一分子生理学の立ち上げ：一個の分子機械の機能と構造変化の直接観察

（研究課題番号：12002012）

平成１２年度～平成１６年度科学研究費補助金（特別推進研究）

研究成果報告書

平成１７年６月

研究代表者　　木　下　一　彦

（大学共同利用機関法人自然科学研究機構
岡崎統合バイオサイエンスセンター・教授）

はしがき

2000年7月に本研究が採択されたとき、掲げた研究目的は以下のようなものであった。

> 今、分子1個を観察し操作することにより、分子機械の働きの仕掛けを探る、「一分子生理学」が誕生しつつある。本研究では、芽生えたばかりの一分子生理学にいくつか大輪の花を咲かせることにより、この新しい学問の展開をリードすることを目指す。手法として巨大プローブと小さな蛍光プローブを光学顕微鏡下で駆使し、たんぱく質分子機械の機能と構造変化の同時測定を試みる。具体的な目標として、(i) F_1-ATPaseの回転機構の解明、(ii) RNA polymeraseのDNAの回りの回転の証明と回転を利用した動作解析、(iii) キネシン・ミオシンのモーター作用における双頭の役割の解明、(iv) 1個のリボソームが蛋白質を作る現場の可視化、などを予定している。

申請当時、たんぱく質（ないしRNA）でできた分子機械1個1個を直接観察し操作することにより、分子機械の働きの仕掛けを探る、「一分子生理学」が新しい学問分野として誕生しつつあった（研究者人口が爆発的に増える兆しが見え始めていた）。我々は、光学顕微鏡下の観察・操作を中心に、一分子を見て初めて仕組みが分かった、といえる例をいくつも示すことにより、生命科学の中に一分子生理学をしっかりと根付かせることを目指した。とくに、分子機械に比べて遙かに大きなプローブ、例えばプラスチックビーズ、を目印ないしハンドルとして結合させる方法と、小さな蛍光色素分子をたんぱく質分子のねらった部分に結合させる方法を相補的に使うことが有効であろうと提案した。

一分子生理学は、目の前で分子が動いて（機能して、あるいは構造変化して）くれないと全く成果にならない。発想・努力・経験に加えて、運が必要である。それ故、数多くの成果を挙げたとは言いがたいが、以下の主要成果を得た。いずれも一分子観察・操作のおかげである。分子機械の働きは確率的なので、複数の機械を互いに同期させられない。回転運動の詳細の解明など（回転の方向すら）、他の手法では非常に困難である。

[1] F_1-ATPaseの回転機構の解明（ATP駆動の分子機械が働く仕組み）

F_1-ATPaseは知られている中で最小の回転分子モーターである。3個のβサブユニット上の活性部位におけるATP加水分解反応により中央のγサブユニットが120度ずつ回転する。その機構がかなり分かってきた。(i) γの向きにより指定される特定のβにATPが結合すると、結合反応に駆動されて80-90度の回転が起きる。(ii) 次に、一つ前に結合していたATPが加水分解される。この間の回転は小さい。(iii) 続いて、分解産物（おそらく燐酸）の解離に駆動されて40-30度の回転が起きる。すなわち、結合と解離が駆動力の主要な発生源であり、ATPの分解反応そのものはほとんど仕事をしない。これらと、すでに示した回転角によらずほぼ一定のトルク（回転力）が出るという事実を合わせることにより、各

化学状態（ATP 待ち、加水分解後、分解産物の解離待ち、解離後＝次の ATP 待ち）における回転のポテンシャルエネルギーの角度依存性を決めることが出来た。いまや F_1-ATPase は、数ある ATP 駆動の分子機械の中で、最も理解が進んだものといってよかろう。実験的に求められた上記のポテンシャルエネルギーを再現するとともに、ATP 濃度依存性など様々な回転特性を説明できる、詳細な回転モデルを構築することもできた。

現時点で残された大きな問題の一つは、３つの活性部位のうちいくつにヌクレオチド（ATP ないし ADP）が結合すると回転が起きるかである。本研究の前半では、結合数が１と２の間を交替するとするいわゆるバイサイト機構が有力と考えていたが、その後、他研究室から２と３の間の交替（トライサイト機構）を示唆する結果が次々と出てきた。本研究の後半では、この問題の解決にかなりの力を注いだが、見かけ上互いに矛盾する結果が得られたりしてまだ結論に至っていない。作業仮説として結合数が２のまま回転するという新説を提唱しており、本研究の終了後もこの検証を進める予定である。

[2] F_1-ATPase の逆回転による ATP 合成（単一ハンドルによる分子機械の逆行の証明）

F_1-ATPase のγサブユニットに磁気ビーズを結合させ、磁気ピンセットを用いて強制的に逆回転させることにより、ATP が合成されることを示すことができた。人類史上初めての、力による化学合成である。生体内ではバクテリアから人までこの回転反応により ATP が合成されることになっているが、もちろん直接の証明はまだない。生体内では、F_1 が膜に埋まった F_o と結合して巨大な ATP 合成酵素複合体を形成しており、そこに膜を介したプロトン駆動力が加わって初めて ATP が合成される。本研究では、その複雑な仕掛けのうち F_1 のみ（$\alpha_3\beta_3\gamma$ の７つのサブユニットのみ）で合成が可能なことが実証されたわけである。F_1-ATPase はそれだけで可逆な分子機械であり、しかもγの回転角というただ一つの自由度の操作だけで逆行させられる（γから離れた活性部位における化学反応まで逆行させられる）。どんな分子機械でも、構成原子のすべてを自在に操ってよければ逆行させられることは自明であるが、F_1-ATPase はγを回すだけで逆行するように「できて」いるのである。リニアーモーターであるミオシンやキネシンの１ヶ所を引っ張って逆向きに歩かせたら ATP 合成ができるか、こちらは今のところ全く不明（大方の予想としては不可能）である。

本研究の範囲では、ATP 合成が出来たことを半定量的に示すのがやっとであった（足かけ７年間にわたる大変な研究であった）。基質（ADP および燐酸）濃度や回転速度、回転力などにより合成効率がどう変わるかといった大切な問題が、すべて取り残されている。これらについても今後研究を進めていきたい。

[3] RNA 合成酵素の遺伝情報読み取り機構

DNA の遺伝情報の読取りに際し、RNA 合成酵素が DNA の右ねじ螺旋構造に忠実に沿って雌ねじのように回転することを示した（RNA 合成酵素を固定すれば DNA が雄ねじとして回転する）。回転は予想されたことではあるが、何百塩基対もほぼスリップ無しに回転することを動画として示すことができ、また遺伝情報読み取りは回転力発生を伴うことを示すこともできた。塩基対あたり 35 度回転するので、DNA 一分子での配列決定に応用出来る可能性もある。

[4] ミオシンVおよびミオシンVIの歩行機構（リニアー分子モーターが動く仕組み）

一分子のミオシンが右巻き二重螺旋構造を持つアクチン上を動くとき、ミオシンVは左ねじ、ミオシンVIは右ねじのように回転しながら進むことを見いだした。この結果は、ミオシンVが歩幅約35nm、VIは36nm強、で「歩く」ことを示す。これらの結果が得られた当時は、ミオシンVIの脚はVに比べ遙かに短いとされており、脚の一部ないし股の部分がほどけないかぎりこの歩幅は説明出来ないと考えられた。その後他研究室から、ミオシンVIの股の部分は実際ほどけており、長いがグニャグニャの2本足（条件により完全にほどけて1本足）であることを示唆する結果が出てきた。長い脚なら歩幅が大きくても矛盾なさそうであるが、グニャグニャの脚で負荷に逆らってどうして前進出来るのか、従来のモデルでは説明できそうもない。これまで見過ごされてきた、持ち上げた足の足首の動き（爪先上下による足裏の向きの制御）を考えれば、ミオシンVIのみならず2本足のリニアーモーター全般の負荷に逆らう歩行を説明できると提案しつつある。

キネシンにビーズを結合させて歩幅を測った、現代一分子生理学の嚆矢と呼ぶべき研究（Svobodaら、1993）以来、リニアーモーターにおいては、巨大プローブの役目はモーター全体の動きを詳細にレポートすることであった。一方小さなプローブ（蛍光プローブ）のほうは、最近、2本の足それぞれの動きを検出できるところまで技術が進んできている。我々は、巨大プローブを用いた「詳細まで一目で分かる」観察が一分子生理学の本命と考えており、2本足のモーターにおいても、1本1本の足の動きをぜひ巨大プローブにより直視したいと考えている。

当初掲げた目的のうち、1個のリボソームがたんぱく質を作る現場の可視化は、実現することが出来なかった。研究代表者にとっては一番思い入れのあるテーマであったが、生体から取り出したリボソームは反応が遅く、その他にも多くの困難に突き当たって、メッセンジャーRNA上のリボソームの動きを見るには至らなかった。リボソームの標識などかなりの準備作業を行ったので、活性の高いリボソームが得られる状況になれば、是非研究を再開したい。

以上の成果の詳細に関しては、巻末に収録した別刷りを参照されたい。刊行論文の掲載誌に紹介記事が出たものに関しては、それも採録した。

末筆ながら、研究活動を全面的に陰から日なたから暖かく支えてくださった深津美紀子・梅沢ひとみ両氏、技術支援および技術指導をしてくださった塩　育氏に心から感謝いたします。本研究は、東京工業大学吉田賢右教授・早稲田大学石渡信一教授・関西先端研究センター大岩和弘博士・国立遺伝学研究所嶋本伸雄教授・マサチューセッツ大学池辺光男教授・大阪大学柳田敏雄教授の研究室を初めとして数多くの方々との共同によるものです。とくに、共著論文を出すに至らなかった方々に、お詫びとともにお礼を申し上げます。慶應義塾大学および岡崎国立共同研究機構統合バイオサイエンスセンター（現自然科学研究機構岡崎統合バイオサイエンスセンター）における木下研究室（現在早稲田大学理工学部）の過去および現在のメンバー、浜松ホトニクス（株）において伊藤博康と共同研究しまた支えてくださった方々、どうもありがとうございました。研究活動はまだ続くので、これからもよろしくお願い致し

ます。慶應義塾大学および岡崎国立共同研究機構の皆様、とくに事務の方々には大変お世話になりました。本当にありがとうございます。

研　究　組　織

研究代表者

木下　一彦
（大学共同利用機関法人自然科学研究機構・岡崎統合バイオサイエンスセンター・教授）
（現：早稲田大学・理工学部・教授）

研究分担者

伊藤　博康
（浜松ホトニクス株式会社・筑波研究所・主任部員）

交付決定額（配分額）

（金額単位：千円）

	直接経費	間接経費	合　　計
平成１２年度	95,000	0	95,000
平成１３年度	95,000	28,500	123,500
平成１４年度	92,000	27,600	119,600
平成１５年度	91,200	27,360	118,560
平成１６年度	14,103	4,230	18,333
総　計	387,303	87,690	474,993

研 究 発 表

1．学会誌等

1) Kengo Adachi, Ryohei Yasuda, Hiroyuki Noji, Hiroyasu Itoh, Yoshie Harada, Masasuke Yoshida, and Kazuhiko Kinosita, Jr.
"Stepping rotation of F_1-ATPase visualized through angle-resolved single-fluorophore imaging"
Proc. Natl. Acad. Sci. USA, **97** (2000) 7243-7247.

2) Takayuki Nishizaka, Ryuzo Seo, Hisashi Tadakuma, Kazuhiko Kinosita, Jr., and Shin'ichi Ishiwata
"Characterization of Single Actomyosin Rigor Bonds: Load Dependence of Lifetime and Mechanical Properties"
Biophys. J., **79** (2000) 962-974.

3) Kiyotaka Y. Hara, Hiroyuki Noji, Dirk Bald, Ryohei Yasuda, Kazuhiko Kinosita, Jr., and Masasuke Yoshida
"The Role of the DELSEED Motif of the β Subunit in Rotation of F_1-ATPase"
J. Biol. Chem., **275** (2000) 14260-14263.

4) Yoshie Harada, Osamu Ohara, Akira Takatsuki, Hiroyasu Itoh, Nobuo Shimamoto, and Kazuhiko Kinosita, Jr.
"Direct observation of DNA rotation during transcription by Escherichia coli RNA polymerase"
Nature, **409** (2001) 113-115.

5) Ryohei Yasuda, Hiroyuki Noji, Masasuke Yoshida, Kazuhiko Kinosita, Jr., and Hiroyasu Itoh
"Resolution of distinct rotational substeps by submillisecond kinetic analysis of F_1-ATPase"
Nature, **410** (2001) 898-904.

6) Hiroyuki Noji, Dirk Bald, Ryohei Yasuda, Hiroyasu Itoh, Masasuke Yoshida, and Kazuhiko Kinosita, Jr.
"Purine but Not Pyrimidine Nucleotides Support Rotation of F_1-ATPase"
J. Biol. Chem., **276** (2001) 25480-25486.

7) Yoko Hirono-Hara, Hiroyuki Noji, Masaya Nishiura, Eiro Muneyuki, Kiyotaka Y. Hara, Ryohei Yasuda, Kazuhiko Kinosita, Jr., and Masasuke Yoshida.
"Pause and rotation of F_1-ATPase during catalysis"
Proc. Natl. Acad. Sci. USA, **98** (2001) 13649-13654.

8) M. Yusuf Ali, Sotaro Uemura, Kengo Adachi, Hiroyasu Itoh, Kazuhiko Kinosita Jr. and Shin'ichi Ishiwata
"Myosin V is a left-handed spiral motor on the right-handed actin helix"
Nature Struct. Biol., **9** (2002) 464-467.

9) Tomoko Masaike, Eiro Muneyuki, Hiroyuki Noji, Kazuhiko Kinosita, Jr., and Masasuke Yoshida
"F_1-ATPase Changes Its Conformations upon Phosphate Release"
J. Biol. Chem., **277** (2002) 21643-21649.

10) Ryohei Yasuda, Tomoko Masaike, Kengo Adachi, Hiroyuki Noji, Hiroyasu Itoh, and Kazuhiko Kinosita, Jr.
"The ATP-waiting conformation of rotating F_1-ATPase revealed by single-pair fluorescence resonance energy transfer"
Proc. Natl. Acad. Sci. USA, **100** (2003) 9314-9318.

11) Katsuya Shimabukuro, Ryohei Yasuda, Eiro Muneyuki, Kiyotaka Y. Hara, Kazuhiko Kinosita, Jr., and Masasuke Yoshida
"Catalysis and rotation of F_1 motor: Cleavage of ATP at the catalytic site occurs in 1 ms before 40° substep rotation"
Proc. Natl. Acad. Sci. USA, **100** (2003) 14731-14736.

12) Hiroyasu Itoh, Akira Takahashi, Kengo Adachi, Hiroyuki Noji, Ryohei Yasuda, Masasuke Yoshida, and Kazuhiko Kinosita, Jr.
"Mechanically driven ATP synthesis by F_1-ATPase"
Nature, **427** (2004) 465-468.

13) Takayuki Nishizaka, Kazuhiro Oiwa, Hiroyuki Noji, Shigeki Kimura, Eiro Muneyuki, Masasuke Yoshida, and Kazuhiko Kinosita, Jr.
"Chemomechanical coupling in F_1-ATPase revealed by simultaneous observation of nucleotide kinetics and rotation"

Nature Struct. Mol. Biol., **11** (2004) 142-148.

14) M. Yusuf Ali, Kazuaki Homma, Atsuko Hikikoshi Iwane, Kengo Adachi, Hiroyasu Itoh, Kazuhiko Kinosita Jr., Toshio Yanagida, and Mitsuo Ikebe
"Unconstrained Steps of Myosin VI Appear Longest among Known Molecular Motors"
Biophys. J., **86** (2004) 3804-3810.

15) Naoyoshi Sakaki, Rieko Shimo-Kon, Kengo Adachi, Hiroyasu Itoh, Shou Furuike, Eiro Muneyuki, Masasuke Yoshida, and Kazuhiko Kinosita, Jr.
"One Rotary Mechanism for F_1-ATPase over ATP Concentrations from Millimolar down to Nanomolar"
Biophys. J., **88** (2005) 2047-2056.

16) Hiroshi Ueno, Toshiharu Suzuki, Kazuhiko Kinosita, Jr., and Masasuke Yoshida
"ATP-driven stepwise rotation of F_oF_1-ATP synthase"
Proc. Natl. Acad. Sci. USA, **102** (2005) 1333-1338.

17) Yoko Hirono-Hara, Koji Ishizuka, Kazuhiko Kinosita, Jr., Masasuke Yoshida, and Hiroyuki Noji
"Activation of pausing F_1 motor by external force"
Proc. Natl. Acad. Sci. USA, **102** (2005) 4288-4293.

○総説・解説（英文）

1) Tomoko Masaike, Noriyo Mitome, Hiroyuki Noji, Eiro Muneyuki, Ryohei Yasuda, Kazuhiko Kinosita, Jr., and Masasuke Yoshida
"Rotation of F_1-ATPase and the hinge residues of the β subunit"
J. Exp. Biol., 203 (2000) 1-8.

2) Kazuhiko Kinosita, Jr., Ryohei Yasuda, and Hiroyuki Noji
"F_1-ATPase: a highly efficient rotary ATP machine"
Essays Biochem. 35 (2000) 3-18.

3) Kazuhiko Kinosita, Jr., Ryohei Yasuda, Hiroyuki Noji, and Kengo Adachi
"A rotary molecular motor that can work at near 100% efficiency"
Phil. Trans. Roy. Soc. Lond. B 355 (2000) 473-489.

4) Shin'ichi Ishiwata, Junko Tadashige, Ichiro Masui, Takayuki Nishizaka, and Kazuhiko Kinosita, Jr.
"Microscopic Analysis of Polymerization and Fragmentation of Individual Actin Filaments"
in Results and Problems in Cell Differentiation, Vol. 32: Molecular Interactions of Actin (2001) C. dos Remedios, Ed. Springer-Verlag, Berlin, 79-94.

5) Kengo Adachi, Hiroyuki Noji, and Kazuhiko Kinosita, Jr.
"Single Molecule Imaging of the Rotation of F_1-ATPase"
Methods Enzymol., 361B (2003) 211-227.

6) Kazuhiko Kinosita, Jr., Kengo Adachi, and Hiroyasu Itoh
"Rotation of F_1-ATPase: How an ATP-Driven Molecular Machine May Work"
Annu. Rev. Biophys. Biomol. Struct., 33 (2004), 245-268.

7) Kazuhiko Kinosita, Jr., M. Yusuf Ali, Kengo Adachi, Katsuyuki Shiroguchi, and Hiroyasu Itoh
"How two-foot molecular motors may walk"
Adv. Exp. Med. Biol., in press.

○総説・解説（和文）

1) 木下一彦、小林　剛、中田千枝子、楠見明弘
　１分子細胞生物学の魅力を語る
　細胞工学、５月号（Ｖｏｌ．２０，Ｎｏ．５）、（２００１）、６３８－６５５。

2) 塩　育
　あれ！　顕微鏡対物レンズが縮んでいる？（対物レンズの温度依存性）
　生物物理、１２月号（Ｖｏｌ．４１）、（２００１）、３１５－３１７。

3) 木下一彦、足立健吾、伊藤博康
　F_1－ＡＴＰａｓｅのステップ回転：ＡＴＰ駆動の分子機械が働く仕組み
　生体の科学、１月号（Ｖｏｌ．５４）、（２００３）、３６－４０。

２．口頭発表

①国内

1) 木下一彦、伊藤博康、原田慶恵「磁気ピンセットによる一分子操作」、単一細胞の分子テクノロジーワークショップ2000, 2000.07.26-27, （青葉記念会館）仙台。

2) 木下一彦「Toward Single-Molecule Physiology under an Optical Microscope」、8th International Conference on Laser Applications in Life Sciences, 2000.08.13-18, （早稲田大学）東京。

3) 木下一彦「たんぱく質分子機械の仕掛けを一分子測定で探る」、第38回年会日本生物物理学会年会, 2000. 09. 10-13, （東北大学川内北キャンパス）仙台。

4) 伊藤博康、野地博行、吉田賢右、木下一彦「F_1-ATPaseによるATP合成の試み」、第38回年会日本生物物理学会年会, 2000. 09. 10-13, （東北大学川内北キャンパス）仙台。

5) 野地博行、伊藤博康、足立健吾、吉田賢右、木下一彦「F_1モーターの回転トルクを直接測定する」、第38回年会日本生物物理学会年会, 2000. 09. 10-13, （東北大学川内北キャンパス）仙台。

6) 足立健吾、安田涼平、野地博行、吉田賢右、木下一彦「結合ヌクレオチド, 構成サブユニット, 温度が与えるF1-ATPaseの活性への影響」、第38回年会日本生物物理学会年会, 2000. 09. 10-13, （東北大学川内北キャンパス）仙台。

7) 西坂崇之、足立健吾、野地博行、大岩和弘、安田涼平、木下一彦「F1-ATPaseによるATPの加水分解と回転の同時観察」、第38回年会日本生物物理学会年会, 2000. 09. 10-13, （東北大学川内北キャンパス）仙台。

8) 有賀隆行、政池知子、野地博行、木下一彦、吉田賢右「ハイブリッドF1-ATPaseを用いた回転ステップの１分子解析」、第38回年会日本生物物理学会年会, 2000. 09. 10-13, （東北大学川内北キャンパス）仙台。

9) 木下一彦「回転分子モーターの一分子生理学」、創成機能科学専攻新設記念シンポジウム, 2000.09.29, （室蘭工業大学）北海道。

10) 木下一彦「回転分子モーターの一分子生理学」、第４回ＶＢＬシンポジウム, 2000.10.16-17, （名古屋大学ﾌﾛﾝﾃｨｱﾌﾟﾗｻﾞ）名古屋。

11) 木下一彦「エネルギーの素を作る回転するタンパク質」、明治大学科学技術研究所公開講座, 2000.11.11, (明治大学) 生田。

12) 足立健吾「1分子偏光測定によるF1-ATPaseの回転の可視化」、第26回レーザー顕微鏡研究会, 2000.11.15, (東京農工大)東京。

13) 木下一彦「分子モーターを観る」、岡崎国立共同研究機構技術課合同セミナー, 2000.12.05, (岡崎ｺﾝﾌｧﾚﾝｽｾﾝﾀｰ) 岡崎。

14) 竹中啓、高槻玲、足立健吾、塩育、伊藤博康、嶋本伸雄、木下一彦「RNA polymeraseによるDNAの回転ｲﾒｰｼﾞﾝｸﾞ」、筋収縮・細胞運動研究会, 2000. 12. 08-09, (帝京大学) 板橋。

15) 西坂崇之、伊藤博康、大岩和弘、木下一彦、野地博行「F1-ATPase 1分子のATP加水分解の可視化」、2001年生体運動研究合同班会議, 2001. 01. 06-08, (早稲田大学) 東京。

16) 安田涼平、野地博行、吉田賢右、木下一彦「F1-ATPaseのサブステップ」、2001年生体運動研究合同班会議, 2001. 01. 06-08, (早稲田大学) 東京。

17) 原田慶恵、竹中啓、高槻玲、足立健吾、塩育、伊藤博康、嶋本伸雄、木下一彦「RNA polymeraseの転写によるDNAの引き込みと回転の同時観察」、2001年生体運動研究合同班会議, 2001. 01. 06-08, (早稲田大学) 東京。

18) 木下一彦「Toward Single-Molecule Physiology」、2001 JRCAT International Workshop on Single-Molecule Technology, 2001. 01. 10-12, (つくば国際会議場エポカル) つくば。

19) 木下一彦「一分子生理学」、JST異分野研究者交流フォーラム“生命科学の新しいメソドロジー”, 2001. 02. 02-05, (大仁ホテル) 静岡。

20) 木下一彦「How an ATP-driven molecular machine may work」、Fifth Membrane Research Forum, 2001. 06. 04-06, (名古屋大学) 名古屋。

21) 木下一彦「たんぱく質1分子でできた回転モーター」、第24回日本バイオレオロジー学会, 2001. 06. 07-08, (慶應義塾大学・矢上) 横浜。

22) 木下一彦「Single-Molocule Physiology under an Optical Microscope」、4th International Conference on Biological Physics, 2001. 07.30-08.03, (Kyoto International Conference Hall) 京都。

23) 足立健吾「1分子で出来た回転分子モーター＝大きなプローブと小さなプローブで見た回転＝」、第120回有機エレクトロニクス研究会，2001. 09.04,（東京大学山上会館）東京。

24) 木下一彦「一分子生理学～光学顕微鏡下で分子機械の働きを探る」、第16回生体機能関連化学シンポジウム、 2001. 09.19,（東京大学）東京。

25) 榊直由、牧泰史、鈴木勉、渡辺公綱、木下一彦「タンパク質合成におけるリボソームに対するmRNAの移動を1分子イメージする試み」、第39回日本生物物理学会年会、2001. 10.06-08,（大阪大学）大阪。

26) 西中太郎、足立健吾、塩育、石部聡子、井川粛子、柴田武彦、原田慶恵、木下一彦「RecA タンパク質によるDNA回転顕微鏡観察」、第39回日本生物物理学会年会、2001. 10.06-08,（大阪大学）大阪。

27) 川島啓佑、宗行英朗、木下一彦「F1-ATPaseの活性に対するMgADPの及ぼす影響」、第39回日本生物物理学会年会、2001. 10.06-08,（大阪大学）大阪。

28) 弘埜（原）陽子、野地博行、宗行英朗、木下一彦、吉田賢右「F1-ATPaseにおけるADP阻害の解析」、第39回日本生物物理学会年会、2001. 10.06-08,（大阪大学）大阪。

29) 島袋勝弥、宗行英朗、安田涼平、原清敬、木下一彦、吉田賢右「β(E190D)F1-ATPase変異体の回転解析」、第39回日本生物物理学会年会、2001. 10.06-08,（大阪大学）大阪。

30) 足立健吾、西坂崇之、野地博行、伊藤博康、塩育、大岩和弘、吉田賢右、木下一彦「F1-ATPaseの回転軸γサブユニットの向きに依存したATPのアフィニティ」、第39回日本生物物理学会年会、2001. 10.06-08,（大阪大学）大阪。

31) 西坂崇之、野地博行、木村成輝、木下一彦、大岩和弘「F1-ATPaseに結合した蛍光性ATPの角度の検出」、第39回日本生物物理学会年会、2001. 10.06-08,（大阪大学）大阪。

32) 野地博行、伊藤博康、塩育、足立健吾、宗行英朗、吉田賢右、木下一彦「磁気ピンセットを用いたF1モーターの回転ポテンシャルの測定」、第39回日本生物物理学会年会、2001. 10.06-08,（大阪大学）大阪。

33) 木下一彦「F1-ATPaseの回転を説明する機械的モデル」、第39回日本生物物理学会年会、2001.

10.06-08, （大阪大学）大阪。

34) 伊藤博康、野地博行、吉田賢右、木下一彦「F1-ATPase による ATP 合成の試み」、第 39 回日本生物物理学会年会、2001. 10.06-08, （大阪大学）大阪。

35) 木下一彦「ATP 駆動の分子機械の動作機構を一分子生理学で探る」、第 74 回日本生化学会大会、2001. 10.25-28, （国立京都国際会館）京都。

36) 木下一彦「タンパク質 1 分子でできた回転モーター：化学・力学エネルギー変換の仕組み」、第 23 回生体膜と薬物の相互作用シンポジウム、2001.11.08-09, （メルパルク熊本）熊本。

37) 木下一彦「Single-molecule physiology under an optical microscope: How molecular machines may work」、The 9th International Colloquium on Scanning Probe Microscopy、2001. 12.06-08, （熱川）静岡。

38) Md. Yusuf Ali, 上村想太郎、足立健吾、石渡信一、伊藤博康、木下一彦「Direct observation of the rotation of myosin V around the axis of an actin filament」、2002 年生体運動研究合同班会議、2002. 01.06-08, （千葉大学）千葉。

39) 西坂崇之、野地博行、木村成輝、宗行英朗、吉田賢右、木下一彦、大岩和弘「F1-ATPase のステップ状の回転と ATP の方向の同時観察」、2002 年生体運動研究合同班会議、2002. 01.06-08, （千葉大学）千葉。

40) 木下一彦「体の中にくるくる回るモーターがある」、ＪＳＴ第 6 回基礎研究報告会、2002. 02.06, （日本科学未来館）東京。

41) 木下一彦「Single-Molecule Physiology: How Protein Molecular Machines May Work」、国際ナノテクノロジー総合展・技術会議、2002. 03.06-08, （幕張メッセ国際展示場）千葉。

42) 木下一彦「Single-Molecule Physiology: How Molecular Machines May Work」、Okazaki Lectures (Asian Winter School), 2002.03.08-11, （岡崎国立共同研究機構）岡崎。

43) 木下一彦「F1-ATPase のステップ回転：ATP 駆動の分子機械の働く仕組み」、第 29 回生体分子化学討論会、2002.07.11-12 (岡崎国立共同研究機構) 岡崎。

44) 木下一彦「一分子の生理学」、第 20 回麻酔メカニズム研究会プログラム、2002.07.13-14, (千里ライフサイエンスセンター）大阪。

45) 木下一彦「一分子生理学：分子機械の働く仕組み」、第 75 回日本生化学会大会、2002.10.14-17(国立京都国際会館)京都。

46) 榊直由、下理恵子、伊藤博康、足立健吾、宗行英朗、吉田賢右、木下一彦「低ＡＴＰ濃度における F1-ATPase の回転とヌクレオチド結合数」、第 40 回日本生物物理学会年会、2002.11.02-04, (名古屋大学) 名古屋。

47) 野地博行、伊藤博康、宗行英朗、足立健吾、吉田賢右、木下一彦「F1 モーターの回転トルクを直接測定する」、第 40 回日本生物物理学会年会、2002.11.02-04, (名古屋大学) 名古屋。

48) 足立健吾、西坂崇之、野地博行、伊藤博康、大岩和弘、吉田賢右、木下一彦「F1-ATPase の multisite catalysis の一分子観察」、第 40 回日本生物物理学会年会、2002.11.02-04, (名古屋大学) 名古屋。

49) 西坂崇之、大岩和弘、木村成輝、木下一彦、吉田賢右、宗行英朗、野地博行「F1-ATPase の回転におけるサブステップと蛍光性ＡＴＰの同時観察」、第 40 回日本生物物理学会年会、2002.11.02-04, (名古屋大学) 名古屋。

50) 政池知子、宗行英朗、野地博行、木下一彦、吉田賢右「F1-ATPase は結合ヌクレオチドのγリン酸解離とともに構造変化する」、第 40 回日本生物物理学会年会、2002.11.02-04, (名古屋大学) 名古屋。

51) 木下一彦「Single-molecule physiology under an optical microscope:How molecular machines may work」、2002 年分子研 COE コンファレンス、2002.11.18-21, (岡崎国立共同研究機構) 岡崎。

52) 木下一彦「Chemo-mechanical coupling in a rotary molecular motor revealed by single-molecule physiology」、電子科学研究所十周年記念シンポジウム、2002.12.09-11,(京王プラザホテル札幌) 札幌。

53) 木下一彦「たんぱく質一分子でできた回転モーター」、第 9 回ナノ・バイオテクノロジー研究会、2003.02.06,(名古屋工業大学)名古屋。

54) 木下一彦「CHEMO-MECHANICAL COUPLING IN A ROTARY MOLECULAR MOTOR REVEALED BY SINGLE-MOLECULE PHYSIOLOGY」、FNB 2003 ナノ・バイオ融合テクノロジー国際シンポジウム、2003.03.09-10,(つくば国際会議場エポカル)つくば。

55) 木下一彦「一分子生理学から学んだ化学－力学エネルギー変換の仕組」、日本顕微鏡学会 2003 年度シンポジウム　分子レベルの顕微鏡学、2003.03.17,（京都大学）京都。

56) 野地博行、黒田綾、伊藤博康、足立健吾、吉田賢右、木下一彦「F1 モーターの回転ポテンシャルの実測」、第 41 回日本生物物理学会年会、2003. 09.23-25,（朱鷺メッセ新潟コンベンションセンター）新潟。

57) 伊藤博康、足立健吾、野地博行、吉田賢右、木下一彦「ATP の力学的な合成」、第 41 回日本生物物理学会年会、2003. 09.23-25,（朱鷺メッセ新潟コンベンションセンター）新潟。

58) 昆-下理恵子、宗行英朗、井合健太郎、榊直由、足立健吾、伊藤博康、古池晶、牧泰史、吉田賢右、木下一彦「ΔNC 変異体を用いたＦ1－ATPase のヌクレオチド結合数と回転速度の測定」、第 41 回日本生物物理学会年会、2003. 09.23-25,（朱鷺メッセ新潟コンベンションセンター）新潟。

59) 足立健吾、西坂崇之、野地博行、伊藤博康、大岩和弘、吉田賢右、木下一彦「F1-ATPase の回転と multistite catalysis の 1 分子イメージング」、第 41 回日本生物物理学会年会、2003. 09.23-25,（朱鷺メッセ新潟コンベンションセンター）新潟。

60) 榊直由、下理恵子、伊藤博康、足立健吾、古池晶、宗行英朗、吉田賢右、木下一彦「極低 ATP 濃度における F1-ATPase の回転」、第 41 回日本生物物理学会年会、2003. 09.23-25,（朱鷺メッセ新潟コンベンションセンター）新潟。

61) 古池晶、榊直由、足立健吾、伊藤博康、下理恵子、吉田賢右、木下一彦「F1-ATPase 回転運動の温度依存性」、第 41 回日本生物物理学会年会、2003. 09.23-25,（朱鷺メッセ新潟コンベンションセンター）新潟。

62) 牧泰史、榊直由、足立健吾、木下一彦「たんぱく質合成反応の光学顕微鏡下に観察の試み」、第 41 回日本生物物理学会年会、2003. 09.23-25,（朱鷺メッセ新潟コンベンションセンター）新潟。

63) 原陽子、石塚康司、木下一彦、吉田賢右、野地博行「F1 モーターを力学的に活性化させる」、第 41 回日本生物物理学会年会、2003. 09.23-25,（朱鷺メッセ新潟コンベンションセンター）新潟。

64) 木下一彦「Chemo-mechanical Coupling in the Rotary Motor F1-ATPase」、第 19 回国際生物学賞記念シンポジウム、2003.12.03-04,（奈良県新公会堂）奈良。

65) 木下一彦「たんぱく質一分子でできた回転モーター」、分子ナノテクノロジー第 174 委員会、

2003.12.07-08,(京都テルサ)京都。

66) 木下一彦「F1-ATPaseの回転機構：ＡＴＰ駆動のたんぱく質分子機械が働く仕組み」、第26回日本分子生物学会年会、2003.12.10-13,(神戸ポートアイランド)神戸。

67) 下理恵子、宗行英朗、榊直由、足立健吾、伊藤博康、古池晶、吉田賢右、木下一彦「ΔNC変異体を用いたＦ１－ATPaseの活性とヌクレオチド結合数の関係」、２００４年生体運動研究合同班会議、2004. 01.08-10, （東京大学）東京。

68) 榊直由、下理恵子、伊藤博康、足立健吾、古池晶、宗行英朗、吉田賢右、木下一彦「低ATP濃度における F1-ATPaseの回転」、２００４年生体運動研究合同班会議、2004. 01.08-10, （東京大学）東京。

69) 伊藤博康、木下一彦「Mechanically-driven ATP synthesis」、２００４年生体運動研究合同班会議、2004. 01.08-10, （東京大学）東京。

70) 木下一彦「How two-foot molecular motors may walk」、Symposium on Mysteries about the Sliding Filament Mechanism in Muscle Contraction: Fifty Years after its Proposal 2004.03.07-10,(国際文化会館)東京。

②海外

1) Kinosita, K., "F1-ATPase : a rotary motor that can work at near 100% efficiency" 2000.03.07-13, Molecular Motors and Cell Dynamics, Les Treilles (France).

2) Kinosita, K., "Toward single-molecule physiology under an optical microscope" 2000.05.03-06, The Sixth Symposium on Recent Advances in Biophysics, National Tsing-Hua University, Hsin-Chu (Taiwan).

3) Kinosita, K., "A rotary molecular motor that can work at near 100% efficiency" 2000.05.24-25, Third East Asian Biophysics Symposium, 慶州 (Korea).

4) Kinosita, K., "F1-ATPase: a rotary motor that can work at near 100% efficiency" 2000.06.04-08, American Society for Biochemistry and Molecular Biology, Hynes Convention Center, Boston (USA).

5) Kinosita, K., "A rotary molecular motor that can work at near 100% efficiency"2000.09.09-13, 3rd European Biophysics Congress, Munchen(Germany).

6) Kinosita, K., "Imaging and Manipulation of Individual Rotary Molecular Machines" 2000.10.21-24, 15th FAOBMB Symposium, Beijing(China).

7) Kinosita, K., "Stepping rotation in a protein machine revealed by single molecule imaging" 2001.01.14-20, Winter Workshop on Single Molecule Biophysics, Aspen Center for Physics(USA).

8) Nishizaka, T., Adachi, K., Itoh, H., Yasuda, R., Noji, H., Oiwa, K., Kinosita, K. Jr., "Simultaneous Imaging of ATP Hydrolysis and Rotation in a Single F1-ATPase Molecule " 45th Annual Meeting of the Biophysical Society, 2001.02.17-21, Boston(USA).

9) Kinosita, K., "Single-Molecule Observation of the Stepping Rotation of F1-ATPase " 2nd International Symposium on Physics, Chemistry and Biology with Single Molecules, 2001.03.05-07, Staffelstein (Germany)

10) Kinosita, K., "F1-ATPase: A Rotary Stepper Motor" 2001 Gordon Research Conference: Molecular Cell Biology, 2001. 06. 10-15, Tilton (USA).

11) Kinosita, K. "Mechanism of Stepping Rotation of F1-ATPase" International Symposium on Biophotonics, 2001. 08.19-21, University of Wisconsin, Madison (USA).

12) Kinosita, K. "F1-ATPase Motor" 34th International Union of Physiological Sciences, 2001. 08.26-31, Christchurch Convention Center, Christchurch (New Zealand).

13) Kinosita, K. "F1-ATPase" The German Biophysical Society Annual Meeting and NanoBioTec Congress, 2001. 09.24-27, Halle Munster land (Germany).

14) Kinosita, K. "Stepping Rotation of Single F1-ATPase Molecues: How a Molecular Machine May Work" Rockefeller University Friday Lecture, 2001. 11.29-12.03, New York (USA).

15) Kinosita, K. "How an ATP-driven molecular machine may work: Clues from single-molecule physiology" 46th Annual Meeting of the Biophysical Society, 2002. 02.23-27, Moscone Convention Center, San Francisco (USA).

16) Adachi, K., Nishizaka, T., Noji, H., Itoh, H., Shio, M., Oiwa, K., Yoshida, M., Kinosita, K. Jr. "Dependence of nucleotide affinity of F1 motor on the rotary angle" 46th Annual Meeting of the Biophysical Society, 2002. 02.23-27, Moscone Convention Center, San Francisco (USA).

17) Itoh, H., Noji, H., Yoshida, M., Kinosita, K. Jr. "ATP Synthesis by reverse rotation of F1-ATPase" 46th Annual Meeting of the Biophysical Society, 2002. 02.23-27, Moscone Convention Center, San Francisco (USA).

18) Noji, H., Itoh, H., Adachi, K., Yoshida, M., Kinosita, K. Jr. "Rotary potentials of F1-motor" 46th Annual Meeting of the Biophysical Society, 2002. 02.23-27, Moscone Convention Center, San Francisco (USA).

19) Nishizaka, T., Noji, H., Oiwa, K., Kinosita, K. Jr. "Orientation of single fluorescent ATP molecule bound to F1-ATPase" 46th Annual Meeting of the Biophysical Society, 2002. 02.23-27, Moscone Convention Center, San Francisco (USA).

20) Ali, M. Y., Uemura, S., Adachi, K., Ishiwata, S., Kinosita, K. Jr. "Direct observation of the rotation of myosin-V around an actin filament" 46th Annual Meeting of the Biophysical Society, 2002. 02.23-27, Moscone Convention Center, San Francisco (USA).

21) Kinosita, K. "Rotary mechanism of F1-ATPase"Gordon Research Conference: Muscle:Contracile Proteins, 2002. 06.09-14,Colby-Sawyer College, New London(USA).

22) Kinosita, K. "Single-molecule physiology under an optical microscope:How molecular machines may work" The-Heraeus-Seminar 282 Bad Honnef 2002, 2002. 06.18-21, Physikzenturm Bad Honnef, (Germany).

23) Kinosita, K. "Single-molecule physiology under an optical microscope:How molecular machines may work" Society for Developmental Biology 61st Annual Meeting , 2002. 07.21-25, University of Wisconsin-Madison, Madison (USA).

24) Kinosita, K. "Single-molecule physiology under an optical microscope:How molecular machines may work" 293th Wilhelm und Else Heraeus Seminar, 2002. 09.22-26, Philipps-University of Marburg, Marburg (Germany).

25) Kinosita, K. "Chemo-Mechanical Coupling in F1-ATPase Revealed by Single-Molecule Physiology" 2003 Winter Conference on Biophysics "The Biophysics of Single Molecules", 2003. 01.05-11, Aspen Center

For Physics (USA).

26) Kinosita, K. "Single-Molecule Studies of the Rotary Mechanism of F1-ATPase" Keystone Symposia, 2003.02.22-27, Sagebrush Inn and Conference Center, Taos (USA).

27) Itoh, H., Noji, H., Yoshida, M., Kinosita, K. Jr. "ATP Synthesis by Reverse Rotation of F1-ATPase" 47th Annual Meeting, 2003.03.01-05, San Antonio(USA).

28) Adachi, K., Nishizaka, T., Noji, H., Itoh, H., Oiwa, K., Yoshida, M., Kinosita, K. Jr. "Imaging of Multisite Catalysis in F1-ATPase" 47th Annual Meeting, 2003.03.01-05, San Antonio(USA).

29) Nishizaka, T., Oiwa, K., Noji, H., Kimura, S., Kinosita, K. Jr. "Observation of Nucleotide Kinetics in F1-ATPase" 47th Annual Meeting, 2003.03.01-05, San Antonio(USA).

30) Kinosita, K. "Single Molecule Physiology" Living matter:A new challenge to physicists?, 2003.03.02-08, The University of Lausanne, Lausanne (Switzerland).

31) Kinosita, K. "Chemo-Mechanical Coupling in F1-ATPase revealed by single-molecule physiology" 225th ACS National Meeting, 2003.03.23-27,the Morial Convention Center, New Orleans (USA).

32) Kinosita, K. "Chemo-Mechanical Coupling in F1-ATPase, a Rotary Motor Made of a Single Protein Molecule " Chairmen of the European Research Councils Chemistry Committees, 2003.04.11-13,Chalmers University of Technology,Goteborg (Sweden).

33) Kinosita, K. "Mechano-Chemical Coupling in F1-ATPase " Bionanotechnology Euroconference on Biomolecular Devices, 2003.07.09-14, Hotel Alixares del Generalife, Granada (Spain).

34) Kinosita, K. "The rotary mechanism of F1-ATPase studied by single-molecule physiology under an optical microscope" 9th International Workshop on "Single Molecule Detection and Ultra Sensitive Analysis in the Life Sciences" 2003.09.24-26, WISTA Campus in Berlin-Adlershof, Berlin-Adlershof (Germany).

35) Kinosita, K. "Single-Molecule Physiology of Protein Machines" Nano-science and technology: Frontiers and opportunities, 2003.12.26-27, Department of Physics National Chung Hsing University, Taichung (Taiwan).

36) Kinosita, K. "Mechano-chemical coupling in F1-ATPase" NCBS Symposium on "Molecules,Machines and Networks", 2004.01.05-09, National Center for Biological Sciences Tata Institute of Fundamental Research, Bangalore(India).

37) Kinosita, K. "How an ATPase driven molecular machine works " 39th Winter Seminar Biophysical Chemistry, Molecular Biology and Cybernetics of Cell Functions, 2004.01.10-24, Hotel Sport Klosters, Klosters (Switzerland).

38) Furuike, S., Sakaki, N., Adachi, K., Itoh, H., Shimo-Kon, R., Yoshida, M., Kinosita, K. Jr. "Temperature Dependence of the Rotation of F_1-ATPase" Biophysical Society, 48th Annual Meeting, 2004.02.14-18, Baltimore Convention Center, Baltimore (USA).

39) Sakaki, N., Shimo-Kon, R., Itoh, H., Adachi, K., Furuike, S., Muneyuki, E., Yoshida, M., Kinosita, K. Jr. "Rotation of F_1-ATPase at Very Low ATP Concentrations" Biophysical Society, 48th Annual Meeting, 2004.02.14-18, Baltimore Convention Center, Baltimore (USA).

40) Adachi, K., Nishizaka, T., Noji, H., Itoh, H., Oiwa, K., Yoshida, M., Kinosita, K. Jr. "Single-Molecule Imaging of the Rotation and Multisite Catalysis in F1-ATPase" Biophysical Society, 48th Annual Meeting, 2004.02.14-18, Baltimore Convention Center, Baltimore (USA).

41) Kinosita, K. "Mechano-Chemical Coupling in F1-ATPase" Symposium "Life Sciences on the Nanometer Scale-Physics Meets Biology", 2004.03.10-12,University Regensburg, Regensburg(Germany).

３．出版物

1) 安田涼平、木下一彦

ＡＴＰ合成酵素の動力学

生体とエネルギーの物理－生命力のみなもと、日本物理学会編（垣谷俊昭、美宅成樹編）、（裳華房、東京、２０００），１９８－２１６。

2) Ryohei Yasuda, Hiroyuki Noji, Kengo Adachi, Takayuki Nishizaka, Yasuyuki Kato-Yamada, Masasuke Yoshida, and Kazuhiko Kinosita, Jr.

"Rotation of ATP synthase"

in Na/K-ATPase and Related ATPases (2000) Kazuya Taniguchi and Shunji Kaya, Eds, Elsevier, Amsterdam, pp. 87-92.

3) 木下一彦

私の生物物理　－　生物物理はＨｏｗの世界

生物物理学とはなにか　－　未解決問題への挑戦（日本生物物理学会シリーズ・ニューバイオフィジクスⅡ－１０、曽我部正博、郷　信広編）、共立出版、東京、２００３，ｐｐ．２３３－２３９。

研　究　成　果

研究論文のコピーをもって代える。

Stepping rotation of F_1-ATPase visualized through angle-resolved single-fluorophore imaging

Kengo Adachi*†, Ryohei Yasuda†, Hiroyuki Noji†, Hiroyasu Itoh†‡, Yoshie Harada†§, Masasuke Yoshida†¶, and Kazuhiko Kinosita, Jr.†§‖

*Department of Physics, Faculty of Science, Kanazawa University, Kakuma-machi, Kanazawa 920-1192, Japan; †Core Research for Evolutional Science and Technology, "Genetic Programming" Team 13, Nogawa, Miyamae-ku, Kawasaki 216-0001, Japan; ‡Tsukuba Research Laboratory, Hamamatsu Photonics K. K., Tsukuba 300-2635, Japan; ¶Research Laboratory of Resources Utilization, Tokyo Institute of Technology, Midori-ku, Yokohama 226-8503, Japan; and §Department of Physics, Faculty of Science and Technology, Keio University, Kohoku-ku, Yokohama 223-8522, Japan

Communicated by Paul D. Boyer, University of California, Los Angeles, CA, April 17, 2000 (received for review February 6, 2000)

Orientation dependence of single-fluorophore intensity was exploited in order to videotape conformational changes in a protein machine in real time. The fluorophore Cy3 attached to the central subunit of F_1-ATPase revealed that the subunit rotates in the molecule in discrete 120° steps and that each step is driven by the hydrolysis of one ATP molecule. These results, unlike those from the previous study under a frictional load, show that the 120° stepping is a genuine property of this molecular motor. The data also show that the rate of ATP binding is insensitive to the load exerted on the rotor subunit.

Conformational changes in protein molecules during function are best studied at the single-molecule level, because the operation of protein machines is always stochastic and thus such operations cannot be synchronized with each other. Individual behaviors can be assessed by single-fluorophore imaging (1–5), which is much less perturbing than imaging through a huge tag such as a plastic bead or actin filament (6). Real-time determination of fluorophore orientation (5, 7, 8) should be particularly useful, because a conformational change necessarily accompanies reorientation of one part against others. Thus far, however, successful applications of this potentially powerful method have been made infrequently. Herein, we show reorientation of a subunit in F_1-ATPase by using angle-resolved single-fluorophore imaging.

The F_1-ATPase is a part of ATP synthase that couples proton flow through its F_o portion to synthesis/hydrolysis of ATP in F_1 (9). Isolated F_1 consisting of $\alpha_3\beta_3\gamma_1\delta_1\varepsilon_1$-subunits only hydrolyzes ATP and is called F_1-ATPase. In a crystal structure of F_1 (10), the γ-subunit is surrounded by a cylinder made of alternating α- and β-subunits. Rotation of γ within the $\alpha_3\beta_3$-hexamer has been suggested (11–13) and confirmed (14–20). In our previous studies (18, 20), the rotation was visualized under a microscope by attaching an actin filament to γ. The filament rotated counterclockwise when viewed from the F_o side and in discrete 120° steps as predicted from the presence of three catalytic sites, one each on β (10). The long actin filament, however, may have altered the genuine kinetics of the F_1 motor, because the filament was subject to a large hydrodynamic friction. Also, the 120° stepping could have resulted from frictional obstruction of the filament motion by the $\alpha_3\beta_3$-hexamer with pseudo-3-fold symmetry. Measurement of rotation with a much smaller probe is desired. Thus, we examined rotational characteristics of F_1 with no load by attaching a single fluorophore to γ and assessing the fluorophore orientation through its polarized fluorescence on a microscope with an extremely low background (4, 21).

Materials and Methods

Protein Preparation. The subcomplex α(C193S)$_3\beta$(His$_{10}$-tag at N terminus)$_3\gamma$(I210C) derived from thermophilic *Bacillus* PS3 was mixed with a 1.1-fold molar excess of Cy3-maleimide (Amersham Pharmacia) in 20 mM Mops-KOH (pH 7.0) and 100 mM KCl for 30 min at room temperature. Unreacted Cy3-maleimide was removed on a Superdex 200 column (Amersham Pharmacia) to terminate the reaction. The labeling ratio was determined to be 0.75 mol Cy3 per mol F_1, by assuming ε_{555}^{Cy3} = 150,000 $M^{-1}\cdot cm^{-1}$ (22), ε_{280}^{Cy3} = 15,000 $M^{-1}\cdot cm^{-1}$, and ε_{280}^{F1} = 154,000 $M^{-1}\cdot cm^{-1}$ (23).

Ni^{2+}-Nitrilotriacetic Acid (Ni-NTA) Surface. Glass coverslips (Micro-Cover Glass, No. 1, 24 × 36 mm^2, Matsunami, Japan) precleaned with KOH were immersed in 0.01% acetic acid containing 2% (vol/vol) 3-glycidyloxypropyl-trimethoxysilane (Fluka) for 3 h at 90°C and washed with water. The glass was incubated in 0.01 M $NaHCO_3$ (pH 10.0) containing 10% (wt/vol) *N*-(5-amino-1-carboxypentyl)-iminodiacetic acid (Qiagen, Hilden, Germany) for 16 h at 60°C and washed with water. Then, the glass was incubated in 10 mM $NiCl_2$ (or $NiSO_4$) and 5 mM glycine (pH 8.0) for 2 h at room temperature, washed with water, and stored in water until use.

Rotation Assay. A flow chamber (18) was constructed of a bottom coverslip (24 × 36 mm^2) coated with Ni-NTA and an uncoated top coverslip (18 × 18 mm^2), and 50 pM Cy3-$\alpha_3\beta_3\gamma$ in buffer A (50 mM KCl/4 mM $MgCl_2$/10 mM Mops-KOH, pH 7.0) was infused. After 2 min, the chamber was washed with five volumes of buffer A and then with five volumes of degassed buffer A containing 0.5% 2-mercaptoethanol, 216 μg/ml glucose oxidase, 360 μg/ml catalase, 4.5 mg/ml glucose, 0.2 mg/ml creatine kinase, 2.5 mM creatine phosphate, and the desired amount of ATP. Washing with buffer A plus 500 mM imidazole removed ≈80% of fluorescent spots, whereas buffer A plus 500 mM KCl removed ≈10%, and <3% of spots were observed with unlabeled F_1.

ATPase Activity. F_1 was passed through a Butyl-Toyopearl column (Tosoh, Tokyo) equilibrated with 10% (vol/vol) $(NH_4)_2SO_4$/2 mM EDTA/100 mM potassium phosphate, pH 7.0 to reduce the bound nucleotide to ≈0.05 mol per mol F_1 as confirmed with reverse-phase HPLC (ODS-80Ts, Tosoh). ATPase activity was determined at 23°C with an ATP-regenerating system (24) containing 1 mM phosphoenolpyruvate, 200 μg/ml pyruvate kinase, 100 μg/ml lactate dehydrogenase, 0.15 mM NADH, and indicated ATP in buffer A. The initial hydrolysis rate was determined from the slope of absorbance decrease at 340 nm, allowing for the mixing time of 1.5 s.

Abbreviation: Ni-NTA, Ni^{2+}-nitrilotriacetic acid.

‖To whom reprint requests should be addressed.

The publication costs of this article were defrayed in part by page charge payment. This article must therefore be hereby marked "*advertisement*" in accordance with 18 U.S.C. §1734 solely to indicate this fact.

Article published online before print: *Proc. Natl. Acad. Sci. USA*, 10.1073/pnas.120174297. Article and publication date are at www.pnas.org/cgi/doi/10.1073/pnas.120174297

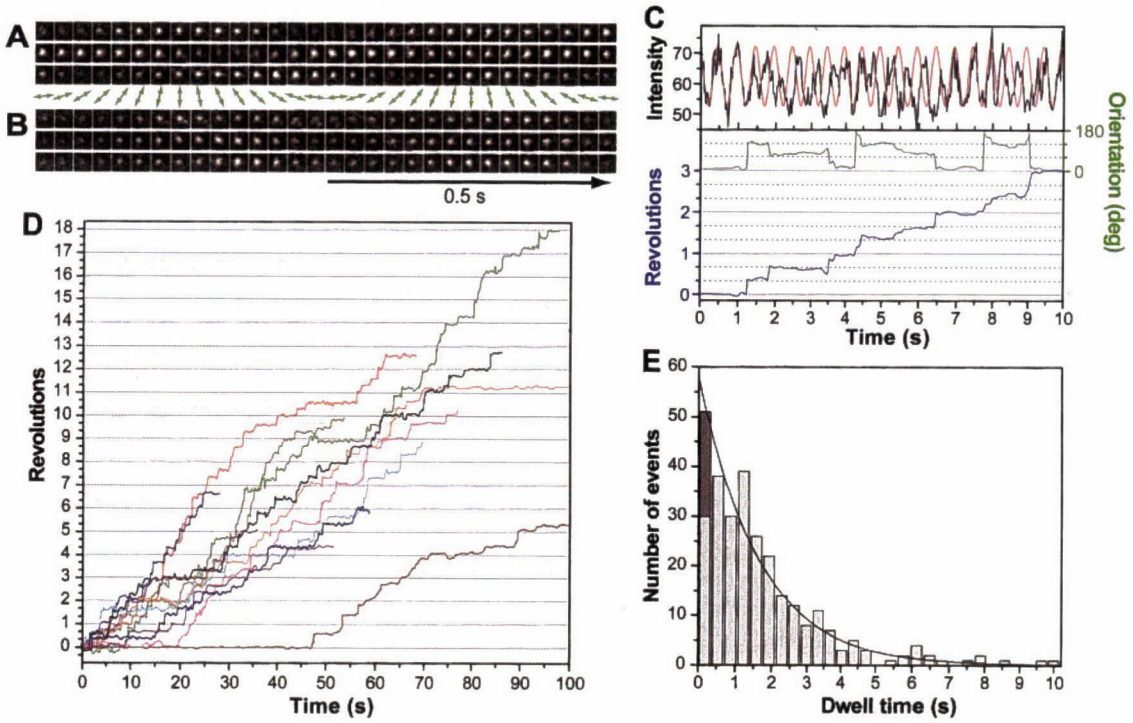

Fig. 1. (*A* and *B*) Sequential fluorescence images, at 33-ms intervals, of single Cy3-F_1 molecules at 20 nM ATP. The direction of excitation polarization is shown in green arrows. Each image was averaged spatially over 3 × 3 pixels (0.30 × 0.30 μm^2); the size of images shown is 17 × 17 pixels. The excitation intensity was 1.1 mW over a sample area of 24 μm in diameter. (*C*) Time courses of the fluorescence intensity and calculated fluorophore angles. The black line shows the intensity at time *t*, *I*(*t*), of the spot in *A* integrated over a square of 0.79 × 0.79 μm^2 enclosing the spot. When a fluorophore lies at an angle θ in the sample plane, its intensity is expected to flicker as $\cos^2[360°\cdot(t/T) - \theta] \propto \cos[360°\cdot(2t/T) - 2\theta]$, where *T* (1 s) is the period of excitation rotation. Thus, $\theta(t)$ was determined by fitting the observed *I*(*t*) with this function over the period between *t* and $t + T/2$. The green curve shows $\theta(t) - \theta_0$, where $\theta_0 = \theta(0)$; values between 0°and 180° were chosen. If this fluorophore had remained at θ_0, *I*(*t*) would have flickered as in the red line which is proportional to $\cos^2[360°\cdot(t/T) - \theta_0] \propto \cos[360°\cdot(2t/T) - 2\theta_0]$. The accumulated rotation angle (blue line) was obtained by assuming that all steps were counterclockwise. (*D*) Time courses of the stepwise rotation of the γ-subunit at 20 nM ATP. Different lines show different fluorophores (F_1). (*E*) Distribution of dwell times between steps. Each negative 120° step in the orientation records was interpreted as a zero dwell between two consecutive counterclockwise steps and counted as one in the dark part. The solid line shows the exponential fit. The average dwell time was 2.0 s.

ATPase activity of F_1 attached on the Ni-NTA glass surface was measured with a Malachite Green Pi assay (25, 26); 15 μl of 0.5 nM Cy3-$\alpha_3\beta_3\gamma$ in buffer A was infused into a chamber with both top and bottom coverslips coated with Ni-NTA. After 2 min, the chamber was washed with 200 μl of buffer A. ATPase reaction was started by infusing buffer A containing 2 mM ATP. After an incubation time of 10–55 min, 50 μl of buffer A was added from one edge of the chamber, and the solution containing liberated Pi was collected from the other edge. This procedure was repeated five times, and 200 μl of the collected solution was mixed with 500 μl of a Malachite Green reagent (Iatron Laboratories, Tokyo). After 10 s, 75 μl of 34% (wt/vol) sodium-citrate was added. After 12 min, the absorbance at 650 nm was measured. In control experiments without F_1, the absorbance was independent of the incubation time. The absorbance for samples with F_1, after subtraction of the control value, was approximately proportional to the ATPase reaction times (10, 25, 40, and 55 min), indicating that a steady state was reached by 10 min. The number of subcomplex molecules in the chamber was estimated from the fluorescence intensity of Cy3.

Fluorescence Microscopy. A 532-nm laser beam (DPSS 532–200, Coherent, Tokyo) was circularly polarized with a quarter-wave plate and introduced into a fluorescence microscope (IX70, Olympus, Tokyo) through a side port as described in ref. 4. To rotate the excitation polarization, a rotating sheet polarizer was inserted after the quarter-wave plate. Fluorescence was collected through an oil-immersion objective (PlanApo 100×, NA 1.4, Olympus) onto an intensified (VS4–1845, Videoscope, Sterling, VA) charge-coupled device camera (CCD-300T-IFG, Dage–MTI, Michigan City, IN). Observations were made at 23 ± 1°C. Images were recorded on a Hi8 video recorder (EVO-9650, Sony, Tokyo) and analyzed with a digital image processor (C2000, Hamamatsu Photonics, Hamamatsu City, Japan) and a personal computer.

Results and Discussion

To detect the rotation of the γ-subunit, the fluorophore should be firmly attached to γ. We thus tested several combinations of a γ-mutant (S107C, I210C, or S107C/I210C) and a fluorescent dye suitable for single-fluorophore imaging (tetramethylrhodamine-5-maleimide, Molecular Probes; Cy3-maleimide or Cy3-bis-maleimide, Amersham Pharmacia). Among these, a suspension of the subcomplex $\alpha_3\beta_3\gamma$(I210C), hereafter referred to as F_1, labeled with Cy3-maleimide at the sole cysteine in γ gave the highest fluorescence anisotropy of 0.32 [λ_{ex} = 550 nm; λ_{em} = 590 nm; measured in a Hitachi (Tokyo) F-4500 spectrofluorometer], indicating that the fluorophore wobble on this subcomplex was within a cone of semiangle <25°. This Cy3-labeled F_1 was fixed on a glass surface coated with Ni-NTA through histidines engineered in β such that the F_o side would be away from the glass. Single Cy3 fluorophores were observed on the inverted epifluorescence microscope. The orientations of individual fluorophores, and thus of γ, were assessed by two methods: (*i*) from the polarization dependence of the efficiency of light ab-

sorption (7) and (*ii*) from the polarization of emitted fluorescence (5).

For method *i*, the polarization axis of excitation light was rotated continuously in the sample plane at 1 Hz, in the counterclockwise direction when viewed from the F_o side. Under these conditions, fluorophores are expected to fluoresce when the excitation polarization becomes parallel with their absorption transition moment. The fluorophore in Fig. 1*A* was initially at a vertical orientation, turned into an 8 o'clock–2 o'clock orientation in the second row, and then turned through 4 o'clock–10 o'clock to the vertical orientation. The fluorophore in Fig. 1*B*, in contrast, remained vertical, presumably being on an inactive F_1.** From the spot in Fig. 1*A*, we calculated the fluorophore orientation as in Fig. 1*C* (see legend for method). The orientation (green), determined within the cyclic redundancy of 180°, stepped among three levels. Because rotation was always counterclockwise in previous studies (18, 20), we interpret all steps as counterclockwise and show the resultant rotation angle in blue; negative 60° steps in green were interpreted as counterclockwise 120° steps. The negative 120° step at ≈9 s in green was interpreted as rapid succession of two counterclockwise 120° steps within the 0.5-s window used for the angle analysis. Stepping records at 20 nM ATP are summarized in Fig. 1*D*.

Fig. 1*E* shows a histogram of the dwell times between steps. Zero dwells between rapid succession of two steps, converted from negative 120° steps above, are distinguished in dark gray, because some of these may represent genuine backward (clockwise 120°) steps. If steps are all driven by one ATP molecule, the histogram should be an exponential function at low ATP concentrations (<μM) where ATP binding is rate limiting: $\exp(-k_{on}[ATP]t)$, where k_{on} is the rate constant for ATP binding and t is the dwell time. The experimental histogram, including the dark part, was indeed exponential with k_{on} of $3.1 \times 10^7\ M^{-1}\cdot s^{-1}$, a value that agrees with the previous estimate with actin of $2 \times 10^7\ M^{-1}\cdot s^{-1}$ to $3 \times 10^7\ M^{-1}\cdot s^{-1}$ (20). Most of the steps counted in the dark bar are thus likely not backward steps. Genuine backward steps were observed with actin (20), but their frequency was at most a few percent.

In method *ii*, fluorescence was excited with circularly polarized light. The emission was decomposed into vertically (*V*) and horizontally (*H*) polarized components in a dual-view apparatus, and the two were simultaneously projected onto the video camera (5, 27). A vertically oriented fluorophore would show up in the *V* image, and a horizontal one would appear in *H*. Alternate appearance, as shown in Fig. 2*A*, indicates rotation of the γ-subunit. From the intensity records (Fig. 2*B*), polarization ($[V - H]/[V + H]$) was calculated (Fig. 2*C*) and showed three levels, a, b, and c. These levels can be explained by three orientations separated by 120° (Fig. 2*D*), again indicating stepping rotation.

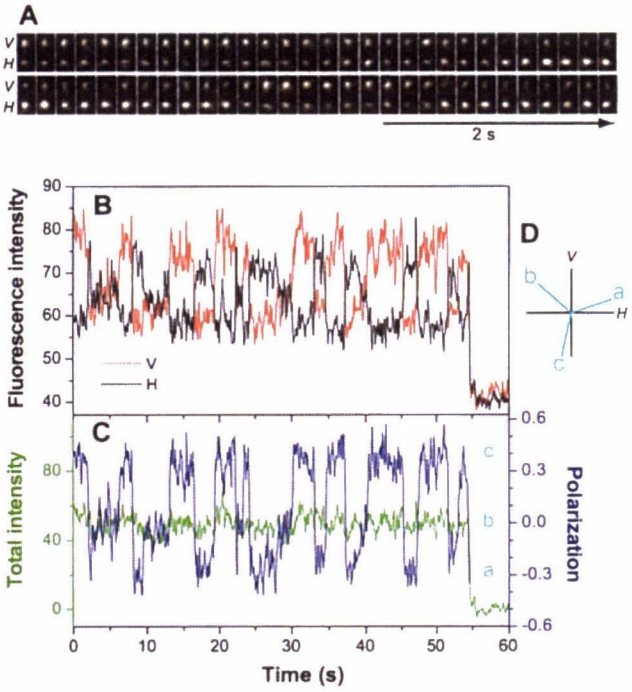

Fig. 2. (*A*) Sequential fluorescence images, at 167-ms intervals, of a single Cy3-F_1 molecule at 20 nM ATP. *V*, vertically polarized fluorescence; *H*, horizontally polarized fluorescence. Each image (15 × 30 pixels or 1.5 × 3.0 μm^2) was averaged spatially over 3 × 3 pixels. (*B*) Time courses of spot intensities for *V* and *H* in *A*, median-filtered over eight video frames (0.27 s). (*C*) Time courses of the polarization, $P = (V - H)/(V + H)$, and total intensity, $I = V + H$, calculated from *B*. The fluorophore photobleached at ≈55 s. Dashed lines (a, b, and c) are calculated *P* for the three orientations in *D*: $P = 0.4 \times [\sin^2(\theta + 18°) - \cos^2(\theta + 18°)]$, where $\theta = 0°$, 120°, and 240°.

The alternation of the spot intensity became faster at higher ATP concentrations, as expected for the ATP-dependent rotation (Fig. 3*A*). Because three levels of polarization were not always apparent in the noisy data, we analyzed the time intervals for a full turn (red lines in Fig. 3*A*). If a turn is comprised of three 120° steps and if each step is driven by one ATP molecule, then the time for a full turn, t, is expected to be distributed, at low ATP concentrations, as $t^2\exp(-k_{on}[ATP]t)$, where k_{on} is the rate constant for ATP binding. The experimental histograms (Fig. 3*B*) could be fitted with this function, indicating 120° stepping. k_{on} was $1.9 \times 10^7\ M^{-1}\cdot s^{-1}$ at 200 nM ATP, $2.3 \times 10^7\ M^{-1}\cdot s^{-1}$ at 60 nM ATP, and $2.9 \times 10^7\ M^{-1}\cdot s^{-1}$ at 20 nM ATP. These values are consistent with the results of method *i* and previous estimates with actin. Slightly smaller values at higher ATP concentrations may be due to limited temporal resolution.

The average stepping rates, defined as the inverse of average stepping time, for individual F_1 are shown in Fig. 4. Rates from single-fluorophore imaging are somewhat higher than the estimates with actin (20), because long actin filaments occasionally made long pauses, presumably caused by surface obstruction, which increased the average stepping time without significantly affecting k_{on} estimated from the histogram analysis. Preliminary measurements with probes of intermediate sizes (submicrometer beads) also show higher rates consistent with the present estimates (R.Y., unpublished work). The stepping rates paralleled the rate of ATP hydrolysis measured in solution (Fig. 4), supporting the contention of one step per one ATP molecule. The hydrolysis rate was not as high, however, probably because of heterogeneity: a small fraction of F_1 in solution was probably inactive, whereas

**Approximately 70% of observed spots were unpolarized both in methods *i* and *ii*, presumably because of imperfect binding to the glass surface (rapid tumbling or wrong orientations of F_1 can result in unpolarized fluorescence). Of the polarized ≈30%, most were inactive, showing no time-dependent change in polarization direction. For *i* and *ii*, we analyzed 59,149 spots and selected for further analysis 76 spots that made three or more revolutions before photobleaching. When an actin filament was used as a marker of rotation (18, 20), the probability of finding a rotating filament was also low, at most a few percent and much less at low ATP concentrations. The reasons for the low yields are not clear but likely include surface denaturation and MgADP inhibition. The steady-state ATPase activity, at 2 mM ATP, of Cy3-F_1 attached to the Ni-NTA glass surface was 19 s^{-1} and was ≈30% of that in solution, suggesting that ≈70% was denatured on the surface. The initial activity in solution at 2 mM ATP was 239 s^{-1}, which decreased to the steady-state level of 67 s^{-1} because of the MgADP inhibition (28). These numbers imply that <10% of the F_1 molecules on the surface are expected to be active. Most of the active ones might have been in the unpolarized, imperfectly bound population, because binding through three histidine tags tethered at widely separated positions could potentially impose strain. The actual causes are yet to be determined.

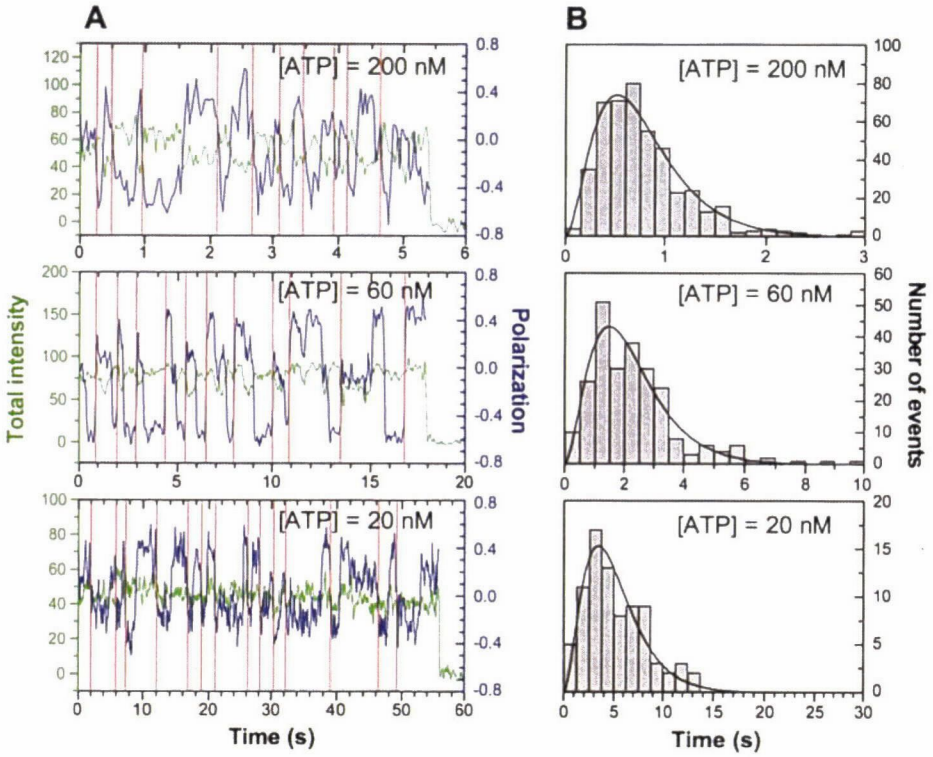

Fig. 3. (*A*) Alternation of polarization at various ATP concentrations. The excitation intensity was 6.2 mW at 200 nM ATP, 3.2 mW at 60 nM ATP, and 1.8 mW at 20 nM ATP over a sample area of 24 μm in diameter (the frequency of alternation did not depend on excitation intensity). The polarizations at 60 and 20 nM ATP were calculated after *V* and *H* were median-filtered over four and eight video frames, respectively. Vertical red lines indicate termination of one revolution, identified by eye as the crossing of polarization through zero in a unique direction. All records were terminated by photobleaching. (*B*) Distribution of times for a turn at various ATP concentrations. The average values were 0.84 s at 200 nM ATP, 2.4 s at 60 nM ATP, and 5.5 s at 20 nM ATP. Solid lines show fits with the equation in the text.

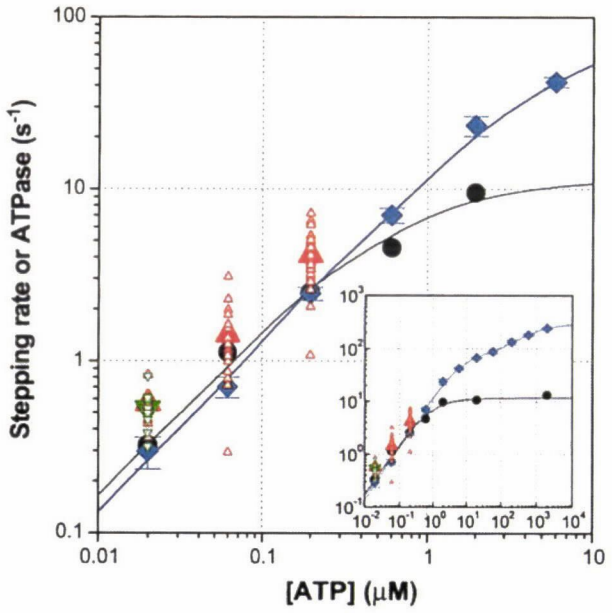

Fig. 4. Comparison of stepping and ATP hydrolysis rates. Stepping rate (3× rotation rate) was determined for each spot as $1/\langle t\rangle$ or $3/\langle 3t\rangle$, where $\langle t\rangle$ and $\langle 3t\rangle$ are average times per step (*i*, green triangles) or turn (*ii*, red triangles), respectively. Larger symbols show averages over spots. Black circles show previous estimates with actin (20). Hydrolysis rate *V* (blue diamonds with error bars showing SD) was estimated in solution (i.e., the rate shown is the ensemble average over all molecules in the solution) and was fitted with $V = (k_{cat}{}^{a}K_m{}^{b}[ATP] + k_{cat}{}^{b}[ATP]^2)/([ATP]^2 + K_m{}^{b}[ATP] + K_m{}^{a}K_m{}^{b})$, where $k_{cat}{}^{a} = 83$ s^{-1}, $k_{cat}{}^{b} = 292$ s^{-1}, $K_m{}^{a} = 6.3$ μM, and $K_m{}^{b} = 680$ μM. Hydrolysis rate of Cy3-labeled F_1 (not shown) agreed within experimental error.

stepping rates were estimated on the most active F_1 in the sample. A likely cause is MgADP inhibition (28), which may also be responsible for the dip in hydrolysis rate around 10^1 to 10^2 μM ATP (Fig. 4 *Inset*). To estimate the hydrolysis rate in fully active samples, we carefully removed nucleotides from the F_1 preparation and measured the initial rate of hydrolysis. However, the possibility of rapid onset of MgADP inhibition during the initial period including the mixing time cannot be ignored.

In summary, by observing no-load rotation of F_1, we have shown that 120° stepping is a genuine characteristic of the F_1 motor, at least at low ATP concentrations and at the video-limited temporal resolution. Individual steps are powered by one ATP molecule. The kinetics of stepping or of ATP binding seem to be independent of the load. Because the rate of ATP binding likely depends on the orientation of γ (28–30), the rate could in principle vary depending on the load. At least for the frictional load on the actin filament, such variation does not seem to occur.

The polarization-analyzed single-fluorophore imaging should be useful in elucidating conformational changes in other protein (and RNA) machines as well. Method *i*, being superior in angular resolution, and method *ii*, having theoretically unlimited time resolution, are complementary.

We thank S. Ishiwata, T. Hisabori, E. Muneyuki, and other Core Research for Evolutional Science and Technology members for critical discussions, K. Steinert of Qiagen for the Ni-NTA protocol, and H. Umezawa for lab management. This work was supported in part by Grants-in-Aid from the Ministry of Education, Science, Sports, and Culture of Japan and a Keio University Special Grant-in-Aid.

1. Moerner, W. E. (1997) *Science* **277,** 1059–1060.
2. Ishikawa, M., Hirano, K., Hayakawa, T , Hosoi, S. & Brenner, S (1994) *Jpn J. Appl. Phys.* **33,** 1571–1576.
3 Funatsu, T., Harada, Y , Tokunaga, M., Saito, K. & Yanagida, T (1995) *Nature (London)* **374,** 555–559.
4 Sase, I., Miyata, H., Corrie, J. E., Craik, J. S. & Kinosita, K., Jr. (1995) *Biophys. J.* **69,** 323–328
5. Sase, I., Miyata, H., Ishiwata, S. & Kinosita, K., Jr. (1997) *Proc Natl. Acad. Sci. USA* **94,** 5646–5650.
6. Kinosita, K., Jr (1999) *FASEB J.* **13,** S201–S208.
7. Ha, T., Enderle, T., Chemla, D. S , Selvin, P. R. & Weiss, S (1996) *Phys. Rev. Lett.* **77,** 3979–3982.
8. Warshaw, D. M., Hayes, E., Gaffney, D., Lauzon, A. M., Wu, J., Kennedy, G., Trybus, K., Lowey, S. & Berger, C (1998) *Proc Natl. Acad. Sci. USA* **95,** 8034–8039.
9. Boyer, P D. (1997) *Annu. Rev Biochem* **66,** 717–749.
10. Abrahams, J. P , Leslie, A. G., Lutter, R. & Walker, J. E (1994) *Nature (London)* **370,** 621–628
11 Boyer, P. D. & Kohlbrenner, W. E (1981) in *Energy Coupling in Photosynthesis*, eds. Selman, B. R. & Selman-Reimer, S. (Elsevier, Amsterdam), pp. 231–240.
12. Oosawa, F & Hayashi, S. (1986) *Adv. Biophys.* **22,** 151–183.
13 Boyer, P. D. (1993) *Biochim. Biophys Acta* **1140,** 215–250.
14. Duncan, T. M., Bulygin, V. V., Zhou, Y., Hutcheon, M. L. & Cross, R. L. (1995) *Proc. Natl. Acad. Sci. USA* **92,** 10964–10968
15. Sabbert, D., Engelbrecht, S. & Junge, W. (1996) *Nature (London)* **381,** 623–625
16. Zhou, Y., Duncan, T. M., Bulygin, V. V , Hutcheon, M L. & Cross, R. L. (1996) *Biochim. Biophys. Acta* **1275,** 96–100.
17. Aggeler, R., Ogilvie, I. & Capaldi, R. A. (1997) *J. Biol. Chem.* **272,** 19621–19624.
18. Noji, H., Yasuda, R., Yoshida, M. & Kinosita, K., Jr. (1997) *Nature (London)* **386,** 299–302.
19. Hasler, K., Engelbrecht, S. & Junge, W. (1998) *FEBS Lett.* **426,** 301–304.
20. Yasuda, R., Noji, H., Kinosita, K , Jr., & Yoshida, M. (1998) *Cell* **93,** 1117–1124
21. Adachi, K., Kinosita, K., Jr , & Ando, T. (1999) *J. Microsc. (Oxford)* **195,** 125–132
22. Ernst, L. A , Gupta, R. K., Mujumdar, R. B. & Waggoner, A. S. (1989) *Cytometry* **10,** 3–10.
23. Matsui, T , Muneyuki, E., Honda, M , Allison, W. S., Dou, C & Yoshida, M. (1997) *J Biol. Chem.* **272,** 8215–8221.
24. Kato, Y , Sasayama, T., Muneyuki, E. & Yoshida, M. (1995) *Biochim. Biophys. Acta* **1231,** 275–281.
25. Ohno, T. & Kodama, T. (1991) *J. Physiol. (London)* **441,** 685–702.
26. Harada, Y., Sakurada, K., Aoki, T., Thomas, D. D. & Yanagida, T. (1990) *J Mol. Biol.* **216,** 49–68.
27 Kinosita, K., Jr., Itoh, H., Ishiwata, S., Hirano, K., Nishizaka, T. & Hayakawa, T (1991) *J. Cell. Biol.* **115,** 67–73.
28. Kinosita, K., Jr., Yasuda, R., Noji, H. & Adachi, K. (2000) *Philos. Trans R Soc London B* **355,** 473–490.
29. Wang, H. & Oster, G. (1998) *Nature (London)* **396,** 279–282.
30. Kinosita, K., Jr., Yasuda, R. & Noji, H. (2000) *Essays Biochem.* **35,** in press.

Characterization of Single Actomyosin Rigor Bonds: Load Dependence of Lifetime and Mechanical Properties

Takayuki Nishizaka,*† Ryuzo Seo,* Hisashi Tadakuma,* Kazuhiko Kinosita, Jr.,†‡ and Shin'ichi Ishiwata*†§¶
*Department of Physics, School of Science and Engineering, Waseda University, Tokyo169-8555; †Core Research for Evolutional Science and Technology, Genetic Programming Team 13, Kanagawa 216-0001; ‡Department of Physics, Faculty of Science and Technology, Keio University, Yokohama 223-8522; §Advanced Research Institute for Science and Engineering, Waseda University, Tokyo; and ¶Materials Research Laboratory for Bioscience and Photonics, Waseda University, Tokyo, Japan

ABSTRACT Load dependence of the lifetime of the rigor bonds formed between a single myosin molecule (either heavy meromyosin, HMM, or myosin subfragment-1, S1) and actin filament was examined in the absence of nucleotide by pulling the barbed end of the actin filament with optical tweezers. For S1, the relationship between the lifetime (τ) and the externally imposed load (F) at absolute temperature T could be expressed as $\tau(F) = \tau(0)\cdot\exp(-F\cdot d/k_BT)$ with $\tau(0)$ of 67 s and an apparent interaction distance d of 2.4 nm (k_B is the Boltzmann constant). The relationship for HMM was expressed by the sum of two exponentials, with two sets of $\tau(0)$ and d being, respectively, 62 s and 2.7 nm, and 950 s and 1.4 nm. The fast component of HMM coincides with $\tau(F)$ for S1, suggesting that the fast component corresponds to single-headed binding and the slow component to double-headed binding. These large interaction distances, which may be a common characteristic of motor proteins, are attributed to the geometry for applying an external load. The pulling experiment has also allowed direct estimation of the number of myosin molecules interacting with an actin filament. Actin filaments tethered to a single HMM molecule underwent extensive rotational Brownian motion, indicating a low torsional stiffness for HMM. From these results, we discuss the characteristics of interaction between actin and myosin, with the focus on the manner of binding of myosin.

INTRODUCTION

Recent developments in microscopic techniques have opened up opportunities of studying "single-molecule physiology," which enables us to elucidate protein-protein interactions and their various biological functions under living circumstances in aqueous media. For molecular motors, their individual behaviors have been successfully studied at the single molecule level. Nanometer steps and piconewton forces generated by single molecular motors have been measured under an optical microscope (Svoboda et al., 1993; Finer et al., 1994; Ishijima et al., 1994, 1998; Miyata et al., 1994, 1995; Molloy et al., 1995; Mehta et al., 1999). Single-fluorophore imaging (Funatsu et al., 1995; Sase et al., 1995a) has revealed individual ATP turnovers by myosin and rotational movement between actin and myosin (Sase et al., 1997), suggesting a hopping character for myosin (Kinosita et al., 1998). The mechanisms of motor operation, however, are still unclear. During one cycle of ATP hydrolysis, molecular motors are considered to form different conformations with different affinities for their substrate filaments and to alternate binding and unbinding. Here we focus on the characteristics of unbinding between myosin and actin.

In general, binding and unbinding interactions of proteins are essential for many biological functions, e.g., adhesion between cells, migration of cells on substratum (Nishizaka et al., 2000), recognition between ligands and receptors, processive movement of molecular motors, and so on. Several techniques have been developed to measure forces of protein bonds in the range from the subpiconewton level to a nanonewton. Glass microneedles were first applied to measure the sliding force generated between a microtubule and dynein motors (Kamimura and Takahashi, 1981) and then successfully used to measure the sliding force and the tensile strength of single actin filaments (Kishino and Yanagida, 1988; Tsuda et al., 1996). Individual ligand-receptor binding has been extensively characterized by atomic force microscopy (Nakajima et al., 1997; Fritz et al., 1998). The interaction between avidin and biotin has been examined in detail, and its molecular dynamics has been simulated (Florin et al., 1994; Moy et al., 1994; Grubmuller et al., 1996; Izrailev et al., 1997; Merkel et al., 1999). In the present study we used optical tweezers to characterize single actomyosin rigor bonds.

Optical tweezers, formed by focusing a laser beam, capture a particle of micrometer size without direct contact (Ashkin et al., 1986, 1990). In our previous studies (Nishizaka et al., 1995b), we measured the force required to unbind a rigor bond formed between an actin filament and a single heavy meromyosin (HMM) molecule in the absence of ATP using optical tweezers under a dual-view (fluorescence and phase-contrast) microscope (Kinosita et al., 1991; Sase et al., 1995b; Arai et al., 1999). The average unbinding force was ~9 pN, which is 2–5 times larger than the sliding force (Finer et al., 1994; Ishijima et al., 1994; Miyata et al., 1995) and an order of magnitude smaller than other intermolecular forces (Florin et al., 1994; Tsuda et al., 1996; Fritz et al., 1998). Unbinding under a constant force was a

Received for publication 28 February 2000 and in final form 26 April 2000.

Address reprint requests to Dr. Shin'ichi Ishiwata, Department of Physics, School of Science and Engineering, Waseda University, 3-4-1 Okubo, Shinjuku-ku, Tokyo 169-8555, Japan. Tel.: 81-3-5286-3437; Fax: 81-3-3200-2567; E-mail: ishiwata@mn.waseda.ac.jp.

0006-3495/00/08/962/13 $2.00

stochastic process, and an increase in the load by 10 pN decreased the lifetime of the rigor bond by a factor of 10^2 to 10^3. Interestingly, two types of HMM molecules were found, one with a large (long) and the other with a small (short) unbinding force (lifetime), suggesting "molecular individualism."

In this study, we measured the lifetime of single actomyosin (either HMM or subfragment-1 of myosin (S1)) rigor bonds under various external loads and could formulate the relationship between the lifetime and the load. The stochastic properties of the rigor bonds have been demonstrated. We developed a microscopic way to count the number of myosin molecules attached to the glass surface. Based on the number density of myosin molecules interacting with an actin filament thus measured, we estimated the minimum number of myosin molecules needed to slide actin filaments continuously. Furthermore, the torsional stiffness of single myosin molecules was estimated by observing the rotational Brownian motion of a short actin filament attached to myosin. Throughout the present study, we tried to characterize the interaction with actin of double-headed HMM molecules compared with that of single-headed S1 molecules.

MATERIALS AND METHODS

Dual-view imaging microscopy and optical tweezers system

Fig. 1 shows a schematic diagram of a dual-view (phase-contrast and fluorescence) video microscope imaging system (Kinosita et al., 1991; Nishizaka et al., 1995a,b; Sase et al., 1995b; Arai et al., 1999) equipped with optical tweezers. The inverted microscope (TMD-300; Nikon Co., Tokyo) with a 100× objective with a phase-contrast plate (NA 1.3, fluor 100 Ph; Nikon) was used on an optical bench (HG-LM; Herz Co., Kanagawa, Japan). The optical system included dichroic mirrors (DM 550, DM infrared, Sigma Koki Co., Saitama, Japan; DM 530, Asahi Spectra Co., Tokyo), filters (F 380–520, F 550, F 590; Asahi Spectra), and mirrors. The beam from the sample, which consisted of two components, the phase-contrast image of the bead (wavelength 380–520 nm, the *once-broken* line in Fig. 1) and the fluorescence image of actin filaments (excitation 550 nm and emission > 590 nm; the *dashed line* in Fig. 1), was separated by a beam separator (DM > 530 nm) Colorless filters (HA-30; Hoya Co., Tokyo, and Asahi Spectra) were placed behind the Hg lamp and before the image intensifier to cut off the infrared light. The field stop was positioned between the microscope and the beam separator, and lenses (DLB-50-150PM; Sigma Koki) were positioned before each camera to focus images clearly. The bead image, acquired with a CCD camera (CCD-72; Dage-MTI, Michigan City, IN), was stored in a digital frame memory (DIPS-C2000; Hamamatsu Photonics K. K., Hamamatsu, Japan). The position of the bead was determined by calculating the centroid of its intensity profile with a spatial resolution of nanometer scale (Fig 2; Miyata et al., 1994; Nishizaka et al., 1995b). The data were analyzed with a personal computer (Apple Japan, Tokyo).

The sample stage of the microscope was replaced with the custom-made stage, on which the position of the objective along the z direction could be controlled by using a piezoelectric microscope positioner (P-720.00; Physik Instrumente GmbH and Co., Waldbronn, Germany) with a power supply (BWS 1202.5; Takasago, Tokyo). Because the drift between the commercial sample stage and the objective is mainly caused by deformation of the gear(s) sustaining a nose piece, the nose piece was removed and the objective was fixed directly to the sample stage to suppress the drift during measurements. Large displacement of the stage (as much as >40 nm) was achieved with the use of high-resolution actuators (HPA-10; Sigma Koki), their controller (Mark-8; Sigma Koki), and a personal computer (Apple Japan, Tokyo) with GPIB (NI488.2; National Instruments Co., Austin, TX). The small displacement (nanometer scale) was adjusted with a piezoelectric substage (p-770.10; Physik Instrumente GmbH and Co.) with a function generator (1915; NF Electronic Instruments, Yokohama, Japan) and an amplifier (BWS 120–2.5, Takasago). The temperature of the microscopic system was stabilized by allowing it to sit for 4–6 h before the measurements.

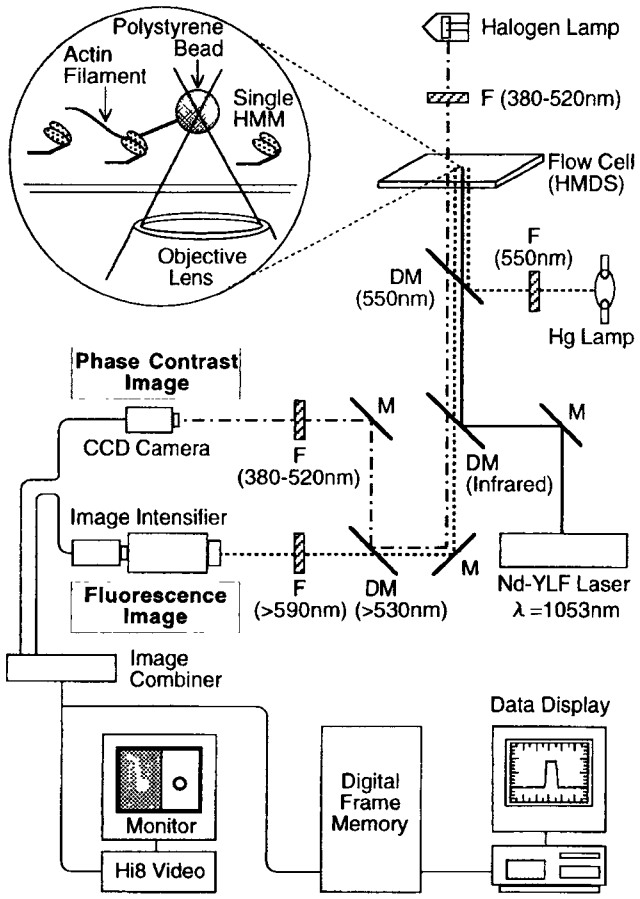

FIGURE 1 Schematic diagram of optical tweezers and dual-view imaging video microscope system. The once-broken lines and the dashed lines represent phase-contrast and fluorescence imaging optical paths, respectively, and the solid lines represent the optical tweezers optical path. The microscope system includes dichroic mirrors (DM) (the wavelength in parentheses shows the wavelength of the reflected light, and the wavelength with the > sign shows the range of wavelength passing through DM), filters (F) (the wavelength in parentheses shows the wavelength of light passing through F), and mirrors (M).

The spatial resolution of the system and the performance of the sample stage were examined by the method shown in Fig. 2. Fig. 2 *A* gives an example showing the position fluctuation of a bead trapped by optical tweezers with a stiffness of 0 27 pN/nm. The standard deviation (SD) of the displacement of the bead trapped for 1 min was 0.84 nm for the x direction and 0.93 nm for the y direction (n = 5). Here these values are considered to be the spatial resolution of our system, with 1/30 s time resolution. In

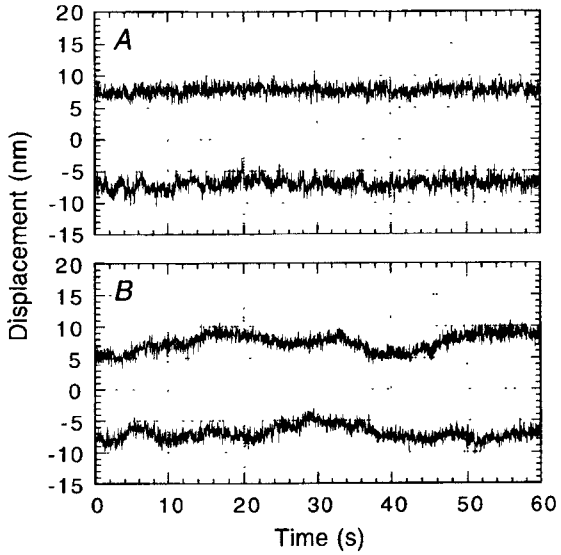

FIGURE 2 Performance of the image analysis system and the sample stage. (*A*) Time course of the displacement of the bead that was trapped in the medium by optical tweezers with a stiffness of 0.27 pN/nm. The displacement reflects both the stability of the trap center and the spatial resolution of our analysis system. (*B*) Displacement of the bead that was fixed to the glass surface The glass surface was covered with nitrocellulose over the bead, so that the bead was fixed between the nitrocellulose membrane and the glass surface. Thus the displacement of the bead reflects the movement of the sample stage. Upper and lower traces in each figure respectively represent the displacements along the x and y axes

contrast, to check the drift of the stage, we measured the displacement of the bead fixed to a glass surface by covering it with nitrocellulose (Fig. 2 *B*). The SD of the displacement of the bead for 1 min was 2.1 nm for the x direction and 2.0 nm for the y direction (n = 10). They were larger than the spatial resolution of our system, indicating the drift of the microscopic stage or the vibration of the system.

The actin filaments labeled with a fluorescent probe were visualized using another CCD camera equipped with an image intensifier (KS1381; Video Scope International, Washington, D.C.). To observe a phase-contrast image of beads simultaneously, the focus of the phase-contrast image plane was displaced ~0.5 μm (the radius of the bead) higher than the focus of the fluorescence image plane by moving the lenses in front of the camera. Two images were electronically combined (MV24-c; For. A Co., Tokyo) on the same screen to compare the behavior of the actin filament against the displacement of the bead at the same time.

The 1 W Nd:YLF laser (1053–1000p: λ = 1.053 μm; Amoco Laser Co , Napervlle, IL) was coupled with an optical fiber, and the laser was not placed on the optical bench, to avoid a vibration. The position of the optical fiber could be moved along three directions (x, y, and z) and tilted in two directions (xy plane) The laser beam was set parallel with the objective (YTL-25-20PY1; Sigma Koki) and then focused with a custom-made optical apparatus (Nikon and Sigma Koki). The laser beam was led into the microscope from the right-hand side to the position just below the dichroic mirror for fluorescence excitation, which was originally designed to set an analyzer of a DIC microscope. The linear polarization of the laser light was changed to a circular polarization with a quarter wave plate. The laser light could be split into two beams with a set of beam splitters (PBN-20-16040; Sigma Koki) if needed. The trap stiffness we used, 0.1–0.3 pN/nm, was calibrated as described before (Nishizaka et al., 1995b).

In vitro assay system and preparation of bead-tailed F-actin

Actin and myosin were prepared from rabbit skeletal white muscle according to a standard procedure (Kondo and Ishiwata, 1976). HMM prepared by chymotryptic digestion, and s1 by papin digestion of myosin was stored in liquid N_2 (Nishizaka et al., 1993). A bead-tailed actin filament was prepared as previously reported (Suzuki et al., 1996). Bovine plasma gelsolin (Kurokawa et al , 1990) was cross-linked to the carboxylated polystyrene bead (1-μm diameter; Polysciences, Warrington, PA) with 1-ethyl-3-(3-dimethyl-aminopropyl)-carbodiimide (Nacalai Tesque Co., Kyoto), such that the barbed end (B-end) of an actin filament, which corresponds to the rear end when the filament slides, was attached to the bead. The average number of actin filaments attached to the bead was controlled by cross-linking an appropriate amount of bovine serum albumin (BSA) to the bead (BSA/gelsolin = 20:1 w/w). BSA labeled with rhodamine X maleimide (Molecular Probes, Eugene, OR) was also attached to the bead surface to visualize the bead as a fluorescence image (cold BSA/labeled BSA = 19:1). The bead was washed with F-buffer (0.1 M KCl, 2 mM $MgCl_2$, 2 mM 3-(*N*-morpholino)propanesulfonic acid (pH 7.0), 1.5 mM NaN_3, 1 mM dithiothreitol (DTT)) and mixed with 0.2 mg/ml actin filament labeled with rhodamine phalloidin (Molecular Probes) (Yanagida et al., 1984). Before infusion to the flow cell, bead-tailed actin filaments were diluted in F-buffer containing 1 mg/ml BSA to avoid adsorption of the bead to the glass surface. The in vitro assay system was prepared according to the report by Toyoshima et al. (1987), with slight modifications (Nishizaka et al., 1995b). The coverslip, cleaned in a sonicator with neutral detergent, was silanized with hexamethyl disilazane (Nacalai Tesque) (Nishizaka et al., 1995b). HMM and S1 were diluted in an assay buffer (AB) (25 mM KCl, 4 mM $MgCl_2$, 25 mM imidazole-HCl (pH 7.4), 1 mM EGTA, 1 mM DTT) and infused with the flow cell from one side and then from the other side after 60 s. The cell was washed with AB-buffer containing 0.5 mg/ml BSA, 10 mM DTT, 0.22 mg/ml glucose oxidase, 0.036 mg/ml catalase, and 4.5 mg/ml glucose. The bead-tailed actin filament, which was a mixture of 20 nM actin and 0.05% (w/v) bead, was infused. After washing with 3 volumes of AB-buffer containing 0.5 mg/ml BSA and the oxygen scavenger system, the edges of the flow cell were sealed with grease (Toray Dow Corning Silicone, Tokyo). All experiments were done at 30–32°C, except the S1 measurement at 27–32°C.

RESULTS

Direct counting of the number of HMM molecules

First we developed a method for directly counting the number of HMM molecules interacting with actin filaments. Our previous studies showed that the location of each HMM molecule attaching to a glass surface could be determined (Nishizaka et al., 1995a,b). When an actin filament was pulled and taut, HMM molecules could be recognized as a nodal point of the fluctuation of actin filament. By imposing the external load, we broke the nodal point and loosened the filament again (figure 1 *A* of Nishizaka et al., 1995a). Although this technique was useful for determining the location of HMM molecules, it was restricted to a very low density of HMM molecules, because the loosened part of the actin filament immediately attached to adjacent HMM molecules when the distance between adjacent molecules was less than ~1 μm. To solve this difficulty, the bead was manipulated not in the direction parallel to the glass surface but perpendicular to the surface (Figs. 3 and 4). This tech-

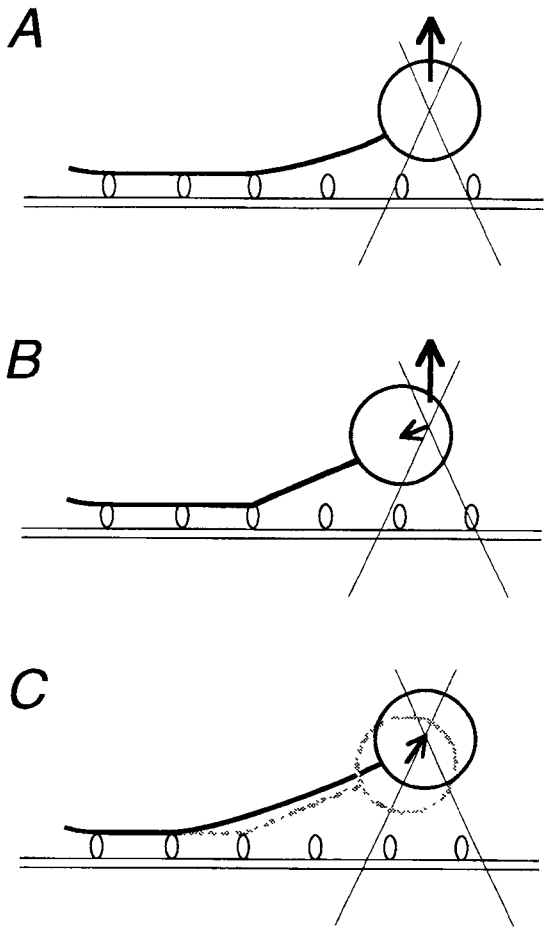

FIGURE 3 Schematic illustration of the technique used to count the number of motor molecules attached to the glass surface. The bead-tailed actin filament bound to HMM molecules was manipulated in the upward (z) direction at a constant rate (A) The filament was pulled taut from the HMM molecule (B), so that the bead was displaced from the trap center in the direction of the HMM. The bead returned to the trap center when the cross-bridge was broken, and subsequently the actin filament was loosened (C).

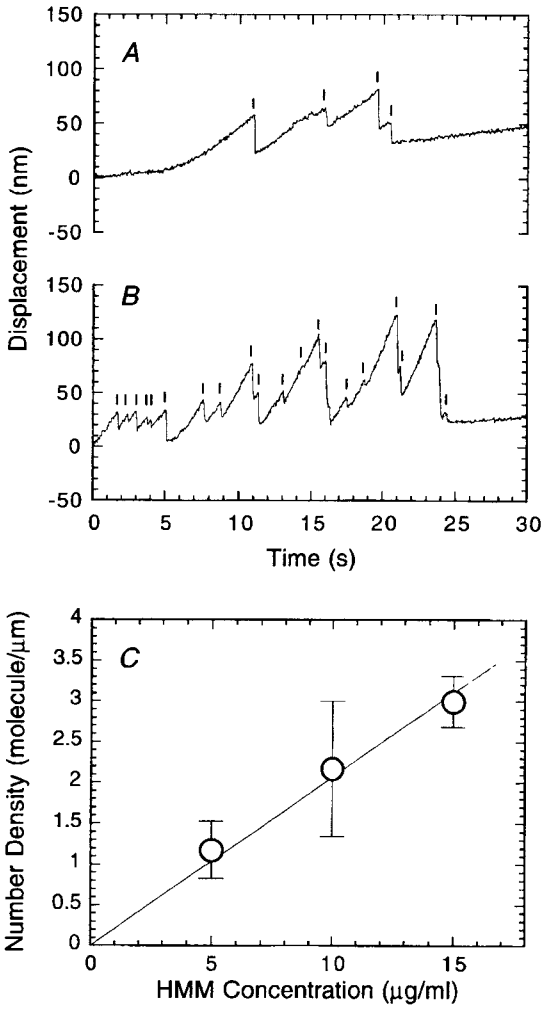

FIGURE 4 (A and B) Examples of the time course of the bead displacement projected onto the xy plane of the glass surface. The objective was moved in the upward (z) direction at a constant rate, 100 nm/s The glass surface was precoated with 5 and 15 μg/ml HMM in A and B, respectively. The small bar indicates the moment at which the cross-bridge was broken (cf. Fig. 3 C). (C) The relation between the concentration of HMM infused into the flow cell and the number density of HMM. Bars indicate the standard deviation (n = 4–5). The slope of a linear approximation is 0.21 molecules/((μg/ml)·μm actin filament).

nique could be used to avoid overcounting the number of molecules.

Fig. 4, A and B, shows examples of the time course of the bead movement projected onto the xy plane with this technique. The trapped bead was manipulated in the upper z direction at a constant rate of 100 nm/s by moving the objective with a piezoelectric positioner (Fig. 3 A). After the part of the actin filament closest to the bead became taut, the bead began to deviate from the trap center (*sawtooth pattern* in Fig. 4, A and B; cf. Fig. 3 B). Then, after a while, the bead returned to the trap center accompanying the unbinding of the rigor bond. Thus each peak in Fig. 4, A and B, indicated by a small bar corresponds to the moment at which the cross-bridge was broken (Fig. 3 C). Finally, the filament was completely detached from the glass surface (at 21 s in Fig. 4 A and 24 s in Fig. 4 B). In 0–5 s and 21–30 s in Fig. 4 A, the trapped bead was displaced to the x direction at a rate of ~2 nm/s, which was accompanied by the upward motion of the objective. This movement is attributable to a slight misalignment between the laser beam and the optical center axis of the objective.

We applied the above method to the HMM solution in the range of 5–15 μg/ml (Fig. 4); at higher HMM concentrations, actin filaments were severed at a nodal point by pulling. The maximum trapping force of our system was estimated to be ~60 pN, indicating that an actin filament can be broken by applying a force less than 60 pN when the

filament is bent at an acute angle (cf. Arai et al., 1999). As shown in Fig. 4 *C*, the average number of HMM molecules that attached to a unit length of an actin filament was proportional to the concentration of infused HMM, and its slope was 0.21 molecules/((μg/ml)·μm actin filament).

We also examined the minimum concentration of HMM needed to achieve smooth sliding movement of actin filaments in the presence of 1 mM ATP. On the glass surface coated with HMM lower than 20 μg/ml, actin filaments could not slide and became detached from the glass surface. At 30 μg/ml HMM, actin filaments ~10 μm in length slid continuously at a speed of 9.3 ± 0.7 μm/s (n = 5), whereas short actin filaments slid intermittently and sometimes became detached. Under these conditions (1 mM ATP and 30 μg/ml HMM), the minimum length of actin filaments that slid continuously for 10 s was 1.4 μm.

Swiveling motion of actin filaments tethered to HMM

On a glass surface that was coated with a low concentration of HMM in the absence of ATP, short actin filaments (1–2 μm long) showed swiveling Brownian motion around a single point over a range of more than 360° (Nishizaka et al., 1995a,b). An example of this swiveling motion is shown in Fig. 7. This observation is analogous to the case of a microtubule tethered by a single kinesin molecule (Hunt and Howard, 1993). By analyzing the swiveling motion of actin filaments, we estimated the torsional stiffness of the flexible part, which is probably located in a HMM molecule.

The direction of a rotating actin filament was estimated from the centroid of its fluorescence image. We chose those actin filaments tethered to the glass surface by a single point that was slightly deviated from the center of the filament. When the filament swiveled around the tether point, the centroid of its fluorescence image also swiveled, showing the direction of the filament (Noji et al., 1997; Yasuda et al., 1998). Before the centroid calculation, noise in the video images was reduced by recording by averaging over 4 consecutive video frames. Actin filaments 1–3 μm long were selected for calculation to avoid the effect of their bending motion in calculation.

Fig. 5 *A* is an example showing the time course of the rotation of the short actin filament. The direction of the filament fluctuated with time. This fluctuation was assumed to be caused by thermal energy, and the torsional stiffness could be estimated as follows: the direction was divided every 1-rad partition, and the probability that the filament existed in each direction of 1 rad width, $P(\theta)$ (θ = torsion angle), was calculated. The energy $E(\theta)$ was thus obtained by the equation $E(\theta) = -k_B T \cdot \ln(P(\theta))$ as shown in Fig. 5 *B*, where k_B is the Boltzmann constant and T is the absolute temperature. The approximation of $E(\theta)$ to a spring shape function, $E(\theta) = \frac{1}{2} k \theta^2$ (k is the spring constant), is shown as a thin line in Fig. 5 *B*. The value of k was estimated to be

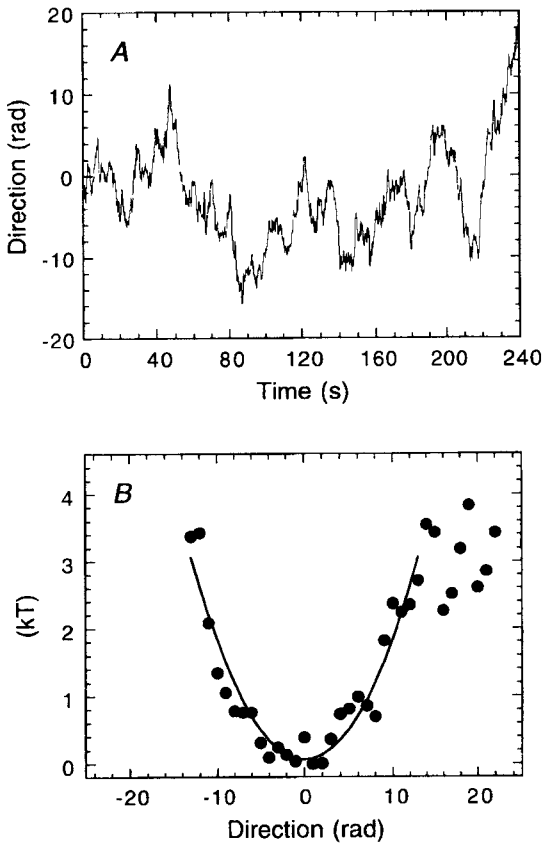

FIGURE 5 (*A*) An example showing the time course of swiveling of a short actin filament tethered to the glass surface through a single HMM molecule (see the short actin filament in Fig. 7, indicated by an *arrow*). (*B*) The energy profile showing the torsional stiffness of the single HMM molecule estimated from *A*. The thin line is an approximation with a spring shape function ($E(\theta) = 1/2 \cdot k\theta^2$, where $E(\theta)$ is energy, k is the spring constant, and θ is the torsion angle), in which the spring constant is 0.074×10^{-21} N · m/rad in the range of ±12 rad.

$2.3 \pm 1.9 \times 10^{-22}$ (± SD, n = 5) N·m/rad. Actin filaments rotated 6.4 times at maximum and 3.8 times on average.

Lifetime of single rigor bonds

In our previous studies (Nishizaka et al., 1995a,b), the unbinding force was measured by moving the trap center with a movable mirror. In the present study, the optical stage was displaced by using a piezoelectric substage, while the trap center was fixed. The advantage of this method is that the imposed load can be precisely determined at any moment. Fig. 6 illustrates how to examine the load dependence of the lifetime of single rigor bonds formed between a single actin filament and a single myosin (HMM or S1) molecule that attached to the glass surface. First the bead attached to the B-end of an actin filament is trapped by optical tweezers (Fig. 6 *A*). When the optical stage is displaced stepwise so as to make the actin filament taut, the

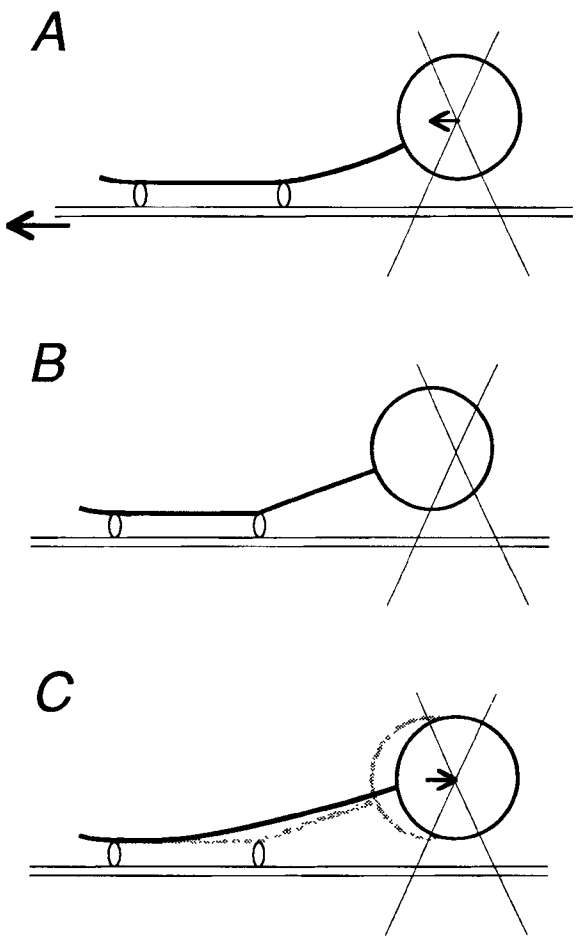

FIGURE 6 Schematic illustration of the procedure to measure the lifetime of the rigor bond between a single actin filament and a single HMM (or S1) molecule. (*A*) The bead-tailed actin filament bound to a motor protein is trapped by optical tweezers, and then the piezoelectric substage is displaced stepwise. (*B*) The filament is pulled taut from the motor protein, and the bead is displaced from the trap center, so that a sudden constant load is imposed on the rigor bond (*C*) Finally, the bead returns to the trap center accompanying the breakage of the rigor bond, and the filament is loosened again The time that elapsed between *B* and *C* corresponds to the lifetime of rigor bond.

bead is subsequently displaced from the trap center (Fig. 6, *A* and *B*). Thus a constant load is imposed stepwise on the rigor bond within a video frame, 1/30 s. After a while, the rigor bond is broken, and the bead is returned to the trap center (Fig. 6 *C*). The actin filament is loosened and shows bending Brownian motion again between the bead and the adjacent myosin molecule.

Fig. 7 is a series of fluorescence micrographs showing how to impose an external load on single rigor bonds. An actin filament was first trapped with optical tweezers (Fig. 7 *A*) and tautened by stepwise displacement to the left by the piezoelectric substage (Fig. 7 *B*) because the bead had located to the right of the HMM molecule. In this example, there were two HMM molecules that tethered the actin filament to the glass surface as identified as a nodal point (*arrowheads*), and the actin filament was pulled taut from the first HMM molecule. After a while, the bond was broken (Fig. 7 *C*), such that the lifetime of the rigor bond under a constant load could be directly measured. The actin filament was immediately loosened and showed bending Brownian motion again. When the stage was moved further, the filament was pulled taut from the next HMM molecule (Fig. 7 *D*). The stage was displaced stepwise again, and the second rigor bond was subsequently broken. Thus the actin filament was completely dissociated from the glass surface and the fluorescence image became out of focus (Fig. 7 *E*). Note that in Fig. 7, there is a short actin filament swiveling around a single point (indicated by a *small arrow*), at which a single HMM molecule is considered to be attached. The data in Fig. 5 were obtained from such a fluorescence image.

Fig. 8 *A* is an example of a record showing the time course of the displacement of the bead after stepwise imposition of an external load. When the stage was displaced stepwise (at 1.3 s, as shown by an *arrow*), the actin filament became taut (cf. Fig. 7, *B* and *D*), and the bead was displaced from the trap center. In this example, the external load imposed on the rigor bond was estimated to be 10.6 pN (we could not determine the external load beforehand, because the degree of loosening of an actin filament before applying the load could not be controlled), and the rigor bond was broken 0.43 s after the load was imposed. This observation showed that the lifetime of the actin-HMM rigor bond at no load, ~1000 s, was decreased to 0.43 s by imposing a load of 10.6 pN.

In the case of acto-S1 rigor bonds, spontaneous unbinding occurred, on the average, in ~100 s (Tadakuma et al., manuscript in preparation). Because of this short lifetime, measurement of the load dependence of the lifetime was technically difficult. To solve this problem, we prepared a flow cell coated with a higher density of S1 as compared with HMM, and actin filament was pulled at an acute angle to avoid the possibility of stretching two rigor bonds simultaneously.

Fig. 8 *B* is a summary showing the relationship between the imposed load and the lifetime. While the lifetime of HMM rigor bonds was distributed over a wide range of imposed loads, that of S1 rigor bonds was limited to a narrower range. In the case where a bond was broken within 66 ms (two video frames), we could not precisely determine the imposed load, so that these data (~5% of measurements) were omitted from Fig. 8 *B*. In the case of S1, there were four exceptional cases in which rigor bonds did not break for 60 s over 20 pN. We judge that they are attributable to the aggregation of S1, and thus they are not included in Fig. 8 *B*.

To elucidate the load dependence of the lifetime, we divided loads on the abscissa of Fig. 8 *B* into 3-pN partitions and replotted the time course of the unbinding occurrence of HMM and S1 rigor bonds in each partition, as shown in Fig. 9. The error bars indicate $N^{1/2}$, corresponding to the stan-

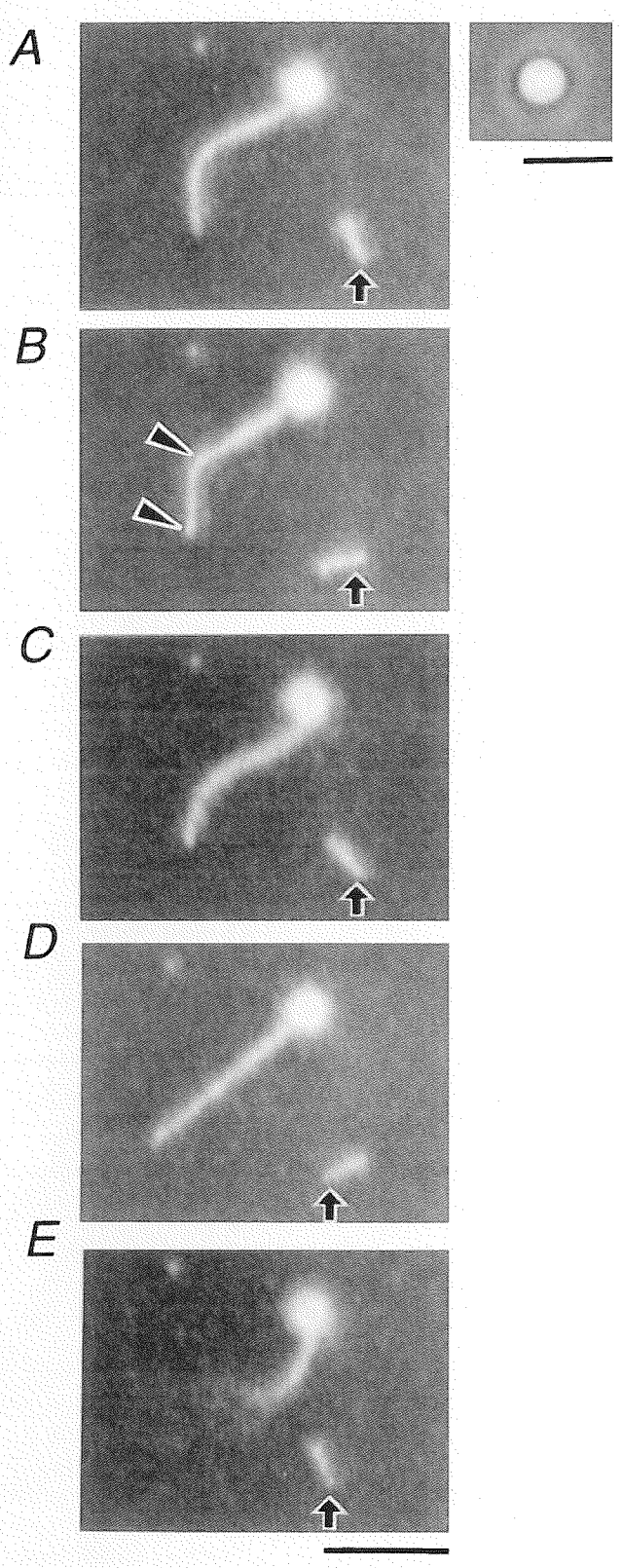

FIGURE 7 A series of fluorescence micrographs showing how to measure the lifetime of single rigor bond(s). (*A*) The bead attached to the B-end of an actin filament was trapped by optical tweezers. (*B*) The flow cell was moved (within 1/30 s) ~200 nm stepwise, using a piezoelectric substage, so that the actin filament was pulled taut from an HMM molecule (*arrowheads*). (*C*) After a while, the rigor bond was broken and the lifetime of the single rigor bond was measured. (*D*) The substage was moved further leftward and displaced stepwise again, such that the filament became nearly straight. (*E*) The filament was detached completely from the glass surface and showed Brownian motion. Note that a short actin filament, tethered to the glass surface through probably only one HMM molecule (indicated by an *arrow*), swiveled in each micrograph. Scale bar, 5 μm. (*upper right*) Phase-contrast image of the bead of *A–E*. Scale bar, 2 μm. The two images were simultaneously observed using the optics of Fig. 1.

dard deviation for events that stochastically occur N times. For S1, and for 9.0–12.0 pN and 12.0- pN of HMM, plots were approximated with the equation of a single exponential decay, $N(t) = N(0)\cdot\exp(-t/\tau)$, where τ is a lifetime of the rigor bond. Deviations of τ were estimated from fitted curves with maximum and minimum τ so as not to deviate from error bars by more than one data point in Fig. 9, and then they were expressed as error bars in Fig. 10. For 0.0–3.0, 3.0–6.0, and 6.0–9.0 pN of HMM, the data were approximated with the sum of two exponential decays, i.e., $N(t) = N_f(0)\cdot\exp(-t/\tau_f) + N_s(0)\cdot\exp(-t/\tau_s)$, where τ_f and τ_s are, respectively, a fast and a slow component of the lifetime, and $N_f(0) + N_s(0) = N_0$ is the total number of data at each region. After an optimum set of τ_f, τ_s, and $N_f(0)$ values was determined, deviations in τ_f and τ_s were independently estimated from fitted curves with maximum and minimum values so as not to deviate from the error bars of all data points. These maximum and minimum values of τ_f and τ_s were expressed as error bars in Fig. 10. The lifetimes thus obtained are summarized in Table 1.

Fig. 10 is a semilogarithmic plot of the data summarized in Table 1. As for the slow component of HMM, the relation between the lifetime, $\tau(F)$, and the imposed load, F, was closely approximated by the equation $\tau(F) = \tau(0)\cdot\exp(-F\cdot d/kT)$ (*thick solid line*). The relations for S1 and for the fast component of HMM were also approximated by this equation, as shown by a dashed line and a thin solid line, respectively. Note that the relation for S1 coincided with that for the fast component of HMM. From these approximation lines, d and $\tau(0)$ were estimated as summarized in Table 2.

DISCUSSION

Minimum number of HMM molecules needed to slide actin filaments continuously

The estimation of the number of myosin molecules interacting with an actin filament is essential for describing the sliding movement of an actin filament in an in vitro motility assay. Unlike myosin V (Mehta et al., 1999) or kinesin (Howard et al., 1989; Vale et al., 1996), the skeletal myosin (myosin II) molecule is not a processive motor, such that multiple motors are required for smooth and continuous

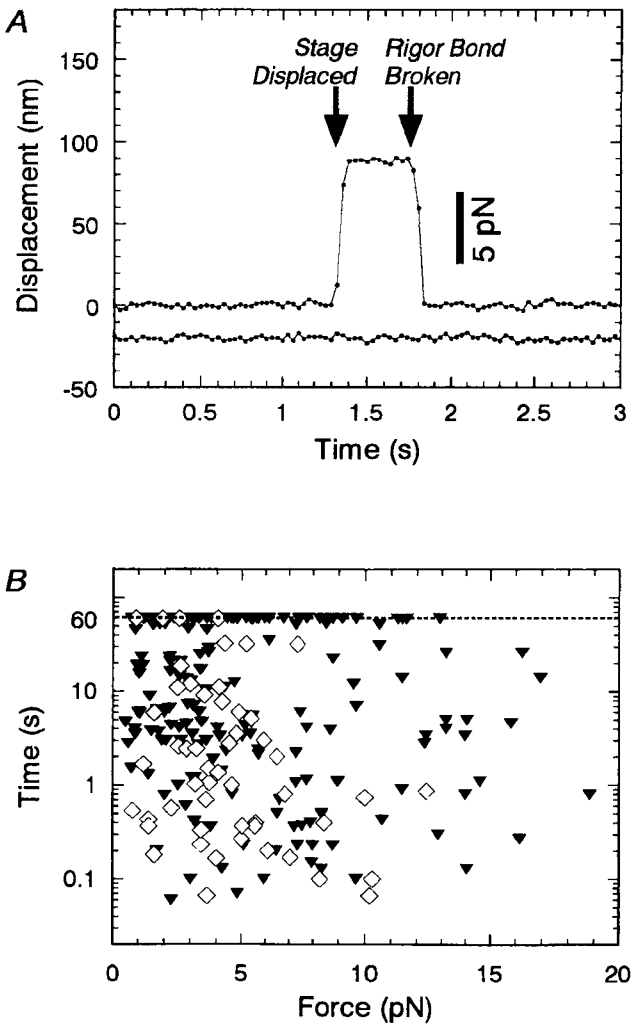

FIGURE 8 Load dependence of the lifetime of single rigor bonds (*A*) An example of the time course of the displacement of the bead (cf. Figs. 6 and 7). Upper and lower plots show, respectively, the displacement of the bead along and perpendicular to the actin filament. Each dot was plotted every 1/30 s. The stage was displaced stepwise at 1.3 s so as to impose a constant external load, and then the bond was broken after 0.43 s in this example. (*B*) Relationship between the imposed load and the lifetime of rigor bonds of HMM (▼) and S1 (◇). For the rigor bonds not broken within 60 s, the lifetimes are plotted on the dashed line indicating 60 s.

sliding of actin filaments without dissociation. Although we could not directly count the number of HMM molecules during the sliding movement, the number required for smooth sliding of an actin filament could be estimated from our results (Fig. 4). The lowest concentration of HMM required for continuous sliding motion of actin filaments was 30 μg/ml in our method, so that the minimum line density of HMM molecules is estimated to be 30 (μg/ml) $\times$ 0.21 (molecules/μm/(μg/ml)) = 6.3 (molecules/μm actin filament). Furthermore, the minimum length of the filament showing the sliding movement was ~1.4 μm under the same conditions. Thus we obtain the minimum number of molecules required for smooth sliding without dissociation, 6.3 (molecules/μm) $\times$ 1.4 (μm) = 8.8 (molecules).

We can assume that one ATP hydrolysis of the actomyosin system takes (10–100) ms, as in an in vitro motile system (Harada et al., 1990) and in solution (cf. Goldman, 1987). On the other hand, the probability that at least one myosin head binds to an actin filament is given by $P = 1 - \{(N - n)/N\}^N$, where N is the total number of myosin heads that can interact with the filament and n is the average number of heads that bind to the filament at one time. Therefore, $(1 - P) \times$ (10–100) ms is the dissociation period during which no myosin heads interact with the filament. The diffusion coefficient perpendicular to the filament axis for a 1.4-μm actin filament is calculated to be 1.4×10^{-8} cm^2/s from the equations $D = k_BT/\Gamma_\perp$ and $\Gamma_\perp = 4\pi\eta L/(\ln(L/2r) + \gamma_\perp)$, where L = 1.4 μm, r = 5 nm, η = 0.010 g/cm·s, $\gamma_\perp$ = 0.89 (Hunt et al., 1994) and T = 300 K. Thus the time required for actin filaments 1.4 μm long to diffuse as far as δx, ~17 nm (the size of myosin heads) to 34 nm (its doubled size), within which the filaments can maintain a sliding motion, is calculated to be 0.1–0.4 ms according to the equation $\delta x = (2Dt)^{1/2}$. To make $(1 - P) \times$ (10–100) ms shorter than 0.1–0.4 ms, P should be larger than 0.96–0.999. Together, n should be larger than 3.0–5.8 under N = 17.6 (= 8.8 $\times$ 2) heads to keep P as 0.96–0.999 ($1 - \{(N - n)/N\}^N = 1 - \{(17.6-3.0)/17.6\}^{17.6} > 0.96$, $1 - \{(17.6-5.8)/17.6\}^{17.6} > 0.999$), suggesting that at least (3.0–5.8)/17.6 $\cong$ 17–30% of myosin heads always bind to the filament during sliding motion. If all n heads are in a state of producing the active force, the value 17–30% corresponds to the "duty ratio," which is the proportion of the period in which a single head produces the force in one ATPase cycle. However, because some head is only capable of holding the filament without producing active force (Goldman, 1987; Ishiwata and Yasuda, 1993), 17–30% could be an overestimation of the duty ratio.

Torsional stiffness of a single HMM molecule

By analysis of the rotational Brownian motion of a short actin filament tethered to a single HMM molecule, the torsional stiffness has been estimated to be $(2.3 \pm 1.9) \times 10^{-22}$ N·m/rad. The flexible part responsible for this small stiffness must be located at the joint between the S1 and S2 regions, and/or within the S2 region of the HMM molecule (Kinosita et al., 1984; Ishiwata et al., 1987, 1988). Note that this stiffness is so small that the thermal fluctuation energy, k_BT (4.1×10^{-21} N·m), can twist myosin 2.8 times ($(4.1 \times 10^{-21})/(2.3 \times 10^{-22})/2\pi = 2.8$). This small stiffness can explain the following mechanical properties of myosin previously reported: myosin can interact with an actin filament under various orientations (Toyoshima et al., 1989; Molloy et al., 1995), although it modifies the motor functions, such as the sliding velocity and force (Yamada et al., 1990; Sellers and Kachar, 1990; Ishijima et al., 1996). The unbinding

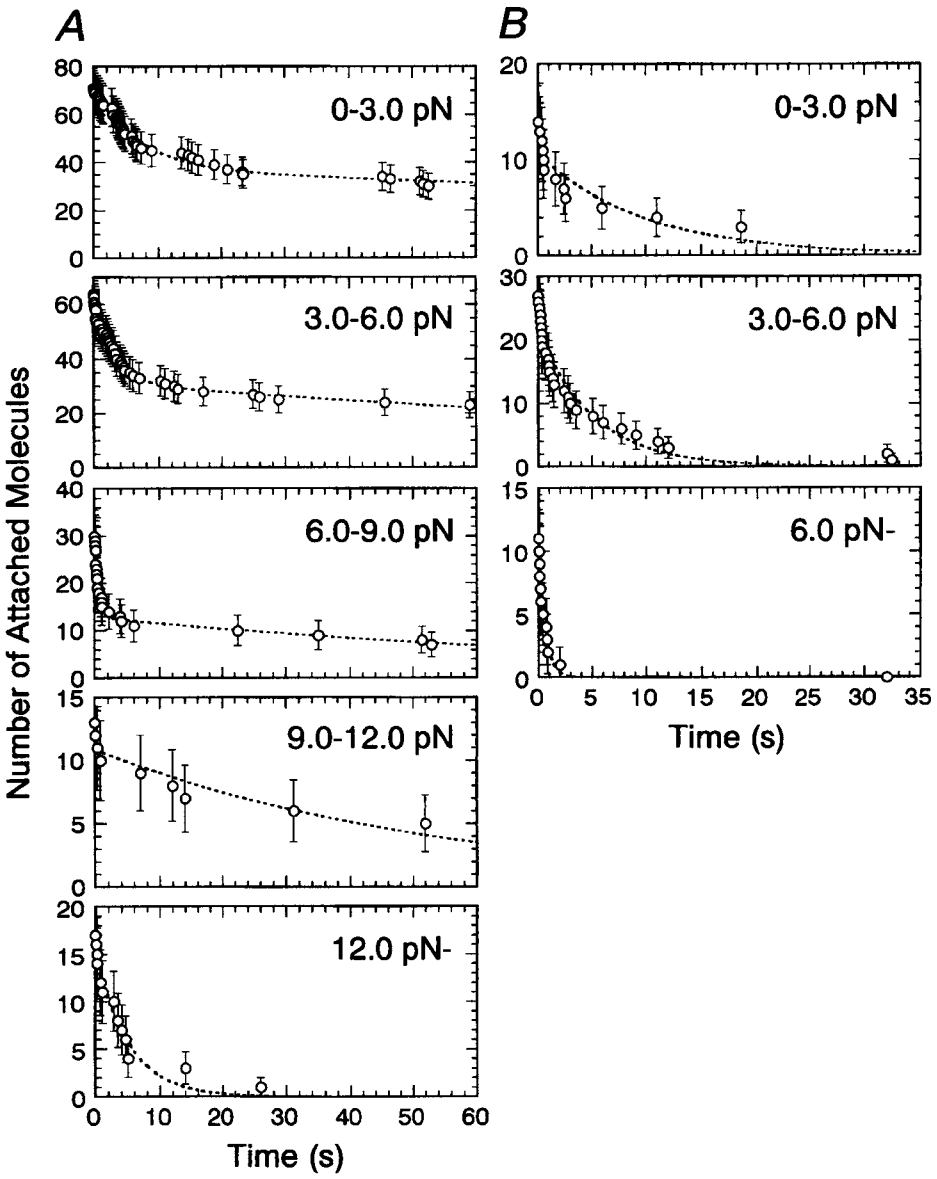

FIGURE 9 Time course of the decrease in the number of attached molecules, N, under various imposed loads, replotted from the data of Fig. 8 *B*. Error bars show standard deviation, which is simply determined as the square of the number of measurements at each point ($\pm N^{1/2}$). (*A*) HMM. Dashed lines indicate the approximation by $N(t) = N(0)\cdot\exp(-t/\tau)$ or $N(t) = N_f(0)\cdot\exp(-t/\tau_f) + N_s(0)\cdot\exp(-t/\tau_s)$ (for details see Results). (*B*) S1. Dashed lines indicate the approximation by $N(t) = N(0)\cdot\exp(-t/\tau)$.

force of rigor bonds is independent of the direction of external load, at least within ±90° (Nishizaka et al., 1995b). Because of the small stiffness, the geometrical relationship of the actin-myosin binding interface is probably maintained.

As for kinesin, the stiffness was estimated to be 1.2×10^{-22} N·m/rad by observing the rotational Brownian motion of an attached microtubule (Hunt and Howard, 1993), which is comparable to that of HMM. Thus such a small torsional stiffness may be common to motor proteins. Surprisingly, kinesin could be twisted more than 30 times by manipulation with optical tweezers without breaking the bond between kinesin and a microtubule (Kuo et al., 1995). This result may not be explainable by twisting of a head-rod junction; thus we alternatively assume that detachment and reattachment occur on one head while the other head binds to a filament. The twisting distortion in the attached head will be released during unbinding, and then the head can bind again without large distortion. If the two heads repeat this process alternately, the filament can rotate in one direction without limitation. We favor this model as an explanation of how protein can rotate more than 30 times without dissociation. If this process also occurred in our actin-HMM complex, the estimated value is an underestimation as a torsional stiffness of single HMM molecules.

Load dependence of lifetime of rigor bonds and binding manner of HMM

In our previous study, we repeatedly measured the load dependence of the lifetime of rigor bonds on the same

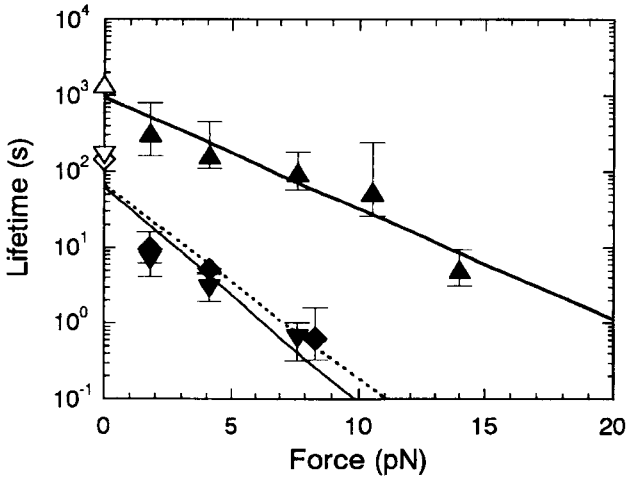

FIGURE 10 Relation between imposed load and lifetime of HMM and S1 rigor bonds. Triangles and inverted triangles show the slow and fast components of HMM, respectively Squares show the lifetime of S1. Filled symbols were determined from Fig. 9, and open symbols are experimental data obtained without load (Tadakuma et al., manuscript in preparation). Fitted lines show the approximation by the equation $\tau(F) = \tau(0)\cdot\exp(-F\cdot d/k_BT)$. The thick and thin solid lines show the approximation of slow and fast components of HMM, respectively. The dashed line shows the approximation for S1.

acto-HMM rigor complexes (figure 4 in Nishizaka et al., 1995b). In the present study, we improved the mechanical stability of the microscopy apparatus to realize more accurate measurements, especially for longer times. As a result, the spatial resolution became less than 1 nm, and the drifting movement of the stage was restricted to within ~2 nm for 1 min. Such an improvement was essential for quantitatively investigating the relationship between the lifetime and the load.

TABLE 1 Lifetimes of HMM and S1 rigor bonds estimated from the approximation with exponential decay shown in Fig. 9

Load (pN)	Ratio, fast/total	Lifetime (s) τ_f	Lifetime (s) τ_s
A HMM			
No load	(0.41)	(170)	(1400)
0–3	0.47	6.9	320
3–6	0.51	2.9	160
6–9	0.57	0.64	97
9–12	—	—	53
12+	—	—	5.1
	Lifetime (s)		
B. S1			
No load	(150)		
0–3	9 9		
3–6	5.2		
6–9	0.63		

The data were approximated by the equation of single exponential decay, $N(t) = N(0)\cdot\exp(-t/\tau)$, or the sum of two exponential decays, $N_f(0)\cdot\exp(-t/\tau_f) + N_s(0)\cdot\exp(-t/\tau_s)$. Ratio, $N_f(0)/(N_f(0) + N_s(0))$, means the proportion of cross-bridges having the fast component. Both ratio and lifetimes without load shown in parentheses were determined by the microscopic observation of spontaneous detachment from a glass surface of swiveling short actin filaments (Tadakuma et al., manuscript in preparation)

TABLE 2 Interaction distance, d, and lifetime without external load, $\tau(0)$, for, respectively, single rigor bonds of HMM and S1, estimated from the slope and the extrapolation of the solid and dashed lines in Fig. 10

	d	$\tau(0)$
HMM (fast)	2.7	62
HMM (slow)	1.4	950
S1	2.4	67

We found that the time course of the decrease in the number of attached S1 molecules under an external load nearly followed a single exponential decay (Fig. 9 *B*). In contrast, the decay for HMM was not expressed by a single exponential, except for a large applied force (Fig. 9 *A*), but could be approximated by the sum of two exponentials with different lifetimes. As shown in Table 1, *A* and *B*, the fast component of the lifetime of HMM nearly coincided with the lifetime of S1. One plausible explanation for this result is that HMM molecules that attached to the glass surface are classified into two groups: one having the slow component of lifetimes in which double-headed binding occurs, and another having the fast component in which only single-headed binding is possible, probably because of the adsorption of either head to the glass surface. This explanation will be examined in the future by using single-headed myosin (Harada et al., 1987) or single-headed HMM. The ratio between single-headed and double-headed molecules in our HMM assay is estimated to be nearly 1:1 (Table 1 *A*). We previously suggested the presence of "molecular individualism" in each HMM, based on the fact that each HMM molecule showed the individual load dependence of the lifetime (Nishizaka et al., 1995b). The difference in the number of active heads may be the main reason for this "individuality."

The lifetime, τ, is generally related to the activation energy for unbinding, $\Delta G^{\ddagger}$, through $\tau \propto \exp(\Delta G^{\ddagger}/k_BT)$. This could be extended to a fundamental property of the binding between a ligand and a receptor under an external load, i.e., $\tau(F) = \tau_0\cdot\exp((\Delta G^{\ddagger} - F\cdot d)/k_BT) = \tau(0)\cdot\exp(-F\cdot d/k_BT)$, where $\tau(F)$ is the lifetime under the load F and d is defined as the distance of an intermolecular interaction beyond which the intermolecular bond is ruptured (Bell, 1978; Erickson, 1994). The value of d is generally assumed to be less than a nanometer. Note that even though there is no load, the intermolecular bonds in an aqueous solution break with a lifetime of $\tau(0)$ in a stochastic manner under thermal equilibrium. This aspect is essential for understanding the unbinding force of the bond between proteins. The unbinding force between proteins was previously estimated to be

larger than 100 pN (Kishino and Yanagida, 1988; Florin et al., 1994; Tsuda et al., 1996; Fritz et al., 1998); however, it has been predicted that these values depend on the rate of the increase in the applied load. The unbinding force could be smaller when the external load is applied slowly, e.g., at a rate comparable to the dissociation rate constant. This was confirmed for actin-HMM rigor complex (cf. Fig. 4 in Nishizaka et al., (1995b)) and for avidin-biotin complex: the unbinding force increases from several piconewtons to hundreds of piconewtons as the velocity is increased by 10^6 (Merkel et al., 1999). In the case of P-selectin, the unbinding force was confirmed to increase logarithmically with the increase in the pulling velocities of ligand against receptor (figure 5 in Fritz et al., 1998). Thus the difference in the pulling velocity is considered to be the main reason why the average unbinding force of actin-HMM rigor complex obtained by AFM (Nakajima et al., 1997), ~14 pN, was larger than that obtained with optical tweezers (Nishizaka et al., 1995b), ~9 pN.

The exponential dependence of lifetime on the external load, which was predicted before (Bell, 1978; Erickson, 1994), fits well with our results as shown in Fig. 10. From the slope of the straight lines in Fig. 10, we obtained the values of d: 1.4 nm for the slow component of HMM, 2.7 nm for the fast component of HMM, and 2.4 nm for S1 (Table 2). The value of d for slow HMM components, which corresponds to the double-headed binding, was nearly one-half of those of d for fast HMM components, corresponding to the single-headed binding, and for S1. This difference by a factor of 2 suggests that the external load (F) is evenly shared on each attached head of HMM, such that the external load imposed on each head effectively becomes a half. This suggests that d for the interaction between single-head myosin and actin is ~2.5 nm.

It is expected that the large d value is attributable to the geometry of application of an external load. In fact, regarding the interaction between actin monomers in a filamentous actin, the tensile strength depends on the direction of the applied load to the molecular interface. Tsuda et al. (1996) reported that 600 pN was required for the breakage of the actin filament by straight pull, whereas Arai et al. (1999) reported that the actin filament broke when they applied 1 pN after tying a knot in it. In both measurements, the process of unbinding was observed at a video rate, so that the duration required for breakage was similar. Thus the apparent value of d for the latter may be an order of magnitude larger than that for the former.

In our system, the load was always imposed toward the long axis of an actin filament. The value of d could be decreased when the external load is applied in the direction parallel to the coordinate axis of the interaction potential, which may usually be the direction perpendicular to the intermolecular interface. The proposed structure of myosin head is longitudinally thin, and the actin-binding site is not located at the tip of the head but relatively at the side of the catalytic domain of the head, such that myosin heads bind to an actin filament at an acute angle (Rayment et al., 1993a,b). As a result, the myosin is being pulled from an angle, which would tend to tilt it out of the interface rather than pulling it out perpendicularly. The applied load could induce the distortion of the myosin head around the binding interface, then the activation energy for unbinding is efficiently decreased by a small load, as shown in Fig. 10, which results in the large value of d. In contrast, in the case of avidin-biotin unbinding force measurement by AFM (Florin et al., 1994; Moy et al., 1994), a symmetrical avidin molecule was sandwiched between an AFM cantilever and an agarose bead that was biotinylated (the 50-μm-diameter agarose bead versus the 6-nm-diameter avidin). It is expected that the load was imposed nearly perpendicularly to the interface of the avidin-biotin bond (Grubmuller et al., 1996; Evans and Ritchie, 1997; Izrailev et al., 1997), so that the small value of d was obtained.

X-ray crystallography showed that the myosin head consists of two domains, i.e., a catalytic domain that contains ATP- and actin-binding sites, and a neck domain. One possible hypothesis for how myosin heads generate force is that the neck domain tilts against the catalytic domain like a lever arm and induces a power stroke accompanied by the release of P_i (Rayment et al., 1993a,b; Corrie et al., 1999; Taylor et al., 1999). This structural dynamic is thought to be coupled with the change in the binding affinity between the myosin head and actin (Goldman and Brenner, 1987), although this hypothesis seems to have difficulty explaining the results showing their uncoupling (Ishijima et al., 1998) and multiple unitary displacements of single myosin head per ATP hydrolysis (Kitamura et al., 1999). In general, it is believed that the post-power stroke state has higher binding affinity for actin, and the pre-power stroke state has relatively lower affinity. In our experiments, the actin filament was always pulled in the direction of the reversal of the power stroke of myosin because the bead was attached to the B-end of an actin filament. In other words, we imposed the load so as to change the state of myosin from a post-power stroke state to a pre-power stroke state. If the structure of the myosin head changes from a high-affinity form to a low-affinity form with the application of an external load, the unbinding that occurs very efficiently with an imposed load can also be explained by this mechanism. In this relation, the following experiment is interesting: measurement of the lifetime by pushing the myosin head, which is in the pre-power stroke state with ATP analogs, toward the post-power stroke state along the direction of the power stroke. In this case, the lifetime may become longer because of the transition from the low-affinity state to the high-affinity state.

Finally, we would like to point out that the geometry for applying an external load in our system is similar to that in muscle fibers. The gradual change in the binding affinity, which is assumed in the Huxley and Simmons model (Hux-

ley and Simmons, 1971), may accompany the change in the number of intermolecular bonds at the actomyosin interface. Thus a large value of d may be a feature common to motor proteins.

We thank Drs. Naoya Suzuki, Hidetake Miyata, Ichiro Sase, and Ryohei Yasuda of Keio University and Mr. Madoka Suzuki of Waseda University for their technical support and advice. This research was partly supported by grants-in-aid for Scientific Research, for Scientific Research for Priority Areas, and for the High-Tech Research Center Project to SI from the Ministry of Education, Science, Sports and Culture of Japan, and by grants-in-aid from the Japan Science and Technology Corporation. TN was a Research Fellow of the Japan Society for the Promotion of Science.

REFERENCES

Arai, Y., R. Yasuda, K Akashi, Y. Harada, H. Miyata, K. Kinosita, Jr., and H. Itoh. 1999. Tying a molecular knot with optical tweezers. *Nature* 399:446–448.

Ashkin, A., J. M. Dziedzic, J. E. Bjorkholm, and S Chu. 1986. Observation of a single-beam gradient force optical trap for dielectric particles. *Optics Lett.* 11:288–290.

Ashkin, A., K Schutze, J. M. Dziedzic, U. Euteneuer, and M. Schliwa. 1990 Force generation of organelle transport measured in vivo by an infrared laser trap. *Nature.* 348.346–348.

Bell, G. I 1978. Models for the specific adhesion of cells to cells. *Science.* 200:618–627.

Corrie, J. E., B. D. Brandmeier, R. E. Ferguson, D. R. Trentham, J. Kendrick-Jones, S. C. Hopkins, U. A. van der Heide, Y. E. Goldman, C. Sabido-David, R. E. Dale, S. Criddle, and M. Irving. 1999. Dynamic measurement of myosin light-chain-domain tilt and twist in muscle contraction. *Nature.* 400:425–430.

Erickson, H. P. 1994. Reversible unfolding of fibronectin type III and immunoglobulin domains provides the structural basis for stretch and elasticity of titin and fibronectin. *Proc. Natl. Acad. Sci. USA.* 91: 10114–10118.

Evans, E., and K. Ritchie. 1997 Dynamic strength of molecular adhesion bonds. *Biophys. J.* 72:1541–1555.

Finer, J. T., R. M. Simmons, and J. A. Spudich. 1994. Single myosin molecule mechanics: piconewton forces and nanometre steps. *Nature.* 368.113–119.

Florin, E. L., V. T. Moy, and H. E. Gaub. 1994. Adhesion forces between individual ligand-receptor pairs. *Science.* 264:415–417

Fritz, J., A. G. Katopodis, F. Kolbinger, and D. Anselmetti. 1998 Force-mediated kinetics of single P-selectin/ligand complexes observed by atomic force microscopy. *Proc. Natl. Acad. Sci. USA.* 95:12283–12288.

Funatsu, T., Y. Harada, M. Tokunaga, K. Saito, and T. Yanagida. 1995. Imaging of single fluorescent molecules and individual ATP turnovers by single myosin molecules in aqueous solution. *Nature.* 374:555–559

Goldman, Y. E. 1987. Kinetics of the actomyosin ATPase in muscle fibers. *Annu. Rev. Physiol.* 49.637–654.

Goldman, Y. E., and B. Brenner. 1987. Special topic. molecular mechanism of muscle contraction. General introduction. *Annu. Rev. Physiol.* 49:629–636.

Grubmuller, H., B. Heymann, and P. Tavan. 1996. Ligand binding: molecular mechanics calculation of the streptavidin-biotin rupture force. *Science.* 271:997–999.

Harada, Y., A. Noguchi, A. Kishino, and T. Yanagida. 1987. Sliding movement of single actin filaments on one-headed myosin filaments. *Nature* 326:805–808.

Harada, Y., K. Sakurada, T. Aoki, D. D. Thomas, and T. Yanagida. 1990. Mechanochemical coupling in actomyosin energy transduction studied by in vitro movement assay. *J Mol. Biol.* 216:49–68.

Howard, J., A. J. Hudspeth, and R. D. Vale. 1989. Movement of microtubules by single kinesin molecules. *Nature.* 342:154–158.

Hunt, A. J., F. Gittes, and J. Howard. 1994. The force exerted by a single kinesin molecule against a viscous load. *Biophys. J.* 67:766–781.

Hunt, A. J., and J. Howard. 1993. Kinesin swivels to permit microtubule movement in any direction. *Proc. Natl. Acad. Sci. USA.* 90: 11653–11657.

Huxley, A. F., and R. M. Simmons. 1971. Proposed mechanism of force generation in striated muscle. *Nature.* 233:533–538.

Ishijima, A., Y. Harada, H. Kojima, T. Funatsu, H. Higuchi, and T. Yanagida. 1994. Single-molecule analysis of the actomyosin motor using nano-manipulation. *Biochem. Biophys. Res. Commun.* 199: 1057–1063.

Ishijima, A., H. Kojima, T. Funatsu, M. Tokunaga, H Higuchi, H. Tanaka, and T. Yanagida. 1998. Simultaneous observation of individual ATPase and mechanical events by a single myosin molecule during interaction with actin. *Cell.* 92:161–171.

Ishijima, A., H. Kojima, H. Higuchi, Y. Harada, T. Funatsu, and T. Yanagida. 1996. Multiple- and single-molecule analysis of the actomyosin motor by nanometer-piconewton manipulation with a microneedle: unitary steps and forces. *Biophys. J.* 70:383–400.

Ishiwata, S., K. Kinosita, Jr., H. Yoshimura, and A. Ikegami. 1987. Rotational motions of myosin heads in myofibril studied by phosphorescence anisotropy decay measurements. *J. Biol. Chem.* 262: 8314–8317.

Ishiwata, S., K. Kinosita, Jr., H. Yoshimura, and A. Ikegami. 1988. Optical anisotropy decay studies of the dynamic structure of myosin filaments. *Adv. Exp. Med. Biol.* 226:267–276.

Ishiwata, S., and K. Yasuda. 1993. Mechano-chemical coupling in spontaneous oscillatory contraction of muscle. *Phase Transitions.* 45: 105–136.

Izrailev, S., S. Stepaniants, M. Balsera, Y. Oono, and K. Schulten 1997 Molecular dynamics study of unbinding of the avidin-biotin complex *Biophys. J* 72:1568–1581.

Kamimura, S., and K. Takahashi. 1981. Direct measurement of the force of microtubule sliding in flagella. *Nature.* 293:566–568.

Kinosita, K., Jr., S Ishiwata, H. Yoshimura, H. Asai, and A. Ikegami. 1984. Submicrosecond and microsecond rotational motions of myosin head in solution and in myosin synthetic filaments as revealed by time-resolved optical anisotropy decay measurements. *Biochemistry.* 23:5963–5975.

Kinosita, K., Jr., H. Itoh, S. Ishiwata, K. Hirano, T. Nishizaka, and T. Hayakawa. 1991. Dual-view microscopy with a single camera: real-time imaging of molecular orientations and calcium. *J. Cell Biol.* 115:67–73.

Kinosita, K., Jr., R. Yasuda, H. Noji, S. Ishiwata, and M. Yoshida. 1998. F_1-ATPase: a rotary motor made of a single molecule *Cell.* 93.21–24.

Kishino, A., and T. Yanagida. 1988. Force measurements by micromanipulation of a single actin filament by glass needles. *Nature* 334·74–76.

Kitamura, K , M. Tokunaga, A. H. Iwane, and T. Yanagida. 1999. A single myosin head moves along an actin filament with regular steps of 5.3 nanometres. *Nature.* 397:129–134.

Kondo, H., and S. Ishiwata. 1976. Uni-directional growth of F-actin. *J. Biochem.* 79:159–171.

Kuo, S. C., K Ramanathan, and B. Sorg. 1995. Single kinesin molecules stressed with optical tweezers. *Biophys. J.* 68:74s.

Kurokawa, H., W. Fujii, K. Ohmi, T. Sakurai, and Y. Nonomura. 1990. Simple and rapid purification of brevin. *Biochem. Biophys. Res. Commun.* 168:451–457.

Marston, S. B. 1982 The rates of formation and dissociation of actin-myosin complexes. Effects of solvent, temperature, nucleotide binding and head-head interactions. *Biochem. J.* 203:453–460.

Mehta, A. D., R. S. Rock, M. Rief, J. A. Spudich, M. S. Mooseker, and R. E. Cheney. 1999. Myosin-V is a processive actin-based motor. *Nature.* 400:590–593.

Merkel, R., P. Nassoy, A. Leung, K. Ritchie, and E. Evans. 1999. Energy landscapes of receptor-ligand bonds explored with dynamic force spectroscopy. *Nature.* 397:50–53.

Miyata, H., H. Hakozaki, H. Yoshikawa, N. Suzuki, K. Kinosita Jr, T. Nishizaka, and S. Ishiwata. 1994. Stepwise motion of an actin filament

over a small number of heavy meromyosin molecules is revealed in an in vitro motility assay *J Biochem.* 115:644–647.

Miyata, H , H. Yoshikawa, H. Hakozaki, N. Suzuki, T. Furuno, A. Ikegami, K. Kinosita, Jr., T. Nishizaka, and S. Ishiwata. 1995. Mechanical measurements of single actomyosin motor force. *Biophys. J.* 68:286s–290s.

Molloy, J. E , J. E. Burns, J. Kendrick-Jones, R. T. Tregear, and D. C. White 1995 Movement and force produced by a single myosin head. *Nature.* 378:209–212.

Moy, V. T., E. L. Florin, and H. E. Gaub. 1994. Intermolecular forces and energies between ligands and receptors. *Science.* 266:257–259.

Nakajima, H., Y. Kunioka, K. Nakano, K. Shimizu, M Seto, and T. Ando 1997. Scanning force microscopy of the interaction events between a single molecule of heavy meromyosin and actin *Biochem. Biophys. Res. Commun.* 234:178–182.

Nishizaka, T., H Miyata, H. Yoshikawa, S. Ishiwata, and K. Kinosita, Jr. 1995a. Mechanical properties of single protein motor of muscle studied by optical tweezers. *Biophys. J* 68:75s.

Nishizaka, T., H. Miyata, H. Yoshikawa, S. Ishiwata, and K. Kinosita, Jr. 1995b. Unbinding force of a single motor molecule of muscle measured using optical tweezers. *Nature.* 377:251–254.

Nishizaka, T., Q. Shi, and M. P. Sheetz. 2000. Position dependent linkages of fibronectin-integrin-cytoskeleton. *Proc. Natl. Acad Sci. USA.* 97: 692–697.

Nishizaka, T., T. Yagi, Y. Tanaka, and S. Ishiwata. 1993 Right-handed rotation of an actin filament in an in vitro motile system. *Nature* 361:269–271.

Noji, H., R. Yasuda, M. Yoshida, and K. Kinosita, Jr. 1997. Direct observation of the rotation of F_1-ATPase. *Nature.* 386:299–302.

Rayment, I., H. M. Holden, M. Whittaker, C B. Yohn, M. Lorenz, K. C. Holmes, and R. A. Milligan. 1993a. Structure of the actin-myosin complex and its implications for muscle contraction. *Science.* 261: 58–65.

Rayment, I., W. R Rypniewski, K. Schmidt-Base, R. Smith, D. R. Tomchick, M. M. Benning, D. A. Winkelmann, G. Wesenberg, and H. M. Holden. 1993b Three-dimensional structure of myosin subfragment-1: a molecular motor *Science.* 261:50–58.

Sase, I., H. Miyata, J. E. Corrie, J. S. Craik, and K. Kinosita, Jr. 1995a. Real time imaging of single fluorophores on moving actin with an epifluorescence microscope. *Biophys. J.* 69:323–328.

Sase, I , H. Miyata, S. Ishiwata, and K. Kinosita, Jr. 1997. Axial rotation of sliding actin filaments revealed by single- fluorophore imaging *Proc. Natl. Acad. Sci. USA.* 94:5646–5650.

Sase, I., T. Okinaga, M. Hoshi, G. W. Feigenson, and K Kinosita, Jr. 1995b. Regulatory mechanisms of the acrosome reaction revealed by multiview microscopy of single starfish sperm. *J. Cell Biol.* 131: 963–973.

Sellers, J. R., and B. Kachar. 1990. Polarity and velocity of sliding filaments· control of direction by actin and of speed by myosin. *Science.* 249.406–408.

Suzuki, N., H. Miyata, S. Ishiwata, and K. Kinosita, Jr. 1996. Preparation of bead-tailed actin filaments· estimation of the torque produced by the sliding force in an in vitro motility assay. *Biophys. J* 70:401–408.

Svoboda, K., C. F. Schmidt, B. J. Schnapp, and S. M. Block. 1993. Direct observation of kinesin stepping by optical trapping interferometry. *Nature.* 365:721–727.

Taylor, K A , H. Schmitz, M. C Reedy, Y. E. Goldman, C. Franzini-Armstrong, H. Sasaki, R T. Tregear, K. Poole, C Lucaveche, R. J. Edwards, L. F. Chen, H. Winkler, and M. K. Reedy. 1999 Tomographic 3D reconstruction of quick-frozen, Ca^{2+}-activated contracting insect flight muscle. *Cell.* 99:421–431

Toyoshima, Y. Y., S. J. Kron, E. M. McNally, K. R. Niebling, C. Toyoshima, and J. A. Spudich. 1987 Myosin subfragment-1 is sufficient to move actin filaments in vitro. *Nature.* 328:536–539.

Toyoshima, Y. Y., C. Toyoshima, and J. A. Spudich. 1989 Bidirectional movement of actin filaments along tracks of myosin heads. *Nature.* 341:154–156.

Tsuda, Y., H. Yasutake, A. Ishijima, and T. Yanagida. 1996 Torsional rigidity of single actin filaments and actin-actin bond breaking force under torsion measured directly by in vitro micromanipulation. *Proc. Natl. Acad. Sci. USA.* 93 12937–12942.

Vale, R. D., T. Funatsu, D. W Pierce, L. Romberg, Y. Harada, and T. Yanagida. 1996. Direct observation of single kinesin molecules moving along microtubules. *Nature.* 380:451–453.

Yamada, A., N. Ishii, and K. Takahashi. 1990. Direction and speed of actin filaments moving along thick filaments isolated from molluscan smooth muscle. *J. Biochem.* 108:341–343.

Yanagida, T., M. Nakase, K. Nishiyama, and F. Oosawa. 1984. Direct observation of motion of single F-actin filaments in the presence of myosin. *Nature.* 307:58–60.

Yasuda, R., H. Noji, K. Kinosita, Jr., and M. Yoshida. 1998. F_1-ATPase is a highly efficient molecular motor that rotates with discrete 120° steps. *Cell.* 93:1117–1124.

THE JOURNAL OF BIOLOGICAL CHEMISTRY
Vol 275, No. 19, Issue of May 12, pp 14260–14263, 2000
Printed in U S A

The Role of the DELSEED Motif of the β Subunit in Rotation of F_1-ATPase*

Received for publication, January 20, 2000

Kiyotaka Y. Hara‡, Hiroyuki Noji§, Dirk Bald§, Ryohei Yasuda§, Kazuhiko Kinosita, Jr.§¶, and Masasuke Yoshida§‖

From the Chemical Resources Laboratory, R-1, Tokyo Institute of Technology, Nagatsuta 4259, Yokohama 226-8503, Japan, §CREST (Core Research for Evolutional Science and Technology) Genetic Programming Team 13, Teikyo University, Biotechnology Research Center 3F, Nogawa 907, Miyamae-ku, Kawasaki 216-000, Japan, and the ¶Department of Physics, Faculty of Science and Technology, Keio University, Yokohama 223-8522, Japan

F_1-ATPase is a rotary motor protein, and ATP hydrolysis generates torque at the interface between the γ subunit, a rotor shaft, and the $\alpha_3\beta_3$ substructure, a stator ring. The region of conserved acidic "DELSEED" motif of the β subunit has a contact with γ subunit and has been assumed to be involved in torque generation. Using the thermophilic $\alpha_3\beta_3\gamma$ complex in which the corresponding sequence is DELSDED, we replaced each residue and all five acidic residues in this sequence with alanine. In addition, each of two conserved residues at the counterpart contact position of γ subunit was also replaced. Surprisingly, all of these mutants rotated with as much torque as the wild-type. We conclude that side chains of the DELSEED motif of the β subunit do not have a direct role in torque generation.

F_1, together with the membrane-embedded proton-conducting unit F_0, forms the F_0F_1-ATP synthase that reversibly couples transmembrane proton flow to ATP synthesis/hydrolysis (1–6). Isolated F_1 has ATP-hydrolyzing activity, F_1-ATPase, and has a subunit structure $\alpha_3\beta_3\gamma\delta\epsilon$ in which the central γ subunit with coiled-coil structure is surrounded by the $\alpha_3\beta_3$ hexagonal ring structure (7). The α and β subunits have amino acid sequences homologous with each other, a similar folding topology, and noncatalytic and catalytic nucleotide binding sites, respectively. F_1 is by itself a rotary motor molecule. Using the $\alpha_3\beta_3\gamma$ complex, a minimum stable ATPase-active complex of F_1 from thermophilic *Bacillus* PS3 (TF_1)[1] (8–10), rotation of the γ subunit relative to the $\alpha_3\beta_3$ ring was visualized under an optical microscope as rotation of a fluorescent actin filament attached to the γ subunit of the immobilized $\alpha_3\beta_3\gamma$ complex (11). The torque of the rotation is invariably ~40 pN·nm for actin filaments with various lengths, and at low ATP concentrations, rotation driven by a single ATP hydrolysis was observed as a discrete 120° step (12).

Since the rotation of the γ subunit was established (11–18), the mechanism of how ATP hydrolysis on the β subunits drives rotation of the γ subunit has attracted keen interest. It is obvious that torque should be generated at the interface between the γ subunit and the $\alpha_3\beta_3$ ring. In the crystal structure of F_1 from bovine mitochondria (MF_1), three β subunits are in different states; one β (β_{TP}) has an ATP analog, Mg-AMP-PNP, at its catalytic site, another β (β_{DP}) has Mg-ADP, the third β_E has none. The structures of β_{TP} and β_{DP} are very similar to each other and they are in the "closed" conformation, in which the carboxyl-terminal helical domain is lifted close to the nucleotide binding domain and in contact with the γ subunit. In contrast, β_E adopts the "open" conformation, in which the crevice for substrate binding is open and the carboxyl-terminal domain is apart from the γ subunit. It was shown that this structure of F_1, characterized by two closed and one open β subunits, is generated as intermediate(s) during the catalytic cycle (19, 20). It seems plausible that the dynamic open-closed motion of the carboxyl-terminal domain of the β subunit caused by the binding of nucleotide may drive the rotation of the γ subunit.

The carboxyl-terminal domain of the β subunit contains the acidic cluster sequence, known as the DELSEED motif. This sequence has been well conserved in all F_1s with minor variations; for example, DELSDED in TF_1-β, DELSEED in MF_1-β, and DELSEED in the β subunit of F_1 from *Escherichia coli* (EF_1). In the closed conformation of the β subunit, this region has contact with the γ subunit. The counterpart contact region of the γ subunit is mainly in the short helix that forms a small protrusion from the straight coiled-coil structure (residues 81–98 in TF_1-γ, 73–90 in MF_1-γ, and 82–99 in EF_1-γ) (Fig. 1). Based on these facts, the β-DELSEED motif has been assumed to play an essential role in the rotation of the γ subunit and hence coupling between catalysis and transport (21). To examine this, we have replaced the DELSDED sequence of TF_1-β and the counterpart contact positions of TF_1-γ with alanine and observed the rotation as well as ATP hydrolysis.

EXPERIMENTAL PROCEDURES

Strains, Plasmids, and Proteins—E. coli strains used were JM109 (22) for preparation of plasmids, CJ236 (23) for generating uracil-containing single-stranded plasmid for site-directed mutagenesis, and JM103Δ (*uncB-uncC*) (24) for expression of the mutant $\alpha_3\beta_3\gamma$ complexes of TF_1. The uracil-containing single-stranded plasmid was generated from M13mp18 containing the inserted fragment encoding α(C193S), β(10H), and γ(S107C) in which αCys-193 was replaced with serine, a 10-histidine tag was attached to the amino terminus of the β subunit, and γSer-107 was replaced with cysteine (11). The expression plasmid for the $\alpha(C193S)_3\beta(10H)_3\gamma(S107C)$ complex was made by exchanging the fragment encoding the above subunits into the plasmid (pKAGB1) for the expression of wild-type $\alpha_3\beta_3\gamma$ complex (9). The mutations were introduced into the uracil-containing single-stranded plasmid by using

* This work was supported in part by grants from CREST (Core Research for Evolutional Science and Technology, Japan). The costs of publication of this article were defrayed in part by the payment of page charges. This article must therefore be hereby marked "*advertisement*" in accordance with 18 U.S.C. Section 1734 solely to indicate this fact.

‡ Supported by Fellowships of the Japan Society for the Promotion of Science for Young Scientists.

‖ To whom correspondence should be addressed. Fax: 81-45-924-5277; E-mail: myoshida@res.titech.ac.jp.

[1] The abbreviations used are; TF_1, F_1 from thermophilic *Bacillus* PS3; MF_1, F_1 from bovine heart mitochondria; EF_1, F_1 from *E. coli*; wt′ complex, a mutant $\alpha(C193S)_3\beta(10H)_3\gamma(S107C)$ complex of TF_1 used as a second wild-type complex for the rotation assays, the enzymatic characteristics are almost unchanged from the real wild-type $\alpha_3\beta_3\gamma$ complex; MOPS, 4-morpholinepropanesulfonic acid; AMP-PNP, adenosine 5′-(β,γ-imino)triphosphate.

TABLE I
Effect of mutations in the β-DELSDED sequence and counterpart residues of the γ subunit on ATP hydrolysis and torque value

Each value of ATP hydrolysis was the mean of three measurements. Torque values were determined from at least 10 continuously rotating actin filaments.

Mutation	ATP hydrolysis	Torque
	μmol/min/mg	*pN · nm*
wt′	27 ± 1	37 ± 2
βD390A	24 ± 1	27 ± 5
βE391A	5 ± 1	30 ± 4
βL392A	17 ± 3	34 ± 5
βS393A	19 ± 1	39 ± 4
βD394A	33 ± 6	43 ± 6
βE395A	27 ± 2	33 ± 6
βD396A	17 ± 2	37 ± 3
γL85A	13 ± 4	28 ± 5
γR95A	27 ± 3	28 ± 6
βAALSAAA	10 ± 0	34 ± 4

synthetic oligonucleotides. The *Mlu*I-*Pst*I fragment from the M13 plasmid was exchanged by that from the expression plasmid to generate mutants with replaced or deleted residues in the βDELSDED sequence. The mutants with replaced residues in γ-short helix were generated by exchanging the *Bgl*II-*Mlu*I fragment. The mutant $\alpha_3\beta_3\gamma$ complexes were purified as described previously (9).

ATPase Activity—ATPase activity was measured at 25 °C in the presence of an ATP-regenerating system in 10 mM MOPS-KOH (pH 7.0) buffer containing 50 mM KCl, 4 mM $MgCl_2$, 50 μg/ml pyruvate kinase, 50 μg/ml lactate dehydrogenase, 5 mM phosphoenolpyruvate, 0.2 mM NADH, and 2 mM ATP. The rate of ATP hydrolysis was determined between 3 and 13 s after addition of the enzyme.

Observation of Rotation—To observe the rotation of the γ subunit under a microscope, we fixed mutant $\alpha_3\beta_3\gamma$ complexes on a surface-bound bead (0.2 μm in diameter) through 10-histidine tags of the β subunits (12). A fluorescently labeled actin filament was attached to the γ subunit through streptavidin (11). The ATP concentration was fixed at 2 mM in an ATP-regenerating system containing 0.2 μg/ml creatine kinase and 2.5 mM creatine phosphate. Rotation was observed at 25 °C on an inverted fluorescence microscope (IX70, Olympus), and images were recorded with an ICCD camera (ICCD-350F, Video scope) on an 8-mm video tape. The rotation angle of the filament was estimated from the circular movement of the centroid of the filament image calculated using a software that we provided. The frictional torque for the rotation of the γ subunit is given, in the simplest approximation, by $(4\pi/3)\omega\eta[L_1^3/[\ln(L_1/2r) - 0.447] + L_2^3/[\ln(L_2/2r) - 0.447]]$. ω, the angular velocity; η, the viscosity of the medium (10^{-3} N·s·m^{-2}); L_1, L_2, the length from the center of rotation to the end of the actin filament; r (5 nm), the radius of the filament.

RESULTS AND DISCUSSION

Alanine Scanning Mutation in the βDELSDED Sequence—We generated seven mutant $\alpha_3\beta_3\gamma$ complexes of TF_1 in which residues in the βDELSDED sequence of the β subunits were individually replaced with alanine (alanine scanning mutation). The mutations were introduced into the wt′ complex, $\alpha(C193S)_3\beta(10H)_3\gamma(S107C)$, which we have routinely used for observation of rotation. As described (11), ATPase activity of the wt′ complex is nearly the same as that of the wild-type $\alpha_3\beta_3\gamma$ complex. ATPase activities at 2 mM ATP were examined for the mutants. Among seven mutants, only one mutant $\alpha_3\beta_3\gamma$ complex containing the E391A mutation in the β subunit (βE391A complex) showed significantly impaired ATPase activity, ~20% of that of the wt′ complex. The ATP-driven proton pumping activity of F_0F_1-ATP synthase reconstituted from the βE391A complex and other components was also impaired to a similar extent (data not shown). ATPase activities of other mutant complexes were less impaired or nearly intact (Table I). Next, rotation of the γ subunit, visualized by attached fluorescently labeled actin filaments, was examined at 2 mM ATP. All of the mutant complexes showed continuous rotation in a manner apparently indistinguishable from the rotation of the wt′ complex. As expected, the rotations were anti-clockwise when viewed from the membrane side. The calculated rotary torques of mutant complexes are all similar to that of the wt′ complex (Table I). As described (12), the apparent discrepancy between the decreased V_{max} values and the unaffected torque results from the difference in rates of catalytic turnover with or without load.[2] The results of the alanine scanning mutation described above indicate that no single residue in the βDELSDED sequence is essential for ATPase and rotation.

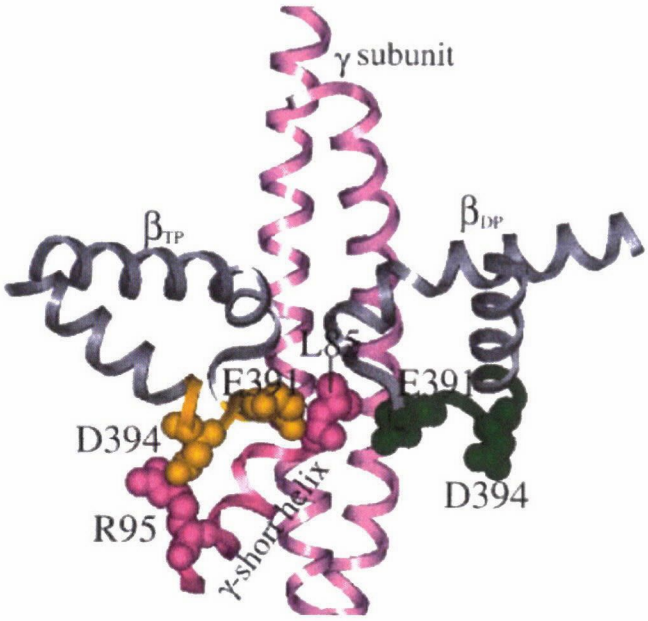

FIG. 1. **A model structure of the region around the βDELSDED sequence and the γ subunit of TF_1.** The model structure of TF_1 was generated from the crystal structure of MF_1 (7) using the software "Insight II." The βDELSDED sequences of the two β subunits in the closed conformation (β_{TP} and β_{DP}) are shown in *yellow* and *green*, respectively, and the rest of the peptide chains (374–417) of β_{TP} and β_{DP} are shown in *gray*. γ subunit is shown in *pink*. Side chains of βGlu-391, βAsp-394, γLeu-85, and γArg-95 (corresponding to βGlu-395, βGlu-398, γLeu-77, and γLys-87 in MF_1, respectively) are shown in space-filling atoms.

Mutants of the γ-Short Helix—Among the residues in the short helix of the γ subunit, γGly-84, γLeu-85, and γArg-95 are highly conserved in F_1s from various sources. As shown in the model structure of TF_1 (Fig. 1), βGlu-391 of β_{TP} and γLeu-85 interact with each other, and βAsp-394 of β_{TP} interacts directly with γArg-95. Biochemical data also support the close location of these residues; in EF_1, cysteine introduced at βGlu-391[3] was cross-linked readily with the intrinsic cysteine residue next to γLeu-85 (25). The alanine scanning mutations of the βDELSDED sequence described above, however, indicate that these interactions may not be critical for the catalysis and rotation. To confirm this indication, we replaced γGly-84, γLeu-85, and γArg-95 individually with alanine. The γG84A mutant did not form a stable $\alpha_3\beta_3\gamma$ complex and was expressed only as inclusion bodies. Therefore, γGly-84 appears to be essential to form the structure of the γ subunit required for stable interaction with the surrounding $\alpha_3\beta_3$ ring. The γL85A and γR95A mu-

[2] In rotation assay at high ATP concentrations, the maximum rate of rotation (and hence ATP hydrolysis) is limited by frictional load of filament rotation in the water. In the ATPase assay, the rate of ATP hydrolysis by free $\alpha_3\beta_3\gamma$ complex (without actin filament and without immobilization) is not limited by the frictional load but by the intrinsic catalytic nature of the enzyme. The change of maximum rotational rate of a 1-μm filament should become apparent only when the V_{max} of the mutant complex decreases to less than 10% of the V_{max} of the wt′ complex.

[3] Unless stated, numbering of the residues is according to TF_1.

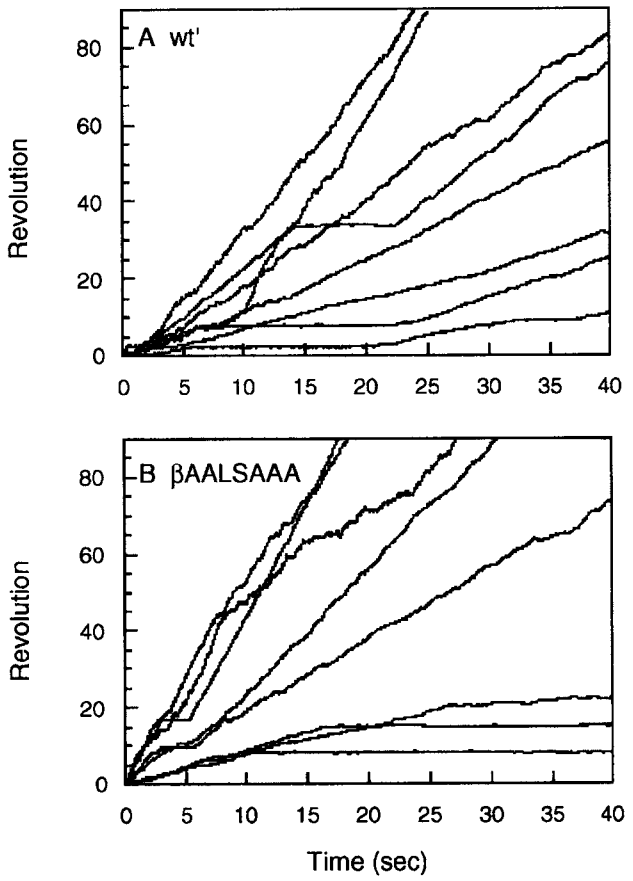

FIG. 2. **Time courses of rotation of the actin filaments attached to the γ subunit in the wt' complex and the βAALSAAA mutant complex.** The *ordinate* represents the number of anti-clockwise revolutions in the presence of 2 mM ATP. Each line represents one filament. The length of the filaments presented here is 1.0–2.5 μm. *A*, wt' complex; *B*, βAALSAAA mutant complex. Details of the experiments are described under "Experimental Procedures."

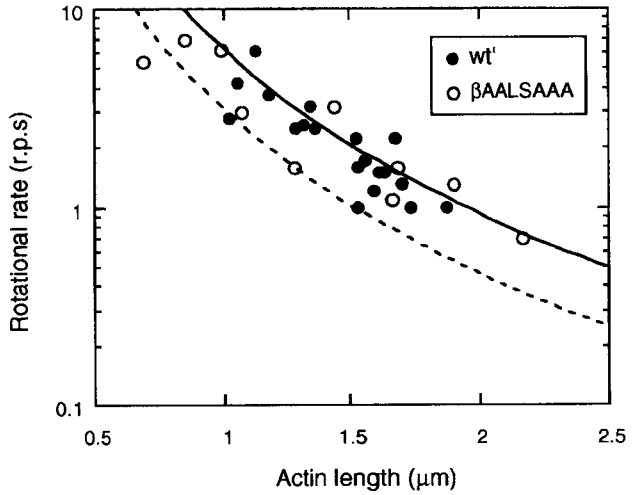

FIG. 3. **Rotational rate *versus* length of the actin filaments.** Rotational rates were estimated by least square linear fitting on the time courses for more than five revolutions and expressed in revolutions per s (*r.p.s.*). *Closed* and *open circles* indicate results of the wt' complex and βAALSAAA mutant complex, respectively. *Solid* and *dotted lines* represent the calculated rotational rate of the filaments with varying lengths, which gives a constant torque value of 40 and 20 pN·nm, respectively.

tants formed stable $\alpha_3\beta_3\gamma$ complexes. The ATPase activity of the γR95A complex was almost unaffected, but the activity of the γL85A complex decreased to about one-half that of the wt' complex (Table I). Nevertheless, torque generated by the γL85A and γR95A complexes was nearly equal to that by the wt' complex (Table I). Even though γLeu-85 and γArg-95 in the short helix of the γ subunit interact directly with the βDELSDED sequence, these interactions by themselves are not necessary for the function.

Elimination of All Negative Charges in the βDELSDED Sequence—Despite the above results, there is a possibility that the βDELSDED sequence plays an essential role for the torque generation, not through specific residue-residue interaction but as a cluster of negative charges. Then, a quintuple alanine mutant in which all five acidic residues in the βDELSDED sequence were replaced with alanines (βAALSAAA mutant) was expressed and purified as a stable $\alpha_3\beta_3\gamma$ complex. ATPase activity of the βAALSAAA complex decreased to 37% of that of the wt' complex, but this mutant complex still showed continuous rotation in a manner apparently indistinguishable from the rotation of the wt' complex (Fig. 2) and exerted rotational torque in normal range (Fig. 3). We also made βAALSDED, βDALSAED, and βDELSAAA mutant complexes, and the results were the same; they showed normal rotation (data not shown). Thus, the negative charge cluster in the βDELSDED sequence does not play an essential role in the rotation of the γ subunit.

Conclusion and Other Possibilities—Although the DELSEED motif is well conserved in all F_1s and has a direct contact with γ subunit, our results presented here indicate that the side chains of this motif do not contribute to the rotation of the γ subunit. This motif contains five acidic residues, and a negative charge cluster has been assumed to contribute to the catalysis (26). However, even a single negative charge is not necessary for the catalysis and rotation. Now several possibilities on the function of the DELSEED motif are worth examining. (i) A possibility should be considered that torque is generated at other β-γ intersubunit contact sites including the portions that have not been solved by x-ray crystallography. (ii) The function of the DELSEED motif could be a steric one; the helix-turn-helix structure including the DELSEED motif acts as a solid protruding "bar" that dynamically moves and pushes the short helix of the γ subunit through the physical contact but not through specific interactions between residues. The motion of the bar is caused by the open-closed motion of the β subunits. We tried to remove this bar by deleting whole DELSDED sequence of TF_1-β, but this mutant failed to assemble into $\alpha_3\beta_3\gamma$ complex. (iii) The role of the DELSEED motif in the enzyme function could be structural. A mutant in which all seven residues in the βDELSDED sequence were replaced with alanine did not assemble. Interestingly, addition of higher negative charge to this region destabilized the complex because a mutant, βDEEEDED, failed to assemble, and the mutant complexes were expressed as inclusion bodies. (iv) The conservation of the DELSEED motif implicates another role of this sequence. An amphipathic cationic reagent binds to this region and inactivates the ATPase activity (27). In EF_1, the ε subunit with cysteines introduced is cross-linked to the βE391C residues of two β subunits (28–30). Interaction with the ε subunit to regulate the catalysis is one of the possible functions of the DELSEED motif.

Acknowledgments—We thank T. Hisabori, E. Muneyuki, H. Taguchi, T. Matsui, T. Nishizaka, Y. Kato-Yamada, T. Suzuki, J. Suzuki, T. Masaike, S. P. Tsunoda, Y. Hirono, Y. Kikuchi, S. Ono, and T. Ariga for their technical assistance and helpful discussion.

REFERENCES

1. Mitchell, P. (1961) *Nature* **191,** 144–148
2. Kagawa, Y., and Racker, E. (1966) *J. Biol. Chem.* **241,** 2467–2474
3. Boyer, P. D. (1997) *Annu. Rev. Biochem* **66,** 717–749

4. Pedersen, P. L. (1996) *J. Bioenerg Biomembr* **28,** 389–395
5. Weber, J., and Senior A. E. (1997) *Biochim. Biophys. Acta* **1319,** 19–58
6. Fillingame, R. H., Jones, P. C., and Jiang, W. (1998) *Biochim. Biophys. Acta* **1365,** 135–142
7. Abrahams, J. P., Leslie, A G W., Lutter, R., and Walker, J. E. (1994) *Nature* **370,** 621–628
8. Yokoyama, K., Hisabori, T., and Yoshida, M. (1989) *J. Biol. Chem.* **264,** 21837–21841
9. Matsui, T., and Yoshida, M. (1995) *Biochim. Biophys. Acta* **1231,** 139–146
10 Kaibara, C., Matsui, T., Hisabori, T., and Yoshida, M (1996) *J. Biol. Chem.* **271,** 2433–2438
11. Noji, H., Yasuda, R., Yoshida, M., and Kinosita, K., Jr. (1997) *Nature* **386,** 299–302
12. Yasuda, R , Noji, H., Kinosita, K., Jr., and Yoshida, M (1998) *Cell* **93,** 1117–1124
13 Duncan, T. M., Bulygin, V. V., Zhou, Y., Hutcheon, M. L., and Cross, R. L. (1995) *Proc. Natl. Acad. Sci U S. A.* **92,** 10964–10968
14. Zhou, Y., Duncan, T. M., Bulygin, V. V., Hutcheon, M L., and Cross, R L (1996) *Biochim. Biophys. Acta* **1275,** 96–100
15. Sabbert, D., Engelbrecht, S., and Junge, W. (1996) *Nature* **381,** 623–625
16. Noji, H., Hasler, K., Junge, W., Kinosita Jr, K., Yoshida, M., and Engelbrecht, S. (1999) *Biochem. Biophys. Res. Commun* **260,** 597–599
17 Omote, H , Sambonmatsu, N , Saito, K., Sambongi, Y , Iwamoto-Kihara, A., Yanagida, T., Wada, Y., and Futai, M. (1999) *Proc. Natl. Acad. Sci. U. S. A.* **96,** 7780–7784
18. Hisabori, T., Kondoh, A., and Yoshida, M. (1999) *FEBS Lett.* **463,** 35–38
19. Tsunoda, S. P., Muneyuki, E., Amano, T., Yoshida, M., and Noji, H. (1996) *J. Biol. Chem.* **274,** 5701–5706
20. Ren, H., Dou, C., Stelzer, M. S., and Allison, W S. (1999) *J. Biol. Chem.* **274,** 31366–31372
21. Ketchum, C. J., Al-Shawi, M. K., and Nakamoto, R. K. (1998) *Biochem. J.* **330,** 707–712
22. Yanisch-Perron, C., Vieira, J., and Messing, J (1985) *Gene* **33,** 103–119
23 Kunkel, T. A., Bebenek, K., and McClary, J. (1991) *Methods Enzymol.* **204,** 125–139
24. Monticello, R. A., Angov, E., and Brusilow, W. (1992) *J. Bacteriol.* **174,** 3370–3376
25. Aggeler, R., and Capaldi, R. A. (1996) *J. Biol. Chem.* **271,** 13888–13891
26. Kagawa, Y., and Hamamoto, T. (1996) *J. Bioenerg. Biomembr* **28,** 421–431
27. Bullough, D. A., Ceccarelli, E. A., Verburg, J. G., and Allison, W. S. (1989) *J. Biol. Chem.* **264,** 9155–9163
28 Dallmann, H. G., Flynn, T. G., and Dunn, S. D. (1992) *J. Biol Chem.* **267,** 18953–18960
29. Aggeler, R., Haughton, M. A., and Capaldi, R. A. (1995) *J. Biol. Chem.* **270,** 9185–9191
30. Tang, C., and Capaldi, R. A. (1996) *J Biol. Chem.* **271,** 3018–3024

12. Wakimoto, B. T. Beyond the nucleosome: epigenetic aspects of position-effect variegation in Drosophila. *Cell* **93,** 321–324 (1998).
13. Boivin, A. & Dura, J. M. In vivo chromatin accessibility correlates with gene silencing in Drosophila. *Genetics* **150,** 1539–1549 (1998).
14. Gottschling, D. E. Telomere-proximal DNA in Saccharomyces cerevisiae is refractory to methyltransferase activity in vivo. *Proc. Natl Acad. Sci. USA* **89,** 4062–4065 (1992).
15. Braunstein, M., Sobel, R. E., Allis, C. D., Turner, B. M. & Broach, J. R. Efficient transcriptional silencing in *Saccharomyces cerevisiae* requires a heterochromatin histone acetylation pattern. *Mol. Cell Biol.* **16,** 4349–4356 (1996).
16. Turner, B. M., Birley, A. J. & Lavender, J. Histone H4 isoforms acetylated at specific lysine residues define individual chromosomes and chromatin domains in *Drosophila* polytene nuclei. *Cell* **69,** 375–384 (1992).
17. Dorer, D. R. & Henikoff, S. Expansions of transgene repeats cause heterochromatin formation and gene silencing in *Drosophila*. *Cell* **77,** 993–1002 (1994).
18. Devlin, R. H., Bingham, B. & Wakimoto, B. T. The organization and expression of the light gene, a heterochromatic gene of *Drosophila melanogaster*. *Genetics* **125,** 129–140 (1990).
19. Dorsett, D. Distant liaisons: long-range enhancer-promoter interactions in *Drosophila*. *Curr. Opin. Genet. Dev.* **9,** 505–514 (1999).
20. Durfee, T. *et al.* The retinoblastoma protein associates with the protein phosphatase type 1 catalytic subunit. *Genes Dev.* **7,** 555–569 (1993).
21. Sandell, L. L., Gottschling, D. E. & Zakian, V. A. Transcription of a yeast telomere alleviates telomere position effect without affecting chromosome stability. *Proc. Natl Acad. Sci. USA* **91,** 12061–12065 (1994).
22. Bourns, B. D., Alexander, M. K., Smith, A. M. & Zakian, V. A. Sir proteins, Rif proteins, and Cdc13p bind *Saccharomyces* telomeres in vivo. *Mol. Cell Biol.* **18,** 5600–5608 (1998).
23. Alexander, C., Grueneberg, D. A. & Gilman, M. Z. Studying heterologous transcription factors in yeast. *Methods Companion Methods Enzymol.* **5,** 147–155 (1993).
24. Braunstein, M., Rose, A. B., Holmes, S. G., Allis, C. D. & Broach, J. R. Transcriptional silencing in yeast is associated with reduced nucleosome acetylation. *Genes Dev.* **7,** 592–604 (1993).

Acknowledgements

We wish to thank S. Kantrow for her technical assistance and G. Bryant for his help with the quantitative PCR analysis. We are grateful to J. V. Ravetch, Head, Laboratory of Molecular Genetics & Immunology, The Rockefeller University, for his support of D.d.B. and R.A.L. during this work. We also thank T. De Lange and M. Grunstein for comments on the manuscript. M.P. is a Ludwig Foundation Professor. This work was supported in part by NIH and a fellowship from the Norman and Rosita Winston Foundation (Z.Z.).

Correspondence and requests for materials should be addressed to either D.d.B (e-mail: derik.debruin@ssmb.com) or M.P. (e-mail: m-ptashne@ski.mskcc.org).

Direct observation of DNA rotation during transcription by *Escherichia coli* RNA polymerase

Yoshie Harada*†‡, Osamu Ohara§, Akira Takatsuki*, Hiroyasu Itoh†‖, Nobuo Shimamoto¶ & Kazuhiko Kinosita Jr*†

** Department of Physics, Faculty of Science and Technology, Keio University, Hiyoshi 3-14-1, Kohoku-ku, Yokohama 223-8522, Japan*
† CREST (Core Research for Evolutional Science and Technology) "Genetic Programming" Team 13, Nogawa 907, Miyamae-ku, Kawasaki 216-0001, Japan
§ Kazusa DNA Research Institute, Yana 1532-3, Kisarazu 292-0812, Japan
‖ Tsukuba Research Laboratory, Hamamatsu Photonics KK, Tokodai, Tsukuba 300-2635, Japan
¶ Structural Biology Center, National Institute of Genetics, Mishima 411-8540, Japan

Helical filaments driven by linear molecular motors are anticipated to rotate around their axis, but rotation consistent with the helical pitch has not been observed. 14S dynein[1] and non-claret disjunctional protein (ncd)[2] rotated a microtubule more efficiently than expected for its helical pitch, and myosin rotated an actin filament only poorly[3]. For DNA-based motors such as RNA polymerase, transcription-induced supercoiling of DNA[4] supports the general picture of tracking along the DNA helix[5]. Here we report direct and real-time optical microscopy measurements of rotation rate that are consistent with high-fidelity tracking. Single RNA polymerase molecules attached to a glass surface rotated DNA for >100 revolutions around the right-handed screw axis of the double helix with a rotary torque of >5 pN nm. This real-time observation of rotation opens the possibility of resolving individual transcription steps.

Linear movement of a single molecule of RNA polymerase relative to DNA has been observed directly, during transcription[6–9] and during a one-dimensional diffusional search for a promoter[8,10,11]. To observe relative rotation between RNA polymerase and DNA, we employed an optical microscopy technique based on the tethered-particle method[6] (Fig. 1a). A DNA template, 4,971 base pairs (1.7 μm) long and containing one strong promoter (T7A1), was constructed (Fig. 1b). Transcription was initiated in a bulk solution in the absence of UTP, such that the polymerase stalled at the adenine at the +20 position (A20), before the thymine at +21 position[12]. The stalled polymerase was attached to a glass surface (Fig. 1a), and a magnetic bead of diameter 850 nm coated with streptavidin was attached to the downstream end of the DNA where nine nucleotide residues were biotinylated. Then, all four nucleoside triphosphates (NTPs) were added to allow further transcription. In a similar system with a non-magnetic bead, Schafer *et al.*[6] observed highly 'processive' (moving over a long distance without detachment) threading of DNA through RNA polymerase,

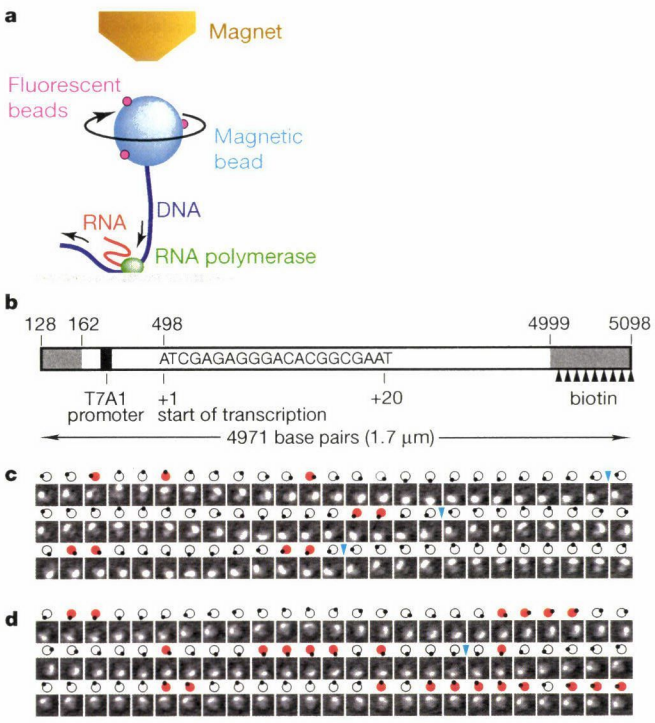

Figure 1 Observation of DNA rotation by RNA polymerase. **a**, Observation system (not to scale). The magnetic bead was pulled upwards by a disk-shaped neodymium magnet, to which a conical iron piece was attached to enhance the magnetic force. Magnetization was vertical and did not prevent bead rotation. Daughter fluorescent beads served as markers of rotation. **b**, The DNA template. Numbers above are from the T7 D111 sequence. Rotation assay started from position +20. The magnetic bead was attached to the nine biotins. Shaded ends denote primers for the polymerase chain reaction. **c**, **d**, Snapshots of rotating beads at 133-ms intervals at NTP concentrations of 50 μM (**c**) and 2.5 μM (**d**). Grey part at the centre, a magnetic bead visualized with transmitted light; moving white spot, a daughter fluorescent bead or probably its aggregates. Diagrams show their relative positions. Blue arrowheads indicate completion of a turn. Red diagrams show moments of anticlockwise rotation due to torsional brownian fluctuations of DNA; these were less noticeable at high [NTP], presumably because supercoiling had reduced the effective tether length. Image size, 2.4 × 2.4 μm^2.

‡ Present address: Department of Molecular Physiology, The Tokyo Metropolitan Institute of Medical Science, 18-22, Honkomagome 3-chome, Bunkyo-ku, Tokyo 113-8613, Japan.

visualized as progressive reduction in the range of the brownian motion of the end bead. We also confirmed this. The high processivity, however, does not necessarily imply precise helical tracking. RNA polymerase might occasionally allow DNA to rotate freely within the active site to relieve torsional stress. Or, the polymerase might allow transient, straight backward slippage of DNA without rotation, while imposing helical rotation for forward movement. This would lead to overwinding. For forward movement, RNA polymerase might bring in DNA several base pairs at a time, in which case tracking of the double helix is not required.

We thus attempted to observe rotation directly by decorating the end bead with smaller fluorescent beads. We pulled the magnetic bead upward at ~0.1 pN with a magnet for two reasons: to confine the rotation in a horizontal plane, and in the hope of restraining the DNA from supercoiling, which would interfere with torque transmission to the end bead. Up to a few per cent of beads in an observation chamber rotated continuously (Fig. 1c, d), invariably clockwise when viewed from top in Fig. 1a. Threading a right-handed double helix of DNA through RNA polymerase will, in a simple mechanism, produce clockwise rotation. Not all beads rotated, some being stuck on the glass surface; others fluctuated in both directions, presumably being attached to nicked DNA or tethered to an inactive polymerase. Below we report only on those beads that made at least five revolutions in one direction. When NTPs were absent, unidirectional rotation was not observed.

Time courses of rotation of individual beads are shown in Fig. 2. Most curves do not start at time zero, because we had to search over several fields of view before finding a continuously rotating bead. The curves are also shifted upwards to give the impression that all beads started rotating at time zero. In fact we could confirm this only for three cases. Generally the rotation was slower at lower NTP concentration, [NTP], although variations among beads were large. Extremely slow beads, among those examined under the same [NTP], often carried large aggregates of fluorescent beads. Rotation rate also varied with time. Thin parts of the curves in Fig. 2 indicate pauses in the bead rotation; we define a pause as a time interval longer than 50 s during which a bead fluctuated no more than ±2 revolutions (this was less well defined at low [NTP]). Observation was terminated after a pause, or after complete immobilization for >30 s, or when the bead tore off and floated into solution. For our DNA template with the full transcript length of ~4,500 bases, the expected number of revolutions is 4,500/10.4 (base pairs per turn of DNA[13]); that is, ~ 430. At least ~180 consecutive revolutions have been observed (an orange curve in Fig. 2), suggesting that thousands of base pairs can be transcribed without extensive rotational slippage.

To compare with the rate of rotation, we measured the rate of RNA elongation in solution, and on individual molecules of RNA polymerase on the glass surface[6] (see Supplementary Information). As summarized in Fig. 3, the two methods gave consistent results (dark versus light green symbols), indicating that surface attachment did not alter the elongation kinetics. The elongation rate divided by 10.4 will be the rotation rate if the polymerase faithfully tracks the DNA helix. Indeed, this seemed to be the case at [NTP] below ~20 μM, as seen in red circles in Fig. 3 (also see legend for the purple curve). Although the scatter in rotation data is large, we believe that data showing faster (and longer) rotation are more reliable, because anything that attaches or touches the bead impedes rotation (aggregates of fluorescent beads, DNA, and so on). These data support high-fidelity tracking, but we cannot dismiss the possibility of underwinding by a factor of up to ~2. Extensive overwinding is unlikely.

The apparent saturation of rotation rate in Fig. 3 is explained if the maximal torque of RNA polymerase, Γ_{max}, is already reached at the observed maximal rotation rate of ~0.2 revolutions per second (r.p.s.). To rotate a bead of diameter D = 850 nm in bulk water at this speed, a torque $\Gamma = 2\pi[0.2\ \text{r.p.s.}]\xi \approx 2.4$ pN nm is required, where $\xi = \pi\eta D^3$ is the rotational frictional drag coefficient and η (= 10^{-9} pN nm^{-2} s) is the viscosity of water. The drag is higher

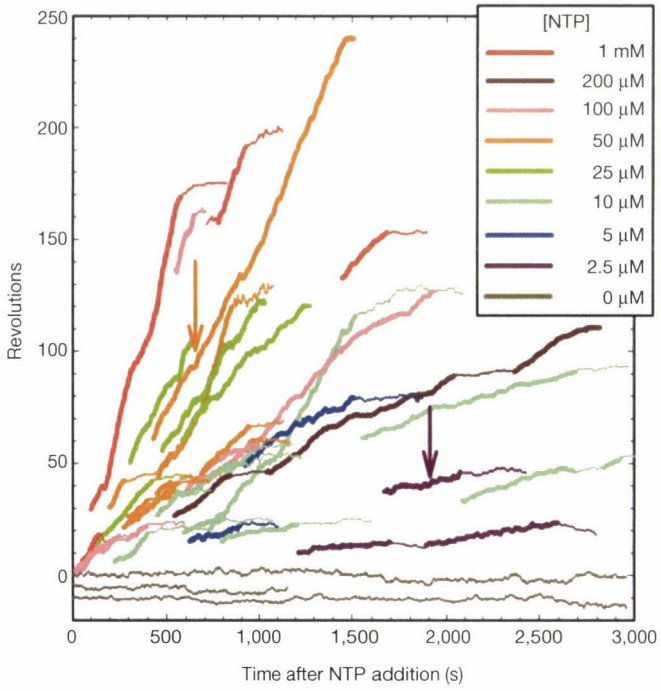

Figure 2 Time courses of bead rotation at various [NTP]. Rotation angles (clockwise positive) were estimated from images as in Fig. 1c, d by centroid analysis[17]. Thin lines indicate portions that were excluded in the estimation of rotation rates in Fig. 3. Arrows show the portions shown in Fig. 1c, d.

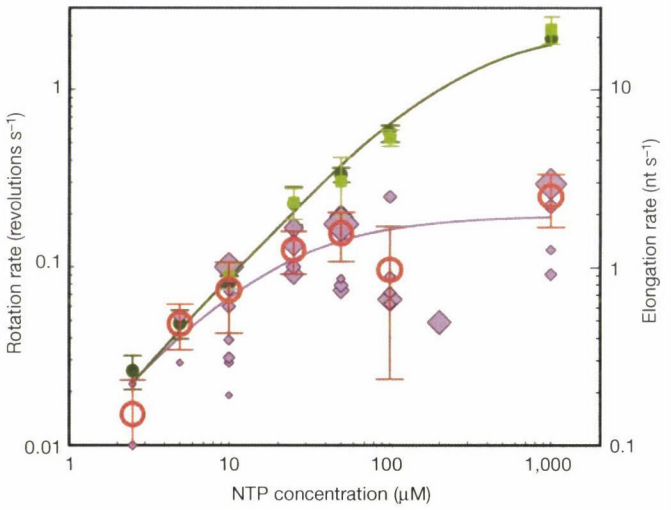

Figure 3 Comparison of rotation and transcription rates. Purple diamonds, rotation rates for individual beads, estimated as the total number of revolutions, N, in the thick portion of a curve in Fig. 2 divided by time; symbol size ∝ $N^{1/2}$. Red circles, rotation rates at indicated [NTP] averaged with weights ∝ N; error bars, root mean square of weighted residuals. Dark green circles, elongation rates in solution; light green squares, elongation rates for individual RNA polymerase molecules on the glass surface (see Supplementary Information). Dark green curve, fit with $V = V_{max}[\text{NTP}]/([\text{NTP}] + K_m)$ where V_{max} = 22 nucleotides s^{-1} and K_m = 250 μM. Purple curve, fit to purple diamonds with rotation rate r given by[17] $1/r = n/V + T_{rot}$; n/V is the time for elongation reaction where n nucleotides are added per revolution; T_{rot} is the time required to rotate the bead against friction; n = 8.7 ± 3.7 nucleotides per revolution (n = 10.4 for precise helical tracking) and T_{rot}^{-1} = 0.21 ± 0.8 r.p.s.

near the glass surface[14]. Pulled at ~0.1 pN by the magnet, the bead centre will be ~1.1 μm from the surface at the initial DNA length of ~1.5 μm (ref. 15). The effective ξ at this height is ~130% of the bulk value, and approaches 300% as the bead comes down towards the surface[14]. DNA itself must also rotate, with a similar magnitude of ξ. Altogether, the required torque will be >5 pN nm. Flexible DNA cannot sustain this much torque and collapses by supercoiling, which is expected to occur at the critical torque $\Gamma_c \approx 6$ pN nm under ~0.1 pN of tension[15]. At high [NTP], beads often rotated steadily without lateral fluctuations, suggesting that extensive supercoiling had made the effective tether length approximately equal to zero. The beads may then touch the surface, further increasing the effective ξ. Presumably, balance between this high drag and Γ_{max} is reached at ~0.2 r.p.s. ($= \Gamma_{max}/2\pi\xi = T_{rot}^{-1}$ in Fig. 3 legend), resulting in saturation. Γ_{max} must be >5 pN nm, but is unlikely to exceed the 40 pN nm which F_1-ATPase produces by converting available energy almost entirely to rotation[16,17]. An alternative explanation for the slow rotation at high [NTP] might be extensive rotary slippage in RNA polymerase at [NTP] > 20 μM. However, simple slippage is unlikely to result in the saturation behaviour, and the transcription obeyed simple Michaelis–Menten kinetics—indicative of an [NTP]-independent mechanism.

In summary, our results indicate that RNA polymerase rotates DNA by tracking its right-handed helix, that the polymerase does so over thousands of base pairs, and that the polymerase can produce >5 pN nm of torque. Whether RNA polymerase rotates around DNA or vice versa is an issue *in vivo*[5], but our experiment with fixed RNA polymerase cannot answer this problem. Some uncertainty remains in the degree of tracking fidelity, but several beads made many revolutions at the rate commensurate with precise helical tracking. Although the mechanism of tracking is yet unknown, genuine rotary motors may also employ tracking as the rotary mechanism. In the bacterial flagellar motor[18,19], the rotor consists of circularly arranged identical subunits. Driving units are also circularly arranged, but one unit suffices to produce efficient rotation[19]. A single unit may thus track along the rotor subunits thereby causing rotation. In the F_1-ATPase in which an asymmetric rotor rotates in 120° steps[17], the tracking mechanism is unlikely.

We expect that the RNA polymerase rotation reported here could provide a means of resolving individual steps of transcription. Transcription of one base will produce a linear translocation of 0.34 nm (ref. 13), which is extremely difficult to resolve. However, accompanying rotation is as much as 35°, and should in principle be detectable. The main problem is torsional brownian motion of DNA, which has to be averaged out. A tag much smaller than the 850-nm bead (and shorter DNA) is needed for averaging within a reasonable time. Determination of the orientation of a tiny tag is feasible, even of a single fluorophore[3,20]. □

Methods

Materials

Escherichia coli RNA polymerase holoenzyme was purified[21] and supplemented with excess σ-subunit. The DNA template for transcription was prepared from T7 D111 DNA[22], by polymerase chain reaction with an upstream primer for segment 128–162 (in the T7 coordinate) and downstream primer for 4999–5098 (Fig. 1b). The downstream primer had been biotinylated at 9 sites at ~10-base intervals. Before use, the template was treated with T4 DNA ligase at 0.1 mM ATP for 30 min at room temperature to remove nicks. Stalled transcription complex[12] was prepared by incubating 0.3 μM RNA polymerase and 0.3 nM DNA in buffer A (20 mM TrisCl pH 8.0, 20 mM NaCl, 14 mM $MgCl_2$, 0.1 mM EDTA, 14 mM 2-mercaptoethanol, 1.5% (w/v) glycerol, 20 μg ml^{-1} acetylated BSA, 250 μM ApU dinucleotide) containing 100 μM each of ATP, GTP and CTP for 3 min at 30 °C.

Fluorescent, carboxylated microbeads (20 nm, excitation 580 nm, emission 605 nm, Molecular Probes) were amino-derivatized with ethylene diamine in the presence of 1-ethyl-3-(3-dimethylaminopropyl)carbodiimide (EDC). The microbeads and Biotin-X cadaverine (Molecular Probes) were conjugated to 850-nm carboxylated magnetic beads (Seradyn) with EDC, and streptavidin was bound to the biotinylated magnetic beads[11].

Transcription on the glass surface

A flow chamber[17] was made of two coverslips, which had been sonicated in water, stored in methanol, and dried by setting fire to the methanol. 5 μl of stalled complex in buffer A was mixed with 50 μl of buffer B (20 mM Tris-acetate pH 8.0, 130 mM NaCl, 4 mM $MgCl_2$, 0.1 mM EDTA, 0.1 mM DTT, 20 μg ml^{-1} acetylated BSA and 80 μg ml^{-1} heparin), infused into the flow chamber, and incubated for 5 min. Further treatments were infusion of 2 mg ml^{-1} α-casein in buffer B for 2 min, washing with buffer B; infusion of beads in buffer C (buffer B minus BSA and heparin, plus 1 mg ml^{-1} α-casein) for 15 min; washing with buffer B plus 1 mM biotin; then washing with buffer B. Transcription was started by infusing NTPs and 0.5% (v/v) 2-mercaptoethanol in buffer B.

Microscopy

Samples were observed at 23 ± 2 °C on an Olympus IX70 inverted microscope with a 100× oil-immersion objective. Magnetic beads were illuminated with a halogen lamp obliquely from above through a ring-shaped optical-fibre assembly. Fluorescent daughter beads were imaged with standard epi-fluorescence optics. Superimposed bright-field and fluorescence images were projected on a silicon-intensified target camera (C2400-08 Hamamatsu Photonics) and recorded on a video tape. A conical magnet was placed above the sample to pull the beads (Fig. 1a). Vertical pulling force was calibrated by tethering the magnetic beads with 16-μm-long λ-phage DNA and measuring the amplitude of brownian motion[15]. The force varied among beads and was 0.05–0.2 pN.

Received 25 August; accepted 18 October 2000

1. Vale, R. D. & Toyoshima, Y. Y. Rotation and translocation of microtubules in vitro induced by dyneins from *Tetrahymena cilia*. *Cell* **52**, 459–469 (1988)
2. Walker, R. A., Salmon, E. D. & Endow, S. A. The *Drosophila claret* segregation protein is a minus-end directed motor molecule. *Nature* **347**, 780–782 (1990)
3. Sase, I., Miyata, H., Ishiwata, S. & Kinosita, K. Jr. Axial rotation of sliding actin filaments revealed by single-fluorophore imaging. *Proc. Natl Acad. Sci. USA* **94**, 5646–5650 (1997)
4. Wang, J. C. & Lynch, A. S. Transcription and DNA supercoiling. *Curr. Opin. Genet. Dev.* **3**, 764–768 (1993)
5. Cook, P. R. The organization of replication and transcription. *Science* **284**, 1790–1795 (1999)
6. Schafer, D. A., Gelles, J., Sheetz, M. P. & Landick, R. Transcription by single molecules of RNA polymerase observed by light microscopy. *Nature* **352**, 444–448 (1991)
7. Wang, M. D. *et al.* Force and velocity measured for single molecules of RNA polymerase. *Science* **282**, 902–907 (1999)
8. Guthold, M. *et al.* Direct observation of one-dimensional diffusion and transcription by *Escherichia coli* RNA polymerase. *Biophys. J.* **77**, 2284–2294 (1999)
9. Davenport, R. J., Wuite, G. J. L., Landick, R. & Bustamante, C. Single-molecule study of transcriptional pausing and arrest by *E. coli* RNA polymerase. *Science* **287**, 2497–2500 (2000)
10. Kabata, H. *et al.* Visualization of single molecules of RNA polymerase sliding along DNA. *Science* **262**, 1561–1563 (1993)
11. Harada, Y. *et al.* Single molecule imaging of RNA polymerase-DNA interactions in real time. *Biophys. J.* **76**, 709–715 (1999)
12. Levin, J. R., Krummel, B. & Chamberlin, M. J. Isolation and properties of transcribing ternary complexes of *Escherichia coli* RNA polymerase positioned at single template base. *J. Mol. Biol.* **196**, 85–100 (1987)
13. Stryer, L. *Biochemistry* 4th edn (Freeman, New York, 1995).
14. Svoboda, K. & Block, S. M. Biological applications of optical tweezers. *Annu. Rev. Biophys. Biomol. Struct.* **23**, 247–285 (1994).
15. Strick, T., Allemand, J.-F., Bensimon, D., Lavery, R. & Croquette, V. Phase coexistence in a single DNA molecule. *Physica A* **263**, 392–405 (1999)
16. Noji, H., Yasuda, R., Yoshida, M. & Kinosita, K. Jr. Direct observation of the rotation of F_1-ATPase. *Nature* **386**, 299–302 (1997)
17. Yasuda, R., Noji, H., Kinosita, K. Jr. & Yoshida, M. F_1-ATPase is a highly efficient molecular motor that rotates with discrete 120° steps. *Cell* **93**, 1117–1124 (1998)
18. DeRosier, D. J. The turn of the screw: the bacterial flagellar motor. *Cell* **93**, 17–20 (1998)
19. Ryu, W. S., Berry, R. M. & Berg, H. C. Torque-generating units of the flagellar motor of *Escherichia coli* have a high duty ratio. *Nature* **403**, 444–447 (2000)
20. Adachi, K. *et al.* Stepping rotation of F_1-ATPase visualized through angle-resolved single-fluorophore imaging. *Proc. Natl Acad. Sci. USA* **97**, 7243–7247 (2000)
21. Kubori, T. & Shimamoto, N. A branched pathway in the early stage of transcription by *Escherichia coli* RNA polymerase. *J. Mol. Biol.* **256**, 449–457 (1996)
22. Studier, F. W. Gene *0.3* of bacteriophage T7 acts to overcome the DNA restriction system of the host. *J. Mol. Biol.* **94**, 283–295 (1975)

Supplementary information is available on *Nature's* World-Wide Web site (http://www.nature.com) or as paper copy from the London editorial office of *Nature*.

Acknowledgements

We thank M. Susa for help in transcription analysis; A. Ishihama, S. Ishiwata, G. W. Feigenson and members of Team 13 for comments; and H. Umezawa for laboratory management. This work was supported in part by Grants-in-Aid from Ministry of Education, Science, Sports and Culture of Japan, Hayashi Memorial Foundation for Female Natural Scientists, and an Academic Frontier Promotional Project.

Correspondence and requests for materials should be addressed to Y. H. (e-mail: yharada@rinshoken.or.jp).

Resolution of distinct rotational substeps by submillisecond kinetic analysis of F_1-ATPase

Ryohei Yasuda*†‖, Hiroyuki Noji*, Masasuke Yoshida‡*, Kazuhiko Kinosita Jr†* & Hiroyasu Itoh§*

* *CREST 'Genetic Programming' Team 13, Teikyo University Biotechnology Center 3F, Nogawa 907, Miyamae-Ku, Kawasaki 216-0001, Japan*
† *Department of Physics, Faculty of Science and Technology, Keio University, Yokohama 223-8522, Japan*
‡ *Chemical Resources Laboratory, Tokyo Institute of Technology, Yokohama 226-8503, Japan*
§ *Tsukuba Research Laboratory, Hamamatsu Photonics KK, Tokodai, Tsukuba 300-2635, Japan*

The enzyme F_1-ATPase has been shown to be a rotary motor in which the central γ-subunit rotates inside the cylinder made of $\alpha_3\beta_3$ subunits. At low ATP concentrations, the motor rotates in discrete 120° steps, consistent with sequential ATP hydrolysis on the three β-subunits. The mechanism of stepping is unknown. Here we show by high-speed imaging that the 120° step consists of roughly 90° and 30° substeps, each taking only a fraction of a millisecond. ATP binding drives the 90° substep, and the 30° substep is probably driven by release of a hydrolysis product. The two substeps are separated by two reactions of about 1 ms, which together occupy most of the ATP hydrolysis cycle. This scheme probably applies to rotation at full speed (~130 revolutions per second at saturating ATP) down to occasional stepping at nanomolar ATP concentrations, and supports the binding-change model for ATP synthesis by reverse rotation of F_1-ATPase.

The ATP synthase is an enzyme ubiquitous in bacteria, plants and animals, which synthesizes ATP from ADP and inorganic phosphate using proton flow through a membrane[1–3]. F_1, a water-soluble portion of the ATP synthase, is the site of ATP synthesis, whereas protons flow through the membrane-embedded F_o portion. At least *in vitro*, F_1 can hydrolyse ATP to pump protons through the F_o portion in the reverse direction. Isolated F_1 only hydrolyses ATP, and is called F_1-ATPase. Its subunit composition is $\alpha_3\beta_3\gamma\delta\epsilon$.

The prevailing view is that ATP hydrolysis/synthesis in F_1 is coupled to proton flow in F_o through the rotation of a common shaft, of which the γ-subunit of F_1 is a part. This rotational coupling mechanism was initially proposed by Boyer[1–3], and by others[4–6]. Later, a crystal structure of F_1 showed that a rod-shaped γ-subunit is surrounded by a cylinder made of three α- and three β-subunits, arranged alternately[7] (Fig. 1a). An analogue of ATP, ADP and none were bound to the three β-subunits, indicating that sequential ATP hydrolysis on the three β-subunits would indeed induce rotation of the central, asymmetrical γ-subunit. Rotation of the γ-subunit in an isolated F_1 during ATP hydrolysis has been demonstrated experimentally by various methods[8–10].

We have visualized the rotation of the γ-subunit under an optical microscope by fixing F_1 on a surface and attaching an actin filament to the γ-subunit as a marker of its orientation[10]. At nanomolar ATP, the actin filament rotated in discrete 120° steps[11], consistent with the pseudo-three-fold symmetrical structure[7] of F_1. The rotation rate was close to one-third of the rate of ATP hydrolysis in solution, suggesting that one ATP molecule is consumed per 120° step[11]. At high ATP concentrations, however, the actin rotation was smooth rather than stepwise, and the rotation was much slower than ATP hydrolysis. Viscous friction imposed on the actin filament prevented fast rotation of F_1 and obscured the stepping behaviour. Here we have used a smaller marker, a colloidal gold bead of 40-nm diameter, for which the viscous friction is 10^{-3} to 10^{-4} times that for actin (Fig. 1b). In the resultant high-speed rotation, we were able to resolve substeps. In this study we investigate the magnitudes, speeds, and timings of the substeps, and we also look at: (1) the motor speeds at no load; (2) whether the motor uses different rotary mechanisms at low and high speeds; (3) which parts of hydrolysis reactions drive the substeps; and (4) what structural changes may underlie the substeps.

Full-speed rotation with 40-nm beads

Bead rotation was imaged by laser dark-field microscopy[12] (Fig. 1c),

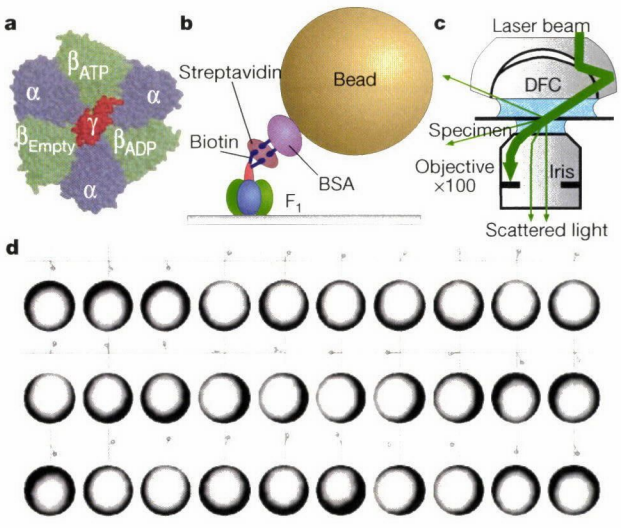

Figure 1 Observation of F_1 rotation. **a**, Atomic structure[7] of F_1-ATPase viewed from the F_o side (top in **b**). **b**, Side view of the observation system. The 40-nm bead gave a large enough optical signal that warranted a submillisecond resolution; but the bead was small enough not to impede the rotation. **c**, Laser dark-field microscopy for observation of gold beads. Only light scattered by the beads exited the objective and was detected. DFC, dark-field condenser. **d**, Sequential images of a rotating bead at 2 mM ATP. Images are trimmed in circles (diameter 370 nm) to aid identification of the bead position; centroid positions are shown above the images at ×3 magnification. The interval between images is 0.5 ms.

‖Present address: Cold Spring Harbor Laboratory, 1 Bungtown Road, Cold Spring Harbor, New York 11724, USA.

and recorded on a fast-framing charge-coupled-device (CCD) camera at speeds up to 8,000 frames per s. The 40-nm bead appeared as a spot of diffraction-limited size (~300 nm; Fig. 1d). When a bead is attached obliquely (Fig. 1b), rotation of the γ-subunit will result in a circular movement of the bead image. Some beads showed rotation (Fig. 1d; movies in Supplementary Information), and motions of these beads were analysed by calculating the centroid of the bead image[13]. The rotation diameter of bead centroid ranged between 25–55 nm. Diameters up to ~60 nm are possible for the height of F_1 of ~10 nm and the linker lengths of ~5 nm for streptavidin[14] and ~10 nm for BSA[15] (Fig. 1b). Rotation was stepwise at all ATP concentrations examined (see below).

To see whether the friction on the 40-nm bead impeded F_1 rotation, we varied the frictional load by attaching single or duplex polystyrene beads (108, 196 or 291 nm) to the γ-subunit. At both 2 mM and 2 μM ATP (Fig. 2; red and blue circles, respectively), time-averaged rotation rates showed saturation behaviour at small friction. Maximal rotation rate depended on ATP concentration [ATP], but increasing [ATP] beyond 2 mM did not accelerate rotation (see below). Thus, at 2 mM ATP, the 40-nm bead rotated at the full speed of the F_1 motor, which was 134 revolutions per second (r.p.s.) at 23 °C; the bead was not an impeding load for F_1. At saturating speeds, all beads rotated stepwise. On the load-dependent portions in Fig. 2, however, bead rotation was smooth, as was rotation of actin at these ATP concentrations[11]. The load dependence of actin rotation[11] (Fig. 2; triangles) is consistent with the bead assay.

One rotary mechanism at all speeds

The time-averaged rate of rotation showed simple Michaelis–Menten dependence on [ATP] (Fig. 3; the maximal rate at infinite [ATP], V_{max} = 129 r.p.s.; Michaelis constant, K_m = 15 μM), suggesting that one mechanism accounts for rotation in the nM–mM range. This idea is corroborated by observations[11,16,17] that the torque and its angle dependence, as well as mechanical work done in a 120° step, are independent of [ATP] over the nM–mM range. Also, the apparent rate of ATP binding, k_{on}^{ATP}, given by $3V_{max}/K_m$ of $(2.6 \pm 0.5) \times 10^7\ M^{-1}\ s^{-1}$ agrees with previous estimates based on the analysis of step intervals at nanomolar ATP[11,18].

As seen in Fig. 3, the rotation rate was close to one-third of the rate of ATP hydrolysis for bead-free F_1 in solution, supporting the contention that one ATP molecule is consumed per 120° rotation[11,16–18]. The hydrolysis rate, however, was lower, particularly around 50 μM. A probable cause is MgADP inhibition: F_1 is stochastically inactivated during ATP hydrolysis, when it binds MgADP tightly[17,19,20]. Although we started with nucleotide-free F_1, some inactivation may have proceeded during the mixing time of ~2 s. Indeed, the rate of inactivation increases with [ATP] and reaches ~0.3 s^{-1} at > 10 μM ATP[20], the position of the concavity in Fig. 3. Higher activity at still higher [ATP] is accounted for by binding of ATP to non-catalytic α-subunits, which tends to restore the hydrolysis activity[19]. Lauryldodecylamine oxide (LDAO), a suppressor of the MgADP inhibition[19], produced hydrolysis kinetics parallel to the rotation kinetics, although $V_{max}/3$ (82 s^{-1}) was only ~60% of V_{max} for rotation (Fig. 3).

The 120° step consists of 90° and 30° substeps

At 8,000 frames per s, steps were clearly resolved in the rotation of 40-nm beads, even at saturating ATP. At 2 mM ATP, only 120° steps were seen (Fig. 4a, b), whereas at 20 μM or 2 μM ATP, the 120° step was further split into roughly 90° and 30° substeps (Fig. 4c–f, where each panel shows a continuous record). We call the interval between a 30° substep and a 90° substep a '0° dwell' and the interval between 90° and 30° substeps a '90° dwell'. In Fig. 4c–f, 0° dwells fall on black horizontal lines that are separated from each other by 120°, and 90° dwells fall on grey lines that are 30° below the black lines. The 90° dwells were about a few ms in duration, on average, both at 2 and 20 μM ATP, whereas 0° dwells became longer at 2 μM. The implication is that F_1 waits for the arrival of ATP during the 0° dwell, which is terminated by a 90° substep induced by ATP binding. The subsequent 90° dwell is for a process or processes independent of [ATP]. This scheme predicts that, at [ATP] ~ K_m = 15 μM, 0° and 90° dwells have approximately equal lengths, as was observed

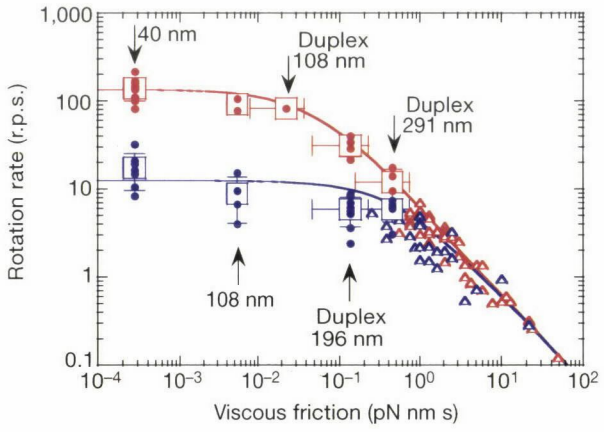

Figure 2 Relationship between rate of bead rotation and viscous friction on the bead. Circles, the average rate for a bead calculated over at least 20 consecutive revolutions; squares, the average over different beads (vertical error bars indicate s.d.). ATP at 2 mM and 2 μM is indicated by red and blue colours, respectively. The abscissa is the rotational frictional drag coefficient ξ calculated as in Methods. Possible range of ξ for each bead is shown by the size of the squares or associated horizontal error bars. For comparison, rotation rates for an actin filament attached to the γ-subunit[11] are also plotted (triangles). Lines show fits with the rate expected for a motor producing a constant torque[11]: $(1/V_{noload} + 2\pi\xi/N)^{-1}$ where N = 40 pN nm (assumed torque) and V_{noload} = 12.5 ± 1.0 r.p.s. for 2 μM ATP and 134 ± 3 r.p.s. for 2 mM ATP (s.e.m.).

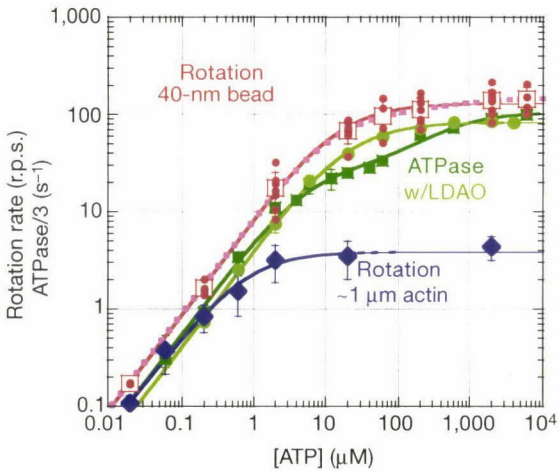

Figure 3 Comparison of rotation and hydrolysis rates. Red circles, time-averaged rotation rate for individual 40-nm beads. Red squares, rotation rate averaged over different beads. Dark green squares, one-third of the initial rate of ATP hydrolysis. Light green circles, one-third of the rate of ATP hydrolysis in the presence of LDAO. Blue diamonds, rotation rate for an actin filament attached to the γ-subunit[11]. Standard deviations greater than the symbol size are shown in bars ($n \geq 2$). Curves show fits with Michaelis–Menten kinetics, $V = V_{max}[ATP]/(K_m + [ATP])$, where V_{max} and K_m are 129 ± 9 r.p.s. and 15 ± 2 μM for bead rotation (red), 4.0 ± 0.3 r.p.s. and 0.7 ± 0.1 μM for actin rotation (blue), and 247 ± 9 s^{-1} and 19 ± 1 μM for hydrolysis in the presence of LDAO (light green). Fits with two K_m values, $V = (V_{max1}K_{m2}[ATP] + V_{max2}[ATP]^2)/([ATP]^2 + K_{m2}[ATP] + K_{m1}K_{m2})$, are also shown, where V_{max1} = 85 ± 9 s^{-1}, K_{m1} = 5.2 ± 0.7 μM, V_{max2} = 306 ± 22 s^{-1}, and K_{m2} = 393 ± 147 μM for hydrolysis without LDAO (dark green), and V_{max1} = 109 ± 30 r.p.s., K_{m1} = 12 ± 4 μM, V_{max2} = 149 ± 32 r.p.s., and K_{m2} = 682 ± 2768 μM for bead rotation (dashed pink). The latter does not show improvement over the simple fit in red. Values are means ± s.e.m.

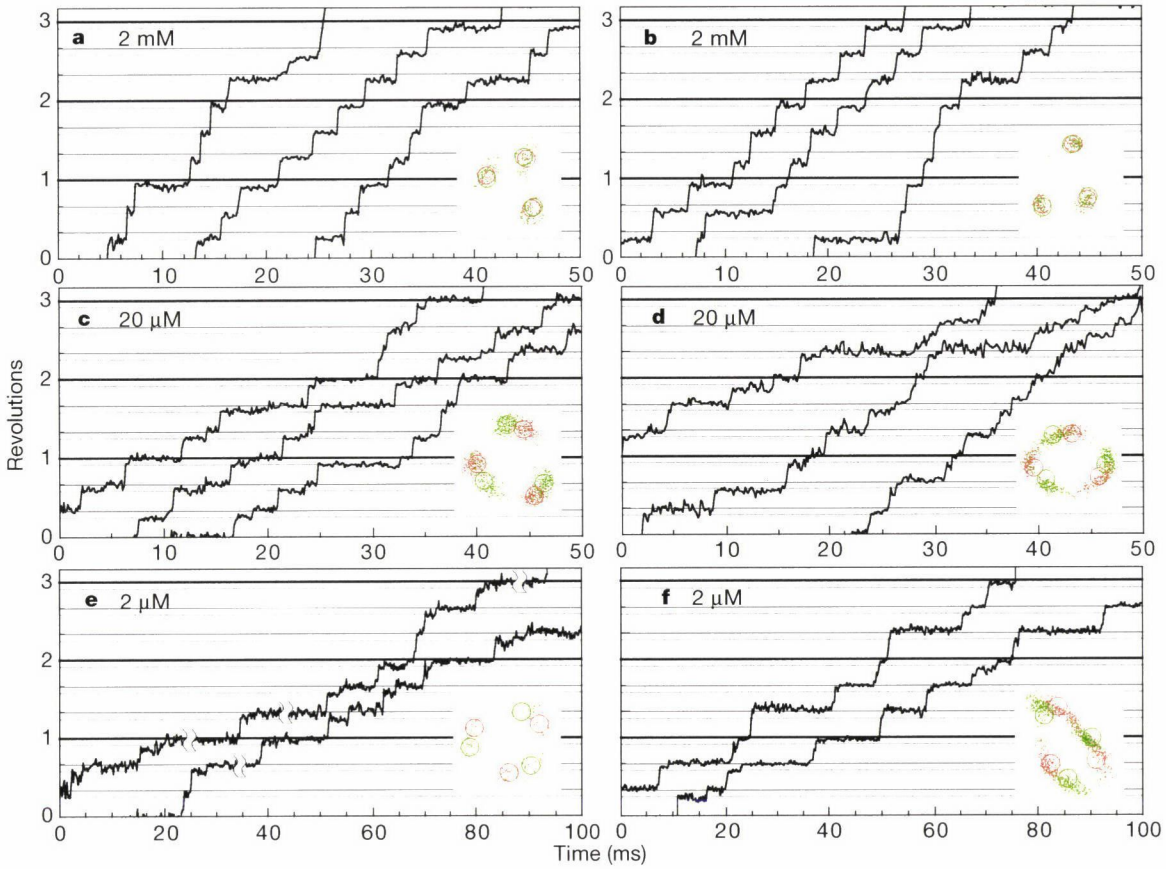

Figure 4 Unfiltered time courses of stepping rotation of 40-nm beads at varying [ATP]. **a**, **b**, 2 mM; **c**, **d**, 20 μM; **e**, **f**, 2 μM [ATP]. All curves in a panel are continuous; later curves are shifted, to save space. Grey horizontal lines are placed 30° below black lines. In **e**, some of the long dwells are cut short. Insets, positions of a bead within 0.25–0.5 ms before (red) and after (green) the main (90° or 120°) steps; runs lasting 0.5 s (2 mM) or 2 s (2 μM and 20 μM) were analysed. Circles indicate projection of ~0° and ~90° dwell points on an obliquely situated circular trajectory that best fit the data. Angles in the time courses and in Fig. 5 are those on the oblique circle.

at 20 μM ATP. At 2 mM ATP, the expected rate of ATP binding is $(2.6\times10^7\ M^{-1}s^{-1}\times2\ mM)\approx5\times10^4\ s^{-1}$. Then, 0° dwells will be ~0.02 ms and will not be detected at the current resolution. The absence of substeps in Fig. 4a, b is thus explained. We place dwells in Fig. 4a, b on grey lines, because they must be 90° dwells according to this explanation (see also Fig. 7).

The 30° substeps were not always clear, but we could easily locate, in rotation records, steps that spanned most of a 120° interval (~90° or ~120° step). Positions of the bead centroid in 0.25–0.5-ms intervals before (red) and after (green) these main steps are shown in the insets of Fig. 4. At 2 μM and 20 μM ATP, red and green spots are separated by ~30°, showing the presence of substeps, whereas spots overlap with each other at 2 mM ATP. The traces are distorted, presumably because of oblique rotation on an obliquely situated F_1. Circles on each trace are the projection of three equally spaced pairs of dwell positions on a circular trajectory oblique to the surface. A search for the best fit with the observed traces show the separation between red and green circles to be 29° ± 7° (mean ± s.d.) for 13 runs at 2, 6 and 20 μM ATP; and 4° ± 3° for 7 runs at 2 and 6 mM.

Figure 5 shows histograms of angular positions. Separations of peaks at 20 μM ATP (crosses) averaged 35° ± 13° (mean ± s.d. for 15 peak pairs). Substeps are less obvious at 2 μM, but histograms for the 2-ms intervals before and after the main steps (green) show similar peak separations. Taking these and other experimental uncertainties into account, we estimate the substep sizes to be within 90° ± 10° and 30° ± 10°.

Steps are fast

Consecutive steps in a rotation record at 2 mM ATP are super-

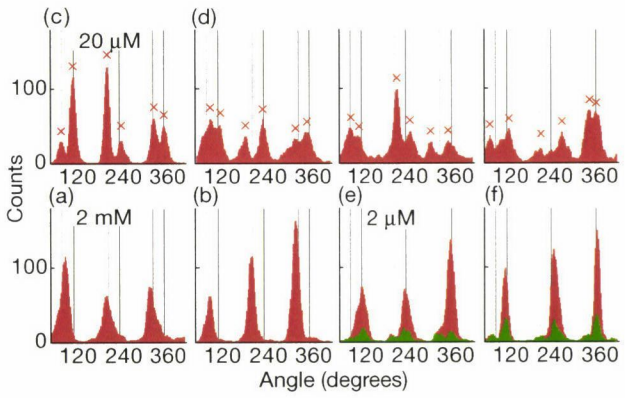

Figure 5 Histograms of angular positions over 0.5 s runs. Labels (a–f) are from records of which Fig. 4, **a**–**f** are a part. Each time course was passed through a five-point median filter, and its histogram was calculated with 2° bins. The histogram was then averaged over 10° intervals. Green parts (**e** and **f**) indicate 2 ms before and after main steps. Crosses indicate peaks identified by eye. To assess the baseline noise in raw data, we also constructed unfiltered, unaveraged histograms at 2 μM ATP with 2° bins (not shown). The histograms gave three peaks, of which the half width at 1/e height was estimated by fitting each peak with a gaussian curve; the half widths averaged 18° ± 7° (mean ± s.d. for 15 peaks).

imposed in Fig. 6a. The average (thick cyan line) shows that a whole 120° step completes within 0.25 ms (two frames) at saturating ATP. This value is an upper boundary because faster transients are unresolved with the camera that we used. Thus, time for the mechanical stepping (the times needed to reorientate the γ-subunit through 90° and 30°) occupies < 10% of the ATPase cycle time. The 90° substeps at 2 μM ATP are also within 0.25 ms (Fig. 6b). Stepping is fast, the instantaneous speed being well above 1,000 r.p.s., whether [ATP] is above or below K_m for rotation.

Substeps of 90° by ATP binding and 30° by product release

Figure 6c shows averages of all steps observed at indicated [ATP]. Presence of distinct and fast ~90° substeps is clear at all [ATP] < 60 μM, although whether the remaining ~30° is also stepwise cannot be judged in this figure. Fit with grey lines indicates the substep size to be 90.2° ± 0.3°.

The averaging was made after steps other than the central one were eliminated from each step record, such that it started with a near −30° dwell and ended with a ~120° dwell. When the last dwell at 120° was too short to be distinguished, the previous dwell at ~90° was extended to the right edge of the figure (see Methods). Thus, the portion of the curves between −30° and 0° reflects the distribution of dwell times at 0° that were started at the end of a substep from −30° to 0°, and terminated by a central 90° substep. The dwell is [ATP]-dependent, and can be explained by termination by ATP binding at the rate $k_{on}^{ATP} = 3.0 \times 10^7\ M^{-1}\,s^{-1}$ estimated from Fig. 8 (Fig. 6c; grey lines). The kinetics above 90°, in contrast, is [ATP]-independent, except that the amplitude decreases with [ATP]. The decrease is accounted for by the fact that, at [ATP] > K_m, the dwell at ~120° becomes too short and is not represented in our averaging procedure. As shown (grey lines), the kinetics are in accord with the scheme in Fig. 7a where two ~1-ms reactions govern the dwell at ~90° (the two reactions are deduced from Fig. 8).

Our proposed scheme is summarized in Fig. 7a. ATP binding drives a 90° substep (A→B). Next are hydrolysis reactions that are mechanically silent (B, C). Eventually, the last hydrolysis product of the previously bound ATP (ADP, phosphate, or both) is released, accompanying a 30° substep (C→A′) and resetting the system to the initial A state except for the 120° rotation that has taken place. At high [ATP], another 90° substep occurs immediately, and thus the two substeps are not resolved (Fig. 7b)—this is why we propose that both of the hydrolysis products must have been released by the end of a 30° substep. At [ATP] ~ K_m, ATP binding and hydrolysis take similar time, and 90° and 30° substeps are equally spaced.

Two ~1-ms reactions before a next step

Figure 8a shows histograms of dwell times between two main steps (90° or 120°) that were easily discerned at all [ATP]. At [ATP] ≪ K_m (0.02 and 0.2 μM), the histograms were fitted with a single exponential (pink lines) with a rate proportional to [ATP] (Fig. 8b; open cirlces), indicating that ATP binding alone sets the pace of rotation at these [ATP]. At 2 μM ATP, the histogram starts at the origin at zero dwell and shows a distinct peak, indicating the appearance of another rate-limiting reaction. Between 2 and 60 μM, the histograms are explained, roughly, by the ATP-binding reaction and an ATP-independent, ~0.5-ms^{-1} reaction (Fig. 8b). At [ATP] >> K_m = 15 μM, the histograms still show a distinct peak, indicating the presence of at least two reactions. A fit with two rate constants indicated both to be ~1 ms (Fig. 8b; filled black circles), which, taken together, can account for the 0.5-ms^{-1} reaction at intermediate [ATP]. Thus, at least three rate constants, two for the ~1-ms reactions and one for ATP binding, are required to describe the rotation kinetics at all [ATP]. Global fit to all histograms (green lines) showed k_{on}^{ATP} to be $(3.0 \pm 0.1) \times 10^7\ M^{-1}\,s^{-1}$ (consistent with the estimate from Fig. 3 (above) and previous values in actin[11] and single-fluorophore[18] assays), and the other two rates to be 1.64 ± 0.06 ms^{-1} and 0.71 ± 0.02 ms^{-1}. Of the latter two reactions, we cannot discriminate which is first, and the two rates do not differ significantly (see also Fig. 8b).

Thus we propose in Fig. 7a that two ~1-ms dwells separate the 90° and 30° substeps. A simple explanation is that the first dwell is terminated by release of a hydrolysis product (phosphate or ADP) and the second by release of the other product. Alternatively, the first reaction may be splitting of ATP to ADP and phosphate, and the second reaction the release of the two. Either interpretation is

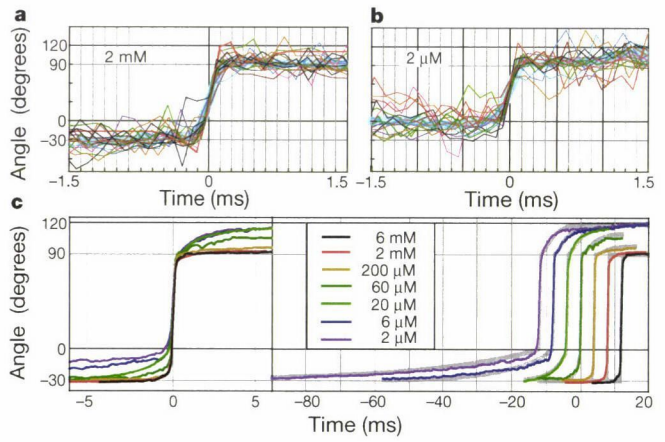

Figure 6 Kinetics of substeps. **a**, **b**, Eighteen consecutive steps and their average (thick cyan line) in a rotation record at 2 mM (**a**) or 2 μM (**b**) ATP (see Methods for the averaging procedure). **c**, Steps in several runs at indicated [ATP], averaged as in **a** and **b**. The averaging procedure retained all dwells at ~0° position in the ordinate, but some dwells at ~120° were converted to a horizontal line at ~90° position when the substep from 90° to 120° was contiguous (within 0.25 ms) with the next substep from 120° to 210°. This is why the curves at high [ATP] do not rise much beyond the 90° line. The curves are reproduced on the right; superimposed grey lines represent fits with theoretical curves based on the scheme in Fig. 7a (see Methods). The best fit was obtained with the size of the 30° substep, $A_{30°}$, of 29.8° ± 0.3° (mean ± s.e.m.).

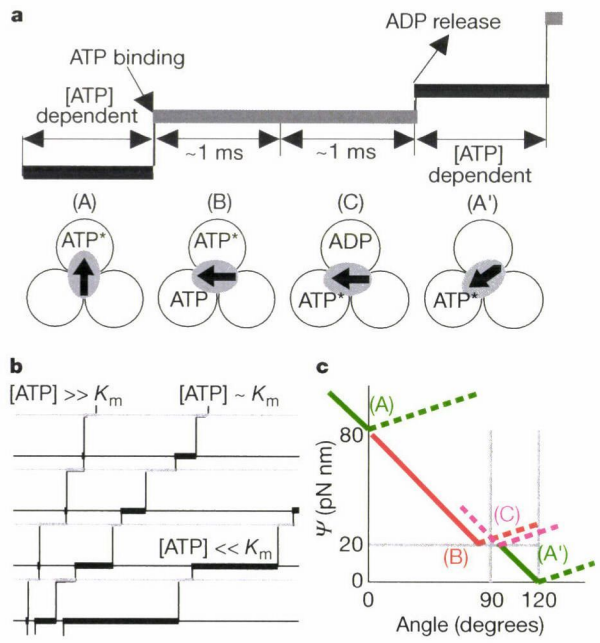

Figure 7 Proposed mechanism for F_1 rotation. **a**, Rotation scheme. ATP with asterisk represents ATP or ADP + phosphate; ADP (alone) may be phosphate or ADP + phosphate. **b**, Stepping time courses expected from **a**. **c**, Highly schematic diagram for the potential energy Ψ for γ-subunit rotation. Each coloured line shows Ψ in one of the four states in **a**. The orientation of the γ-subunit in state A (in **a**) is taken as 0°.

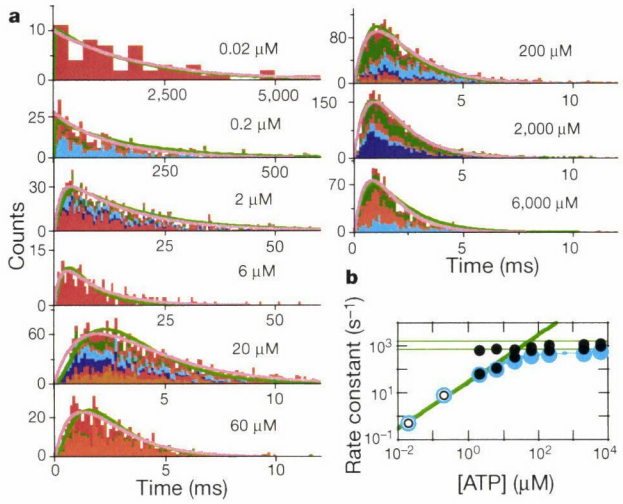

Figure 8 Dwells between main steps. **a**, Histograms of dwell times between two main (90° or 120°) steps at various [ATP]. Total counts in each histogram are 60, 463, 1,145, 2,862, 631, 2,384, 3,262 and 1,457 in the order of 0.02–6,000 μM. Histograms for individual runs are distinguished by colours; they are added to constitute a whole histogram. Pink lines at 0.02 and 0.2 μM ATP are single-exponential fits, constant·exp($-kt$), with k shown in open circles in **b**. Pink lines at other [ATP] are fits with two rate constants, constant·[exp($-k_a t$) − exp($-k_b t$)], with k_a and k_b shown (filled black circles in **b**). Green lines show the result of a global fit to the individual histograms ($n = 38$; equal weight for each count) with sequential reactions (Fig. 7a) starting with ATP binding at the rate k_{on}^{ATP}[ATP] and two ATP-independent reactions with rates k_1 and k_2: $k_{on}^{ATP} = (3.0 \pm 0.1) \times 10^7\ M^{-1}\ s^{-1}$, $k_1 = 1.64 \pm 0.06\ ms^{-1}$, and $k_2 = 0.71 \pm 0.02\ ms^{-1}$ (s.e.m.). **b**, ATP dependence of the rate constants. Blue circles show the total rate, k or $k_a k_b/(k_a + k_b)$ for the individual fits. Green lines show the rate constants obtained in the global analysis, and the total rate, $[k_1^{-1} + k_2^{-1} + (k_{on}^{ATP}[ATP])^{-1}]^{-1}$, is shown by the blue line.

consistent with the biochemical evidence that the releases of ADP and phosphate occur at similar rates[21].

Discussion

In our rotation scheme (Fig. 7a) one or two of the three catalytic sites are filled at any time with ATP or its product(s) of hydrolysis. This is the so-called bi-site mechanism[2,3,17], which is the norm at least at submicromolar [ATP]. Previously we have demonstrated rotation at [ATP] as low as 20 nM, indicating that bi-site hydrolysis accompanies rotation[11] and that bi-site is the fundamental mode of rotation[17]. Present results suggest bi-site to be the norm also at physiological (mM) [ATP]. Alternation between two-filled and three-filled states (the tri-site mechanism) has been proposed for hydrolysis at high [ATP], from non-Michaelis–Menten kinetics[22,23] as in Fig. 3, and from quenching of tryptophan fluorescence in the active sites[24]. These results indicating the tri-site mechanism may have been influenced by the MgADP inhibition[25]. In contrast, ATP synthesis by ATP synthase is insensitive to the inhibition and seems to proceed by a bi-site mechanism[26]. Our rotation assay focuses only on active F_1, and is unaffected by the inhibition. The rotation rate was higher than one-third of the hydrolysis rate at all [ATP] (Fig. 3), implying that part of F_1 in solution was not fully active already at several seconds after exposure to ATP. We do not necessarily deny possible occupancy of three sites, but we claim that filling all sites does not significantly accelerate, nor add power to, rotation.

Presence of the substeps indicates the appearance of two metastable structures during rotation, in which the equilibrium positions of the γ-subunit differ by ~90° (Fig. 7a: A versus B or C). If our bi-site interpretation is correct, the crystal structure in Fig. 1a probably corresponds to the two-nucleotide structure B (or C). The other central structure with one nucleotide (A) is yet to be solved. A structure[27] reported recently indicates that the protruding portion of the γ-subunit, where the bead was attached, is torsionally flexible, therefore it is possible that the substeps revealed here might be an artefact: intrinsic steps of the γ-subunit are always 120°, whereas the bead is somehow obstructed at 90° and lags behind for a few ms. We dismiss this possibility because (1) the bead rotated over 120° within 0.25 ms at 2 mM ATP; (2) the dwell time at 90° was independent of the radius of bead rotation, which presumably reflects differences in bead attachment; and (3) larger beads did not show any sign of obstruction.

In Fig. 7a, binding of ATP drives the 90° substep. By reciprocity, the affinity of the β-subunit for ATP, on the left of the arrow on the central γ-subunit, must increase as the γ-subunit rotates[6,16,17,28]. Likewise, because release of ADP (or phosphate, or both) drives the 30° substep, the affinity of the β-subunit for ADP, on the right of the arrow, must decrease as the γ-subunit rotates over the last 30°. The magnitude of these affinity changes can be estimated as below. We have shown that, at least under a high load, F_1 does 80–90 pN nm of mechanical work per 120° step[11] and that the torque it produces is nearly independent of the rotation angle[16,17] (the potential energy Ψ for γ-subunit rotation is linearly downhill). Rotation of 291-nm beads gave similar results (R.Y., unpublished observations). These results, combined with Fig. 7a, suggest the diagram in Fig. 7c for Ψ: in state A in Fig. 7a, Ψ_A is minimal at 0°; ATP binding produces state B where Ψ_B is linearly downhill toward its minimum at ~90°; Ψ_C is also minimal at ~90°; product release recovers state A′ where $\Psi_{A'}$ is again linearly downhill toward 120°. Solid lines have the constant slope of 80 pN nm of work per 120° as indicated by experiment, whereas dashed lines are drawn arbitrarily to provide minima at experimental positions. Affinity for ATP is proportional to $\exp[(\Psi_A - \Psi_B)/k_BT]$, where k_BT ~4.1 pN nm is the thermal energy at room temperature[6,28]. Thus, rotation from 0° to 90° accompanies an increase in the affinity of more than $\exp[(60\ pN\ nm)/k_BT] \sim 2 \times 10^6$. The affinity for ADP, $\propto \exp[(\Psi_{A'} - \Psi_C)/k_BT]$, decreases more than $\exp[(20\ pN\ nm)/k_BT] \sim 10^2$.

These affinity changes account for ATP synthesis by forced clockwise rotation of the γ-subunit. Starting from state A′ in Fig. 7a, the affinity for ADP of the empty β-subunit on the right of the arrow increases as the γ-subunit rotates clockwise, and this β-subunit will pick up ADP from the medium. Further rotation decreases the affinity for ATP of the β-subunit carrying the previously synthesized ATP (on the left of the arrow), and this ATP will eventually be released. In this simple scheme, it is the central, asymmetrical γ-subunit that dictates which of the three β-subunits should change its affinity, and to what extent. A corollary of the 'γ-dictator model' is that tri-site operation may take place during hydrolysis if ADP release is somehow slowed down, for example by partial inhibition. After a 90° substep, the γ-subunit is already pointing close to the next β-subunit and signals this β-subunit to bind ATP. ATP binding may therefore occur without waiting for the 30° substep accompanying ADP release; however, this would be an inefficient tri-site mechanism with no additional power and speed, as we claim above.

Synthesis (or hydrolysis) of ATP on a β-subunit does not require much energy, because ATP and ADP + phosphate are in equilibrium on the β-subunit[21,26]. This is in accord with our observation that the hydrolysis reaction, which we presume to occur during the two ~1-ms reactions, is mechanically silent. The principal function of hydrolysis is to allow the release of bound ATP by converting it to products, thereby resetting the machine for the next round of stepping. Complete mechanical silence, however, is unfavourable for efficient ATP synthesis, because clockwise rotation should release ATP, not ADP + phosphate. Indeed, it has been indicated that the equilibrium shifts toward ATP during synthesis[26]. One such mechanism (a switch-less model for F_1 motor[16,17]) is suggested in Fig. 7c, where the minimum in Ψ_C (after hydrolysis) is placed slightly to the right of the minimum in Ψ_B (before hydrolysis). Such a slight shift would be undetectable at the present resolution.

Our work is essentially a consolidation and embodiment of the binding-change model[1–3]. Similar to F_1-ATPase, myosin hosts ATP and its hydrolysis product at near equilibrium[29,30]. This may be the general tactics adopted by many ATP-dependent molecular machines. If so, much of the free-energy drop accompanying ATP hydrolysis occurs in the ATP-binding step[17,29,30]. ATP binding may be the principal source of power in these molecular machines. Indeed, ATP binding induces large conformational changes in molecules such as myosin[31], kinesin[32,33] and chaperonin[34]. □

Methods

Proteins

A mutant (α-C193S, β-His_{10} at amino terminus, γ-S107C, γ-I210C) $\alpha_3\beta_3\gamma$ subcomplex (referred to here as F_1) derived from a thermophilic *Bacillus* PS3 was biotinylated at two cysteines (γ-107C and γ-210C) by incubation with fourfold molar excess of 6-*N*′-[2-(*N*-maleimido)ethyl]-*N*-piperazinylamidohexyl-D-biotinamide for 1 h at 23 °C. Unbound biotin was removed with PD10 (Amersham Pharmacia). Two biotin moieties per protein were found in an assay using 4-hydroxyazobenzene-2-carboxylic acid[35]. Eight molar excess of streptavidin (Pierce) was added to the biotinylated F_1 and purified on Superdex-200HR (Amersham Pharmacia).

Beads

Colloidal gold (diameter 40 nm; British BioCell International) was coated with biotinylated BSA by incubating 0.2% colloidal gold in 2 mM potassium phosphate pH 7.0 with 0.4 mg ml^{-1} BSA and 0.2 mg ml^{-1} sulphosuccinimidyl-*N*-[*N*′-(D-biotinyl)-6-aminohexanoyl]-6′-aminohexanoate (biotin-$(AC_5)_2$ sulpho-OSu; Dojin) for 1 h at 23 °C. We stored modified gold particles in a solution containing 2 mM potassium phosphate and 0.05% polyethylene glycol. Polystyrene beads were biotinylated as follows: 2.7% amino beads (108 nm; Polyscience) in 20 mM potassium phosphate pH 7.0 was incubated with 1 mg ml^{-1} of biotin-$(AC_5)_2$ sulpho-OSu for 1 h at 23 °C. We incubated 2.5% of carboxy beads (196 or 291 nm; Bangs) in 20 mM potassium phosphate with 3.6 mM 5-(((*N*-(biotinoyl)amino)hexanoyl)amino)pentylamine trifluoroacetate salt (Molecular Probes), 1% 1-ethyl-3-(3-dimethylaminopropyl)-carbodiimide hydrochloride and 1% *N*-hydroxysulphosuccinimide for 1 h at 23 °C.

Rate of ATP hydrolysis

Nucleotide-depleted F_1 was prepared[18], and its ATPase activity was determined at 23 °C with an ATP-regenerating system[18,36] containing 1 mM phosphoenolpyruvate, 200 μg ml^{-1} pyruvate kinase, 100 μg ml^{-1} lactate dehydrogenase, 0.15 mM NADH, and indicated MgATP in buffer A (50 mM KCl, 2 mM $MgCl_2$, 10 mM 3-[*N*-morpholino]propanesulfonic acid-KOH, pH 7.0). The initial hydrolysis rate was determined from the slope of absorbance decrease at 340 nm; the average slope was estimated for the period of 2–5 s (2 mM–12 μM ATP), 2–7 s (6–2 μM) or 2–12 s (0.2–0.06 μM) after the start of the reaction. In the presence of LDAO, hydrolysis kinetics showed a lag, and thus the rate was estimated at steady state during 400–500 s (2 mM–60 μM), 1,000–1,500 s (20–6 μM) or 4,500–5,000 s (2–0.6 μM).

Microscopy

Beads of 196 nm and 291 nm were observed with transmitted light on an Olympus IX-70 microscope. We observed 40-nm and 108-nm beads with laser dark-field microscopy[12] (Fig. 1c). A laser beam (532 nm, diameter 3 mm, 200 mW, Millenia II, Spectra Physics) was introduced into a dark-field condenser (numerical aperture, NA 1.2–1.4; Olympus) to illuminate the specimen obliquely. Light scattered by beads was collected with a ×100 objective (NA 1.35; Olympus) with its iris diaphragm set to NA ~1.1 to block the direct ray. The field of view was ~50 μm. To confirm that we observed single 40-nm beads and not their aggregates, we measured the intensity of beads with regular dark-field microscopy with a halogen lamp, which provided homogeneous illumination. The intensity distribution had a single, large peak and a second small peak at four times the intensity of the first peak. Because an object smaller than the wavelength scatters light in proportion to the square of its volume[37], these peaks should correspond to single and duplex beads. Most beads were thus single. Twenty-fold reduction in the laser intensity did not affect the rotation speed, indicating that heating by the laser was insignificant.

Bead rotation assay

A flow cell was made of two KOH-cleaned coverslips separated by two spacers with 50 μm thickness[11]. Mixture of 0.1–1 nM beads and F_1 at 10–100 times the bead concentration in buffer B (buffer A plus 5 mg ml^{-1} BSA) was applied to the flow cell. Unbound beads were washed out with buffer B, and then buffer B plus MgATP (Mg^{2+} 2 mM in excess), 0.1 mg ml^{-1} creatine kinase, and 1 mM creatine phosphate was infused. Bead images were recorded as an eight-bit AVI file with a fast framing CCD camera (HiD-Cam, Nac) at 8,000 frames per s at [ATP] ≥ 2 μM; 125 frames per s at 0.2 μM; and 60 frames s^{-1} at 0.02 μM. The temperature was 23 °C. From each unmodified image, the bead centroid was calculated as $\Sigma x_i(I_i-I_{th})/\Sigma(I_i-I_{th})$, where x_i (or y_i) is the pixel coordinate, I_i the pixel intensity, I_{th} a threshold value, and the summation was for $I_i \geq I_{th}$.

The rotational frictional drag coefficient ξ for the beads was calculated as follows: for a single bead of radius a rotating in water with viscosity η (= 10^{-9} pN nm^{-2} s), minimal ξ is given by $8\pi\eta a^3$ when the rotation axis is at the bead centre, and maximal ξ by $8\pi\eta a^3 + 6\pi\eta a^3 = 14\pi\eta a^3$ when the axis is at a bead edge; for a bead duplex, minimal ξ is given by $2\times 8\pi\eta a^3 = 16\pi\eta a^3$ for a vertical duplex rotating around its centre, whereas maximal ξ is $2\times 8\pi\eta a^3 + 6\pi\eta a^3 + 6\pi\eta a\,(3a)^2 = 76\pi\eta a^3$ for a horizontal duplex rotating around an edge.

Analysis of substep kinetics

We superimposed and averaged time courses of individual steps as in Fig. 6a, b. First, we identified all main (90° or 120°) steps in a continuous run by eye. Then, individual steps were aligned on the time axis by positioning the midpoint of each step at time 0 (to within ± one frame). Vertical alignment was made by shift, by multiples of 120°. Next, steps other than the central one were eliminated from individual step records: the part earlier than 0.25 ms after the preceding 90° substep (or 120° step when substeps were contiguous) was replaced with a horizontal line at the angle at the 0.25-ms point (for example, a red line in Fig. 6a), and the part later than 0.25 ms before the following 90° substep (or 120° step) was replaced with the angle at that point (Fig. 6a; red line). Finally, we averaged all step records (Fig. 6a, b; thick cyan lines).

Step records averaged over several runs (Fig. 6c, coloured lines) were fitted with theoretical kinetics (Fig. 6c; grey lines) on the basis of the scheme in Fig. 7a; rate constants in the scheme were fixed to the values determined in Fig. 8. For the [ATP]-dependent kinetics for the rise from −30° to 0°, the grey lines show $A_{30°}\exp(k_{on}^{ATP}[ATP]t) - A_{30°}$, where $A_{30°}$ is the size of the 30° substep, $k_{on}^{ATP} = 3.0\times10^7$ M^{-1} s^{-1}, and t (< 0) is time from the central 90° substep. For the rise from 90° to 120°, two reactions with rates k_1 = 1.64 ms^{-1} and k_2 = 0.71 ms^{-1} are assumed, giving $A_{30°}B\{1-[k_2\exp(-k_1t) - k_1\exp(-k_2t)]/(k_2-k_1)\} + (120°-A_{30°})$ where $B = \exp(-k_{on}^{ATP}[ATP]\ 0.25\ ms)$ accounts for the loss of some of the 30° substeps in the averaging process. Global fit to all experimental curves (allowing a vertical shift for each curve) yielded $A_{30°} = 29.8 \pm 0.3°$.

Received 4 October 2000, accepted 26 February 2001

1 Boyer, P. D. & Kohlbrenner, W. in *Energy Coupling in Photosynthesis* (eds Selman, B. R. & Selman-Reimer, S.) 231–240 (Elsevier, Amsterdam, 1981)
2 Boyer, P. D. The binding change mechanism for ATP synthase—some probabilities and possibilities. *Biochim. Biophys. Acta* **1140,** 215–250 (1993).
3 Boyer, P. D. Catalytic site forms and controls in ATP synthase catalysis. *Biochim. Biophys. Acta* **1458,** 252–262 (2000).
4. Cox, G. B., Jans, D. A., Fimmel, A. L., Gibson, F. & Hatch, L. The mechanism of ATP synthase. Conformational change by rotation of the b-subunit. *Biochim. Biophys. Acta* **768,** 201–208 (1984).
5. Mitchell, P. Molecular mechanics of protonmotive F_oF_1 ATPases. Rolling well and turnstile hypothesis. *FEBS Lett.* **182,** 1–7 (1985).
6. Oosawa, F. & Hayashi, S. The loose coupling mechanism in molecular machines of living cells. *Adv. Biophys.* **22,** 151–183 (1986).
7. Abrahams, J. P., Leslie, A. G. W., Lutter, R. & Walker, J. E. Structure at 2.8 Å resolution of F_1-ATPase from bovine heart mitochondria. *Nature* **370,** 621–628 (1994).
8. Duncan, T. M., Bulygin, V. V., Zhou, Y., Hutcheon, M. L. & Cross, R. Rotation of subunits during catalysis by *Escherichia coli* F_1-ATPase. *Proc. Natl Acad. Sci. USA* **92,** 10964–10968 (1995).
9. Sabbert, D., Engelbrecht, S. & Junge, W. Intersubunit rotation in active F-ATPase. *Nature* **381,** 623–625 (1996).
10. Noji, H., Yasuda, R., Yoshida, M. & Kinosita, K. Jr. Direct observation of the rotation of F_1-ATPase. *Nature* **386,** 299–302 (1997).
11. Yasuda, R., Noji, H., Kinosita, K. Jr & Yoshida, M. F_1-ATPase is a highly efficient molecular motor that rotates with discrete 120° steps. *Cell* **93,** 1117–1124 (1998).
12. Kudo, S., Magariyama, Y. & Aizawa, S. Abrupt changes in flagellar rotation observed by laser dark-field microscopy. *Nature* **346,** 677–680 (1990).
13. Miyata, H. *et al.* Stepwise motion of an actin filament over a small number of heavy meromyosin molecules is revealed in an *in vitro* motility assay. *J. Biochem. (Tokyo)* **115,** 644–647 (1994).
14. Weber, P. C., Ohlendorf, D. H., Wendoloski, J. J. & Salemme, F. R. Structural origins of high-affinity biotin binding to streptavidin. *Science* **243,** 85–88 (1989).
15. He, X. M. & Carter, D. C. Atomic structure and chemistry of human serum albumin. *Nature* **358,** 209–215 (1992).
16. Kinosita, K. Jr, Yasuda, R. & Noji, H. F_1-ATPase: a highly efficient rotary ATP machine. *Essays Biochem.* **35,** 3–18 (2000).
17. Kinosita, K. Jr, Yasuda, R., Noji, H. & Adachi, K. A rotary molecular motor that can work at near 100% efficiency. *Phil. Trans. R. Soc. Lond. B* **355,** 473–489 (2000).
18. Adachi, K. *et al.* Stepping rotation of F_1-ATPase visualized through angle-resolved single-fluorophore imaging. *Proc. Natl Acad. Sci. USA* **97,** 7243–7247 (2000).
19. Jault, J.-M. *et al.* The $\alpha_3\beta_3\gamma$ complex of the F_1-ATPase from the thermophilic *Bacillus* PS3 containing the $\alpha D_{261}N$ substitution fails to dissociate inhibitory Mg ADP from a catalytic site when ATP binds to noncatalytic sites. *Biochemistry* **34,** 16412–16418 (1995).
20. Matsui, T. *et al.* Catalytic activity of the $\alpha_3\beta_3\gamma$ complex of F_1-ATPase without noncatalytic nucleotide binding site. *J. Biol. Chem.* **272,** 8215–8221 (1997).
21. Cunningham, D. & Cross, R. L. Catalytic site occupancy during ATP hydrolysis by MF_1-ATPase. Evidence for alternating high affinity sites during steady-state turnover. *J. Biol. Chem.* **263,** 18850–18565 (1988).
22. Gresser, M. J., Myers, J. A. & Boyer, P. D. Catalytic site cooperativity of beef heart mitochondrial F_1 adenosine triphosphatase. Correlations of initial velocity, bound intermediate, and oxygen exchange measurements with an alternating three-site model. *J. Biol. Chem.* **257,** 12030–12038 (1982).
23. Jault, J.-M. *et al.* The $\alpha_3\beta_3\gamma$ subcomplex of the F_1-ATPase from the thermophilic *Bacillus* PS3 with the βT165S substitution does not entrap inhibitory MgADP in a catalytic site during turnover. *J. Biol. Chem.* **271,** 28818–28824 (1996).
24. Weber, J., Wilke-Mounts, S., Lee, R. S., Grell, E. & Senior, A. E. Specific placement of tryptophan in the catalytic sites of *Escherichia coli* F_1-ATPase provides a direct probe of nucleotide binding: maximal ATP hydrolysis occurs with three sites occupied. *J. Biol. Chem.* **268,** 20126–20133 (1993).
25. Milgrom, Y. M., Murataliev, M. B. & Boyer, P. D. Bi-site activation occurs with the native and nucleotide-depleted mitochondrial F_1-ATPase. *Biochem. J.* **330,** 1037–1043 (1998).

26 Zhou, J.-M. & Boyer, P. D. Evidence that energization of the chloroplast ATP synthase favors ATP formation at the tight binding catalytic site and increases the affinity for ADP at another catalytic site. *J. Biol. Chem.* **268,** 1531–1538 (1993).
27 Gibbons, C., Montgomery, M. G., Leslie, A. G. W. & Walker, J. E. The structure of the central stalk in bovine F_1-ATPase at 2.4 Å resolution. *Nature Struct. Biol.* **7,** 1055–1061 (2000).
28 Wang, H. & Oster, G. Energy transduction in the F_1 motor of ATP synthase. *Nature* **396,** 279–282 (1998).
29 Wolcott, R. G. & Boyer, P. D. The reversal of the myosin and actomyosin ATPase reactions and the free energy of ATP binding to myosin. *Biochem. Biophys. Res. Commun.* **57,** 709–716 (1974).
30 Mannherz, H. G., Schenck, H. & Goody, R. S. Synthesis of ATP from ADP and inorganic phosphate at the myosin-subfragment 1 active site. *Eur. J. Biochem.* **48,** 287–295 (1974).
31 Houdusse, A., Szent-Gyorgyi, A. G. & Cohen, C. Three conformational states of scallop myosin S1. *Proc. Natl. Acad. Sci. USA* **97,** 11238–11243 (2000).
32. Rice, S. *et al.* A structural change in the kinesin motor protein that drives motility. *Nature* **402,** 778–784 (1999).
33 Schnitzer, M. J., Visscher, K. & Block, S. M. Force production by single kinesin motors. *Nature Cell Biol.* **2,** 718–723 (2000).
34 Sigler, P. B. *et al.* Structure and function in GroEL-mediated protein folding. *Annu. Rev. Biochem.* **67,** 581–608 (1998).
35 Kunioka, Y. & Ando, T. Innocuous labeling of the subfragment-2 region of skeletal muscle heavy meromyosin with a fluorescent polyacrylamide nanobead and visualization of individual heavy meromyosin molecules. *J. Biochem. (Tokyo)* **119,** 1024–1032 (1996).
36 Kato, Y., Sasayama, T., Muneyuki, E. & Yoshida, M. Analysis of time-dependent change of *Escherichia coli* F_1-ATPase activity and its relationship with apparent negative cooperativity. *Biochim. Biophys. Acta* **1231,** 275–281 (1995).
37 Born, M. & Wolf, E. *Principles of Optics* 7th edn (Cambridge Univ. Press, Cambridge, 1999).

Supplementary information is available on *Nature*'s World-Wide Web site (http://www.nature.com).

Acknowledgements

We thank T. Ariga for sample preparation; A. Kusumi for colloidal gold; T. Hisabori, E. Muneyuki, T. Nishizaka, K. Adachi, C. Gosse, M. Y. Ali, S. Ishiwata and G. W. Feigenson for critical discussions; and H. Umezawa for laboratory management. This work was supported in part by Grants-in-Aid from the Ministry of Education, Science, Sports and Culture of Japan.

Correspondence and requests for materials should be addressed to K.K.

polarizable Cs^+ ions, you have the recipe for a good ionic conductor.

For a couple of decades, $CsHSO_4$ has been the model high-temperature proton conductor. But no one tested it in a real fuel cell. They may have been discouraged by its softness in the superionic phase, its solubility in water, the difficulty of synthesizing the compound with electrodes attached and the narrow operating window available (between 140 °C and its melting/decomposition temperature above 200 °C). Haile *et al.*[1] have now responded to the increasing clamour for intermediate-temperature solid electrolytes, and proton conductors in particular, and tried out $CsHSO_4$ in a laboratory set-up.

They made a fuel cell by sandwiching the solid acid between two electrode layers made from $CsHSO_4$ powder mixed with platinum and carbon and a volatile organic. The entire fuel cell was compressed to provide good contact between the electrolyte and electrode layers. On heating, the organic component evaporated, leaving behind a porous electrode structure with the possibility of multiple contacts between the fuel (or oxygen, at the other end of the cell), the electrolyte and the electrodes.

Next came the question of whether the solid acid electrolyte was stable when exposed to the operating conditions of the fuel cell: a temperature of 160 °C, hydrogen gas at one electrode and oxygen at the other. The laboratory fuel cell performed stably over several days, burning the world's cleanest fuel — hydrogen — and emitting the most environmentally friendly effluent, pure water.

Haile and her colleagues[1] have been studying for some time another class of proton conductors, in which the protons are not part of the structure, but merely defects dissolved in water-containing atmospheres. The breakthrough for these materials came in the early 1980s when Iwahara and coworkers showed that chemically doped $SrCeO_3$ and other perovskite-related oxides became proton-conducting in humid atmospheres and at high temperatures up to 800 °C. Iwahara demonstrated fuel cells and other devices based on a number of perovskite-related oxides, and conceived the term protonics for the rapidly expanding field of solid-state proton conductors[4].

These high-temperature perovskite conductors lose protons at high temperatures, so the optimum temperature of proton conduction is a compromise between proton concentration and mobility. The proton conductivity typically peaks at around 400–600 °C. From these temperatures and down to those of solid acids such as $CsHSO_4$ (160 °C) there is a gap in fuel-cell temperatures for which, as yet, there is no real candidate for a solid electrolyte. This is an important temperature range because it should allow good materials stability, fast reaction kinetics, and manageable heat recovery for a wide variety of applications.

Haile *et al.*[1] are applying for a patent for fuel cells based on solid acid salts, but are otherwise realistically modest about their results. The $CsHSO_4$ electrolyte they used was a millimetre or more thick, whereas real applications will require micrometre-thin films to reduce the resistance of the electrolyte layer. The performance of the electrodes may also be of concern; slow charge transfer appears to cause further drops in voltage. Overall, the laboratory fuel cell delivers a modest 44 milliwatts per square centimetre, which compares unfavourably with the output of state-of-the-art PEFCs and SOFCs. More importantly, one can imagine that operation times of tens of thousands of hours will reveal degradation of the electrolyte due to creep, evaporation and reduction of sulphate in the solid acid by the fuel. From a practical point of view, accidental overheating would melt or decompose the electrolyte and water flooding would easily dissolve it.

Nonetheless, Haile *et al.* have proved the concept; true solid-state proton conductors can indeed be put to work in fuel cells, and the relevance of protonics has been extended into the intermediate temperature range. If $CsHSO_4$ is not the most practical electrolyte, then there is a rich chemistry of solid acids and hydroxides with much yet to discover. ■

Truls Norby is in the Department of Chemistry, University of Oslo, Centre for Materials Science, Gaustadalleen 21, NO-0349 Oslo, Norway.
e-mail: truls.norby@kjemi.uio.no

1. Haile, S. M., Boysen, D. A., Chisholm, C. R. I. & Merle, R. B. *Nature* **410**, 910–913 (2001)
2. Glasser, L. *Chem. Rev.* **75**, 21–65 (1975)
3. Baranov, A. I. *et al. JETP Lett.* **36**, 459–462 (1982)
4. Iwahara, H. in *Proc. 17th Risø Int. Symp. Mat. Sci.* (eds Poulsen, F. W. *et al.*) 13–28 (Risø National Laboratories, Roskilde, Denmark, 1996)

Molecular motors

Doing a rotary two-step

Mark J. Schnitzer

By spinning around, the ATP synthase converts energy from electrochemical to chemical form for storage. A cunning assay reveals intricate details of the rotation.

How do organisms power themselves? This simple question marked the start of a decades-long quest that led eventually to a rotary enzyme called ATP synthase. Using energy derived from proton gradients created during photosynthesis or respiration, this enzyme produces ATP (adenosine triphosphate) molecules — the main cellular energy store. A challenge now is to understand how ATP synthase works. It is thought to contain two rotary motors, called F_0 and F_1, which are rotationally coupled through their drive shafts. This device uses motion, in the form of 120° rotary steps by F_1, as an intermediate, converting energy from electrochemical through mechanical to chemical form[1]. On page 898 of this issue[2], Yasuda and colleagues describe their elegant studies of the F_1 motor, and show that each rotary step actually consists of two smaller substeps. More generally, their work highlights some central issues concerning energy flow in proteins.

The F_0 and F_1 motors have specialized functions (Fig. 1). The F_0 motor is bound to membranes of energy-generating cellular structures such as mitochondria, and channels protons through its rotor and non-rotating stator to drive rotation. Meanwhile, the stator of F_1 catalyses the production of ATP from ADP (adenosine diphosphate) and inorganic phosphate, provided that F_0 drives the F_1 rotor with sufficient torque (rotary force). The catalytic sites of F_1 are within the three so-called β-subunits, which are arranged with tripartite symmetry in the stator. Both F_0 and F_1 can operate in reverse, and isolated F_1 is called the F_1-ATPase because, in the absence of torque from F_0, it hydrolyses ATP to power reverse rotation.

There is only indirect evidence that F_0 can drive rotation[3–5]. But rotation of F_1 subcomplexes has been visualized directly *in vitro*, by fixing the stator to a glass surface and using a micrometre-sized filament attached to the rotor's γ-subunit as a marker[6,7]. With this assay, 120° rotary steps can be detected by monitoring the movement of the filament at low ATP concentrations, such that the binding of ATP to F_1 is the rate-limiting event between steps[7]. The distribution of times between steps is consistent with one ATP molecule being hydrolysed per step.

Once a step begins, the time taken for the 120° turn depends on the frictional drag imposed by the filament and so on the filament's length. Drag also smoothes out any rapid fine structure within the protein's 120° movement when monitored via the filament. This obscures how rotor movements are linked to hydrolysis events, which probably occur in reverse during ATP synthesis. So, to break the speed barrier imposed by the filament, Yasuda *et al.*[2] have revved up the assay by using a bead with a diameter of a mere 40 nanometres as the marker. Using

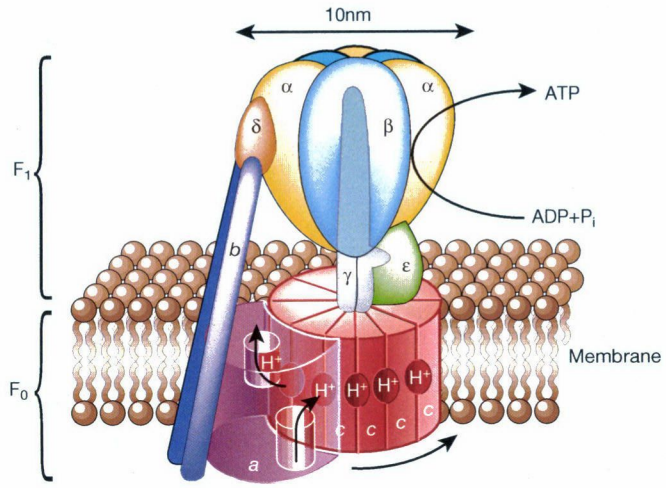

Figure 1 **ATP synthase — energy converter. The enzyme consists of two motors, F_0 and F_1. The transmembrane F_0 motor has one *a*, two *b* and nine to twelve *c* subunits. The soluble F_1 motor has three α and three β subunits, and one each of the ε, δ and γ subunits. The F_0 rotor (consisting of the *c* subunits) and the F_1 rotor (ε and γ subunits) are connected, as are the respective stators (the F_0 stator comprises the *a* and *b* subunits; the F_1 stator consists of the δ subunit and the three α and three β subunits). During ATP synthesis, F_0 channels protons across the membrane to drive rotation, which in F_1 occurs as 120° rotational steps. Yasuda *et al.*[2] show that each 120° step is composed of two smaller substeps of 90° and 30°. Modified from refs 14, 15.**

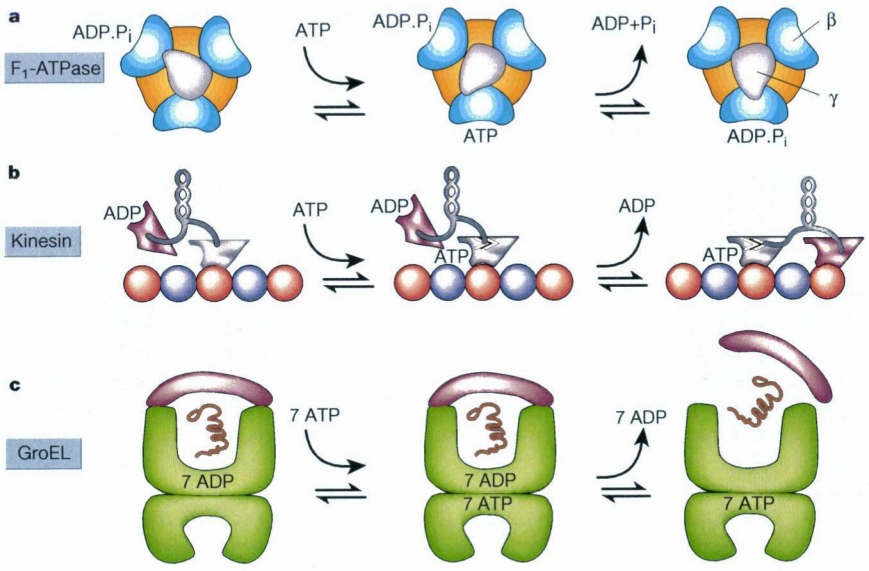

Figure 2 **Molecular machines that use ATP binding at one catalytic site to trigger a large conformational change and the release of ADP from another catalytic site. P_i is inorganic phosphate. a, F_1-ATPase, with the catalytic β-subunits in dark blue, the α-subunits in yellow, and the γ-subunit in light blue. When ATP binds to one β-subunit, the γ-subunit rotates by 90°. ADP and P_i are released from another β-subunit, and the γ-subunit rotates a further 30°. b, Kinesin, a linear motor with two catalytic heads (purple and grey) that move along a microtubule filament (red and blue). ATP binding to the front head triggers a conformational change (shown by double arrowheads) in its adjoining neck linker domain[9] and induces the rear head to step forward and to release ADP. c, The chaperone GroEL (green), its co-chaperone GroES (purple) and a substrate protein (squiggly line). GroES acts as a cap, containing the substrate protein within GroEL while the substrate folds. GroEL has two rings, each of which bind seven ATP or ADP molecules. Cooperative binding of seven ATP to one ring triggers the other ring to release GroES, the substrate protein and seven ADP molecules.**

a high-speed camera to capture footage of bead rotation, the authors find that, when attached to the γ-subunit off the rotational axis, the bead spins in an eccentric orbit during ATP hydrolysis. Rotational frictional drag is so slight that, at saturating ATP concentrations, 120° steps begin roughly every 2 milliseconds, and an entire step is complete within about 0.25 milliseconds.

A potential problem with these rapid speeds is that they might make it hard to detect substeps within a step, given that the camera acquires data only twice during a 120° step. However, it was known through the Nobel-Prize-winning work of Paul Boyer[8] that a large fraction of the energy liberated during the ATP-hydrolysis cycle is released when ATP binds tightly to one catalytic site. Most of the remaining energy is freed about 2 milliseconds later, when the products of hydrolysis (ADP and inorganic phosphate) are released from another catalytic site (Fig. 2a). It seemed plausible that these large energy changes might be accompanied by large conformational changes in F_1. If those changes involved rotational substeps, then it might prove possible to increase the average time between successive substeps to at least 2 milliseconds. The trick would be to pause rotation after the product-release substep, by lowering the ATP concentration enough to delay the next ATP-binding substep by 2 milliseconds or more. So, each substep would now follow a pause.

Yasuda *et al.*[2] adopt this tactic, and records of motion at 20 μM ATP or below reveal $90 \pm 10°$ and $30 \pm 10°$ substeps, separated by about 2 milliseconds. The 90° movement must be the binding substep — its mean initiation time following a 30° movement depends on ATP concentration. Histograms of initiation times reveal the delay between 90° and 30° rotations, and show a time distribution consistent with two kinetic transitions, each requiring about 1 millisecond. A remaining challenge is to correlate these transitions and the substeps with structural forms of the catalytic β-subunits.

ATP synthase was one of the first enzymes known to show cooperative interactions between its catalytic sites. We now have explicit proof[2] that ATP binding to F_1 triggers rotation. F_1 thereby joins a growing list of molecular machines that use ATP binding at one catalytic site to induce product release from another catalytic site through large mechanical movements (Fig. 2b, c). Two other examples are the motor protein kinesin and the chaperone molecule GroEL, which helps newly formed protein chains to fold into the correct shape. Kinesin has two catalytic head regions that somehow allow the molecule to advance in discrete 8-nanometre steps. ATP binding at one head triggers a conformational change in the protein, allowing ADP to be released from the other head[9] and stepping to occur. GroEL has two ring domains; binding of seven ATP molecules to one ring triggers the other ring to release the substrate protein[10] and seven ADP molecules.

In all of these proteins, how does energy flow outwards from an ATP-binding site to initiate movement and product release? Energy must travel between catalytic sites — about 5 nanometres in F_1-ATPase[11], some 9 nanometres in GroEL[10], and potentially

up to 16 nanometres in kinesin[9]. Detailed modelling[12] of F_1 indicates that ATP binding might trigger elastic bending in the catalytic β-subunit, which then applies torque to the γ-subunit in the rotor. In kinesin, a rigid helical structure may act as a mechanical relay between a phosphate-sensing loop at the ATP/ADP-binding site and a linker region that is usually mobile but which becomes immobilized upon ATP binding[9]. Energy flow in GroEL is poorly understood. Indeed, questions about all three enzymes remain; for example, do mechanical signals generally occur as elastic strain, as in F_1, or can some protein domains become thermally activated upon ATP binding? Temperature-dependent kinetic studies and efficiency considerations may help to separate entropic and enthalpic contributions, but energy flow will probably remain murky until investigated further. The hope is that new experimental approaches, such as those relying on protein databases to enable statistical comparisons of closely related proteins[13], will speed our understanding. ■

Mark J. Schnitzer is in the Biological Computation Research Department, Bell Laboratories, Lucent Technologies, Murray Hill, New Jersey 07974, USA.
e-mail: schnitzer@lucent.com

1. Boyer, P. D. *Annu. Rev. Biochem.* **66,** 717–749 (1997).
2. Yasuda, R., Noji, H., Yoshida, M., Kinosita, K. Jr & Itoh, H. *Nature* **410,** 898–904 (2001).
3. Dimroth, P. *Biochim. Biophys. Acta* **1458,** 374–386 (2000).
4. Sambongi, Y. *et al. Science* **286,** 1722–1724 (1999).
5. Rastogi, V. K. & Girvin, M. E. *Nature* **402,** 263–268 (1999).
6. Noji, H., Yasuda, R., Yoshida, M. & Kinosita, K. *Nature* **386,** 299–302 (1997).
7. Yasuda, R., Noji, H., Kinosita, K. & Yoshida, M. *Cell* **93,** 1117–1124 (1998).
8. Boyer, P. D. *Biochim. Biophys. Acta* **1140,** 215–250 (1993).
9. Vale, R. D. & Milligan, R. A. *Science* **288,** 88–95 (2000).
10. Sigler, P. B. *et al. Annu. Rev. Biochem.* **67,** 581–608 (1998).
11. Abrahams, J. P., Leslie, A. G., Lutter, R. & Walker, J. E. *Nature* **370,** 621–628 (1994).
12. Wang, H. & Oster, G. *Nature* **396,** 279–282 (1998).
13. Lockless, S. W. & Ranganathan, R. *Science* **286,** 295–299 (1999).
14. Elston, T., Wang, H. & Oster, G. *Nature* **391,** 510–513 (1998).
15. Boyer, P. D. *Nature* **402,** 247–249 (1999).

Fundamental physics

Newton rules (for now)

Frank Wilczek

Three hundred years after Newton explained the falling of an apple and the motion of the planets, physicists are beginning to test his universal law of gravity down to micrometre distances — with interesting results.

Newton's formula for the force of gravitational attraction is the oldest, and perhaps the most revered, universal law of physics. Yet it is not sacred. The experimental support for Newton's force law at sub-centimetre distances is surprisingly weak. There are theoretical suggestions about why and how deviations from Newton's law might arise at these distances. A group of experimentalists at the University of Washington, Seattle, has tackled the question, using ingenious but surprisingly low-tech, small-science techniques to test newtonian gravity down to 200 μm. As they report in *Physical Review Letters*[1], Newton's law still rules, which puts some theoretical speculation about large 'extra dimensions' on the ropes.

In modern physics, the precise form of Newton's formula for the gravitational force — proportional to mass, inversely proportional to distance squared — is rooted in profound principles. Force proportional to mass means acceleration independent of mass. Thus Newton's law implies that the motion induced by gravity is independent of the material properties of the body it acts upon. This idea is deeply engrained in Einstein's theory of general relativity, in which gravitational fields (produced by matter) change the geometry of space-time, causing it to become curved. It is the curvature of space-time that controls the natural acceleration of bodies. The inverse square form of Newton's law is a consequence of the field equations for gravity. The form of these equations, in turn, is dictated by the general principles of quantum field theory (specifically, the requirement that they derive from a local lagrangian function).

How, then, might deviations arise? One way is through the existence of extra, non-gravitational forces. Indeed, we know that there are other forces in physics, even at macroscopic distances. For example, there are $1/r^2$ electric forces between charged bodies, and $1/r^4$ magnetic forces (with complicated angular dependence) between magnetic bodies, where r is the separation. Even between unscreened neutral, non-magnetic bodies there are attractive short-range $1/r^7$ van der Waals forces. If our goal is to test the foundations of physics, however, our focus must be on non-electric, non-magnetic bodies, and forces beyond van der Waals.

Within the framework of quantum field theory, forces are associated with the exchange of virtual particles. Thus new forces are associated with new particles. The range of the force depends inversely on the mass of the particle. If the particle mass is m, then the range of the corresponding force is $\hbar/mc$, where $\hbar$ is Planck's constant and c is the speed of light. Numerically, a particle of mass 2×10^{-5} electron volts (25 billion times lighter than the electron) yields a force with a range of 1 centimetre. Thus in looking for deviations from Newton's force law — specifically new forces operating at supermolecular but sub-centimetre distances — we are probing for the existence of extremely light, extremely weakly interacting particles[2,3].

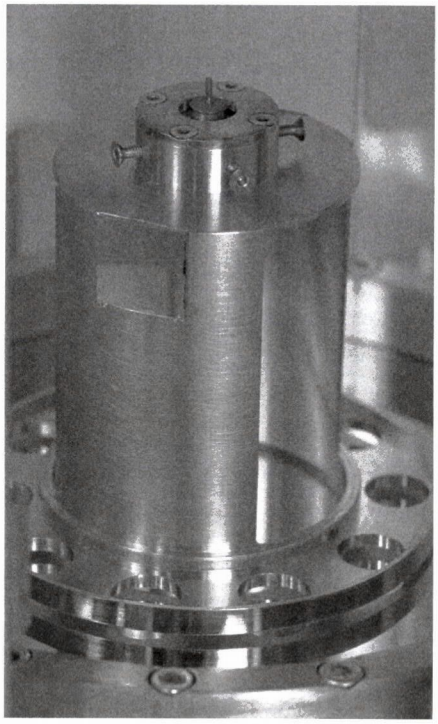

UNIV. WASHINGTON

Figure 1 **Apparatus used at the University of Washington[1] to test Newton's inverse square law. They measured the motion of a metal ring suspended above a rotating disk to show that Newton is correct down to ring–disk separations of at least 200 μm. The photograph shows the metal ring, which has ten holes bored in it, suspended from a torsion pendulum. The rotating disk below the metal ring is hidden from view by a sheet of metal foil that minimizes electrical forces on the pendulum. As the disk rotates, the gravitational force causes the ring to twist back and forth ten times for each revolution of the disk. The twisting of the pendulum is measured by reflecting a laser beam from a small mirror attached to the upper part of the pendulum. The entire apparatus is coated in gold to prevent electrical forces interfering with the weak gravitational signal.**

Many examples of such particles have been suggested, with various motivations. So-called axions[4] arise in attempts to explain the accurate time-reversal symmetry of the 'strong force' — the short-range interaction that holds protons and neutrons together in nuclei. Dilatons arise in superstring theory (a fundamental theory of elementary particles that requires extra dimensions). Familons and modulons arise in attempts to understand the origin of the subtle differences between particles in different families — for example the difference between the electron and its heavier cousins, the muon and tau leptons[5].

None of these exotic particles has yet been

THE JOURNAL OF BIOLOGICAL CHEMISTRY
Vol 276, No 27, Issue of July 6, pp 25480–25486, 2001
Printed in U S A

Purine but Not Pyrimidine Nucleotides Support Rotation of F_1-ATPase*

Received for publication, March 12, 2001, and in revised form, March 28, 2001
Published, JBC Papers in Press, March 28, 2001, DOI 10.1074/jbc.M102200200

Hiroyuki Noji‡§, Dirk Bald‡¶, Ryohei Yasuda‡‖, Hiroyasu Itoh‡, Masasuke Yoshida‡‡‡, and Kazuhiko Kinosita, Jr‡§§¶¶**

From ‡CREST "Genetic Programming" Team 13, Teikyo University Biotechnology Research Center 3F, Nogawa 907, Miyamae-ku, Kawasaki 216-0001, Japan, §PRESTO, Chemical Resources Laboratory, Tokyo Institute of Technology, Yokohama 226-8503, Japan, ‖Tsukuba Research Laboratory, Hamamatsu Photonics KK, Tokodai, Tsukuba 300-2635, Japan, ‡‡‡Chemical Resources Laboratory, Tokyo Institute of Technology, Yokohama 226-8503, Japan, and §§Faculty of Science and Technology, Keio University, Yokohama 223-8522, Japan

The binding change model for the F_1-ATPase predicts that its rotation is intimately correlated with the changes in the affinities of the three catalytic sites for nucleotides. If so, subtle differences in the nucleotide structure may have pronounced effects on rotation. Here we show by single-molecule imaging that purine nucleotides ATP, GTP, and ITP support rotation but pyrimidine nucleotides UTP and CTP do not, suggesting that the extra ring in purine is indispensable for proper operation of this molecular motor. Although the three purine nucleotides were bound to the enzyme at different rates, all showed similar rotational characteristics: counterclockwise rotation, 120° steps each driven by hydrolysis of one nucleotide molecule, occasional back steps, rotary torque of ~40 piconewtons (pN)·nm, and mechanical work done in a step of ~80 pN·nm. These latter characteristics are likely to be determined by the rotational mechanism built in the protein structure, which purine nucleotides can energize. With ATP and GTP, rotation was observed even when the free energy of hydrolysis was −80 pN·nm/molecule, indicating ~100% efficiency. Reconstituted F_oF_1-ATPase actively translocated protons by hydrolyzing ATP, GTP, and ITP, but CTP and UTP were not even hydrolyzed. Isolated F_1 very slowly hydrolyzed UTP (but not CTP), suggesting possible uncoupling from rotation.

The F_oF_1 ATP synthase is an enzyme that synthesizes ATP from ADP and inorganic phosphate (P_i) using proton flow across a membrane (1). The F_o portion of the enzyme resides in the membrane and mediates proton translocation. The F_1 portion, consisting of $\alpha_3\beta_3\gamma_1\delta_1\epsilon_1$ subunits, is external to the membrane and catalyzes ATP synthesis. The ATP synthase is a completely reversible molecular machine in that ATP hydrolysis in F_1 can produce a reverse flow of protons through F_o. Isolated F_1 only catalyzes ATP hydrolysis and hence is called F_1-ATPase. Its minimal, stable subcomplex capable of ATP hydrolysis is $\alpha_3\beta_3\gamma$ (2).

For the coupling between the proton flow in F_o and the chemical reaction (ATP synthesis/hydrolysis) in F_1, Boyer and Kohlbrenner (3) and Oosawa and Hayashi (4) independently suggested a rotational catalysis model. The essence is that F_o is a rotary motor (or turbine) driven by the proton flow, that F_1 is another rotary motor driven by ATP hydrolysis, and that the two motors have a common rotary shaft, yet their genuine rotary directions are opposite to each other's. Rotation of the shaft in F_o's genuine direction, as occurs in cells, results in the reverse rotation of the F_1 motor and thus in ATP synthesis in F_1. When F_1 gains control and hydrolyzes ATP, protons are pumped through F_o in the reverse direction.

A crystal structure of F_1 (5) strongly supported the rotation model and has inspired many experiments, which, together, have proved that the γ subunit is (part of) the common rotor shaft and that $\alpha_3\beta_3$ subunits, which surrounded γ in the crystal, are the stator in the F_1 motor (6–8). Single-molecule imaging of F_1, in particular, has revealed that the γ subunit rotates in a unique direction consistent with the crystal structure, that γ makes discrete 120° steps, and that the energy conversion efficiency of the F_1 motor driven by ATP hydrolysis can reach ~100% (9, 10). The precise mechanism of rotation, however, is not yet clear.

In Boyer's model, binding changes play the major role (1). On the three β subunits, each of which hosts a catalytic site, ATP and its hydrolysis products, ADP and P_i, are in equilibrium. Thus, in the absence of an external energy supply, the change in free energy associated with ATP hydrolysis should manifest as the higher affinity for ATP than for ADP and P_i. During ATP synthesis, the mechanical energy supplied by the γ rotation driven by F_o somehow decreases the affinity for ATP (and probably increases the affinity for ADP and P_i), resulting in the appearance of ATP in the medium. In the reverse reaction of ATP hydrolysis, the free energy difference between the stronger ATP binding and weaker ADP/P_i binding drives the rotation of γ. Boyer proposes that these binding changes occur sequentially on the three catalytic sites, synchronously with the γ rotation. In the crystal structure of F_1 (5), the three β subunits carried a different nucleotide, an analog of ATP, ADP, and none, in support of the sequential binding change mechanism.

If binding and release, rather than the cleavage of the terminal phosphate, are indeed the source of mechanical torque production in the F_1 motor, the rotational characteristics are expected to differ among different NTPs. The free energy gain in overall hydrolysis is similar among NTPs, but the operation of the F_1 motor, which can work at near 100% efficiency, may well depend on delicate energy balances in various steps of hydrolysis. Here we show that purine but not pyrimidine nu-

* The costs of publication of this article were defrayed in part by the payment of page charges. This article must therefore be hereby marked "*advertisement*" in accordance with 18 U.S.C. Section 1734 solely to indicate this fact.

¶ Present address: Dept. of Structural Biology, Free University of Amsterdam, De Boelelaan 1087, 1081, Amsterdam, Netherlands.
‖ Present address: Cold Spring Harbor Laboratory, 1 Bungtwon Rd., Cold Spring Harbor, NY 11724.
¶¶ To whom correspondence should be addressed. Tel.: 81 44 750 1710; Fax: 81 44 750 1712

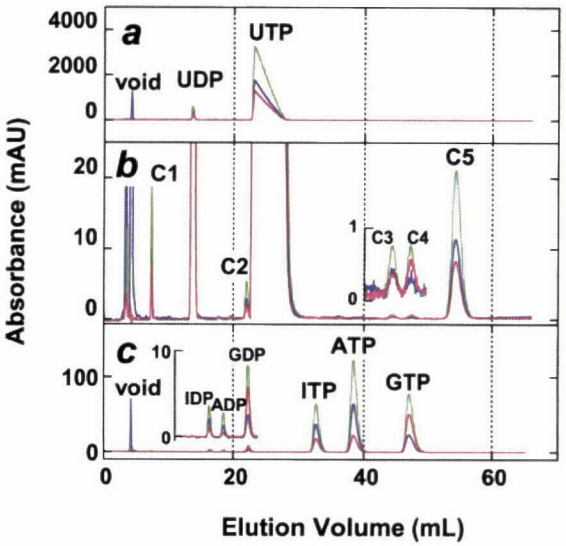

FIG. 1. **Contaminants in UTP.** 775 nmol of UTP was loaded on the anion exchange column equilibrated with 50 mM sodium phosphate (pH 7.0) and eluted with an isocratic flow of the equilibration buffer. *a*, elution profiles monitored as A_{220} (*blue*), A_{260} (*green*), and A_{280} (*red*). UTP contained UDP at 3%. *b*, expansions of profiles in *a*. *Inset*, further expansion. Five contaminant peaks, C1–C5, were resolved. *c*, elution profiles for combined purine nucleotides. 20 nmol of ATP, 10 nmol of GTP, and 10 nmol of ITP were loaded together. *Inset*, their expanded profiles. Contaminating ADP, GDP, and IDP were eluted before ATP, GTP, and ITP. Peak C4 was identified as GTP from the coincidence in the elution time and the relative magnitudes of A_{220}, A_{260}, and A_{280}. The amounts of the contaminants in C1–C5 were 0.10, 0.03, 0.01, 0.01, and 0.39% of UTP, respectively.

cleotides support F_1 rotation, suggesting that the interaction between the catalytic site and the additional ring in purines is critical to the proper operation of this molecular machine.

EXPERIMENTAL PROCEDURES

Chemicals and Proteins—Nucleotides (GTP, ITP, UTP, and CTP) were purchased from Sigma. ATP and other enzymes were from Roche Molecular Biochemicals. The purity of each nucleotide was assessed on an anion exchange column. Nucleotides were applied on DEAE 2SW (Tosoh, Japan) equilibrated with 50 mM sodium phosphate (pH 7.0) and eluted with an isocratic flow of the same buffer. Because DEAE 2SW has higher affinity for compounds with more negative charges, nucleotides are eluted in the order of nucleoside mono-, di-, and triphosphate. The elution profiles for UTP are shown in Fig. 1, *a* and *b*. Besides the UDP peak at 13 ml (identical with the peak for commercial UDP), several contaminant peaks (C1–C5) were resolved. The void peak at 4 ml is unlikely to be a nucleotide(s), because A_{260} (*green*) and A_{280} (*red*), within an absorbance peak of a nucleotide, were extremely low compared with A_{220} (*blue*). C1 at 7 ml was probably UMP, because it was eluted earlier, and the relative magnitudes of A_{220}, A_{260} and A_{280} were the same as those for UTP and UDP. C4 was judged as contaminating GTP, because its elution volume and the relative magnitudes of A_{220}, A_{260}, and A_{280} all matched with those for GTP (Fig. 1*c*). The GTP contamination amounted to 0.01% of UTP, as determined from the peak area of A_{260}. The other contaminants, C2, C3, and C5, were of unknown origin; their signatures did not match with those of ATP, GTP, ITP, dATP, or their diphosphates. C2, C3, and C5 in UTP amounted to 0.03, 0.01, and 0.39%, respectively. Although the levels of contaminants were low, they may nevertheless affect the rotation assay, because the affinity of F_1-ATPase for UTP is extremely low (see "Results"). We therefore used the fraction at the UTP peak (23 ml) for the rotation assay. CTP was also found to be contaminated by unknown compounds (1.5%); thus, its peak fraction was used for the rotation assay. ATP, GTP, and ITP contained less than 5% contaminants, which were mostly their hydrolysis products; these were used without purification.

The $\alpha_3\beta_3\gamma$ subcomplex (β-His tag/γS107C) of F_1 derived from thermophilic *Baccillus* strain PS3 (TF_1)[1] was expressed in *Escherichia coli* as described previously (9) and purified as follows. The cell lysate containing the enzyme was applied on a Ni^{2+}-NTA Superflow column (Qiagen) equilibrated with 50 mM imidazole (pH 7.0) and 100 mM NaCl. The column was washed with 100 mM imidazole (pH 7.0) and 100 mM NaCl, and then the enzyme was eluted with 500 mM imidazole (pH 7.0) and 100 mM NaCl. Ammonium sulfate was added to the fraction containing the enzyme to a final concentration of 10% saturation and the sample was applied to a butyl-Toyopearl column (Tosoh, Japan) equilibrated with 500 mM imidazole (pH 7.0), 100 mM NaCl, and 10% saturated ammonium sulfate. The column was washed with 10 column volumes of a solution containing 100 mM sodium phosphate (pH 7.0), 2 mM EDTA, and 10% saturated ammonium sulfate to remove endogenously bound nucleotides. The enzyme was eluted with 50 mM Tris-Cl (pH 8.0) and 2 mM EDTA and stored as precipitant in 70% saturated ammonium sulfate containing 2 mM dithiothreitol. Before use, the enzyme was dissolved in 100 mM sodium phosphate (pH 7.0) and 2 mM EDTA and passed through a size exclusion column (Superdex 200 HR 10/30; Amersham Pharmacia Biotech) equilibrated with 100 mM sodium phosphate (pH 7.0) and 2 mM EDTA. The amount of nucleotides remaining on the enzyme was determined as described previously (11). Samples with less than 0.1 mol of nucleotide/mol of enzyme were used for the measurement of hydrolysis activity. Whole TF_oF_1 complex was reconstituted from the mutant TF_1 (β-His tag/γS107C) and authentic F_o from the thermophile and was incorporated into liposomes as described previously (12).

NTPase Activity—ATP, GTP, ITP, and UTP hydrolysis activities of $\alpha_3\beta_3\gamma$ were measured at 23 °C in a medium containing 50 mM MOPS-KOH (pH 7.0), 50 mM KCl, 2 mM $MgCl_2$, and an ATP (or GTP, ITP, or UTP)-regenerating system consisting of 2.5 mM phosphoenolpyruvate, 100 μg/ml lactate dehydrogenase, 0.2 mM NADH, and pyruvate kinase at 200 μg/ml for ATP hydrolysis, 500 μg/ml for GTP and ITP hydrolysis, or 750 μg/ml for UTP hydrolysis. The reaction was initiated by the addition of the enzyme to 1.3 ml of assay mixture, and hydrolysis was monitored as NADH oxidation determined from the absorbance decrease at 340 nm. The CTP hydrolysis activity was estimated from P_i released in the same medium without a regenerating system during a 60-min incubation at 23 °C. Hydrolysis by the reconstituted TF_oF_1 was also measured as P_i released in 50 mM MOPS-KOH (pH 7.0), 25 mM $NaSO_4$, 25 mM K_2SO_4, 4 mM $MgCl_2$, and 2 mM indicated nucleotide during a 20-min incubation at 23 °C.

Rotation Assay—Streptavidin-conjugated TF_1 for the rotation assay was prepared as described previously (9). Rotation in the presence of ATP, GTP, or ITP was observed in the TF_1 adsorbed on a Ni^{2+}-NTA-modified polystyrene bead by attaching an actin filament to the γ subunit (10). The assay mixture contained 50 mM MOPS-KOH, (pH 7.0), 50 mM KCl, 2 mM $MgCl_2$, 10 mg/ml bovine serum albumin, and an indicated Mg-nucleotide. Fluorescent actin filaments at the bottom of a flow chamber were observed with an inverted epifluorescence microscope (IX70; Olympus). Assays at less than 10 μM GTP or ITP were made on the TF_1 directly attached to coverslips to which Ni^{2+}-NTA had been bound covalently (13); the probability of finding a rotating actin filament was higher than on the Ni^{2+}-NTA-modified polystyrene bead. Images were taken with an intensified CCD camera (ICCD-350F; VideoScope) and recorded on 8-mm videotapes. Rotation by UTP or CTP was observed through an aggregate of biotinylated polystyrene beads with a diameter of 440 nm, which was attached to γ (14). Images of bead aggregates were obtained in the bright field in the absence of the oxygen scavenger system and recorded with a CCD camera (CCD-300-RC; Dage-MTI). Possible nucleotide contamination from actin filaments and the oxygen scavenger system was thus excluded.

Proton Pump by Reconstituted TF_oF_1—Nucleotide-driven proton-translocation into TF_oF_1 liposomes was detected as the decrease in the pyranine fluorescence in an FP 777 fluorometer (JASCO, Japan) at 23 °C. TF_oF_1 liposomes (about 5 μg of TF_oF_1) containing pyranine inside were preincubated at 23 °C in 1.5 ml of a reaction mixture containing 10 mM MOPS-KOH (pH 7.0), 50 mM KCl, 2 mM nucleotide, 25 mM K_2SO_4, 25 mM Na_2SO_4, and 20 mM *p*-xylene-bispyridinium bromide, which quenched the pyranine fluorescence outside the liposomes. Excitation and emission wavelengths were 460 and 510 nm, respectively. The reaction was started by the addition of 4 mM $MgCl_2$. After recording the fluorescence change, 10 μM FCCP was added to recover the initial fluorescence, which would ensure that the fluorescence decrease was caused by the proton uptake into the liposomes.

[1] The abbreviations used are: TF_1, the $\alpha_3\beta_3\gamma$ subcomplex (β-His tag/γS107C) of F_1 derived from thermophilic *Baccillus* strain PS3; NTA, nitrilotriacetic acid; FCCP, carbonyl cyanide *p*-(trifluoromethoxy) phenylhydrazone; TF_oF_1, F_oF_1-ATPase derived from thermophilic *Baccillus* strain PS3; MOPS, 4-morpholinepropanesulfonic acid; pN, piconewton(s).

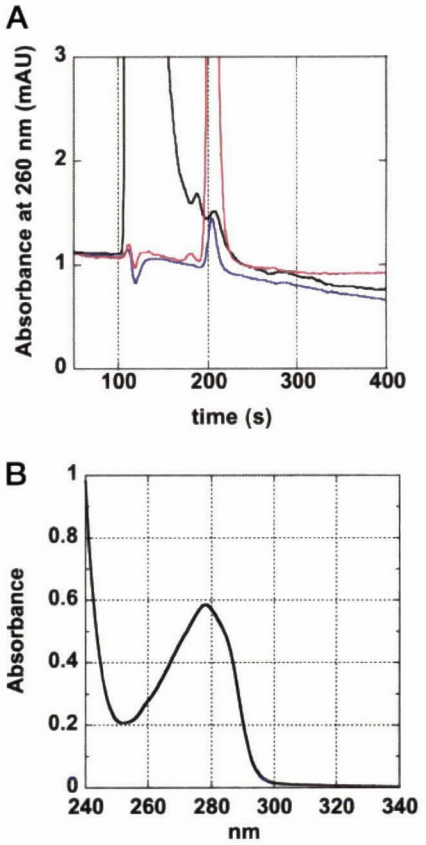

FIG. 2. **Nucleotide-depleted $\alpha_3\beta_3\gamma$ subcomplex.** *a*, assessment of nucleotides tightly bound to the $\alpha_3\beta_3\gamma$ subcomplex. 100 pmol of the purified subcomplex was precipitated by perchloric acid and subjected to reverse-phase chromatography with the monitor wavelength of 260 nm (*black line*). Bound ATP and ADP gave peaks at 188 and 208 s, respectively, with a height of 0.49 and 0.23 milliabsorbance units above the tail of the main peak. As controls, 10 pmol of ADP gave a peak at 204 s with a height of 1.28 milliabsorbance units (*blue line*), and 100 pmol of the commercial ADP showed a contaminant ATP peak at 183 s (*red line*). *b*, absorbance spectrum of the nucleotide-depleted $\alpha_3\beta_3\gamma$ subcomplex. The ratio of A_{280} (0.57) to A_{260} (0.279) was 2.04.

RESULTS

Nucleotide-depleted F_1-ATPase—F_1-ATPase is known to be inhibited by Mg-ADP tightly bound to a catalytic site (15, 16). TF_1 used in the previous study (10) contained ~0.3 mol of tightly bound nucleotide/mol of enzyme; thus, the hydrolysis activity might have been underestimated. Here, we employed an improved purification protocol (see "Experimental Procedures") and obtained a sample containing only 0.084 mol of bound nucleotide (0.037 mol of ATP and 0.047 mol of ADP) per mol of enzyme as determined from the peak heights in the reverse-phase chromatography (Fig. 2*a*). Before use, the protein was further purified by size exclusion chromatography, because TF_1 tended to aggregate upon storage. For the final sample, the ratio of A_{280} to A_{260}, a convenient measure of the purity, was greater than 2.0 (Fig. 2*b*). As expected, the ATP hydrolysis activity of this nucleotide-depleted enzyme was higher than that reported previously (see below).

Hydrolysis Activities—ATP, GTP, ITP, and UTP hydrolysis activities of the nucleotide-depleted TF_1 were determined as the rate of oxidation of NADH using the ATP-, GTP-, ITP-, or UTP-regenerating system. Hydrolysis of the purine nucleotides, ATP, GTP, and ITP, gradually decelerated to a steady state as shown in Fig. 3, *a* and *b*. This turnover-dependent inactivation is attributed to the Mg-ADP (GDP, IDP) inhibition. The hydrolysis rates were therefore determined during the initial 10 s after the injection of the enzyme into the assay mixture (Fig. 3, *a* and *b*, *insets*).

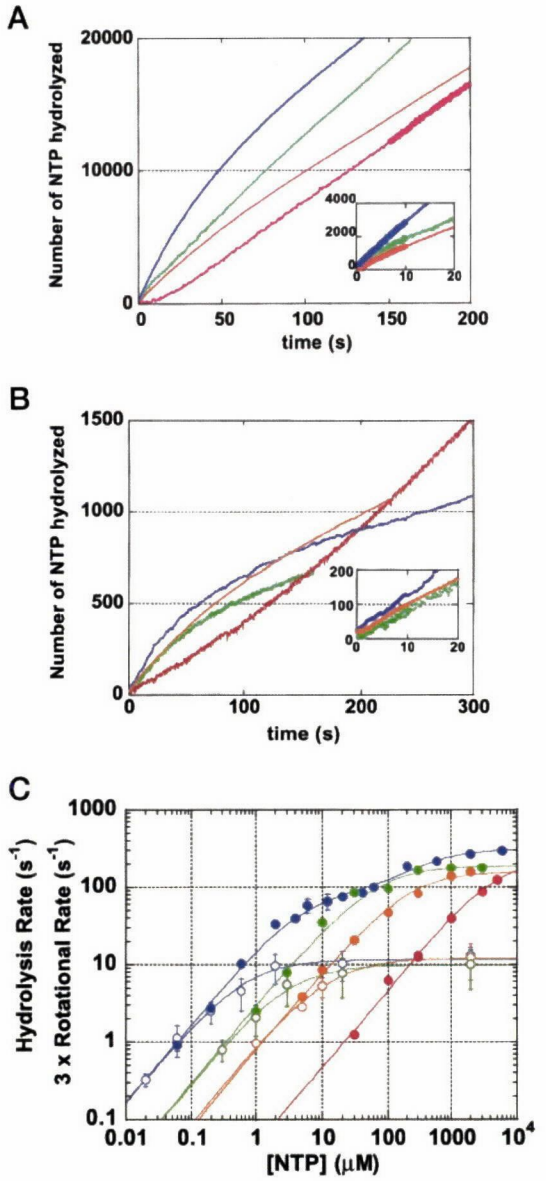

FIG. 3. **Comparison of the hydrolysis and rotational rates for different nucleotides.** *a*, time courses of hydrolysis monitored as NADH oxidation through the regeneration system. *Blue*, 2 mM ATP; *green*, 1 mM GTP; *orange*, 1 mM ITP; *red*, 3 mM UTP. *Inset*, enlarged view of the initial portion. The *thick parts* of the *lines* show the portion in which the hydrolysis rate shown in *c* was estimated. *b*, time courses of hydrolysis at lower nucleotide concentrations. *Blue*, 600 nM ATP; *green*, 3 μM GTP; *orange*, 10 μM ITP; *red*, 100 μM UTP. *c*, comparison between hydrolysis and rotational rates. *Closed circles*, hydrolysis rates determined as in *a* and *b*. *Open circles*, rotational rates for 0.5–1.2-μm actin filaments; 3 times the measured rates in revolutions s^{-1} are plotted for comparison with the hydrolysis rates. *Error bars*, S.D. *Blue*, ATP; *green*, GTP; *orange*, ITP; *red*, UTP. Rotational rates for ATP are from Ref. 10. *Solid lines*, except the one for ATP hydrolysis, show fit with $V = V_{max}[NTP]/([NTP] + K_m)$, where V_{max} and K_m are 187 s^{-1} and 64 μM for GTP hydrolysis, 157 s^{-1} and 202 μM for ITP hydrolysis, 256.8 s^{-1} and 5.5 mM for UTP hydrolysis, 3.82 revolutions s^{-1} and 0.69 μM for ATP-driven rotation, 3.28 revolutions s^{-1} and 3.43 μM for GTP-driven rotation, and 3.95 revolutions s^{-1} and 13.3 μM for ITP-driven rotation. The rates of ATP hydrolysis were fitted with $V = (V_{max}{}^a K_m{}^b[NTP] + V_{max}{}^b[NTP]^2)/([NTP]^2 + K_m{}^b[NTP] + K_m{}^a K_m{}^b)$, where $V_{max}{}^a$ = 87.5 s^{-1}, $V_{max}{}^b$ = 313 s^{-1}, $K_m{}^a$ = 5.25 μM, and $K_m{}^b$ = 429 μM.

The rate of ATP hydrolysis did not obey simple Michaelis-Menten kinetics and was fitted with two sets of K_m and V_{max}: $V_{max}{}^a$ = 87.5 s^{-1}, $V_{max}{}^b$ = 313 s^{-1}, $K_m{}^a$ = 5.25 μM, and $K_m{}^b$ = 429 μM (Fig. 3*c*). The maximum rate of ATP hydrolysis, $V_{max}{}^b$,

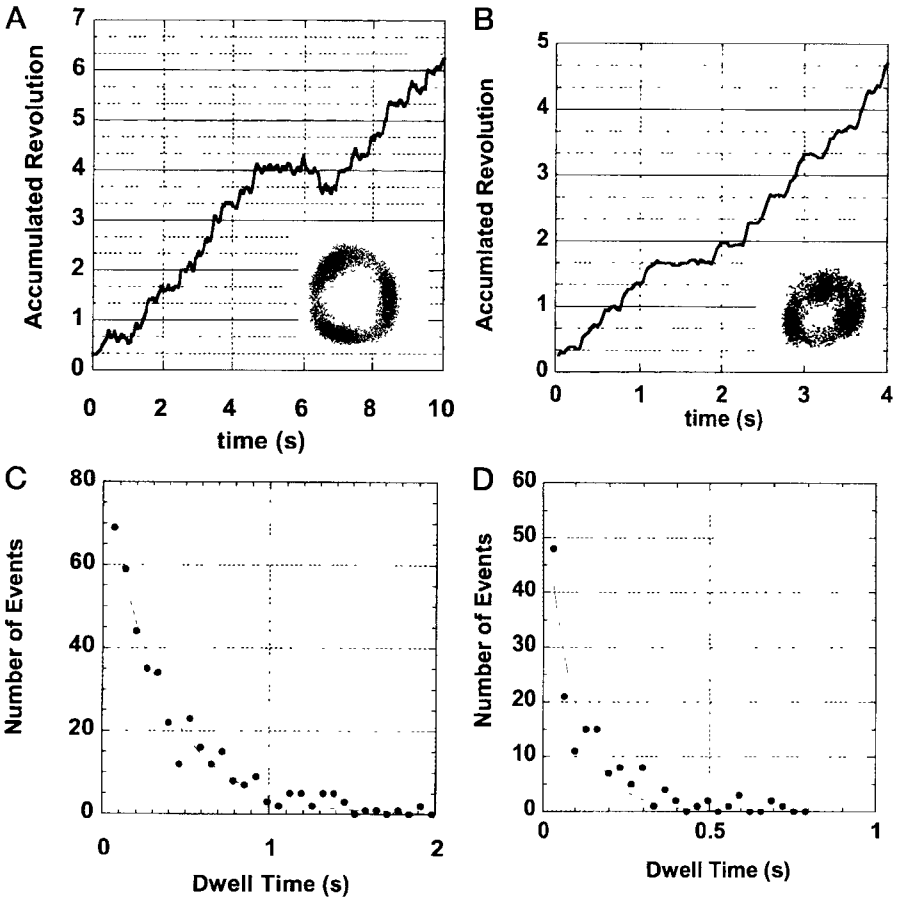

FIG. 4. **Stepping rotation at low nucleotide concentrations.** *a* and *b*, time courses of rotation at 1 μM GTP (actin length 0.95 μm) and at 10 μM ITP (actin length 1.01 μm). *Insets*, traces of the centroid of the actin filament. *c* and *d*, histograms of dwell times between steps. Rotation records in *a* and *b* were analyzed and are shown in *c* and *d*. *Lines* indicate an exponential fit. constant $\times$ exp($-kt$), where k is the rate for nucleotide binding (2.9 s^{-1} for 1 μM GTP and 11.1 s^{-1} for 10 μM ITP).

of 313 s^{-1} is higher than the previous value (10) of 177 s^{-1}, presumably because of the thorough removal of the bound nucleotide and aggregated enzyme. An additional factor is the increase of the amount of pyruvate kinase, which may limit the overall reaction rate, to 0.2 mg/ml, compared with 0.05 mg/ml in the previous study. The rates for GTP and ITP hydrolysis could be accounted for by simple Michaelis-Menten kinetics; V_{max} and K_m were 187 s^{-1} and 64 μM, respectively, for GTP and 157 s^{-1} and 202 μM for ITP.

In contrast to the purine nucleotides, UTP hydrolysis activity gradually increased with time (Fig. 3, *a* and *b*). This cannot be ascribed to the slow response of the UTP-regenerating system, because it could generate UTP from UDP much faster (0.5 s^{-1}) than the acceleration (0.017 s^{-1} at 1 mM UTP). Slow binding of UTP to noncatalytic sites could explain the acceleration, but evidence is absent. Because the activation took a longer time at lower UTP concentrations, fully activated rate of UTP hydrolysis was estimated from the slope between 150 and 200 s at >300 μM, between 250 and 300 s at 100 μM, and between 1000 and 1200 s at 30 μM. As seen in Fig. 3*c*, hydrolysis of UTP was much slower than that of the purine nucleotides. To confirm that the measured hydrolysis rate was that of UTP and not of contaminants, we also measured P_i released in the medium. Although the rate of P_i release was around half the hydrolysis rate determined from NADH oxidation, presumably because of the absence of the UTP-regenerating system, TF_1 produced P_i equivalent to >40% of UTP in 5 min. Thus, TF_1 did hydrolyze UTP, not contaminating other nucleoside-triphosphates, which amounted to <0.5% (see "Experimental Procedures"). CTP, in contrast, was not hydrolyzed; the rate of P_i release at 2 mM CTP measured over 60 min was indistinguishable from the rate without the enzyme (<0.01 s^{-1}).

As seen in Fig. 3*c*, the maximal hydrolysis rates for the four nucleotides, ATP, GTP, ITP, and UTP, do not differ greatly. The major difference among the four is in the apparent K_m values, UTP being the highest. In this regard, it is possible that CTP is also hydrolyzed with a similar V_{max} but with a K_m far above 10 mM. Another difference is that ATP hydrolysis shows significant deviation from the simple Michaelis-Menten kinetics, which is not apparent for the other nucleotides. This may be correlated with the stronger tendency toward inhibition with ATP than with the other nucleotides (Fig. 3, *a* and *b*). The possibility that the other nucleotides also show deviation at much higher concentrations (giving possibly the same V_{max}) cannot be dismissed.

GTP- and ITP-driven Rotation—GTP and ITP supported the rotation of the γ subunit in TF_1. The rotation, observed through the motion of a fluorescent actin filament attached to the γ subunit, was counterclockwise without exception, as in the case of ATP-driven rotation. Rotation assays at less than 10 μM GTP or 10 μM ITP were made on the enzyme directly attached to a coverslip that had been covalently modified with Ni^{2+}-NTA (13). Compared with the previous method (10) of attaching the enzyme on Ni^{2+}-NTA-coated beads, the direct attachment resulted in a higher percentage of finding rotating filaments at low nucleotide concentrations.

Because the F_1 motor has been shown to be a 120° stepper (10), we compare 3 times the rotational rate of a short actin filament (0.5–1.3 μm) with the corresponding hydrolysis rate (Fig. 3). At low nucleotide concentrations ([ATP] < 0.1 μM, [GTP] < 1 μM, [ITP] < 10 μM) where nucleotide binding is rate-limiting, the two rates agreed with each other, indicating that three molecules of purine nucleotide, whether ATP, GTP, or ITP, drive a full turn. The agreement also shows that the rotation in the presence of GTP or ITP was not due to possible ATP contamination, which was far below 5%. At higher nucle-

otide concentrations, the rotational rate saturated around 4 revolutions s^{-1}. This is simply due to the hydrodynamic friction against the rotating actin filament (10). At low nucleotide concentrations, the rotation was resolved into discrete 120° steps (Fig. 4, *a* and *b*). The histograms of dwell times between steps were fitted with a single exponential decay with the rate of 2.9 s^{-1} for 1 μM GTP and 11.1 s^{-1} for 10 μM ITP (Fig. 4, *c* and *d*), implying that a first order reaction, binding of GTP (ITP), triggers each 120° step. These rate constants agree with the hydrolysis rates (Fig. 3*c*), confirming again that each 120° step is driven by the hydrolysis of one molecule of GTP or ITP.

As seen in Fig. 4*a*, back steps occurred occasionally in GTP-driven rotation. ITP-driven rotation also showed occasional back steps (data not shown). The velocity of back steps was as fast as the forward one and thus is unlikely to be of purely thermal origin (10). A stochastic mistake in the order of substrate binding or product release among the three catalytic sites could explain the back steps.

UTP Does Not Drive γ Rotation—With commercial UTP at 4 mM, we occasionally observed slow rotation (*e.g.* 1.4 revolutions s^{-1}). We suspected that this might have been due to contaminants, because ATP at a concentration as low as 300 nM, for example, could account for the observed speed. Indeed, even CTP, which the $\alpha_3\beta_3\gamma$ does not hydrolyze, produced rotation at 0.3 revolutions s^{-1} at 2 mM. We therefore purified UTP and CTP (see "Experimental Procedures") and examined rotation at 300 μM, the highest concentration available after the column purification. To avoid possible nucleotide contamination from other sources, we attached an aggregate of biotinylated polystyrene beads to the γ subunit in place of an actin filament and observed the beads in bright field in the absence of the oxygen scavenger system. No rotating beads were found in six assays with UTP in which 5543 beads only fluctuated around a fixed point. Observation in each assay continued for more than 30 min, much longer than the time needed to activate UTP hydrolysis at 300 μM (~5 min). Six assays with CTP also gave negative results.

If hydrolysis of each UTP molecule produces a 120° step as with purine nucleotides, the rotational rate is expected to be 4.4 s^{-1} at 300 μM UTP. We therefore carried out parallel assays with 600 nM ATP where the rotational rate would be 1.5 s^{-1}. 40 rotating beads were found out of 4299 fluctuating beads (five assays). We also made an "unpredicted test" in which we observed beads without knowing the identity of the nucleotide. No rotation was found with 300 μM UTP, and rotating beads were readily found in the presence of 600 nM ATP. We conclude that UTP cannot support rotation of the γ subunit carrying a bead aggregate, at least not at the rate expected from the hydrolysis rate. One possibility is that UTP hydrolysis, unlike the hydrolysis of purine nucleotides, is completely decoupled from γ rotation, even at no load. The other possibility is that UTP, with a different base structure, cannot supply sufficient power to drive the beads through 120°; in this case, the rate of UTP hydrolysis by the loaded TF_1 would also be very low.

Torque and Efficiency—To compare torque and energy conversion efficiency among three purine nucleotides, ATP, GTP, and ITP, that supported γ rotation, the rotational velocities of actin filaments attached to the γ subunit on Ni^{2+}-NTA coated-beads were examined. Fig. 5 shows time courses of rotation for actin filaments with length around 2 μm (Fig. 5*a*) and 3–4 μm (Fig. 5*b*). The average rotational velocity was determined for each curve over a portion containing at least five consecutive revolutions without noticeably unnatural intermissions (*e.g.* the last part of the *brown curve* in Fig. 5*b* was omitted). The results are summarized in Fig. 5*c*. Most data for GTP-driven (*green*) and ITP-driven rotation (*orange*) are *on or below* the

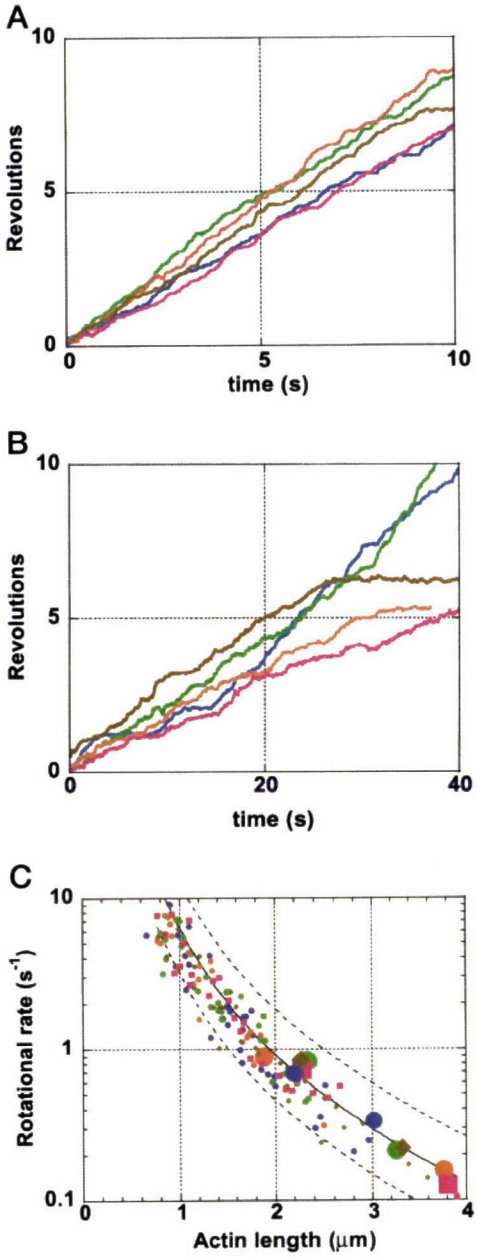

FIG. 5. **Estimation of torque in GTP- and ITP-driven rotations.** *a*, time courses of the rotation of an actin filament with length around 2 μm. *Blue*, 2 mM ATP; *green*, 2 mM GTP; *orange*, 2 mM ITP; *pink*, 2 mM ATP, 10 μM ADP, and 100 mM P_i; *gold*, 2 mM GTP, 10 μM GDP, and 100 mM P_i. *b*, time courses of the rotation with actin length of 3–4 μm. See *a* for color coding. *c*, rotational rate *versus* the length of the actin filament. *Blue circles*, 2 mM Mg-ATP; *green circles*, 2 mM Mg-GTP; *orange circles*, 2 mM Mg-ITP; *pink squares*, 2 mM ATP, 10 μM ADP, and 100 mM P_i (ΔG_{ATP} = −80 pN·nm/molecule); *gold diamonds*, 2 mM GTP, 10 μM GDP, and 100 mM P_i (ΔG_{GTP} = −80 pN·nm/molecule). *Large symbols* indicate the data in *a* and *b*. *Solid line*, calculated rotational rate under an assumed constant torque of 40 pN·nm; *dashed lines*, constant torque at 80 and 20 pN·nm.

line representing the constant torque of 40 pN·nm, as is also the case for ATP-driven rotation (*blue*). We think that higher velocity values are more reliable, because any obstructions against rotation would reduce the velocity, and we conclude that TF_1 exerts a constant rotary torque of about 40 pN·nm regardless of the differences among the structures of purine rings. (The average torque calculated over all points in Fig. 5*c* is 32 ± 11 pN·nm for ATP, 35 ± 11 pN·nm for GTP, and 32 ± 10 pN·nm for ITP; these average values, however, are not

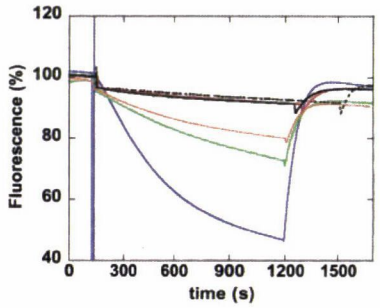

FIG. 6. **Proton pump activity of TF_oF_1 reconstituted into liposomes.** Translocation of protons into TF_oF_1 liposomes was monitored as the decrease in pyranine fluorescence. The reaction mixture contained 2 mM ATP (*blue line*), 2 mM GTP (*green line*), 2 mM ITP (*orange line*), 2 mM CTP (*black line*), 2 mM UTP (*red line*), or no nucleotide (*dashed black line*). The reaction was started by the addition of 4 mM $MgCl_2$. At 1200 s, 10 μM FCCP was added to collapse the pH gradients.

meaningful, because the data in Fig. 5*c* have been selected for high torque values.)

The torque of 40 pN·nm times the angular displacement of $2\pi/3$ radians (equal to 120°), ~80 pN·nm, is the mechanical work done in a 120° step. In the previous study (10), it was shown that TF_1 does this much work even when the free energy available from ATP hydrolysis, ΔG_{ATP}, was reduced to −90 pN·nm/molecule. Here, we examined the torque and work in the presence of 2 mM ATP (or GTP), 10 μM ADP (GDP), and 100 mM inorganic phosphate. Under these conditions, ΔG_{ATP} is calculated as −80 pN·nm/molecule from $\Delta G_{ATP} = \Delta G_0 + k_BT \cdot \ln[ADP] \cdot [Pi]/[ATP]$, where ΔG_0 = −50 pN·nm/molecule (17), k_BT = 4.1 pN·nm/molecule is thermal energy at room temperature, and ΔG_{GTP} should be of a similar value. As seen in Fig. 5*c*, the experimental points at ΔG_{ATP} = −80 pN·nm/molecule (*purple*) and ΔG_{GTP} = −80 pN·nm/molecule (*brown*) are indistinguishable from other points and also fall on or below the line for the constant torque of 40 pN·nm or constant work of 80 pN·nm (the torque averaged over plotted points is 35 ± 10 pN·nm for ΔG_{ATP} = −80 and 32 ± 9 pN·nm for ΔG_{GTP} = −80 pN·nm/molecule) This strengthens our contention that the efficiency of the energy conversion in this motor, from the hydrolysis (of purine nucleotides) into the mechanical work, can reach ~100%.

Proton Pump—Nucleotide-driven proton uptake by the reconstituted TF_oF_1 liposome was measured, to see whether γ rotation is mechanically coupled to the proton pump. Liposomes were incubated with 2 mM nucleotide until the base line became stable, and then 4 mM $MgCl_2$ was added to start the reaction (Fig. 6). After 20 min, 10 μM FCCP was added to collapse the pH gradients so as to ensure that the fluorescence decrease indicated the proton uptake. Fig. 6 clearly shows that the purine nucleotides ATP, GTP, and ITP drove the formation of pH gradient but UTP and CTP did not; the latter two gave signals that were indistinguishable from the control in the absence of a nucleotide. The initial rates of proton uptake by GTP and ITP in 1 min after starting the reaction were 30 and 27% of the ATP-driven uptake, respectively. The rate of nucleotide hydrolysis by TF_oF_1, determined from the amount of inorganic phosphate released in 20 min, was 7.2 ± 1.4 s^{-1} for ATP, 3.4 ± 0.5 s^{-1} for GTP, and 2.7 ± 0.5 s^{-1} for ITP. The three nucleotides show the same order in proton pumping and hydrolysis activities. The agreement suggests that GTP and ITP hydrolysis are coupled to proton pumping as efficiently as with ATP. Pyridine nucleotides were not good substrates for hydrolysis by TF_oF_1; the hydrolysis activity was not detected by the phosphate measurement (<0.12 s^{-1} for 2 mM CTP and <0.09 s^{-1} for 2 mM UTP).

DISCUSSION

In this paper, we have shown that the purine ring of a nucleotide is indispensable for γ rotation and for proton pumping in the F_oF_1-ATPase. Both rotation and proton pumping were supported by the purine nucleotides, ATP, GTP, and ITP, but not by the pyrimidine nucleotides, CTP and UTP. Our results are consistent with the report by Perlin *et al.* (18), where GTP and ITP were shown to drive proton pumping in the F_oF_1-ATPase, and support the idea that nucleotide hydrolysis is coupled to proton pumping through mechanical rotation of the γ subunit.

Our rotation assay has revealed that many of the rotational characteristics are common to all three purine nucleotides. (i) The rotary torque is constant around 40 pN·nm. (ii) The rotation consists of discrete 120° steps. (iii) Each 120° step is driven by the hydrolysis of one nucleotide molecule. (iv) Backward steps as fast as the forward ones occur occasionally. The first three points imply that the mechanical work done in a 120° step is about 80 pN·nm for all three nucleotides, and thus the energy conversion efficiency can reach ~100% with all three purine nucleotides. As to the last statement, we have shown in this study that the mechanical work of ~80 pN·nm is done even when ΔG_{ATP} or ΔG_{GTP} is reduced to −80 pN·nm/molecule. We did not ascertain a high efficiency in ITP-driven rotation, but Sorgato *et al.* (19) have reported that the energy from ITP hydrolysis is converted into a membrane potential by submitochondrial particles as efficiently as ATP hydrolysis. Thus, the efficiency of ITP-driven rotation is expected also to be close to 100%. The similarities among the three nucleotides suggest that the mechanical characteristics of the rotation such as the stepping, torque, and work per step are inherent in the (structure of the) F_1 motor. Purine nucleotides can trigger and let proceed the stepping mechanism in which the step angle, torque, and work are preset, whereas pyrimidine nucleotides cannot.

Chemical kinetics, in contrast, are different among the three purine nucleotides. First, the hydrolysis curves in Fig. 3*c* are shifted toward higher concentrations in the order of ATP, GTP, and ITP, and the rotation curves follow the same trend. Apparently, this is due to the difference in the rate of nucleotide binding, ATP being the fastest and ITP the slowest. Analysis of step intervals at low nucleotide concentrations supported this view; the rate constant was 2.5×10^7 M^{-1} s^{-1} for ATP (10), 2.9×10^6 M^{-1} s^{-1} for GTP, and 1.1×10^6 M^{-1} s^{-1} for ITP.

According to the binding change mechanism for ATP synthase (1), much of the energy available from γ rotation during synthesis is used to release a tightly bound ATP into the medium. Conversely, during hydrolysis, binding of ATP powers the reverse rotation of γ. If the above difference in the rate constant of nucleotide binding reflects a similar difference in the affinity for the nucleotide, then the energy provided by ITP binding will be the smallest and might have been insufficient to power the stepping mechanism. Because all three purine nucleotides supported rotation, it seems either that the affinity for ITP is high enough (a 20-fold difference in the binding constant is equivalent to a free energy difference of only 12 pN·nm/molecule), or that the rate of nucleotide release decreases in the order of ATP to ITP and makes the affinities more or less the same. In this regard, it is possible that UTP, of which the hydrolysis curve in Fig. 3*c* is further shifted toward the right, cannot confer sufficient binding energy to the stepping mechanism.

A second difference in the chemical kinetics is that the ATP hydrolysis was described by two sets of K_m and V_{max}, whereas one set sufficed for GTP and ITP. The two sets for the case of ATP are usually ascribed to two modes of catalysis: bisite and

trisite, where one or two, or two or three, respectively, of the three catalytic sites are alternately filled with a nucleotide. The possibility, however, exists that the enzyme operates in the bisite mode at all concentrations at or above micromolar and that the apparent deviation from the simple Michaelis-Menten kinetics is due to the Mg-ADP inhibition. Single K_m values for the hydrolysis of GTP and ITP, which are shown to be less prone to inhibition, support this view, although two sets of K_m and V_{max} with similar V_{max}/K_m could also explain the simple kinetics. Resolution calls for the determination of the number of nucleotides bound in the catalytic sites of uninhibited enzyme, which is not an easy experiment.

The pyrimidine nucleotides, CTP and UTP, were poor substrates for the TF_1 and TF_oF_1. CTP was not hydrolyzed and, naturally, did not drive γ rotation or proton pump. UTP was hydrolyzed by TF_1, yet UTP did not support rotation and pumping. Ca-ATP has also been reported to be an uncoupling substrate for F_oF_1, in that Ca-ATP was hydrolyzed without pumping protons (20). The kinetics of Ca-ATP hydrolysis, however, was similar to that of Mg-ATP hydrolysis. Thus, the nature of uncoupling seems different between the two cases, Ca-ATP and (Mg-)UTP. Interestingly, the reconstituted TF_oF_1 did not hydrolyze UTP, while TF_1 (the $\alpha_3\beta_3\gamma$ subcomplex) did. This finding is consistent with the report by Yokoyama *et al.* (21) that the substrate specificity of this enzyme is higher when it contains a fuller complement of subunits. The UTP hydrolysis activity of the $\alpha_3\beta_3\gamma$ subcomplex may be ascribed to some flexibility in and around the catalytic site that would be suppressed in F_oF_1; such hydrolysis may proceed without a major structural change of the β subunit and thus without rotation of the γ subunit.

Acknowledgments—We thank Y. Harada, T. Nishizaka, K. Adachi, T. Hisabori, and E. Muneyuki for technical assistance and helpful discussions and H. Umezawa for laboratory management.

REFERENCES

1. Boyer, P. D. (2000) *Biochim. Biophys. Acta* **1458,** 252–262
2. Matsui, T., and Yoshida, M. (1995) *Biochim. Biophys. Acta* **1231,** 139–146
3. Boyer, P. D., and Kohlbrenner, W. E. (1981) in *Energy Coupling in Photosynthesis* (Selman, B. R., and Selman-Reimer, S., eds) pp. 231–240, Elsevier, Amsterdam
4. Oosawa, F., and Hayashi, S. (1986) *Adv. Biophys.* **22,** 151–183
5. Abrahams, J. P., Leslie, A. G., Lutter, R., and Walker, J. E. (1994) *Nature* **370,** 621–628
6. Aggeler, R., Haughton, M. A., and Capaldi, R. A. (1995) *J. Biol. Chem.* **270,** 9185–9191
7. Duncan, T. M., Bulygin, V. V., Zhou, Y., Hutcheon, M. L., and Cross, R. L. (1995) *Proc. Natl. Acad. Sci. U. S. A.* **92,** 10964–10968
8. Sabbert, D., Engelbrecht, S., and Junge, W. (1996) *Nature* **381,** 623–625
9. Noji, H., Yasuda, R., Yoshida, M., and Kinosita, K., Jr. (1997) *Nature* **386,** 299–302
10. Yasuda, R., Noji, H., Kinosita, K., Jr., and Yoshida, M. (1998) *Cell* **93,** 1117–1124
11. Tsunoda, S. P., Muneyuki, E., Amano, T., Yoshida, M., and Noji, H. (1999) *J. Biol. Chem.* **274,** 5701–5706
12. Bald, D., Amano, T., Muneyuki, E., Pitard, B., Rigaud, J. L., Kruip, J., Hisabori, T., Yoshida, M., and Shibata, M. (1998) *J. Biol. Chem.* **273,** 865–870
13. Adachi, K., Yasuda, R., Noji, H., Itoh, H., Harada, Y., Yoshida, M., and Kinosita, K., Jr. (2000) *Proc. Natl. Acad. Sci. U. S. A.* **97,** 7243–7247
14. Yasuda, R., Noji, H., Yoshida, M., Kinosita, K., Jr., and Itoh, H. (2001) Nature **410,** 898–904
15. Jault, J. M., Matsui, T., Jault, F. M., Kaibara, C., Muneyuki, E., Yoshida, M., Kagawa, Y., and Allison, W. S. (1995) *Biochemistry* **34,** 16412–16418
16. Matsui, T., Muneyuki, E., Honda, M., Allison, W. S., Dou, C., and Yoshida, M. (1997) *J. Biol. Chem.* **272,** 8215–8221
17. Stryer, L. (1995) *Biochemistry*, 4th Ed., pp. 443–462, Freeman, New York
18. Perlin, D. S., Latchney, L. R., Wise, J. G., and Senior, A. E. (1981) *Biochemistry* **23,** 4998–5003
19. Sorgato, M. C., Galiazzo, F., Valente, M., Cavallini, L., and Ferguson, S. J. (1982) *Biochim. Biophys. Acta* **681,** 319–322
20. Papageorgiou, S., Melandri, A. B., and Solaini, G. (1998) *J. Bioenerg. Biomembr.* **30,** 533–541
21. Yokoyama, K., Hisabori, T., and Yoshida, M. (1989) *J. Biol. Chem.* **264,** 21837–21841

Pause and rotation of F_1-ATPase during catalysis

Yoko Hirono-Hara*, Hiroyuki Noji[†‡§], Masaya Nishiura[¶], Eiro Muneyuki*, Kiyotaka Y. Hara*, Ryohei Yasuda[‡], Kazuhiko Kinosita, Jr.[‡‖], and Masasuke Yoshida*[‡**††]

[†]Precursory Research for Embryonic Science and Technology (PRESTO), **Exploratory Research for Advanced Technology (ERATO), *Chemical Resources Laboratory, Tokyo Institute of Technology, 4259 Nagatsuta, Yokohama 226-8503, Japan; [¶]Department of Life Sciences, Graduate School of Arts and Sciences, University of Tokyo, 3-8-1 Komaba, Meguro-ku, Tokyo 153-8902, Japan, [‡]Core Research for Evolutional Science and Technology (CREST) Genetic Programming Team 13, Teikyo University Biotechnology Research Center 3F, 907 Nogawa, Miyamae, Kawasaki 216-0001, Japan; and [‖]Department of Physics, Faculty of Science and Technology, Keio University, Hiyoshi 3-14-1, Kohoku-ku, Yokohama 223, Japan

Edited by Susan S Taylor, University of California at San Diego, La Jolla, CA, and approved September 25, 2001 (received for review July 16, 2001)

F_1-ATPase is a rotary motor enzyme in which a single ATP molecule drives a 120° rotation of the central γ subunit relative to the surrounding $\alpha_3\beta_3$ ring. Here, we show that the rotation of F_1-ATPase spontaneously lapses into long (≈30 s) pauses during steady-state catalysis. The effects of ADP-Mg and mutation on the pauses, as well as kinetic comparison with bulk-phase catalysis, strongly indicate that the paused enzyme corresponds to the inactive state of F_1-ATPase previously known as the ADP-Mg inhibited form in which F_1-ATPase fails to release ADP-Mg from catalytic sites. The pausing position of the γ subunit deviates from the ATP-waiting position and is most likely the recently found intermediate 90° position.

ATP synthase of mitochondria, chloroplasts, and bacteria catalyzes ATP synthesis coupled with a transmembrane proton flow (1–4). The enzyme consists of a membrane-embedded, proton-conducting portion (F_0) and a protruding portion (F_1) in which catalytic sites for ATP synthesis/hydrolysis exist. The isolated F_1 portion has ATPase activity; hence, it is often called F_1-ATPase. It is composed of five different subunits with a stoichiometry of $\alpha_3\beta_3\gamma\delta\varepsilon$. The $\alpha_3\beta_3\gamma$ subcomplex is the minimum ATPase-active complex, which has catalytic features similar to F_1-ATPase. In the crystal structure (5), the central γ subunit is surrounded by an $\alpha_3\beta_3$ cylinder where three α and three β subunits are arranged alternately, and the six nucleotide binding sites are located at the α/β subunit interfaces. Three of the binding sites are catalytic, and the β subunits provide most of the catalytic residues. The other three are noncatalytic, and the α subunits provide most residues contributing nucleotide binding.

It has been postulated that the energy of the proton flow liberated at F_0 is transformed into the energy of ATP synthesis at F_1 through rotation of the central γ subunit and vice versa—the energy of ATP hydrolysis can be converted into the energy of proton pumping through reverse rotation of the γ subunit (6). By using an $\alpha_3\beta_3\gamma$ subcomplex of thermophilic F_1-ATPase (F_1-ATPase) immobilized on a glass surface, we have observed ATP hydrolysis-driven rotation of the fluorescent actin filament attached to the γ subunit (7).

At nanomolar ATP concentration, F_1-ATPase binds and hydrolyzes a single ATP molecule, makes a 120° rotation, and waits for the next ATP molecule. As the ATP concentration increases, the ATP-waiting period becomes shorter until it is finally undetectable, and rotation of the actin filament becomes apparently continuous over hundreds of revolutions (8). However, when the rotation was observed for long periods, occasional pauses of rotation were recognized, even at high ATP concentrations (7, 9). Here, we show that these pauses occur at an intermediate step of rotation and mostly correspond to the ADP-Mg inhibition, which has been observed in bulk-phase kinetics as a general feature of the F_1-ATPases (and ATP synthases). Slow interconversion between rotating and pausing states thus contributes to the attenuation of ATPase during steady-state catalysis.

Materials and Methods

Protein Preparation. *Escherichia coli* strains used were JM109 (10) for preparation of plasmids, CJ236 (11) for generating uracil-containing single-stranded plasmids for site-directed mutagenesis, and JM103Δ (uncB-uncD) for expression of the mutant complexes of F_1 from the thermophilic *Bacillus* PS3. Plasmids M13mp18 and pKAGB1 (12), which carried genes for the α, β, and γ subunits of F_1 from the thermophilic *Bacillus* PS3, were used for mutagenesis and for gene expression, respectively. Site-directed mutagenesis was accomplished as described by Kunkel *et al.* (11). The plasmid pKAGB1/αC193S/γS107C/βHis10tag has been described (7). The plasmids pKAGB1/αK175A/T176A and pKAGB1/βT165S, which have been described (13, 14), were used to generate plasmids for this study.

pKAGB1/ΔNC/βT165S/γS107C, βHis10-tags was prepared by removing the fragment containing the ΔNC (α K175A/T176A) substitution (*Eco*RI-*Bgl*II fragment) and ligating it into the pKABG1/βT165S/αC193S, γS107C, βHis10-tags (*Eco*RI-*Bgl*II fragment) from which the wild-type gene fragment had been removed. The plasmid pKAGB1/αC193S/γS107C/βHis10-tag was used to express protein α (C193S)$_3\beta_3\gamma$(S107C), which was considered to be wild type, and plasmid pKAGB1/ΔNC/βT165S/αC193S, γS107C, βHis10-tags was used to express protein $\alpha(\Delta NC)_3\beta(T165S)_3\gamma(S107C)$, which was named ΔNC′ mutant. The α $(C193S)_3\beta_3\gamma$(S107C/I210C) was used for the measurement of angular position (15). These F_1 subcomplexes were purified as described (12, 16). Purified F_1 was passed through a DEAE column equilibrated with 100 mM potassium phosphate/0.2 mM EDTA (pH 7.0) to reduce the bound nucleotide to 0.01 mol per mol F_1, which was confirmed with reverse-phase HPLC.

Rotation Assay. The wild type and the ΔNC′ mutant were biotinylated at the cysteines of the γ subunit and conjugated with streptavidin (7). To visualize the rotation of the γ subunit under the microscope, a fluorescent actin filament or duplex of beads (ϕ = 440 nm, 517 nm) was attached to the γ subunit. A flow cell (10 μl) was made of two coverslips separated by two spacers of 50-μm thickness. The glass surface was coated with Ni-nitrilotriacetic acid. Beads (0.1–1 nM) or actin (1–10 nM) were mixed with 1/100× to 1/10× the molar concentration of F_1 in buffer A [10 mM 4-morpholinepropanesulfonic acid (Mops)-KOH/50 mM KCl/1% (vol/vol) BSA, pH 7.0]. The mixture was applied to the flow cell. Unbound beads or actin filaments were removed from the flow cell by washing with buffer A, followed

This paper was submitted directly (Track II) to the PNAS office

Abbreviations F_1-ATPase, $\alpha_3\beta_3\gamma$ subcomplex of thermophilic F_1-ATPase, LDAO, lauryl dimethyl amine oxide, ΔNC, mutant F_1-ATPase with defective noncatalytic sites

[§]Present address Institute of Industrial Science, 4-6-1, Komaba, Meguro ku, Tokyo 153, Japan.

[††]To whom reprint requests should be addressed E-mail myoshida@res.titech ac jp

The publication costs of this article were defrayed in part by page charge payment This article must therefore be hereby marked "*advertisement*" in accordance with 18 U S C §1734 solely to indicate this fact

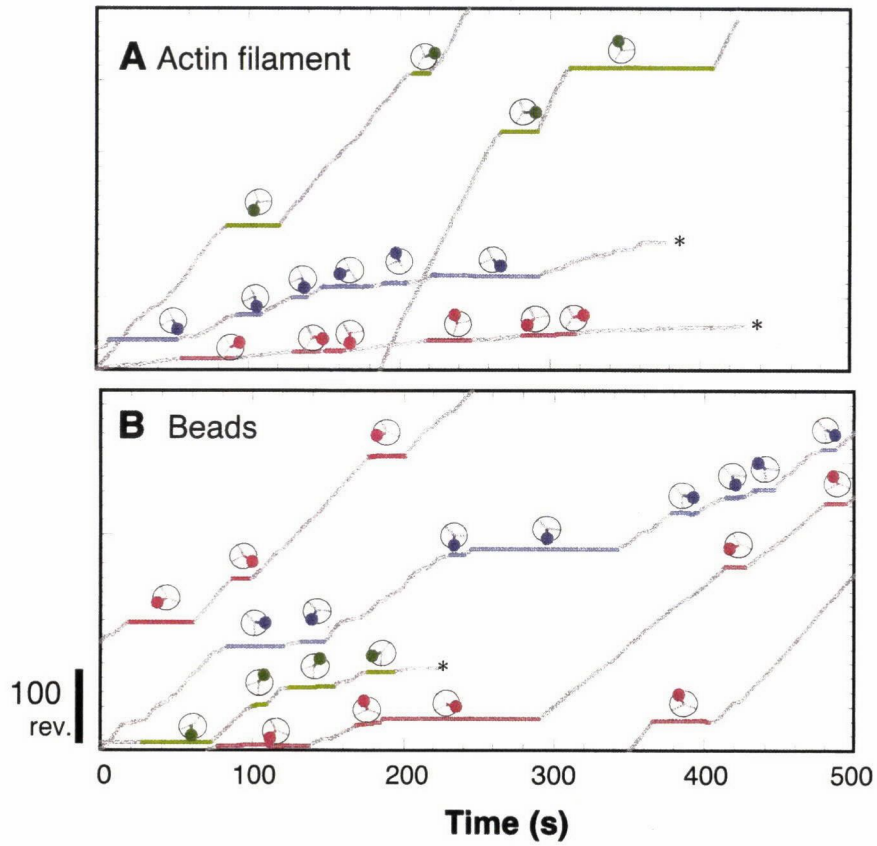

Fig. 1. Time courses of the rotation of F_1-ATPase labeled with actin filaments or beads. (*A*) Rotation of the actin filament attached to the γ subunit in the presence of 2 mM ATP-Mg. Each colored line represents the pausing of rotation for longer than 10 s. The same colored pauses were derived from a single filament. The average images of each pause are trimmed in circles to identify the filament position; inner gray lines show average angular positions of the pauses made by that molecule. The rotations of the beads are shown in *B*. The position indicated by asterisks (*) marks when the actin filament or beads disappeared from the observation field.

by applying buffer A or buffer B (100 mM potassium phosphate buffer, pH 7.0) containing 2 mM $MgCl_2$, 0.2 μM–2 mM ATP, and the ATP-regenerating system (0.2 mg/ml creatine kinase and 2.5 mM creatine phosphate). In the presence of 0.1% lauryl dimethyl amine oxide (LDAO), the rotation of the F_1 particles were observed in the presence of buffer B. The rotation of the ΔNC′ mutant also was observed in buffer B (17). Buffer exchange was performed as described. To visualize induction of ADP-Mg inhibition, after the observation of the rotation in ATP-containing buffer A (1 mM ATP-Mg), an ADP-containing buffer A (1 mM ATP-Mg, 1 mM ADP or 0.1 mM ADP) was infused into the same chamber for rotation observation (see Fig. 2 *A* and *B*). To visualize release from the ADP-Mg inhibited state, the ADP buffer was exchanged to ATP+re buffer (ATP-containing buffer and ATP-regenerating system; see Fig. 2*C*).

The fluorescent actin filament was observed with a fluorescence microscope (IX70; Olympus, New Hyde Park, NY). Photobleaching of the fluorescent actin filament was minimized by the use of a filter (ND20). The rotation of the actin filament could be observed for 40–50 min. The 440-nm and 517-nm beads were observed with a transmission light microscope.

Images from actin- or bead-labeled F_1-ATPase were recorded with an intensified charge-coupled device (350 F; Videoscope, Dallas) camera on an 8-mm videotape. Analysis of rotational angle was performed as described (7).

Measurement of ATPase Activity. ATPase activity was measured at 25°C in the presence of an ATP-regenerating system (18) consisting of 300 μg/ml pyruvate kinase, 300 μg/ml lactate dehydrogenase, 2.5 mM phosphoenolpyruvate, and 0.2 mM NADH in buffer A or buffer B containing 2 mM $MgCl_2$ and the indicated ATP concentrations. Typically, the reaction was initiated by the addition of F_1 to 1.2 ml of assay mixture. The rate of ATP hydrolysis was monitored as the rate of oxidation of the NADH, which was determined by the absorbance decrease at 340 nm. The spectrophotometer was equipped with a small stirrer to ensure rapid mixing. The maximum dead time of measurement was less than 0.75 sec after initiation of the reaction. The data from 2 to 300 s were usually used for analysis. The initial rapid activity (the activity of wild type is 187 s^{-1} and that of ΔNC′ mutant is 54 s^{-1}) decreased to the steady-state activity at 2 mM ATPMg.

Materials. LDAO (30% aqueous solution) was purchased from Calbiochem.

Results

Pauses of Rotation of F_1-ATPase at High ATP. Fig. 1*A* shows the typical time courses of the rotation of a fluorescent actin filament attached to the γ subunit of immobilized F_1-ATPase in the presence of 2 mM ATP. At this ATP concentration, ATP binding should take place within 0.1 ms (8) and does not result in a pause of rotation. However, each F_1-ATPase molecule made several distinct pauses during 500 s, some of which were longer than 60 s. Noticeably, paused filaments always stayed within one of three angular positions, consistent with the pseudo-3-fold symmetrical structure of F_1-ATPase. There is no obvious preference among the three angular positions for pauses to occur.

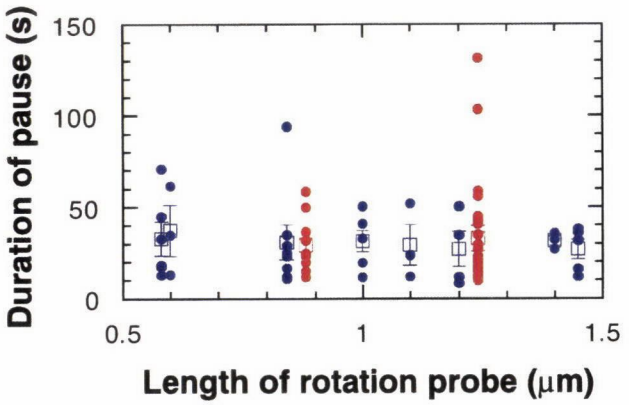

Fig. 2. Effect of load of attached probes on the durations of the pauses (longer than 10 s). Blue circles, actin filaments; red circles, pair of biotin-coated beads (diameter 440 nm or 517 nm); squares, the average for one molecule ± SE.

Sometimes, the time-averaged centers of three positions deviated slightly from the exact 3-fold symmetry, probably because of the oblique attachment of the F_1-ATPase molecule to the glass surface. To confirm that these pauses are not due to obstruction by nearby proteins or surface, we observed the single molecule for a long period by using plastic beads of diameter 440 nm or 517 nm as a rotation probe under transmission light microscopy. Despite the difference in the observation system, the pauses in the rotation of a pair of biotin-coated beads attached to the γ subunit also occurred at three positions with a frequency and duration similar to those observed in the rotation of actin filament (Fig. 1*B*).

The duration of all pauses longer than 10 s observed in the rotation of actin filaments and beads were plotted as a function of the length of the probes (Fig. 2). Values are scattered, but, on average, pauses continue for ≈30 s irrespective of the length of the probes. If pauses were caused by nearby obstacles, they should occur at random positions, and longer probes would generate more pauses because of an increased chance of encountering obstacles. Thus, the observed properties of pauses, the three angular-pause positions, and load-independence all suggest that the pause is not due to accidental obstruction by nearby proteins or by the surface, but that it reflects intrinsic properties of the F_1 motor.

State of F_1-ATPase Corresponding to the Pauses. It is natural to assume that the F_1-ATPase in the pausing phase should be in an

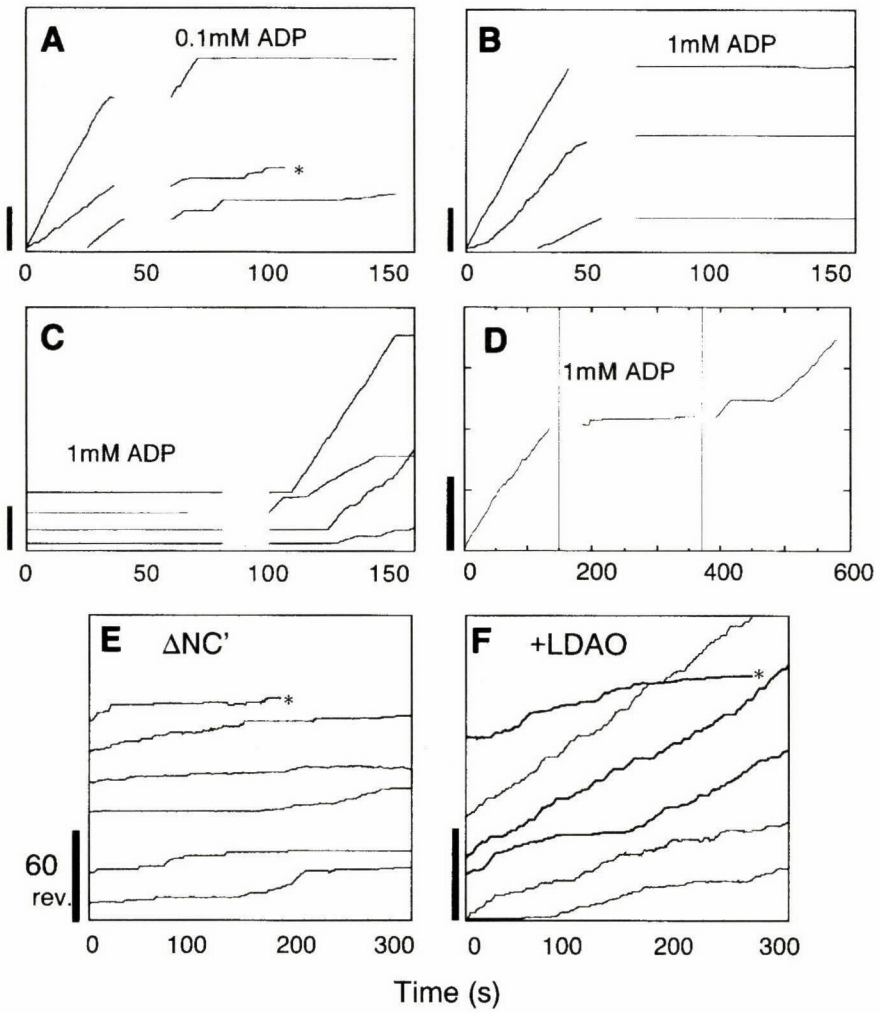

Fig. 3. Effect of ADP or ΔNC′ mutation on rotation. (A–D) Each line shows the rotation of wild-type F_1-ATPase. Buffer containing 0.1 mM ADP (*A*) or 1 mM ADP (*B*) was infused into the chamber for rotation observation. (*C*) ADP containing buffer was exchanged to ATP+re buffer. (*D*) Buffer containing 1 mM ADP was slowly introduced into the chamber (the center trace). The chamber was again exchanged for the ATP+re buffer (the right trace). Each line shows the rotation of the ΔNC′ mutant in buffer B in the absence (*E*) or in the presence (*F*) of 0.1% LDAO. Each bar indicates 60 revolutions.

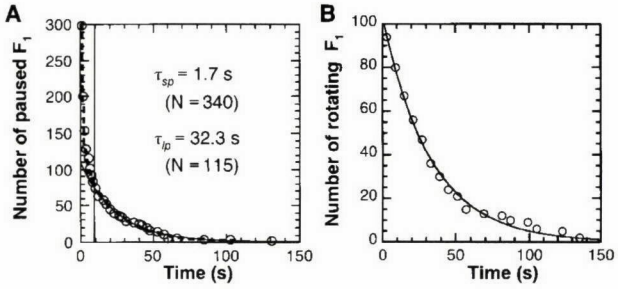

Fig. 4. Kinetic analyses of the rotation of single molecules. (*A*) The decay of the number of the pausing F_1-ATPases in 2 mM ATP-Mg. The data are fitted with a double exponential function (dashed line) assuming two kinds of pauses, short pause and long pause, in the following manner: $y = N_{sp} \cdot \exp(-t/\tau_{sp}) + N_{lp} \cdot \exp(-t/\tau_{lp})$, where N_{sp} (number of the short pauses) = 340, N_{lp} (number of the long pauses) = 115, τ_{sp} (life-time of the short pause) = 1.7 s, τ_{lp} (life-time of the long pause) = 32.3 s, with an error of about ±15%. The solid line shows a single exponential curve calculated from N_{lp} = 115 and τ_{lp}' = 32.2 s. (*B*) The decay of the number of the rotating F_1-ATPase in 2 mM ATP-Mg. The rotation between pauses longer than 10 s were measured. The solid line shows a single-exponential function with k_{r-lp}' (= $1/\tau_r'$) (rate of conversion from rotation to the long pause) = 0.029 s^{-1}.

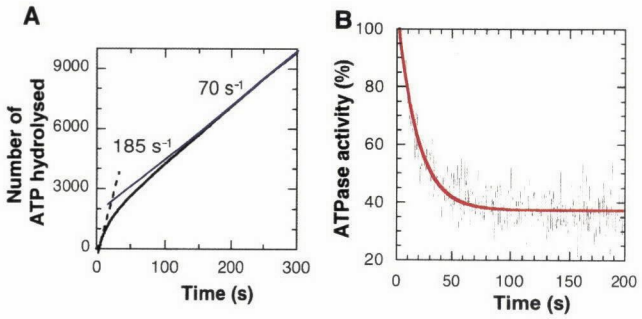

Fig. 5. Kinetic analyses of ADP-Mg inhibition as derived from the ATPase activity measurements. (*A*) The time course of ATP hydrolysis catalyzed by wild-type F_1-ATPase (black line) in Buffer A at 2 mM ATP-Mg. Dashed line, the initial rate; blue line, steady-state rate. (*B*) Inactivation of ATPase activity (black line) was fitted with a single exponential function (red line): const. · exp ($-k_{app} \cdot t$), where k_{app} (the apparent rate constant for inhibition) = 0.054 s^{-1}.

inactive form that is not hydrolyzing ATP. Because rotation resumes after awhile, this inactive form should be activated again in the presence of ATP-Mg. The candidate for the inactive form of F_1-ATPase that shows the above features is the ADP-Mg inhibited form, a state commonly found in F_1-ATPases from mitochondria (19), chloroplasts (20), and bacteria (13, 18, 21). The ADP-Mg inhibited form is generated in a stochastic manner during catalytic turnover of ATP hydrolysis by stable entrapment of ADP-Mg at a catalytic site. The ADP-Mg can be either an immediate hydrolysis product that is left bound to the enzyme or it can be picked up from the bulk phase medium (21). If pausing F_1-ATPase is really in the ADP-Mg inhibited form, inclusion of ADP-Mg in the solution during the rotation assay should result in an increase in the number of pauses. At first, rotation was observed in the presence of 1 mM ATP, and then a solution containing 0.1 mM ADP + 1 mM ATP (Fig. 3*A*) or 1 mM ADP + 1 mM ATP (Fig. 3*B*) was infused into the chamber. As expected, rotation was frequently (0.1 mM ADP) or almost completely (1 mM ADP) prevented after the infusion. Physical damage of the immobilized F_1-ATPase by the infusion is unlikely to be the reason for stopping rotation, because the reverse order of addition produced the opposite result—the molecules were unable to rotate in the presence of 1 mM ADP + 1 mM ATP and began rotation after the ADP was removed (Fig. 3*C*). Further, the rotating molecules in 1 mM ATP lapsed into a pause after the infusion of the ADP-containing solution, and started rotation again after the second infusion by the ADP-free solution (Fig. 3*D*).

Binding of ATP to the noncatalytic nucleotide-binding site on the α subunits stimulates the recovery of F_1-ATPase from the ADP-Mg inhibited form (14). Therefore, the mutant F_1-ATPase that has defective noncatalytic sites (ΔNC; ref. 13) is soon converted completely to the ADP-Mg inhibited form during catalysis. We examined whether the ΔNC mutant could rotate but were unable to find any rotating molecules. A second mutation, β-T165S, was introduced into the ΔNC mutant. The single β-T165S mutant is less susceptible to attaining the ADP-Mg inhibited form (14). The propensity of the ΔNC+β-T165S mutant (ΔNC′ mutant) to achieve the ADP-Mg inhibited form was intermediate, as it was greater than the wild-type F_1-ATPase but less than the ΔNC mutant. When we observed rotation of the ΔNC′ mutant, the number of actively rotating molecules was much smaller than in wild-type F_1-ATPase; even if they rotated, they stopped readily and stayed in the pausing phase for a long time (Fig. 3*E*). The inclusion of LDAO, which is known to be a potent activator of the ADP-Mg inhibited form (13, 21), resulted in a sharp decrease in the length of the long pauses (Fig. 3*F*). The same effect of LDAO was observed for the wild-type F_1-ATPase (data not shown). These results support the contention that the state of F_1-ATPase during the pause is the ADP-Mg inhibited form.

Kinetic Analysis of the Pause. We collected the data from all pauses longer than 1 s from many rotating molecules at 2 mM ATP. The duration of each pause was plotted as the time-dependent decay of the number of pausing F_1-ATPases, which remained in the pause and had not yet resumed rotation (Fig. 4*A*). The pauses observed for the rotation of probes of various lengths were analyzed together because the load, as shown in the previous section, does not affect the pausing (Fig. 2). The plot could not be fitted with a single exponential but was well fitted with the sum of two exponentials, suggesting that there are at least two kinds of pauses: the short-lived pause with a life-time (τ_{sp}) of 1.7 s, and the long-lived pause with a life-time (τ_{lp}) 32 s. On average, actively working F_1 in the presence of 2 mM ATP spent 33.5% of its time in rotation, 4.5% in the short pause, and 62% in the long pause. A curve calculated from the long pause alone (the solid line in Fig. 4*A*) indicates that most (96% of the total) of the observed pauses longer than 10 s belong to the category of the long pauses. The frequency of the incidence for the rotating F_1-ATPase to pause also was examined. For the short pauses, however, the incidence did not seem to be statistically random, and simple analysis was impossible. For the long pauses, the periods between one long pause (>10 s) and the next long pause (>10 s) were collected and analyzed. They were plotted as the time-dependent decay of the number of the "rotating" F_1-ATPases that escaped from one long pause but had not lapsed into the next long pause yet (Fig. 4*B*). The data were fitted with a single exponential with a 34 s life-time (τ_r'). This value was obtained for the 72 pauses longer than 10 s and should be corrected by the uncounted long pauses shorter than 10 s (calculated to be 43). The corrected value of τ_r is 22 s; that is, rotating F_1-ATPase lapses into the long pauses after 22 s, on average.

Kinetic Analysis of the ADP-Mg Inhibited Form. To compare the kinetic parameters of the long pauses to those of the ADP-Mg inhibited form, we estimated from the bulk-phase experiments the rates of conversion from the active to the ADP-Mg inhibited form ($k_{a\text{-}i}$) and those of reverse conversion ($k_{i\text{-}a}$) during catalysis, with the equation:

Table 1. Lifetimes obtained from single-molecule analysis and ATPase activity measurements under several conditions

Protein	ATP, μM	Lifetimes, s: Single molecule pausing F_1-ATPase (τ_{lp})	Lifetimes, s: ATPase ADP-Mg inhibition (τ_i)
Wild type	2000	32	56
		31	71*
	200	48	30
	20	77	59
	2	694	1429
ΔNC′	2000	167	143*
		12	22†

*Buffer contains 100 mM potassium phosphate.
†Buffer contains 100 mM potassium phosphate and 0.1% LDAO.

$$\text{the active form of } F_1 \underset{k_{i-a}}{\overset{k_{a-i}}{\longleftrightarrow}} \text{the ADP-Mg inhibited form of } F_1. \quad [1]$$

When the ATP hydrolysis assay was started by the addition of F_1-ATPase to the solution, the initial rapid hydrolysis decelerated within 1 min and reached a slow steady-state of hydrolysis (Fig. 5*A*). This time course suggests that the initial rapid hydrolysis is catalyzed by the F_1-ATPase free from ADP-Mg inhibition, and that the ADP-Mg inhibited form gradually accumulates, causing a decrease in the rate of hydrolysis. The final, steady-state hydrolysis at a stable rate is catalyzed by the active F_1-ATPase that is in a dynamic equilibrium with the ADP-Mg inhibited form. Based on the above scheme, $k_{a\text{-}i}$ and $k_{i\text{-}a}$ at 2 mM ATP were calculated to be 0.034 s^{-1} and 0.018 s^{-1} from the apparent rate constant of deceleration ($k_{a\text{-}i} + k_{i\text{-}a}$) and the ratio of steady-state activity to the initial activity ($k_{i\text{-}a}/[k_{a\text{-}i} + k_{i\text{-}a}]$) (9). A calculated curve using these rate constants can approximate the experimental data well (Fig. 5*B*, solid line). Thus, the life-time of the ADP-Mg inhibited form ($\tau_i = 1/k_{i\text{-}a}$) in 2 mM ATP is 56 s, and that of the active molecule ($\tau_a = 1/k_{a\text{-}i}$) is 29 s. These life-times coincide well with τ_{lp} and τ_r obtained from single-molecule analysis. Next, we compared the life-times of ADP-Mg inhibition from bulk-phase experiments and the life-times of pauses at several ATP concentrations. When the ATP concentration was decreased from 20 μM to 2 μM, both the life-times τ_i and τ_{lp} increased dramatically (≈25 times) (Table 1). The dependency of τ_a on ATP concentration is also very similar to that of τ_r (data not shown). The transitions at this concentration range are consistent with our previous observations that the rates of ADP-Mg inhibition were ATP-concentration dependent with an apparent K_d for ATP of 4 μM (13) or 13 ± 7 μM (22). By the same procedures, life-times in the presence of 100 mM potassium phosphate (Pi) and those of ΔNC′ mutant in 100 mM Pi with or without LDAO also were obtained. It is clear that the values of τ_i and τ_{lp} change in parallel and are always in the same range.

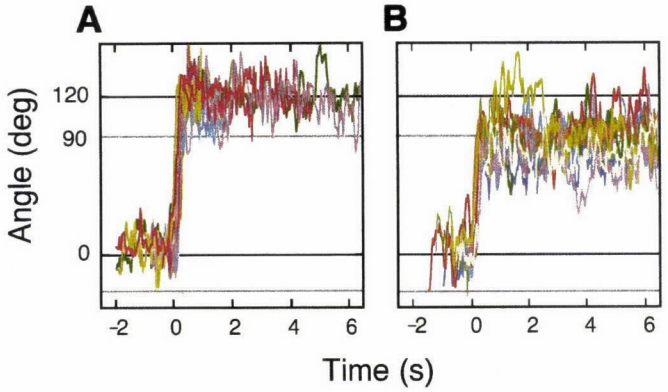

Fig. 7. Motions of rotation probe stepping from the ATP-waiting position (*A*) to the next ATP waiting positions or (*B*) to the ADP-Mg inhibition. The ATP concentration was 200 nM. (*A*) The stepping motions (of which subsequent pauses were shorter than 5 s) are collected and overlayed (n = 13). (*B*) The stepping motions (of which subsequent pauses were longer than 2 min) are collected and overlayed (n = 13).

Orientation of γ Subunit in the ADP-Mg Inhibited Form. The γ subunit makes a 120° rotation by using a single ATP and waits at this position (ATP-waiting position) for the next ATP. At low-ATP concentrations, this stepping rotation is well observed (8). As described, the pausing caused by ADP-Mg inhibition takes place in three angular positions that are separated by 120° from each other. To compare the relative positions of the long pause and the ATP-waiting state, we recorded the stepping rotation at 20

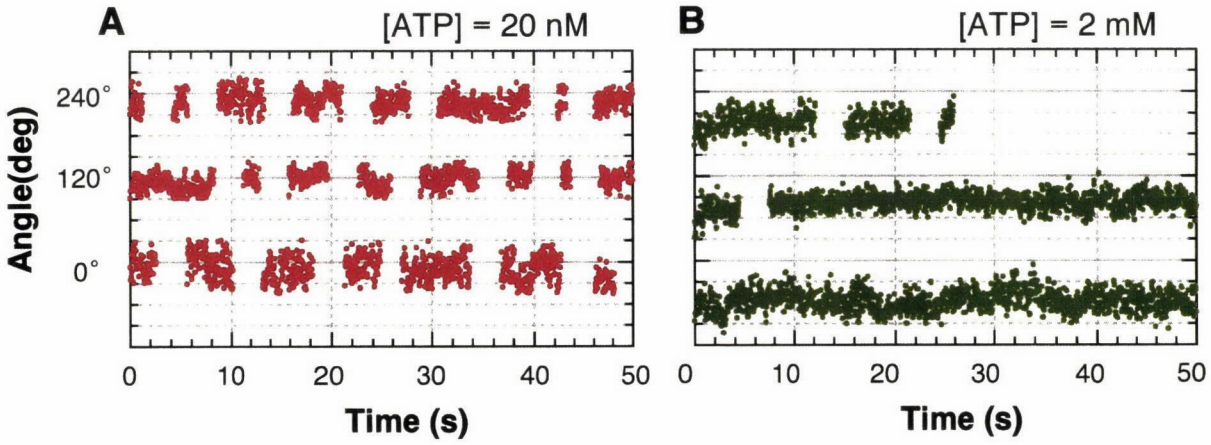

Fig. 6. Comparison of angular positions of ATP-waiting state and ADP-Mg inhibition. (*A*) The stepwise rotation of F_1-ATPase caused by waiting ATP was observed at 20 nM ATP. Each discrete 120° step was caused by ATP binding. (*B*) The pausing positions at 2 mM ATP. A reaction mixture containing 2 mM ATP was slowly introduced into the same chamber. Instead of the stepwise rotations, we could detect both continuous rotation and long pauses, as in Fig. 1. The angles of the long pauses, which are assumed to be caused by ADP-Mg inhibition, are shown. The positions of probes during the pausing period are presented at each of three angular positions.

nM ATP at first, then infused the buffer containing 2 mM ATP into the observation chamber and observed the long pauses of the same molecule. As seen in Fig. 6, the positions of ADP-Mg inhibition and the ATP-waiting positions are significantly different and separated by 37.6° ± 2.5°. The same particle started stepwise rotation again at 0°, 120°, and 240° after exchange of the buffer for 200 nM ATP.

At 200 nM ATP, both 120° steps caused by ATP-waiting and the pauses caused by the ADP-Mg inhibition were observed frequently enough for analysis (Fig. 7). Under these conditions, the ATP-waiting period is short (≈0.4 s), whereas ADP-Mg inhibition continues for a long period (≈30 min). Therefore, we can easily separate these two kinds of pauses; the result of the short ones define the ATP-waiting state, and long ones are the result of ADP-Mg inhibition. Moreover, the two paused states can be distinguished by the angle of rotation after the pause. Whereas steps between two adjacent ATP-waiting positions were 120°, the long pauses always started after ≈90° rotation.

Discussion

Here, we showed that individual single molecules of active F_1-ATPase alternate between at least three phases: continuous rotation, short pauses, and long pauses during catalysis at saturating ATP concentrations. The origin of the short pause is not yet known, but the long pause has been identified as the ADP-Mg inhibited state that has been recognized previously by bulk-phase kinetics. ADP-Mg inhibition is a common feature of the F_1-ATPases and ATP synthases from various sources and, hence, likely to have functional significance. ATP hydrolysis and ATP-driven proton-pumping activity by ATP synthase are susceptible to this inhibition. Conversely, the ADP-Mg inhibition is relieved when membrane potential exists (23); ATP synthesis by ATP synthase is completely free from this inhibition (24, 25).

F_1-ATPase rotates in discrete 120° steps, consistent with sequential ATP hydrolysis on the three β subunits. Recently, it was revealed that each 120° step is further divided to the 90° and 30° substeps, each taking only a fraction of a msec (15). ATP binding drives the 90° substep. The enzyme spent about 2 msec on average at the 90° position (the 90° dwell), irrespective of medium ATP concentrations. During the 90° dwell, at least two 1-msec events occur; the latter one, resetting the enzyme to start the next cycle, accompanies the 30° rotation. ADP-Mg inhibition arises at ≈83°, measured from the ATP-waiting position (Figs. 6 and 7), and therefore it is likely to be generated in a stochastic manner at the 90° dwell by some off-the-catalytic-pathway event.

We thank T. Nishizaka for actin preparation. We also thank Drs. J. Hardy and M. T. Stumpp for critical reading of the manuscript. Y.H.-H. and K.Y.H. are supported by Research Fellowships of Japan Society for the Promotion of Science for Young Scientists.

1 Deckers-Hebestreit, G. & Altendlf, K. (1996) *Annu. Rev. Microbiol.* **50,** 791–824.
2 Boyer, P D (2000) *Biochim Biophys Acta* **1458,** 252–262.
3. Weber, J & Senior, A. E (2000) *Biochim. Biophys. Acta* **1458,** 300–309
4 Cross, R. I (2000) *Biochem Biophys. Acta* **1458,** 270–275.
5. Abrahams, J P, Leslie, A G, Lutter, R. & Walker, J. E. (1994) *Nature (London)* **370,** 621–628
6 Boyer, P D (1993) *Biochim Biophys Acta* **1140,** 215–250.
7 Noji, H, Yasuda, R, Yoshida, M & Kinosita, K J (1997) *Nature (London)* **386,** 299–302
8 Yasuda, R, Noji, H., Kinosita, K J & Yoshida, M (1998) *Cell* **93,** 1117–1124
9 Masaike, T, Mitome, N, Noji, H, Muneyuki, E, Yasuda, R., Kinosita, K J & Yoshida, M (2000) *J Exp. Biol* **203,** 1–8.
10. Yanisch-Perron, C., Vieria, J & Messing, J. (1985) *Gene* **33,** 103–119.
11. Kunkel, I A, Bebenek, K & McClary, J. (1991) *Methods Enzymol.* **204,** 125–139
12 Matsui, T & Yoshida, M (1995) *Biochim Biophys. Acta* **1231,** 139–146
13. Matsui, T, Muneyuki, L, Honda, M, Allison, W. S., Dou, C & Yoshida, M (1997) *J Biol Chem* **272,** 8215–8221
14 Jault, J M, Dou, C, Grodsky, N B, Matsui, T, Yoshida, M. & Allison, W S (1996) *J Biol Chem* **271,** 28818–28824
15. Yasuda, R, Noji, H, Yoshida, M, Kinosita, K J. & Itoh, H (2001) *Nature (London)* **410,** 898–904.
16. Amano, T, Hisabori, T., Muneyuki, E & Yoshida, M (1996) *J. Biol. Chem.* **271,** 18128–18133
17. Bald, D., Muneyuki, E, Amano, T, Kruip, J, Hisabori, T. & Yoshida, M. (1999) *Eur J Biochem* **262,** 563–568
18. Kato, Y., Sasayama, T, Muneyuki, E & Yoshida, M. (1995) *Biochim. Biophys. Acta* **1231,** 275–281.
19. Milgrom, Y M & Boyer, P D. (1990) *Biochim. Biophys. Acta* **1020,** 43–48
20. Guerrero, K J, Xue, Z X. & Boyer, P. D. (1990) *J Biol Chem* **265,** 16280–16287
21 Jault, J M, Matsui, T, Jault, F. M, Kaibara, C, Muneyuki, E., Yoshida, M, Kagawa, Y & Allison, W. S (1995) *Biochemistry* **34,** 16412–16418.
22 Muneyuki, L, Makino, M, Kamata, H, Kagawa, Y, Yoshida, M & Hirata, H (1993) *Biochim Biophys. Acta* **1144,** 62–68
23 Galkin, M A & Vinogradov, A. D (1999) *FEBS Lett* **448,** 123–126
24 Syroeshkin, A V, Vasilyeva, E A & Vinogradov, A D (1995) *FEBS Lett* **366,** 29–32
25 Bald, D., Amano, T, Muneyuki, E., Pitard, B., Rigaud, J. L, Kruip, J, Hisabori, T., Yoshida, M & Shibata, M. (1998) *J Biol. Chem* **273,** 865–870

Myosin V is a left-handed spiral motor on the right-handed actin helix

M. Yusuf Ali[1–3], Sotaro Uemura[4], Kengo Adachi[1,2], Hiroyasu Itoh[2,5], Kazuhiko Kinosita Jr[1–3] and Shin'ichi Ishiwata[2,4]

[1]*Center for Integrative Bioscience, Okazaki National Research Institutes, Higashiyama 5-1, Myodaiji, Okazaki 444-8585, Japan.* [2]*CREST (Core Research for Evolutional Science and Technology), 'Genetic Programming' Team 13, Nogawa 907, Miyamae-ku, Kawasaki 216-0001, Japan.* [3]*Department of Physics, Faculty of Science and Technology, Keio University, Hiyoshi 3-14-1, Kohoku-ku, Yokohama 223-8522, Japan.* [4]*Department of Physics, School of Science and Engineering, Waseda University, Okubo 3-4-1, Shinjuku-ku, Tokyo 169-8555, Japan.* [5]*Tsukuba Research Laboratory, Hamamatsu Photonics KK, Tokodai, Tsukuba 300-2635, Japan.*

Published online: 13 May 2002, DOI: 10.1038/nsb803

Myosin V is a two-headed, actin-based molecular motor implicated in organelle transport. Previously, a single myosin V molecule has been shown to move processively along an actin filament in discrete ~36 nm steps. However, 36 nm is the helical repeat length of actin, and the geometry of the previous experiments may have forced the heads to bind to, or halt at, sites on one side of actin that are separated by 36 nm. To observe unconstrained motion, we suspended an actin filament in solution and attached a single myosin V molecule carrying a bead duplex. The duplex moved as a left-handed spiral around the filament, disregarding the right-handed actin helix. Our results indicate a stepwise walking mechanism in which myosin V positions and orients the unbound head such that the head will land at the 11th or 13th actin subunit on the opposing strand of the actin double helix.

Class V myosin has two globular motor domains that interact with an actin filament to generate force upon ATP hydrolysis; the motor supports a wide variety of cellular movements[1–5]. Myosin V consists of two identical heavy chains, each composed of an N-terminal motor domain ('head'), six IQ motifs that bind light chains ('neck'), a coiled coil tail domain and a globular cargo-binding domain[1]. A single myosin V molecule moves along an actin filament for many catalytic cycles without dissociating from the filament[6–8]. Steps of ~36 nm have been identified in this processive movement[6,7,9], and the two heads of myosin V have been shown to bind to actin ~36 nm apart[10], suggesting that myosin V 'walks' on actin with 36 nm strides by alternate binding of the two heads.

Whether myosin V really walks and, if so, how its step size is determined are fundamental issues relating to the motor mechanism. The step size measurements above were made either with myosin V fixed on a surface[6,9] or actin filaments lying on a surface[7,10] such that myosin V could approach an actin filament only from one side. Myosin V had to move straight on actin; thus, the motor may well have been forced to step on blue actin subunits (Fig. 1*a*), which are 36 nm apart. Here we allow myosin V to freely rotate around an actin filament and monitor how or whether the motor walks. If myosin V walks but its natural step size is slightly longer or shorter than 36 nm, unconstrained motion should be a right- or left-handed, long-pitch spiral.

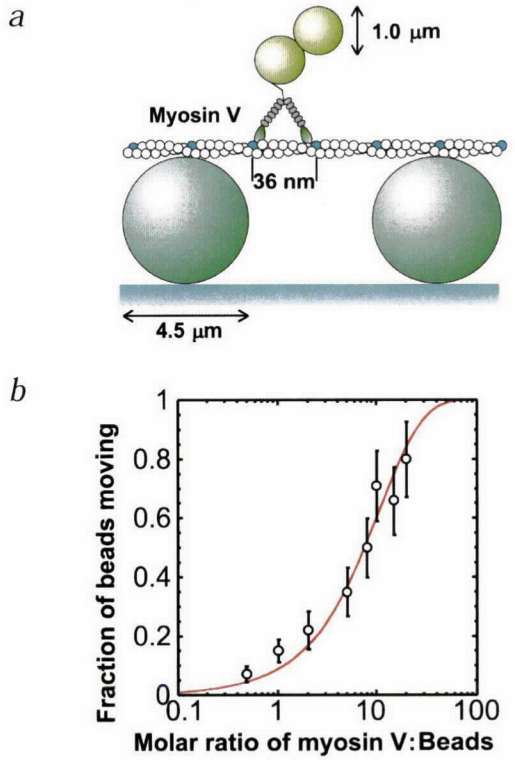

Fig. 1 Experimental design. ***a***, Motility assay system (not to scale). The heads of myosin V are green; the necks, gray. Every 13th actin subunit is blue. ***b***, Fraction of beads that moved more than ~0.5 μm along an actin filament (see Methods). Error bars indicate $\pm n^{1/2} N^{-1}$, where n is the number of beads that moved and N (50 or 100) is the number of trials. Line shows the theoretical probability that a bead carries one or more active motors, $1 - \exp(-\lambda c)$, where c is the molar ratio of myosin V to beads and λ (0.092) is the fit parameter[30].

Alternatively, steps may be so short that myosin V sequentially interacts with neighboring actin subunits in one of the two helical strands (crossing onto the other strand would require extremely 'bowlegged' necks). In this case, myosin V would undergo extensive right-handed rotation, as does RNA polymerase around DNA[11]. A single head might glide over many actin subunits in a strand during one ATPase cycle[12]. Such gliding is not necessarily inconsistent with the observed ~36 nm steps, because gliding would be forced to stop at ~36 nm when rotation around the actin filament is prohibited. Direct observation of rotation will distinguish between these cases.

Myosin V rotates as a left-handed screw

To allow myosin V to freely rotate around an actin filament, we suspended an actin filament between two large (4.5 μm) beads immobilized on a glass surface[13] (Fig. 1*a*); a similar system has been reported[14]. Using optical tweezers, we positioned a duplex of smaller (1 μm) beads that were pre-incubated with myosin V at the molar ratio of 1:1 onto the midpoint of the filament. When the laser trap was turned off, the duplex started to move along and, at the same time, rotate around the actin filament. Results from experiments in which single 1 μm beads prepared at various myosin:bead ratios were allowed to move along an actin filament (Fig. 1*b*) indicate that a single myosin V molecule is most likely responsible for this motion. The fraction of moving beads as a function of myosin:bead ratio fit well to a

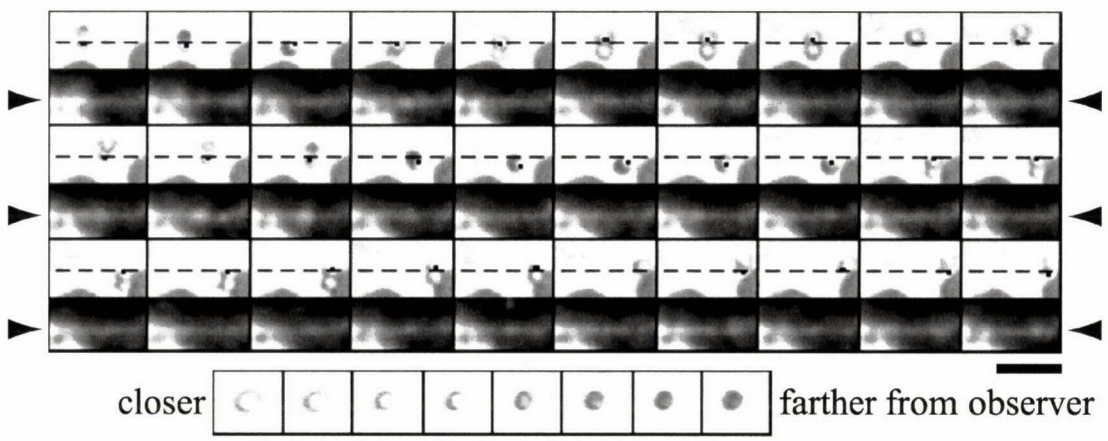

Fig. 2 Spiral motion of myosin V around an actin filament at 400 μM ATP. ***a***, Sequential images at 1 s intervals. Upper and lower panels show bright-field and corresponding fluorescence images, respectively. The bar corresponds to 5 μm. Dashed lines are the position of the actin filament deduced from lower panels (arrow heads); dots, center of the beads that are judged to be on actin. Note that the actin filament remained straight. ***b***, Images of a 1 μm bead at decreasing heights (left to right at ~0.2 μm intervals) from the glass surface. Because our images represent views from above the sample[27], white beads in (*a*) and (*b*) are closer to the observer, whereas the black beads are farther away.

Poisson distribution (solid line); this fit indicates that >95% of moving beads were driven by only one myosin V molecule. These single beads also rotated around the actin filament, but precise analysis was far easier with the bead duplex.

Myosin V-decorated bead duplexes were allowed to move along an actin filament at 400 μM ATP, where the linear velocity of the motor was maximal. Sequential video images of such a system reveal that the bead duplex rotates around the actin filament (Fig. 2a; movies at http://k2.ims.ac.jp). In these images, a bead that appears white is closer to the observer, whereas a black one is farther from the observer (Fig. 2b). Thus, the duplex moved as a left-handed screw, making two revolutions while traveling over ~4.4 μm. Such complete rotations were observed at all ATP concentrations examined, and all complete rotations were left-handed. This is in contrast to myosin II, which rotates as a right-handed screw[15]. Not all bead duplexes bound to an actin filament showed clear rotation (Table 1), the primary reasons being either that they did not move long enough or the filament was <2 μm from the surface. There were 10 instances where, with no apparent reason, the duplex moved for >1 μm without appreciable rotation (Fig. 3c; Table 1). Presumably, the filament height was ~2 μm or some debris was attached to the duplex and impeded rotation. Indeed, we occasionally observed beads carrying relatively large debris, including short actin filaments, in the fluorescence image. Smaller debris would have been unnoticed. That myosin V can move without rotation is consistent with the previous observations of stepping on actin lying on a surface.

Table 1 Summary of bead duplex experiments at 1:1 myosin V:bead

Total number of bead duplexes tested at 1–1,000 μM ATP	1,040
Duplexes bound to actin	229
Active duplexes[1]	156 (100%)
Moved only for <1 μm	57 (37%)[2]
Moved for >1 μm and made >0.5 revolution	43 (28%)
Moved for >1 μm without rotation[3]	46 (29%)
Moved for >1 μm without rotation[4]	10 (6%)

[1]Defined as having moved along actin for >0.5 μm.
[2]Actin filaments were not long enough in 22 cases.
[3]The filament height was <2 μm.
[4]Reason for no rotation is unknown.

Unconstrained step size is 34.8 nm

From the time courses of rotation and displacement along actin for individual bead duplexes (Fig. 3a–c), we determined the relation between rotation and displacement for all duplexes that made >~1 revolution (solid lines in Fig. 3d). All of these curves (Fig. 3d) are within a narrow zone, showing that the rotation and displacement are well correlated, except for the presumably impeded cases (Fig. 3c, dotted lines in Fig. 3d). Myosin V travels a distance of 2.2 ± 0.3 μm per one left-handed revolution (mean ± s.d. for linear fits to 22 solid curves in Fig. 3d), which is constant over ATP concentrations from 1 μM to 1 mM, where the linear velocity of the motor changes from 5 to 320 nm s^{-1}.

The left-handed rotation of single myosin V molecules indicates a step size slightly smaller than the actin helical repeat of 36 nm (Fig. 4). Steps shorter than 18 nm, including the case of sliding along one helical strand[12], would result in right-handed rotation. Because the difference between the helical repeat of actin and the step size of myosin V motor (blue/cyan versus red in Fig. 4) must add up to one full turn of actin helix (72 nm) over the travel distance of 2.2 μm, the average step size is given by 36 nm × (2,200 nm – 72 nm) / (2,200 nm) = 34.8 nm. This number derived from the actin repeat is rather precise (±0.1 nm) and is insensitive to the uncertainty in the 2,200 nm value. On average, myosin V rotates 6° (360° × 34.8 nm / 2,200 nm) per step left around the actin filament.

Step size is constant

The step size of 34.8 nm above is the one at no load. Hydrodynamic friction against the bead duplex is given by $2 \times 6\pi\eta av$, where η (0.001 N m^{-2} s) is the viscosity of water; a (0.5 μm), the bead radius; and v (<320 nm s^{-1}), the bead velocity. Thus, the frictional load is at most 0.006 pN, far less than the maximal pulling force, 3 pN, produced by a single myosin V molecule[6]. The frictional torque against rotation is given by[16]: $(2 \times 8\pi\eta a^3 + 6\pi\eta a^3 + 6\pi\eta ar^2)\omega$, where r is the distance between

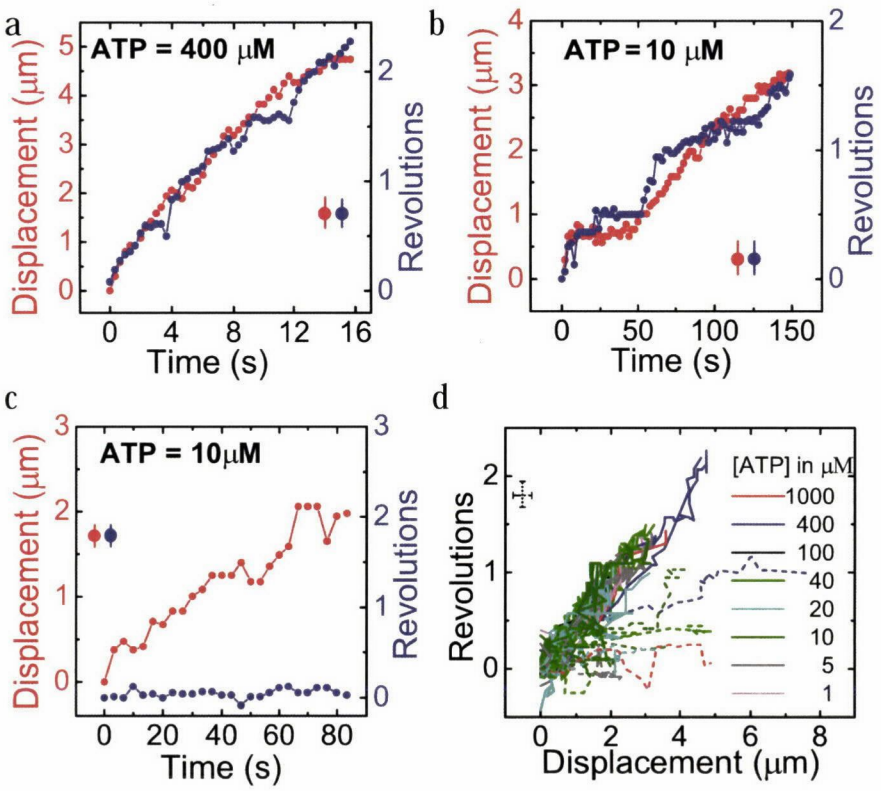

Fig. 3 Correlations between displacement and rotation. ***a,b***, Typical time courses. Error bars are likely uncertainties in human judgment (see Methods). ***c***, A case of linear motion. ***d***, Relationship between sliding distance and rotation. ATP concentrations are distinguished by color and indicated in μM. Dashed lines represent linear motion or irregular rotation.

the center of the outer bead and actin filament, and ω is the angular velocity. A duplex with r = 1.2 μm was found to rotate at ω = 0.9 radian s^{-1}, giving the highest torque of 20 pN nm, and several other duplexes showed the torque at >10 pN nm. These values are apparently quite high, comparable to the 40 pN nm of torque produced by the rotary molecular motor F_1ATPase[17]. In one step, however, myosin V rotates only 6° = 0.1 radian; thus, the work done for rotation is at most 2 pN nm (20 pN nm × 0.1 radian), only half the thermal energy. The frictional torque is completely negligible at low ATP concentrations.

The step size of myosin V is ~35 nm under a variety of conditions. Duplexes prepared at 10^4 myosin V molecules per bead also made one left-handed rotation per 2.5 ± 0.5 μm at 40 μM ATP (n = 8). This is a loaded condition, because a stepping myosin V molecule has to work against others that are simultaneously bound to actin. Consistent with this, a step size of 35 nm has recently been reported[9] under a load of 1 pN. Load independence of the step size may imply that myosin V does not readily fluctuate toward right or left when it stands on one foot ('head'). To determine if myosin V tends to interact with intervening actin subunits during the long strides, we examined bead motions at increasing ionic strengths, which would result in diminished actin–myosin interaction[18]. The average distances traveled at 50, 100, 200 and 300 mM KCl were 2.1, 2.1, 1.5 and 1.1 μm (n = 8, 23, 7 and 7), respectively, indicating reduction in processivity as expected. Rotations, however, were all left-handed and one revolution per 2.3 ± 0.5 μm at all ionic strengths. Myosin V seems to stride over intervening actin subunits.

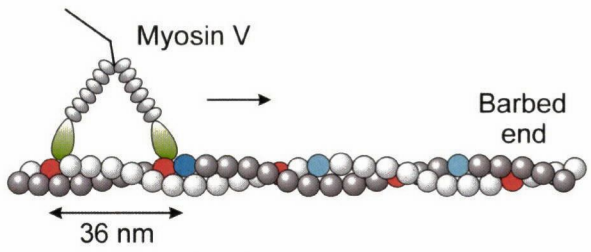

Fig. 4 Interpretation of the left-handed rotation. Stepping on every 11th actin subunit (red) would result in left-handed spiral movement, whereas linear movement is expected on the 13th subunits (blue/cyan). The estimated step size of 34.8 nm is between the 11th and 13th subunits.

Discussion

Spiral motion of a single motor molecule around a helical track should reveal how the motor successively interacts with the repeating units composing the track. To our knowledge, myosin V is the first example of a processive motor spiraling with a pitch incommensurate to the helical pitch of the track; kinesin[19] and RNA polymerase[11] precisely follow their respective helical track. The deduced step size of 34.8 nm for myosin V is much larger than the intersubunit distance of 5.5 nm in one strand of the actin filament, indicating that myosin V walks with long strides; sliding along one strand of actin helix[12] is unlikely.

There are 13 actin subunits per 36 nm, counting both strands. Our results indicate that, during unconstrained walking, myosin V aims at the 11th (red, Fig. 4) or 13th (blue) actin subunit on the opposing strand (binding to the 12th subunit on the opposite side of the filament would be sterically hindered). This almost straight walking is not a trivial task, because, unlike a human, the two feet ('heads') of myosin V are identical and related by basic two-fold symmetry. Landing on the 13th subunit would require 180° twist of the neck from its symmetry-related orientation. Although the twist would imply extensive flexibility in the neck (and/or head), a proper posture of the bound head and neck is to aim at a correct target among identical actin subunits in the double helix. Recent reports[20,21] suggest that ~25 nm of the step size of ~35 nm is accounted for by the swing of the bound neck and the rest by diffusion of the unbound head. The swing, then, must be a delicate combination of bending and twisting that ensures diffusional landing on, mostly, the 11th or 13th subunit, irrespective of load.

The natural way of walking is one in which the two heads move forward alternately[22]. Alternate binding of two identical heads should result in 180° rotation of the entire molecule

around its symmetry axis every time the motor steps[22], but kinesin failed to show this[23]. We examined whether our bead duplex would rotate around the point of attachment to actin at low concentrations of ATP (500 nM–1 μM), but, similar to kinesin, we have seen no convincing evidence of 180° rotation. This is apparently inconsistent with simple walking, although oblique attachment of myosin V to the bead surface may have impeded the rotation of the bead duplex. Simple walking has also been challenged by recent findings: myosin VI[9,24] and mutated myosin V[12], both short necked, made large steps apparently incompatible with the head and neck sizes. Conformational changes, or melting, in the head/neck region would be required to allow a long stride, as in kinesin[25]. Whether, or in which direction, these short-necked myosins rotate remains to be seen.

Methods

Sample preparation. Myosin V was purified from chick brain[26]. Rabbit skeletal actin was biotinylated and stained with phalloidin-tetramethylrhodamine essentially as described[27] but without crosslinking; the molar ratio of actin to biotin-PE-maleimide was 1:2. Polystyrene beads (1 μm, F-8814, Molecular Probes) were incubated for 30 min in buffer A (10 mM imidazole, pH 7.6, 100 mM KCl, 4 mM $MgCl_2$, 1 mM EGTA and 5 mM dithiothreitol (DTT)) containing 10 mg ml^{-1} BSA and centrifuged for 15 min at 18,000× *g*. Of the beads, ~10% formed duplexes. The beads were coated with myosin V as described[7]. To assess the coating efficiency (Fig. 1*b*), a single bead was selected and held in an optical trap[28] near an actin filament suspended in buffer A containing 1 mM ATP (see below). Then, the filament was moved across the bead in various directions by moving the microscope stage until the bead attached to the filament. If attachment did not occur within ~1 min, the bead was repositioned and the manipulation was repeated several times. After attachment, the trap was turned off to allow movement of the bead along actin. The fraction of beads that were bound but did not move >–0.5 μm was <–0.1 (0.03 at the myosin/bead ratio, c, of 0.5 and 0.09 at c = 1). The motility assay below was done on duplex beads prepared at c = 1, unless stated otherwise.

Motility assay. Carboxylated polystyrene beads (4.5 μm; Polyscience) were amino-derivatized and biotinylated[29]. The beads were incubated with 10 mg ml^{-1} streptavidin, washed and infused in a flow chamber. After 10 min, 5 mg ml^{-1} BSA was infused and incubated for 1 min. Biotinylated and labeled actin filaments were infused and allowed to bind to the 4.5 μm beads to form actin bridges. Then, 0.25–1 pM of beads decorated with myosin V in buffer A containing ATP, 6 mg ml^{-1} glucose, 0.2 mg ml^{-1} glucose oxidase, 0.02 mg ml^{-1} catalase and 0.2% β-mercaptoethanol were infused into the flow cell. To minimize Brownian motion, only tightly suspended actin filaments were used. If such a filament was not found, we moved the 4.5 μm beads with the optical tweezers to form a tight actin bridge. Torsional Brownian motion of actin is <±50° for a 10 μm filament[13]. Finally, we positioned a bead duplex onto an actin filament using the optical tweezers, moved the filament until it bound the duplex and turned off the optical trap to let the duplex move along the actin filament. If unsuccessful, this maneuver was repeated 10–30×. The microscope system has been described[28]; bright-field images showing bead movement and fluorescence images showing actin filaments were simultaneously recorded with video cameras. Positions and orientations of bead duplexes were analyzed by eye to the precision of ±0.5 μm and ±0.25 revolutions. For the orientation, video images were compared with pairs of overlapping circles representing views of two spheres at known angles. Because of drift in the microscope focus, there were rare occasions where distinction between the two beads became difficult; large deviations from linear relationship in Fig. 3*d*, seen in some curves, may be due to human error. Observations were made at 23 °C.

Acknowledgments

We thank R. Yasuda, H. Noji, T. Nishizaka, Y. Harada and T. Nishinaka for discussion, L.B. Roksana, K. Kawashima, K. Yogo, R. Shimo, J. Yamaguchi and H. Kubota for sample preparation. M. Shio for microscope setup and H. Umezawa for laboratory management. M.Y.A. was a research fellow of the Japan Society for the Promotion of Science. This work was supported in part by Grants-in-Aid from the Ministry of Education, Culture, Sports, Science, and Technology of Japan.

Competing interests statement

The authors declare that they have no competing financial interests.

Correspondence should be addressed to K.K. *email: kazuhiko@ims.ac.jp*

Received 7 March, 2002; accepted 16 April, 2002.

1 Cheney, R.E. *et al. Cell* **75**, 13–23 (1993)
2 Mermall, V., Post, P.L. & Mooseker, M.S. *Science* **279**, 527–533 (1998)
3 Rogers, S.L. & Gelfand, V.I. *Curr. Biol.* **8**, 161–164 (1998)
4 Tabb, J.S., Molyneaux, B.J., Cohen, D.L., Kuznetsov, S.A. & Langford, G.M. *J. Cell Sci.* **111**, 3221–3234 (1998)
5 Hodge, T. & Cope, M.J. *J. Cell Sci.* **113**, 3353–3354 (2000)
6 Mehta, A.D. *et al. Nature* **400**, 590–593 (1999)
7 Rief, M. *et al. Proc. Natl. Acad. Sci. USA* **97**, 9482–9486 (2000)
8 Sakamoto, T., Amitani, I., Yokota, E. & Ando, T. *Biochem. Biophys. Res. Commun.* **272**, 586–590 (2000)
9 Rock, R.S. *et al. Proc. Natl. Acad. Sci. USA* **98**, 13655–13659 (2001)
10 Walker, M.L. *et al. Nature* **405**, 804–807 (2000)
11 Harada, Y. *et al. Nature* **409**, 113–115 (2001)
12 Tanaka, H. *et al. Nature* **415**, 192–195 (2002)
13 Yasuda, R., Miyata, H. & Kinosita, K. Jr. *J. Mol. Biol.* **263**, 227–236 (1996)
14 Yamada, T. *et al. Biophys. J.* **80**, 80a (2001)
15 Nishizaka, T., Yagi, T., Tanaka, Y. & Ishiwata, S. *Nature* **361**, 269–271 (1993)
16 Suzuki, N., Miyata, H., Ishiwata, S. & Kinosita, K. Jr. *Biophys. J.* **70**, 401–408 (1996)
17 Yasuda, R., Noji, H., Kinosita, K. Jr. & Yoshida, M. *Cell* **93**, 1117–1124 (1998)
18 Homsher, E., Wang, F. & Sellers, J.R. *Am. J. Physiol.* **262**, 714–723 (1992)
19 Gelles, J., Schnapp, B.J. & Sheetz, M.P. *Nature* **331**, 450–453 (1988)
20 Moore, J.R., Krementsova, E.B., Trybus, K.M. & Warshaw, D.M. *J. Cell Biol.* **155**, 625–635 (2001)
21 Veigel, C., Wang, F., Bartoo, M.L., Sellers, J.R. & Molloy, J.E. *Nature Cell Biol.* **4**, 59–65 (2002)
22 Howard, J. *Annu. Rev. Physiol.* **58**, 703–729 (1996)
23 Hua, W., Chung, J. & Gelles, J. *Science* **295**, 844–848 (2002)
24 Nishikawa, S. *et al. Biochem. Biophys. Res. Commun.* **290**, 311–317 (2002)
25 Rice, S. *et al. Nature* **402**, 778–784 (1999)
26 Cheney, R.E. *Methods Enzymol.* **298**, 3–18 (1998)
27 Noji, H., Yasuda, R., Yoshida, M. & Kinosita, K. Jr. *Nature* **386**, 299–302 (1997)
28 Miyata, H. *et al. Biophys. J.* **68**, 286s–290s (1995)
29 Harada, Y. *et al. Biophys. J.* **76**, 709–715 (1999)
30 Block, S.M., Goldstein, L.S. & Schnapp, B.J. *Nature* **348**, 348–352 (1990)

THE JOURNAL OF BIOLOGICAL CHEMISTRY
Vol 277, No 24, Issue of June 14, pp 21643-21649, 2002
Printed in U S A

F_1-ATPase Changes Its Conformations upon Phosphate Release*

Received for publication, October 26, 2001, and in revised form, March 5, 2002
Published, JBC Papers in Press, March 5, 2002, DOI 10.1074/jbc.M110297200

Tomoko Masaike‡§, Eiro Muneyuki‡, Hiroyuki Noji¶‖, Kazuhiko Kinosita, Jr.‡‡, and Masasuke Yoshida‡ ‡‡§§¶¶**

*From the ‡Chemical Resources Laboratory, Tokyo Institute of Technology, 4259 Nagatsuta, Yokohama, 226-8503, Japan, ¶PRESTO (Precursory Research for Embryonic Science and Technology), Japan Science and Technology Corporation 332-0012, Japan, the ‖Institute of Industrial Science, University of Tokyo, 4-6-1 Komaba Meguro-ku, Tokyo 153-8505, Japan, the **Center for Integrative Bioscience, Okazaki National Research Institutes, 38 Aza Nishigonaka, Myodaiji-Cho, Okazaki, Aichi, 444-8585, Japan, ‡‡CREST (Core Research for Evolutional Science and Technology) Genetic Programming Team 13, Teikyo University Biotechnology Center 3F, 907 Nogawa, Miyamae-ku, Kawasaki 216-0001, Japan, and §§ERATO (Exploratory Research for Advanced Technology), Japan Science and Technology Corporation 332-0012, Japan*

Motor proteins, myosin, and kinesin have γ-phosphate sensors in the switch II loop that play key roles in conformational changes that support motility. Here we report that a rotary motor, F_1-ATPase, also changes its conformations upon phosphate release. The tryptophan mutation was introduced into Arg-333 in the β subunit of F_1-ATPase from thermophilic *Bacillus* PS3 as a probe of conformational changes. This residue interacts with the switch II loop (residues 308–315) of the β subunit in a nucleotide-bound conformation. The addition of ATP to the mutant F_1 subcomplex $\alpha_3\beta(R333W)_3\gamma$ caused transient increase and subsequent decay of the Trp fluorescence. The increase was caused by conformational changes on ATP binding. The rate of decay agreed well with that of phosphate release monitored by phosphate-binding protein assays. This is the first evidence that the β subunit changes its conformation upon phosphate release, which may share a common mechanism of exerting motility with other motor proteins.

ATP synthase is composed of the major subcomplexes F_1 and F_o. F_1-catalyzed synthesis of ATP from ADP and P_i is coupled with proton translocation through F_o, which resides in the membrane. F_1 part can be separated from F_o part as a water-soluble ATPase that has subunit composition $\alpha_3\beta_3\gamma\delta\epsilon$ and hence is often called F_1-ATPase. Catalytic nucleotide-binding sites are located on the β subunits, whereas the α subunits contain noncatalytic nucleotide-binding sites. In the crystal structure of the bovine mitochondrial F_1-ATPase (MF_1),[1] the coiled-coil structure of the γ subunit is surrounded by a semi-hexagonal ring of $\alpha_3\beta_3$ (1). F_1-ATPase is a rotary motor enzyme; ATP-dependent rotation of the γ subunit relative to the $\alpha_3\beta_3$ ring, as predicted by biochemical studies (2–4), was visualized using the thermophilic F_1-ATPase (TF_1) (5). Consistent with the presence of three β subunits in the ring, hydrolysis of a single ATP molecule drives a 120° rotation of the γ subunit (6). It is intriguing how the local conformational changes accompanied by each of reaction steps in the catalytic cycle, such as ATP binding, hydrolysis, and release of ADP and P_i, are amplified and transformed into the force to dislocate the γ subunit. Recent progress shows that each 120° rotation is further divided into a 90° substep that is driven by ATP binding and a 30° substep presumably driven by the release of the product, most likely ADP (7).

Nucleotide binding induces a large conformational change of the β subunit (8). Each of the three β subunits in the initial MF_1 structure, which was disclosed in 1994 (1), takes one of the two conformations: an "open" form in which catalytic site is empty or a "closed" form in which the catalytic site is occupied by AMP-PNP or ADP. Consistent with that, the β subunits of the crystal structure of the TF_1 subcomplex $\alpha_3\beta_3$ without bound nucleotides were all in the open form (9). Compared with the open form, the carboxyl-terminal domain of the β subunit in the closed form swings ~30° toward the amino-terminal domain so that the catalytic cleft located between two domains is closed. A nucleotide-induced transition from the open to the closed conformation is inherent in the nature of the β subunit, because even the isolated β subunit undergoes the open-close motion responding to nucleotide binding (10, 11). Thus, it has been proposed that the coordinated open-to-closed and closed-to-open motions of the β subunits in F_1-ATPase accompanied by ATP binding and ADP release drive 90° and 30° rotations of the γ subunit, respectively.

In contrast to the nucleotide-dependent open-close motion, the conformational events of the β subunit at the steps of hydrolysis of ATP and release of P_i are unclear. In the case of other ATP-driven motor proteins, myosin and kinesin, the structures of the ATP-bound form and the ADP-bound form are different (12, 13), and P_i release is assumed to be the step of power stroke (14, 15). The initial structure of MF_1, however, shows that the ADP-bound β subunit and the AMP-PNP-bound β subunit are in a very similar, closed conformation. Therefore, it appears that the loss of P_i from the catalytic site does not cause significant conformational changes or that the intermediate species of the enzyme generated upon P_i release is too unstable to form crystals even though its conformation is different from the known structures. Indeed, a third conformation of the β subunit was reported recently (16); one of the β subunits in the AlF_4^--inhibited MF_1 exists in a "half-closed" conformation, the catalytic site of which is occupied by ADP and sulfate in mimicry of P_i. Biochemical studies on the kinetics of P_i release and the related conformational changes are few,

* The costs of publication of this article were defrayed in part by the payment of page charges. This article must therefore be hereby marked "*advertisement*" in accordance with 18 U.S.C. Section 1734 solely to indicate this fact.

§Supported by Fellowships of the Japan Society for the Promotion of Science for Young Scientists.

¶¶ To whom correspondence should be addressed. Tel.: 81-45-924-5233; Fax: 81-45-924-5277; E-mail: myoshida@res.titech.ac.jp.

[1] The abbreviations used are: MF_1, bovine heart mitochondrial F_1; TF_1, thermophilic F_1-ATPase; AMP-PNP, adenosine 5′-(β,γ-imino) triphosphate; MDCC, [2-(1-maleimidyl)ethyl]-7-(diethylamino)-coumarin-3-carboxamide; PBP, phosphate-binding protein; ATPγS, adenosine 5′-*O*-(3-thiotriphosphate).

mainly because of the absence of methods to monitor P_i release from F_1-ATPase.

The present work has aimed at real time monitoring of conformational changes of the β subunit caused by P_i release. Some Trp residues introduced into the β subunits of *Escherichia coli* F_1-ATPase were reported to confer different fluorescence between AMP-PNP binding and ADP binding (17–19). Fluorescently labeled γ subunit was also reported to change its conformations upon ATP cleavage (20, 21). Nevertheless, none of them reported fluorescence changes of the β subunit caused by P_i release by time-resolved measurements. We have sought for new positions for the Trp mutation that can monitor changes of fluorescence upon P_i release. Concurrently for that purpose, we have adopted the P_i-binding protein that enabled real time monitoring of P_i release from the enzyme. Analyses, including kinetic comparison of fluorescence changes and P_i release after addition of ATP, have established that a Trp introduced at position 333 (R333W) reflects P_i release well. The residue 333 of the β subunit, located in helix H, which interacts with the "switch II loop," appears to sense γ-phosphate of the bound nucleotide and changes its conformation upon loss of P_i from the catalytic site.

EXPERIMENTAL PROCEDURES

Reagents and Buffers—Nucleotides were purchased from Sigma and Roche Molecular Biochemicals. Mop reagents 7-methylguanosine and purine nucleotide phosphorylase were purchased from Sigma. The fluorescent probe for phosphate-binding protein, [2-(1-maleimidyl)ethyl]-7-(diethylamino)-coumarin-3-carboxamide (MDCC) was purchased from Molecular Probes. The buffers used in the measurements are abbreviated as follows: TK buffer, 50 mM Tris-HCl, pH 8.0, 100 mM KCl; TKM2 buffer, 50 mM Tris-HCl, pH 8.0, 100 mM KCl, 2 mM $MgCl_2$; TKM4 buffer, 50 mM Tris-HCl, pH 8.0, 100 mM KCl, 4 mM $MgCl_2$; KP_i buffer, 100 mM KP_i, pH 7.0, 100 mM KCl, 2 mM EDTA; NaP_i buffer, 100 mM NaP_i, pH 7.0, 200 mM NaCl; and reverse phase buffer: 100 mM NaP_i, pH 6.9, 4 mM EDTA. Unless otherwise indicated, TKM2 buffer was used for measurements. To eliminate contaminated P_i from buffers, TKM and TK buffers for PBP assays contain 200 μM 7-methylguanosine and 0.01 unit/ml purine nucleotide phosphorylase (named P_i mop) (22, 23).

Strains, Plasmids, and Preparation of Subcomplexes—*E. coli* strain JM109 was used for plasmid amplification. JM103Δ(*unc*B-*unc*D) was used for overexpression of the α, β, and γ subunits of F_1-ATPase. Plasmids used were pucβ, which carried a gene for the β subunit, for mutagenesis and expression, and pkk$\alpha\gamma$, which carried genes for the α and γ subunits, for expression. The βR333W and βD311W mutations into the β subunit were introduced by the Kunkel method (24) using primer oligonucleotides annealed to the single strand DNA of pucβ: 5′-GATAAATCCCCATCTCCGCAAGCTTCCACTCCAGGTTCGTC-3′ for βR333W introducing cleavage site of *Hind*III and 5′-CGTCGTGG-CCGGAGCCGGATCCGTATAGTCCCAGGCCGGGACGTAAATC-3′ for βD311W introducing cleavage site of *Bam*HI (mutated bases are underlined). For preparation of the isolated β(R333W) and $\alpha_3\beta$(D311W)$_3\gamma$, mutated plasmids were transformed into JM103Δ(*unc*B-*unc*D) for overexpression and purified using NaP_i buffer as previously described (25). Because $\alpha_3\beta$(R333W)$_3\gamma$ and $\alpha_3\beta$(D311W/R333W)$_3\gamma$ could not be expressed using the pkk$\alpha\gamma\beta$ system, a novel lysate reassembly method was developed. The plasmids pkk$\alpha\gamma$, pucβ(R333W), and pucβ(D311W/R333W) were each expressed separately in JM103Δ(*unc*B-*unc*D). Pellets from centrifugation of the cultures were diluted in NaP_i buffer. The cells containing mutated β subunits were each mixed with those containing the α and γ subunits. The mixture was disrupted by a French pressure cell and was incubated at 30 °C for 30 min for reassembly of the subcomplex. It was then incubated at 60 °C for 15 min, and the insoluble denatured proteins were removed by centrifugation for 40 min at 40,000 rpm. Purification of the subcomplexes were performed by ammonium sulfate gradient in NaP_i buffer using a Butyl-Toyopearl 650M column (Tosoh). The purified β subunit and subcomplexes were stored as ammonium sulfate precipitates. They were diluted in TK buffer, concentrated by Vivaspin (Sartorius), and applied twice to a gel filtration (Superdex 200; Amersham Biosciences) for final purification (flow was 0.5 ml/min first with TK buffer and second with KP_i buffer) on the day of measurements.

Analyses of Bound Nucleotides—Analysis of residual nucleotides after purification of the enzyme was performed as previously described (26). The number of residual nucleotides bound to $\alpha_3\beta$(R333W)$_3\gamma$ was less than 0.1 mol/mol after gel filtration with KP_i buffer and TK buffer.

The number of nucleotides bound to $\alpha_3\beta$(R333W)$_3\gamma$ at the end points of the fluorescence measurements was estimated by the following protocol. The mixtures of nucleotides and $\alpha_3\beta$(R333W)$_3\gamma$ from stopped flow measurements were each applied to an Ultrafree filtration device (molecular weight, 5 k cutoff; Millipore). After centrifugation for 2 min at 2 kilorounds per minute at 25 °C, the nucleotide contents in 100 μl of the filtrates were quantified by reverse phase high pressure liquid chromatography (ODS-80Ts; Tosoh) using reverse phase buffer. The amount of nucleotides bound to $\alpha_3\beta$(R333W)$_3\gamma$ was estimated by subtracting the concentration of the nucleotides free in solution (concentration in the filtrate) from the initial concentration.

Measurements of Trp Fluorescence—The fluorescence measurements of the Trp mutant subcomplexes and the isolated β(R333W) subunit were carried out by excitation at 295 nm, and detection of emission at 345 nm was carried out using a spectrofluorometer (FP-6500; Jasco). In a cuvette, 1.2 ml of 5 μM β(R333W) or 1 μM $\alpha_3\beta_3\gamma$ mutants was mixed with 20 μl of ATP or ADP while stirring.

Measurements of $\alpha_3\beta$(R333W)$_3\gamma$ were carried out also by a stopped flow apparatus (SFM-400, BioLogic) using a xenon lamp as a source of light. ATP in TK buffer (30 μl of 1.0 or 0.5 or 0.25 μM)[2] was mixed with the same volume of 2 μM $\alpha_3\beta$(R333W)$_3\gamma$ in TKM4 buffer over 20 ms. The same method was applied to ADP, AMP-PNP, and ADPγS. TK buffer prevents ATP at submicromolar concentrations from decomposition into ADP and P_i before addition to $\alpha_3\beta$(R333W)$_3\gamma$. The same stopped flow experiments were also performed using buffers that were treated with P_i mop to ensure that the buffer conditions were the same as those used for measurement of P_i release. There was no change in the Trp fluorescence profile between with and without P_i mop in solutions (data not shown).

Measurement of Unisite Catalysis—The unisite catalysis was measured using the stopped flow apparatus in the quenched flow mode. It was started by mixing 250 μl of 2 μM $\alpha_3\beta$(R333W)$_3\gamma$ with the same volume of 1 μM ATP and stopped after various time periods by perchloric acid quenching. Hydrolyzed nucleotides were analyzed by a reverse phase column (ODS-80Ts; Tosoh) using the reverse phase buffer as previously described (26).

Measurement of P_i Release—Release of P_i from $\alpha_3\beta$(R333W)$_3\gamma$ was measured using a PBP assay (22, 23). PBP labeled with MDCC was prepared as previously described (22, 23). Binding of P_i to MDCC-labeled PBP (MDCC-PBP) increases the fluorescence emission at 464 nm when the complex is excited at 425 nm. By virtue of rapid binding of P_i to MDCC-PBP (k_{on} = 1.36 × 10^8 M^{-1} s^{-1}) and high affinity of PBP for P_i (K_d = ~0.1 μM) (22), the increase in the P_i concentration in the solutions could be monitored as the increase of fluorescence emission in real time.

PBP assays were carried out using a stopped flow apparatus (SFM-400; BioLogic) under the same conditions as the Trp fluorescence measurements. 30 μl of 2 μM $\alpha_3\beta$(R333W)$_3\gamma$ in TKM4 buffer was mixed with the same volume of 4 μM MDCC-PBP and 1 μM ATP in TK buffer. The buffers contain P_i mop for elimination of P_i to avoid saturation of MDCC-PBP with contaminated P_i.

Measurement of the Rate of Formation of the MgADP-inhibited Form—To estimate the rate of formation of the MgADP-inhibited form under the fluorescence measurement conditions, the following experiment was carried out. 20 μl of 11 μM $\alpha_3\beta$(R333W)$_3\gamma$ and 200 μl of 0.55 μM ATP were manually mixed and preincubated at 25 °C for varying periods of time. 150 μl of the incubated solution was injected into the ATP-regenerating system (27) containing 2 mM ATP-Mg (mixture of equal concentrations of ATP and $MgCl_2$) in TKM2 buffer. The time course of ATP hydrolysis was measured by monitoring the absorbance at 340 nm using a spectrophotometer (V-550; Jasco). The slope of the absorbance is initially small as the majority of the molecules are in the MgADP-inhibited form, but it gradually increases because of reactivation by binding of ATP to the α subunit (28). Therefore, the ratio of active $\alpha_3\beta$(R333W)$_3\gamma$ was estimated from the initial slope of 10 s of absorbance at 340 nm compared with that without preincubation.

Other Assays—The concentrations of β(R333W), $\alpha_3\beta$(R333W)$_3\gamma$, $\alpha_3\beta$(D311W/R333W)$_3\gamma$, and $\alpha_3\beta$(D311W)$_3\gamma$ were analyzed by BCA assay (Pierce) and absorbance at 280 nm.

[2] All the stopped flow measurements and bound nucleotide measurements were repeated with 75 μl of mixing shots to be sure that the effects of carry-over from the previous shots were minimum. The rate constants and the amount of bound nucleotides (except for AMP-PNP, 0.41 mol/mol in Table I) were essentially the same (± 5%) as those obtained with 30 μl/shot.

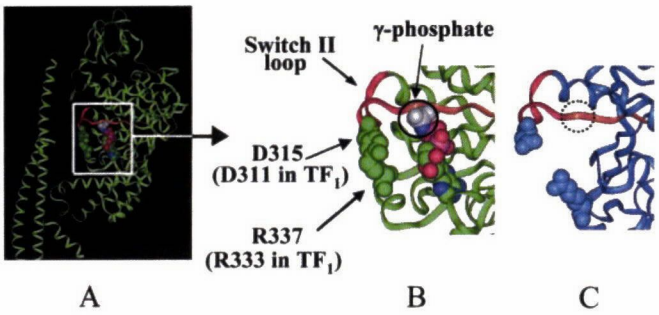

FIG. 1. **Positions of the residues Asp-315 and Arg-337 in bovine mitochondrial F_1 β subunit.** AMP-PNP and residues Asp-315 and Arg-337 are shown as space-filling models. The switch II loop is in *red*, and γ-phosphate of the bound nucleotide is in *white*. *A*, β subunit in the AMP-PNP bound form and the γ subunit. *B* and *C*, close-ups of the regions of Asp-315 and Arg-337 in AMP-PNP-bound β subunit (*B*) and nucleotide-free β subunit (*C*).

Data Processing—Data processing was performed by BioKine software (BioLogic), Origin 6.0 (Microcal Software), Excel 97 (Microsoft), and Dynafit (BioKin) (29).

RESULTS

Transient Increase in Trp Fluorescence upon ATP Binding—The initial crystal structure of MF_1 suggests that Arg-333 in TF_1-β (Arg-337 in MF_1-β) in helix H interacts with Asp-311 in TF_1-β (Asp-315 in MF_1-β) of the switch II loop only when the β subunit is in the closed conformation (Fig. 1) (1). Ren *et al.* (30) showed that cysteines introduced at positions 311 and 333 of TF_1-β can readily form an intramolecular cross-link in two of the three β subunits in the $\alpha_3\beta_3\gamma$ subcomplex of TF_1. Cross-linking abolished ATPase activity almost completely by fixing two β subunits in the closed conformation. We introduced Trps into the same positions and examined the fluorescence response of the mutant, expecting to have enabled fluorescent detection of nucleotide-induced open-close motion of the β subunits. Trp fluorescence of 1 μM $\alpha_3\beta$(D311W/R333W)$_3\gamma$ subcomplex decreased when 0.5 μM ADP was added (Fig. 2*A*). The fluorescent response to the same concentration of ATP was very different from that observed for ADP; a transient fluorescence increase was followed by rapid decay. The final level of fluorescence after decay was similar to that attained by ADP. Then, to determine which (or both) Trp was responsible for this transient fluorescence change, we made two single mutants, $\alpha_3\beta$(D311W)$_3\gamma$ and $\alpha_3\beta$(R333W)$_3\gamma$. The fluorescence response of $\alpha_3\beta$(D311W)$_3\gamma$ to ADP was similar to that of ATP, that is, a similar extent of increase and no further rapid changes (Fig. 2*B*). On the other hand, fluorescence of $\alpha_3\beta$(R333W)$_3\gamma$ showed a two-phase response to ATP addition: transient increase and rapid decay (Fig. 2*C*). The addition of ADP caused only a slight increase in fluorescence. The final level of fluorescence change by ATP was almost the same as that attained by ADP. It appeared that these two phases might represent certain steps in the catalysis occurring at a single catalytic site. Therefore, further fluorescence measurements were focused on $\alpha_3\beta$(R333W)$_3\gamma$, using a stopped flow apparatus, which could provide higher time resolution than manual mixing. It should be added that the three mutants mentioned above retained ATPase activity of rotary catalysis at a saturating ATP concentration (2 mM): 140 turnovers/s ($\alpha_3\beta$(D311W/R333W)$_3\gamma$), 29 turnovers/s ($\alpha_3\beta$(D311W)$_3\gamma$), and 106 turnovers/s ($\alpha_3\beta$(R333W)$_3\gamma$), which are 61, 13, and 46%, respectively, of that of the $\alpha_3\beta_3\gamma$ subcomplex without these mutations. Hereafter, we focus on the characteristics of $\alpha_3\beta$(R333W)$_3\gamma$.

Isolated β(R333W) Responds to ATP and ADP Differently—To understand whether the different fluorescence response

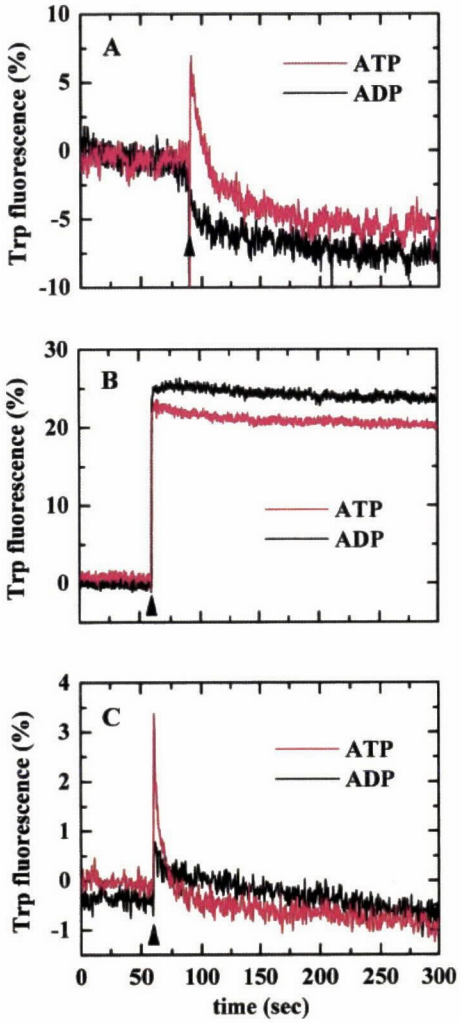

FIG. 2. **Time courses of fluorescence changes of the Trp mutants.** At the times indicated by *arrowheads*, ATP or ADP was manually mixed with $\alpha_3\beta$(D311W/R333W)$_3\gamma$ (*A*), $\alpha_3\beta$(D311W)$_3\gamma$ (*B*), and $\alpha_3\beta$(R333W)$_3\gamma$ (*C*). The concentrations of subcomplexes and nucleotides in the mixtures were 1 and 0.5 μM, respectively. The details of the experiments are described under "Experimental Procedures."

of $\alpha_3\beta$(R333W)$_3\gamma$ to ATP or ADP is generated from intersubunit interaction in the subcomplex or from conformational changes within a β subunit, fluorescence response of the isolated β(R333W) subunit to ATP or ADP was examined. Because the isolated β subunit can bind nucleotide but does not retain catalytic ability (31), the nucleotide-induced change of Trp fluorescence of β(R333W) can be solely attributed to the nucleotide binding. The addition of ATP or ADP to the isolated β(R333W) caused an instantaneous increase in Trp fluorescence that was followed by a slow increase (~30 s), and the fluorescence remained constant after saturation (Fig. 3*A*). The reason for the slow increase is not known, but it is worth noting that the extent of the fluorescence increase by ATP is significantly larger than by ADP, just as observed for initial fluorescence increase of $\alpha_3\beta$(R333W)$_3\gamma$. The K_d values for ATP and ADP estimated from fluorescence changes at various concentrations of nucleotide (Fig. 3*B*) are similar to each other: 20 μM for ATP and 27 μM for ADP, consistent with the values reported previously (32). These results suggest that conformational changes within a β subunit induced by AT(D)P binding can explain the initial increase of fluorescence observed for the $\alpha_3\beta$(R333W)$_3\gamma$ subcomplex. The different magnitude of fluorescence increase in response to ATP and ADP indicates that the

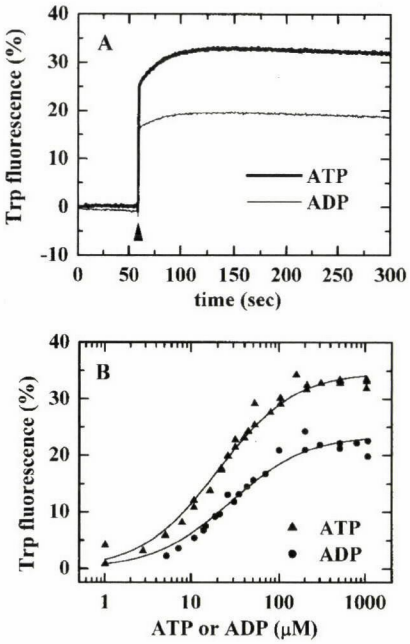

FIG. 3. **Trp fluorescence changes of the isolated β(R333W) subunit induced by binding of ATP and ADP.** *A*, time course of Trp fluorescence changes induced by manual mixing with ATP or ADP at the time indicated by an *arrowhead*. Final concentrations of the β(R333W) subunit and nucleotides were 5 μM and 1 mM, respectively. *B*, the extent of Trp fluorescence changes of the isolated β(R333W) subunit (final concentration, 5 μM) induced by manual mixing with various concentrations of ATP or ADP. The *lines* indicate fits for calculations of the dissociation constant (K_d) by the following equation: $y = C \cdot [1 + x + K_d - sqrt\ \{(1 + x + K_d)^2 - 4x\}]/2$. The details of the experiments are described under "Experimental Procedures."

Trp residue introduced at position 333 of the β subunit is able to sense the presence of γ-phosphate of the bound adenine nucleotides, and this ability is inherent in the β(R333W) subunit.

Initial Fluorescence Increase Reflects ATP Binding—For $\alpha_3\beta(R333W)_3\gamma$, the initial increase in fluorescence by the addition of ATP was our initial focus (Fig. 4). The addition of a nonhydrolyzable ATP analog, AMP-PNP, to $\alpha_3\beta(R333W)_3\gamma$ induced an increase in fluorescence that was similar to that observed for ATP, but no subsequent decay was observed (Fig. 4*A*). Similarly, the decay was not observed for binding of ATP in the absence of Mg, where hydrolysis was blocked (data not shown). Another ATP analog, ATPγS, which is a poor substrate for F_1, also induced a similar fluorescence increase (Fig. 4*A*) that was followed by a slower decay. Taken together, we concluded that the initial fluorescence increase reflected the occupation of a catalytic site of the β subunit by ATP (*step 1* of Scheme 1). The rates of nucleotide binding calculated from the fluorescence changes of $\alpha_3\beta(R333W)_3\gamma$ were $(1.7 \pm 0.3) \times 10^7$ M^{-1} s^{-1} for ATP, $(4.1 \pm 0.7) \times 10^7$ M^{-1} s^{-1} for ADP, $(1.3 \pm 0.0) \times 10^6$ M^{-1} s^{-1} for AMP-PNP, and $(2.8 \pm 0.2) \times 10^7$ M^{-1} s^{-1} for ATPγS.

Nucleotide Binding Is Not the Cause of Fluorescence Decay—Decay of the fluorescence of $\alpha_3\beta(R333W)_3\gamma$ after the initial increase was observed under the conditions where unisite catalysis (33–35) was occurring and hence may correspond to a certain step of catalysis after the capture of ATP by a catalytic site. 0.5, 0.25, and 0.125 μM ATP caused the decay at comparable rates,[3] which indicates that the binding step is not involved in the decay (time courses are not shown). From the time courses of Trp fluorescence upon the addition of various nucleotides (Fig. 4*A*), it is assumed that ATP hydrolysis or an event that occurs immediately after that causes fluorescence decay.

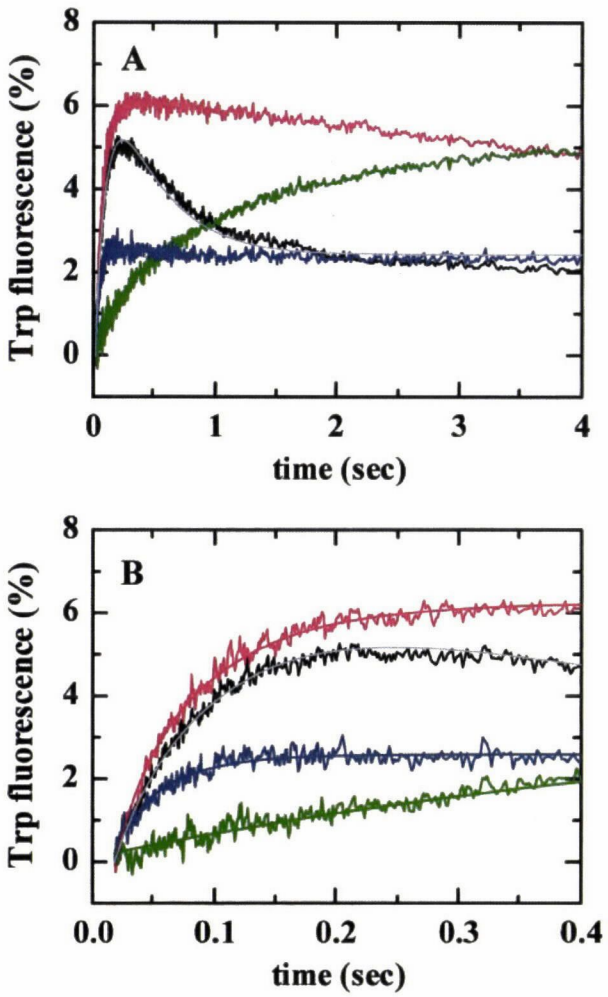

FIG. 4. **Time courses of Trp fluorescence changes of $\alpha_3\beta(R333W)_3\gamma$ induced by mixing with various nucleotides using a stopped flow apparatus.** Final concentrations of $\alpha_3\beta(R333W)_3\gamma$ and nucleotides were 1 and 0.5 μM, respectively. ATP is in *black*, ADP is in *blue*, AMP-PNP is in *green*, and ATPγS is in *red*. The base line is subtracted from each trace. The changes from the start of the measurements (18.6 ms) are plotted. *A*, changes in 4 s. A *line* overlaid with the *trace* of ATP is a simulation curve according to the following scheme: $F_1 + ATP \rightarrow F_1{\cdot}ATP \rightarrow F_1{\cdot}ADP{\cdot}P_i \rightarrow F_1{\cdot}ADP + P_i$. The rate constants used for the simulation are $k_{on} = 1.4\times10^7$, $k_{cat} = 14.2$, and $k_{off} = 2.73$, assuming that the increase in Trp fluorescence occurs by binding of ATP and that the decay occurs by release of P_i from F_1. These rate constants are within the standard error of those derived from measurements of ATP hydrolysis and P_i release in the following sections (see also Figs. 5 and 6 and Table I). *B*, changes in 0.4 s. The *lines* indicate fitting curves for calculating the binding rates (k_{on}) by the following scheme: F_1 + nucleotide → F_1·nucleotide. In the case of ATP, the same fitting curve as *A* is shown. The details of the experiments are described under "Experimental Procedures."

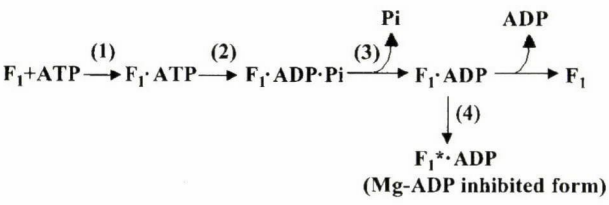

SCHEME 1. **Reaction scheme of uni-site ATP hydrolysis by F_1 ATPase.**

[3] The rates of decay estimated by the simple fitting scheme $F_1 + ATP \rightarrow F_1{\cdot}ATP \rightarrow F_1{\cdot}ADP + P_i$ attributing fluorescence increase to binding of ATP and decay to hydrolysis were $k_{decay} = 1.9 \pm 0.3$, 1.8, and 2.0 s^{-1} for 0.5, 0.25, and 0.125 μM ATP, respectively.

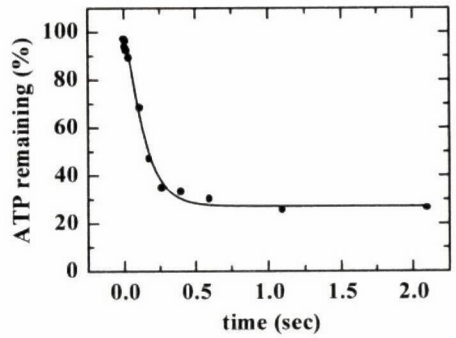

FIG. 5. **Time course of ATP hydrolysis by $\alpha_3\beta$(R333W)$_3\gamma$ under unisite conditions.** The reactions were performed by the quenched flow mode of stopped flow apparatus. Concentrations of $\alpha_3\beta$(R333W)$_3\gamma$ and nucleotides in the mixture were 1 and 0.5 μM, respectively. The reactions were stopped by the addition of perchloric acid, and the amounts of ATP and ADP were measured. The *line* is a fitting curve according to the following scheme: F_1 + ATP → F_1·ATP → F_1·ADP·P_i using k_{on} = 1.7 × 10^7. The details of the experiments are described under "Experimental Procedures."

Typically, a slowly hydrolyzed ATP analog, ATPγS, causes slow decay.

ATP Hydrolysis Precedes Fluorescence Decay—To test the assumption described above, the time course of generation of ADP (*step 2* of Scheme 1) was measured. $\alpha_3\beta$(R333W)$_3\gamma$ and ATP were mixed using a stopped flow apparatus under the same conditions as the fluorescence measurements, and the reactions were stopped after various periods of time by the addition of perchloric acid. Acid quenching liberates substrates from denatured enzymes. Therefore, irrespective of whether the substrate is released or still bound to the enzyme, the generation of ADP can be detected by this method. The generation of ADP occurred with the rate constant of 14.4 s^{-1} (Fig. 5), which is greater than the rate of fluorescence decay (2.7 s^{-1}; Fig. 4). Therefore, the cause of fluorescence decay can be assigned to a step after ATP hydrolysis such as P_i release and/or ADP release, etc. To determine which is the case, the release of ADP and P_i was examined.

ADP Remains Bound after Hydrolysis—Analysis of the enzyme-bound nucleotides was carried out by sampling the mixtures of 1 μM $\alpha_3\beta$(R333W)$_3\gamma$ and 0.5 μM nucleotides from stopped flow fluorescence measurements and applying them each to an Ultrafree filtration device. The amount of nucleotides in the filtrates was analyzed. Virtually all (92%) of the product ADP remained bound to the enzyme even after all of the ATP had been hydrolyzed (Table I). Therefore, it is not feasible to assign the fluorescence decay to ADP release as the cause of the fluorescence decrease. We also measured the amount of enzyme-bound nucleotide when ADP, AMP-PNP, and ATPγS were added. Again, nearly all of the added nucleotides were stably bound to the enzyme (Table I). Taking this into account, the highest Trp fluorescence level by ATP, ATPγS, and AMP-PNP (Fig. 4*A*) can be assigned to the γ-phosphate (γ-thiophosphate)-bound form.

P_i Release Proceeds at the Same Rate as Fluorescence Decay—To monitor the time course of P_i release from the enzyme (*step 3* of Scheme 1), a PBP assay was adopted. Fluorescence of a coumarin-labeled PBP (MDCC-PBP) increases severalfold when P_i binds. The versatility of monitoring of P_i release from $\alpha_3\beta$(R333W)$_3\gamma$ by the PBP assay was carefully assessed and established (see "Experimental Procedures"). Thus, real time, continuous monitoring of P_i released from F_1-ATPase became possible for the first time. We found that P_i was released from $\alpha_3\beta$(R333W)$_3\gamma$ with a rate constant of 2.8 ± 0.1 s^{-1} (Fig. 6), which is the same rate as that of the fluorescence decay (Fig. 4). Thus, it is suggested that the decay of fluorescence after the initial increase reflects the decay of the enzyme form with bound ADP-P_i to the enzyme form with bound ADP only, that is, release of P_i from the enzyme. However, if there is a rapid conversion from the active enzyme-ADP complex into inactive enzyme-ADP complex, this conversion is also a candidate for the fluorescence decay. This possibility should be considered because it is known that the so-called MgADP-inhibited form, an inactive form of enzyme-ADP complex, tends to be generated under these conditions. We examined this possibility next.

TABLE I

Concentrations of nucleotides remained bound to 1 μM of $\alpha_3\beta$(R333W)$_3\gamma$ after incubation with 0.5 μM of nucleotides

The samples were the same as those used for fluorescence observation using a stopped flow apparatus. ATP and ATPγS were detected as ADP because of hydrolysis by $\alpha_3\beta$(R333W)$_3\gamma$. The details of the experiments are described under "Experimental Procedures."

Nucleotide	Bound concentration
	μM
ATP	0.46
ADP	0.45
AMP-PNP	0.46
ATPγS	0.45

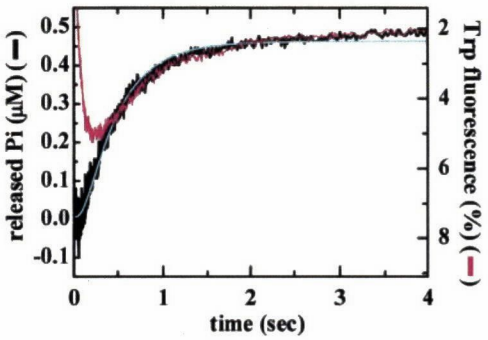

FIG. 6. **Time course of P_i release from $\alpha_3\beta$(R333W)$_3\gamma$ monitored by fluorescence increase of MDCC-PBP.** ATP was mixed with $\alpha_3\beta$(R333W)$_3\gamma$ using a stopped flow apparatus. The final concentrations of $\alpha_3\beta$(R333W)$_3\gamma$ and nucleotides were 1 and 0.5 μM, respectively. The saturated level of MDCC-PBP fluorescence is set 0.5 μM. For comparison, the profile of Trp fluorescence changes under the same conditions is superimposed (*red*). A *blue line* indicates the fit of the MDCC-PBP fluorescence by the following scheme: F_1 + ATP → F_1·ATP → F_1·ADP·P_i → F_1·ADP + P_i using k_{on} = 1.7 × 10^7 and k_{cat} = 14.4. The details of the experiments are described under "Experimental Procedures."

Transition to the MgADP-inhibited Form Is Slower than Fluorescence Decay—The MgADP-inhibited form (*step 4* of Scheme 1) is not caused by a mere product inhibition but by stable retention of MgADP at the catalytic site. The MgADP can either be picked up from the bulk phase medium or can be a remnant of hydrolysis that remains bound to the enzyme (27). When the MgADP-inhibited form of F_1-ATPase is exposed to ATP and Mg^{2+}, it shows no ATPase activity initially but is gradually reactivated with a time constant of ~30 s (27, 43). Therefore, the population of the MgADP-inhibited form in a certain preparation of F_1-ATPase can be assessed from the initial rate of ATP hydrolysis. Under the same conditions used for the fluorescence measurement, we took an aliquot from the solution at the indicated times, injected it into the ATPase assay mixture and measured the initial ATPase activity. The initial ATPase activities were plotted as a function of the time and the rate of generation of the MgADP-inhibited form in the solution was estimated (Fig. 7). The time constant of the onset of MgADP inhibition thus estimated was 15 s, which is much slower than the fluorescence decay. Therefore, the possibility that the fluorescence decay is caused by generation of the MgADP-inhibited state is unlikely. In other words, the lifetime of active MgADP bound form is long enough to be maintained during fluorescence changes of several seconds. Taking these

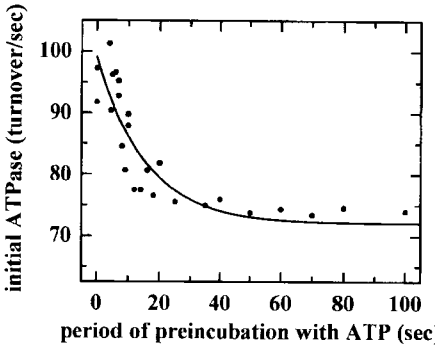

FIG. 7. **Formation of the MgADP-inhibited form under the unisite conditions.** $\alpha_3\beta$(R333W)$_3\gamma$ (1 μM) was preincubated with 0.5 μM ATP. An aliquot of the mixture was taken out after the indicated preincubation period and injected into the ATPase assay mixture, and an initial velocity of ATP hydrolysis was measured that reflected the proportion of the active form and the MgADP-inhibited form of the subcomplex generated during preincubation with ATP. The details of the experiments are described under "Experimental Procedures."

results together, we can conclude that under unisite conditions, the increase in Trp fluorescence of the $\alpha_3\beta$(R333W)$_3\gamma$ subcomplex occurs upon ATP binding, and the decay occurs as a function of P_i release (Table II).

DISCUSSION

The novel Trp mutant $\alpha_3\beta$(R333W)$_3\gamma$ revealed that the residue Arg-333 senses the presence of γ-phosphate at the catalytic site of β subunit as well as changes in the surrounding structure upon nucleotide binding and P_i release. Although Arg-333 does not directly contact the γ-phosphate of the bound nucleotide in the crystal structure, this residue somehow recognizes conformational differences between ATP-bound (or ADP-P_i-bound) and ADP-bound conformations of the β subunit.

It is worth noting that when a nucleotide is bound to the catalytic site, the mutated residue Arg-333 interacts with the switch II loop, a switch region common to a wide range of nucleotide triphosphate-utilizing proteins including GTP-binding proteins and motor proteins (12, 13, 36–40). A function of switch II in myosin and kinesin is to transmit conformational changes caused by γ-phosphate release to a distant point where motility of motor proteins is exerted (41). For example, in the case of myosin, an alanine mutation introduced into Gly-457 in the switch II loop causes loss of motility (42). In the crystal structure of monomeric kinesin motor KIF1A, the switch II loops of the ADP-bound and ATP-bound forms were in different conformations (12). Moreover, studies using fluorescence energy transfer and other analyses of conventional kinesin indicated a difference between ATP-bound and ADP-bound forms in the flexibility of the neck linker (15). Therefore, it is natural to assume that F_1-ATPase, another motor protein, might undergo an analogous conformational change when P_i is released.

However, real images of the conformational change of F_1-ATPase that we detected by the fluorescence change cannot be directly assumed by comparing crystal structures of various nucleotide binding states that are solved to date. The crystal structure of F_1-ATPase containing β subunits in the ATP-bound, ADP-bound, and empty forms in one molecule (1) suggested that P_i release does not cause drastic conformational changes because the structure of AMPPNP-bound and ADP-bound β subunits are very similar to each other, both in the same closed conformation. There is a possibility that introduced Trp reflects a very subtle change in the conformation accompanying P_i release. A new crystal structure (16) was discovered recently that contains a third half-closed conformation of the β subunit, which is in between the closed and open

TABLE II
Rate constants of the reaction steps and corresponding Trp fluorescence changes

Reaction step	Step in Scheme 1	Rate constant	Trp fluorescence
ATP binding	1	$(1.7 \pm 0.3) \times 10^7 M^{-1}s^{-1}$	Increase
ATP hydrolysis	2	$14.4 \pm 0.2\ s^{-1}$	Negligible change
P_i release	3	$2.8 \pm 0.1\ s^{-1}$	Decay
ADP inhibition	4	$6.7 \times 10^{-2}\ s^{-1}$	

forms. This new conformation is thought to be in a transition state where the products ADP and P_i are both bound. The existence of this half-closed conformation indicated partial opening of the β subunit during ATP hydrolysis. As a next step, further opening of ADP-bound form induced by P_i release can naturally be assumed. Therefore, another possibility is that the fluorescence change reflects the difference of these two partially open states: one with bound ADP-P_i and the other with bound ADP. This problem has direct implications on the conformational transitions accompanying the catalytic cycle but awaits further studies to be clarified.

The present research also revealed new information about the ATPase reaction by direct, real time measurements of some of the kinetic parameters of the unisite catalysis (Table II). The parameters shown here give insights into the reaction mechanism. The first is the rate of nucleotide binding. Comparing the results of stopped flow measurements (unisite catalysis conditions) with the previous single molecule observation of rotating F_1-ATPase at low ATP concentrations (bi-site or tri-site catalysis conditions), the rates of ATP binding are in the same range ($(1.7 \pm 0.3) \times 10^7\ M^{-1}\ s^{-1}$ and $2.7 \times 10^7\ M^{-1}\ s^{-1}$, respectively). This indicates that the rates of ATP binding are almost the same for the first and second (or third) catalytic sites. The second is that P_i release predominantly occurs while ADP remains bound to the enzyme in unisite catalysis. The third is that the rate of P_i release is slower than that of ATP hydrolysis, suggesting that the F_1·ADP·P_i complex has to wait for some conformational change that allows P_i release.

Future studies should be directed at the observation of conformational changes of the β subunit in F_1-ATPase at each step (including P_i release) of during rotational catalysis. For this purpose, a new probe that is tractable by single molecule observation is necessary.

Acknowledgments—Dr. Martin R. Webb is gratefully acknowledged for advice on preparation and measurements of phosphate-binding protein. We thank K. Kawashima, Dr. Motojima, Dr. Kato-Yamada, Dr. Watanabe, Dr. Georges, Dr. T. Suzuki, Dr. Motohashi, Dr. Tabata, Dr. Hisabori, Dr. Taguchi, and J. Suzuki for valuable discussion and technical advice and Dr. Hardy for critically reading the manuscript.

REFERENCES

1 Abrahams, J. P., Leslie, A. G. W., Lutter, R., and Walker, J. E. (1994) *Nature* **370,** 621–628
2. Boyer, P. D. (1993) *Biochim. Biophys. Acta* **1140,** 215–250
3. Boyer, P. D., and Kohlbrenner, W. E. (1981) in *Energy Coupling in Photosynthesis*, pp. 407–426, Elsevier Science Publishing Co., Inc., New York
4 Duncan, T. M., Bulygin, V. V., Zhou, Y., Hutcheon, M. L., and Cross, R. L. (1995) *Proc. Natl. Acad. Sci. U. S. A.* **92,** 10964–10968
5. Noji, H., Yasuda, R., Yoshida, M., and Kinosita, K., Jr. (1997) *Nature* **386,** 299–302
6. Yasuda, R., Noji, H., Kinosita, K., Jr., and Yoshida, M. (1998) *Cell* **93,** 1117–1124
7 Yasuda, R., Noji, H., Yoshida, M., Kinosita, K. Jr., and Ito, H. (2001) *Nature* **410,** 898–904
8 Tsunoda, S. P., Muneyuki, E., Amano, T., Yoshida, M., and Noji, H. (1999) *J. Biol. Chem.* **274,** 5701–5706
9 Shirakihara, Y., Leslie, A. G. W., Abrahams, J. P., Walker, J. E., Ueda, T., Sekimoto, Y., Kambara, M., Saika, K., Kagawa, Y., and Yoshida, M. (1997) *Structure* **5,** 825–836
10 Tozawa, K., Sekino, N., Soga, M., Yagi, H., Yoshida, M., and Akutsu, H. (1995) *FEBS Lett.* **376,** 190–194
11 Yagi, H., Tozawa, K., Sekino, N., Iwabuchi, T., Yoshida, M., and Akutsu, H. (1999) *Biophys. J.* **77,** 2175–2183
12 Kikkawa, M., Sablin, E. P., Okada, Y., Yajima, H., Fletterick, R. J., and

Hirokawa, N. (2001) *Nature* **411,** 439–445
13. Houdusse, A., Kalabokis, V. N., Himmel, D., Szent-Gyorgyi, A. G., and Cohen, C. (1999) *Cell* **97,** 459–470
14. Suzuki, Y., Yasunaga, T., Ohkura, R., Wakabayashi, T., and Sutoh, K. (1998) *Nature* **396,** 380–383
15. Rice, S., Lin, A. W., Safer, D., Hart, C. L., Naber, N., Carragher, B. O., Cain, S. M., Pechatnikova, E., Wilson-Kubalek, E. M., Whittaker, M., Pate, E., Cooke, R., Taylor, E. W., Milligan, R. A., and Vale, R. D. (1999) *Nature* **402,** 778–783
16. Menz, R. I., Walker, J. E., and Leslie, A. G. W. (2001) *Cell* **106,** 331–341
17. Weber, J., Wilke-Mounts, S., Lee, R. S.-F., Grell, E., and Senior, A. E. (1993) *J. Biol. Chem.* **268,** 20126–20133
18. Weber, J., Bowman, C., and Senior, A. E. (1996) *J. Biol. Chem.* **271,** 18711–18718
19. Weber, J., Wilke-Mounts, S., Hammond, S. T., and Senior, A. E. (1998) *Biochemistry* **37,** 12042–12050
20. Turina, P., and Capaldi, R. A. (1994) *J. Biol. Chem.* **269,** 13465–13471
21. Turina, P., and Capaldi, R. A. (1994) *Biochemistry* **33,** 14275–14280
22. Brune, M., Hunter, J. L., Corrie, J. E. T., and Webb, M. R. (1994) *Biochemistry* **33,** 8262–8271
23. Brune, M., Hunter, J. L., Howell, S. A., Martin, S. R., Hazlett, T. L., Corrie, J. E. T., and Webb, M. R. (1998) *Biochemistry* **37,** 10370–10380
24. Kunkel, T. A., Bebenek, K., and McClary, J. (1991) *J. Methods Enzymol.* **204,** 125–139
25. Matsui, T., and Yoshida, M. (1995) *Biochim. Biophys. Acta* **1231,** 139–146
26. Hisabori, T., Muneyuki, E., Odaka, M., Yokoyama, K., Mochizuki, K., and Yoshida, M. (1992) *J. Biol. Chem.* **267,** 4551–4556
27. Matsui, T., Muneyuki, E., Honda, M., Allison, W. S., Dou, C., and Yoshida, M. (1997) *J. Biol. Chem.* **272,** 8215–8221
28. Jault, J. M., Matsui, T., Jault, F. M., Kaibara, C., Muneyuki, E., Yoshida, M., Kagawa, Y., and Allison, W. S. (1995) *Biochemistry* **34,** 16412–16418
29. Kuzmic, P. (1996) *Anal. Biochem.* **237,** 260–273
30. Ren, H., Dou, C., Stelzer, M., and Allison, S. W. (1999) *J. Biol. Chem.* **274,** 31366–31372
31. Yoshida, M., Sone, N., Hirata, H., and Kagawa, Y. (1977) *J. Biol. Chem.* **252,** 3480–3485
32. Odaka, M., Kaibara, C., Amano, T., Matsui, T., Muneyuki, E., Ogasahara, K., Yutani, K., and Yoshida, M. (1994) *J. Biochem. (Tokyo)* **115,** 789–796
33. Grubmeyer, C., Cross, R. L., and Penefsky, H. S. (1982) *J. Biol. Chem.* **257,** 12092–12100
34. Milgrom, Y. M., and Cross, R. L. (1997) *J. Biol. Chem.* **272,** 32211–32214
35. Milgrom, Y. M., Murataliev, M. B., and Boyer, P. D. (1998) *Biochem. J.* **330,** 1037–1043
36. Lambright, D. G., Sondek, J., Bohm, A., Skiba, N. P., Hamm, H. E., and Sigler, P. B. (1996) *Nature* **379,** 311–319
37. Rayment, I., Rypniewski, W. R., Schmidt-Base, K., Smith, R., Tomchick, D. R., Benning, M. M., Winkelmann, D. A., Wesenberg, G., and Holden, H. M. (1993) *Nature* **261,** 50–58
38. Fisher, A. J., Smith, C. A., Thoden, J. B., Smith, R., Sutoh, K., Holden, H. M., and Rayment, I. (1995) *Biochemistry,* **34,** 8960–8972
39. Smith, C. A., and Rayment, I. (1996) *Biochemistry* **35,** 5404–5417
40. Dominguez, R., Freyzon, Y., Trybus, K. M., and Cohen, C. (1998) *Cell,* **94,** 559–571
41. Vale, R. D., Milligan, R. A. (2000) *Science* **288,** 88–95
42. Sasaki, N., Shimada, T., and Sutoh, K. (1998) *J. Biol. Chem.* **273,** 20334–20340
43. Hirono-Hara, Y., Noji, H., Nishiura, M., Muneyuki, E., Hara, K. Y., Yasuda, R., Kinosita, K., Jr., and Yoshida, M. (2001) *Proc. Natl. Acad. Sci. U. S. A.* **98,** 13649–13654

The ATP-waiting conformation of rotating F_1-ATPase revealed by single-pair fluorescence resonance energy transfer

Ryohei Yasuda*†, Tomoko Masaike‡§, Kengo Adachi¶, Hiroyuki Noji‖, Hiroyasu Itoh, and Kazuhiko Kinosita, Jr.¶**

*Cold Spring Harbor Laboratory, Cold Spring Harbor, NY 11724; ‡ATP System Project, Exploratory Research for Advanced Technology, Japan Science and Technology Corporation, 5800-3 Nagatsuta, Yokohama 226-0026, Japan, §Chemical Resources Laboratory, Tokyo Institute of Technology, 4259 Nagatsuta, Yokohama 226-8503, Japan; ¶Center for Integrative Bioscience, Okazaki National Research Institutes, Higashiyama 5-1, Myodaiji, Okazaki 444-8585, Japan; ‖Precursory Research for Embryonic Science and Technology, Japan Science and Technology Corporation, Institute of Industrial Science, University of Tokyo, 4-6-1 Komaba, Tokyo 153-8505, Japan, and **Hamamatsu Photonics KK, Tokodai, Tsukuba 300-2635, Japan

Edited by Paul D. Boyer, University of California, Los Angeles, CA, and approved June 16, 2003 (received for review December 23, 2002)

F_1-ATPase is an ATP-driven rotary motor in which a rod-shaped γ subunit rotates inside a cylinder made of $\alpha_3\beta_3$ subunits. To elucidate the conformations of rotating F_1, we measured fluorescence resonance energy transfer (FRET) between a donor on one of the three βs and an acceptor on γ in single F_1 molecules. The yield of FRET changed stepwise at low ATP concentrations, reflecting the stepwise rotation of γ. In the ATP-waiting state, the FRET yields indicated a γ position $\approx$40° counterclockwise (= direction of rotation) from that in the crystal structures of mitochondrial F_1, suggesting that the crystal structures mimic a metastable state before product release.

The F_1-ATPase is a part of F_oF_1-ATP synthase that synthesizes ATP in F_1, the water-soluble portion of the ATP synthase, from ADP and inorganic phosphate (P_i) when protons pass through F_o, the membrane-embedded portion. Isolated F_1, consisting of $\alpha_3\beta_3\gamma\delta\varepsilon$ subunits, hydrolyzes ATP as the reverse reaction. The minimum ATPase unit, $\alpha_3\beta_3\gamma$ (hereafter referred to as F_1), is pseudo 3-fold symmetric: a rod-shaped, asymmetric γ subunit is surrounded by an $\alpha_3\beta_3$ cylinder (1). Rotation of γ inside the $\alpha_3\beta_3$ cylinder has been suggested (2–5) and confirmed by chemical (6) and optical (7, 8) methods. Direct observation under an optical microscope (8–11) has shown that F_1 rotates in discrete 120° steps, each fueled by a single ATP molecule.

Several kinds of high-resolution crystal structures of mitochondrial F_1 (MF_1) have been solved (1, 12, 13), but it is unknown which rotation states these crystal structures correspond to or how closely these are related to the structure of actively rotating F_1. To investigate the transient structures in rotating F_1, we applied a single-pair fluorescence resonance energy transfer (FRET) technique (14). We measured FRET between a donor (Cy3) on one of three βs and an acceptor (Cy5) on γ in single thermophilic F_1 molecules fixed on a glass surface (Fig. 1). Because the FRET yield strongly depends on the distance between the two fluorophores, the FRET yield will change cyclically as the γ subunit rotates (15). The distance between labeled residues were estimated from the FRET yield and used to analyze the transient conformation of F_1.

Materials and Methods

Proteins. Cy5-maleimide was prepared as in ref. 16. The sole cysteine of a mutant subcomplex of F_1, α(C193S)$_3\beta$(His-10 tag at N terminus)$_3\gamma$(S107C) derived from thermophilic *Bacillus* PS3, was labeled with Cy5-maleimide (molar ratio 1:2) in 20 mM Mops-KOH (pH 7.0), 100 mM KCl, and 5 mM glycine at 23°C for 30 min. The cysteine of a mutant β(S205C) (without His tag) was labeled with Cy3-maleimide at 1:2 in the same buffer excluding glycine at 23°C for 30 min. Free dyes were removed on a PD10 column (Amersham Pharmacia). The (Cy5-γ)F_1 was incubated with Cy3-β at 1:10 at 45°C for 2 days, and free β subunit was removed on a size exclusion column (Superdex 200, Amersham Pharmacia). The final preparation contained 0.7–1 mol Cy5 and 0.05–0.2 mol Cy3 per mol F_1 (estimated from absorption spectra, using ε_{555}^{Cy3} = 150,000 $M^{-1}\cdot cm^{-1}$, ε_{555}^{Cy5} = 15,000 $M^{-1}\cdot cm^{-1}$, ε_{655}^{Cy5} = 250,000 $M^{-1}\cdot cm^{-1}$, ε_{280}^{Cy3} = 15,000 $M^{-1}\cdot cm^{-1}$, ε_{280}^{Cy5} = 25,000 $M^{-1}\cdot cm^{-1}$, and $\varepsilon_{280}^{F_1}$ = 154,000 $M^{-1}\cdot cm^{-1}$). A solution of 0.05–0.5 nM labeled F_1 in 50 mM KCl, 2 mM $MgCl_2$, 10 mM Mops-KOH (pH 7.0), 0.06–1 μM ATP, 70 mM 2-mercaptoethanol, 200 μg/ml glucose oxidase, 20 μg/ml catalase, and 4.5 mg/ml glucose was sandwiched between two KOH-cleaned quartz coverslips for microscopic observation. Resulting thickness of the solution was $\approx$3 μm. Previously, we found that His-tagged F_1 rotates on a clean glass surface (11), presumably bound by the negatively charged surface. To determine the activity of labeled β, a construct α(C193S)$_3\beta$(S205C)$_3\gamma$(S107C) was expressed and labeled with Cy3 at 1:8–20, resulting in 0.5–1.0 mol of Cy3 per cysteine. ATPase activity was measured as described (9).

Microscope. A laser beam (532 nm, DPSS 532–200, Coherent Radiation, Palo Alto, CA) was introduced into an inverted microscope (IX70, Olympus) through a water-immersion objective (PlanApo ×60, numerical aperture 1.2, Olympus). Fluorescence was divided into <620-nm (Cy3) and >620-nm (Cy5) components (17) and focused onto an intensified (VS4–1845, Videoscope, Dallas) charge-coupled device (CCD-300T-IFG, Dage-MTI, Michigan City, IN) camera. Bandpass filters (Chroma Technology, Brattleboro, VT) reduced the cross talk between Cy3 and Cy5 channels to <3%. The excitation efficiency of Cy5 at 532 nm was <0.03 times that of Cy3. Images recorded on a videotape were captured in a personal computer (LG3, Scion, Frederick, MD) and analyzed off-line with custom software. Because only Cy5 close to a donor emitted fluorescence, we could find FRET pairs (F_1 having both Cy3 and Cy5) by looking for fluorescence of Cy5. Most FRET pairs (>99%) did not show time-dependent change of the FRET yield, presumably because of surface denaturation (18). In the Cy3 channel, we observed many more fluorescent spots that lack companion spots in the Cy5 channel. Most of them photobleached in a single step. These presumably represent F_1 carrying a single Cy3 fluorophore without Cy5 acceptor.

Calculation of Distance Between FRET Pairs. The FRET yield f was obtained experimentally as $f = a\text{Cy5}/(\text{Cy3} + a\text{Cy5})$, where Cy5 and Cy3 denote the fluorescence intensities above the background and a is the ratio of the intensity change of two dyes,

This paper was submitted directly (Track II) to the PNAS office

Abbreviations: FRET, fluorescence resonance energy transfer, MF_1, mitochondrial F_1, DCCD, dicyclohexylcarbodiimide

†To whom correspondence should be addressed E-mail yasuda@cshl org

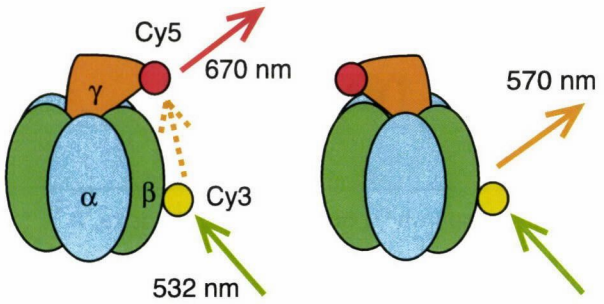

Fig. 1. Visualization of the rotation of F_1 through single-pair FRET: principle of the experiment.

ΔCy3/ΔCy5 (see Fig. 3*E*). The distance between the donor and acceptor was calculated as $R = R_0(1/f - 1)^{1/6}$, where f is the experimental FRET yield and R_0 is the Förster distance (19). R_0 was determined as $[(8.79 \times 10^{17}) \cdot n^{-4} \cdot \kappa^2 \cdot Q_D \cdot J]^{1/6}$ (nm), where J, the overlap integral, was calculated from measured emission spectrum of (Cy5-γ)F_1 and absorption spectrum of (Cy3-β)F_1 to be 8.85×10^{-13} $M^{-1} \cdot cm^3$, $Q_D = 0.25$ is the quantum yield of the donor measured with rhodamine-B (quantum yield = 0.49; ref. 20) as reference, $n = 1.33$ is the refractive index of water, and $\kappa^2 = 0.667 \pm 0.524$ (see below) is the orientation factor. The error in R_0 was mainly from κ^2 and was estimated as $\delta R_0 = R_0 \cdot \delta(\kappa^2)/(6\kappa^2)$. Resulting R_0 was 5.9 $\pm$ 0.8 nm. The error in R was estimated as $(R_0^6/6R^5f^2)\delta f + (R/R_0)\delta R_0$, where δf is the standard error for f.

Calculation of Orientation Factor. The orientation factor κ^2 is defined as $\kappa^2 = \langle(cos\theta_T - 3\,cos\theta_D\,cos\theta_A)^2\rangle$, where θ_T is the angle between $\boldsymbol{\mu}_D$ and $\boldsymbol{\mu}_A$, the donor emission and acceptor absorption transition moments, and θ_D is the angle between $\boldsymbol{\mu}_D$ and $\boldsymbol{d}$ and θ_A between $\boldsymbol{\mu}_A$ and $\boldsymbol{d}$, where $\boldsymbol{d}$ is the vector connecting the donor and acceptor (19). Because none of these angles are known, we assigned arbitrary orientations to $\boldsymbol{\mu}_D$, $\boldsymbol{\mu}_A$, and $\boldsymbol{d}$ and calculated average κ^2 for that combination while allowing $\boldsymbol{\mu}_D$ and $\boldsymbol{\mu}_A$ to wobble within a cone around the assigned axis. This calculation was repeated for all combinations of $\boldsymbol{\mu}_D$, $\boldsymbol{\mu}_A$, and $\boldsymbol{d}$, giving the average and standard deviation for κ^2. The cone angle ϕ_X (X = A or D) for the subnanosecond wobble of the fluorophore is related to the limiting and residual fluorescence anisotropy r_0 and r_{inf} (21) by $r_{inf} = r_0 \cdot [cos\phi_X(1 + cos\phi_X)/2]^2$. r_0 and r_{inf} in turn are related with the steady-state anisotropy r_s (21) by $r_s = (r_0 - r_{inf})/(1 + \tau/\tau_r) + r_{inf}$, in which τ is the fluorescence lifetime and τ_r the rotation correlation time of the dye. τ/τ_r was estimated, by assuming that τ_r is not much different from the correlation time of free dye in water, as $(\tau/\tau_r)_{water}Q_{protein}/Q_{water}$, where $Q_{protein}$ and Q_{water} are the quantum yields of the dye on protein and in water, and $(\tau/\tau_r)_{water}$ is the quantity for free dye in water that was measured as $(\tau/\tau_r)_{water} = (r_0/r_{water} - 1)$, where r_{water} is the steady-state anisotropy of the free dye in water. The steady-state fluorescence anisotropy r_s was measured in a cuvette by using a spectrofluorometer (F-4500, Hitachi, Tokyo) to be 0.29, 0.30, 0.26, and 0.17 for (Cy3-β)F_1 (some proteins contain multiple Cy3), (Cy5-γ)F_1, free Cy3, and free Cy5, respectively (λ_{ex} = 550 and 650 nm, λ_{em} = 590 and 690 nm, respectively for Cy3 and Cy5). Lower limit of r_0 (giving lower limit of the cone angle) was measured as the steady-state anisotropy of the dyes in glycerol at 0°C to be 0.36 for Cy3 and 0.39 for Cy5. The quantum yield Q was measured as 0.25, 0.26, 0.03, and 0.25, respectively, for Cy3-F_1, Cy5-F_1, free Cy3, and free Cy5, using rhodamine-B as a reference. From measured r_s, r_0, and Q, the wobble cone semiangles were obtained as $\phi_D > 25°$ and $\phi_A > 33°$ for Cy3 and Cy5 on F_1.

Derivation of Possible Positions of FRET Pair. The linker length from the dye center to the labeled cysteine sulfur was estimated to be 1.2 and 1.7 nm for Cy3 and Cy5, respectively, from the bond angles and lengths. The donor and acceptor were assumed to be within the linker lengths of the labeled cysteines (β205 and γ107; β203 and γ99 in the MF_1 sequence). Because γ97–100 in MF_1 are unresolved in the crystals, possible positions of γ99-S (mutated to cysteine) were calculated as follows: the peptide backbone was extended from the visible γ101 to γ99 by assigning standard bond lengths and angles while allowing arbitrary rotations around N—C_α (Φ) and C—C_α (Ψ) bonds. If resultant γ99-C is not within 1.0 nm (maximum possible length between γ99-C and γ96-C) from γ96-C, the structure was discarded. Carbonyl oxygens and amino nitrotgens and γ99-C_β were modeled automatically assuming the standard L-amino acid configuration (no need to model a side chain for γ100 glycine). Finally, C_α—C_β bond in γ99 was rotated into an arbitrary angle to locale γ99S. During the construction, if an added atom (excluding hydrogen) was within 0.15 nm of the visible atoms in the crystal, that structure was also discarded. After 5,000 trials, we obtained 562, 462, and 2,323 possible γ99S locations for native MF_1, (ADP AlF_4^-)$_2MF_1$, and MF_1-dicyclohexylcarbodiimide (DCCD). For each location, we assigned a sphere of radius 1.7 nm and assumed that the acceptor could be anywhere in the sphere with the same probability. The acceptor spheres seen in Fig. 5 show the outermost circumference enclosing all possible acceptor position. In the native MF_1 (1), γ91–96 and γ101 are also missing, and we adopted the (ADP AlF_4^-)$_2MF_1$ structure (12) for this part.

Positions of the acceptor compatible with our FRET results (see Fig. 5 *A* and *B*, red dots) were obtained as follows. First, we randomly assigned a donor position from the donor sphere, removing the positions inside the protein by discarding the positions within 0.4 nm of the atoms in the crystal structure. We also chose $\boldsymbol{\mu}_D$ and $\boldsymbol{\mu}_A$ randomly. Instead of rotating the acceptor, we rotated the donor into three equivalent positions, assuming the same linker vector and $\boldsymbol{\mu}_D$ for the three (simple 120° rotations). Then we selected three FRET efficiency values f, one for a high-FRET state and two for low-FRET states, assuming a Gaussian distribution for f with half-width at $1/e$ maximum equaling the experimental standard error. The remaining task was to find three donor-acceptor vectors $\boldsymbol{d}$ that are compatible with the chosen conditions. This was done in an iterative search for the orientation and absolute value of $\boldsymbol{d}$ by first assigning random orientations to the three vectors $\boldsymbol{d}$. (*i*) We calculated three orientation factors from the chosen orientations of $\boldsymbol{d}$, $\boldsymbol{\mu}_D$, and $\boldsymbol{\mu}_A$, while allowing $\boldsymbol{\mu}_D$ and $\boldsymbol{\mu}_A$ to wobble in the respective cones. (*ii*) This gave three distances $|\boldsymbol{d}|$, from which we determined the acceptor position. Two answers were obtained, above and below F_1, and we always chose the one above. (*iii*) From the acceptor position, we extracted three orientations of $\boldsymbol{d}$, disregarding the absolute values, and repeated steps *i-iii*. We stopped the iteration when the differences in the three orientations between two adjacent iteration cycles all became <0.5°. In ≈10% of trials, the calculation did not converge within 500 iterations and we gave up. For a chosen set from ≈1,800 donor positions, $\boldsymbol{\mu}_D$ and $\boldsymbol{\mu}_A$, we always attempted five independent iterations starting from different and randomly selected orientations of $\boldsymbol{d}$. These gave consistent results within 0.2 $\pm$ 0.04 nm (mean $\pm$ SD), when converged. Finally, if the obtained acceptor position was within 0.4 nm of the crystal atoms that position was discarded (to avoid physical conflicts). Red dots seen in Fig. 5 *A* and *B* represent results obtained in this way. When we rotated γ for a better fit with the experimental FRET efficiencies (see Fig. 5), the final check of physical conflicts was made for each γ orientation; the number of remaining red dots did not depend significantly on the γ angle, ranging from 1,340 to 1,414, 1,144 to 1,308, and 1,078 to 1,187, respectively, for native MF_1, (ADP AlF_4^-)$_2MF_1$, and MF_1-DCCD.

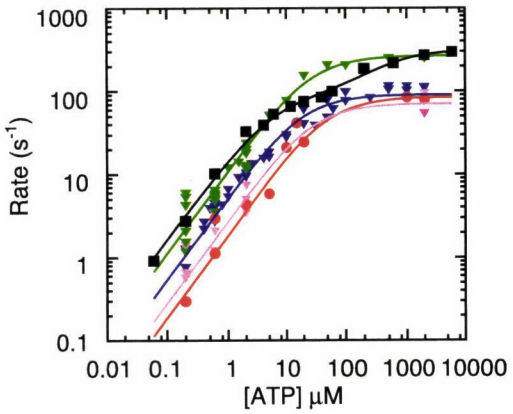

Fig. 2. Effect of labeling on ATPase activity (11). F_1 with a sole cysteine at γ was labeled with Cy3 (green) or unlabeled (black). F_1 with four cysteines (one each in βs and γ) were fully labeled (red), 50% labeled (pink), or unlabeled (blue). Smooth curves are fits with V_{max}[ATP]/([ATP] + k_M) (green, red, pink, blue) or with ($V_{max}k_M$ + V_{max2}[ATP]^2)/([ATP]^2 + k_{M2}[ATP] + k_Mk_{M2}) (black). The rate of ATP binding, k_{on}, was estimated as V_{max}/k_M = (1.1 ± 0.3) × 10^7 M^{-1}·s^{-1} (green), (5.4 ± 0.9) × 10^6 M^{-1}·s^{-1} (blue), (1.9 ± 1.1) × 10^6 M^{-1}·s^{-1} (red), (2.8 ± 1.2) × 10^6 M^{-1}·s^{-1} (pink), and (1.65 ± 0.32) × 10^7 M^{-1}·s^{-1} (black).

The probability of finding a FRET-compatible acceptor position (see red dots in Fig. 5 *A* and *B*) among the possible acceptor positions in the crystal structures was estimated by counting the number of red dots within the acceptor-linker length of a possible γ99-S position, averaging this number over all possible γ99-S positions, and dividing the average by the total number of the red dots. We also calculated the probabilities for rotated γ by rotating the acceptor spheres.

Results

Visualization of F_1 Rotation Through Single-Pair FRET. To label one of the three βs with Cy3 (Fig. 1), we expressed β alone with an engineered cysteine and labeled it with Cy3. The labeled β was exchanged into an independently expressed F_1 of which γ had been labeled with Cy5, resulting in 0.05–0.2 mol of labeled β and 0.7–1.0 mol of labeled γ per mol of F_1. The effect of β mutation and labeling was checked in yet another F_1 construct where all three βs had the cysteine and were fully labeled (Fig. 2): at low [ATP] where hydrolysis rate was proportional to [ATP], the apparent rate of ATP binding was estimated as $k_{on}^{labeled}$ = 1.9 × 10^6 M^{-1}·s^{-1} and $k_{on}^{unlabeled}$ = 1.7 × 10^7 M^{-1}·s^{-1} for the labeled and unlabeled F_1. When only one of three β was labeled, therefore, the rotation at low [ATP] where ATP binding is rate limiting will consist of alternate one slow and two fast steps, as has been demonstrated for an F_1 chimera of normal and slow β subunits (22).

Under an epi-fluorescence microscope, Cy3 was selectively excited at 532 nm, and emissions from Cy3 and Cy5 were simultaneously imaged. The two showed alternate and stepwise intensity changes in the presence of ATP (Fig. 3 *A–C*), indicating alternation of the FRET yield between high and low states. The rate of alternation was faster at higher [ATP], as expected for ATP-dependent stepwise rotation of γ. When Cy3 lost its companion acceptor by photobleaching of Cy5, the fluorescence of Cy3 increased (arrow in Fig. 3*A*). If Cy3 bleaches before Cy5, both are expected to disappear simultaneously, as was indeed observed (arrows in Fig. 3 *B* and *C*). There was a clear correlation between Cy3 and Cy5 fluorescence, showing the existence of two FRET states (Fig. 3 *D–F*).

The transition rates between the high- and low-FRET states, defined as the inverse of the averaged dwell times, ($1/\langle\tau_H\rangle$ and $1/\langle\tau_L\rangle$), were each proportional to [ATP] (Fig. 4), confirming that the change in the FRET yield represents rotation steps. The

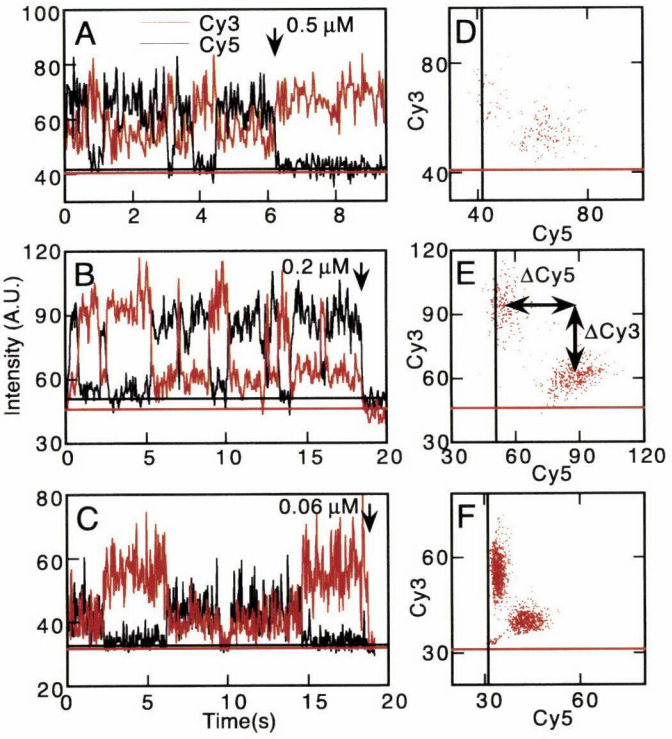

Fig. 3. Changes in the FRET yield accompanying rotation. (*A–C*) Time courses of Cy3 (red) and Cy5 (black) fluorescence at different [ATP]. Arrows indicate photobleaching of Cy5 (*A*) or Cy3 (*B* and *C*). (*D–F*) Correlation between Cy3 and Cy5 intensities in *A–C* (data up to the arrow are scored). Straight lines in *A–F* represent the background intensities for Cy3 (red) and Cy5 (black) channels measured near the FRET pair.

rate of rotation, estimated as $1/(\langle\tau_H\rangle + \langle\tau_L\rangle)$, was also proportional to [ATP] (Fig. 4*A*).

For 120° stepping, three FRET states are expected, as observed for a different donor-acceptor pair (15). In our experiments, two of three states were indistinguishable, leading to two possibilities: (*i*) the high-FRET state with a longer dwell ($\langle\tau_H\rangle/\langle\tau_L\rangle$ = 2.3 ± 0.3) involved one slow step associated with the labeled β and the low-FRET state involved two normal steps, or (*ii*) the high-FRET state involved one normal and one slow steps and the low-FRET state involved one normal step. For each case, the rates of ATP binding, $k_{on}^{labeled}$ and $k_{on}^{unlabeled}$ were calculated from the observed dwell times and compared with the rates estimated from ATP hydrolysis. For case *i*, $k_{on}^{labeled}$ is given as $\langle\tau_H\rangle^{-1}$[ATP]$^{-1}$ = (3.8 ± 0.7) × 10^6 M^{-1}·s^{-1} and $k_{on}^{unlabeled}$ as $2\langle\tau_L\rangle^{-1}$[ATP]$^{-1}$ = (1.6 ± 0.3) × 10^7 M^{-1}·s^{-1}, both of which agree with $k_{on}^{labeled}$ and $k_{on}^{unlabeled}$ estimated from the ATPase activity. For case *ii*, $k_{on}^{labeled}$ = ($\langle\tau_L\rangle - \langle\tau_H\rangle$)$^{-1}$[ATP]$^{-1}$ = (7.4 ± 3.8) × 10^6 M^{-1}·s^{-1} and $k_{on}^{unlabeled}$ = $\langle\tau_L\rangle^{-1}$[ATP]$^{-1}$ = (7.8 ± 1.3) × 10^6 M^{-1}·s^{-1}, inconsistent with the ATPase results. Thus, the low-FRET state involved two normal steps, and the high-FRET state involved one slow step. Histograms of dwell times (Fig. 4*B*) were also better fit with model *i*.

ATP-Waiting Conformation of F_1. The FRET yields in the high- and low-FRET states were calculated from the observed fluorescence intensities as 0.56 ± 0.06 and 0.15 ± 0.03, respectively, corresponding to the donor-acceptor distances of 5.7 ± 0.9 and 7.9 ± 1.0 nm. Because the low-FRET state involves two rotation steps, the distance between the two dyes will change as 5.7, 7.9, and 7.9 nm during rotation. These values are to be compared with the known crystal structures of F_1.

Three different crystal structures of MF_1 have been solved: a

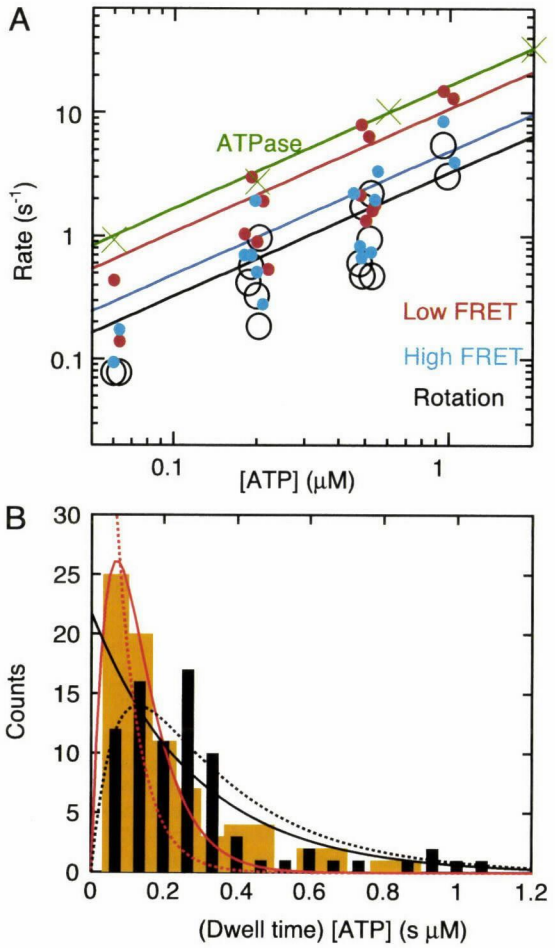

Fig. 4. (*A*) ATP dependence of the transition rate from the high and low FRET states ($1/\langle\tau_H\rangle$ and $1/\langle\tau_L\rangle$) and the rotation rate estimated as $1/(\langle\tau_H\rangle + \langle\tau_L\rangle)$ (160 FRET states were analyzed in 15 FRET pairs). For comparison, the rate of ATP hydrolysis in F_1 without the subunit labeling is shown (Fig. 2*A*). Lines show linear fits with slopes (± SE) of (4.9 ± 0.7), (10.9 ± 1.3), (3.3 ± 0.4), and (16.5 ± 0.2) × 10^6 $M^{-1}\cdot s^{-1}$ for $1/\langle\tau_H\rangle$, $1/\langle\tau_L\rangle$, rotation, and ATPase, respectively. (*B*) Histogram of dwells, τ, of the high (black) and low (orange) FRET states. Solid curves show fit for case *i* in the text: low FRET dwell (red) with $constant\cdot\tau[ATP]\exp(-k_{on}^{unlabeled}\tau[ATP])$, where $k_{on}^{unlabeled} = 1.65 \times 10^7\ M^{-1}\cdot s^{-1}$ is the ATP binding constant of unlabeled F_1 from Fig. 2, and high FRET dwells (black) with $constant\cdot\exp(-k_{on}^{labeled}\tau[ATP])$, where $k_{on}^{labeled} = 1.9 \times 10^6\ M^{-1}\cdot s^{-1}$ is for labeled β (χ^2 = 257, 80 dwells, 15 FRET pairs). Dashed curves show fit for case *ii* in the text: low FRET dwells (red) with $constant\cdot\exp(-k_{on}^{unlabeled}\tau[ATP])$, and high FRET dwells (black) with $constant\cdot\{\exp(-k_{on}^{labeled}\tau[ATP]) - \exp(-k_{on}^{unlabeled}\tau[ATP])\}$, where $k_{on}^{labeled}$ and $k_{on}^{unlabeled}$ are fixed to the experimental values above (χ^2 = 497, 80 dwells, 15 FRET pairs).

"native MF_1" structure in which AMP-PNP, ADP, and none occupy the three catalytic sites (1), an "MF_1-DCCD" structure that is inhibited with DCCD and has the same nucleotides as the native MF_1 (12), and an "(ADP AlF_4^-)$_2MF_1$" structure, which is inhibited with aluminum fluoride and has two ADP AlF_4^- and one ADP (13). To compare these structures, we adopt the triangle made of three α-carbons of α-GLU26 as the frame of reference (23); a line perpendicular to, and passing through the center of, the triangle is assumed to be the rotation axis. The conformation of γ inside the $\alpha_3\beta_3$ cylinder varies little among the three crystal structures, whereas part of γ near the upper orifice of the $\alpha_3\beta_3$ cylinder is twisted clockwise (opposite to the rotation direction) up to 20° and 11° in (ADP AlF_4^-)$_2MF_1$ and MF_1-DCCD, respectively, compared with the native MF_1 when viewed from above in Figs. 1 and 5 (13).

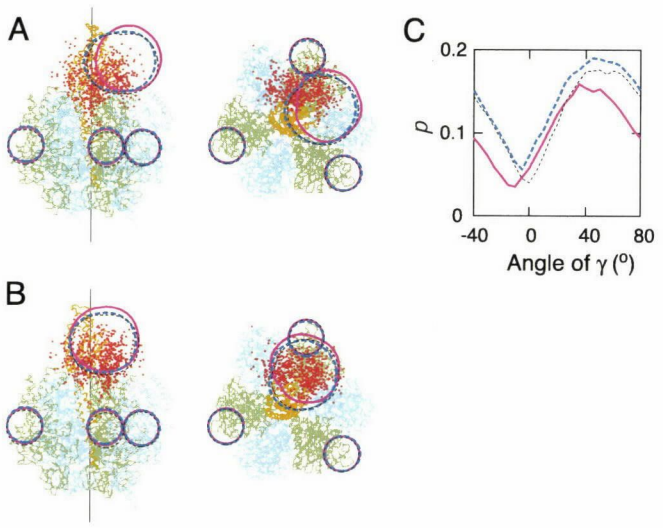

Fig. 5. (*A*) Side (*Left*) and top (*Right*) views of the backbone trace of the structure of (ADP.AlF_4)$_2$ MF_1 (13), color-coded as in Fig. 1*A*. Small and large spheres represent geometrically allowed positions of the donor (Cy3) and acceptor (Cy5), respectively, on the native MF_1, (ADP AlF_4^-)$_2MF_1$, and MF_1-DCCD structures (blue, black, and pink); the degree of twist in γ varies among the three structures, resulting in the slight deviations of large circles. Red dots indicate possible acceptor positions calculated from the FRET results (see *Materials and Methods*). The black line indicates the putative rotation axis. (*B*) The acceptor sphere (and γ) is rotated counterclockwise by 40°. (*C*) Probability (p) of finding red dots in the acceptor sphere as functions of γ angle (θ) for native MF_1 (blue), MF_1-DCCD (pink), and (ADP AlF_4^-)$_2$ MF_1 (black). Larger values between $p(\theta)$ and $p(\theta + 120°)$ are plotted.

In these structures, the position of the residue labeled with the acceptor, which is on the protruding portion of γ, varies to some extent, while the donor residues occupy the same positions. Possible positions of the donor and acceptor in the three MF_1 structures are essentially the same (Fig. 5*A*, small and large spheres for the donor and acceptor, respectively). The acceptor spheres are larger, because several residues around the acceptor site are unresolved in the structures and linker length of the acceptor is longer than that of the donor. Starting with the donor positions that are common to all structures, we calculated acceptor positions that are compatible with the three FRET efficiencies above (red dots in Fig. 5 *A* and *B*). The FRET-estimated acceptor positions overlap best with the acceptor sphere (large ones) when γ was rotated counterclockwise by ≈40° in all MF_1 crystals (Fig. 5*C*). Because FRET measurements were done at low ATP concentrations where binding of ATP limits the rotation rate, this conformation corresponds to the ATP-waiting state of F_1.

Discussion

Rotation Mechanism of F_1-ATPase. Our FRET results suggest that the conformation of γ in the ATP-waiting state of F_1 is ≈40° counterclockwise, or ≈40° in the rotation direction, from that in the MF_1 crystal structures. Then, which kinetic state do the MF_1 structures correspond to? At least one intermediate state during rotation, other than the ATP-waiting state, has so far been resolved: binding of ATP to F_1 in the ATP-waiting state induces a counterclockwise ≈90° substep, and F_1 remains at this intermediate angle for ≈2 ms before undergoing a further ≈30° substep induced by product release (11). When F_1 is inhibited on tight binding of MgADP, the rotation stalls at ≈80° (24), suggesting that the inhibited conformation resembles that of the intermediate state after the ≈90° substep. Naively, crystal structures are expected to be close to the 90°/80° conformation rather than the ATP-waiting conformation, because crystalliza-

tion involves long incubation with MgADP or MgATP, a condition that favors the formation of the MgADP-inhibited enzyme (25), as has been suggested in cross-linking studies (26). If so, expected acceptor positions in the ATP-waiting state should be 30°/40° ahead the crystal structures (Fig. 5*B*). Our FRET results (Fig. 5, red dots) indeed point to this position, suggesting that the crystal structures are closer to the 90°/80° conformation rather than the ATP-waiting conformation (0° or 120°).

Whether rotation of F_1-ATPase requires filling of all three catalytic sites with a nucleotide (27) or filling two is sufficient (28) is an important, but unresolved, issue. Because γ orientation in both the 2- and 3-nt crystal structures differ from our results by 40°, the ATP-waiting conformation likely binds a single nucleotide. If so, rotation under our experimental conditions occurs by filling at most two catalytic sites.

The protruding part of γ in crystals of F_1 from *Escherichia coli* (29) or the thermophilic bacterium (Y. Shirakihara, personal communication) is twisted counterclockwise compared with the MF_1 structures, such that possible acceptor positions in these bacterial crystals are close to the large circles in Fig. 5*B*. Our FRET results obtained with the thermophilic F_1 are consistent with these positions. In particular, the thermophilic bacterial crystal contained only 1 nt, suggesting again that the ATP-waiting state corresponds to a single-nucleotide state.

Our interpretations above rest on the assumption that the crystal structures closely mimic an active rotation intermediate hosting the same number of nucleotides. However, the lattice packing may have deformed the F_1 structure in the crystals (12, 13). The twist of γ in $(ADP\ AlF_4^-)_2MF_1$ and MF_1-DCCD, relative to native MF_1, is maximal around the orifice of the $\alpha_3\beta_3$ cylinder and is smaller both above and below the orifice, suggesting some distortion. In particular, native MF_1 and MF_1-DCCD both have two catalytic nucleotides, and yet γ in MF_1-DCCD is twisted clockwise up to 11°. Significantly, the MF_1-DCCD crystal is more closely packed than the native MF_1 crystal, and the bacterial crystals in which γ is twisted counterclockwise are less densely packed. A possibility thus exists that 2-nt MF_1 in a relaxed crystal might show a γ orientation similar to the bacterial one. If so, our FRET results might point to the necessity of three-site filling. FRET with different donor-acceptor pairs will help resolve the remaining ambiguity.

Analysis of Protein Conformation Through Single-Pair FRET. FRET is a standard technique for measuring distances in the 1- to 10-nm range and often used for analyzing conformation of proteins and nucleotides in solution (30). For analysis of transient protein conformations, FRET measurement on individual donor-acceptor pairs is essential because protein molecules behave stochastically and their operations cannot be synchronized.

In this study, we have demonstrated that single-pair FRET reveals a transient conformation of F_1-ATPase with nanometer precision. The resolution, limited mainly by the ambiguity in the orientation factor and the relatively large linker length between the fluorophore and target residue, could be improved by synthesizing short-linker fluorophores and searching for a proper fluorophore-residue combination that warrants an extensive wobble of the fluorophore on the protein surface.

We thank T. Nishizaka, T. Ariga, and Y. Shirakihara for critical discussions. This work was supported by the Japan Society for the Promotion of Science (to R.Y.), the Burroughs Wellcome Fund (to R.Y.), Core Research for Evolutional Science and Technology, and Grants-in-Aid from the Ministry of Education, Science, Sports, and Culture of Japan.

1 Abrahams, J P., Leslie, A. G., Lutter, R. & Walker, J E. (1994) *Nature* **370,** 621–628.
2 Boyer, P. & Kohlbrenner, W. (1981) in *Energy Coupling in Photosynthesis*, eds. Selman, B. R & Selman-Reimer, S. (Elsevier, Amsterdam), pp. 231–240.
3. Cox, G., Jans, D. A., Fimmel, A., Gibson, F. & Hatch, L. (1984) *Biochim. Biophys. Acta* **849,** 62–69
4. Oosawa, F. & Hayashi, S. (1986) *Adv. Biophys* **22,** 151–183
5 Boyer, P. D. (2000) *Biochim. Biophys Acta* **1458,** 252–262
6 Duncan, T. M., Bulygin, V. V., Zhou, Y., Hutcheon, M L & Cross, R. L. (1995) *Proc. Natl. Acad. Sci. USA* **92,** 10964–10968
7. Sabbert, D., Engelbrecht, S & Junge, W (1996) *Nature* **381,** 623–625
8 Noji, H., Yasuda, R., Yoshida, M. & Kinosita, K., Jr. (1997) *Nature* **386,** 299–302.
9 Yasuda, R., Noji, H., Kinosita, K., Jr., & Yoshida, M (1998) *Cell* **93,** 1117–1124.
10 Adachi, K., Yasuda, R., Noji, H., Itoh, H, Harada, Y., Yoshida, M & Kinosita, K., Jr. (2000) *Proc Natl. Acad. Sci USA* **97,** 7243–7247.
11. Yasuda, R, Noji, H, Yoshida, M., Kinosita, K., Jr, & Itoh, H (2001) *Nature* **410,** 898–904
12. Gibbons, C., Montgomery, M G., Leslie, A G. W. & Walker, J. E (2000) *Nat. Struct. Biol.* **7,** 1055–1061
13. Menz, R I., Walker, J E & Leslie, A G. (2001) *Cell* **106,** 331–341.
14 Kelley, A., Michalet, X. & Weiss, S. (2001) *Science* **292,** 1671–1672.
15 Borsch, M., Diez, M., Zimmermann, B., Reuter, R. & Graber, P (2002) *FEBS Lett.* **527,** 147–152.
16 Funatsu, T, Harada, Y., Tokunaga, M, Saito, K. & Yanagida, T (1995) *Nature* **374,** 555–559.
17. Kinosita, K., Jr., Itoh, H., Ishiwata, S., Hirano, K., Nishizaka, T. & Hayakawa, T (1991) *J. Cell Biol.* **115,** 67–73.
18. Kinosita, K., Jr., Yasuda, R., Noji, H. & Adachi, K. (2000) *Philos. Trans R. Soc London B* **355,** 473–489.
19. Forster, T. (1948) *Annalen Physik* **2,** 55–75.
20 Ishikawa, M., Hirano, K., Hayakawa, T, Shigeru, H & Brenner, S (1994) *Jpn J. Appl. Phys.* **33,** 1571–1576.
21 Kinosita, K., Jr., Kawato, S & Ikegami, A (1984) *Adv. Biophys.* **17,** 147–203
22. Ariga, T., Masaike, T., Noji, H. & Yoshida, M. (2002) *J. Biol. Chem.* **277,** 24870–24873.
23 Wang, H. & Oster, G. (1998) *Nature* **396,** 279–282
24 Hirono-Hara, Y., Noji, H., Nishiura, M, Muneyuki, E, Hara, K. Y, Yasuda, R., Kinosita, K., Jr., & Yoshida, M. (2001) *Proc Natl. Acad. Sci. USA* **98,** 13649–13654.
25. Milgrom, Y. M. & Boyer, P. D. (1990) *Biochim. Biophys. Acta* **1020,** 43–48
26 Tsunoda, S. P., Muneyuki, E., Amano, T., Yoshida, M. & Noji, H. (1999) *J. Biol. Chem* **274,** 5701–5706
27. Weber, J. & Senior, A. E. (2001) *J. Biol. Chem.* **276,** 35422–35428.
28. Boyer, P. D. (2002) *FEBS Lett.* **512,** 29–32.
29 Hausrath, A C, Gruber, G, Matthews, B. W. & Capaldi, R A. (1999) *Proc Natl. Acad. Sci. USA* **96,** 13697–13702.
30. Selvin, P. R. (2000) *Nat. Struct Biol* **7,** 730–734.

Catalysis and rotation of F_1 motor: Cleavage of ATP at the catalytic site occurs in 1 ms before 40° substep rotation

Katsuya Shimabukuro*, Ryohei Yasuda†, Eiro Muneyuki*, Kiyotaka Y. Hara‡, Kazuhiko Kinosita, Jr.§, and Masasuke Yoshida*‡¶

*Chemical Resources Laboratory, Tokyo Institute of Technology, 4259 Nagatsuta, Midori-ku, Yokohama 226-8503, Japan; †Cold Spring Harbor Laboratory, 1 Bungtown Road, Cold Spring Harbor, NY 11724, ‡ATP System Project, Exploratory Research for Advanced Technology (ERATO), Japan Science and Technology Corporation, 5800-3, Nagatsuta, Midori-ku, Yokohama 226-0026, Japan; and §Center for Integrative Bioscience, Okazaki National Research Institute, Yamate Building 1, Higashiyama 5-138, Myodaiji, Okazaki, Aichi 444-8585, Japan

Edited by Paul D. Boyer, University of California, Los Angeles, CA, and approved October 10, 2003 (received for review August 6, 2003)

F_1, a water-soluble portion of F_oF_1-ATP synthase, is an ATP hydrolysis-driven rotary motor. The central γ-subunit rotates in the $\alpha_3\beta_3$ cylinder by repeating the following four stages of rotation: ATP-binding dwell, rapid 80° substep rotation, interim dwell, and rapid 40° substep rotation. At least two 1-ms catalytic events occur in the interim dwell, but it is still unclear which steps in the ATPase cycle, except for ATP binding, correspond to these events. To discover which steps, we analyzed rotations of F_1 subcomplex ($\alpha_3\beta_3\gamma$) from thermophilic *Bacillus* PS3 under conditions where cleavage of ATP at the catalytic site is decelerated: hydrolysis of ATP by the catalytic-site mutant F_1 and hydrolysis of a slowly hydrolyzable substrate ATPγS (adenosine 5′-[γ-thio]triphosphate) by wild-type F_1. In both cases, interim dwells were extended as expected from bulk phase kinetics, confirming that cleavage of ATP takes place during the interim dwell. Furthermore, the results of ATPγS hydrolysis by the mutant F_1 ensure that cleavage of ATP most likely corresponds to one of the two 1-ms events and not some other faster undetected event. Thus, cleavage of ATP on F_1 occurs in 1 ms during the interim dwell, and we call this interim dwell catalytic dwell.

F_oF_1-ATP synthase is an enzyme ubiquitous from bacteria to animals and plants. It synthesizes ATP from ADP and inorganic phosphate by using $\Delta\mu_H^+$-driven proton flow through a membrane (1, 2). F_oF_1-ATP synthase can easily be separated into two major portions: water-soluble F_1 and membrane-embedded F_o. The isolated F_1 ($\alpha_3\beta_3\gamma\delta\varepsilon$) has an ATP hydrolysis activity and is often called F_1-ATPase (3, 4). The crystal structure of F_1 shows that the rod-shaped γ-subunit is surrounded by a cylinder made of three α- and three β-subunits arranged alternatively (5). The catalytic sites are located in β-subunits but residues from adjacent α-subunits also contribute. It has been thought that F_oF_1-ATP synthase is a complex of F_o motor and F_1 motor that share a common rotor: a downhill proton flow through F_o drives rotation of the rotor, causing conformational changes in F_1 that result in ATP synthesis. Conversely, ATP hydrolysis in F_1 causes a reverse rotation of the rotor that enforces F_o to pump protons in the reverse direction (6). The rotor is made of a c-subunit ring of F_o (7–11) and $\gamma\varepsilon$ subunits of F_1 (12–15).

We have visualized and analyzed the ATP-driven rotation of the γ-subunit in the minimum assembly of F_1 motor, $\alpha_3\beta_3\gamma$ subcomplex (hereafter in this article, this subcomplex is called F_1) (13, 16). To date, the following features have been established. The γ-subunit makes a 120° step per one ATP consumption (17), which is further divided into 90° and 30° substeps (18). The dwelling time before the 90° substep rotation depends on ATP concentration and disappears beyond the limit of time resolution of the observation methods as ATP concentration ([ATP]) increases. Therefore, the dwell before the 90° substep rotation is a dwell for ATP binding, and the 90° substep rotation is certainly driven by ATP binding to one of β-subunits of F_1. On the contrary, dwelling time before the 30° substep rotation is independent of [ATP] and is observed even at a high [ATP] that gives a near V_{max} hydrolysis rate. Obviously, during this dwell the enzyme carries out subsequent catalytic events after ATP binding. We call the dwells before the 90° and 30° substep rotation an "ATP-binding dwell" and an "interim dwell," respectively. Histogram of the dwelling times at the 0.12-ms time resolution in the rotation assay with a probe of 40-nm bead showed that at least two events, both with a 1-ms time constant, occur in this interim dwell; the first event comes in 1 ms after ATP binding and the second event occurs in next 1 ms, which is followed by the 30° substep rotation to finish one round of catalysis (18).

Then, an immediate question is which steps in the ATPase cycle correspond to these events? Provided that the 90° substep rotation is driven by ATP binding, the subsequent steps of the ATPase reaction, namely, cleavage of ATP into ADP and P_i, release of P_i, and release of ADP, can be candidates for the two 1-ms events in the interim dwell. However, although the 90° substep rotation is clearly initiated by ATP binding, this finding does not necessarily mean that the step is driven solely by ATP binding. Taking the positive catalytic cooperativity of ATP hydrolysis by F_1 (19, 20) into account, it is possible that both ATP binding and immediately after ATP hydrolysis may drive the 90° substep rotation as proposed by Senior *et al.* (21). To address this question, we have generated two systems where the step of ATP cleavage on the enzyme is greatly decelerated. First, we have generated a catalytic-site mutant $F_{1(\beta\text{-L190D})}$, which hydrolyzes ATP extremely slowly (22). Second, we have adopted ATPγS as a slowly hydrolyzable substrate (23). The analysis of rotations under these conditions allowed us to assign one of the 1-ms events to be the cleavage of ATP at a catalytic site. In addition, the previously described "90° and 30° substeps" have been revised to the more appropriate "80° and 40° substeps."

Materials and Methods

Materials and Reagents. ATP, ADP, phospho*enol*pyruvate, and BSA were purchased from Sigma. 6-{*N*′-[2-(*N*-maleimido)-ethyl]-*N*-piperazinylamide}hexyl D-biotinamide (Biotin-PEAC$_5$-maleimide) and 1-ethyl-3-(3-dimethylaminopropyl) carbodiimide (EDC) were obtained from Dojindo (Kumamoto, Japan). Pyruvate kinase, lactate dehydrogenase, NADH, and ATPγS were acquired from Roche Diagnostics. (+)-Biotinyl-3, 6-dioxaoctanediamine (Biotin-PEO-amine) and NeutrAvidin were ob-

This paper was submitted directly (Track II) to the PNAS office

Abbreviations ATPγS, adenosine 5′-[γ-thio]triphosphate, fps, frames per second, rps, revolutions per second; LDAO, *N*,*N*-dimethyldodecylamine-*N*-oxide

¶To whom correspondence should be sent at the * address E-mail myoshida@res titech ac.jp

tained from Pierce. Carboxylate bead (diameter, 0.2 μm) was acquired from Polysciences. *N,N*-dimethyldodecylamine-*N*-oxide (LDAO) was obtained from Fluka.

Protein Preparation. Subcomplex ($\alpha_3\beta_3\gamma$) of F_1 from thermophilic *Bacillus* strain PS3 (called F_1 unless otherwise specified) was expressed in *Escherichia coli* JM103Δunc(uncB-D) by using an expression plasmid, pKAGB1/HC95, that carries genes for the α(C193S), γ(S107C/I210C), and β(10 His-tag at N terminus) (18). Although several residues in the expressed F_1 (called HC95) were altered from the original F_1, it functions in the same manner as the original one, and we consider HC95 as a wild type in this article. Glu-190 of β-subunit was mutated to Asp by the Kunkel method (24) with *E. coli* strain JM109 as a host. The mutant (called $F_{1(\beta\text{-L190D})}$) was expressed in JM103Δunc(uncB-D) and purified as described (25, 26). The purified F_1 was further applied to gel-filtration HPLC (Superdex 200 H/R; Amersham Biosciences) equilibrated with 100 mM KP_i, pH 7.0, containing 100 mM KCl and 2 mM EDTA, and the peak fractions were used for the experiments. The above purification procedures were carried out at room temperature. The concentration of F_1 was estimated by absorbance at 280 nm (ε = 154,000 $M^{-1}\cdot cm^{-1}$).

Hydrolysis of ATP and ATPγS. All reactions were carried out at 25°C. ATPase activity was measured in the presence of an ATP-regenerating system containing 0.2 mM NADH, 2.5 mM phospho*enol*pyruvate, 50 μg/ml pyruvate kinase, 25 μg/ml lactate dehydrogenase, and an indicated amount of ATP in solution A (50 mM KCl/2 mM $MgCl_2$/10 mM 3-[*N*-morpholino]propanesulfonic acid-KOH, pH 7.0) (27). To examine the phosphate or thiophosphate inhibitions, 0.1% LDAO was added to the assay solution to avoid effects of F_1 reactivation from the ADP-inhibited form by phosphate or thiophosphate (28). The reaction was initiated by the addition of F_1 to 1.2 ml of assay solution, and the hydrolysis rate was determined from the absorbance decrease at 340 nm. The hydrolysis rate of ATPγS was measured without an ATP-regenerating system because it replaces ATPγS with ATP during the assay. The reaction was started by mixing F_1 with indicated amount of ATPγS and stopped after various times by adding perchloric acid. The amount of produced ADP was measured by anion-exchange HPLC (10 SAX column, Whatman) eluted with 500 mM $(NH_4)_2HPO_4$-H_3PO_4, pH 4.0, monitoring absorbance at 260 nm.

Bead Preparation. Beads for rotation experiments were biotinylated as follows. The carboxylate beads (diameter, 0.2 μm) were washed twice by centrifugation with solution B (50 mM 2-morpholinoethanesulfonic acid-KOH, pH 5.5) and resuspended in solution B containing 200 μM 1-ethyl-3-(3-dimethylaminopropyl) carbodiimide and 2 mM (+)-biotinyl-3, 6-dioxaoctanediamine. After a 2-h incubation at room temperature for biotinylation, the beads were centrifuged, washed six times, suspended in solution B, and stored at 4°C.

Rotation Assay. For rotation assay, cysteines of γ-subunit were biotinylated as follows. F_1 and 6-{*N'*-[2-(*N*-maleimido)ethyl]-*N*-piperazinylamide}hexyl D-biotinamide were reacted at a molar ratio of 1:3 overnight at room temperature, and unreacted biotin was removed by PD-10 column (Amersham Biosciences). A flow chamber was made of a cover glass and a slide glass with a spacer of 50-μm thickness. Biotinylated F_1 (0.2–0.5 μM) in solution A containing 10 mg/ml BSA was loaded into the flow chamber first, and, after 2 min, F_1 unattached to the glass surface was washed away with 100 μl of solution A. Then, 2 μM NeutrAvidin in solution A was loaded. After 2 min, unbound NeutrAvidin was removed with 100 μl of solution A, and 2 pM biotinylated beads in solution A containing 10 mg/ml BSA were loaded. After a 12-min incubation, unbound beads were removed with 100 μl of solution A containing indicated amount of ATP or ATPγS. In the case of ATP, solution A was complemented by an ATP-regenerating system. Rotating duplex beads were observed with dark-field microscopy (IX-70; Olympus, Tokyo) with a ×100 objective lens (numerical aperture, 1.35; Olympus). The images of rotating beads were recorded directly to a hard disk of a computer as an 8-bit .avi file with a fast-framing charge-coupled device camera (Hi-Dcam; nac Image Technology, Tokyo) at the indicated frame rate. Custom software (created by R.Y.) was used for analyses of the bead movements and dwelling times of steps. With this experimental setup, the wild-type F_1 rotated at a rate of 24.6 ± 2.6 revolutions per second (rps) (mean ± SE; n = 5) at 2 mM ATP, far below the rate observed by the 8,000-frames per second (fps) charge-coupled device camera with 40-nm bead (≈130 rps) where viscous load did not impede the rotation (18). Therefore, the 2-ms interim dwell observed in the previous study was not seen. Nonetheless, this setup is good for observation of rotations slower than ≈10 rps because it allows long-time data collection and is easy to handle.

Results and Discussion

Bulk Phase Enzymatic Properties of $F_{1(\beta\text{-E190D})}$. To obtain a mutant F_1 in which a chemical cleavage of ATP at the catalytic site is greatly decelerated while other catalytic steps are less affected, we replaced Glu-190 of β-subunit with Asp, and $F_{1(\beta\text{-L190D})}$ was generated. Glu-190 was suggested to be an essential residue for catalysis of F_1 (29), and, indeed, the mutant $F_{1(\beta\text{-L190Q})}$ with the replacement of this critical Glu with Gln has lost ATPase activity completely (22, 30). Crystal structure of mitochondrial F_1 suggests that the carboxyl group of Glu-188 of the β-subunit (equivalent to Glu-190 of β-subunit of thermophilic F_1) acts as a general base to polarize a water molecule to make nucleophilic attack on the γ-phosphorus of ATP (Fig. 1*A*). Crystal structure also shows that βGlu-188 of mitochondrial F_1 does not directly contribute to binding AT(D)P to the catalytic site. Indeed, it was shown that a mutant *E. coli* F_1 equivalent to $F_{1(\beta\text{-L190Q})}$ had binding affinities to ATP and ADP similar to those of the wild-type F_1 (31). The $F_{1(\beta\text{-L190D})}$, as expected, retained only very low ATP hydrolytic activity. Hydrolysis of substoichiometric amount of ATP (unisite catalysis) by $F_{1(\beta\text{-L190D})}$ (time constant, 126 s) was 1,800 times as slow as the wild-type F_1 (time constant, 6.9×10^{-2} s) (32). Steady-state ATPase activity of $F_{1(\beta\text{-L190D})}$ showed simple Michaelis–Menten-type dependence on [ATP], and the V_{max} and K_m values (mean ± SE) were determined to be 2.4 ± 0.0 s^{-1} and 1.4 ± 0.1 μM, respectively (Fig. 1*B*). This V_{max} value is ≈100 times smaller than that of the wild-type F_1 (≈250 s^{-1}). This K_m value is one order smaller than that of the wild-type F_1 (19 ± 1 μM) measured in the presence of LDAO, a suppressor of the MgADP inhibition (18).

Rotation of $F_{1(\beta\text{-E190D})}$. We observed rotation of $F_{1(\beta\text{-L190D})}$ at various [ATP]s. At all [ATP]s, the rotation rate averaged over 30 s roughly agreed with the ATP hydrolysis rate measured in the bulk divided by 3 (Fig. 1*B*). Some 20% of the higher rate of the rotation than ATP hydrolysis can be explained by MgADP inhibition in the latter condition. In bulk phase kinetics, some fraction of enzyme is always in the state of MgADP inhibition. On the other hand, rotation rate was measured for only actively rotating molecules and hardly was affected by MgADP inhibition. A rotation vs. [ATP] curve could be fitted with a simple Michaelis–Menten-type kinetics, where V_{max} and K_m values (mean ± SE) were calculated to be 0.9 ± 0.1 rps (for 2.7 s^{-1} ATP hydrolysis) and 1.0 ± 0.4 μM, respectively. Unlike the wild-type F_1, $F_{1(\beta\text{-E190D})}$ rotated with discrete 120° steps even at 2 mM ATP (Fig. 2*A*). As will be discussed later, these dwells are not the ATP-binding dwells but the interim dwells. At low [ATP] (<2 μM), the 120° steps were further divided into two substeps, and

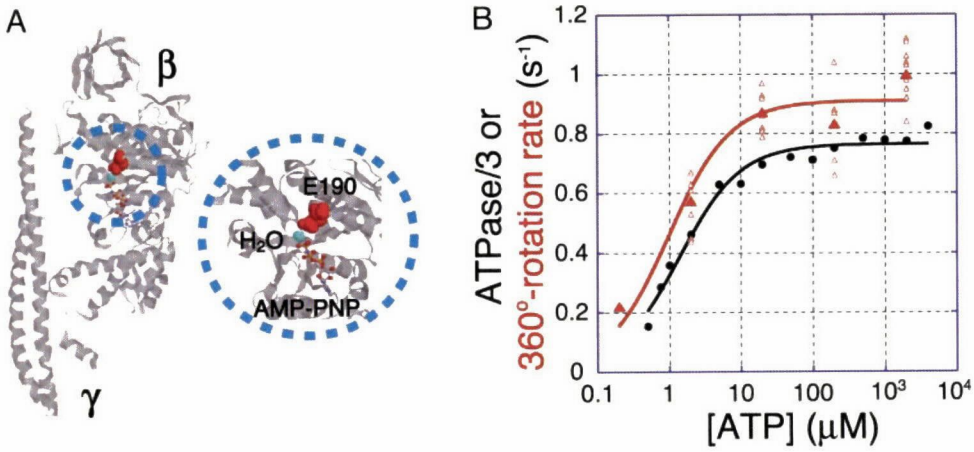

Fig. 1. (*A*) The position of Glu-190 of β-subunit. The structural data are taken from chain F of bovine mitochondrial F_1-ATPase (Protein Data Bank ID code 1BMF; ref. 5). β-Subunit and γ-subunit are shown as ribbon models (*Left*). Residue Glu-188 (red), equivalent to Glu-190 in this study, and a water (cyan), which is thought to be important for catalysis, are shown as space-filling models. 5′-(β,γ-Imino)triphosphate (AMP-PNP), an analogue of ATP, is shown as a stick model. Close-ups of the regions near Glu-188 and AMP-PNP are shown (*Right*). (*B*) Comparison of the 360° rotation rate and hydrolysis rates in the bulk. Black circle, the rate of the ATP hydrolysis in the bulk divided by 3; red open triangle, averaged 360° rotation rate for the individual 0.2-μm duplex beads attached to γ-subunit of $F_{1(\beta\text{-E190D})}$; red filled triangle, the 360° rotation rate averaged over different beads. The black and red lines show fit with Michaelis–Menten equation, $V = V_{max} \times [ATP]/(K_m + [ATP])$. $V_{max} = 0.8 \pm 0.0\ s^{-1}$ and $K_m = 1.4 \pm 0.1\ \mu M$ for the bulk, $V_{max} = 0.9 \pm 0.1\ s^{-1}$ and $K_m = 1.0 \pm 0.4\ \mu M$ for rotation. Values are means ± SE.

the steps at six regular positions were observed in one revolution (Fig. 2*B* and *Inset*). The angles of the two substep rotations were ≈80° (80.9 ± 1.8°; mean ± SE; $n = 15$) and ≈40° (39.1 ± 1.7°). The dwelling time before the 80° substep rotation depended on [ATP], therefore, this dwell is the ATP-binding dwell. On the other hand, the dwelling time before the 40° substep rotation was independent of [ATP], and this dwell is the interim dwell.

The 80° and 40° substeps described here correspond to the previously reported 90° and 30° substeps (18). The apparent discrepancy in the angles seems to arise from the difference between the observation methods. In the previous study, a 40-nm single bead obliquely attached to the γ-subunit was used as a probe of rotation, whereas we used 0.2-μm duplex beads in the present study. With a larger probe, better angular resolution was attained in the present study. The study on MgADP inhibition also presented 37.6 ± 2.5° as an angle of substep rotation that precedes the ATP-binding dwell (33). Therefore, although the very accurate angles of substep rotations should be determined in future studies, the terms 80° and 40° substeps are more appropriate at present than the previous 90° and 30° substeps.

Dwelling Times of Rotation of $F_{1(\beta\text{-E190D})}$. Histogram of the ATP-binding dwell before 80° substeps obeyed an exponential function (data not shown), and the second-order rate constant for ATP binding to F_1 (k_{on}) was estimated to be $(3.1 \pm 0.1) \times 10^6\ M^{-1}\cdot s^{-1}$ (mean ± SE). This k_{on} value of $F_{1(\beta\text{-E190D})}$ is approximately one order smaller than that of the wild-type [$(3.0 \pm 0.1) \times 10^7\ M^{-1}\cdot s^{-1}$] (18), probably because of the subtle change of environments near γ-phosphate of ATP caused by replacing Glu with Asp. If we apply a simple Michaelis–Menten scheme,‖ the 10-fold decrease in K_m is consistent with the observed 10-fold decrease in k_{on} and 100-fold decrease in k_{cat} on the assumption that k_{off} is negligible compared with k_{cat}. Histogram of the interim dwell has a distinct peak, which can be fit with double exponentials with two time constants of 321 ± 22 ms and 19.9 ± 0.1 ms (mean ± SE) (Fig. 2*C*). Thus, the interim dwell of $F_{1(\beta\text{-E190D})}$ is comprised of at least two kinds of successive dwells: a relatively long dwell of 320 ms and a relatively short dwell of 20 ms. Considering the properties of the mutant described above, it is most likely that the longer dwell corresponds to the time required for the chemical cleavage of ATP.

Hydrolysis of ATPγS by F_1. ATPγS often has been regarded as a nonhydrolyzable ATP analogue and used as an inhibitor of phosphatases and ATPases. However, when ATPγS was incubated with F_1, the amount of ATPγS was slowly decreased (Fig. 3*A Inset*) and an equivalent amount of ADP was produced (not shown). Without F_1, no such change occurred. Thus, ATPγS is a slowly hydrolyzable substrate for F_1-ATPase. The hydrolysis rate of ATPγS did not show simple Michaelis–Menten dependence on ATPγS concentration ([ATPγS]) and could be fitted with an equation assuming two K_m values (27). The total V_{max} value of ATPγS hydrolysis by the wild-type F_1 was 5.8 ± 0.3 s^{-1} (mean ± SE), and this value is 43 times smaller than that of ATP hydrolysis (≈250 s^{-1}). The K_m values are 1.0 ± 0.3 μM and (2.4 ± 1.0) × 10^2 μM (Fig. 3*A*). The higher K_m value of several hundred micromolar also was observed during ATP hydrolysis by wild-type F_1 in the absence of LDAO, and it was concluded as representing MgATP binding to noncatalytic sites, which reactivates the MgADP-inhibited enzyme (34–36). Similarly, we regard the high K_m value of (2.4 ± 1.0) × 10^2 μM observed for ATPγS as also reflecting MgATPγS binding to noncatalytic sites. The reason for the slow hydrolysis of ATPγS is mainly the sluggish cleavage of ATPγS on the catalytic site. Actually, the binding property of ATPγS to the catalytic site is not so different from ATP as examined by rapid mixing experiments (32). If the release of thiophosphate, one of the hydrolyzed products of ATPγS, from the catalytic site were extremely slow, it would cause the decrease of V_{max} value. However, it does not seem to be the case, because even in the presence of 100 mM thiophosphate, the ATPase activity was decreased by only 57% (Fig. 3*B*). This inhibition, although a little greater than that exhibited by P_i, which decreased by 51% at 100 mM, cannot explain the extent of decrease in V_{max} value of ATPγS hydrolysis.

Rotation of F_1 by ATPγS. The rotation rate at 20 μM ATPγS (5.9 rps; mean; $n = 2$) was similar to the rate at 2 mM ATPγS (4.4 ± 0.3 rps; mean ± SE; $n = 5$), and discrete 120° steps were observed (Fig. 4*A*). The hydrolysis rate estimated from rotation assay was

‖Here we assume that K_m is expressed as $(k_{off} + k_{cat})/k_{on}$, where k_{on} is a second-order ATP-binding rate constant, k_{off} is an ATP-release rate constant, and k_{cat} is a rate constant to produce products from enzyme-substrate complex.

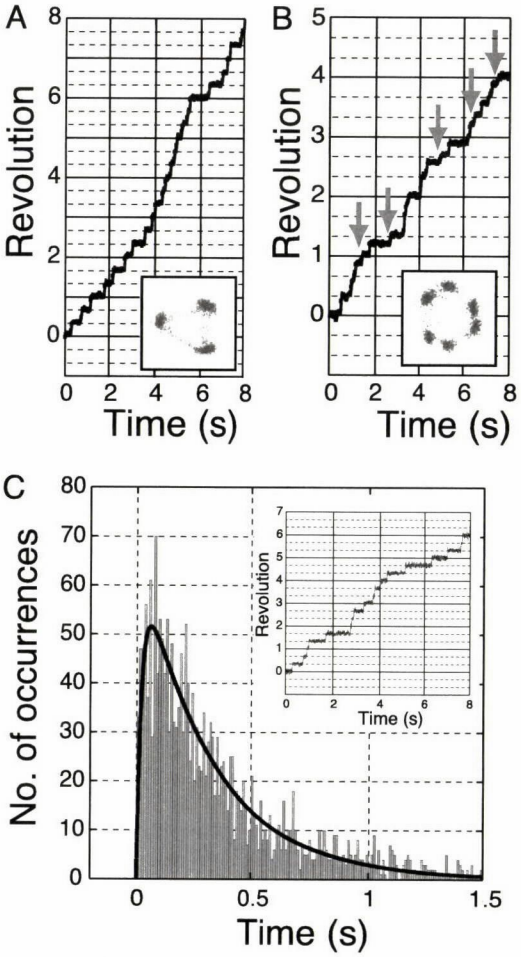

Fig. 2. (*A* and *B*) Typical time course of the stepwise rotations of $F_{1(\beta\text{-E190D})}$ at 2 mM (*A*) and 2 μM (*B*) ATP at 30 fps. (*Insets*) The trace of the centroid of the beads images. Arrows indicate the positions at which 40° substep was observed. (*C*) The histogram of dwelling times between steps in the presence of 2 mM ATP at 500 fps. Total counts are 2,068. (*Inset*) The time course of rotation at 500 fps. Black line shows fit with two exponentials assuming there were two rate-limiting reactions: constant × (exp($-k_1 \times t$) −exp($-k_2 \times t$)), where k_1 = 50.3 ± 0.2 s^{-1} (mean ± SE; time constant, 19.9 ± 0.1 ms) and k_2 = 3.12 ± 0.22 s^{-1} (time constant, 321 ± 22 ms).

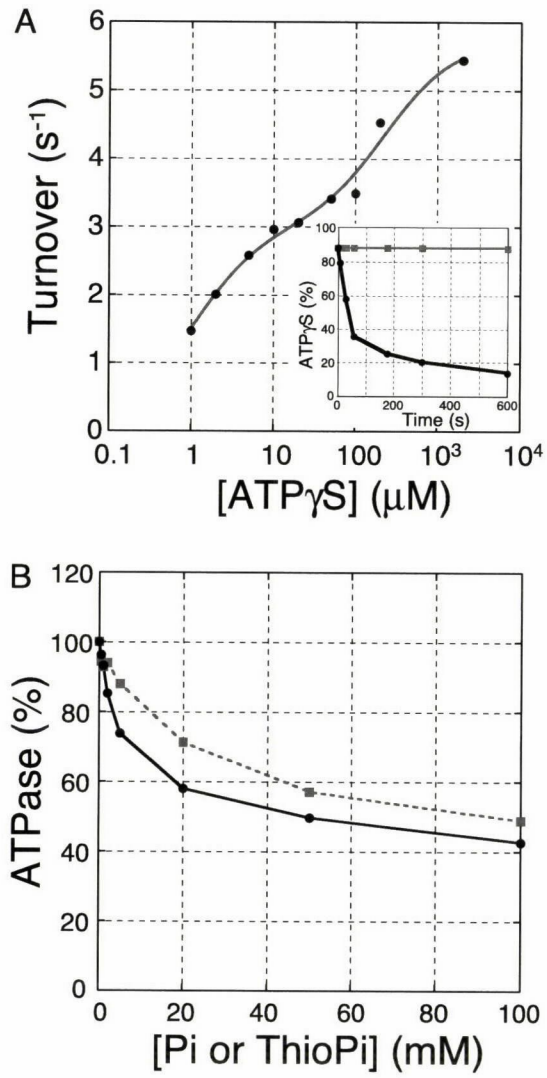

Fig. 3. (*A*) ATPγS hydrolysis rate as a function of ATPγS concentration. The solid curve is the fit with two K_m values: $V = (V_{max1} \times K_{m2} \times [ATP] + V_{max2} \times [ATP]^2)/([ATP]^2 + K_{m2} \times [ATP] + K_{m1} \times K_{m2})$, where V_{max1} = 3.0 ± 0.2 s^{-1}, V_{max2} = 5.8 ± 0.3 s^{-1}, K_{m1} = 1.0 ± 0.3 μM, and K_{m2} = (2.4 ± 1.0) × 10^2 μM. (*Inset*) The time courses of ATPγS hydrolysis. Black circles, in the presence of 200 μM ATPγS and 0.5 μM F_1 (wild type); gray squares, in the absence of F_1. (*B*) The rate of ATP hydrolysis in the presence of phosphate (gray squares) or thiophosphate (black circles). Values are means ± SE.

twice as high as that measured in the bulk solution, presumably because some of the F_1 molecules in the solution were in the MgADP-inhibited form. The difference was greater than in the case of ATP because we could not use an ATP-regenerating system for ATPγS. The dwells between the steps are independent of [ATPγS], indicating that they are the interim dwells. This finding also excluded a possibility that rotation was driven by contaminated ATP that was <0.1%, as assessed with an anion-exchange HPLC. At 0.5 μM ATPγS,** rotations with 80° and 40° substeps were observed (Fig. 4*B*). From analysis of ATPγS-binding dwells, the second-order rate constant for ATPγS binding to F_1 (k_{on}) was estimated to be (2.6 ± 0.1) × 10^7 $M^{-1}{\cdot}s^{-1}$ (mean ± SE), which is similar to that of ATP [(3.0 ± 0.1) × 10^7 $M^{-1}{\cdot}s^{-1}$] (18) and agrees well with the value determined from a biochemical experiment [(2.8 ± 0.2) × 10^7 $M^{-1}{\cdot}s^{-1}$] (32). Histogram of the interim dwells showed an upward convex shape passing through the origin (Fig. 4*C*), which can be fit by double exponentials with two time constants of 61.0 ± 2.6 ms and 8.20 ± 0.6 ms (mean ± SE). Biochemical studies suggest that ATPγS decelerates the cleavage rate by 30-fold (23). Thus, the longer dwell most likely corresponds to the slow cleavage of ATPγS and the short one corresponds to the product release, as discussed later.

Rotation of $F_{1(\beta\text{-E190D})}$ by ATPγS. We assume that both the 320-ms event of $F_{1(\beta\text{-E190D})}$ in hydrolysis of ATP and the 61-ms event of F_1 in hydrolysis of ATPγS correspond to the same rate-limiting reaction, that is, cleavage of terminal (thio)phosphate moiety of ATP or ATPγS. To further confirm this point, we analyzed the rotation of $F_{1(\beta\text{-E190D})}$ driven by the hydrolysis of ATPγS. At 2 mM ATPγS, very slow rotation (2.3 × 10^{-2} ± 0.3 rps; mean ± SE; n = 5) was observed, and rotation proceeded with discrete 120° steps (Fig. 5*A*). Histogram of the dwelling times showed an apparent single-exponential decay, and a value of 12.5 ± 0.4 s

**At low ATPγS concentrations (<2 μM), rotating beads were rarely seen in the observation field, probably because of the MgADP inhibition. Usually the ATP-regenerating system eliminates ADP, but it cannot be used in these experiments because it replaces ATPγS with ATP.

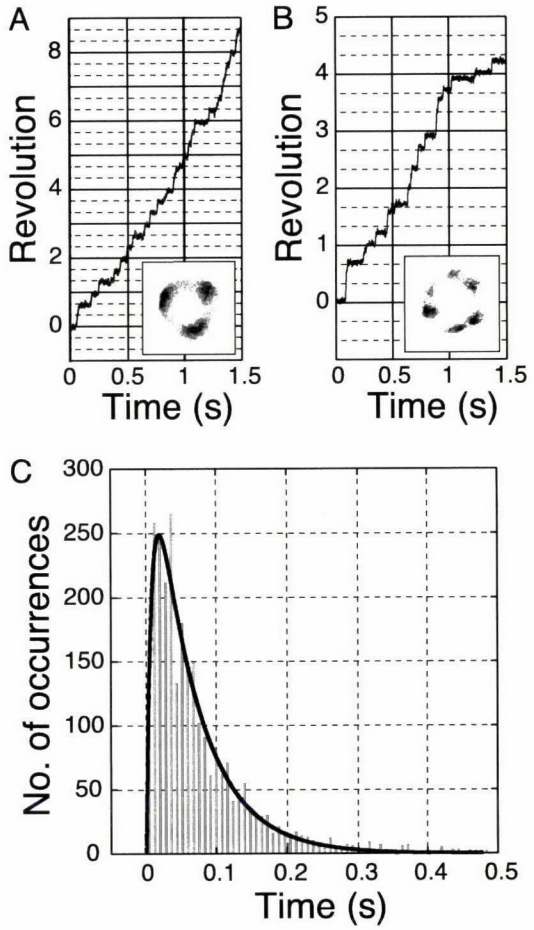

Fig. 4. (*A* and *B*) Typical time course of the rotation of 0.2-μm duplex beads attached to γ-subunit of F_1 (wild type) with 2 mM (*A*) and 0.5 μM (*B*) ATPγS at 500 fps. (*Insets*) The trace of the centroid of the bead images. (*C*) The histogram of the dwelling times between steps at 2 mM ATPγS by using a fast-framing camera at 500 fps (2,674 dwells). Black line shows fit with two exponentials as in Fig. 2C: $k_1 = (1.22 \pm 0.09) \times 10^2\ s^{-1}$ (mean $\pm$ SE; time constant, 8.20 $\pm$ 0.6 ms) and $k_2 = 16.4 \pm 0.7\ s^{-1}$ (time constant, 61.0 $\pm$ 2.6 ms).

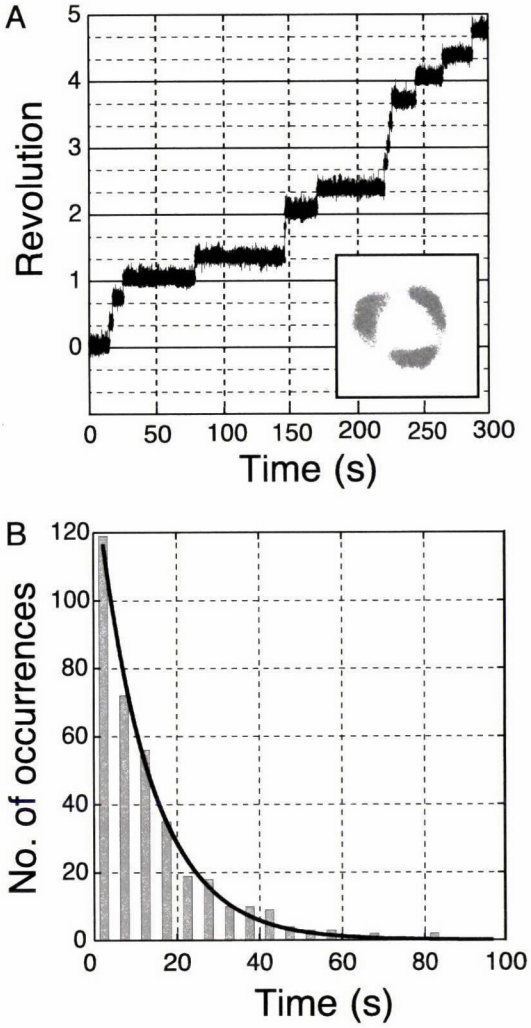

Fig. 5. (*A*) Time course of the stepwise rotation of $F_{1(\beta\text{-E190D})}$ in the presence of 2 mM ATPγS at 250 fps. (*Inset*) The trace of the centroid of 0.2-μm beads. (*B*) The histogram of dwelling times between steps in the presence of 2 mM ATPγS at 250 fps (363 dwells). Black line shows a single exponential fit: constant $\times$ exp($-k \times t$), where k is the rate constant and t is the dwelling time; $k = (8.00 \pm 0.27) \times 10^{-2}\ s^{-1}$ (mean $\pm$ SE; time constant, 12.5 $\pm$ 0.4 s)

(mean $\pm$ SE) was obtained as the time constant[††] (Fig. 5*B*). The very long time constant observed in the combination of the mutation and ATPγS is consistent with the contention that the main effect of βE190D mutation and ATPγS is to retard the same step of ATP(γS) cleavage. Furthermore, if we assume that their effects are energetically additive, the very long time constant leads a conclusion that one of the two 1-ms events in the interim dwell of the wild-type F_1 is the cleavage of ATP. Actually, if we assume that one of the two 1-ms events in the interim dwell of the wild-type F_1 is the cleavage of ATP at the catalytic site, the mutation βE190D and ATPγS slowed down the time constant of this event 320-fold and 61-fold, respectively. Then, if modification of a catalytic residue and a substrate might exhibit a dual effect on the catalytic rate (rotation rate), the time constant of ATPγS cleavage by $F_{1(\beta\text{-E190D})}$ is predicted to be 19.5 s (for 1 ms $\times$ 320 $\times$ 61). The value obtained from the experiment, 12.5 s, is fairly close to this predicted value and strongly suggests that these assumptions are valid. This agreement also exclude the possibility that a third, unidentified event with a faster time constant corresponds to the ATP cleavage. For example, if an event of 0.1 ms corresponded to the ATP cleavage at the catalytic site, the mutation βE190D and ATPγS would retard the step by 3,200-fold and 610-fold, respectively. Then, the combination of the mutant and ATPγS would cause 1,952,000-fold deceleration, resulting in a time constant as long as 195.2 s. This value is far larger than the experimental value observed, and the above possibility is proved to be unlikely. Thus, cleavage of ATP on F_1 occurs in 1 ms during the interim dwell, and we call this interim dwell the catalytic dwell. The present results also indicate that the 80° substep rotation takes place before the cleavage of ATP into ADP and P_i and the 40° substep rotation requires completion of the cleavage.

Conclusion

In the function of F_1, catalysis and rotation seems to be tightly coupled. Therefore, altered catalysis, either by mutation or different substrate, results in altered rotation, and analysis of the latter with good reference of the former can bring a insight into the mechanism of F_1 motor. We have adopted this approach and obtained results leading to the conclusion that the ATP cleavage reaction at the catalytic site is one of the 1-ms events in the

[††]A short dwell with a time constant <0.2 s might exist but could not be seen in the present observations.

catalytic dwell. Contrary to the previous hypothesis (21), it is clearly indicated that the 80° substep rotation takes place before the cleavage of ATP into ADP and P_i. It also is established that the 40° substep rotation requires completion of the cleavage. This conclusion was to be expected but needed to be examined experimentally because the two 1-ms events can be any events (except ATP binding) that occur in F_1 during catalysis. Even a conformational isomerization of F_1 without changes of chemical species of bound substrate/product cannot be excluded as a candidate. Now that one of the 1-ms events is determined to be an ATP cleavage, the next challenge will be the identification of another 1-ms event and clarification of the sequence of the events.[‡‡]

[‡‡]If the two catalytic events occur at the same β-subunit, ATP hydrolysis must occur first followed by release of products But in the case where the two events occur at different β-subunits, ATP hydrolysis could occur after product release from another β-subunit

We thank H. Noji, R. Iino, T. Masaike, Y. Hirono-Hara, T. Ariga, H. Ueno, T. Suzuki, and M. Takeda for critical discussions and technical advice. K.S. is supported by research fellowships from the Japan Society for the Promotion of Science for Young Scientists.

1 Mitchell, P (1961) *Nature* **191,** 144–148
2 Boyer, P. D (2000) *Biochim Biophys Acta* **1458,** 252–262
3 Yoshida, M , Muneyuki, E & Hisabori, T (2001) *Nat. Rev. Mol Cell Biol* **2,** 669–677
4 Noji, H & Yoshida, M (2001) *J. Biol Chem.* **276,** 1665–1668
5 Abrahams, J P , Leslie, A. G , Lutter, R & Walker, J E (1994) *Nature* **370,** 621–628.
6 Boyer, P D (1993) *Biochim Biophys Acta* **1140,** 215–250.
7 Kaim, G & Dimroth, P. (1998) *EMBO J.* **17,** 5887–5895.
8 Sambongi, Y., Iko, Y , Tanabe, M., Omote, H , Iwamoto-Kihara, A., Ueda, I , Yanagida, T , Wada, Y & Futai, M. (1999) *Science* **286,** 1722–1724
9 Hutcheon, M L , Duncan, T. M , Ngai, H & Cross, R. L (2001) *Proc. Natl Acad Sci USA* **98,** 8519–8524.
10 Nishio, K , Iwamoto-Kihara, A , Yamamoto, A., Wada, Y. & Futai, M (2002) *Proc. Natl Acad Sci. USA* **99,** 13448–13452.
11 Tsunoda, S. P., Aggeler, R , Yoshida, M & Capaldi, R A (2001) *Proc Natl. Acad. Sci. USA* **98,** 898–902.
12 Sabbert, D , Engelbrecht, S. & Junge, W. (1996) *Nature* **381,** 623–625.
13 Noji, H., Yasuda, R , Yoshida, M. & Kinosita, K., Jr. (1997) *Nature* **386,** 299–302
14 Kato-Yamada, Y , Noji, H., Yasuda, R , Kinosita, K., Jr., & Yoshida, M. (1998) *J Biol Chem.* **273,** 19375–19377
15 Omote, H , Sambonmatsu, N , Saito, K , Sambongi, Y , Iwamoto-Kihara, A., Yanagida, T , Wada, Y & Futai, M (1999) *Proc Natl Acad. Sci. USA* **96,** 7780–7784
16 Adachi, K , Yasuda, R., Noji, H , Itoh, H , Harada, Y., Yoshida, M. & Kinosita, K , Jr (2000) *Proc Natl Acad Sci. USA* **97,** 7243–7247.
17 Yasuda, R , Noji, H , Kinosita, K , Jr , & Yoshida, M. (1998) *Cell* **93,** 1117–1124
18 Yasuda, R , Noji, H , Yoshida, M., Kinosita, K., Jr., & Itoh, H. (2001) *Nature* **410,** 898–904
19 Cross, R L., Grubmeyer, C. & Penefsky, H S. (1982) *J Biol Chem.* **257,** 12101–12105
20. Grubmeyer, C , Cross, R L & Penefsky, H. S. (1982) *J Biol. Chem* **257,** 12092–12100.
21 Senior, A E., Nadanaciva, S & Weber, J (2002) *Biochim Biophys Acta* **1553,** 188–211
22 Amano, T , Tozawa, K , Yoshida, M. & Murakami, H. (1994) *FEBS Lett* **348,** 93–98
23. Turina, P & Capaldi, R A. (1994) *Biochemistry* **33,** 14275–14280.
24. Kunkel, T A., Bebenek, K & McClary, J. (1991) *Methods Enzymol.* **204,** 125–139.
25 Amano, T., Hisabori, T , Muneyuki, E. & Yoshida, M. (1996) *J Biol. Chem* **271,** 18128–18133.
26 Matsui, T. & Yoshida, M. (1995) *Biochim. Biophys. Acta* **1231,** 139–146.
27 Kato, Y , Sasayama, T., Muneyuki, E & Yoshida, M (1995) *Biochim. Biophys. Acta* **1231,** 275–281
28 Mitome, N., Ono, S., Suzuki, T., Shimabukuro, K., Muneyuki, E. & Yoshida, M (2002) *Eur. J. Biochem* **269,** 53–60.
29. Yoshida, M., Posper, J. W., Allison, W. S. & Esch, F S. (1981) *J. Biol. Chem.* **256,** 148–153
30 Ohtsubo, M., Yoshida, M , Ohta, S , Kagawa, Y., Yohda, M. & Date, T. (1987) *Biochem. Biophys Res Commun* **146,** 705–710
31 Lobau, S., Weber, J , Wilke-Mounts, S & Senior, A. E. (1997) *J. Biol Chem* **272,** 3648–3656.
32. Masaike, T , Muneyuki, E., Noji, H , Kinosita, K , Jr., & Yoshida, M (2002) *J. Biol Chem.* **277,** 21643–21649.
33 Hirono-Hara, Y., Noji, H , Nishiura, M , Muneyuki, E., Hara, Y. K., Yasuda, Y., Kinosita, K., Jr., & Yoshida, M. (2001) *Proc. Natl. Acad Sci. USA* **98,** 13649–13654.
34 Jault, J M & Allison, W S (1993) *J. Biol. Chem.* **268,** 1558–1566
35 Ren, H & Allison, W. S (2000) *J. Biol. Chem.* **275,** 10057–10063.
36 Ono, S , Hara, Y. K., Hirao, T , Matsu, T., Noji, H., Yoshida, M & Muneyuki, E (2003) *Biochim Biophys Acta* **1607,** 35–44

centrifugation. Respiration and OXPHOS enzyme activities were normalized for protein concentration using the Coomassie Stain kit (Pierce)[9,19]. Mitochondrial membrane potential was calculated from mitochondrial uptake of TPP^+ using a TPP^+-sensitive electrode[12]. The sensitivity of the mtPTP to undergo permeability transition was examined in liver mitochondria of 10-month-old *Ant1*$^{-/-}$, *Ant2*$^{fl/fl}$, *Alb-Cre* animals by TPP^+ release after sequential additions of 10 nM $CaCl_2$ (ref. 13). The mtPTP modulators used were 1 mM *t*-H_2O_2, 0.1 mM diamide, 100 μM ATR and 125 μM ADP (Fig. 3).

Mitochondrial PTP activation was also monitored by mitochondrial swelling using light scattering at 546 nm for 10 min in 1.5 ml with 1 mg mitochondrial protein and 16.5 nmol $CaCl_2$. The reaction was initiated by the addition of 0.1 μM ruthenium red and 1 μM FCCP.

Hepatocytes were isolated from 12- to 15-month-old anaesthetized mice, perfused *in situ* with collagenase-dispase medium (Invitrogen). Hepatocytes were gently released, filtered and cultured on collagen-coated cover glasses or plates in Waymouth's MB-752/1 medium[3]. Hepatocyte sensitivity to Ca^{2+} ionophore was examined by extent of cell death assessed by the percentage of total cellular lactate dehydrogenase (LDH) released into the medium[20] after treatment with 5 to 50 μM Bt-A23187 for 1 h, without or with a 30 min pretreatment of either 1 μM CsA or 50 μM *z*-VAD 17 (Fig. 4). Receptor-induced cell death was monitored by analysis of nuclear morphology using Hoechst 33258 (Molecular Probes) staining after treatment with 100 ng ml^{-1} of murine recombinant TNF-α (R&D Systems) or 4 ng ml^{-1} of human recombinant Fas ligand (Upstate), with or without 0.2 μg ml^{-1} actinomycin D (Fig. 4).

Received 14 August; accepted 10 November 2003; doi:10.1038/nature02229

1. Zoratti, M. & Szabo, I. The mitochondrial permeability transition. *Biochim. Biophys. Acta* **1241**, 139–176 (1995).
2. Marzo, I. *et al.* Bax and adenine nucleotide translocator cooperate in the mitochondrial control of apoptosis. *Science* **281**, 2027–2031 (1998).
3. Levy, S. E., Chen, Y. S., Graham, B. H. & Wallace, D. C. Expression and sequence analysis of the mouse adenine nucleotide translocase 1 and 2 genes. *Gene* **254**, 57–66 (2000).
4. Ellison, J. W., Salido, J. C. & Shapiro, L. J. Genetic mapping of the adenine nucleotide translocase 2 gene (*Ant2*) to the mouse proximal X chromosome. *Genomics* **36**, 369–371 (1996).
5. Graham, B. *et al.* A mouse model for mitochondrial myopathy and cardiomyopathy resulting from a deficiency in the heart/skeletal muscle isoform of the adenine nucleotide translocator. *Nature Genet.* **16**, 226–234 (1997).
6. Stepien, G., Torroni, A., Chung, A. B., Hodge, J. A. & Wallace, D. C. Differential expression of adenine nucleotide translocator isoforms in mammalian tissues and during muscle cell differentiation. *J. Biol. Chem.* **267**, 14592–14597 (1992).
7. Lunardi, J., Hurko, O., Engel, W. K. & Attardi, G. The multiple ADP/ATP translocase genes are differentially expressed during human muscle development. *J. Biol. Chem.* **267**, 15267–15270 (1992).
8. Postic, C. & Magnuson, M. A. DNA excision in liver by an albumin-Cre transgene occurs progressively with age. *Genesis* **26**, 149–150 (2000).
9. Boss, O., Hagen, T. & Lowell, B. B. Uncoupling proteins 2 and 3: potential regulators of mitochondrial energy metabolism. *Diabetes* **49**, 143–156 (2000).
10. Petronilli, V., Nicolli, A., Costantini, P., Colonna, R. & Bernardi, P. Regulation of the permeability transition pore, a voltage-dependent mitochondrial channel inhibited by cyclosporin A. *Biochim. Biophys. Acta* **1187**, 255–259 (1994).
11. Bernardi, P. Modulation of the mitochondrial cyclosporin A-sensitive permeability transition pore by the proton electrochemical gradient. Evidence that the pore can be opened by membrane depolarization. *J. Biol. Chem.* **267**, 8834–8839 (1992).
12. Esposito, L. A. *et al.* Mitochondrial oxidative stress in mice lacking the glutathione peroxidase-1 gene. *Free Radic. Biol. Med.* **28**, 754–766 (2000).
13. Kokoszka, J. E., Coskun, P., Esposito, L. & Wallace, D. C. Increased mitochondrial oxidative stress in the Sod2$^{+/-}$ mouse results in the age-related decline of mitochondrial function culminating in increased apoptosis. *Proc. Natl Acad. Sci. USA* **98**, 2278–2283 (2001).
14. Halestrap, A. P., Woodfield, K. Y. & Connern, C. P. Oxidative stress, thiol reagents, and membrane potential modulate the mitochondrial permeability transition by affecting nucleotide binding to the adenine nucleotide translocase. *J. Biol. Chem.* **272**, 3346–3354 (1997).
15. Lapidus, R. G. & Sokolove, P. M. The mitochondrial permeability transition. Interactions of spermine, ADP, and inorganic phosphate. *J. Biol. Chem.* **269**, 18931–18936 (1994).
16. Novgorodov, S. A., Gudz, T. I., Brierley, G. P. & Pfeiffer, D. R. Magnesium ion modulates the sensitivity of the mitochondrial permeability transition pore to cyclosporin A and ADP. *Arch. Biochem. Biophys.* **311**, 219–228 (1994).
17. Qian, T., Herman, B. & Lemasters, J. J. The mitochondrial permeability transition mediates both necrotic and apoptotic death of hepatocytes exposed to Br-A23187. *Toxicol. Appl. Pharmacol.* **154**, 117–125 (1999).
18. Hatano, E. *et al.* The mitochondrial permeability transition augments Fas-induced apoptosis in mouse hepatocytes. *J. Biol. Chem.* **275**, 11814–11823 (2000).
19. Trounce, I. A., Kim, Y. L., Jun, A. S. & Wallace, D. C. Assessment of mitochondrial oxidative phosphorylation in patient muscle biopsies, lymphoblasts, and transmitochondrial cell lines. *Methods Enzymol.* **264**, 484–509 (1996).
20. Leist, M. *et al.* Murine hepatocyte apoptosis induced *in vitro* and *in vivo* by TNF-α requires transcriptional arrest. *J. Immunol.* **153**, 1778–1788 (1994).

Acknowledgements We thank M. Magnuson for providing the *Alb-Cre* transgenic mice, L. Hayes for mouse husbandry and genotyping, and H. Yi for the electron microscope analysis. This work was funded by US National Institutes of Health grants awarded to D.C.W., G.R.M. and D.P.J.

Competing interests statement The authors declare competing financial interests: details accompany the paper on **www.nature.com/nature**

Correspondence and requests for materials should be addressed to D.C.W. (dwallace@uci.edu).

Mechanically driven ATP synthesis by F_1-ATPase

Hiroyasu Itoh[1,2], Akira Takahashi[3], Kengo Adachi[4], Hiroyuki Noji[5], Ryohei Yasuda[6], Masasuke Yoshida[7] & Kazuhiko Kinosita Jr[4]

[1]*Tsukuba Research Laboratory, Hamamatsu Photonics KK, and* [2]*CREST "Creation and application of soft nano-machine, the hyperfunctional molecular machine" Team 13*, Tokodai, Tsukuba 300-2635, Japan*
[3]*System Division, Hamamatsu Photonics KK, Joko, Hamamatsu 431-3103, Japan*
[4]*Center for Integrative Bioscience, Okazaki National Research Institutes, Okazaki 444-8585, Japan*
[5]*Institute of Industrial Science, University of Tokyo, Tokyo 153-8505, Japan*
[6]*Cold Spring Harbor Laboratory, Cold Spring Harbor, New York 11724 USA*
[7]*ERATO "ATP System", 5800-3 Nagatsuta, Yokohama 226-0026, Japan*

ATP, the main biological energy currency, is synthesized from ADP and inorganic phosphate by ATP synthase in an energy-requiring reaction[1–3]. The F_1 portion of ATP synthase, also known as F_1-ATPase, functions as a rotary molecular motor: *in vitro* its γ-subunit rotates[4] against the surrounding $\alpha_3\beta_3$ subunits[5], hydrolysing ATP in three separate catalytic sites on the β-subunits. It is widely believed that reverse rotation of the γ-subunit, driven by proton flow through the associated F_o portion of ATP synthase, leads to ATP synthesis in biological systems[1–3,6,7]. Here we present direct evidence for the chemical synthesis of ATP driven by mechanical energy. We attached a magnetic bead to the γ-subunit of isolated F_1 on a glass surface, and rotated the bead using electrical magnets. Rotation in the appropriate direction resulted in the appearance of ATP in the medium as detected by the luciferase–luciferin reaction. This shows that a vectorial force (torque) working at one particular point on a protein machine can influence a chemical reaction occurring in physically remote catalytic sites, driving the reaction far from equilibrium.

When isolated F_1 hydrolyses ATP, its central γ-subunit rotates anticlockwise[4] when viewed from above in Fig. 1a, with an efficiency of chemical-to-mechanical energy conversion approaching 100% (ref. 8). The purpose of this study was to show that the chemo-mechanical coupling in the F_1 motor is completely reversible, and that reversal is achieved by manipulating a single variable—that is, the rotary angle of the γ-subunit. Any molecular machine would be reversible if one could manipulate all constituent atoms at will. Whether one or a few thermodynamic handles exist in a chemo-mechanical molecular machine such that its operation can be controlled through that handle in both directions is an important but unresolved issue. For example, whether one can synthesize ATP by pulling back a linear molecular motor such as myosin or kinesin—and if so, where to pull—is unknown. Reversal of the whole ATP synthase is well documented[1,9], including the demonstration of γ-subunit reorientation under synthesis conditions[10], but whether or not the γ-subunit angle serves as a single handle for F_1 reversal has not been tested.

To prove this reversibility, we used $\alpha_3\beta_3\gamma$, the minimal subcomplex of F_1 that shows ATP-catalysed rotation[4]. The subcomplex was attached to a glass surface through histidine residues engineered at the amino terminus of the β-subunits, and a magnetic bead coated with streptavidin was attached to the γ-subunit, which had been biotinylated at two engineered cysteines (Fig. 1a). The beads were rotated with magnets (Fig. 1b–d) in a medium containing ADP and phosphate as substrates and the luciferin–luciferase system[11,12], which emits a photon when it captures and hydrolyses ATP. The initial idea was to count these chemiluminescent photons (Fig. 1b); however, background luminescence originating from contaminant ATP present in ADP even after purification was a problem. Thus, the

volume of medium per active F_1 molecule had to be small.

First, we tried to reduce the volume by making microdroplets in oil (Fig. 2a). Figure 2b shows data from a 4×4 array of droplets in one chamber. The beads in droplets were rotated at 10 Hz alternately for 5 min each in the direction of hydrolysis (anticlockwise when viewed from top in Fig. 1a) and synthesis (clockwise). As seen in Fig. 2b, 14 out of 16 droplet curves showed the M-shaped pattern of photon counts expected for the sequence of rotation direction when the overall decline was taken into account. The decline was due to the gradual disappearance of the aqueous phase into oil: although we saturated the oil with water before the experiment, droplets tended to shrink over time. For random photon counts, the probability of observing a slanting M shape is 8^{-1}. The probability of observing 14 or more M shapes out of 16 is 2×10^{-11}. The data set shown in Fig. 2b thus strongly indicates mechanical synthesis. The experiment is extremely difficult (at most a few beads rotate in each droplet), however, and we have obtained only a few more data sets that contained several M-shaped patterns.

We thus tried to increase the number of rotating beads in an ordinary observation chamber (Fig. 1c) by infusing a concentrated solution of beads carrying F_1. To allow F_1 to rotate in the proper direction, we derivatized only the bottom surface of the chamber with nickel nitrilo-triacetic acid (Ni^{2+}-NTA), which would specifically bind the β-histidines. In control experiments done in 4 mM ATP (no ADP) and without magnets, we found in the field of view of $1.0 \times 10^5\ \mu m^2$ as many as 480 ± 70 F_1 molecules rotating anticlockwise at the bottom (three chambers). However, the high density of beads resulted in nonspecific binding to the ceiling, where 100 ± 20 beads rotated clockwise (as viewed from above the chamber). We also tested in the ATP medium whether forced rotation by external magnets would damage F_1. After confirming ATP-driven rotation, we turned on the magnets and applied several bursts of hundreds of revolutions at 10 Hz in both directions. When the magnets were turned off, ATP-driven rotation resumed.

Synthesis was shown in the ADP–luciferase medium by accumulating chemiluminescence photons over a series of 5-min intervals in which the magnetic field was rotated at 10 Hz in either direction or turned off. All series produced the expected pattern (Fig. 3a): higher photon counts during clockwise rotation (S, synthesis) than during anticlockwise rotation (H, hydrolysis) or no rotation (N). This graph compiles all data taken in consecutive experiments (about half of the experiments failed at some point, for example during chamber preparation or because of a large focus drift, and did not produce data). Mechanical synthesis in the flat chamber was reproducible, although variation among data was still large.

We note that in most curves shown in Fig. 3a including the total counts, counts during anticlockwise rotation (H) are higher than those at no rotation (N). This is due to the presence of F_1 at the ceiling of the chamber as stated above. For these upside-down F_1 molecules, anticlockwise bead rotation will drive ATP synthesis. Indeed, when we flipped the chamber upside down after obtaining the unbroken blue line in Fig. 3a, the count pattern was reversed, as shown by the broken blue line. Another reason for the higher counts during anticlockwise rotation was that luciferase did not consume all of the newly synthesized ATP in 5 min: as shown by the unbroken lines in Fig. 3b, the luminescence at no rotation was high after ATP synthesis at the arrows. Luminescence decay after ATP mixing was shown to involve a component with a lifetime of about 3 min (see Supplementary Information). Taking all of the above points into account, we consider that mechanical synthesis has been conclusively demonstrated.

Figure 4 shows the effect of rotary speed on the efficiency of ATP synthesis. The synthesis rate apparently saturated above 3 Hz (Fig. 4b). This was because larger beads or bead aggregates failed to rotate at high speeds, as confirmed by direct observation (uncoupling between magnet and bead rotations). Calibration of the

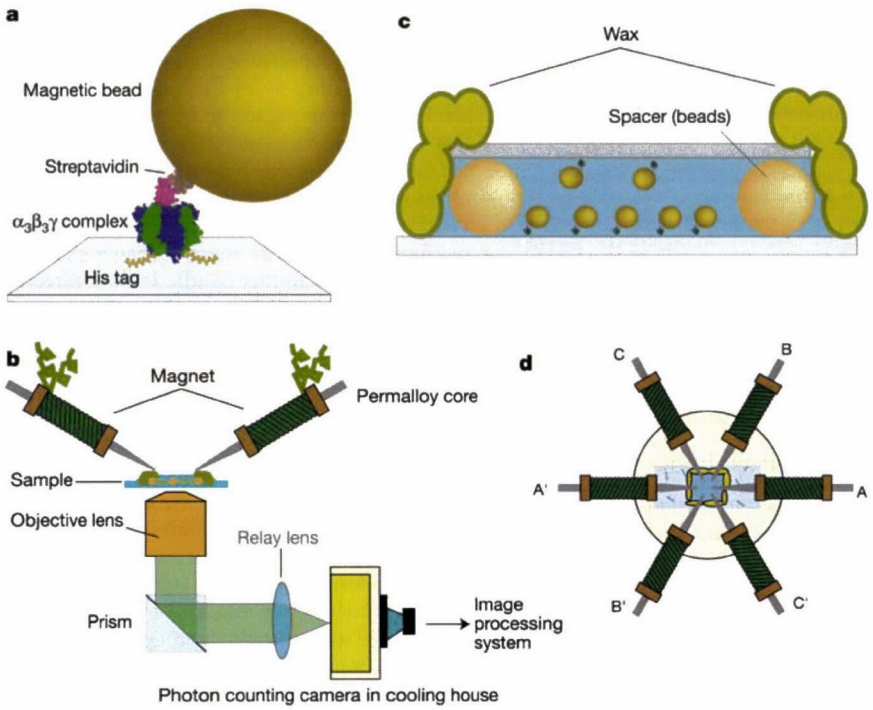

Figure 1 Experimental set-up. **a**, Basic design. The structures of F_1 and streptavidin are from ref. 21 and ref. 22, respectively. The bead is not to scale and the orientation of streptavidin is unknown. **b**, Side view of the optical system. **c**, Observation chamber. Ni^{2+}-NTA was applied only to the bottom surface, but some F_1-conjugated beads rotated on the ceiling. **d**, Top view of the magnets.

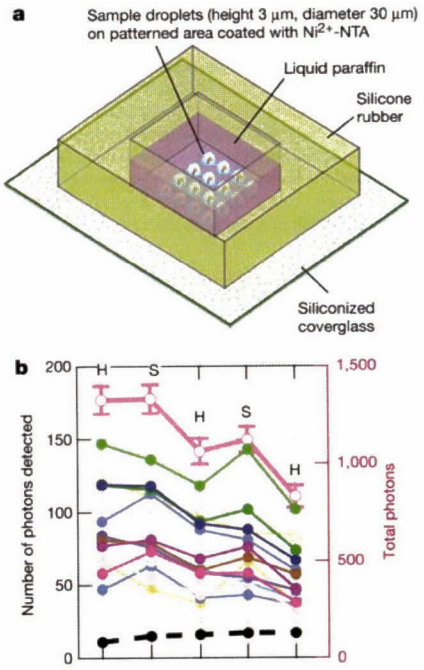

Figure 2 Rotational synthesis in microdroplets. **a**, Observation chamber. On the silanized bottom coverglass, 4 × 4 spots separated by ~50 μm and measuring 20–30 μm were derivatized with Ni^{2+}-NTA, which rendered the spots hydrophilic. An oil layer with a thickness of ~3 mm was placed on top. Using a glass micropipette, we formed a droplet of ~1 pl containing F_1 on each spot and then replaced the solution with one containing beads, ADP, phosphate and the chemiluminescence system. **b**, Simultaneous observation of 16 droplets. Thick magenta curve with open circles represents the sum of all unbroken curves; error bars represent ± 2σ, where σ is the expected s.d. for photon statistics (square root of the total count). The broken curve at the bottom represents a control in which an area outside the droplets was imaged. See Supplementary Information for details.

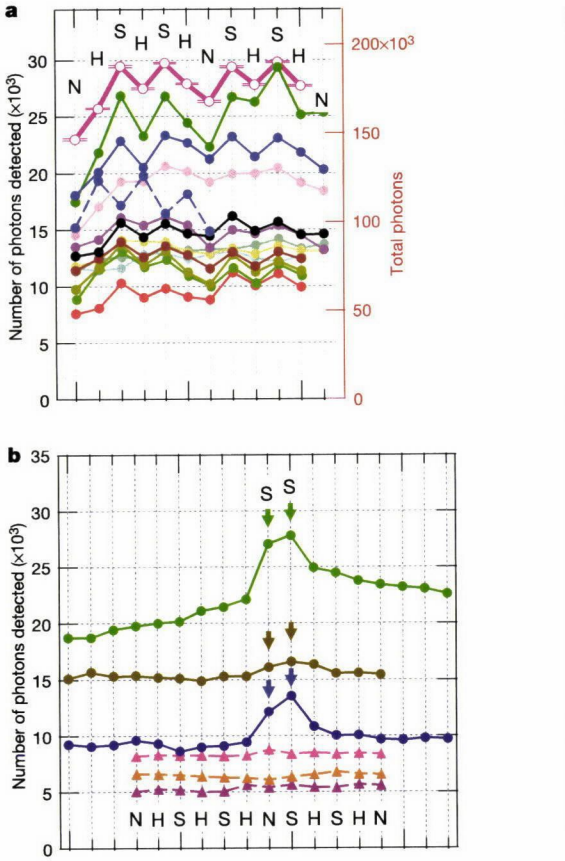

Figure 3 Rotational synthesis in a flat chamber. Each symbol shows the number of photons detected over 5 min in an image area of 7.8 × 10^4 μm^2. N, no rotation; H, 10-Hz rotation in the hydrolysis direction (for F_1 on the bottom of the chamber); S, 10-Hz rotation in the synthesis direction. **a**, Results from 12 chambers, distinguished by different colours. Broken blue curve represents results obtained after the chamber giving rise to the unbroken blue curve was flipped upside down. Thick magenta curve with open circles represents the sum of all unbroken curves; error bars represent ± 4σ (>99.99% confidence). For clarity, some curves have been shifted vertically within ± 1,000 counts. **b**, Control experiments. Unbroken curves show results either without rotation or with imposed clockwise rotation for synthesis at 10 Hz (arrows). Broken curves show experiments carried out as in **a** except that phosphate was omitted from the medium. The counts in the broken curves are low in comparison to the others because phosphate tended to increase the background, apparently by increasing the portion of luciferase that reacted with ATP extremely slowly (see Supplementary Information).

photon-to-ATP ratio (see Supplementary Information) indicated a synthesis rate of about five molecules of ATP per second under rotation at 3 Hz, as compared with the nine molecules of ATP per second expected for the one ATP molecule per 120° scheme[8].

Although Fig. 4 represents our best data so far and variation among chambers is large (Fig. 3a), we anticipate that the coupling between mechanical rotation of the γ-subunit and chemical synthesis is tight, at least at low speeds. The significant synthesis at low speeds (Fig. 4), which were much lower than the maximal rotary speed of 130 Hz of this motor during ATP hydrolysis[13], merits attention. Because the slow rotation was at a constant speed, it is likely that chemical reactions were at quasi-equilibrium at all angles. Rotation by ATP hydrolysis can also be made slow and at a constant speed by attaching a long actin filament to the γ-subunit[8], again suggesting quasi-equilibrium. The implication is that ATP synthesis in F_1 proceeds as a straightforward reversal of the hydrolysis reaction, tracking the same reaction pathway in the opposite direction. On that pathway, both hydrolysis and synthesis reactions are controlled by one mechanical handle, the rotary angle of the γ-subunit. The situation contrasts with the more complex rotary motor of bacterial flagella, where rotational directions can be switched without reversing the proton motive force[14].

ATP synthesis is a chemical reaction that is energetically uphill, requiring 80–100 pN nm of energy under physiological conditions[2]. In the experiments shown here, contaminant ATP amounted to about 1 nM, implying that roughly 30 pN nm of free energy was needed per molecule of ATP synthesized (see Supplementary Information). If F_1, or the motor enzyme myosin, is mixed with high concentrations of ADP and phosphate in the absence of ATP, some ATP is spontaneously formed on the enzyme without input of energy[15–18]. This, however, is a dead-end reaction and the ATP that has been formed is not available in the medium: release of the tightly bound ATP requires an external supply of energy[1,13].

Here we have demonstrated repetitive synthesis by F_1 (~10^3 ATP molecules in 5 min), leading to appearance of the product in the medium. To our knowledge, this is the first accomplishment of artificial chemical synthesis by a vectorial force (although nature presumably has been doing this for millions of years). Pressure could also shift a chemical equilibrium by acting on substrates (and solvent); however, in our experiments the chemical equilibrium *per se* is on the side of almost complete hydrolysis, and a force on a point remote from substrates counters the hydrolysis reaction and pushes the equilibrium to the point of favouring synthesis. Because we still have to rely on nature's nanomachine, the F_1 motor, our

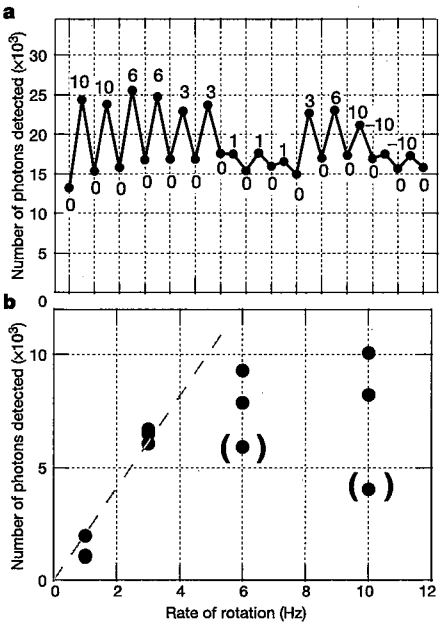

Figure 4 Dependence of synthesis efficiency on the rate of magnet rotation. **a**, Photons detected over an image area of $1.0 \times 10^5\ \mu m^2$ in 5-min periods at various rotary speeds (shown in Hz; negative numbers indicate rotation in the hydrolysis direction). **b**, Photon increments during rotation. From the photon count for each synthesis rotation in **a**, the average of the adjacent no-rotation counts was subtracted. Symbols in the parentheses show the last two measurements for synthesis in **a**; low values for these presumably reflect sample deterioration.

primary goal is to understand fully how it works and thereby to exploit the mechanism in artificial ways. Improving the present system for more quantitative assays, such as the torque and speed dependence of the coupling efficiency, that can be compared with theoretical predictions[7,19] should be our next task. The key is to obtain magnetic beads that are small and uniform in size. □

Methods

Materials

A mutant $\alpha_3\beta_3\gamma$ subcomplex (comprising C193S α-, His_{10}–β-, and S107C, I210C γ-subunits; referred to as F_1 in this paper), derived from the thermophilic *Bacillus* strain PS3, was biotinylated at the only cysteines on the γ-subunit (ref. 8). Streptavidin-coated magnetic beads (Seradyn; nominally 0.7 μm) were lightly centrifuged to remove large beads and aggregates (but elimination was incomplete). Biotinylated F_1 (400 pM) was incubated with beads (~50 pM) in buffer A (50 mM 3-(*N*-morpholino)propanesulphonic acid/KOH, 20 mM K_2SO_4, 4 mM $MgSO_4$, pH 7.6) for 10 min at 23 °C, washed with buffer A, and concentrated with a magnet. Luciferase[12] was a kind gift from Kikkoman Co. We purified ADP (K-salt; Sigma) as described[20] on a Poros HQ/L column (Applied Biosystems).

Observation chamber

For the chamber shown in Fig. 1c, a $32 \times 24\ mm^2$ coverglass was functionalized by a silane coupling agent with an SH group (TSL 8380; GE Toshiba Silicone), and reacted first with 10 mg ml^{-1} maleimide-C_3-NTA (Dojindo) and then with 10 mM $NiCl_2$. Two parallel strips of Lumirror polyester film (TORAY) were placed on the coverglass, and a $18 \times 18\ mm^2$ coverglass coated with hexamethyldisilazane was placed on top to form a flow chamber. We infused ~500 pM F_1-conjugated magnetic beads in buffer A_3 (buffer A containing 3 mg ml^{-1} bovine serum albumin (BSA)) and incubated the chamber for 30 min at 23 °C. After infusing buffer A_3 several times, buffer A containing 10 μM luciferase, 1 mM luciferin, 10 mM K_2PO_4, 200 μM ADP and 1.5 mg ml^{-1} BSA, together with a small number of 3-μm Dynabeads M-280 beads (Dynal) that would eventually serve as spacers, was infused. The spacer strips were carefully removed and the upper coverglass was pressed to reduce the chamber height to ~3 μm, as determined by the spacer beads. The chamber was then sealed with wax and subjected to observation.

Microscopy

The chamber was placed on an inverted ICM 450 microscope (Zeiss). Luminescence was collected with an oil immersion ×60 objective, numerical aperture 1.45 (Olympus) and deflected with a prism to a factory-made side port (Fig. 1b). The beam was focused with an ED Plan ×2 objective (Nikon) onto a cooled photon-counting camera (V8070U-64-N230/C4566 equipped with an Argus 50 image processing system; Hamamatsu Photonics), which recorded centroid positions of incoming photons (counts in the dark: ~15 s^{-1} over the whole image plane). To rotate the beads, we placed three opposing pairs of custom-made electromagnets with a Permalloy core on the chamber (Fig. 1d). The three pairs were activated with a custom circuit 120° out of phase to produce a rotating magnetic field (in either direction).

Received 5 May; accepted 31 October 2003; doi:10.1038/nature02212.

1. Boyer, P. D. The ATP synthase—a splendid molecular machine. *Annu. Rev. Biochem.* **66**, 717–749 (1997).
2. Kinosita, K. Jr, Yasuda, R., Noji, H. & Adachi, K. A rotary molecular motor that can work at near 100% efficiency. *Phil. Trans. R. Soc. Lond. B* **355**, 473–489 (2000).
3. Yoshida, M., Muneyuki, E. & Hisabori, T. ATP synthase—a marvellous rotary engine of the cell. *Nature Rev. Mol. Cell Biol.* **2**, 669–677 (2001).
4. Noji, H., Yasuda, R., Yoshida, M. & Kinosita, K. Jr Direct observation of the rotation of F_1-ATPase. *Nature* **386**, 299–302 (1997).
5. Abrahams, J. P., Leslie, A. G. W., Lutter, R. & Walker, J. E. Structure at 2.8 Å resolution of F_1-ATPase from bovine heart mitochondria. *Nature* **370**, 621–628 (1994).
6. Boyer, P. D. & Kohlbrenner, W. E. in *Energy Coupling in Photosynthesis* (eds Selman, B. R. & Selman-Reimer, S.) 231–240 (Elsevier, Amsterdam, 1981).
7. Oosawa, F. & Hayashi, S. The loose coupling mechanism in molecular machines of living cells. *Adv. Biophys.* **22**, 151–183 (1986).
8. Yasuda, R., Noji, H., Kinosita, K. Jr & Yoshida, M. F_1-ATPase is a highly efficient molecular motor that rotates with discrete 120° steps. *Cell* **93**, 1117–1124 (1998).
9. Turina, P., Samoray, D. & Gräber, P. H^+/ATP ratio of proton transport-coupled ATP synthesis and hydrolysis catalysed by CF_0F_1-liposomes. *EMBO J.* **22**, 418–426 (2003).
10. Zhou, Y., Duncan, T. M. & Cross, R. L. Subunit rotation in *Escherichia coli* F_0F_1–ATP synthase during oxidative phosphorylation. *Proc. Natl Acad. Sci. USA* **94**, 10583–10587 (1997).
11. McElroy, W. D., Seliger, H. H. & White, E. H. Mechanism of bioluminescence, chemiluminescence and enzyme function in the oxidation of firefly luciferin. *Photochem. Photobiol.* **10**, 153–170 (1969).
12. Hattori, N., Kajiyama, N., Maeda, M. & Murakami, S. Mutant luciferase enzymes from fireflies with increased resistance to benzalkonium chloride. *Biosci. Biotechnol. Biochem.* **66**, 2587–2593 (2002).
13. Yasuda, R., Noji, H., Yoshida, M., Kinosita, K. Jr & Itoh, H. Resolution of distinct rotational substeps by submillisecond kinetic analysis of F_1-ATPase. *Nature* **410**, 898–904 (2001).
14. Berg, H. C. The rotary motor of bacterial flagella. *Annu. Rev. Biochem.* **72**, 19–54 (2003).
15. Yoshida, M. The synthesis of enzyme-bound ATP by the F_1-ATPase from the thermophilic bacterium PS3 in 50% dimethylsulfoxide. *Biochem. Biophys. Res. Commun.* **114**, 907–912 (1983).
16. Sakamoto, J. Effect of dimethylsulfoxide on ATP synthesis by mitochondrial soluble F_1-ATPase. *J. Biochem.* **96**, 483–487 (1984).
17. Wolcott, R. G. & Boyer, P. D. The reversal of the myosin and actomyosin ATPase reactions and the free energy of ATP binding to myosin. *Biochem. Biophys. Res. Commun.* **57**, 709–716 (1974).
18. Mannherz, H. G., Schenck, H. & Goody, R. S. Synthesis of ATP from ADP and inorganic phosphate at the myosin-subfragment 1 active site. *Eur. J. Biochem.* **48**, 287–295 (1974).
19. Wang, H. & Oster, G. Energy transduction in the F_1 motor of ATP synthase. *Nature* **396**, 279–282 (1998).
20. Oishi, N. & Sugi, H. *In vitro* ATP-dependent F-actin sliding on myosin is not infuenced by substitution or removal of bound nucleotide. *Biochim. Biophys. Acta* **1185**, 346–349 (1994).
21. Menz, R. I., Walker, J. E. & Leslie, A. G. W. Structure of bovine mitochondrial F_1-ATPase with nucleotide bound to all three catalytic sites: implications for the mechanism of rotary catalysis. *Cell* **106**, 331–341 (2001).
22. Freitag, S., Trong, I. L., Klumb, L., Stayton, P. S. & Stenkamp, R. E. Structural studies of the streptavidin binding loop. *Protein Sci.* **6**, 1157–1166 (1997).

Supplementary Information accompanies the paper on **www.nature.com/nature.**

Acknowledgements We thank T. Hayakawa and T. Hiruma of Hamamatsu Photonics KK who allowed H.I. to work on this project for more than 6 years; S. Brenner for the idea of using microdroplets; M. Sugai for initial work; M. Shio, members of the former CREST Team 13 and the current Kinosita and Yoshida laboratories for help and advice; I. Mizuno, K. Suzuki, S. Uchiyama and Y. Mizuguchi for the photon-counting system; C. Gosse and H. Miyajima for the magnetic tweezers; K. Abe and K. Rikukawa for microscopy; S. Murakami for luciferase; and H. Umezawa and M. Fukatsu for laboratory management. This work was supported in part by Grants-in-Aid from the Ministry of Education, Culture, Sports, Science and Technology of Japan, and Burroughs Wellcome Fund (R.Y.).

Competing interests statement The authors declare that they have no competing financial interests.

Correspondence and requests for materials should be addressed to H.I. (hiritoh@hpk.trc-net.co.jp).

Supplementary Information

Contents

I. Preparation of Micro-Droplet System

We functionalized a 32×24 mm^2 coverglass, pre-cleaned with KOH, with a silane coupling agent having an –SH group (TSL 8380, GE Toshiba Silicone) and reduced the –SH groups with 50 mM DTT. Then we applied, using a glass micropipette, 10 mg ml^{-1} maleimide-C_3-NTA (Dojindo) to a surface such that a droplet of diameter ~10 μm and height <2 μm was formed. After making 4×4 droplets separated by ~50 μm (Fig. S1) and waiting for 5-10 min in a humid atmosphere, we rinsed the coverglass with water. We then applied 10 mM $NiCl_2$ to the treated surface to form 4×4 dots coated with Ni-NTA. After 10 min, we extensively washed the coverglass with water and dried it. We placed a silicone-rubber frame on the coverglass to form a rectangular well, and filled it with mineral oil (Sigma) which had been bubbled with water-saturated oxygen (Fig. S1). Using a micropipette, we applied 2.6 pM F_1 in buffer B (10 mM Tris, 15 mM K_2SO_4, 2 mM $MgSO_4$, pH 8.0) to each Ni-NTA dots, where a micro droplet stayed stably under oil, thanks to the hydrophilic nature of the Ni-NTA surface. After 10 min, we removed unbound F_1 by flushing the droplet with buffer B_6 (buffer B plus 6 mg ml^{-1} BSA), using infusion and suction micropipettes. We then added ~0.5 pM magnetic beads coated with streptavidin in buffer B_6 to the droplet and waited for 20 min. Unbound beads were removed by flushing with buffer B_6. Finally, we replaced the droplet medium with buffer B containing 3 mg ml^{-1} BSA, 5 μM luciferase, 1 mM luciferin, 3 mM K_2PO_4 (pH 7.5) and 100 μM ADP. At this stage, typical droplet size was 30 μm wide (BSA widened the hydrophilic spot) and 3 μm high; with time, droplets tended to flatten and shrink in volume.

The image in Fig. S1, lower right, shows photons detected over a 5-min interval during the synthesis experiment. Droplets were identified in a transmitted image, shown on the left, acquired after the experiment. Photons within a droplet periphery identified by eye (image on lower left) were counted. Photons in one area outside droplets (bottom of the image on

lower left) were also counted to estimate the background level.

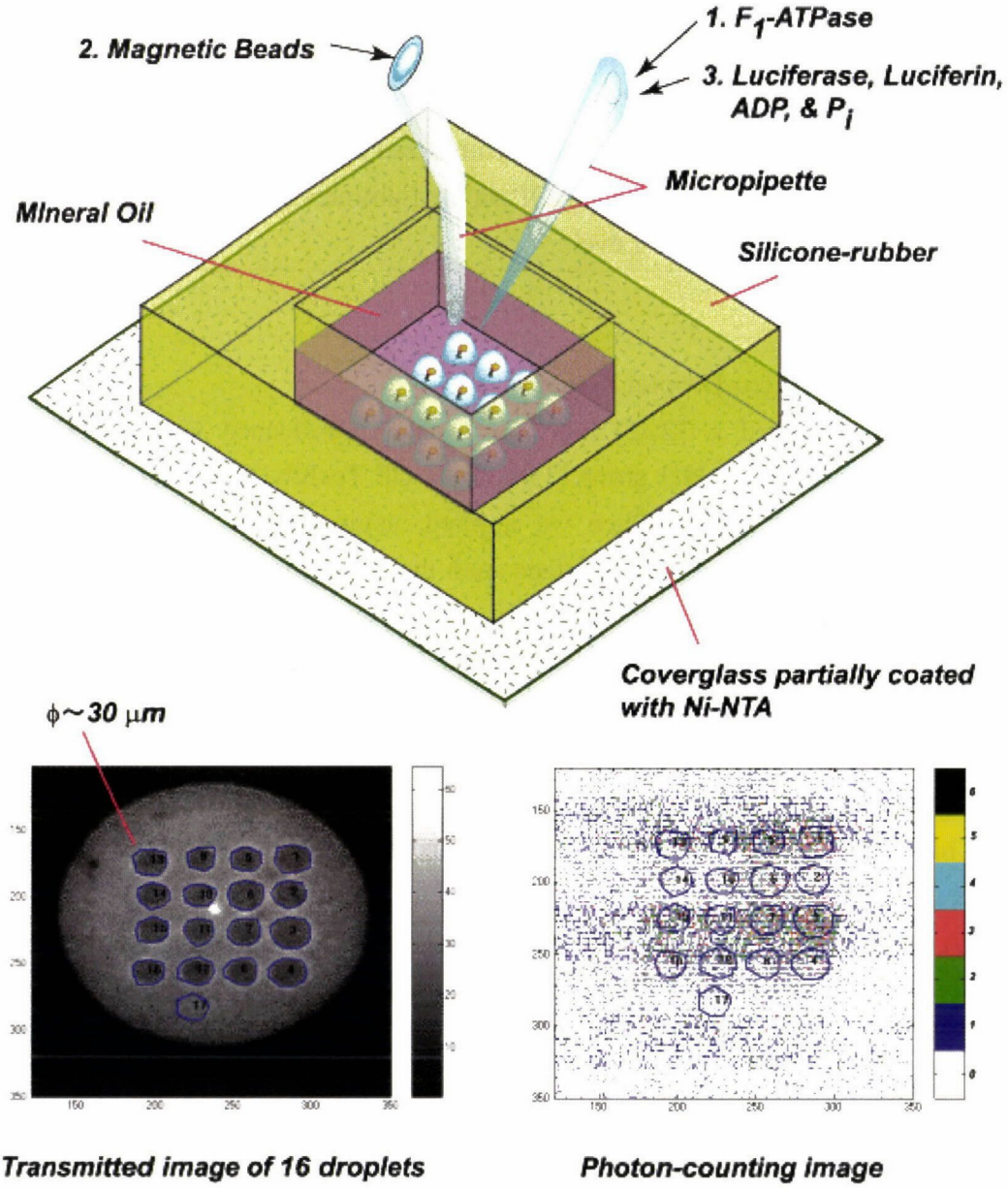

Figure S1. Demonstration of ATP synthesis in micro droplets.

II. Photon-Counting System

The photon-counting camera that we used is made of an image intensifier (V8070U-64-N230, Hamamatsu Photonics) connected to a CCD camera (C2400-77, Hamamatsu) via a tapered optical fibre and housed in a cooling box at -16 °C (C4566,

Hamamatsu). The image of an incident photon is blurred by the intensifier and occupies, typically, 4-5 pixels of the CCD camera; most electrical noises produce a similar point image, but noise due to intra-tube ionization produces a much more intense and wide image. A built-in electronic circuit calculates the centroid of these images and registers one count at the centroid position; even the large ionization noise is reduced to one count. The overall detection efficiency is such that one in about ten incident photons produces one count in the final image (quantum efficiency of the GaAsP photo-cathode is about 40%, but some loss of photoelectrons and the fibre coupling reduce the overall efficiency to ~10%). In the complete darkness, electrical noise in the camera produced 15 counts per second over the whole imaging area of 512×480 pixels. In the experiment shown in Fig. 3 in the main text, we counted photons from a circular area of a sample (7.8×10^4 μm^2), which was projected onto a circle of diameter ~310 pixels on the camera. The dark counts in the circle amounted to ~5 counts per second or 1.5×10^3 counts per 5 min, lower than the count due to the background luminescence from the ADP-luciferase solution.

III. Efficiency of ATP Detection

To estimate the overall efficiency of ATP detection, we put a 3-mm thick silicone rubber sheet, having a 5-mm hole at the centre, on a coverglass and placed it on the microscope stage. 20 μl of the luciferase solution without beads and F_1 (buffer A containing 10 μM luciferase, 1 mM luciferin, 10 mM K_2PO_4, 200 μM ADP, and 1.5 mg ml^{-1} BSA) was placed in the hole. In the complete darkness, 2 μl of a known concentration of ATP was mixed with a pipette and the luminescence flash was monitored with the photon-counting camera (Fig. S2). Over the ATP concentrations of 0.2-2.4 nM, the flash could be approximated by the sum of two exponential decays, one with a time constant of 27±10 s and amplitude 66±15 % and the other 2.9±1.1 min and 34±15 % (11 measurements). The integrated counts over 800 s, excluding the final constant level which constitutes the background luminescence, were proportional to the ATP concentration (Fig. S2, inset) and amounted to 0.009±0.001 detected photons per ATP molecule. Here, the number of ATP molecules contributing to the luminescence was calculated as [image area = 1.0×10^4 μm^2 corresponding to 100×100 pixels on the camera]×[solution height = 1.1 mm]×[ATP concentration], because molecules at different heights h from the focal plane contribute equally to an image pixel: brightness per molecule is proportional to h^{-2} and the number of contributing molecules to h^2. Varying the sample volume in the hole, and thus height (0.25-1.25 mm), verified that the intensity was proportional to the sample height.

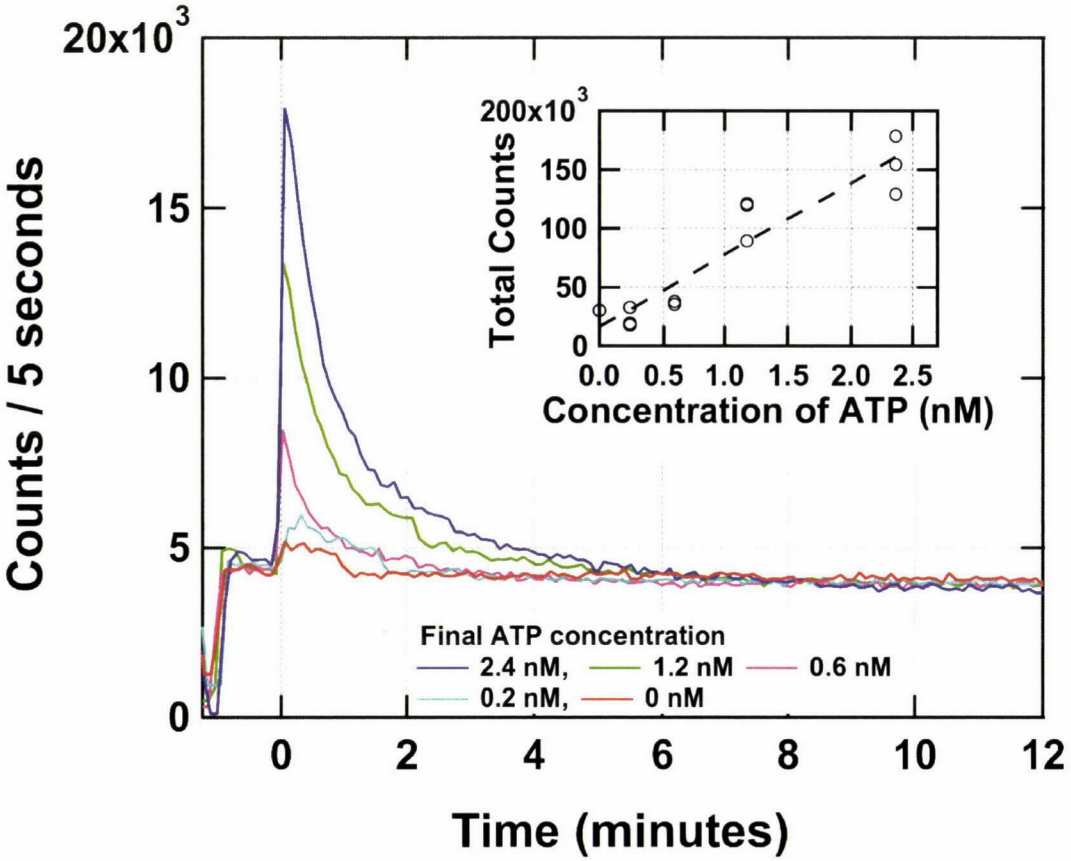

Figure S2. Luminescence flash at various ATP concentrations. The ordinate shows the total number of photons detected over 100×100 pixels on the camera per 5-s exposure time. At about -1 min, a shutter before the camera was closed to bring the pipette tip just above the solution in the chamber. After opening the shutter, ATP was mixed with the pipette at time 0. To aid comparison, the curves are slightly shifted vertically, within 1×10^3 counts, so that the background levels before mixing appear the same. Inset shows the integrated counts, above the final constant level, for 11 measurements (some symbols overlap with another). Linear regression line has a slope of 6.1×10^4 integrated photons per 100×100 pixels per nM ATP.

IV. Number of ATP Molecules Synthesized per Turn

In the experiments with a flat chamber (Figs. 3 and 4 in the main text), there were, on average, 480 F_1 molecules on the bottom and 100 F_1 molecules on the ceiling in the field of view of 1.0×10^5 μm^2. When the beads were rotated clockwise, F_1 on the bottom would synthesise ATP while F_1 on the ceiling would rotate in the hydrolysis direction. Below we

neglect the possible consumption of newly synthesized ATP by F_1 on the ceiling, because most of ATP synthesised on the bottom would be captured by 10 μM luciferase in the solution and because hydrolysis (but not synthesis) of ATP by F_1 tends to be inhibited by MgADP in the medium. We also neglect possible diffusional escape of newly synthesised ATP toward periphery of the observation chamber (18×18 mm^2), because the electromagnets (tip separation ~5 mm) generated torque over the central area of ~10 mm in diameter and diffusion of ATP over 5 mm would take hours.

The data in Fig. 4 in the main text shows that 6,500 photons were detected during 5 min of clockwise rotation at 3 Hz. This amounts, according to the detection efficiency of 0.009 photon per ATP above, to the synthesis of 2,400 ATP molecules s^{-1} in the image area or 5 ATP molecules s^{-1} per F_1. The last number is to be compared with 9 ATP molecules s^{-1} expected at 3 Hz for 100% coupling efficiency.

For the data in Fig. 3a in the main text, there are seven curves for which 12 measurements were made including the last (third) no-rotation data. For these, the difference between the average counts in clockwise and no rotation (S-N) is 2,500 counts per 5 min or 930 ATP molecules s^{-1}. This number is for the imaging area of 7.8×10^4 μm^2 where 370 F_1 molecules would rotate at the bottom. The synthesis rate is thus 2.5 ATP s^{-1} per F_1 at bottom for clockwise rotation, which is considerably lower than the expected rate of 30 ATP s^{-1} for 10 Hz rotation. One reason is that 10 Hz was too fast, as seen in Fig. 4b in the main text, another the large chamber to chamber variation, a third the carry-over of ATP-induced luminescence to the next 5-min period due to slow reaction of luciferase (see below). The apparent rate of synthesis during anticlockwise rotation (H), due to F_1 on the ceiling, is higher than the rate during clockwise rotation (S), but this is also accounted for by the carry-over effect (the sequence was such that H always followed S except for the first H).

V. Effect of Phosphate and ADP on the Luminescence Kinetics of Luciferase

In Fig. 3b in the main text, we report that the luminescence background from luciferase-ADP solution without phosphate was considerably lower than that in the presence of phosphate. Here we show kinetic data possibly explaining this behaviour. Measurements were made as in III, except that phosphate was removed from the solution. As seen in Fig. S3, phosphate adds a slow component to the ATP-induced luminescence flash.

Without ADP, luminescence decayed exponentially to a low level (Fig. S3), suggesting that the long-lasting background luminescence was due to ADP (also see VI below). The integrated photon counts above the background level are within ±10% of each other among the three conditions, implying that the photon/ATP ratio estimated in III above is valid

whether ADP and Pi are absent or not.

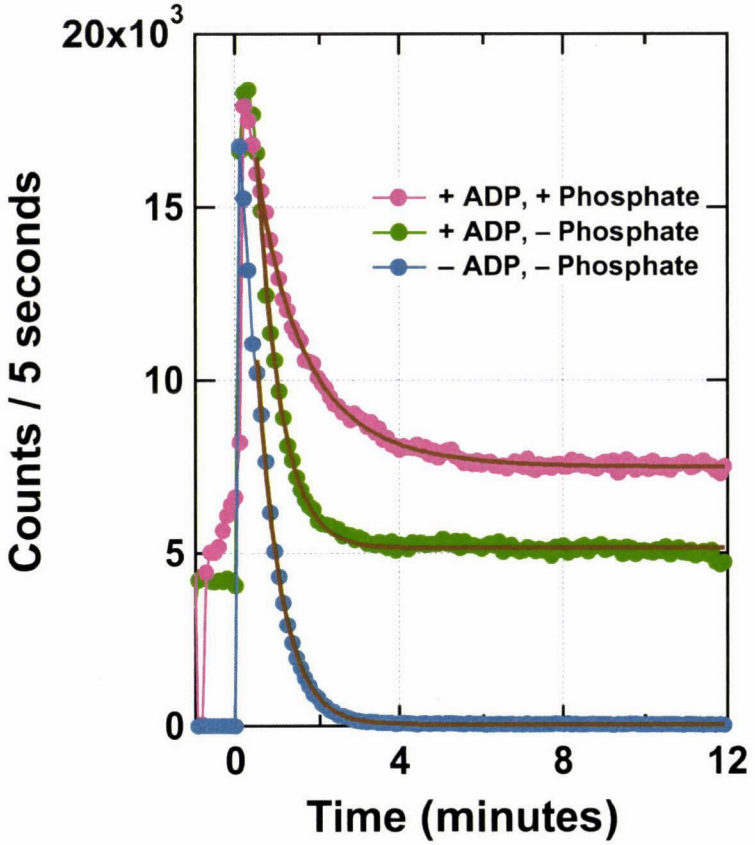

Figure S3. Effects of phosphate and ADP on luminescence flash. Experiments similar to Fig. S2. At time 0, 1.8 nM ATP (final concentration) was mixed with the luciferase solution with 200 μM ADP and 10 mM phosphate (magenta), with 200 μM ADP and without phosphate (green), or without ADP and without phosphate (cyan). Gold lines show exponential fit: $7100\exp(-t/0.64) + 7600\exp(-t/1.62) + 7500$ for +ADP/+phosphate; $28700\exp(-t/0.55) + 5100$ for +ADP/-phosphate; $26400\exp(-t/0.56) + 45$ for –ADP/-phosphate.

VI. Background ATP Level

In Fig. S2, the peak intensities represent the luminescence levels before the added ATP was consumed by luciferase. The peak height would be twice the background level at an added ATP concentration between 0.6 and 1.2 nM, indicating that the background ATP level was about 1 nM in our experiments. Somehow, this much of ATP remained in the solution even after the luminescence due to added ATP had decayed; the background luminescence did not decrease appreciably when the solution was left overnight. The background luminescence was practically negligible in the absence of ADP (Fig. S3). We suspect that

our samples were contaminated by adenylate kinase, which produces ATP (and AMP) from 2ADP: a steady-state ATP level would be reached when ATP production by adenylate kinase and ATP consumption by luciferase balance. As shown in Fig. S4, as little as a few pM of adenylate kinase can explain our background level. We tried to obtain direct proof of contamination by adenylate kinase by adding Ap5A which is a specific inhibitor of adenylate kinase. However, Ap5A somehow induced strong and sustaining luminescence, preventing any meaningful measurement.

Although we could not identify the source of the background luminescence unambiguously, the steady level of ~1 nM ATP in our samples has an important consequence. That is, the mechanically-driven ATP synthesis was made under the condition where free-energy balance strongly favoured hydrolysis. The free energy for ATP hydrolysis is given by

$$\Delta G = \Delta G_0 + k_B T \ln[\mathrm{ADP}][\mathrm{phosphate}]/[\mathrm{ATP}]$$

where ΔG_0 = -58 pN nm (extrapolated to the value at pH 7.6 from ref. 9 in the main text) and $k_B T$ = 4.1 pN nm is the thermal energy at room temperature. For our experiments at [ADP] = 200 μM, [phosphate] = 10 mM, and [ATP] = 1 nM, ΔG is -28 pN nm, the negative sign implying that the equilibrium is on the side of hydrolysis. Thus, the ATP synthesis in our experiments was uphill, requiring 28 pN nm of energy input.

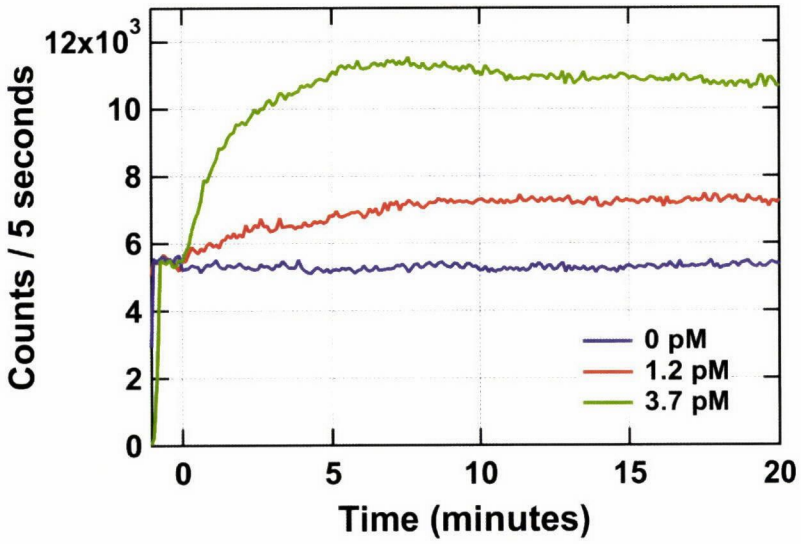

Figure S4. Effect of adenylate kinase on the luminescence level. At time 0, indicated concentrations (final) of adenylate kinase (rabbit muscle, Sigma) was added. Other conditions were as in Fig. S2.

Cell biology

Pathogen propulsion

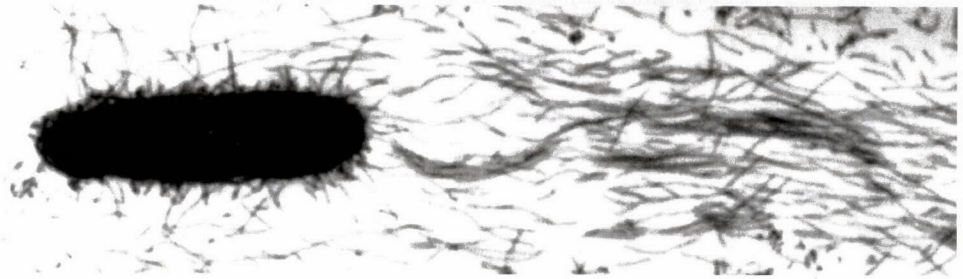

Bacterial pathogens have a cunning way of moving about inside the cells they infect — they harness components of the host's cytoskeletal machinery, in particular, the protein actin.

One such pathogen, *Rickettsia conorii*, is transmitted to humans through tick bites, and causes Mediterranean spotted fever. This bacterium assembles an elaborate 'tail' made of actin filaments (pictured) to propel itself through the cytoplasm of the infected host cell and to invade neighbouring cells. *Rickettsia* tails consist of parallel, unbranched filaments that closely resemble those present in thread-like cellular projections called filopodia.

Elsewhere in this issue, Pascale Cossart and colleagues shed light on the molecular mechanism that generates *Rickettsia* tails (E. Gouin *et al. Nature* **427,** 457–461; 2004). The authors had previously identified a *Rickettsia* protein, RickA, that is structurally similar to members of the WASP family found in higher organisms. WASPs are potent activators of the Arp2/3 complex, which nucleates actin filaments.

In the latest development, Cossart's group has found that RickA occurs on the bacterial surface, where actin filaments are generated. Using an *in vitro* actin polymerization assay, they go on to show that although RickA on its own cannot form actin filaments, it can activate the Arp2/3 complex — thereby stimulating actin polymerization. They extend these studies to show that *Rickettsia* uses the Arp2/3 complex *in vivo* to form actin tails, and that RickA can induce the formation of filopodium-like projections when it is targeted to the plasma membrane. So future work on *Rickettsia* motility might help to clarify the poorly understood process of filopodium formation.

Rickettsia actin tails are very different to those created by another pathogen, *Listeria monocytogenes*, which consist of shorter, highly branched arrays of actin filaments. Nevertheless, the *Listeria* tails are also formed by the Arp2/3 complex, which the bacterium recruits from the host cell using the surface protein ActA. So pathogens may have evolved different ways to induce actin polymerization using the same effector, the Arp2/3 complex. **Deepa Nath**

Ashassi-Sorkhabi and colleagues' work got me wondering whether there were any other natural compounds that act as inhibitors. A quick bibliographic search revealed a long history of research on the anti-corrosion properties of naturally occurring materials: extracts of prickly pear[2], henna[3], rosemary[4] and honey[5] have all been cited as providing a greater than 50% reduction in the corrosion rate of carbon steels, aluminium alloys and copper alloys, in chloride media of up to one-molar concentrations. And historically, tannins[6] were used in the steam age to reduce boiler corrosion.

Particularly fascinating, however, is recent work using organisms (bacillae or fungi) that have been genetically modified to secrete corrosion-inhibiting species, such as polyphosphate[7]. Normally, biofilms tend to accelerate corrosion, but inoculation with these 'smart' organisms can, in appropriate environments, substantially reduce it. Such technology potentially offers immense benefits for environmentally friendly corrosion control. I look forward to the day when we might all be advised to add yoghurt to our central heating systems! Corrosion might then cease to be the hidden enemy no one wants to discuss. ■

Stuart Lyon is in the Corrosion and Protection Centre, University of Manchester Institute of Science and Technology, Manchester M60 1QD, UK.
e-mail: stuart.lyon@umist.ac.uk

1. Ashassi-Sorkhabi, H., Majidi, M. R. & Seyeddi, K. *Appl. Surf. Sci.* doi:10.1016/j.apsusc.2003.10.007 (2003).
2. El-Etre, A. Y. *Corros. Sci.* **45,** 2485–2495 (2003).
3. Chetouani, A. & Hammouti, B. *Bull. Electrochem.* **19,** 23–25 (2003).
4. Kliskic, M. *et al. J. Appl. Electrochem.* **30,** 823–830 (2000).
5. El-Etre, A. Y. & Abdallah, M. *Corros. Sci.* **42,** 731–738 (2000).
6. Matamala, G., Smeltzer, W. & Droguett, G. *Corros. Sci.* **42,** 1351–1362 (2000).
7. Ornek, D. *et al. Appl. Microbiol. Biotechnol.* **58,** 651–657 (2002).

Molecular motors

Turning the ATP motor

Richard L. Cross

A long-standing question regarding ATP synthase — a cellular energy-generator — has been which direction it spins in when generating ATP. Some elegant experiments have revealed the answer.

The ATP synthase not only lays claim to being nature's smallest rotary motor, but also has an extremely important role in providing most of the chemical energy that aerobic and photosynthetic organisms need to stay alive. On page 465 of this issue, Itoh and colleagues[1] describe how they used electromagnets to force this motor to rotate and generate chemical energy (adenosine trisphosphate, ATP). In the process, they determined the direction of rotation during ATP synthesis.

ATP synthase is composed of two linked multi-subunit complexes, called F_0 and F_1. F_0 is embedded in cellular membranes and conducts protons, whereas F_1 is a peripheral complex and contains the catalytic sites. Together they couple the flow of protons down an electrochemical gradient to the synthesis of ATP from ADP (adenosine diphosphate) and inorganic phosphate.

The major — and initially controversial — features of this process were first recognized by Paul Boyer, who developed the concept of the 'rotary binding-change' mechanism. The first surprise came from his discovery that the energy derived from proton transport is not used to promote the synthesis of ATP at the catalytic sites on F_1. Instead, ATP forms spontaneously from tightly bound ADP and phosphate (Fig. 1a, step 2, overleaf); the energy instead drives the subsequent release of ATP from that site[2]. Also associated with this dissociation step (Fig. 1a, step 1) is an increase in the affinity of adjacent catalytic sites for ADP and phosphate[3]. A second surprise was the recognition that the coupling process probably involves subunit rotation[4].

In the binding-change model, then, F_0 and F_1 function as a pair of rotary motors linked by a central rotor and a peripheral stator (Fig. 1b). Rotation of the ring of *c*-subunits in F_0 is proposed to allow protons to be carried between two channels, formed by the *a*-subunit, that connect to opposite sides of the membrane. Because of the existence of the stator[5,6], and because the γ- and ϵ-subunits of the central rotor are firmly attached to the top of the *c*-ring[7], rotation of the *c*-ring forces the γ-subunit to rotate in the centre of F_1. This in turn drives net ATP synthesis by inducing cyclical conformational changes in the surrounding subunits, thereby altering binding affinities at the catalytic sites (hence 'binding-change' model; Fig. 1a, step 1). Strikingly, under

conditions in which more energy is stored in the ATP pool than in the electrochemical proton gradient, the engine can carry out the opposite reaction, consuming (hydrolysing) ATP to rotate F_0 and pump protons up a concentration gradient.

The rotary aspect of this theory remained a popular but speculative idea for years, until compelling evidence was provided by structural[8], biochemical[9] and spectral[10] studies. Then, in a dramatic visual demonstration, a fluorescent actin filament attached to one end of the γ-subunit of immobilized F_1 was seen by fluorescence microscopy to undergo multiple unidirectional rotations during ATP hydrolysis[11]. The direction of rotation, as viewed from the position of F_0, was anticlockwise. Subsequent biochemical experiments[12] established that energy-driven rotation of the γ-subunit occurs during ATP synthesis as well. But in this case the direction of rotation could not be determined by the approach used. So the question of whether or not the direction of rotation reverses when the direction of catalysis reverses has, until now, remained unanswered.

In this regard, it is interesting that the only other well-characterized biological rotary motor — the bacterial flagellar motor — has a transmission that, in response to regulatory signals, can shift the direction of rotation between forward and reverse without changing the direction of proton movement through the membrane. In contrast, the ATP synthase is smaller and simpler, and because of this it has long been thought that the direction of the coupled chemical events (ATP synthesis or hydrolysis) and proton transport (down or up a gradient) would indeed be reversed upon reversing the direction of subunit rotation. In the experiments presented by Itoh *et al.*[1], this prediction is at last confirmed.

The authors accomplished this feat by attaching magnetic beads to the γ-subunits on isolated F_1 complexes, which were immobilized by fixing their tops to a glass surface. The authors then used electromagnets to rotate the beads (substituting for proton transport), which in turn forced the γ-subunits to rotate. ADP and inorganic phosphate were included in the experiment, as well as an assay for monitoring the concentration of ATP. Itoh *et al.* found that rotating the γ-subunit in the anticlockwise direction — previously shown to accompany ATP hydrolysis — caused a decrease in ATP levels. But rotating the γ-subunit in a clockwise direction caused an increase in ATP. The results establish a hard-wired reversibility in the F_0F_1 rotary motor.

An interesting feature of Itoh and colleagues' experiment is that it works only at low rotational speeds, that is, roughly 5% of the maximal ATP-driven rate. As the speed increases, bead rotation becomes uncoupled from the magnet. This is not surprising because the rotary torque is applied at a constant rate in the experiments, whereas under physiological conditions the γ-subunit can stop rotating for significant periods during substrate binding, product release, and catalysis[13,14]. So it might have been predicted that, with increasing speed, a point would be reached at which the pauses limit bead rotation such that it falls out of synchronization with the rotating magnetic field.

As often happens with significant advances, another laboratory has independently reached the same conclusion about the mechanical properties of ATP synthase. Diez and colleagues[15] report the use of fluorescence resonance energy transfer to measure the distance between a pair of probes attached to the *b*- (stator) and γ- (rotor) subunits. Three distinct distances are clearly evident, and correspond to the orientation of the γ-subunit when paused at 120° intervals (see Fig. 1a). As expected, the distance between the probes changes during catalytic turnover, in repeat sequences that progress at a rate equal to that of catalysis. Furthermore, the order of the sequence reverses in going from ATP hydrolysis (close to intermediate to distant) to ATP synthesis (distant to intermediate to close), again establishing a correspondence between the direction of catalysis and the direction of rotation. These studies[1,15] not only further our understanding of an essential energy-transducing complex but also enhance the prospects for exploiting this rotary motor to develop nanodevices. ■

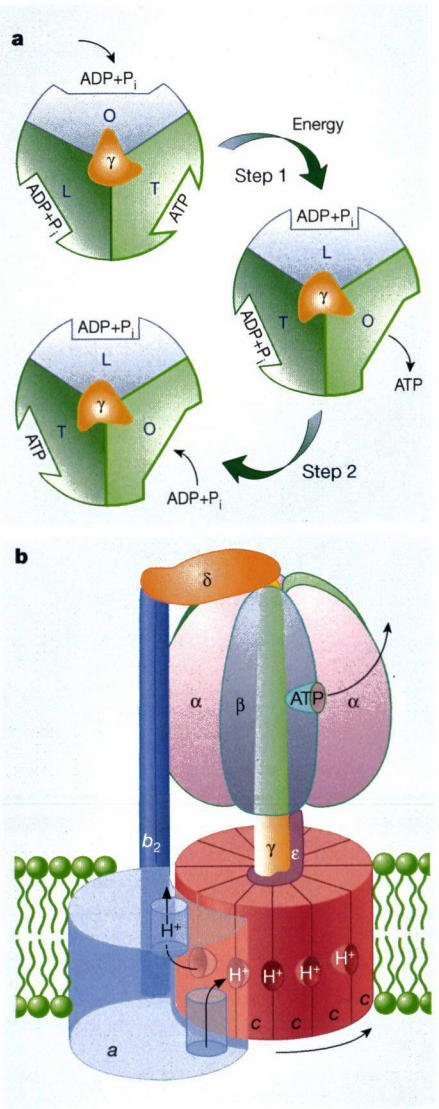

Figure 1 **The binding-change model for F_0F_1 ATP synthase.** a, **Looking up at F_1 from the membrane. Each blue or green area represents a pair of α- and β-subunits, in which the catalytic sites are interfacial but mostly on the β-subunit. In step 1, the γ-subunit rotates through 120°, driving conformational changes in the three surrounding catalytic sites that alter their affinities (O, L or T, for open, loose or tight) for substrates and product. In step 2, ATP forms spontaneously from tightly bound ADP and inorganic phosphate (P_i).** b, **View from the side of F_0F_1. The *a*-subunit contains two partial channels. For a proton to traverse the membrane, it must move through one channel to the centre, bind to one of the *c*-subunits and then be carried to the other partial channel by rotation of the *c*-ring. The *c*-subunits are anchored to the γ-subunit (part of the rotor), whereas the *a*-subunit is anchored through $b_2\delta$ (the stator) to the $\alpha_3\beta_3$ hexamer. Hence, rotation of the *c*-ring relative to the *a*-subunit in F_0 will drive the rotation of the γ-subunit relative to the $\alpha_3\beta_3$ hexamer in F_1. New results[1,15] show that the γ-subunit rotates in a clockwise direction when the engine generates ATP.**

Richard L. Cross is in the Department of Biochemistry and Molecular Biology, SUNY Upstate Medical University, Syracuse, New York 13210, USA.
e-mail: crossr@upstate.edu

1. Itoh, H. *et al. Nature* **427,** 465–468 (2004).
2. Boyer, P. D., Cross, R. L. & Momsen, W. *Proc. Natl Acad. Sci. USA* **70,** 2837–2839 (1973).
3. Kayalar, C., Rosing, J. & Boyer, P. D. *J. Biol. Chem.* **252,** 2486–2491 (1977).
4. Boyer, P. D. & Kohlbrenner, W. E. in *Energy Coupling in Photosynthesis* (eds Selman, B. & Selman-Reiner, S.) 231–240 (Elsevier North-Holland, New York, 1981).
5. Boekema, E. J., Ubbink-Kok, T., Lolkema, J. S., Brisson, A. & Konings, W. N. *Proc. Natl Acad. Sci. USA* **94,** 14291–14293 (1997).
6. Wilkens, S., Zhou, J., Nakayama, R., Dunn, S. D. & Capaldi, R. A. *J. Mol. Biol.* **295,** 387–391 (2000).
7. Hermolin, J., Dmitriev, O. Y., Zhang, Y. & Fillingame, R. H. *J. Biol. Chem.* **274,** 17011–17016 (1999).
8. Abrahams, J. P., Leslie, A. G., Lutter, R. & Walker, J. E. *Nature* **370,** 621–628 (1994).
9. Duncan, T. M., Bulygin, V. V., Zhou, Y., Hutcheon, M. L. & Cross, R. L. *Proc. Natl Acad. Sci. USA* **92,** 10964–10968 (1995).
10. Sabbert, D., Engelbrecht, S. & Junge, S. *Nature* **381,** 623–625 (1996).
11. Noji, H., Yasuda, R., Yoshida, M. & Kinosita, K. Jr *Nature* **386,** 299–302 (1997).
12. Zhou, Y., Duncan, T. M. & Cross, R. L. *Proc. Natl Acad. Sci. USA* **94,** 10583–10587 (1997).
13. Sabbert, D. & Junge, W. *Proc. Natl Acad. Sci. USA* **94,** 2312–2317 (1997).
14. Adachi, K. *et al. Proc. Natl Acad. Sci. USA* **97,** 7243–7247 (2000).
15. Diez, M. *et al. Nature Struct. Mol. Biol.* **11,** 135–141 (2004).

nature
structural &
molecular biology

Chemomechanical coupling in F_1-ATPase revealed by simultaneous observation of nucleotide kinetics and rotation

Takayuki Nishizaka[1,2,7], Kazuhiro Oiwa[1], Hiroyuki Noji[3], Shigeki Kimura[1], Eiro Muneyuki[4], Masasuke Yoshida[4,5] & Kazuhiko Kinosita Jr[6]

F_1-ATPase is a rotary molecular motor in which unidirectional rotation of the central γ subunit is powered by ATP hydrolysis in three catalytic sites arranged 120° apart around γ. To study how hydrolysis reactions produce mechanical rotation, we observed rotation under an optical microscope to see which of the three sites bound and released a fluorescent ATP analog. Assuming that the analog mimics authentic ATP, the following scheme emerges: (i) in the ATP-waiting state, one site, dictated by the orientation of γ, is empty, whereas the other two bind a nucleotide; (ii) ATP binding to the empty site drives an ~80° rotation of γ; (iii) this triggers a reaction(s), hydrolysis and/or phosphate release, but not ADP release in the site that bound ATP one step earlier; (iv) completion of this reaction induces further ~40° rotation.

The enzyme F_oF_1-ATP synthase catalyzes the synthesis of ATP from ADP and phosphate using proton-motive force across a membrane. The F_1 sector has catalytic sites responsible for the synthesis reaction; when isolated, it solely hydrolyzes ATP, and is thus called F_1-ATPase. F_1 contains five different subunits with the stoichiometry $\alpha_3\beta_3\gamma\delta\varepsilon$: the central stalk γ is surrounded by a hexagonal cylinder in which three α and three β subunits are alternately arranged[1]. The catalytic sites are located at the interfaces between α and β subunits, mainly on a β subunit, and are thus arranged 120° apart around the γ subunit. It has been proposed that the synthesis reactions in the three catalytic sites occur not independently but sequentially, one site after another[2,3]. In this proposal's 'binding-change mechanism,' the three catalytic sites have different affinities for nucleotides at any moment, and each undergoes conformational transitions that lead to the sequence of substrate binding → ATP synthesis → ATP release. This mechanism was proposed to involve rotation of a shaft domain: proton-motive force is converted, in F_o, to mechanical rotation of the shaft, which drives conformational changes of the catalytic domains in F_1 to synthesize ATP. Conversely, hydrolysis of ATP induces reverse conformational changes, and thus reverse rotation of the shaft domain (reviewed in ref. 4). Rotation has ultimately been confirmed by direct observation as rotation of the γ subunit in an isolated $\alpha_3\beta_3\gamma$ subcomplex[5].

Observation of F_1 rotation under an optical microscope has clarified that rotation of the γ subunit is unidirectional and can be driven by hydrolysis of ATP, GTP or ITP[5,6], as well as that rotation is resolved into discrete 120° steps, each of which consumes one ATP molecule[7,8]. On the basis of these and previous biochemical studies, possible mechanisms of F_1 rotation have been discussed[9–11]. However, the precise correspondence between chemical reactions and mechanical rotation remains to be established, that is: which chemical event on which catalytic site drives a particular phase of rotation? This is not a trivial task, because both rotation and chemical reactions are stochastic, and because the three catalytic sites are basically identical. A recent high-speed imaging study has shown that a 120° step consists of ~90° and ~30° substeps, and that ATP binding drives the 90° substep[12]. However, the reaction that drives the 30° substep and the reactions that precede and govern its timing have not yet been identified. Here we have attempted to disentangle the complex relationships between chemical and mechanical events by imaging individual F_1 molecules under an optical microscope.

RESULTS

Distinguishing three catalytic sites by polarization

We visualized rotation by attaching a bead duplex to the γ shaft, and simultaneously detected binding of a fluorescent ATP analog to a particular site through angle-resolved fluorescence imaging (Fig. 1, and see Supplementary Fig. 1 online for microscope diagram). We used the fluorescent ATP analog 2′-*O*-Cy3-EDA-ATP[13], which we refer to hereafter as Cy3-ATP.

[1]Kansai Advanced Research Center, Protein Biophysics Group, Iwaoka 588-2, Nishi-ku, Kobe 651-2492, Japan [2]Precursory Research for Embryonic Science and Technology (PRESTO), Japan Science and Technology Agency, Honcho 4-1-8, Kawaguchi, Saitama 332-0012, Japan [3]Institute of Industrial Science, University of Tokyo, Tokyo 153-8505, Japan [4]Chemical Resources Laboratory, Tokyo Institute of Technology, Yokohama 226-8503, Japan [5]ATP system, Exploratory Research for Advanced Technology (ERATO), Japan Science and Technology Agency Yokohama 226-0026, Japan [6]Center for Integrative Bioscience, Okazaki National Research Institutes, Myodaiji, Okazaki 444-8585, Japan [7]Present address Department of Physics, Gakushuin University, Mejiro 1-5 1, Toshima-ku, Tokyo 171-8588, Japan
Correspondence should be addressed to T N (takayuki nishizaka@gakushuin ac jp)

Published online 18 January 2004, doi 10 1038/nsmb721

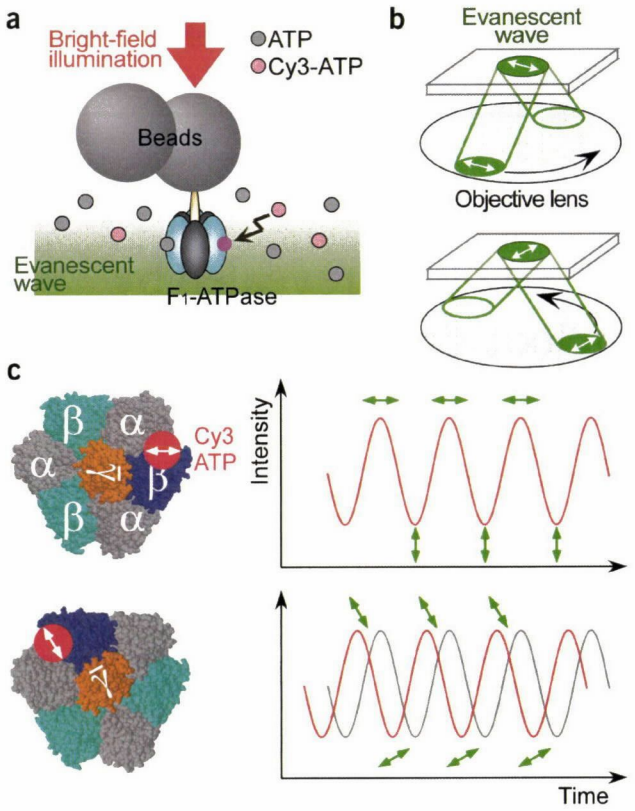

Figure 1 Experimental system. (**a**) Simultaneous-observation system (not to scale). Single turnovers of ATP hydrolysis on catalytic sites in F_1-ATPase are visualized with fluorescently labeled ATP (Cy3-ATP), which is excited by an evanescent wave under total internal reflection fluorescence microscopy. Rotation of a bead duplex attached to the γ shaft is simultaneously observed under bright-field illumination at a wavelength different from the emission of Cy3-ATP. (**b**) Schematic illustrations describing the optical system for angle-resolved imaging, with which we distinguish among the three catalytic sites on F_1 from Cy3 orientation. The incident laser is rotated along the periphery of the objective (black arrow), keeping its polarization parallel with the circular trajectory (white arrows). The direction of polarization of the evanescent wave is rotated within the image plane (white arrows at top). (**c**) Expected intensity time courses for a single Cy3-ATP molecule (right panels) bound to different catalytic sites 120° apart on F_1 (left). The fluorescence intensity (red curves) reaches maxima and minima when the excitation polarization becomes parallel and orthogonal, respectively (green arrows), to the absorption transition moment of the Cy3.

In this study, evanescent-wave excitation was realized by passing a laser beam through the edge of an objective in a method developed for visualization of single fluorophores[14]. Cy3-ATP appears as a stable fluorescent spot when it binds to a surface-immobilized F_1 molecule, whereas unbound Cy3-ATP is virtually invisible because of its rapid Brownian motion[15,16]. We rotated the polarization of the near-field excitation in the image plane at a constant speed by rotating the polarization of the incident laser beam and, at the same time, the beam itself along the periphery of the objective (**Fig. 1b**, and see **Supplementary Fig. 2** online for optical system; note that rotation of laser polarization alone, as done in far-field excitation[8,17,18], is insufficient because the evanescent wave has a small (<10%) polarization component along the direction of the incident laser beam between a numerical aperture of 1.33 and 1.45 (ref. 19). Under the rotating polarized excitation, fluorescence intensity from a single fluorophore is expected to show sinusoidal oscillation (**Fig. 1c**). The intensity reaches a peak every 180°, when the excitation polarization becomes parallel with the absorption transition moment of the fluorophore. Thus, we can determine the fluorophore orientation with the ambiguity of multiples of 180°. The three catalytic sites should host the fluorophore at three different angles that are 120° apart in the image (x-y) plane; therefore, a particular site binding a fluorescent ATP analog can be distinguished with this method.

Newly bound ATP dictates the orientation of the γ subunit

We used an $\alpha_3\beta_3\gamma$ subcomplex of F_1 with mutations that rendered the subcomplex much less prone to MgADP inhibition than the wild type (a 'GT' mutant; E.M., unpublished data; for details, see Methods). During ATP hydrolysis and rotation, F_1 becomes inactive by stochastic and tight binding of MgADP[20–22]; thus rotation lapses into long pauses. Because we wanted to observe repeated binding of Cy3-ATP to the same F_1 molecule, we used the GT mutant. The rotation rate of this mutant by authentic ATP was somewhat slower than that of the active (uninhibited) wild type, and rotation by Cy3-ATP was even slower (see below). Because other rotation characteristics seemed normal, we assume that the chemomechanical coupling in this mutant is basically the same as that of the wild type, and that Cy3-ATP induces the same series of events as authentic ATP, albeit slowly. In this study we sought to relate chemical events on the three catalytic sites with mechanical events, and thus here we disregard (until Discussion) the differences in absolute values of rate constants, assuming these differences are not the result of a grossly different reaction scheme. Another advantage of using the GT mutant was that we could observe substeps in its rotation under pure Cy3-ATP with a conventional video camera (**Fig. 4a**). The average rate of rotation of wild-type F_1 with Cy3-ATP was also slow, but we did not observe the video-rate substeps with the wild type. Below, we refer to the mutant subcomplex simply as F_1.

To allow, at most, one Cy3-ATP molecule at a time to bind, excess unlabeled ATP was added to Cy3-ATP. Before binding of Cy3-ATP, the bead duplex on the γ subunit rotated with clear counterclockwise 120° steps by unlabeled ATP (**Fig. 2a**). When a Cy3-ATP molecule bound to the F_1 molecule, a fluorescent spot appeared at the center of bead rotation, and began to blink regularly, indicating fluorophore angle.

We first observed that the binding of Cy3-ATP is synchronous with a 120° step (**Fig. 2b**; this example was chosen to show the intensity oscillations clearly, and therefore the total duration of Cy3-ATP binding is longer than most others). Second, while Cy3-ATP is still bound, the bead duplex makes another 120° step, indicating that a nucleotide is bound to F_1 for at least two-thirds of a revolution. Third, release of Cy3-nucleotide, presumably in the form of Cy3-ADP, is also synchronous with the third 120° step.

The fluorophore angle θ remained constant during each binding event, even though the γ subunit rotated by 120° in the middle (**Fig. 2a,b**; θ was 107 ± 2° in this binding-release event). Thus, this 120° step was not caused by the binding of another Cy3-ATP to a different site. As shown below, the expected rate of binding at 50 nM Cy3-ATP is once in 5 min, and thus successive binding of two Cy3-ATP molecules is extremely improbable.

In another binding event on the same F_1 molecule, the orientation of bound Cy3 and the bead orientation immediately after Cy3-ATP binding keep a fixed relationship, maintaining the same constant offset angle (compare right top panels in **Fig. 2b–d**; ~120° counterclockwise in this example). We summarize all results of simultaneous observation in which Cy3-ATP bound at least once to each of the three catalytic sites (**Fig. 2e**). The two (bead and Cy3) angles are well correlated without exception, reinforcing the contention that, as soon as a catalytic site binds ATP, the γ subunit always turns the same 'face'

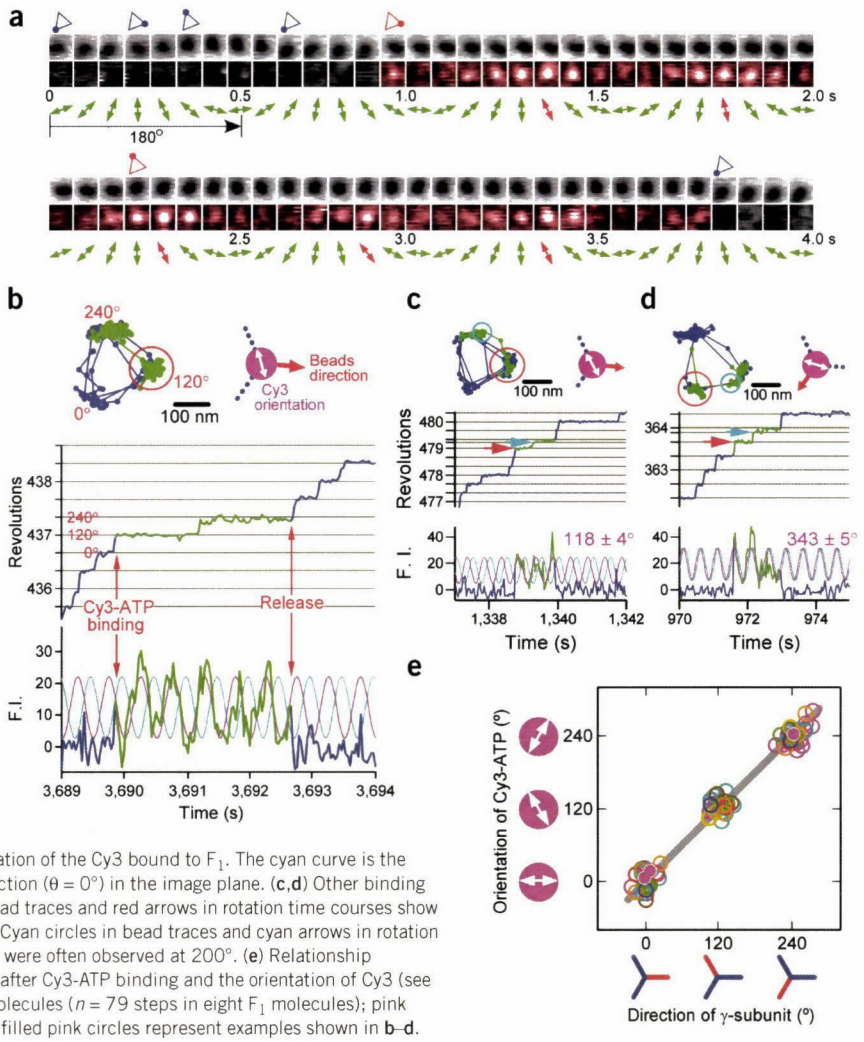

Figure 2 Simultaneous observation of F_1 rotation and Cy3-ATP binding. (**a**) Examples of simultaneous observation of bead stepping as bright-field images (upper rows) and Cy3-ATP binding as fluorescence images (lower rows) in a mixture of Cy3-ATP (50 nM) and excess unlabeled ATP (550 nM). Triangles above the image pairs indicate bead directions immediately after a counterclockwise step. The period during which one catalytic site in F_1 is occupied with Cy3-nucleotide (Cy3-ATP or product Cy3-ADP) is highlighted with red in the lower images. Green arrows below the image pairs show the orientation of the excitation polarization, and red arrows highlight the orientation when the fluorescence intensity becomes maximal and thus show the orientation of the bound Cy3. The bead orientation immediately after Cy3-ATP binding (the first red triangle) is near 3 o'clock, and the orientation of bound Cy3 (red arrows) is near 11 o'clock (equivalent to 5 o'clock) and ~120° counterclockwise (or 60° clockwise) from the bead orientation. Frame width, 0.7 μm for upper rows and 1.4 μm for lower rows. (**b**) Analyses of **a**. Left top, trace of bead motion. The centroid of the image of the bead duplex was calculated in each video frame (33 ms). Right top, diagram indicating the bead direction, and Cy3 orientation estimated from the bottom panel. Middle, time course of bead rotation. Time zero is the start of observation. The angle immediately before Cy3-ATP binding is designated 0°. Bottom, time course of the fluorescence intensity (F.I.) in the vicinity of the F_1 molecule. In **b**–**d**, the period during which Cy3-AT(D)P was judged bound to F_1 is highlighted in green. The green portion of the intensity time course is fitted with the pink curve representing $\cos^2(\omega t + \theta) \propto \cos(2\omega t + 2\theta)$, where ω is the angular rate of prism rotation and θ is the orientation of the Cy3 bound to F_1. The cyan curve is the reference representing a fluorophore lying in the *x* direction ($\theta = 0°$) in the image plane. (**c**,**d**) Other binding events for the same molecule as in **a**. Red circles in bead traces and red arrows in rotation time courses show the angles immediately after Cy3-ATP binding (120°). Cyan circles in bead traces and cyan arrows in rotation time courses show pauses after an 80° substep, which were often observed at 200°. (**e**) Relationship between the direction of the bead duplex immediately after Cy3-ATP binding and the orientation of Cy3 (see Methods for details). Different colors show different molecules ($n = 79$ steps in eight F_1 molecules); pink circles are the same molecule as in **a**–**d**, and the three filled pink circles represent examples shown in **b**–**d**.

(the bar on γ in Fig. 1c) to the β subunit hosting that site. Conversely, the γ subunit dictates which of the three β subunits should bind the next ATP: it must be the β subunit that is 120° ahead from the face of γ. It has been shown that ATP binding drives ~90° rotation of the γ subunit, which is immediately (in ~2 ms) followed by ~30° rotation[12]. We show here that this ATP must bind to the particular β subunit dictated by the orientation of the central γ subunit.

Binding accompanies rotation

Because of the oscillation of fluorescence intensity and the inherent noise in single-fluorophore detection, we cannot be certain that we detected all binding events. Binding events that persisted for one oscillation cycle (0.5 s) or longer were clear, and we scored altogether 163 such events on 27 F_1 molecules. In 155 out of the 163 cases, a 120° step was observed in synchrony with the binding; when binding occurred in a dark phase of fluorescence oscillation, we could not be completely certain if the step was precisely synchronous, but all 155 steps were well within the first oscillation cycle (0.5 s) of the binding (see Methods for the exceptional eight cases). In 31 of the 155 binding events, binding of Cy3-ATP occurred near a peak of the intensity oscillation (within 20% of the peak intensity), allowing precise determination of the timing. In all 31 cases, a forward 120° step was observed within ±1 video frame (33 ms) of the binding (see examples in Fig. 3a). Combining this information with the angle determinations already made, we conclude that binding to the correct β subunit, dictated by the γ subunit, is required for a forward 120° step, and that binding immediately induces a rotational step.

Because the temporal resolution is limited to the video rate, one could argue that stepping might have preceded binding, and thus stepping could be the cause, rather than a result, of binding (as in a thermal-ratchet model[23–25]). Indeed, Brownian fluctuation could help bind ATP, because earlier work[12] has indicated that rotation in the correct (counterclockwise) direction increases the affinity for ATP, and thus rotation and binding are cooperative events. A full 120° step before ATP binding, however, must be extremely rare, judging from the size of angular fluctuations at low ATP concentrations. Also, we cannot claim that binding of Cy3-ATP or ATP invariably induces a 120° step: stepping initiated by binding of Cy3-ATP or ATP might immediately be reversed by premature release of the nucleotide, and such a brief binding associated with a small-amplitude mechanical pulse would not be detected in our video-rate analysis.

Cy3-nucleotide (presumably in the form of Cy3-ADP) was released, in 142 out of the 163 binding events, after the γ subunit had rotated ~240°. The release of Cy3-ADP accompanied a further step toward

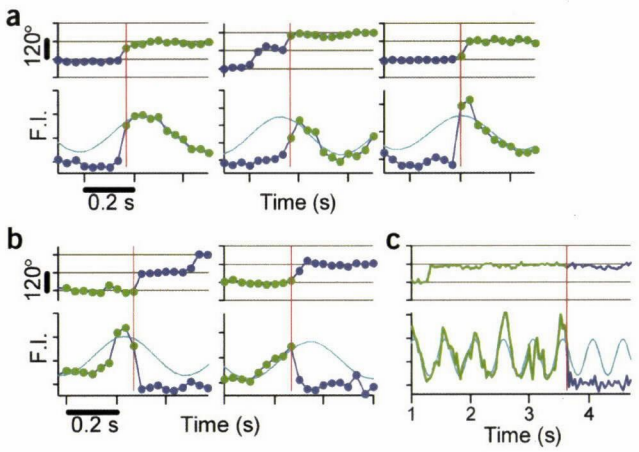

Figure 3 Timing between a rotational step of the γ subunit (upper panels) and binding or release of Cy3-nucleotide (lower panels). Examples of cases in which either binding or release occurred in a bright phase of the oscillation of fluorescence intensity (F.I.). (**a**) Binding. (**b**) Release. Dots correspond to video frames. (**c**) An exceptional case in which Cy3 disappeared without a step, probably as a result of photobleaching (see text). Red vertical lines show the video frame in which we judge binding or release of Cy3-nucleotide occurred.

360°, well within 0.5 s in 129 of the 142 cases, and confirmed to be within ±1 video frame when the release occurred in a bright phase of fluorescence (20 cases including Fig. 3b). The exceptional 13 cases (Fig. 3c) are probably due to photobleaching, because the 'releases' (disappearance of Cy3 fluorescence) without a step occurred mostly after an exceptionally long dwell time (at 200–240°, the angles at which even the GT mutant seemed prone to inhibition when Cy3-ADP was bound): the average dwell time in the exceptional cases was 16.9 s, whereas the dwell times before a release accompanying a step averaged 2.9 s. With the level of excitation intensity used in this study, the mean lifetime of photobleaching of Cy3-ATP was 8 s (T.N., data not shown), and thus long dwells are necessarily affected by photobleaching at some point. Apparently, therefore, release of ADP is also coupled to mechanical stepping. Binding and release of a nucleotide seem always to be tightly coupled to a mechanical event (120° rotation).

Kinetics of rotation driven by Cy3-ATP

The kinetics of the rotation driven by pure Cy3-ATP is basically similar to that driven by unlabeled ATP except that certain kinetic steps are slower. Cy3-ATP alone supported rotation for hundreds of revolutions, at least at such high concentrations as 20 μM. The average rate of rotation, however, was much lower with Cy3-ATP than with ATP (Fig. 4a,b). This difference is mainly due to the lower rate of Cy3-ATP binding: the average rotation rate was proportional to the nucleotide concentration for both Cy3-ATP and ATP, indicating that binding was rate-limiting in the concentration ranges examined; the binding rate k_{on} for Cy3-ATP was ~20-fold lower than k_{on} for ATP (Fig. 4c). The k_{on} for Cy3-ATP coincided with the hydrolysis rate in solution, corroborating the scheme of one Cy3-ATP molecule per 120°, as in the case of rotation of wild type F_1 by unlabeled ATP[7]. The k_{on} for unlabeled ATP in the GT mutant is small compared with that of the wild type, and was approximately half the bulk hydrolysis rate of this mutant in solution. In a modification of the method used in earlier studies, we used different buffer for the rotation assay (see Methods). This difference led to the lower rate of rotation by unlabeled ATP. Incidentally, an isomer of Cy3-ATP, 3′-*O*-Cy3-ATP, which normally coexists with the 2′ isomer that we used[13], gave a poor rotation rate (Fig. 4c), and the rotation often exhibited a long pause. We therefore purified the 2′ isomer from a mixture before use.

Because the rate is limited by substrate binding, rotation is expected to be stepwise, and so it was for Cy3-ATP as well: 120° steps were clearly resolved, as with unlabeled ATP (Fig. 4b). Remarkably, most of the 120° steps with Cy3-ATP were further resolved into substeps (Fig. 4a). Rotation traces showed six dwelling positions, from which the amplitudes of the substeps were obtained as 79 ± 7° (mean ± s.d.; n = 238 displacements in 19 F_1 molecules) and 41 ± 7° (n = 248). The distribution of substep sizes is given in **Supplementary Figure 3a** online. The appearance of video-rate substeps is not due to interaction of the Cy3 moiety with F_1, because EDA-ATP lacking the dye portion also showed the substep behavior (T.N., data not shown). In the rotation of wild-type F_1 driven by unlabeled ATP, substep amplitudes have been estimated as 90 ± 10° and 30 ± 10°, and the two substeps are contiguous within ~2 ms (ref. 12), beyond the temporal resolution of the ordinary video camera used in this study. Despite the difference in timing (and the small difference in amplitudes, which is within experimental uncertainty), we consider the substeps of ~80° and ~40° observed here to be of the same origin as the ~90° and ~30° substeps, for the following reason.

The dwells before an 80° substep, 0° dwells, were, on average, inversely proportional to the Cy3-ATP concentration, whereas the dwells after an 80° substep, 80° dwells, were independent of this concentration (Fig. 4d, and see **Supplementary Fig. 3b** online). These characteristics are common to the 0° dwells and 90° dwells in the ATP-driven rotation in the wild type[12], suggesting common underlying processes. The concentration dependence suggests that the 80° substep is triggered by binding of Cy3-ATP (to the site dictated by the γ subunit), and the 40° substep by a process subsequent to the binding, such as splitting of ATP in, or release of phosphate or ADP from, one of the three sites.

In experiments with the mixture of ATP and Cy3-ATP, the video-rate substeps are a signature of the site that carries Cy3-ATP. Below, we attempt an analysis using this signature, assuming that the same chemomechanical sequence occurs in F_1-ATPase whether it is driven by ATP or Cy3-ATP. We refer to previous 90° and 30° substeps as 80° and 40° substeps.

40° substep governed by site –1

Here we analyze the sequence of events induced by (infrequent) binding of Cy3-ATP during rotation in a mixture of Cy3-ATP and excess unlabeled ATP. The first event after binding was 120° stepping of the γ subunit, as already stated. Let the first step be from 0° to 120°: we designate the angle of the γ subunit (the bead duplex) immediately before binding of Cy3-ATP as 0° (Fig. 2b, middle panel). While the Cy3-ATP was still bound, the motor made another step toward ~240°. A closer look revealed that the second steps were often resolved into 80° and 40° substeps (Fig. 2c,d), reminiscent of the substeps seen in the rotation by pure Cy3-ATP. The 40° substep from 200° to 240° was not always clear because of noise, but a tendency to linger around 200° was noticeable in most cases (Fig. 2b; see **Supplementary Fig. 4** online for averages of the step record).

Our interpretation here is that all 120° steps are composed of 80° and 40° substeps, as in the wild type F_1 driven by unlabeled ATP[12], and that only substeps from 200° to 240° are discerned at the video rate because they are delayed by slow reaction(s) in the site hosting the Cy3-ATP or Cy3-nucleotide. If we call the catalytic site that has most recently bound ATP site 0, the site that governs the substep behavior is site –1, the site that bound ATP one step earlier.

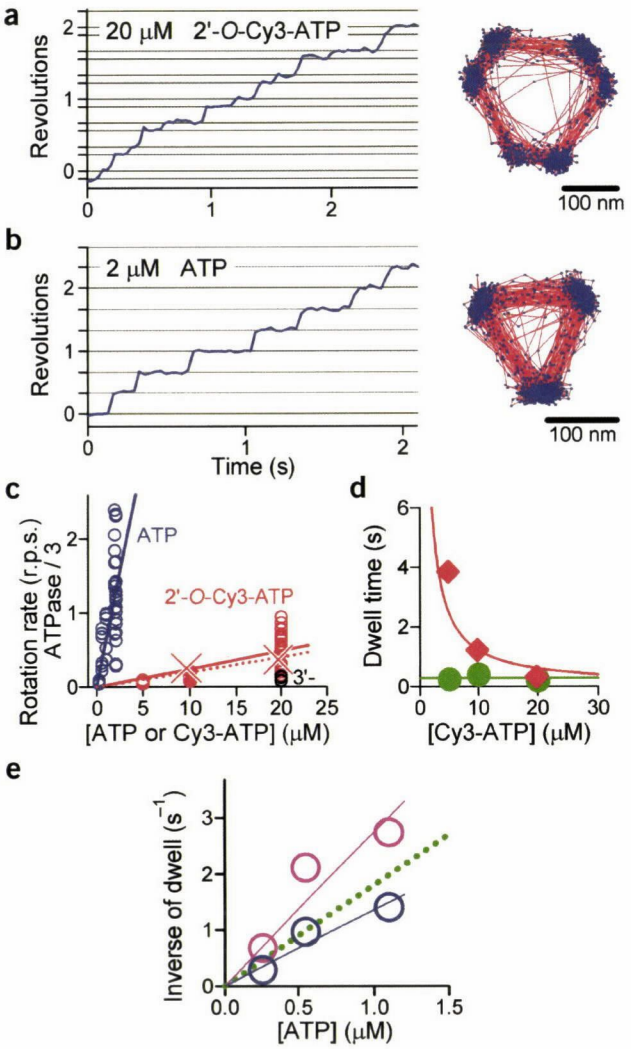

Figure 4 F_1 rotation driven by Cy3-ATP. (**a**) Left, a time course of F_1 rotation in 100% 2′-*O*-Cy3-ATP. Horizontal gray lines are 80° and 40° apart. Right, the trace of bead rotation for 70 s. Centroid positions at all video frames (blue dots) are connected by red lines. (**b**) A rotation time course of F_1 (left) and corresponding trace for 70 s (right) in 100% unlabeled ATP. (**c**) Time-averaged rotation rates by ATP (blue circles), 2′-*O*-Cy3-ATP (red) and 3′-*O*-Cy3-ATP (black). Samples that showed clear 120° steps (or 80° and 40° substeps) during 5–20 consecutive revolutions were chosen. Solid lines show fits with k_{on} (3× rotational rate) of 1.8×10^6 $M^{-1}s^{-1}$ (blue) and 0.073×10^6 M^{-1} s^{-1} (red), assuming consumption of three nucleotides per revolution. The rate of 2′-*O*-Cy3-ATP hydrolysis in solution (red crosses and red dashed line), 0.06×10^6 M^{-1} s^{-1}, coincided with rotation rate. (**d**) ATP dependence of average dwell times before an 80° substep ('0° dwell' $\tau_{0°}$, red diamonds) and dwell times after an 80° substep ('80° dwell' $\tau_{80°}$, green circles). Red line shows fit with $\tau_{0°} = (0.08 \times 10^6\ M^{-1}\ s^{-1})^{-1} \times [\text{Cy3-ATP}]^{-1}$, which agrees with the estimation in **c**, and green line, $\tau_{80°}$ = constant = 0.3 s. (**e**) ATP dependence of the average dwell time in the mixture. Pink circles are at 120° (see **Fig. 2b** and text for angle definition) (total n at three different ATP concentrations = 138) and blue circles, 200–240° (n = 122). Green line is the binding rate of unlabeled ATP estimated from rotation in 100% ATP (see **c**).

Both the 80° substep from 120° to 200° and the next 80° substep from 240° to 320° (part of the observed 120° step from 240° to 360°) must be driven by ATP binding, if the presence of Cy3 fluorophore in bound nucleotide does not alter the basic reaction sequence. In support of this, the rates of occurrence of these substeps, estimated as the inverse of dwell times at 120° and at 200–240° (the interval between a 120–200° substep and the next 240–360° step), were each proportional to the concentration of unlabeled ATP, and both approximately agreed with the rate of ATP binding (Fig. 4e), allowing for relatively large uncertainties due to low counting statistics (the ATP-independent dwell time at 200° is partially responsible for the apparently longer dwell time at 200–240°).

DISCUSSION

In the scheme that emerges (Fig. 5a,b) at least two of the three catalytic sites are always filled with a nucleotide, and thus the occupancy must be two when F_1 is waiting for the next ATP molecule. Four successive ATP-waiting states are shown (Fig. 5a), with the step from 0° to 120° driven by binding of Cy3-ATP. Events between 120° and 240° are detailed (Fig. 5b): (I) ATP binds to the remaining empty site of the β subunit. We call this site, as before, site 0. (II) The binding drives the 80° substep from 120° to 200°. (III) Before the γ subunit makes the next substep from 200° to 240°, reaction(s) must take place at site −1. This rate-limiting reaction must take place at site −1, based on the Cy3-ATP's slow substep signature. Candidates of the rate-limiting reactions include hydrolysis at, or release of phosphate from, site −1, but not the release of ADP from this site (because Cy3 remained bound at least until 240°). (IV) A 40° substep occurs, and the γ subunit reaches 240°. There, the F_1 motor waits for the next ATP molecule to initiate the same sequence (except that event III is now fast).

At some point between events I and IV, ADP must be released from site −2 to vacate that site for the next ATP. Unfortunately, we have not been able to determine the timing of ADP release because substeps were not resolved in the step synchronous with the release of Cy3-ADP. ADP release is unlikely to be after event IV, because in the wild-type F_1 rotating at a high concentration of unlabeled ATP, a 40° substep is followed by the next 80° substep within 0.1 ms: as soon as the 40° substep is complete, the motor is ready to bind the next ATP, and thus one site must be empty[12]. A probable timing for ADP release is during the 40° substep (IV), because F_1 inhibited by failing to release MgADP has been shown to pause around ~80° (ref. 22). Also, because ATP binding produces the major substep of 80°, or the major conformational change of F_1, we do not expect complete mechanical silence for the essentially reverse process of ADP release: some rotation accompanying ADP release is quite probable. A possible scenario could consist of (i) hydrolysis in, or the release of phosphate from, site −1 initiating a 40° substep; (ii) site −2 sensing the slight movement of the γ subunit and (iii) releasing ADP, which drives (iv) the rest of the 40° substep. Another possible timing for ADP release is during the 80° substep (II) ATP binding to site 0 initiates this substep, and ADP release from site −2 helps complete the 80° substep. In this scenario, site occupancy is always two except for the brief (<0.1 ms) interchanging period.

Other, more complex scenarios cannot be dismissed, because a small-amplitude rotation, for example by 10°, would not have been detected in our analyses. In this regard, the difference between the 80° substep observed here and the previous 90° substep[12] might be important. For example, ATP binding to site 0 induces a 80° substep, ATP hydrolysis in site −1 induces another 10° substep, and phosphate release[26] from site −1 and/or ADP release from site −2 drives the last 30° rotation. Consistent with this, a slowly hydrolyzed substrate ATP-γ-S produces 80° substeps at video rate[27]. A notable feature is the

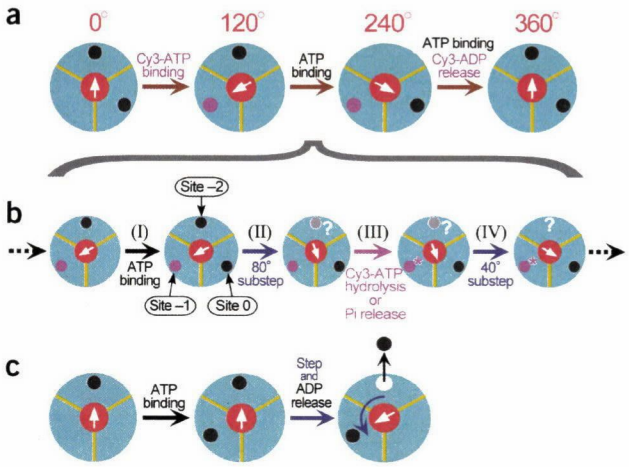

Figure 5 Mechanism of F_1 rotation. (**a**) Rotation scheme consistent with **Figure 2**. Four successive ATP-waiting states are shown. (**b**) Events between 120° and 240°. Nucleotide occupancy in schemes **a** and **b** alternates between two and three. (**c**) An alternative scheme in which the occupancy alternates between one and two (see Discussion).

coupling of rotation with ATP hydrolysis, which will help achieve a high efficiency in the reverse reaction of ATP synthesis[10].

According to the scheme shown here (**Fig. 5b**), at least two catalytic sites (two β subunits) carry out major functions in rotating the γ subunit by 120°. One is the site that has just bound ATP (site 0), which produces the 80° substep. The other is site –1, which controls the timing of (and possibly drives) the 40° substep. As stated above, site –2 also probably assists rotation by releasing ADP. Coordination among the three sites has been proposed[2,3], and now this coordination is beginning to be unraveled.

A current debate regarding F_1 rotation concerns whether the motor operates under bi- or tri-site mode[10,28,29]. In the simplest definition, bi-site is the mode in which the nucleotide occupancy of the three catalytic sites alternates between one and two (**Fig. 5c**), whereas the tri-site mode involves alternation between two and three (**Fig. 5a,b**). The bi-site view has recently been challenged[11,28] with the claim that, on the basis of site occupancy estimated from fluorescence quenching of tryptophan residues introduced in the catalytic sites, hydrolysis and rotation do not occur until a third site binds ATP, and thus bi-site activity does not exist. The present study also supports a tri-site scheme, because Cy3-nucleotide remained bound at least for 240° of rotation of the γ subunit, or until two more ATP molecules bound and a step from 240° to 360° (320°) occurred. Cy3-ATP always bound to the correct β subunit, consistent with a tri-site scheme that leaves only one vacant site for binding, although the asymmetric β could also dictate a particular site to bind ATP in the bi-site mode. We cannot completely exclude the possibility that Cy3-ADP may be stickier than ADP and have a greater tendency to linger in the catalytic site; thus only Cy3-nucleotide, and not nucleotide, might remain bound for 240° or more.

The major questions remaining are when, and from which site, phosphate is released, and what is the timing of ADP release. To answer these questions, techniques must be developed to allow high-speed imaging of fluorescent ATP, as well as detection and resolution of two or more fluorescent ATP molecules on one F_1 molecule. We emphasize that orientation imaging, used here to distinguish among three catalytic sites, is a powerful tool for studying multisite enzymes in general, and also for detecting local conformational changes in different parts of a protein and/or RNA machine (through fluorophore angle changes) simultaneously with an assessment of its function (through a large tag such as a bead or a bead duplex).

METHODS

Proteins. The GT mutant of the $\alpha_3\beta_3\gamma$ subcomplex was derived from a thermophilic *Bacillus* strain PS3 F_1-ATPase and contained the following mutations: β-G181A (ref. 30) and β-T165S (ref. 20) for minimizing MgADP inhibition; α-C193S, γ-S107C and γ-I210C for specific biotinylation of the γ subunit[8,12]; β-His_{10} at the N terminus[5], α-W463F and β-Y341W (refs. 31–33). The GT mutant showed a V_{max} of 250 ± 20 (mean ± s.d.) s^{-1} and a K_m of 37 ± 10 μM for the hydrolysis reaction at 25 °C in buffer A (50 mM KCl, 2 mM $MgCl_2$, 10 mM MOPS-KOH, pH 7.0; the GT mutant does not require lauryldodecylamine oxide (LDAO) for hydrolysis measurement because of its resistance to MgADP inhibition), which are comparable to the values of 247 s^{-1} and 19 μM for the wild type F_1 in the presence of LDAO in buffer A[12]. In buffer B (2 mM $MgCl_2$, 20 mM potassium phosphate, pH 8.0) used for the rotation assay, V_{max} was 210 ± 10 s^{-1} and K_m 50 ± 3 μM, yielding an apparent k_{on} for ATP binding of $V_{max}/K_m = 4.2 \times 10^6$ $M^{-1}s^{-1}$, which is smaller than k_{on} of 13×10^6 $M^{-1}s^{-1}$ for wild type F_1 in buffer A with LDAO[12]. k_{on} from the rotation assay (**Fig. 4c**) is half these values, presumably because of surface hindrance.

Rotation assay. 1.4% (w/v) amino-modified polystyrene beads (amino-modified, 0.22 μm in diameter; Polysciences) were modified with 1 mg ml^{-1} biotin-$(AC_5)_2$-Sulfo-Osu (Dojindo) at room temperature for 4 h, and unreacted biotin was removed by centrifugation (20,000*g* for ~10 min). Then, 0.2 mg ml^{-1} streptavidin (Sigma) was added, and excess streptavidin was washed away. Biotin (biotin-$PEAC_5$-maleimide; Dojindo) was coupled to cysteines in the γ subunit of F_1 by a 30-min incubation at room temperature at 1–8 μM F_1 at F_1/biotin = 1:2. To observe rotation, ~100 pM F_1 in buffer A was infused into a flow chamber comprising two glass coverslips; the top coverslip was coated with 3-glycidyloxypropyl-trimethoxysilane (Fluka) to avoid binding of the protein, and the bottom one had been cleaned in 10 M KOH overnight and washed with distilled water. F_1 attached nonspecifically to the bottom surface. After 2 min, the chamber was washed with 20 mM potassium phosphate, and then the streptavidin-coated beads at 0.1% (w/v) were infused. Avidin on the beads specifically attached to the γ subunit in a single F_1, whereas $\alpha_3\beta_3$ subcomplexes were immobilized on the surface; therefore, stepping between $\alpha_3\beta_3$ and γ was visualized as displacement of beads. For simultaneous observation of Cy3-ATP binding, buffer B plus the oxygen scavenger system[34], 0.5% (v/v) 2-mercaptoethanol, 35–65 nM Cy3-ATP, the desired amount of unlabeled ATP, 0.02 mg ml^{-1} creatine kinase, 0.08 mg ml^{-1} creatine phosphate, was infused. For rotation in Cy3-ATP, buffer B only with the desired amount of Cy3-ATP was infused instead. In both cases, rotating beads often showed large-angle fluctuations, and these did not show clean steps. For analysis, we selected those that showed steady and consistent 120° steps (**Figs. 2** and **4a,b**). A possible reason for the slightly slower rotation of this GT mutant by authentic ATP as compared with the wild type is that the selected F_1 molecules were probably attached to the surface firmly and thus may have been impeded by surface interactions. Observations were made at 23 ± 2 °C.

Cy3-ATP and its hydrolysis by F_1. Cy3-ATP and its isomers were synthesized and purified as reported[13]. The bulk hydrolysis rate of 2′-*O*-Cy3-ATP was measured by mixing 10 nM F_1 with 2′-*O*-Cy3-ATP in buffer B. Aliquots of the reaction solution were then taken and quenched with buffer C (20% (v/v) acetonitrile and 0.6 M $NH_4H_2PO_4$, pH 4.2–4.3). They were analyzed by anion-exchange chromatography (Partisil 10 SAX; Whatman) in buffer C and quantified by the integrated fluorescence intensity of Cy3-ADP. The hydrolysis rate was determined from the amount of 2′-*O*-Cy3-ADP present after the first 1 min of reaction, which was <3% of the initial Cy3-ATP.

Microscopy and analyses. For imaging Cy3-ATP, a green laser beam (wavelength 532 nm; Compass, Coherent) was introduced into an Olympus IX-70 microscope. The beam power at the base of the objective (60×; numerical aperture 1.45; Olympus) was 0.16–0.20 mW for 100 μm^2 illumination at the sample plane. Polarization of the evanescent wave in the image plane was

rotated at a constant speed (0.9990 r.p.s.). For quantitative analysis of the intensity of Cy3, the average intensity over a 0.78-μm square enclosing the center of Cy3 was calculated[8]. The background intensity either before Cy3-ATP binding or after Cy3-ADP release was averaged for 10–30 cycles, and the averaged intensity was subtracted from the Cy3 signal. To determine the Cy3 angle, the intensity record corresponding to a binding event (judged visually) was fitted with a 1.9980-Hz cosine curve with three variables, the amplitude, offset and phase. The difference between this phase and that of the excitation polarization gave the Cy3 angle. For bead imaging, a halogen lamp illuminated the condenser through a 660- to 880-nm filter. The fluorescence (Cy3-ATP) and bright-field (bead duplex) images were separated with a dichroic mirror and recorded with two electronically synchronized cameras[34,35]. The diagram of the microscope system is given (**Supplementary Fig. 1** online). Typically, one record continued for 0.5–1 h, during which 3–20 Cy3-ATP molecules bound to an F_1 molecule. For each F_1 molecule, the angle between the catalytic sites and bead orientations is different because the bead duplex can attach to the γ subunit at any angle. Therefore, in the illustration (**Fig. 2e**), a constant angle values specific for each molecule have been subtracted from the abscissa and ordinate, such that the bead angles close to the 3 o'clock position average 0°, and the corresponding Cy3 angles also average 0°. Cy3 angles have been chosen from the 180° redundancies such that they match the bead angles. For Cy3-ATP binding (**Fig. 3a**), the 8 exceptions of the 163 cases were as follows: 5 cases in which the bead duplex did not rotate during the whole binding event, 1 case in which Cy3-ATP bound in the middle of the dwell time between two steps (we dismissed these events as binding to a nearby F_1 molecule or as nonspecific binding to the glass surface) and 2 cases in which binding of Cy3-ATP induced a backward 120° step[7].

Note: Supplementary information is available on the Nature Structural & Molecular Biology website

ACKNOWLEDGMENTS

We thank R. Yasuda, K. Adachi and H. Itoh for technical assistance and critical discussion, R. Nakamori and Y. Funamoto for technical assistance, D.R. Trentham for initiation of our collaboration; T. Masaike, B. Brenner and H. Kojima for critical discussion, M. Shio, K. Abe and I. Sase for the microscope techniques, and M. Uno and H. Umezawa for management of laboratories and collaboration. This work was supported in part by grants-in-aid from the Ministry of Education, Culture, Sports, Science and Technology of Japan, and by a Core Research for Evolutional Science and Technology (CREST) grant.

COMPETING INTERESTS STATEMENT

The authors declare that they have no competing financial interests.

Received 27 August; accepted 13 November 2003
Published online at http://www.nature.com/natstructmolbiol/

1 Abrahams, J.P., Leslie, A.G., Lutter, R. & Walker, J.E. Structure at 2.8 Å resolution of F_1-ATPase from bovine heart mitochondria. *Nature* **370**, 621–628 (1994)
2 Boyer, P.D. The binding change mechanism for ATP synthase—some probabilities and possibilities. *Biochim. Biophys. Acta* **1140**, 215–250 (1993)
3 Boyer, P.D. The ATP synthase—a splendid molecular machine. *Annu. Rev. Biochem.* **66**, 717–749 (1997)
4 Yoshida, M., Muneyuki, E. & Hisabori, T. ATP synthase—a marvelous rotary engine of the cell. *Nat. Rev. Mol. Cell Biol.* **2**, 669–677 (2001)
5 Noji, H., Yasuda, R., Yoshida, M. & Kinosita, K. Jr. Direct observation of the rotation of F_1-ATPase. *Nature* **386**, 299–302 (1997)
6 Noji, H. *et al.* Purine but not pyrimidine nucleotides support rotation of F_1-ATPase. *J. Biol. Chem.* **276**, 25480–25486 (2001)
7 Yasuda, R., Noji, H., Kinosita, K. Jr. & Yoshida, M. F_1-ATPase is a highly efficient molecular motor that rotates with discrete 120° steps. *Cell* **93**, 1117–1124 (1998)
8 Adachi, K. *et al.* Stepping rotation of F_1-ATPase visualized through angle-resolved single-fluorophore imaging. *Proc. Natl. Acad. Sci. USA* **97**, 7243–7247 (2000)
9 Boyer, P.D. Catalytic site forms and controls in ATP synthase catalysis. *Biochim. Biophys. Acta* **1458**, 252–262 (2000)
10 Kinosita, K. Jr., Yasuda, R., Noji, H. & Adachi, K. A rotary molecular motor that can work at near 100% efficiency. *Phil. Trans. R. Soc. Lond. B* **355**, 473–489 (2000)
11 Weber, J. & Senior, A.E. ATP synthase: what we know about ATP hydrolysis and what we do not know about ATP synthesis. *Biochim. Biophys. Acta* **1458**, 300–309 (2000)
12 Yasuda, R., Noji, H., Yoshida, M., Kinosita, K. Jr. & Itoh, H. Resolution of distinct rotational substeps by submillisecond kinetic analysis of F_1-ATPase. *Nature* **410**, 898–904 (2001)
13 Oiwa, K. *et al.* Comparative single-molecule and ensemble myosin enzymology: sulfoindocyanine ATP and ADP derivatives. *Biophys. J.* **78**, 3048–3071 (2000)
14 Tokunaga, M., Kitamura, K., Saito, K., Iwane, A.H. & Yanagida, T. Single molecule imaging of fluorophores and enzymatic reactions achieved by objective-type total internal reflection fluorescence microscopy. *Biochem. Biophys. Res. Commun.* **235**, 47–53 (1997)
15 Funatsu, T., Harada, Y., Tokunaga, M., Saito, K. & Yanagida, T. Imaging of single fluorescent molecules and individual ATP turnovers by single myosin molecules in aqueous solution. *Nature* **374**, 555–559 (1995)
16 Ishijima, A. *et al.* Simultaneous observation of individual ATPase and mechanical events by a single myosin molecule during interaction with actin. *Cell* **92**, 161–171 (1998)
17 Ha, T., Enderle, T., Chemla, S., Selvin, R. & Weiss, S. Single molecule dynamics studied by polarization modulation. *Phys. Rev. Lett.* **77**, 3979–3982 (1996)
18 Sase, I., Miyata, H., Ishiwata, S. & Kinosita, K. Jr. Axial rotation of sliding actin filaments revealed by single-fluorophore imaging. *Proc. Natl. Acad. Sci. USA* **94**, 5646–5650 (1997)
19 Axelrod, D. Total internal reflection fluorescence at biological surfaces. in *Noninvasive Techniques in Cell Biology* (eds. Foskett, J.K. & Grinstein, S.) 93–127 (Wiley-Liss, New York, 1990)
20 Jault, J.M. *et al.* The $\alpha_3\beta_3\gamma$ subcomplex of the F_1-ATPase from the thermophilic bacillus PS3 with the βT165S substitution does not entrap inhibitory MgADP in a catalytic site during turnover. *J. Biol. Chem.* **271**, 28818–28824 (1996)
21 Matsui, T. *et al.* Catalytic activity of the $\alpha_3\beta_3\gamma$ complex of F_1-ATPase without noncatalytic nucleotide binding site. *J. Biol. Chem.* **272**, 8215–8221 (1997)
22 Hirono-Hara, Y. *et al.* Pause and rotation of F_1-ATPase during catalysis. *Proc. Natl. Acad. Sci. USA* **98**, 13649–13654 (2001)
23 Vale, R.D. & Oosawa, F. Protein motors and Maxwell's demons: does mechanochemical transduction involve a thermal ratchet? *Adv. Biophys.* **26**, 97–134 (1990)
24 Astumian, R.D. & Bier, M. Fluctuation driven ratchets: molecular motors. *Phys. Rev. Lett.* **72**, 1766–1769 (1994)
25 Hunt, A.J., Gittes, F. & Howard, J. The force exerted by a single kinesin molecule against a viscous load. *Biophys. J.* **67**, 766–781 (1994)
26 Masaike, T., Muneyuki, E., Noji, H., Kinosita, K. Jr. & Yoshida, M. F_1-ATPase changes its conformations upon phosphate release. *J. Biol. Chem.* **277**, 21643–21649 (2002)
27 Shimabukuro, K. *et al.* Catalysis and rotation of F_1 motor: cleavage of ATP at the catalytic site occurs in 1 ms before 40° substep rotation. *Proc. Natl. Acad. Sci. USA* **100**, 14731–14736 (2003)
28 Weber, J. & Senior, A.E. Bi-site catalysis in F_1-ATPase: does it exist? *J. Biol. Chem.* **276**, 35422–35428 (2001)
29 Boyer, P.D. Catalytic site occupancy during ATP synthase catalysis. *FEBS Lett.* **512**, 29–32 (2002)
30 Masaike, T. *et al.* Rotation of F_1-ATPase and the hinge residues of the β subunit. *J. Exp. Biol.* **203**, 1–8 (2000)
31 Dou, C., Fortes, P.A. & Allison, W.S. The $\alpha_3(\beta Y341W)_3\gamma$ subcomplex of the F_1-ATPase from the thermophilic *Bacillus* PS3 fails to dissociate ADP when MgATP is hydrolyzed at a single catalytic site and attains maximal velocity when three catalytic sites are saturated with MgATP. *Biochemistry* **37**, 16757–16764 (1998)
32 Ren, H. & Allison, W.S. Substitution of betaGlu$_{201}$ in the $\alpha_3\beta_3\gamma$ subcomplex of the F_1-ATPase from the thermophilic *Bacillus* PS3 increases the affinity of catalytic sites for nucleotides. *J. Biol. Chem.* **275**, 10057–10063 (2000)
33 Mitome, N. *et al.* The presence of phosphate at a catalytic site suppresses the formation of the MgADP-inhibited form of F_1-ATPase. *Eur. J. Biochem.* **269**, 53–60 (2002)
34 Nishizaka, T., Seo, R., Tadakuma, H., Kinosita, K. Jr. & Ishiwata, S. Characterization of single actomyosin rigor bonds: load dependence of lifetime and mechanical properties. *Biophys. J.* **79**, 962–974 (2000)
35 Nishizaka, T., Miyata, H., Yoshikawa, H., Ishiwata, S. & Kinosita, K. Jr. Unbinding force of a single motor molecule of muscle measured using optical tweezers. *Nature* **377**, 251–254 (1995)

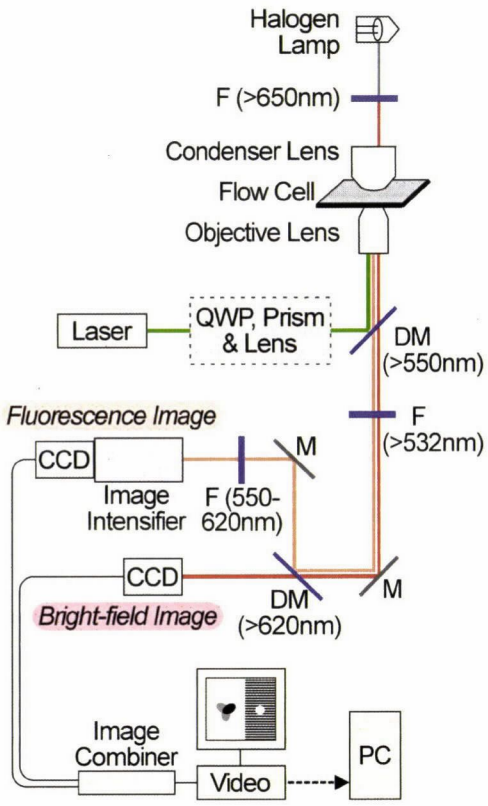

Supplementary Figure 1
Schematic diagram of the microscope system. Optical paths for different wavelengths are distinguished by color. DM, dichroic mirrors; F, filters (transmission range in parentheses); M, mirrors. Bright-field and fluorescence images were separated by a beam splitter at 620 nm, and captured by two cameras (CCD-300; Dage-MTI), the one for fluorescence after an image intensifier (VS4-1845; Video Scope). The two cameras were operated synchronously and combined images were videotaped.

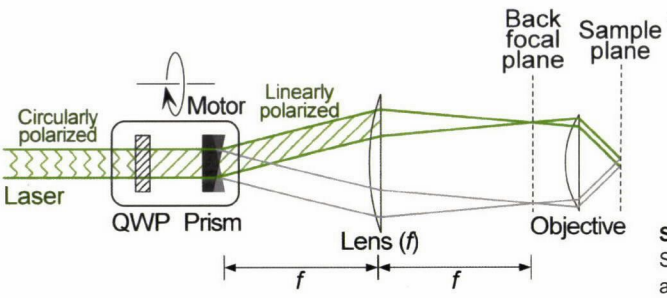

Supplementary Figure 2
Schematic illustration describing the optical configuration to realize the illumination shown in Figure 1*b* in text. A quarter-wave plate (QWP), which transforms the circularly polarized laser beam into a linearly polarized beam, is rotated together with a beam-deflecting prism in a hollow stepping motor. We placed a lens (focal length f = 200 mm) at distance f from the back focal plane of the objective, and a custom-made prism at distance f from the lens. The beam, which was refracted by the prism rotated at a constant speed together with a quarter-wave plate, was collimated and focused at the back focal plane.

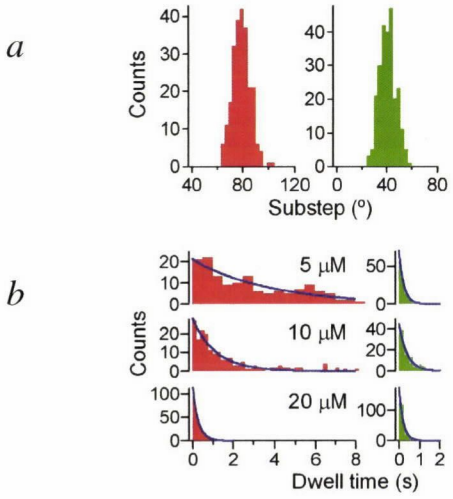

Supplementary Figure 3
Analyses of substeps in rotation by Cy3-ATP. ***a,*** Distribution of substep sizes. We selected by eye those angle-displacements that were completed within one video-frame and accompanied by dwells of more than two video-frames both before and after the displacements. The dwelling angles before and after each displacement were averaged, and the difference was taken as a substep angle. ***b,*** Histograms of dwell times before an 80° substep ('0° dwell', red) and dwell times after an 80° substep ('80° dwell', green) at indicated Cy3-ATP concentrations. The average dwell times τ were estimated by fit with $P(t) = P_0 \cdot \exp(-t/\tau)$ (blue lines). Figure 4*d* in text is the summary of these data.

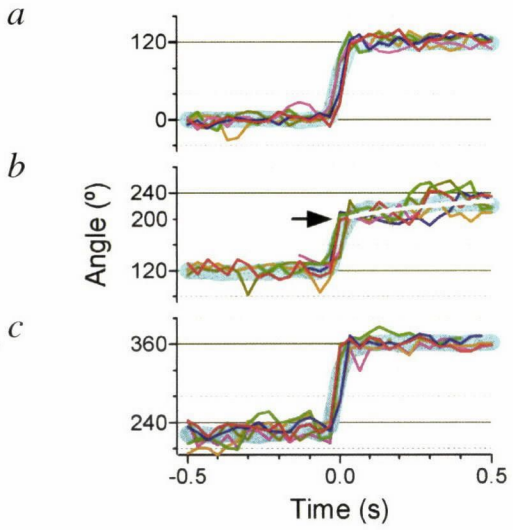

Supplementary Figure 4
Substepping behaviors in the mixture of Cy3-ATP and ATP. The angles in the ordinate are measured from '0°', defined as the angle immediately before binding of Cy3-ATP (see Fig. 2*b* in text). ***a,*** Stepping from 0° to 120°; ***b,*** from 120° to ~240°; ***c,*** from ~240° to 360° (0°). Six examples of step records (thin lines) and averages of 27 steps (thick cyan lines) in the mixture of 50 nM Cy3-ATP and 550 nM unlabeled ATP. Those data that showed dwells of more than two video-frames at all four angles (0°, 120°, 240° and 360°) were chosen and analyzed. After positioning individual steps at time 0, the preceding and subsequent steps and records beyond those were removed, and one further frame was trimmed off from each end. Before averaging, step records shorter than the -0.5 s to 0.5 s interval were extrapolated with a horizontal line(s) with the value of the end point. Then all steps were averaged. In *b*, the white line shows $-40° \times \exp(-t/0.4\ \text{s}) + 240°$. The time constant, 0.4 s, was in good agreement with the average 80° dwell of 0.3 s in the rotation by pure Cy3-ATP (see Fig. 4*d* in text).

Happy motoring with ATP synthase

Alan E Senior & Joachim Weber

ATP synthase research has reached a milestone as single-molecule techniques are used to examine the direction and stepping of the proton gradient–driven rotation, to determine the effect of forced rotation on ATP synthesis and to synchronously monitor rotation and nucleotide kinetics.

Purposeful generation and utilization of energy define living organisms. The central molecule of biological energetics is ATP, and the enzyme responsible for the majority of ATP synthesis in organisms from bacteria to man is ATP synthase. A rush of excitement ran through this field in 1997 when Noji *et al.*[1] discovered that ATP synthase is not just an enzyme, but also a tiny motor. One part of the enzyme rotates, at ~100 Hz, and rotation is integral to the mechanism—as you read this article, billions of these 'nanomotors' are turning at this speed in your tissues and cells. This striking discovery revolutionized experimentation: it was evident that a field that had been previously dominated by membrane biochemistry and enzymology would need to import technologies of physics and biophysics. There was the feeling that this might take some time. Not so. Apparently, the physicists and biophysicists were primed, and in three articles published this month[2–4] (two in this issue of *Nature Structural & Molecular Biology* and one in *Nature*), major advances are reported. The direction and stepping of proton gradient–driven rotation is demonstrated for the first time[2]; rotation forced by external electromagnets is shown to generate ATP[3]; and synchronous monitoring of rotation and nucleotide kinetics has clarified enzyme mechanism and chemomechanical coupling[4].

Proton gradients generated across membranes of chloroplasts, mitochondria and bacteria, by either sunlight capture or nutrient oxidation, provide the natural driving force for ATP synthesis. They consist of a chemical component (a proton concentration difference) and an electrical component (one side is positive, the other negative). By inserting ATP synthase into the membranes, nature devised a way to capture the potential energy of the gradient. ATP synthase allows H^+ to flow down the gradient through the enzyme, transducing gradient energy into chemical energy by converting ADP and phosphate (P_i) into ATP.

A.E.S. is in the Department of Biochemistry and Biophysics, University of Rochester Medical Center, Rochester, New York 14642, USA, and J.W. is in the Department of Cell Biology and Biochemistry, Texas Tech University Health Sciences Center, Lubbock, Texas 79430, USA. e-mail: alan_senior@urmc.rochester.edu

The ATP synthase from *Escherichia coli*[5] is composed of two major domains (**Fig. 1**). The membrane-embedded part (F_o) provides a specific H^+ conduction path, between the *c* subunit ring and the *a* subunit. The catalytic sites, three in number, are located at α/β subunit interfaces of the $\alpha_3\beta_3$ hexagon in the membrane-external F_1. The 'rotor' consists of γ and ε subunits firmly fastened to the *c* ring. A helical region of the γ subunit passes through the center of the $\alpha_3\beta_3$ hexagon, providing communication with the catalytic sites. At the periphery, the 'stator' ($b_2\delta$) prevents co-rotation of catalytic sites with the rotor due to viscous drag. Visualization of single molecules fixed to a surface proved to be the key to demonstration of rotation. In their landmark paper, Noji *et al.*[1] immobilized the $\alpha_3\beta_3\gamma$ subcomplex and demonstrated that upon hydrolysis of added ATP, the γ subunit rotated. The original experiment used fluorescent actin filaments coupled to γ as the visual probe; later experiments showed that γ, ε and *c* ring rotate together as a shaft. Mechanical rotation is therefore the mode of energy transfer between catalytic sites and the membrane.

During ATP hydrolysis, rotation of γ is counterclockwise when viewed from the membrane, and the efficiency of the motor is remarkable[6]. ATP synthase operates only in the direction of ATP synthesis in chloroplasts and mitochondria, but in bacteria both ATP hydrolysis and synthesis are catalyzed, depending on metabolic requirements. Hydrolysis is coupled to outward proton pumping (opposite to that shown in **Fig. 1**). It is generally agreed that ATP synthesis and hydrolysis occur essentially by reversal of the same mechanism. Thus it has been widely anticipated that ATP synthesis requires rotation of the shaft consisting of γε and the *c*-ring in the opposite direction to that seen during hydrolysis, driven by inward proton flow (**Fig. 1**). However, this had not been experimentally proven.

Börsch and colleagues[2] have now established that proton gradients do drive rotation of γ, in the anticipated direction. Their technique depends on observation of single molecules, achieved by incorporating intact ATP synthase into liposomes at a density of one enzyme molecule per liposome and use of a confocal fluorescence detection system. By rapid dilution ('pH jump') they transiently generate a proton gradient across the liposomal membrane, causing ATP synthase to generate ATP. Rotation is recorded by intramolecular fluorescence resonance energy transfer (FRET). A donor fluorophore was attached covalently to the rotor on γ, and an acceptor fluorophore to the stator on b_2. When the donor is excited, energy is transmitted to the acceptor. The efficiency of energy transfer is a function of the distance between fluorophores. In this case, because the donor on γ is rotating, this distance keeps changing. However, it has been established[6] that during ATP hydrolysis, consumption of one ATP yields one 120° step of γ rotation, and that the rotor pauses between steps as the enzyme waits for productive collision with an incoming ATP. Thus, three pauses

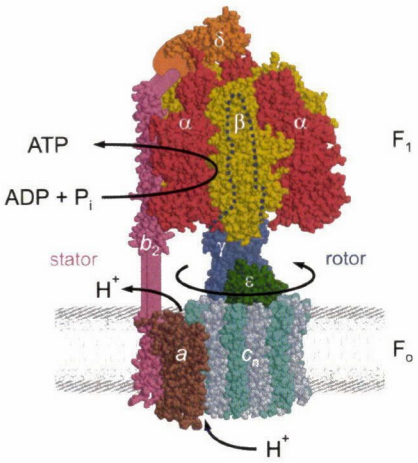

Figure 1 Structure of ATP synthase. The enzyme from *E. coli*, with subunit stoichiometry $\alpha_3\beta_3\gamma\delta\varepsilon ab_2c_n$. In mitochondria and chloroplasts additional subunits are present. Stoichiometry of the *c* ring (*n*) varies (it is believed to be 10–12 in *E. coli* and 10, 11 or 14 in other organisms). See ref. 5 for further details.

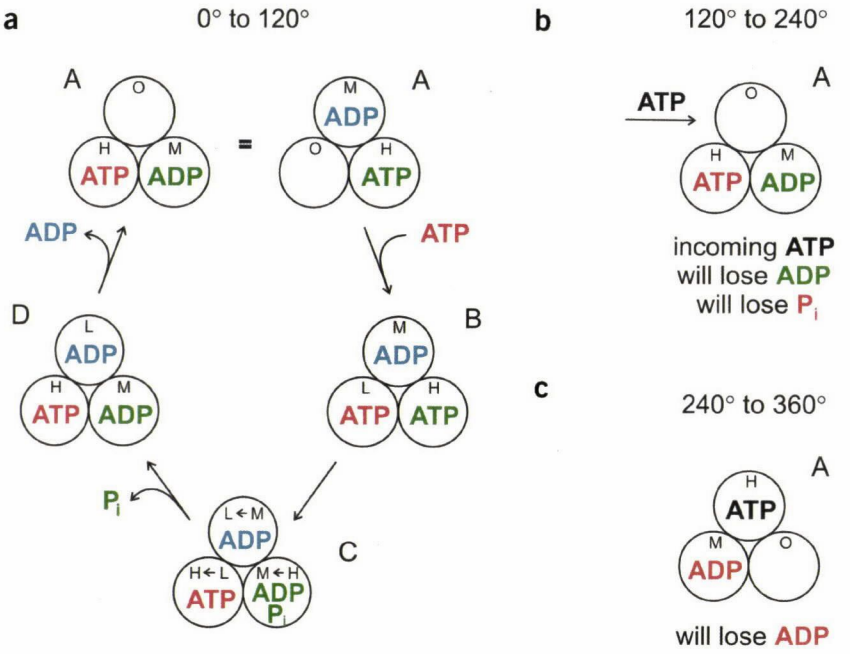

Figure 2 Enzymatic mechanism of ATP hydrolysis by ATP synthase. (**a**) Each circle represents one of the three catalytic sites. O, open (unoccupied); L, lowest affinity for ATP; M, medium affinity; H, highest affinity. The series of enzyme states ABCDA describes what happens during consumption of one molecule of ATP and one 120° step of γ rotation. Binding of an incoming ATP (red) to the ATP-waiting state (A) brings about hydrolysis of already-resident ATP (green), with the chemical reaction transition state occurring between states B and C. Concomitantly, γ rotation is initiated, leading to a switch in site conformations (arrows in C). P_i derived from the already-resident ATP (green) is released (the exact timing is unsolved; see text and ref. 7). Release of already-resident ADP (blue) occurs from state D. Note that ATP binding (red), ATP hydrolysis (green) and ADP release (blue) occur at three different sites, and that at the end of the first 0°-to-120° rotation step, incoming ATP (red) is still bound intact. (**b**) The ATP-waiting state at the beginning of the second (120° to 240°) step. In this step the red ATP will be hydrolyzed. (**c**) The ATP-waiting state at the beginning of the third (240° to 360°) rotation step. In this step the red ADP will be released.

occur during one complete 360° turn. Börsch and colleagues detected three pause positions, each with a distinct FRET level. The important findings were that during proton gradient–driven ATP synthesis, the same three FRET levels were observed as in ATP hydrolysis, indicating that the same 120° rotor stepping occurred. Furthermore, the order in which FRET levels appeared was opposite to that during ATP hydrolysis, demonstrating an opposite direction of rotation. How 120° steps of γ are harmonized with varied *c* ring stoichiometry (*n*, Fig. 1) now becomes a pertinent question.

Itoh *et al.*[3] determined the direction of rotation during ATP synthesis using a totally different approach. They attached magnetic beads to γ in $\alpha_3\beta_3\gamma$ subcomplex and fixed this molecule to a glass surface in an observation chamber, above which was mounted a circular set of electromagnets. After confirmation of robust rotation in the expected direction during ATP hydrolysis, the chamber was infused with buffer containing ADP and Pi, plus luciferin–luciferase, a system that emits photons when it reacts with ATP. And indeed, when γ was forcibly rotated by the magnets in the 'ATP synthesis direction,' at speeds from 3 to 10 Hz, photons were detected, indicating substantial ATP production with multiple turnovers (~5 s^{-1}) occurring on each molecule. From this elegant example of bioengineering, the authors conclude that ATP synthesis requires opposite rotational direction to that of hydrolysis, and that in a biological motor, applied mechanical force can reverse a chemical reaction that lies far from equilibrium.

The enzymatic mechanism of ATP hydrolysis has been elucidated previously using tryptophan probes to correlate catalytic site occupancy with function[5,7]. At physiological rate, in time average, all three catalytic sites are occupied, two by ADP and one by ATP. The mechanism is temporally intricate. Progression through enzyme intermediate states A–D (**Fig. 2a**) corresponds to hydrolysis of one ATP and release of one ADP, concomitant with one step of γ from 0° to 120°. State A for the two subsequent steps (120° to 240° and 240° to 360°) is shown in **Figure 2b,c**. Major features are: (i) the 'ATP-waiting state' (state A, **Fig. 2a**) to which incoming (red) ATP binds, contains two already-resident nucleotides, one ATP and one ADP; (ii) in the first 0°-to-120° step the already-resident ATP (green) is hydrolyzed; (iii) red ATP is hydrolyzed in the second step (120° to 240°) (**Fig. 2b**); (iv) the ADP derived from this ATP (red) is released in the third step (240° to 360°) (**Fig. 2c**).

All of these features have now been verified beautifully in a technical *tour de force* by Nishizaka *et al*[4]. Simultaneous observation of rotation of a bead duplex attached to γ, and binding, hydrolysis and release of a fluorescent ATP analog (Cy3-ATP) have been achieved, allowing temporal correlation of mechanical with enzymatic events. Evanescent wave excitation used to visualize Cy3-ATP allowed discrimination of the three catalytic site positions 120° apart. Thus, it was possible to track Cy3-ATP, establishing its binding in rotation step 1, hydrolysis in step 2 and release of Cy3-ADP in step 3. This convergence to an agreed enzymatic mechanism of ATP hydrolysis from independent approaches marks a milestone in ATP synthase research.

Nishizaka *et al.*[4] go much further, significantly advancing understanding of chemomechanical coupling in ATP synthase. The 120° steps of γ are discriminated into 80° and 40° substeps and binding of an incoming ATP is shown to induce the 0°-to-80° substep. This ATP binding also triggers hydrolysis of the already-resident ATP, and completion of this reaction is necessary to permit the 40° substep. ADP is released concomitantly with the 40° substep. Although Nishizaka *et al.*[4] discuss alternative scenarios, one with ADP released in the 80° substep, we believe this is contradicted by the observation of three sites occupied at V_{max}. From the direct demonstration of ATP binding, hydrolysis and ADP release, occurring in three different sites contemporaneously, evidently all three sites are involved in mechanically rotating γ, and the γ subunit maintains a constant spatial orientation toward this moving ensemble of chemical events. The P_i release event could not be accessed by the techniques used[4] and so its relation to mechanical movement remains an important unsolved issue. Extension of the approach to understanding the detailed mechanoenzymology of ATP synthesis will now be eagerly anticipated.

None of the above would have been possible without X-ray structural information derived by Walker, Leslie and colleagues[8], which was critical for guiding insertion of optical probes. A major advance would be to construct a pictorial series of ATP synthase structures corresponding to progression through the mechanoenzymatic sequence. So far there are structures of the ATP-waiting state (or a close relative) and of the trapped chemical transition state, but not of ground states with all three sites occupied[5].

Looking toward the future, an understanding of ATP synthase will clearly set the stage for biological nanomotor applications, whether by direct bioengineering of the enzyme itself, or by incorporation of the principles into manmade motors. There has been the feeling that this might take some time, but we could be pleasantly surprised.

ACKNOWLEDGMENTS

A.E.S. gratefully acknowledges support from US National Institutes of Health grant GM25349.

1. Noji, H., Yasuda, R., Yoshida, M. & Kinosita, K. *Nature* **386**, 299–302 (1997).
2. Diez, M. *et al. Nat. Struct. Mol. Biol.* **11**, 135–141 (2004).
3. Itoh, H. *et al.* Mechanically-driven ATP synthesis by F_1-ATPase. *Nature* in the press (2004).
4. Nishizaka, T. *et al. Nat. Struct. Mol. Biol.* 142–148 (2004).
5. Weber, J. & Senior, A.E. *FEBS Lett.* **545**, 61–70 (2003).
6. Noji, H., & Yoshida, M. *J. Biol. Chem.* **276**, 1665–1668 (2001).
7. Weber, J. & Senior, A.E. *Biochim. Biophys. Acta* **1458**, 300–309 (2000).
8. Leslie, A.G.W. & Walker, J.E. *Phil. Trans. R. Soc. Lond. B* **355**, 465–472 (2000).

Sizing up small RNAs

Plants use small interfering RNAs (siRNAs), in a process called RNA silencing, to mediate sequence-specific degradation of viral RNAs and thereby defend against attack. Viruses have developed a counter-defense. Their genomes encode proteins that specifically suppress siRNA-mediated degradation. The mechanisms of this suppression are not yet understood.

RNA silencing, a conserved gene inactivation mechanism, involves sequential processing of a double-stranded RNA into short (21–26 nucleotides in length) duplex siRNAs with 3′ overhangs of two nucleotides. One strand of the duplex is incorporated into the RNA-induced silencing complex (RISC) and targets mRNAs with sequence complementarity for degradation. How then is a foreign RNA, such as that of a virus, targeted for degradation? Most plant viruses replicate their genome via double-stranded RNA intermediates that are substrates for the siRNA-generating machinery. The viral RNA is cut, processed and incorporated into RISC, thereby targeting the viral genome and mRNAs.

Some viruses have evolved proteins that inhibit destruction of their RNA. For example, tombusviruses express a protein, p19, that is proposed to sequester viral-based siRNAs and prevent their incorporation into RISC. Two groups, Ye *et al.* (*Nature* **426**, 874–878; 2003) and Vargason *et al.* (*Cell* **115**, 799–811; 2003), now present crystal structures of p19 from tomato bushy stunt virus (TBSV) and *carnation Italian* ringspot virus (CIRV) bound to a 21-nucleotide siRNA. The structures and accompanying biochemical data show how p19 selects siRNA based on the length of the duplex region.

The structures yield two surprises. First, the mode of recognition of the double-stranded RNA is unusual among RNA-binding proteins. Specifically, p19 binds the RNA as a dimer (blue and green ribbons) and uses primarily β-strand rather than loop and helical residues to bind the A-form RNA (gray helix). The concave saddle-shaped surface of the protein facing the RNA is rich in serine and threonine residues (ten per dimer). These residues form a network of interactions through their hydroxyl groups to the 2′-OH of the RNA. Ye *et al.* propose that p19 uses these interactions to distinguish between RNA and DNA duplexes. The second structural

surprise is that p19 acts as a caliper to measure and specifically select siRNA based on the length of the duplex region. Two tryptophans from each monomer (red ball-and-stick models) stack on the terminal base pairs and bracket the RNA. The tryptophans are located on two helices that are linked to the core of the protein through flexible loops (dashed lines). These reading head helices accommodate siRNA with a duplex region of 18–20 nucleotides while maintaining relatively tight (nanomolar) binding.

Biochemical studies from both Ye *et al.* and Vargason *et al.* confirm that RNA size does matter for high-affinity binding to p19. This affinity decreases about five-fold when one base pair is added or deleted from the siRNA. Removal of a second base pair results in a more dramatic, 320-fold decrease in affinity. Vargason *et al.* also show that mutation of either one or both tryptophans is detrimental to *in vivo* suppressor activity of p19.

These structural and biochemical results have broad implications for the understanding of RNA silencing and possibly microRNA (miRNA)-controlled endogenous gene expression. In the latter, short-lived double-stranded intermediates, similar to siRNAs, precede incorporation of miRNA into RISC. The observation that p19 recognizes siRNA of a specific size but in a sequence-independent manner suggests that this protein could also bind double-stranded miRNA intermediates. This ability of p19 to recognize small RNAs by size and not sequence can be exploited to dissect the fundamental mechanisms of RNA silencing and miRNA-mediated gene expression in different eukaryotes. ***Evelyn Jabri***

Unconstrained Steps of Myosin VI Appear Longest among Known Molecular Motors

M. Yusuf Ali,*† Kazuaki Homma,‡ Atsuko Hikikoshi Iwane,§ Kengo Adachi,* Hiroyasu Itoh,¶‖ Kazuhiko Kinosita Jr.,* Toshio Yanagida,§ and Mitsuo Ikebe‡

Okazaki Institute for Integrative Bioscience, National Institutes of Natural Sciences, Higashiyama 5-1, Myodaiji, Okazaki 444-8787, Japan; †Department of Physics, Faculty of Physical Sciences, Shahjalal University of Science and Technology, Sylhet-3114, Bangladesh; ‡Department of Physiology, University of Massachusetts Medical School, Worcester, Massachusetts 01655-0127, USA; §Department of Physiology and Biosignaling, Graduate School of Medicine, Osaka University, Yamadaoka 2-2, Suita 565-0871, Japan; ¶Tsukuba Research Laboratory, Hamamatsu Photonics KK, Tokodai, Tsukuba 300-2635, Japan; and ‖Core Research for Evolutional Science and Technology "Creation and Application of Soft Nano-Machine, the Hyperfunctional Molecular Machine" Team 13, Tokodai, Tsukuba 300-2635, Japan

ABSTRACT Myosin VI is a two-headed molecular motor that moves along an actin filament in the direction opposite to most other myosins. Previously, a single myosin VI molecule has been shown to proceed with steps that are large compared to its neck size: either it walks by somehow extending its neck or one head slides along actin for a long distance before the other head lands. To inquire into these and other possible mechanism of motility, we suspended an actin filament between two plastic beads, and let a single myosin VI molecule carrying a bead duplex move along the actin. This configuration, unlike previous studies, allows unconstrained rotation of myosin VI around the right-handed double helix of actin. Myosin VI moved almost straight or as a right-handed spiral with a pitch of several micrometers, indicating that the molecule walks with strides slightly longer than the actin helical repeat of 36 nm. The large steps without much rotation suggest kinesin-type walking with extended and flexible necks, but how to move forward with flexible necks, even under a backward load, is not clear. As an answer, we propose that a conformational change in the lifted head would facilitate landing on a forward, rather than backward, site. This mechanism may underlie stepping of all two-headed molecular motors including kinesin and myosin V.

INTRODUCTION

Myosin VI is a member of the myosin superfamily that consists of adenosine 5′-triphosphate (ATP)-driven molecular motors that track along an actin filament. It is believed that myosin VI plays a role in intracellular vesicle and organelle transport (Mermall et al., 1994). Myosin VI is distinct from other members in that it moves in the opposite direction on an actin filament toward the pointed, or minus, end (Wells et al., 1999; Homma et al., 2001). The movement is stepwise, and processive in that a single molecule of myosin VI moves for many steps without detaching from actin (Rock et al., 2001; Nishikawa et al., 2002). Another class of myosin, myosin V that moves toward the barbed, or plus, end, has also been shown to be a processive stepper (Mehta et al., 1999; Rief et al., 2000; Tanaka et al., 2002; Ali et al., 2002). Both myosin VI and V, like most other myosins, have two globular motor domains, usually called heads. The heads are connected through a neck-like structure, reinforced with light chains, to a central stalk (Fig. 1 *a*). A head of myosin binds to actin and hydrolyzes ATP to produce a mechanical step, possibly by tilting the neck forward as a lever (Huxley, 1969; Walker et al., 2000). The neck of myosin V indeed appears to tilt (Walker et al., 2000; Burgess et al., 2002; Forkey et al., 2003), and tilting of the long neck can account for the observed step size (Mehta et al., 1999; Rief et al., 2000; Tanaka et al., 2002; Ali et al., 2002) of ~36 nm (Fig. 1 *a*). However, myosin VI (Rock et al., 2001; Nishikawa et al., 2002) and a truncation mutant of myosin V (Tanaka et al., 2002), both of which are short necked, also showed similar step sizes, casting doubt on simple walking.

Most of these previous studies did not allow free rotation of myosin around an actin filament, and thus myosin may have been forced to step between binding sites that are 36 nm apart along one side of the actin filament. Unconstrained motion of myosin V on an actin bridge (Fig. 1 *b*) has been shown to be a long-pitch (2.2 μm) left-handed spiral (Ali et al., 2002), indicating an average step size of 34.8 nm that is slightly shorter than the actin helical repeat. Short-necked myosin VI would spiral with a shorter pitch (<2 μm) to the left or spiral with the 72-nm actin pitch to the right if the step size is <18 nm. To see if, or how, myosin VI spirals, we constructed the system in Fig. 1 *b*. The result was an unexpected one, a long-pitch right-handed spiral, which is difficult to explain by the lever action alone. We propose that a conformational change in a lifted head is an important mechanism that assures these and other linear molecular motors to proceed in the correct direction even under a backward load.

Submitted November 18, 2003, and accepted for publication February 24, 2004

Address reprint requests to Kazuhiko Kinosita Jr., Okazaki Institute for Integrative Bioscience, National Institutes of Natural Sciences, Higashiyama 5-1, Myodaiji, Okazaki 444-8787, Japan. Tel.: 81-564-59-5230; Fax: 81-59-564-5234; E-mail: kazuhiko@ims.ac.jp.

0006-3495/04/06/3804/07 $2.00

MATERIALS AND METHODS

Proteins and beads

A recombinant, full-length myosin VI (M6WT) was expressed and purified as described (Nishikawa et al., 2002). Actin was biotinylated and stained

doi: 10.1529/biophysj.103.037416

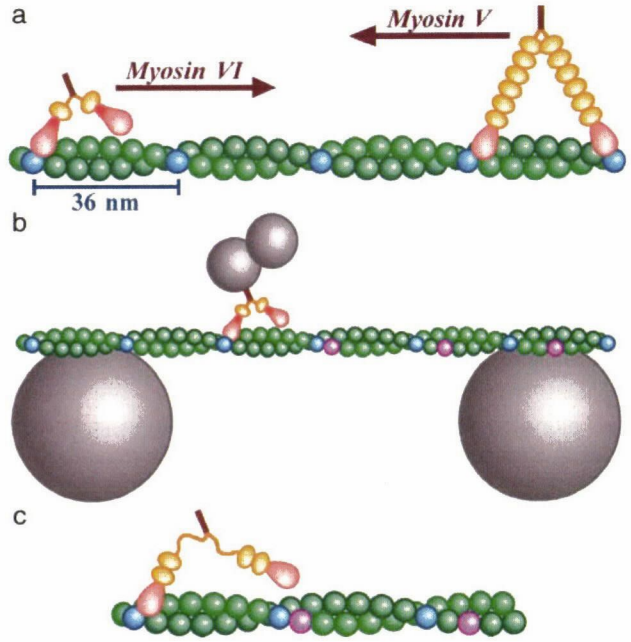

FIGURE 1 Experimental design. (*a*) Movement of myosin VI and V along an actin filament. Heads of myosins are in pink, and necks in orange, orange balls representing a light chain or calmodulin that binds to the neck. Myosin VI contains an extra insert in the head (*red*). Every 13th monomers of actin (*green*), counting both strands, are shown in blue. The barbed (fast growing) end of the filament is on the left. (*b*) Motility assay system (not to scale). An actin bridge was made on two beads, either 4.5 or 6 μm in diameter. A duplex of smaller beads carrying a myosin VI molecule was allowed to move freely along and around the filament. (*c*) Recent work indicates that the extra insert in myosin VI is a second calmodulin binding domain and that a flexible region connects it to the stalk (see text).

with phalloidin-tetramethylrhodamine (Ali et al., 2002). A quantity of 1-μm polystyrene beads (F-8814, Molecular Probes, Eugene, OR), or a mixture of 1- and 0.45-μm beads, were treated (Ali et al., 2002) in buffer A (10 mM imidazole (pH 7.6), 150 mM KCl, 1 mM $MgCl_2$, 1 mM EGTA, 10 mM dithiothreitol (DTT)) containing 10 mg/ml bovine serum albumin (BSA) to form duplexes (~10% of all beads). The beads were coated with myosin VI by mixing at myosin/bead molar ratio c in buffer A containing 10 mg/ml bovine serum albumin, as described (Rief et al., 2000). The coating efficiency was estimated (Ali et al., 2002) by challenging a single (not duplex) bead against an actin filament to see if it bound and moved in buffer A containing 5 mM ATP. The fractions of beads that bound to actin, p_b, and that bound and moved, p_m, could be fitted with $p = 1 - \exp(-\lambda c)$, which represents the theoretical probability (based on Poisson statistics) that a bead carries one or more active motors (Block et al., 1990); λ_b was 0.028, and λ_m was 0.010. Motility assay was performed at $c = 1$ ($p_m = 0.01$ and $p_b = 0.03$), $c = 20$ ($p_m = 0.18$ and $p_b = 0.43$), or $c = 1000$ ($p = 1$).

Motility assay

Actin bridges between 4.5- or 6.0-μm carboxylated polystyrene beads (Polyscience, Warrington, PA) were formed in a flow chamber (Ali et al., 2002). Then, beads decorated with myosin VI in buffer A containing ATP, 6 mg/ml glucose, 0.2 mg/ml glucose oxidase, 0.02 mg/ml catalase, and 0.2% β-mercaptoethanol were infused. To minimize Brownian motion, we selected a tightly suspended actin filament, and positioned a bead duplex onto the filament using optical tweezers (Suzuki et al., 1996). We moved the filament by moving the microscope stage until it bound the duplex, and turned off the optical trap to let the duplex move along the actin filament. Bright-field images showing bead movement and fluorescence images showing actin filaments were simultaneously recorded with video cameras (Suzuki et al., 1996). Positions and orientations of bead duplexes were analyzed by eye to the precision of ± 1 pixel (0.13 μm) and ± 0.2 revolutions (Ali et al., 2002). Observations were made at 26°C.

RESULTS AND DISCUSSION

Spiral motion of myosin VI

After confirming the formation of a fluorescently stained actin bridge between large beads (Fig. 1 *b*), we selected a bead duplex carrying myosin VI with optical tweezers and manipulated it around the actin bridge, in the presence of ATP, until the duplex started to move along actin. Most duplexes did not move at the myosin/bead ratio $c = 1$ or 20 (Table 1), indicating, on the assumption of Poisson statistics (Block et al., 1990), that >98% ($c = 1$) or >90% ($c = 20$) of duplexes that moved carried only one active myosin molecule (also see Materials and Methods above); most duplexes moved at $c = 1000$. At 5 mM ATP, the average velocity was 230 nm/s, consistent with previous studies (Rock et al., 2001; Nishikawa et al., 2002).

Fig. 2 *a* shows sequential images of a bead duplex (*upper rows*) and actin filament (*lower rows*) at 0.4-s intervals. The dashed lines in the upper images show the position of the actin filament deduced from the lower images. The focus for the upper images was set such that a bead appears white when it is closer to the observer and black when it is away. The upper images thus show that the bead duplex moved as a right-handed spiral around the actin filament. In 10.8 s, the duplex moved 1.4 μm while making 1.0 turn, indicating a spiral pitch of 1.4 μm. Fig. 2, *b* and *c*, compile six time courses, of which three show right-handed spiraling and the others straight movement without significant rotation. Except for one left-handed spiral at $c = 1000$, we observed only these two patterns, and we observed mostly straight

TABLE 1 Summary of bead-duplex experiments

Myosin/bead (c)	1	20	1000
Total number tested*	694	729	31
Duplexes bound to actin	40	243	30
Moved for >0.5 μm	24	143	25
Rotated for >0.5 turn†	5	18	7
Pitch (μm/turn)	2.2 ± 1.1	2.5 ± 1.3	5.6 ± 2.9
Run length (μm)	1.0 ± 0.4	1.8 ± 0.9	3.0 ± 1.1
Moved straight	19	125	18
Run length (μm)	1.2 ± 0.5	1.3 ± 1.3	3.6 ± 1.4

ATP concentrations were 100 μM, 400 μM, or 5 mM. The average velocity estimated on randomly chosen data was 230 ± 91 nm/s at 5 mM ($n = 18$), 48 ± 30 nm/s at 400 μM ($n = 40$), and 18 ± 11 nm/s at 100 μM ($n = 20$); no significant dependence on c. All ranges are standard deviations.

*A duplex was manipulated for ~30 s from various directions toward actin. This maneuver was repeated at least 5 times (10 at $c = 1$) until binding occurred.

†All rotations were right handed except for one at $c = 1000$, which was left handed with a pitch of 3.3 μm/turn and run length of 5 μm. Pitch and run length in this table do not include this datum.

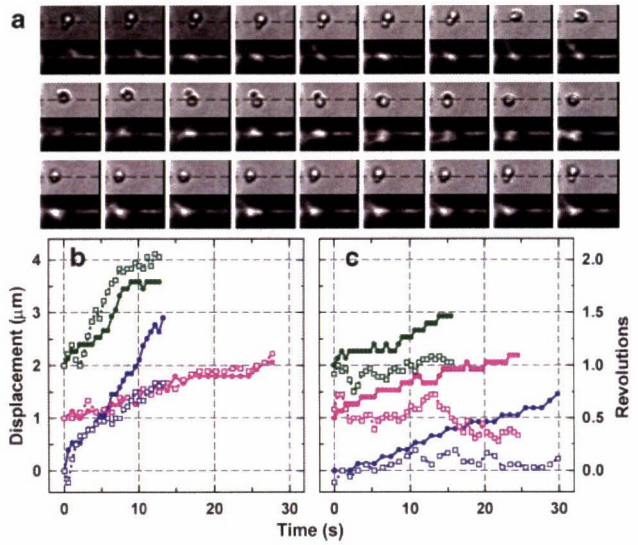

FIGURE 2 Examples of duplex movement. (*a*) Sequential images at 0.4-s intervals. Upper and lower panels show bright-field and corresponding fluorescence images; width of each panel, 7.4 μm. (*Dashed lines*) Position of the actin filament deduced from lower panels. This bead duplex (1 and 0.45 μm) carried a short actin filament that also rotated. (*b* and *c*) Time courses for spiral (*b*) and straight (*c*) movements at $c = 1$ (*green*), 20 (*magenta*), and 1000 (*blue*). (*Closed symbols*) Displacement along actin; (*open symbols*) rotation. ATP concentration was 400 μM, except for the blue curve in *b* (5 mM). For clarity, curves are shifted vertically. Images in *a* correspond to part of green curves in *b*. Also see movies in Supplementary Material.

motion as shown in Table 1. Also, as with kinesin (Hua et al., 2002) and myosin V (Ali et al., 2002), we did not observe clear 180° rotation of myosin VI around its own axis that is expected to accompany every step if a motor with two identical heads attains the same posture after each step (Howard, 1996). The absence of 180° rotation is accounted for if a free joint(s) exists in the necks to give the motor the freedom of adopting different postures after even and odd steps. For myosins (including VI and V) with necks reinforced with light chains, a free joint must exist to orient both heads in the same direction, breaking their twofold symmetry, when the two heads attach to actin during processive walking. Electron micrographs of myosin V (Walker et al., 2000) indeed indicate the presence of a free joint near the neck-stalk junction. The absence of extensive rotation, either spiraling or the 180° rotation, could be due to the attachment of a bead duplex that would impede fast rotation. However, slowing down the overall motion by a factor of >10, by reducing the ATP concentration down to 100 μM, did not change the motional patterns (Table 1).

The straight movement of myosin VI on one side of the actin filaments implies an average step size coincident with the actin helical repeat of 36 nm (*blue* subunits in Fig. 1). The right-handed spiral indicates larger steps (*purple* in Fig. 1 *b*). The pitch of 2.4 μm (mean at $c \leq 20$) implies (Ali et al., 2002) a step size of 36 nm $\times$ (2400 nm + 72 nm)/(2400 nm) = 37.1 nm. These step sizes are slightly longer than those of myosin V or of myosin XI (Tominaga et al., 2003), which are both long necked: to walk with such long strides, myosin VI has to somehow extend its necks. Another possibility is the sliding of an attached head along one strand of actin, whereby short-necked myosin VI could produce an apparently large step size (Nishikawa et al., 2002; Tanaka et al., 2002). The essentially straight motion observed here could be explained if the short-pitch (72 nm) spiraling expected to accompany the sliding is precisely cancelled by crossing, with the other head, onto the other strand. Here we focus on the simpler mechanism of neck extension.

Myosin VI may move like kinesin

The idea of neck extension is not unprecedented. Conventional kinesin, which proceeds along a microtubule with 8-nm steps (Svoboda et al., 1993), has two rather short necks that are not reinforced with light chains and are considered flexible. In a likely scenario (Vale and Milligan, 2000), an unattached head makes a diffusional search for a next binding site. The sites are distributed 8-nm apart, and reaching the site 8-nm ahead requires almost full extension of the flexible necks. To bias the diffusion of the unattached head in the forward direction, the attached head docks a part of its neck, called neck-linker, such that the docked part is oriented forward. It is undocked again to extend the neck when the associate head is to be thrown forward. For myosin VI, two possibilities have been suggested for its neck extension: undocking or unfolding of the extra insert in the head (*red* parts in Fig. 1) (Rock et al., 2001), or unzippering of part of the stalk coiled coil (Nishikawa et al., 2002). An electron micrograph indeed showed necks of myosin VI that were somehow extended (Nishikawa et al., 2002). More recent work indicates that the extra insert in myosin VI is actually a second calmodulin binding domain (Bahloul et al., 2004), and that a flexible region follows this part before the two necks join to form a coiled coil (B. R. Rami and J. A. Spudich, Stanford University, and H. L. Sweeney and C. Franzini-Armstrong, Pennsylvania University, personal communications, 2004). Thus, myosin VI seems to be able to span the observed ~36-nm step size by extending the flexible portion of its two necks (Fig. 1 *c*). The probably stiff calmodulin-binding region could serve as a lever, but the lever is too short (~8 nm) to carry a lifted head 36 nm forward. The head must reach the forward binding site by diffusion. Myosin VI likely walks in a way similar to kinesin (biased diffusional search).

Biasing of diffusion, however, is not trivial in the presence of an opposing external force. In kinesin, the free energy difference between the docked and undocked states is small (Rice et al., 2003), implying that docking would fail when the stalk is pulled back by a load. For myosin V, rotating a landed neck forward as a lever (Moore et al., 2001; Veigel et al., 2002; Burgess et al., 2002) could serve the purpose of biasing the diffusion of the lifted head. For forward bias,

however, the pivot near the neck-stalk junction (Fig. 3 *a*) has to pass the attached head by moving forward by $>\approx 18$ nm (Fig. 1 *a*). But the pivot would be pulled back by 10 nm at 2 pN of backward load where myosin V still moves forward (Rief et al., 2000), given an estimated neck stiffness (Veigel et al., 2002) of 0.2 pN/nm. Also, rotating the attached neck, ~23 nm long, against the backward load of 2 pN requires a torque of more than 40 pN·nm, the torque of a powerful rotary motor F_1-ATPase (Yasuda et al., 1998). For myosin V, too, simple biasing seems difficult at a high load. This is more serious with myosin VI for which the lever is short and the rest of the neck is flexible: when the stalk is pulled backward, the unattached head would tend to diffuse backward rather than forward. Nevertheless, myosin VI moves forward under a backward load up to ~2 pN (Rock et al., 2001; Nishikawa et al., 2002).

Toe up-down mechanism

Here we propose a new concept for biasing. Because we discuss walking mechanisms in this section, we call the heads "feet" and necks "legs," and construct a toy model as in Fig. 3. The ankle between a foot and leg is assumed to be bent forward or backward, depending on the state of bound nucleotide. This has been shown for myosin V (Walker et al., 2000; Burgess et al., 2002), and the ankle action in a landed foot is the basic idea of the lever action mechanism. The ankle action is yet to be demonstrated for myosin VI, for which forward implies the opposite direction. For kinesin, docking/undocking of the neck linker may be regarded as the ankle action. Our proposal here is that the ankle action in a lifted foot is equally, or possibly more, important: through the ankle action, the sole is correctly oriented such that landing on a forward site is favored compared to a backward site. This mechanism is distinct from the biasing of diffusion itself, whereby a lifted foot is positioned above a forward site (e.g., Woehlke and Schliwa, 2000) irrespective of whether the sole is oriented properly or not. The mechanism is also distinct from the selection of a proper prepowerstroke configuration that would ensure an efficient lever action after landing (Xu and Root, 2000).

First, we deal with the case of elastic legs that are connected to the stalk through a free joint (Fig. 3 *a*). Legs of myosin V are presumably semirigid and elastic. The case of flexible legs, expected for kinesin, will be considered later, followed by discussion of myosin VI. We assume that bending an elastic leg requires a considerable amount of energy. Key features to note in Fig. 3 are whether a leg is straight and thus is relaxed and whether a sole is parallel to the surface to allow rapid and stable landing. 1), When both feet land on actin, the posture with least strain (bending) in the legs is the one in which the forward toe (*red*) is down and rear toe (*green*) is up (Fig. 3 *d1*). 2), Bending of the red ankle into toe up position, e.g., upon phosphate release, pulls the green foot and brings it up, e.g., by promoting adenosine 5′-diphosphate (ADP) release and subsequent ATP binding in the rear foot (Fig. 3, *d2* and *d3*). This is the lever action. 3), The red leg leans forward and biases the diffusion of the green leg forward. 4), If the green toe remains up, however, its landing on a distant forward site would be difficult because the sole is not in the correct orientation (Fig. 3 *d4*), and forced landing would result in leg bending (Fig. 3 *d5*); natural landing would be on a site close to the red foot (Fig. 3 *d6*). 5), If the green toe goes down upon lifting (Fig. 3 *e1*), e.g., in response to ATP binding or subsequent hydrolysis, its natural landing site will be a distant forward site (Fig. 3, *e3* and *e4*), whereas other sites would induce leg bending (Fig. 3, *e2*, *e5*, and *e6*). Thus, toe up-down in the lifted foot correctly selects a distant forward site for landing, independent of biased diffusion.

The biased landing by toe up-down operates even if the body (stalk) of the motor is pulled back by an external load. If the leg-stalk junction is pulled back beyond the red foot, simple biasing through leg fluctuation around the junction would fail and tend to promote backward landing (Fig. 3 *f1*). With the green toe down, however, the green foot still tends to land on a distant forward site (Fig. 3, *f3* and *f4*) and not on a backward site (Fig. 3 *f2*), although landing near the red foot would also be allowed if the external force is very high (Fig. 3 *f6*).

The biased landing by toe up-down can operate even if legs are completely flexible, as in kinesin, as long as the landing sites are far apart and require full extension of legs (Fig. 3, *h1* and *h3*). This is because the orientation of the sole on a fully extended leg is restricted, and the sole orientation in the extended leg is dependent on the bend of the ankle (compare Fig. 3, *h1* and *h2*).

Legs of myosin VI are presumably semirigid in the lower half and flexible in the upper half (Fig. 1 *c*). Unless the ankle action occurs obliquely (see below), the stiff lower legs would make landing at intermediate distances difficult, because that would require an extremely bowlegged posture (Fig. 3, *g2* and *g3*). This accounts for the observed long strides. Because the long strides require almost full extension of the flexible part, landing on a forward site will be warranted, as with kinesin (Fig. 3 *h*). Unlike a microtubule, however, an actin filament offers landing sites close to a landed foot. If the upper leg is flexible over a sizable length, landing on a nearby forward site (Fig. 3 *f6*) will not add much strain, particularly in the presence of a backward force. Thus, with an increase in the backward load, we expect to observe frequent short steps in myosin VI, resulting in a smaller average step size. In this regard, the right-handed spiral that we observe here in the absence of a load could also be due to occasional landing on a nearby site (Fig. 3 *e5*), although most of the steps must still be made onto a site ~36 nm forward.

Because both myosin VI and V move essentially straight along actin, the ankle actions in Fig. 3 are all assumed to be along the axis of actin. One could, in principle, design a spiral

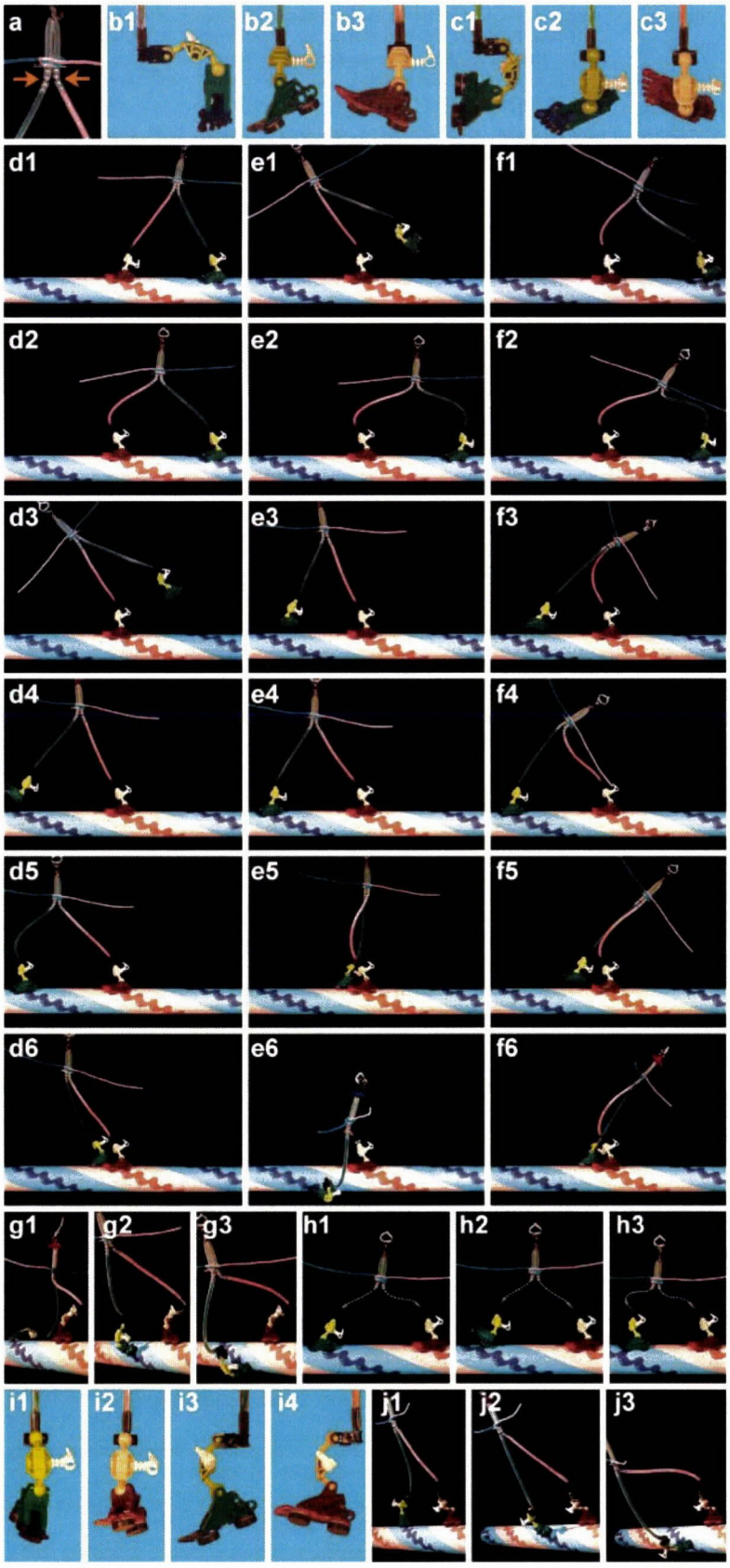

FIGURE 3 A toy model showing various walking postures. Note whether a leg is straight and strain free and whether a sole is parallel to the surface to allow rapid and stable landing. (*a*) Free joints likely reside near the leg (neck)-stalk junction in myosin V (Walker et al., 2000) and in other parts, too, in kinesin and myosin VI. (*b*) Toe down (*green*) and toe up (*red*) positions are assumed. (*c*) Various ankle structures are possible, such as this where the leg and sole are parallel, but toe up/down always means the toe being closer to (*red*)/farther from (*green*) the leg. (*d*) Walking forward with the lifted toe in the up position is difficult. (*e*) Walking is easy if the lifted toe is down. (*f*) With the lifted toe down, landing will be on a forward, rather than backward, site even in the presence of a backward force. (*g*) Straight toe up-down makes spiral landing difficult. (*g1*) On 17th subunit; (*g2*) on 11th; (*g3*) on 7th. (*h*) Even with flexible legs (many free joints), toe down in the lifted foot assures forward landing if landing requires full extension of the legs. (*i*) Ankles that work obliquely. (*j*) Oblique ankles make a spiral motor; compare the straight legs in *j2* and the bent legs in *g2*.

motor using oblique ankles (Fig. 3, *i* and *j*). Nature, though, would not adopt such a design unless she finds a merit in extensive spiraling. One might think that, starting from Fig. 3 *j2*, the red foot could move straight forward and land on the blue site 36 nm ahead. If the green foot then also moves straight forward and lands on the red site 36 nm ahead, the result would be a straight motion of the whole motor without spiraling, with the average step size of 18 nm, not 36 nm. This, however, is extremely unlikely, because the red ankle would alternate between forward-left (Fig. 3 *j2*) and backward-left configurations, whereas the green ankle would alternate between forward right and backward right (Fig. 3 *j2*): the two ankles, which are basically identical, would undergo completely different series of conformational changes to power the motor. Oblique ankles are thus destined to make a spiral motion, through the alternation of forward left and backward right (or forward right and backward left).

Previously suggested mechanisms, docking/undocking in kinesin and lever action in myosin, focus on the ankle action in the landed foot (*red foot* in Fig. 3). Here we propose that the toe up-down in the lifted foot is equally important, and that the selection of a correct binding site by this mechanism may in fact be the most essential mechanism of assuring forward stepping in all linear motors with multiple legs. Another important mechanism for forward stepping is the preferential detachment of the rear foot after, and only after, the fore foot has landed. This will be achieved by strain dependence of ATPase kinetics, as has been suggested by many researchers. For myosin, landing of the fore foot will introduce strain in the rear foot, such that ADP release is promoted in the rear foot, leading to subsequent ATP binding and detachment of the rear foot (see, e.g., Veigel et al., 2002), possibly aided by toe down (= heel up) action. The affinity of kinesin for ADP has been shown to be strain dependent (Uemura and Ishiwata, 2003).

SUPPLEMENTARY MATERIAL

An online supplement to this article can be found by visiting BJ Online at http://www.biophysj.org. Two movies are available: movie 1 corresponds to part of Fig. 2 *a* and movie 2 to part of magenta curve in Fig. 2 *c*. Both are 4× slow replay when played at 30 frames/s.

We thank S Uemura and S. Ishiwata for valuable advices and comments, Y. Onoue, K. Yogo, N. Sakaki, and other members of Kinosita lab for help, M. Shio for optical tweezers, H L Sweeney, C. Franzini-Armstrong, B. R. Rami, and J. A. Spudich for communicating unpublished work, and M. Fukatsu for the toy model and lab management.

This work was supported in part by Grants-in-Aid from the Ministry of Education, Culture, Sports, Science and Technology of Japan.

REFERENCES

Ali, M. Y., S. Uemura, K. Adachi, H Itoh, K. Kinosita, Jr., and S. Ishiwata. 2002. Myosin V is a left-handed spiral motor on the right-handed actin helix. *Nat Struct Biol* 9:464–467.

Bahloul, A., G Chevreux, A. L. Wells, D. Martin, J. Nolt, Z. Yang, L.-Q. Chen, N. Potier, A. Van Dorsselaer, S. Rosenfeld, A. Houdusse, and H. L Sweeney. 2004 The unique insert in myosin VI is a structural calcium-calmodulin binding site *Proc Natl Acad. Sci USA* 101: 4787–4792

Block, S. M., L. S. Goldstein, and B. J. Schnapp. 1990. Bead movement by single kinesin molecules studied with optical tweezers. *Nature* 348: 348–352

Burgess, S , M. Walker, F. Wang, J. R. Sellers, H. D White, P. J Knight, and J Trinick 2002. The prepower stroke conformation of myosin V *J Cell Biol* 159:983–991.

Forkey, J. N., M. E. Quinlan, M. A. Shaw, J. E. T. Corrie, and Y. E Goldman. 2003. Three-dimensional structural dynamics of myosin V by single-molecule fluorescence polarization *Nature* 422:399–404.

Homma, K , M. Yoshimura, J. Saito, R. Ikebe, and M. Ikebe. 2001. The core of the motor domain determines the direction of myosin movement *Nature* 412 831–834.

Howard, J. 1996. The movement of kinesin along microtubules. *Annu Rev Physiol* 58:703–729

Hua, W., J. Chung, and J. Gelles. 2002. Distinguishing inchworm and hand-over-hand processive kinesin movement by neck rotation measurements. *Science* 295:844–848.

Huxley, H. E. 1969 The mechanism of muscular contraction. *Science* 164:1356–1366.

Mehta, A. D , R S. Rock, M. Rief, J. A. Spudich, M. S. Mooseker, and R. E. Cheney. 1999. Myosin-V is a processive actin-based motor. *Nature* 400:590–593.

Mermall, V., J. G. McNally, and K. G. Miller. 1994. Transport of cytoplasmic particles catalysed by an unconventional myosin in living *Drosophila* embryos. *Nature* 369:560–562.

Moore, J. R., E. B Krementsova, K. M. Trybus, and D. M. Warshaw. 2001. Myosin V exhibits a high duty cycle and large unitary displacement. *J Cell Biol* 155.625–635.

Nishikawa, S , K Homma, Y Komori, M Iwaki, T. Wazawa, A. H. Iwane, J. Saito, R. Ikebe, E. Katayama, T. Yanagida, and M. Ikebe. 2002 Class VI myosin moves processively along actin filaments backward with large steps. *Biochem Biophys Res Commun* 290:311–317.

Rice, S., Y. Cui, C Sindelar, N. Naber, M. Matuska, R. Vale, and R. Cooke. 2003. Thermodynamic properties of the kinesin neck-region docking to the catalytic core. *Biophys J* 84.1844–1854

Rief, M., R. S. Rock, A. D Mehta, M. S Mooseker, R E Cheney, and J. A. Spudich. 2000. Myosin-V stepping kinetics a molecular model for processivity. *Proc Natl Acad Sci USA* 97:9482–9486

Rock, R. S., S E Rice, A. L Wells, T. J. Purcell, J A. Spudich, and H. L. Sweeney. 2001. Myosin VI is a processive motor with a large step size. *Proc Natl Acad Sci USA* 98:13655–13659

Suzuki, N , H. Miyata, S. Ishiwata, and K. Kinosita Jr. 1996. Preparation of bead-tailed actin filaments: estimation of the torque produced by the sliding force in an in vitro motility assay *Biophys J* 70:401–408

Svoboda, K., C. F. Schmidt, B J. Schnapp, and S. M. Block. 1993. Direct observation of kinesin stepping by optical trapping interferometry. *Nature* 365:721–727.

Tanaka, H., K Homma, A. H. Iwane, E. Katayama, R. Ikebe, J. Saito, T. Yanagida, and M. Ikebe. 2002. The motor domain determines the large step of myosin-V. *Nature* 415:192–195.

Tominaga, M., H. Kojima, E. Yokota, H. Orii, R. Nakamori, E. Katayama, M. Anson, T Shimmen, and K. Oiwa. 2003. Higher plant myosin XI moves processively on actin with 35 nm steps at high velocity. *EMBO J* 22:1263–1272

Uemura, S., and S. Ishiwata. 2003. Loading direction regulates the affinity of ADP for kinesin *Nat Struct Biol* 10:308–311.

Vale, R. D., and R A. Milligan. 2000. The way things move: looking under the hood of molecular motor proteins. *Science* 288:88–95.

Veigel, C., F. Wang, M L. Bartoo, J R. Sellers, and J. E Molloy 2002 The gated gait of the processive molecular motor, myosin V. *Nat Cell Biol* 4:59–65.

Walker, M. L., S. A. Burgess, J. R. Sellers, F. Wang, J. A. Hammer, J. Trinick, and P. J. Knight. 2000. Two-headed binding of a processive myosin to F-actin. *Nature* 405:804–807.

Wells, A. L., A. W. Lin, L.-Q. Chen, D. Safer, S. M. Cain, T. Hasson, B. O. Carragher, R. A. Milligan, and H. L. Sweeney. 1999. Myosin VI is an actin-based motor that moves backwards. *Nature*. 401: 505–508.

Woehlke, G., and M. Schliwa. 2000. Directional motility of kinesin motor proteins. *Biochim Biophys Acta* 1496:117–127.

Xu, J., and D. D. Root. 2000. Conformational selection during weak binding at the actin and myosin interface. *Biophys J* 79:1498–1510.

Yasuda, R., H. Noji, K. Kinosita, Jr., and M. Yoshida. 1998. F_1-ATPase is a highly efficient molecular motor that rotates with discrete 120° steps. *Cell* 93:1117–1124.

One Rotary Mechanism for F_1-ATPase over ATP Concentrations from Millimolar down to Nanomolar

Naoyoshi Sakaki,*† Rieko Shimo-Kon,† Kengo Adachi,† Hiroyasu Itoh,‡§ Shou Furuike,† Eiro Muneyuki,¶ Masasuke Yoshida,¶‖ and Kazuhiko Kinosita Jr.†

Department of Functional Molecular Science, The Graduate University for Advanced Studies, Nishigonaka 38, Myodaiji, Okazaki 444-8585, Japan; †Okazaki Institute for Integrative Bioscience, National Institutes of Natural Sciences, Higashiyama 5-1, Myodaiji, Okazaki 444-8787, Japan; ‡Tsukuba Research Laboratory, Hamamatsu Photonics KK, and §CREST "Creation and Application of Soft Nano-Machine, the Hyperfunctional Molecular Machine" Team 13, Tokodai, Tsukuba 300-2635, Japan; ¶Chemical Resources Laboratory, Tokyo Institute of Technology, Nagatsuta 4259, Yokohama 226-8503, Japan; and ERATO "ATP System", Japan Science and Technology Agency, Nagatsuta 5800-3, Yokohama 226-0026, Japan

ABSTRACT F_1-ATPase is a rotary molecular motor in which the central γ-subunit rotates inside a cylinder made of $\alpha_3\beta_3$-subunits. The rotation is driven by ATP hydrolysis in three catalytic sites on the β-subunits. How many of the three catalytic sites are filled with a nucleotide during the course of rotation is an important yet unsettled question. Here we inquire whether F_1 rotates at extremely low ATP concentrations where the site occupancy is expected to be low. We observed under an optical microscope rotation of individual F_1 molecules that carried a bead duplex on the γ-subunit. Time-averaged rotation rate was proportional to the ATP concentration down to 200 pM, giving an apparent rate constant for ATP binding of $2 \times 10^7\ M^{-1}s^{-1}$. A similar rate constant characterized bulk ATP hydrolysis in solution, which obeyed a simple Michaelis-Menten scheme between 6 mM and 60 nM ATP. F_1 produced the same torque of ~40 pN nm at 2 mM, 60 nM, and 2 nM ATP. These results point to one rotary mechanism governing the entire range of nanomolar to millimolar ATP, although a switchover between two mechanisms cannot be dismissed. Below 1 nM ATP, we observed less regular rotations, indicative of the appearance of another reaction scheme.

INTRODUCTION

F_1-ATPase is a rotary molecular motor made of a single protein molecule (composed of several subunits). Its unidirectional rotation, driven by ATP hydrolysis, has been demonstrated under an optical microscope (Noji et al., 1997). In vivo, the F_1 motor is connected to a membrane-embedded F_o ("ef-ou" for *o*ligomycin sensitivity conferring *f*actor; see Kagawa and Racker, 1966) complex to constitute the ATP synthase, which synthesizes ATP from ADP and inorganic phosphate to support cellular activities (for reviews, see, e.g., Boyer, 1997; Yoshida et al., 2001; Weber and Senior, 2003). When protons flow through the F_o portion of ATP synthase, the F_1 motor is forced to rotate in its reverse direction; the chemical reaction in the catalytic sites of F_1 is also reversed, resulting in the synthesis of ATP. This scenario of rotational synthesis was suggested two decades ago (Boyer and Kohlbrenner, 1981; Oosawa and Hayashi, 1986), and now one sees experimentally that proton flow indeed leads to reverse rotation of F_1 (Diez et al., 2004) and that reverse rotation of isolated F_1 by a human artifact leads to ATP synthesis (Itoh et al., 2004). The ATP synthase is a reversible molecular machine in which the two reactions, proton translocation (in the direction from F_o to F_1) and ATP hydrolysis, couple with each other in an opposing fashion and can be balanced (Turina et al., 2003). Molecular mechanisms of the coupling between proton flow and rotation, and between rotation and ATP synthesis/hydrolysis, are yet to be worked out in detail.

The ATP-driven rotation in isolated F_1, without F_o, has been characterized relatively well (Kinosita et al., 2000a,b, 2004). Much of the work has been done on the minimal subcomplex of F_1 consisting of seven subunits, $\alpha_3\beta_3\gamma$, in which γ, the rotor, is surrounded by a stator cylinder made of three α and three β subunits arranged alternately (Abrahams et al., 1994). In this article, we call this subcomplex as F_1. The central γ rotates counterclockwise when viewed from the F_o side (Noji et al., 1997), in 120° steps each driven by hydrolysis of one ATP molecule (Yasuda et al., 1998). The rotary torque is almost independent of the rotary angle (Kinosita et al., 2000a), and the mechanical work done in a 120° step amounts to ~90 pN·nm (Yasuda et al., 1998), comparable to the free energy obtained by hydrolyzing one ATP molecule and thus suggesting a near 100% efficiency (but see Kinosita et al., 2004). The 120° step is resolved into 80–90° and 40–30° substeps (Yasuda et al., 2001; Shimabukuro et al., 2003; Nishizaka et al., 2004), separated by at least two chemical reactions each taking ~1 ms (Yasuda et al., 2001). The 80–90° substep is driven by ATP binding, and the 40–30° substep likely by the release of a hydrolysis product (Yasuda et al., 2001). ATP is hydrolyzed in one of the two 1-ms reactions between substeps (Shimabukuro et al., 2003).

The hydrolysis (and synthesis) of ATP occurs in three catalytic sites, each hosted primarily by a β-subunit (Abrahams et al., 1994). A major unanswered question is how the

Submitted October 28, 2004, and accepted for publication December 16, 2004

Address reprint requests to Kazuhiko Kinosita Jr., Okazaki Institute for Integrative Bioscience, National Institutes of Natural Sciences, Higashiyama 5-1, Myodaiji, Okazaki 444-8787, Japan. Tel.: 81-564-59-5230; Fax: 81-564-59-5234; E-mail: kazuhiko@ims ac.jp.

0006-3495/05/03/2047/10 $2.00

doi: 10 1529/biophysj.104.054668

stepwise rotation is coupled to distinct chemical reactions in the three sites. Even the site occupancy, the number of catalytic sites filled with a nucleotide during rotation, is yet in dispute. We suggested a bi-site mechanism in which the occupancy alternates between one and two, on the basis of Michaelis-Menten dependence of the rotation rate on the ATP concentration, [ATP], down to 20 nM (Yasuda et al., 2001). This view has been seriously questioned by Senior and colleagues, who introduced a tryptophan residue in the catalytic sites of *Escherichia coli* F_1 to probe the site occupancy (Weber et al., 1993): when the concentration of a substrate (ATP or ITP) was lowered, hydrolysis activity decreased disproportionately faster than the nucleotide concentration, and the activity was proportional to the fraction of F_1 with three sites filled (Weber and Senior, 2001), indicating that tri-site filling is a must for hydrolysis activity. With F_1 of thermophilic origin that we use, tryptophan mutation has suggested a similar conclusion (Ren and Allison, 2000; Ono et al., 2003). A crystal structure in which three sites are filled with a nucleotide (Menz et al., 2001) supports the tri-site view. When binding of a fluorescent ATP analog was imaged under a microscope, the nucleotide remained bound for at least 240° of rotation (Nishizaka et al., 2004), indicating an occupancy number of two or more for the ATP analog. A complication, however, exists in that F_1-ATPase tends to be inhibited by binding MgADP tightly (Jault et al., 1996; Matsui et al., 1997; Hirono-Hara et al., 2001) and the fraction of inhibited enzyme, often a majority, is difficult to assess. Bulk experiments could report properties of the inhibited form(s). Boyer (2002) maintains that bi-site activation is fundamental and retention of ADP could explain the apparent tri-site filling.

Here we have investigated the rotational properties of F_1 at low [ATP]s, down to 200 pM. Unlike solution studies with an unknown fraction of inhibited enzyme, imaging of individual rotations focuses only on active molecules. Our expectation was that the time-averaged rotation rate would decrease disproportionately faster than the reduction in [ATP], as reported for hydrolysis by Weber and Senior (2001). Actually, the rotation rate was found to be proportional to [ATP] down to 200 pM. If this rotation occurred in a tri-site mode, the enzyme must have kept two nucleotides extremely tightly, with a dissociation constant of ~1 nM or less.

MATERIALS AND METHODS

Unless stated otherwise, operations described below were done at room temperature (23–25°C), and solutions were at pH 7.0. When MgATP was present in a medium, $[Mg^{2+}]$ was always 2 mM in excess over [ATP].

Preparation of F_1

A mutant (α-C193S, β-His_{10} at amino terminus, γ-S107C, γ-I210C) $\alpha_3\beta_3\gamma$ subcomplex derived from a thermophilic *Bacillus* PS3 was purified as described (Adachi et al., 2003) with some modifications. Supernatant of cell lysate was heat-treated at 65°C for 10–15 min followed by centrifugation. The supernatant was applied to a Ni-NTA Superflow column (Qiagen, Hilden, Germany) equilibrated with 40 mM imidazole and 100 mM KCl, with the addition of 50 mM potassium phosphate to aid removal of the endogenously bound nucleotides (Noji et al., 2001). The column was washed with five column volumes of the same solution with imidazole at 100 mM, and the enzyme was eluted by raising the imidazole concentration to 500 mM. Ammonium sulfate was added to the final concentration of 10% saturation, and the solution was applied to a butyl-Toyopearl column (Tosoh, Tokyo) equilibrated with 2 mM EDTA, 50 mM Tris-HCl, 100 mM potassium phosphate, and 10% saturated ammonium sulfate. Bound nucleotides were removed by washing the column with 40 volumes of the same solution, and the enzyme was eluted with 2 mM EDTA, 50 mM Tris-HCl (pH 8.0), and ammonium sulfate at successive concentrations of 5, 3, 2, 1, and 0% saturation. The enzyme in the major fraction, normally at 2%, was stored at 4°C as precipitate in 70% saturated ammonium sulfate containing 1 mM dithiothreitol (DTT). Before use, the precipitate was dissolved in 100 mM potassium phosphate, 2 mM EDTA, and 1 mM DTT, and was incubated overnight at 4°C. To remove DTT and possible denatured enzyme, the sample was passed through a size exclusion column (Superdex 200 HR 10/30, Amersham Biosciences, Piscataway, NJ) equilibrated with 100 mM potassium phosphate and 2 mM EDTA. The concentration of F_1 was determined from the absorbance at 280 nm of 0.45 per mg/ml (Matsui et al., 1997), assuming the molecular weight of 356,000.

The nucleotides that remained on F_1 were assessed as follows: 100 μl of F_1 at a few μM was mixed with 5 μl of 24% (w/w) perchloric acid. After incubation for 5 min at room temperature, 5 μl of 1 M K_2CO_3 was added to neutralize the suspension. After 5-min incubation on ice and centrifugation, 50 μl of the supernatant was applied to a reverse phase column (TSK-GEL ODS-80Ts, Tosoh) equilibrated with 100 mM potassium phosphate (pH 6.8). Nucleotides (ATP or ADP) were undetectable, indicating that <0.05 mol nucleotide was bound per mol of F_1.

F_1 was biotinylated at two cysteines (γ-S107C, γ-I210C) by incubation with fourfold molar excess of 6-{*N'*-[2-(*N*-maleimido)ethyl]-*N*-piperazinyl-amido}hexyl D-biotinamide (Dojindo, Kumamoto, Japan) for 1 h at room temperature. Unbound biotin was removed with Superdex 200 HR 10/30 equilibrated with 100 mM sodium phosphate and 2 mM EDTA. Biotinylated F_1 was frozen with liquid nitrogen and stored at −80°C.

Hydrolysis activity

The ATP hydrolysis activity of F_1 was measured before biotinylation. Because phosphate exerts subtle but complicated effects on the hydrolysis kinetics (R. Shimo-Kon, unpublished) and free phosphate was absent in rotation assays, phosphate in the F_1 sample was removed on the size exclusion column above equilibrated with 100 mM KCl and 10 mM 3-(*N*-morpholino)propanesulfonic acid (MOPS)-KOH at pH 7.0.

ATP hydrolysis by F_1 was followed by coupling the reaction with the oxidation of NADH through an ATP-regenerating system and monitoring the disappearance of NADH from the absorbance at 340 nm (Matsui et al., 1997). The assay mixture contained 0.15 mM NADH, 2.5 mM phosphoenolpyruvate, 0.5 mg/ml pyruvate kinase (rabbit muscle, Roche Diagnostics, Mannheim, Germany; glycerol solution) supplemented with 3.3 mg/ml of the same enzyme (rabbit muscle, Sigma-Aldrich, St Louis, MO; powder with an activity lower than that of the Roche enzyme) to ensure rapid regeneration, and 0.05 mg/ml lactate dehydrogenase (hog muscle, Roche) in buffer A (10 mM MOPS-KOH, 50 mM KCl, 2 mM $MgCl_2$). After adding a desired amount of MgATP to 1.6 ml of the assay solution in a thermostatted (25°C) spectrophotometer (U-3300, Hitachi, Tokyo), reaction was initiated by rapid addition with a cuvette mixer of phosphate-free F_1 (01.5–1.5 μM) to a final concentration of 1.5–15 nM. The rate of ATP hydrolysis was estimated between 2 and 5 s after the mixing.

Ni^{2+}-nitrilotriacetic acid (Ni-NTA) surface

Coverslips to serve as the bottom of an observation chamber were functionalized with Ni-NTA essentially as described (Itoh et al., 2004)

Glass coverslips (Micro Cover Glass, No.1, 24 × 32 mm^2, Matsunami, Osaka) were immersed in 20N KOH for ~13 h, washed with water, immersed in 0.02% (v/v) acetic acid containing 2% (v/v) 3-mercaptopropyltrimethoxysilane (TSL8380, Toshiba GE Silicone, Tokyo) at 90°C for 1 h, washed with water, and baked at 120°C for 10 min. After cooling to room temperature, the SH groups of the silane on the glass surface were reduced with 100 mM DTT for 10 min, washed with water, reacted with 20 mg/ml *N*-[5-(3′-maleimidopropylamido)-1-carboxypentyl]iminodiacetic acid (Dojindo) in 10 mM MOPS-KOH for 30 min, washed with water, reacted with 10 mM $NiCl_2$ for 10 min, and washed with water. Ni-NTA coated coverslips were stored in air at room temperature until use.

Rotation assay

A flow chamber was constructed of two coverslips, a Ni-NTA coated bottom (24 × 32 mm^2) and an uncoated top (18 × 18 mm^2; Matsunami), which were separated by ~50-μm spacers. For rotation assays at 600 nM ATP or below, biotinylated F_1 (1–333 nM) was preincubated for 1 h in a test tube with 2 or 6 μM MgATP in buffer A containing an ATP-regenerating system consisting of 0.2 mg/ml creatine kinase (rabbit muscle, Roche) and 200 mM creatine phosphate (Roche). The preincubated F_1 was diluted with buffer B (buffer A plus 1 mM creatine phosphate and creatine kinase at 2 μg/ml for 200–600 pM ATP and 20 μg/ml for 2 nM ATP or above) to adjust $[F_1]$ to 0.1 nM and [ATP] to a desired final level between 0.2–600 nM. This solution was infused into the flow chamber. After 10 min, unbound F_1 was washed out with five chamber volumes of buffer C (buffer B containing the same desired level of MgATP). For [ATP] above 600 nM, the preincubation was omitted, and the washing was with buffer A except that buffer C was infused at the end. Streptavidin-coated beads (nominal diameter 0.287, 0.49, or 0.95 μm, Seradyn, Indianapolis, IN, or Bangs, Fishers, IN), washed with buffer A to remove preservatives and suspended at ~0.1% (w/w) in solution C containing 5 mg/ml BSA ("ultrapure", Nacalai Tesque, Kyoto), were infused into the F_1-containing chamber. After 30 min, unbound beads were washed out with 10 chamber volumes of buffer C. Finally, the flow chamber was sealed with silicone grease to avoid evaporation.

Bead rotation was observed at 23 ± 0.2°C on an inverted phase-contrast microscope (IX70, Olympus, Tokyo) using a 100× objective (numerical aperture 1.35, Ph3, Olympus). Images were captured with a charge-coupled-device camera (CCD-300-RC, Dage-MTI, Michigan, IN) and recorded on an 8-mm video tape at 30 frames s^{-1} (EVO-9720, Sony, Tokyo). Centroids of bead images were calculated as described (Yasuda et al., 2001).

To ensure that the low ATP concentrations that we adopted were correct, we estimated the contaminant ATP level in buffer B by luciferin-luciferase assay (DeLuca and McElroy, 1978; Itoh et al., 2004) using a luminometer (BSL-100, Hamamatsu Photonics, Hamamatsu, Japan). Free ATP in buffer B was <20 pM in experiments at 200 or 600 pM ATP and <500 pM at 2 nM ATP or above (creatine kinase was different). To achieve these low levels, creatine kinase and creatine phosphate, the major sources of contamination, had to be selected lot by lot.

RESULTS

Preincubation with ATP increases the number of rotating molecules

In our experience, the probability of finding a rotating F_1 molecule on a glass surface is noticeably low at [ATP] below ~1 μM for an unknown reason. Once a rotating F_1 is found, however, it continues to rotate for many turns at an average speed that is proportional to [ATP] at least down to 20 nM (Yasuda et al., 1998, 2001). In this study where we wanted to work at even lower ATP concentrations, the low probability of rotation seriously hampered experiment. In our attempts to circumvent this problem, we found that preincubation with ATP increases the rotation probability significantly.

The effect was assessed quantitatively in a preliminary experiment made under slightly different buffer conditions. We incubated 300 nM biotinylated F_1 with or without 6 μM MgATP for 1 h in the presence of the ATP-regenerating system as described in Methods. After dilution to 1 nM F_1 and 20 nM MgATP (MgATP was added to the control at this point), the solution was infused into an observation chamber. Paramagnetic beads (diameter 0.7 μm, Seradyn) in a buffer at pH 7.6 were infused, and the chamber was washed with buffer A containing 20 nM MgATP, 2.5 mM creatine phosphate, and 0.2 mg/ml creatine kinase. We searched for rotating beads in ten fields of view per chamber, taking ~2 min for each field (3 × 10^3 μm^2). A bead that made three or more revolutions in the 2 min was judged active. For the sample preincubated with 6 μM ATP, we found in five chambers 1728 beads, of which 4% (68 beads) rotated. In the control preincubated without ATP, rotating beads were only 0.2% (five out of 2358 beads). Preincubation had to be long: after 1-min preincubation, we found only one rotating bead out of 458 (0.2%). The effect of preincubation lasted at least for 2 h: we did not notice a clear tendency toward inactivation in the sample preincubated with ATP. The speed of rotating beads was not affected by the ATP preincubation. In the results that we report below, all rotation assays at [ATP] of 600 nM or below were made after ATP preincubation, as described in Methods.

Average rotation rate is proportional to [ATP] down to 200 pM

We imaged rotation of F_1 that was attached to a Ni-NTA treated glass surface (Itoh et al., 2004) through 10 histidines introduced at the N-terminus of the three β-subunits (Noji et al., 1997). To visualize rotation, we attached a streptavidin-coated polystyrene bead(s) to the central γ-subunit that had been biotinylated at two cysteines. We searched for a rotating F_1 that happened to bind a bead duplex, which shows clearer rotation than a single bead, and recorded the rotation for up to 2 h. The centroid of the image of the bead duplex was calculated as described (Yasuda et al., 2001), from which the time course of rotation was constructed as in Fig. 1.

A major concern in this study was to ensure that the low concentrations of ATP we worked with were set reliably. We used beads rather than actin filaments that were used in earlier studies for visualization of rotation (Noji et al., 1997; Yasuda et al., 1998), because actin filaments might release ATP, or ADP that would be converted to ATP by the ATP-regenerating system. We selected the ATP preincubation conditions such that, after dilution, the ATP level would match that in the final rotation assay; the preincubation might have been more effective if we had increased [ATP] during incubation to a higher level. Also, we measured the amount

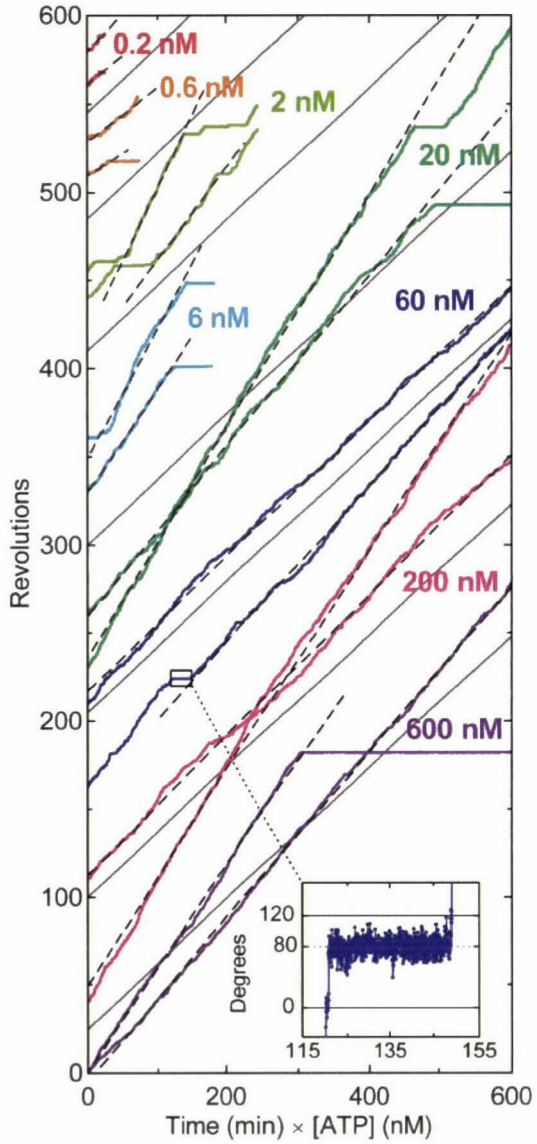

FIGURE 1 Time courses of F_1 rotation at different [ATP]s. Rotation records of the fastest two bead duplexes (0.287 μm) at each [ATP] are selected and shown. Dashed lines indicate the slope estimated on an uninterrupted portion (>50 consecutive revolutions for [ATP] $\geq$ 2 nM, and >7 revolutions at 200 and 600 pM ATP); rotation rates plotted in Fig. 2 are estimated in this way. Solid gray lines have the slope of 0.37 revolutions min^{-1} nM^{-1}, corresponding to the apparent rate constant for ATP binding, k_{on}^{app}, of 1.9 $\times$ 10^7 $M^{-1}s^{-1}$ estimated from data including more bead duplexes (red line in Fig. 2). Note that the horizontal axis is time times [ATP]. Inset shows a magnified portion of the blue curve (60 nM ATP), indicating that the long pause occurred ~80° ahead of an ATP-waiting angle.

of contaminant ATP, mostly from the ATP-regenerating system, in the final assay medium. The actual [ATP] may have been higher by at most 25% at nominal 2 nM, and at most 10% in all other cases (see Methods).

Fig. 1 compiles rotation time courses of 0.287-μm bead duplexes at 0.2–600 nM ATP. The horizontal axis is time times [ATP], and thus the figure shows that the rotation rate is basically proportional to [ATP] more than three decades of magnitude down to 200 pM. This implies that ATP binding was rate limiting in this concentration range. Indeed, the rotation was resolved into 120° steps, the dwells between steps representing the ATP-waiting state, except at the highest [ATP] where stepping was not always clear and in the sub-nanomolar range where the rotation tended to be irregular (see below).

In Fig. 1, data for two bead duplexes that showed the fastest rotation at each [ATP] are selected and shown. We focus on fast bead duplexes, because slower motion can be easily explained by surface obstructions or surface denaturation, whereas fast rotation that sustained for >50 revolutions (>7 revolutions at 600 and 200 pM ATP) is unlikely to represent a statistical exception. Slow beads often showed short pauses at a particular angle(s), suggesting surface obstruction. Fast beads also fell into a long pause occasionally, but the pause angle was usually ~80° ahead of an ATP-waiting position (Fig. 1, *inset*), indicating that the pause was due to the MgADP inhibition (Hirono-Hara et al., 2001). When a fast bead duplex recovered from the inhibited state, it normally resumed fast rotation (Fig. 1). In general, fast bead duplexes always rotate fast, whereas sluggish ones almost never show fast rotations except for up to a few fast revolutions that happen rarely.

In Fig. 2, we summarize time-averaged rotation rates of all bead duplexes that made >20 continual revolutions (mostly >100; >7 revolutions at 600 and 200 pM ATP) without a clearly irregular interruption. The trend that the rate is proportional to [ATP] is reconfirmed, although the rotation rates averaged over several bead duplexes are slightly lower than the rates in Fig. 1. The rotation rate for the 0.49-μm bead duplexes saturates above 1 μM ATP, because hydrodynamic friction against the larger beads sets the upper limit for the rotation rate (Yasuda et al., 1998) at ~3 revolutions s^{-1}. In the linear range, the slope is 6–7 revolutions $\mu M^{-1}s^{-1}$ for both bead duplexes, indicating an apparent rate constant of ATP binding, k_{on}^{app}, of 2 $\times$ 10^7 $M^{-1}s^{-1}$. This value is in good accord with the previous estimates using an actin filament (1.5 $\times$ 10^7 $M^{-1}s^{-1}$; Yasuda et al., 1998) or a 40-nm colloidal gold (2.6 $\times$ 10^7 $M^{-1}s^{-1}$; Yasuda et al., 2001). With the colloidal gold for which hydrodynamic friction is negligible, the rotation rate obeys Michaelis-Menten kinetics with the Michaelis constant, K_m, of ~15 μM and maximal rate, v_{max}, of 129 revolutions s^{-1} (Yasuda et al., 2001; *cyan squares* in Fig. 2). This simple Michaelis-Menten kinetics has now been shown to cover a broad range of [ATP] from 200 pM to 6 mM. In particular, the linear portion in Fig. 2 indicates that the ATP that directly drives rotation is bound with the same rate constant, k_{on}^{app}, of 2 $\times$ 10^7 $M^{-1}s^{-1}$ from 200 pM to at least ~10 μM (rates at 600 and 200 pM ATP tended to be somewhat lower). There is no clear sign of switching between different rotary mechanisms, except possibly in the sub-nanomolar range as discussed below.

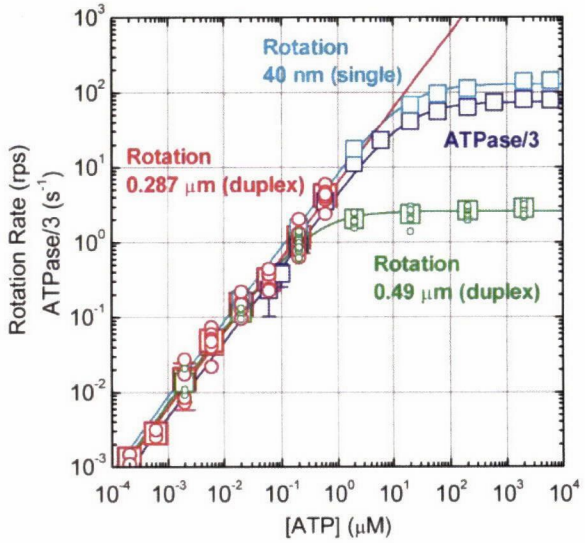

FIGURE 2 [ATP] dependence of the time-averaged rotation rate v and ATP hydrolysis rate V. Red circles, rotation rates of 0.287-μm bead duplexes with their average shown in red squares; red line, a linear fit showing $v/[ATP] = (6.2 \pm 1.0) \times 10^6$ revolutions $M^{-1}s^{-1}$, corresponding to the apparent rate constant for ATP binding, k_{on}^{app}, of 1.9×10^7 $M^{-1}s^{-1}$. Green circles and green squares, for 0.49-μm bead duplexes; green curve, a Michaelis-Menten fit with $v = v_{max}[ATP]/([ATP]+K_m)$, where $v_{max} = 2.6 \pm 0.4$ revolutions s^{-1} and $K_m = 0.37 \pm 0.13$ μM, giving $k_{on}^{app} = 2.1 \times 10^7$ $M^{-1}s^{-1}$. Red and green circles represent a time-averaged rotation rate over >50 consecutive revolutions (>20 at 2 nM, and >7 at 600 and 200 pM ATP). Error bars, where indicated, show SD that exceeds the size of the symbol. Cyan squares, the average rotation rate for a 40-nm colloidal gold (Yasuda et al., 2001); v_{max} = 129 ± 27 revolutions s^{-1} and K_m = 15 ± 6 μM, giving $k_{on}^{app} = 2.6 \times 10^7 M^{-1}s^{-1}$. Blue squares, one third of the average hydrolysis rate for two or three measurements (one at 6 mM ATP), error bars showing SD that exceeds the size of the symbol; blue line, a fit with $V = V_{max}[ATP]/([ATP]+K_m)$ where $V_{max} = 223 \pm 68$ s^{-1} (without division by three) and $K_m = 16 \pm 8$ μM, giving $k_{on}^{app} = 1.4 \times 10^7$ $M^{-1}s^{-1}$. Values here are mean ± SE.

Hydrolysis activity is parallel to rotary speed

In Fig. 2, blue squares show the initial rate of ATP hydrolysis measured in a cuvette. The rate was measured between 2–5 s after the addition of nucleotide-free F_1, to minimize the effect of MgADP inhibition. For comparison with the rotation rate, one third of the hydrolysis rate is plotted in Fig. 2. As seen, the two rates are close to each other, indicating that three ATP molecules would be hydrolyzed per turn. In fact, the hydrolysis rate is slightly lower, apparently suggesting that one ATP molecule could sometimes drive two 120° steps. Our interpretation is that the hydrolysis rate measured in the bulk sample is the average including inhibited or inactive portion, whereas the rotation rate is estimated on a single molecule over a period of active rotation. Assuming that the inhibition was not too serious in the initial 2–5 s of the reaction, we anticipate that three, or slightly more than three, ATP molecules are hydrolyzed per turn. Precise correspondence between hydrolysis and rotation cannot be established unless one could somehow measure ATP hydrolysis in a single, rotating F_1 molecule.

The hydrolysis rate in Fig. 2 can be fitted, to within experimental uncertainty, with a simple Michaelis-Menten curve (*blue line*). This result is different from the previous one where at least two sets of Michaelis constants were needed to fit the hydrolysis kinetics (Yasuda et al., 2001). The simpler kinetics here, with a somewhat lower rate at saturating [ATP], was obtained when phosphate was removed before hydrolysis measurement (R. Shimo-Kon, unpublished). The reason is unknown, but a similar result was obtained in the presence of a detergent lauryldimethylamine oxide (Yasuda et al., 2001), which is a suppressor of MgADP inhibition (Jault et al., 1996; Matsui et al., 1997), or with a mutant lacking noncatalytic nucleotide binding sites (Ono et al., 2003). Hydrolysis of GTP, less prone to the inhibition, also follows Michaelis-Menten kinetics (Noji et al., 2001). Except for the complication likely associated with the MgADP inhibition, hydrolysis kinetics also fails to suggest [ATP]-dependent switching between two different hydrolysis mechanisms.

Torque is independent of [ATP]

When a large probe such as a bead is attached to the γ-subunit, F_1 has to rotate against viscous friction imposed on the probe. The torque N that F_1 produces can be estimated directly from the rotary speed ω (in radians s^{-1}):

$$N = \omega\xi, \tag{1}$$

where ξ is the frictional drag coefficient given, for the case of a spherical bead, by

$$\xi = 8\pi\eta a^3 + 6\pi\eta a x^2, \tag{2}$$

where a is the bead radius, x the radius of rotation, i.e., the distance between the bead center and rotation axis, and η the viscosity of the medium ($\sim 0.93 \times 10^{-3}$ N s m^{-2} at 23°C). In the case of a bead duplex with radii of rotation x_1 and x_2, ξ is given by

$$\xi = 2 \times 8\pi\eta a^3 + 6\pi\eta a x_1^2 + 6\pi\eta a x_2^2. \tag{3}$$

Near a (glass) surface, viscous drag is higher than in the bulk (Hunt et al., 1994; Svoboda and Block, 1994), and thus Eqs. 2 and 3 would lead to an underestimate of the torque (Pänke et al., 2001). We do not correct for this surface effect, because the correction factor depends critically on the bead height, which we cannot estimate reliably. The torque values we report are thus likely underestimated.

With this principle, we inquired if the torque that F_1 produces varies with [ATP]. We used 0.95-μm bead duplexes for this purpose, to better resolve stepping kinetics at the regular video rate of 30 frames s^{-1}. First we recorded stepping rotation at 2 nM ATP, and then infused 60 nM ATP and observed the same bead duplex, and finally infused 2 mM ATP to record continuous rotation of the same bead duplex. In Fig. 3, we overlay 15 consecutive stepping records for each [ATP], all from the same bead duplex. The averages are

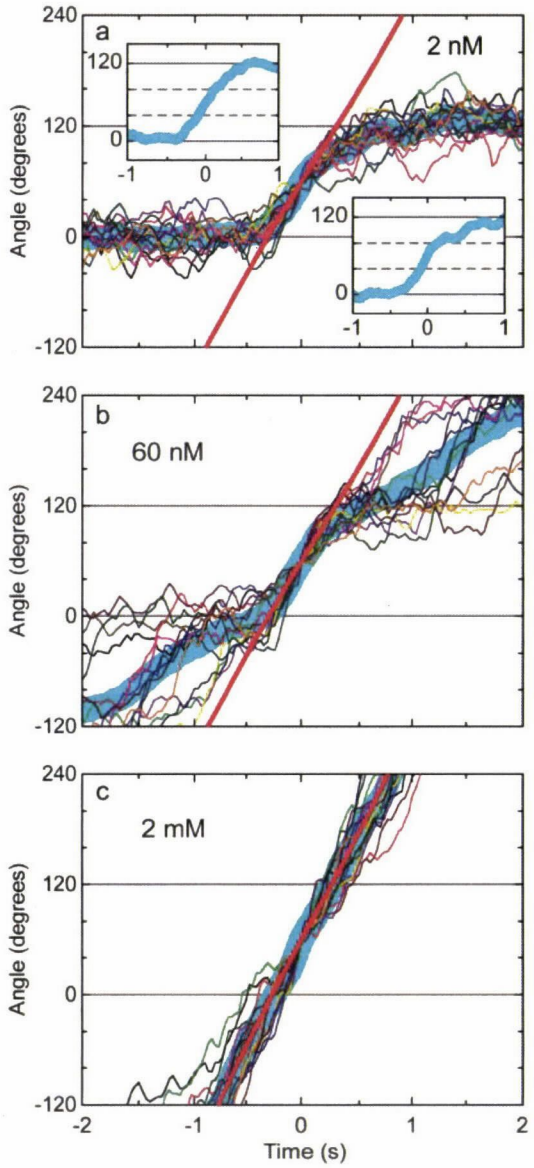

FIGURE 3 Magnified stepping records of a 0.95-μm bead duplex at 2 nM (*a*), 60 nM (*b*), and 2 mM (*c*) ATP. The same bead duplex was observed first at 2 nM ATP, then 60 nM, and finally at 2 mM. From each rotation record, contiguous 15 steps have been chosen and their central parts are overlaid in different colors, thick cyan line being the average. The angles in the vertical axes refer to three ATP-waiting angles identified at low [ATP]; individual step records have been shifted vertically by a multiple of 120° to obtain the overlap. Time zero for each step record was assigned by eye to the data point closest to 60°. Straight red lines indicate the slope of the average step record judged by eye: 0.56, 0.57, 0.65 revolutions s^{-1} at 2 nM, 60 nM, and 2 mM ATP, respectively, corresponding to the torque of 40, 40, and 46 pN·nm. Insets in *a*: upper left, the average over six steps that do not show a conspicuous pause at ~80°; lower right, the average over the rest of nine steps.

shown in thick cyan lines, from the slope (*straight red lines*) of which we estimated the torque, using Eqs. 1 and 3, to be 46, 40, and 40 pN·nm at 2 mM, 60 nM, and 2 nM ATP, respectively. Another data set gave 37, 35, 37 pN·nm for the three ATP concentrations, a third gave 46 pN·nm at 2 mM ATP and 41 pN·nm at 2 nM ATP, and a fourth gave 43 pN·nm at 2 nM ATP. Because regularly stepping bead duplexes at 2 nM ATP were scarce and the infusions afterwards were not always successful, these are the only data we have obtained so far. Although the statistics may not be sufficient, we consider, taking previous results (Yasuda et al., 1998; Kinosita et al., 2000a) also into account, that the torque is ~40 pN·nm from 2 mM to 2 nM ATP, again pointing to one rotary mechanism over mM-nM ATP.

The thick cyan line at 2 nM ATP in Fig. 3 is noticeably curved at the end of the 120° step, and the same trend is also seen at 60 nM ATP. This is due to the tendency of the bead duplex to pause for ~1 s or less at the substep angle of ~80°. In Fig. 3 *a*, the inset at lower right is the average of nine steps with a relatively clear pause, showing a flat portion at ~80°. The inset at upper left is the average of the rest of six steps, showing continuous rise across 80°. The thick cyan line in Fig. 3 *b* is less curved, presumably because the ~80° pause is terminated when the next ATP binds and drives the bead duplex toward 240°. The ~80° pause is almost absent in Fig. 3 *c* (2 mM ATP). The pause duration varied among different bead duplexes, and some duplexes displayed frequent, short pauses even at 2 mM ATP. In general, larger beads, such as the 0.95-μm bead duplex in Fig. 3, often show clear pauses, whereas ~80° pauses are much less conspicuous with smaller beads. This load dependence, together with the large variation among beads with the same size, suggest that these ~80° pauses are not an intrinsic property of the F_1 motor. Our interpretation is that a reaction(s) at the substep angle of ~80°, possibly one of the two 1-ms reactions, is sensitive to mechanical hindrance: hydrodynamic or surface friction against rotation obstructs that reaction, implying that the reaction is coupled to a small degree of γ-rotation. We failed to notice these short pauses in experiments with a long actin filament (Yasuda et al., 1998; Kinosita et al., 2000a), presumably because actin filaments are flexible. Short pauses that we have reported for relatively short actin filaments (Hirono-Hara et al., 2001) may represent the ~80° pauses described here, although the pause angle relative to an ATP-waiting angle was not established in the previous study.

Irregular rotations at subnanomolar ATP

At 600 pM ATP, we noticed that bead duplexes sometimes dwelled around the substep angle, ~80° ahead of an ATP-waiting angle for minutes (Fig. 4 *a*). This was more frequent at 200 pM ATP (Fig. 4 *b*). Finding a bead duplex that rotates in one direction was extremely difficult at these ATP concentrations, and we have so far obtained only a few runs that involve >7 revolutions at each [ATP]. Below we describe apparent characteristics of these runs, which may not be typical, without quantitative statistics. These irregular rotations at extremely low ATP concentrations are not physiologically relevant, but may nevertheless provide some clues about the rotary mechanism at higher [ATP].

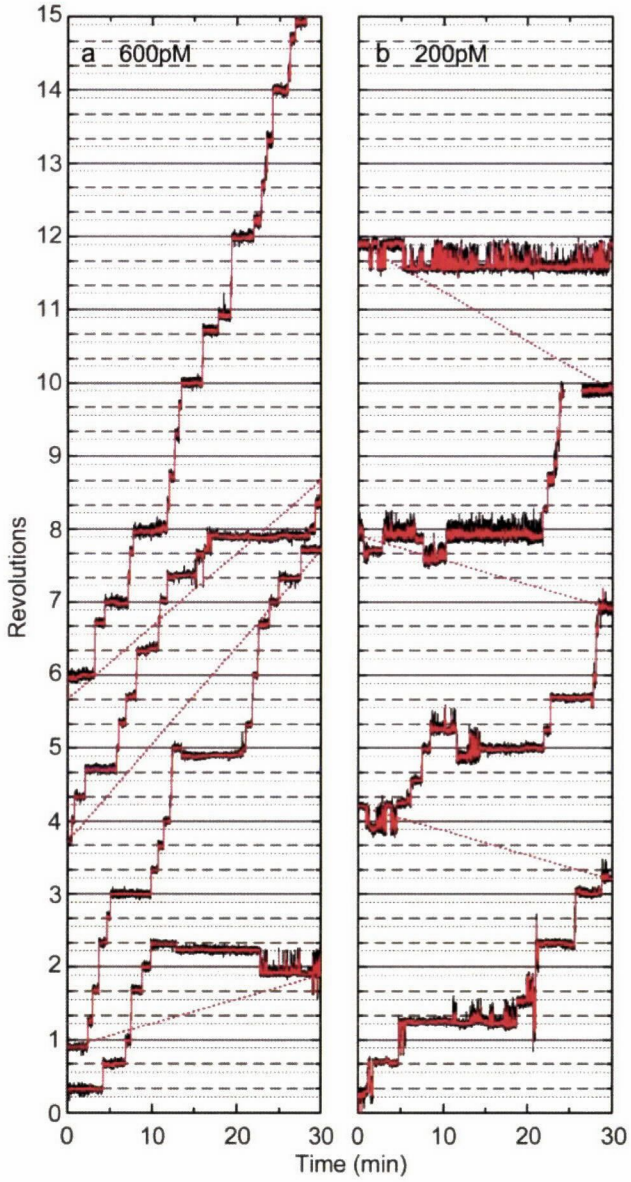

FIGURE 4 Time courses of F_1 rotation at 600 pM (*a*) and 200 pM (b) ATP. Black curves, raw data showing the rotary angle of a 0.287-μm bead duplex; red curves, 15-point (0.5-s) running average. To save space, a continuous record is split into contiguous 30-min segments and plotted on one graph; red dotted lines indicate connection. Solid and dashed horizontal lines are drawn at intervals of 120°, and dotted lines are drawn 40° below a solid or dashed line. The image went out of focus at the break in record *b*.

An ~80° dwell was reached through a (sub)step of various origin: a forward 80° substep from 0°, backward 40° substep from 120°, forward 120° step from −40°, or backward 120° step from 200° (Fig. 4); the latter two modes represent a 120° jump between neighboring substep angles. In contrast, entry into a MgADP-inhibited state at ~80° in high ATP media (200 nM ATP and above) is almost always through a forward 80° substep from 0° (Hirono-Hara et al., 2001); the inset of Fig. 1 also shows this behavior, but some of the long pauses at 2–20 nM ATP in Fig. 1 are through a 40° backward substep from 120°. Escape from an ~80° dwell to a regular ATP-waiting angle was often, though not always, by a 160° forward jump to 240° that was complete in a fraction of a second; these 160° jumps might be a combination of 40° and 120° steps, but a clear dwell (>0.1 s) in the course of a 160° jump was undetectable in most cases.

During an ~80° dwell at pM ATP, the bead duplex often fluctuated extensively. Large-amplitude fluctuations tended to occur in the forward direction, as seen in Fig. 4. This could imply that, in the yet unknown chemical state of the ~80° intermediate, the potential energy for γ-rotation is less steep, or poses lower barriers, against forward rotation than against backward rotation, and that the forward slope/barrier in the potential is smaller in the ~80° intermediate than in the ATP-waiting state. Or, large-amplitude forward fluctuations, occasionally reaching 120° ahead (at ~200°) and staying there for a fraction of a second, might have resulted from transient ATP binding: although an effective ATP binding that eventually leads to a regular 120° step from an ATP-waiting angle is seldom at pM ATP (~0.2 min^{-1} at 200 pM), diffusion-limited encounter of ATP with F_1 could be ~10^2 times as frequent.

These behaviors at pM ATP are clearly different from the mostly regular 120° stepping at nM ATP and above. If tri-site is the norm at nM ATP and above, the irregular rotations may be attributed to a bi-site mode. Or, rotation at nM ATP (and possibly above) might be by a bi-site mode and picomolar rotation by a uni-site mode. Other more complicated schemes are also possible, and what we can conclude here is that a clearly different rotation regime(s) emerges at hundreds of picomolar ATP. In this regard, we also noticed that, at 200 pM ATP, some bead duplexes rotated in both directions, mainly in steps of 120° that could accumulate in net rotation of several revolutions in either direction. This may represent Brownian hopping among the three equivalent orientations in a nucleotide-free F_1, although other possibilities such as a denatured F_1 cannot be dismissed.

DISCUSSION

ATP preincubation

The reason why preincubation with ATP increases the number of rotating F_1 at low [ATP] is not clear. One possibility is that active rotation requires filling of at least two of the three catalytic sites with a nucleotide (tri-site operation) and that the probability of filling two is extremely low at nM ATP or below. Once two or more sites are filled by preincubation, the enzyme starts to rotate, and the active enzyme somehow maintains two nucleotides in the catalytic sites. In this scenario, if the enzyme happens to lose one catalytic nucleotide while waiting for ATP, the enzyme

cannot resume rotation at low [ATP]. Because the number of rotating F_1 did not decrease appreciably at least for 2 h after preincubation, this scenario is rather unlikely.

In a mutant thermophilic F_1 that incorporates a reporter tryptophan near each catalytic site, binding of the first ATP to nucleotide-depleted F_1 has been shown to occur with a bimolecular rate constant of 1.7×10^7 M ^{1}s ^{1} (Masaike et al., 2002), a value close to the rate constant for ATP binding that directly drives rotation, k_{on}^{app}, of $\sim 2 \times 10^7$ $M^{-1}s^{-1}$. If binding of the second ATP occurs at a similar or lower rate, the binding takes a few seconds or more at 20 nM ATP where the preincubation effect was significant. The mutant study has also shown that F_1 that binds only one catalytic nucleotide tends to fall into an MgADP-inhibited state with a time constant of 15 s. Thus, a significant portion would be inhibited before a second catalytic site is filled. Preincubation at high [ATP] will bypass this inhibition process. We are, however, not sure if this alone can explain the preincubation effect. After dilution into an extremely low [ATP], there will be an occasion, however scarce it may be, where only one catalytic nucleotide remains bound to F_1, and then the F_1 would be inhibited. In fact, the preincubation effect lasted at least for 2 h.

Binding of ATP to the three noncatalytic sites during preincubation may explain the sustained effect. Filling the noncatalytic sites takes minutes (for mitochondrial F_1) at 50 μM ATP (Jault and Allison, 1993), suggesting that release would also be extremely slow. Nucleotides bound to the noncatalytic sites greatly reduces the propensity of F_1 to fall into the MgADP-inhibited state, at least for the kind(s) of inhibition that takes place at μM ATP and above (Jault et al., 1996; Matsui et al., 1997; Hirono-Hara et al., 2001). Preincubation with ATP will lead to filling of the noncatalytic sites, and will also help avoid the one-nucleotide inhibition above. The slow manifestation of the preincubation effect, 1 min being ineffective, is consistent with the slow filling of noncatalytic sites.

If the preincubation effect is due to filling of noncatalytic sites, the irregular rotation at subnanomolar ATP might result from the release of a noncatalytic nucleotide(s). This, however, is rather unlikely because the release must take many minutes whereas the irregular rotation was noticeable from the beginning of observation (Fig. 4).

Rotary mechanism

In principle, the events of ATP binding by F_1 can be classified into two categories: productive binding that leads to and that drives a forward 120° step, and futile binding where the ATP is released back into the medium without net rotation. The latter may include rotary spikes where forward rotation initiated by ATP binding is reversed when the ATP is released prematurely. Futile events may also include the case where ATP is hydrolyzed and then released without net rotation. Such futile ATP hydrolysis, or decoupling between hydrolysis and rotation, is likely rare, in view of the relatively good agreement between the rotation and hydrolysis rates (Fig. 2).

What this study clearly shows, together with previous studies (Yasuda et al., 1998, 2001; Adachi et al., 2000; Noji et al., 2001), is that the rate constant for the productive ATP binding, k_{on}^{app}, remains the same at $\sim 2 \times 10^7$ $M^{-1}s^{-1}$ over the broad range of $\sim$1 nM to $\sim$100 μM ATP, and probably up to at least 6 mM (Yasuda et al., 2001). Below $\sim$1 nM, a new rotation regime involving long dwells at $\sim$80° position begins to appear, but, at least down to 200 pM, the overall rotation rate is commensurate with the rate constant for productive ATP binding above of $\sim 2 \times 10^7$ $M^{-1}s^{-1}$ (Figs. 1, 2, and 4). Models of F_1 rotation must take this [ATP] independence of the binding rate constant, and the [ATP] independence of the rotary torque (Fig. 3), into account.

A simple answer is that one rotary mechanism operates in the whole range of [ATP] except for pM and below. Is it a tri-site mechanism, as stated in introduction? A tryptophan residue introduced in the catalytic site reports that the catalytic site occupancy is >2 at several μM and above for *E. coli* F_1 (Weber and Senior, 2001) and also for the thermophilic F_1 that we used in this study (Ren and Allison, 2000; Ono et al., 2003). Although these studies do not suggest tri-site activity at 1 μM ATP and below where the occupancy is apparently <2, the occupancy in our F_1 that lacks the tryptophan mutation may remain high down to 1 nM ATP. Or, the relation between the fluorescence signal and site occupancy may be nonlinear and the actual occupancy in the tryptophan mutants may also be above two down to nM ATP (Ono et al., 2003). A fluorescent ATP analog, Cy3-ATP, remains bound on F_1 for $\geq$240° of rotation at 0.3–2 μM ATP, supporting a tri-site mechanism below 1 μM ATP. A stronger support comes from direct observation of the number of bound Cy3-ATP, in the sample in which the same F_1 mutant as used in this study rotates in the presence of Cy3-ATP at $\sim$100 nM without unlabeled ATP (K. Adachi, unpublished): the number of bound Cy3 basically remains two during regular 120° stepping, but irregular stepping involving $\sim$80° dwells appears when bound Cy3 drops to one. The irregular stepping is reminiscent of one we observed here at 200 and 600 pM ATP (Fig. 4). If the affinity of Cy3-ADP for F_1 is 10^2–10^3 times lower than that of unlabeled ADP, rotation at $\sim$1 nM and above of authentic ATP is likely driven by a tri-site mechanism. Here we define a tri-site mechanism as one in which the catalytic site occupancy in the ATP-waiting state is two, without specifying further details. It is conceivable that the occupancy remains two all the time (ATP binding and ADP release being simultaneous), and then the term "tri-site" may not be appropriate.

The tri-site view, even with the modest definition above, may yet be disputable. Milgrom et al. (1998) have observed full hydrolysis activity of mitochondrial F_1 when the molar ratio of added ATP to F_1 exceeded one. This result indicates

that only one nucleotide is bound in the ATP-waiting state, at least at low [ATP] (bi-site mechanism). We are obtaining similar, though not identical, results with a mutant of thermophilic F_1 (R. Shimo-Kon, unpublished). Note that the [ATP] independence of the rate constant for productive ATP binding, k_{on}^{app}, is compatible with the possibility of bi-site filling at low [ATP] and tri-site filling at high [ATP] if the rate constants are similar in the two regimes. The estimation of site occupancy with the tryptophan mutant has so far been made in the absence of an ATP-regenerating system, where F_1 rapidly falls into an MgADP-inhibited state(s). If F_1 remained active in these experiments where [F_1] was rather high (in the order of 100 nM), ATP in the medium must have been quickly (in the order of 10 s except at ≥mM ATP) converted into ADP. The tryptophan signal is stationary over minutes in most cases, suggesting that the signal comes primarily from inactive enzyme. Results with Cy3-ATP must also be interpreted with caution, because of the presence of the Cy3 moiety, which impedes the hydrolysis reaction (Nishizaka et al., 2004). More experiments are needed to firmly establish the catalytic site occupancy in active, rotating F_1. And, of course, site occupancy is only one part of the jigsaw puzzle. We hope that the results we report here turn out to be a solid piece of the puzzle of how F_1-ATPase rotates.

We thank Y. Onoue, M. D. Hossain, and K. Shiroguchi for discussion, M. Shio for the microscope techniques, and M. Fukatsu for encouragement and lab management.

This work was supported in part by grants-in-aid from the Ministry of Education, Culture, Sports, Science and Technology of Japan.

REFERENCES

Abrahams, J. P., A. G W. Leslie, R. Lutter, and J. E. Walker. 1994. Structure at 2.8 Å resolution of F_1-ATPase from bovine heart mitochondria. *Nature* 370:621–628.

Adachi, K., R Yasuda, H. Noji, H. Itoh, Y. Harada, M. Yoshida, and K Kinosita Jr. 2000. Stepping rotation of F_1-ATPase visualized through angle-resolved single-fluorophore imaging. *Proc. Natl. Acad. Sci. USA* 97:7243–7247.

Adachi, K., H. Noji, and K. Kinosita Jr. 2003. Single-molecule imaging of rotation of F_1-ATPase. *Methods Enzymol* 361B:211–227.

Boyer, P. D. 1997. The ATP synthase—a splendid molecular machine. *Annu Rev Biochem* 66:717–749.

Boyer, P D. 2002. Catalytic site occupancy during ATP synthase catalysis. *FEBS Lett* 512:29–32.

Boyer, P D., and W. E Kohlbrenner. 1981. The present status of the binding-change mechanism and its relation to ATP formation by chloroplasts. *In* Energy Coupling in Photosynthesis. B. R. Selman, and S. Selman-Reimer, editors. Elsevier, Amsterdam. 231–240.

DeLuca, M., and W. D. McElroy. 1978. Purification and properties of firefly luciferase. *Methods Enzymol.* 57:3–15.

Diez, M., B. Zimmermann, M. Börsch, M. König, E. Schweinberger, S. Steigmiller, R. Reuter, S. Felekyan, V. Kudryavtsev, C. A. M. Seidel, and P. Gräber. 2004. Proton-powered subunit rotation in single membrane-bound F_oF_1-ATP synthase. *Nat Struct Mol Biol* 11:135–141.

Hirono-Hara, Y., H. Noji, M. Nishiura, E. Muneyuki, K. Y. Hara, R. Yasuda, K Kinosita Jr., and M. Yoshida. 2001. Pause and rotation of F_1-ATPase during catalysis *Proc Natl Acad Sci USA* 98:13649–13654.

Hunt, A J., F. Gittes, and J. Howard 1994. The force exerted by a single kinesin molecule against a viscous load. *Biophys J* 67:766–781.

Itoh, H., A. Takahashi, K. Adachi, H. Noji, R. Yasuda, M. Yoshida, and K. Kinosita Jr. 2004 Mechanically driven ATP synthesis by F_1-ATPase. *Nature* 427:465–468.

Jault, J -M , and W S. Allison. 1993. Slow binding of ATP to noncatalytic nucleotide binding sites which accelerates catalysis is responsible for apparent negative cooperativity exhibited by the bovine mitochondrial F_1-ATPase. *J Biol Chem* 268:1558–1566

Jault, J.-M., C. Dou, N. B. Grodsky, T. Matsui, M. Yoshida, and W. S. Allison. 1996. The $\alpha_3\beta_3\gamma$ subcomplex of the F_1-ATPase from the thermophilic *Bacillus* PS3 with the βT165S substitution does not entrap inhibitory MgADP in a catalytic site during turnover. *J Biol Chem* 271:28818–28824.

Kagawa, Y., and E. Racker. 1966. Partial resolution of the enzymes catalyzing oxidative phosphorylation. IX. Reconstruction of oligomycin-sensitive adenosine triphosphatase. *J Biol Chem* 241 2467–2474.

Kinosita, K., Jr , K Adachi, and H. Itoh. 2004 Rotation of F_1-ATPase: how an ATP-driven molecular machine may work. *Annu Rev Biophys Biomol Struct* 33:245–268.

Kinosita, K , Jr , R. Yasuda, and H. Noji. 2000a F_1-ATPase: a highly efficient rotary ATP machine. *Essays Biochem* 35:3–18.

Kinosita, K , Jr., R. Yasuda, H. Noji, and K. Adachi 2000b. A rotary molecular motor that can work at near 100% efficiency. *Philos Trans R Soc Lond B Biol Sci* 355:473–489.

Masaike, T., E Muneyuki, H Noji, K. Kinosita Jr., and M. Yoshida. 2002. F_1-ATPase changes its conformations upon phosphate release. *J. Biol Chem* 277:21643–21649.

Matsui, T., E Muneyuki, M. Honda, W. S. Allison, C. Dou, and M. Yoshida. 1997. Catalytic activity of the $\alpha_3\beta_3\gamma$ complex of F_1-ATPase without noncatalytic nucleotide binding site. *J. Biol Chem* 272:8215–8221.

Menz, R. I., J. E. Walker, and A. G. W. Leslie. 2001 Structure of bovine mitochondrial F_1-ATPase with nucleotide bound to all three catalytic sites: implications for the mechanism of rotary catalysis *Cell* 106:331–341.

Milgrom, Y. M., M. B. Murataliev, and P. D. Boyer. 1998. Bi-site activation occurs with the native and nucleotide-depleted mitochondrial F_1-ATPase. *Biochem J* 330:1037–1043.

Nishizaka, T., K. Oiwa, H. Noji, S. Kimura, E. Muneyuki, M. Yoshida, and K. Kinosita Jr. 2004. Chemomechanical coupling in F_1-ATPase revealed by simultaneous observation of nucleotide kinetics and rotation. *Nat Struct Mol Biol* 11:142–148.

Noji, H., R. Yasuda, M. Yoshida, and K. Kinosita Jr. 1997. Direct observation of the rotation of F_1-ATPase. *Nature* 386:299–302.

Noji, H., D. Bald, R. Yasuda, H. Itoh, M. Yoshida, and K. Kinosita Jr. 2001. Purine but not pyrimidine nucleotides support rotation of F_1-ATPase *J Biol Chem* 276:25480–25486.

Ono, S., K. Y Hara, J. Hirao, T. Matsui, H. Noji, M. Yoshida, and E. Muneyuki. 2003. Origin of apparent negative cooperativity of F_1-ATPase *Biochim Biophys Acta* 1607:35–44.

Oosawa, F., and S. Hayashi. 1986. The loose coupling mechanism in molecular machines of living cells. *Adv Biophys* 22:151–183.

Panke, O., D. A. Cherepanov, K. Gumbiowski, S. Engelbrecht, and W. Junge 2001. Viscoelastic dynamics of actin filaments coupled to rotary F-ATPase: angular torque profile of the enzyme. *Biophys J.* 81:1220–1233.

Ren, H., and W. S. Allison. 2000. Substitution of βGlu^{201} in the $\alpha_3\beta_3\gamma$ subcomplex of the F_1-ATPase from the thermophilic *Bacillus* PS3 increases the affinity of catalytic sites for nucleotides. *J Biol Chem* 275: 10057–10063.

Shimabukuro, K., R. Yasuda, E. Muneyuki, K. Y. Hara, K. Kinosita Jr., and M. Yoshida. 2003. Catalysis and rotation of F_1 motor: cleavage of ATP

at the catalytic site occurs in 1 ms before 40° substep rotation. *Proc Natl Acad Sci USA* 100:14731–14736.

Svoboda, K., and S. M Block 1994. Biological applications of optical forces. *Annu Rev Biophys Biomol Struct* 23:247–285.

Turina, P., D. Samoray, and P. Graber. 2003. H^+/ATP ratio of proton transport-coupled ATP synthesis and hydrolysis catalysed by CF_oF_1-liposomes. *EMBO J* 22.418–426.

Weber, J , S. Wilke-Mounts, R. S.-F. Lee, E. Grell, and A. E Senior. 1993 Specific placement of tryptophan in the catalytic sites of *Escherichia coli* F_1-ATPase provides a direct probe of nucleotide binding: Maximal ATP hydrolysis occurs with three sites occupied. *J Biol Chem* 268: 20126–20133

Weber, J., and A. E. Senior. 2001 Bi-site catalysis in F_1-ATPase: does it exist? *J Biol Chem* 276:35422–35428.

Weber, J., and A. E Senior. 2003. ATP synthesis driven by proton transport in F_1F_o-ATP synthase. *FEBS Lett* 545:61–70.

Yasuda, R , H. Noji, K. Kinosita Jr., and M. Yoshida. 1998. F_1-ATPase is a highly efficient molecular motor that rotates with discrete 120° steps. *Cell* 93:1117–1124.

Yasuda, R , H. Noji, M. Yoshida, K. Kinosita Jr., and H. Itoh. 2001. Resolution of distinct rotational substeps by submillisecond kinetic analysis of F_1-ATPase. *Nature* 410.898–904.

Yoshida, M., E. Muneyuki, and T. Hisabori. 2001. ATP synthase — a marvellous rotary engine of the cell. *Nat Rev Mol Cell Biol* 2: 669–677.

ATP-driven stepwise rotation of F_oF_1-ATP synthase

Hiroshi Ueno*, Toshiharu Suzuki*†, Kazuhiko Kinosita, Jr.‡, and Masasuke Yoshida*†§

*Chemical Resources Laboratory, Tokyo Institute of Technology, Nagatsuta 4259, Yokohama 226-8503, Japan; †ATP System Project, Exploratory Research for Advanced Technology, Japan Science and Technology Agency, Nagatsuta 5800-3, Yokohama 226-0026, Japan; and ‡Okazaki Institute for Integrative Bioscience, National Institutes of Natural Sciences, Higashiyama 5-1 Myodaiji, Okazaki 444-8787, Japan

Edited by Paul D. Boyer, University of California, Los Angeles, CA, and approved December 13, 2004 (received for review October 21, 2004)

F_oF_1-ATP synthase (F_oF_1) is a motor enzyme that couples ATP synthesis/hydrolysis with a transmembrane proton translocation. F_1, a water-soluble ATPase portion of F_oF_1, rotates by repeating ATP-waiting dwell, 80° substep rotation, catalytic dwell, and 40°-substep rotation. Compared with F_1, rotation of F_oF_1 has yet been poorly understood, and, here, we analyzed ATP-driven rotations of F_oF_1. Rotation was probed with an 80-nm bead attached to the ring of c subunits in the immobilized F_oF_1 and recorded with a submillisecond fast camera. The rotation rates at various ATP concentrations obeyed the curve defined by a K_m of ≈30 μM and a V_{max} of ≈350 revolutions per second (at 37°C). At low ATP, ATP-waiting dwell was seen and the $k_{on\text{-}ATP}$ was estimated to be 3.6×10^7 $M^{-1}\cdot s^{-1}$. At high ATP, fast, poorly defined stepwise motions were observed that probably reflect the catalytic dwells. When a slowly hydrolyzable substrate, adenosine 5′-[γ-thio]triphosphate, was used, the catalytic dwells consisting of two events were seen more clearly at the angular position of ≈80°. The rotational behavior of F_oF_1 resembles that of F_1. This finding indicates that "friction" in F_o motor is negligible during the ATP-driven rotation. Tributyltin chloride, a specific inhibitor of proton translocation, slowed the rotation rate by 96%. However, dwells at clearly defined angular positions were not observed under these conditions, indicating that inhibition by tributyltin chloride is complex.

ATP hydrolysis | binding change mechanism | membrane protein | single-molecule imaging

F_oF_1-ATPase/synthase (F_oF_1) is a large protein complex (≈500 kDa) that catalyzes ATP synthesis/hydrolysis coupled with a transmembrane H^+ (proton)-translocation in bacteria, chloroplasts, and mitochondria (1–5). The enzyme is easily and reversibly separated into two portions, termed F_1 and F_o. In its simplest prototype bacterial enzyme, a water-soluble F_1 portion consists of five different subunits, $\alpha_3\beta_3\gamma_1\delta_1\varepsilon_1$, and catalyzes ATP hydrolysis (hence, often called F_1-ATPase). Three α-subunits and three β-subunits are arranged alternately, forming a hexagonal cylinder around the coiled-coil structure of the γ-subunit (6). Membrane-integrated F_o portion has three different subunits, $a_1b_2c_n$ (n; variable among species) and mediates proton transport across the membrane. The c-subunits forms a ring structure, and ab_2 associates with the c-subunit ring peripherally (7–10). F_oF_1 is a motor enzyme. When the magnitude of electrochemical potential of protons is large enough, downhill proton flow through F_o causes rotation of the rotor subunits (c_n-γε) relative to the stator subunits (ab_2-$\alpha_3\beta_3\delta$), and rotation of the γ-subunit forces the β-subunits of F_1 to change conformations sequentially that result in ATP synthesis. In the reverse reaction, ATP hydrolysis at F_1 causes the reverse rotation of the rotor subunits that drives F_o to pump protons (Fig. 1) (11).

We have been studying rotation of thermophilic *Bacillus* F_1 since the first direct visualization of ATP-driven rotation of F_1 immobilized on the glass surface (12). A rotation probe attached on the γ-subunit rotates unidirectionally counterclockwise when viewed from membrane side. It repeats a pause and a 120° step rotation when medium ATP concentration ([ATP]) is low (13). The duration of the pause becomes shorter as [ATP] increases and is finally invisible beyond the limit of the observation system. This [ATP]-dependent pause corresponds to the period during which the enzyme waits for medium ATP to come into the empty catalytic site, and, hence, is called the ATP-waiting dwell. With high-speed imaging, it was found that the 120° step of rotation is further split into 90° and 30° substeps (14). A pause between two substeps, ≈2 ms at 23°C, is not influenced by [ATP]. This [ATP]-independent nature of the pause means that catalytic events after substrate binding should occur during this pause, and we call this pause the catalytic dwell. The histogram of durations of the catalytic dwells did not obey a single exponential but did obey double exponentials, indicating that two catalytic reactions of ≈1 ms occur in the catalytic dwell (14). More recent experiments using a slowly hydrolyzable ATP analog, adenosine 5′-[γ-thio]triphosphate (ATPγS) and a slow mutant in ATP hydrolysis, clarified that one of the two 1-ms events is cleavage of a bound ATP at a catalytic site (15). Also, previous 90° and 30° substeps were recently revised to be 80° and 40° substeps (15, 16). Thus, F_1 rotates by repeating four stages: ATP-waiting dwell, rapid 80° substep rotation upon ATP binding, catalytic dwell in which ATP hydrolysis occurs, and rapid 40° substep rotation, probably upon the release of the last product.

ATP-driven rotation of F_oF_1 was demonstrated for *Propionigenium modestum* F_oF_1 with single-fluorophore polarization (17), and for *Escherichia coli* F_oF_1 with disulfide cross-linking (18, 19), direct visualization (20), and fluorescence resonance energy transfer (21). In general, ATP-driven rotation of F_oF_1 can differ from that of F_1 because proton transport through F_o and interaction between the c-subunit ring (rotor) and ab_2 (stator) during rotation may modify the rotation. It was reported that the central rotor rotates counterclockwise when viewed from membrane side, and there are three pauses (each 19–30 ms) in one revolution, likely corresponding to the catalytic dwell (21, 22). The rotation of F_oF_1 driven by proton flow was also observed, and the direction of the rotation is opposite of that of the ATP-driven rotation (22). However, in general, knowledge on rotation of F_oF_1 has yet been very limited. For example, even the following basic motor natures of F_oF_1 remain unknown: (*i*) whether ATP-binding dwell appears at low [ATP], (*ii*) how the rotation depends on [ATP], (*iii*) whether the observed rotation consists of the sequence of 80° and 40° substep rotation or other new substep(s) exists at different angular position(s), (*iv*) whether catalytic dwell is composed of two events, as observed for F_1, and (*v*) how rotation changes when a reversible F_o inhibitor is present. To address these questions, we isolated thermophilic F_oF_1, which kept structural integrity in a detergent, immobilized it on a glass surface through the β-subunits, attached a small (80 nm) bead to the c-subunit ring as a rotation probe whose viscous friction was low enough to allow full-speed rotation, and observed ATP-driven rotation with a fast camera. The results reveal that basic natures of ATP-driven rotation of

This paper was submitted directly (Track II) to the PNAS office.

Freely available online through the PNAS open access option.

Abbreviations. ATPγS, adenosine 5′-[γ-thio]triphosphate, DCCD, *N,N′*-dicyclohexylcarbodiimide, LPC, lysophosphatidylcholine; Ni^{2+}-NTA, Ni^{2+}-nitrilotriacetic acid, rps, revolutions per second; TBT-Cl, tributyltin chloride.

§To whom correspondence should be addressed. E-mail: myoshida@res.titech.ac.jp

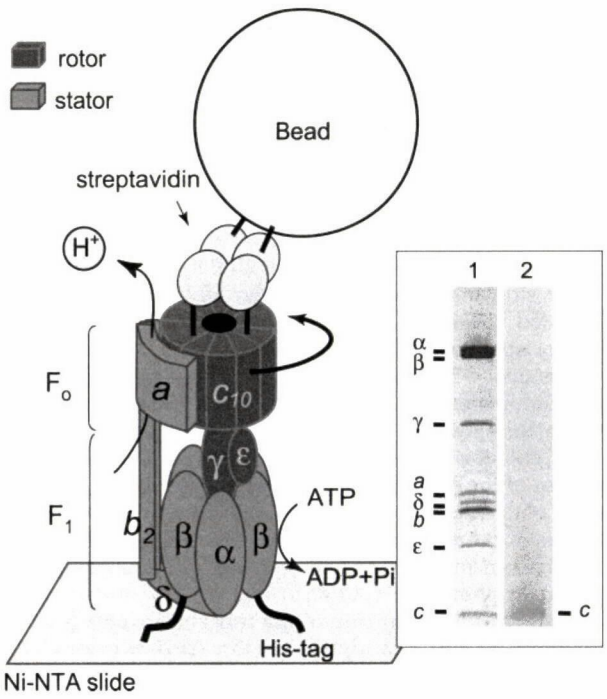

Fig. 1. Experimental system. ATP-driven rotation of the bead attached to the *c*-subunit ring in F_oF_1 was observed under dark-field microscopy and recorded with a fast camera. (*Inset*) F_oF_1 from thermophilic *Bacillus* PS3 used for observation of rotation. Lane 1, PAGE in the presence of sodium dodecyl sulfate of F_oF_1 purified in LPC and stained by Coomassie brilliant Blue; lane 2, immunoblots stained by alkaline phosphatase-streptavidin conjugates that show specific biotin labeling of the *c*-subunit.

F_oF_1 are almost unaltered from those of F_1, except for the response to an F_o-specific inhibitor.

Materials and Methods

Isolation of F_oF_1. A plasmid pTR19-ASDS-CNCR3 for mutant F_oF_1 (*c*Ser2Cys/*β*-His_{10} tags) was made by the Mega-primer method (23) using a plasmid, pTR19-ASDS (24), an expression vector for F_oF_1 complex of thermophilic *Bacillus* PS3. The mutant F_oF_1 was expressed constitutively in *E. coli* strain DK8 [Δ(*uncB-uncC*), *ilv*::Tn*10*] that lacks whole F_oF_1 genes, and the inverted membrane vesicles were prepared by the procedures described (24). After washing a 1-ml suspension of the vesicles (20 mg of protein per ml) with 5-fold volume of buffer PA3 (10 mM Hepes/KOH, pH 7.5/5 mM $MgCl_2$/10%glycerol) containing 2% sodium cholate by centrifugation, the vesicles were dissolved in 2 ml of buffer PA3 containing 2% (wt/vol) octaethylene glycol monododecyl ether and 100 μM Tris (2-carboxyethyl) phosphine, and incubated for 30 min at room temperature. After adjusting the pH of the solution to 7.0 by phosphate buffer, 6-*N*′-[2-(*N*-maleimido)ethyl]-*N*-piperazinyl-amidohexyl-D-biotinamide (Dojindo) was added (50 μM), and incubated for 30 min at room temperature. Biotinylation was quenched with 100 μM DTT, and the suspension was diluted 6-fold with buffer M (20 mM potassium phosphate buffer, pH 7.5/100 mM KCl) containing 0.1% lysophosphatidylcholine (LPC) and 20 mM imidazole. This suspension was applied to a Ni^{2+}-nitrilotriacetic acid (Ni^{2+}-NTA) column (Qiagen, Valencia, CA) equilibrated with the same buffer. After washing with 10 volumes of the equilibration buffer, the protein was eluted with buffer M containing 0.1% LPC and 200 mM imidazole. The eluate containing F_oF_1 was applied to a Soft-Link avidin column (Promega) equilibrated with buffer M containing 0.05% LPC. The column was washed with 10 volumes of the same buffer, and the protein was eluted with buffer M containing 0.05% LPC and 10 mM D-biotin. The purification was finished within 4 h, and the purified sample was used within 1 day. The purified F_oF_1 contained 0.9 mol of ADP and 0.8 mol of ATP per mol of F_oF_1 as endogenously bound nucleotides. Specific biotinylation of the F_oc-subunit was confirmed by immunoblotting using streptavidin-alkaline phosphatase conjugates (Promega).

Beads. Colloidal gold (diameter of 40 or 80 nm; British BioCell International) was incubated in 100 mM borate buffer, pH 8.2, containing 20 mg/ml BSA for 16 h at 37°C. BSA-coated colloidal gold was precipitated by centrifugation, and resuspended in 100 mM borate buffer, pH 8.2, with 10 mg/ml BSA. The suspension was biotinylated with 0.4 mg/ml 15-([biotinoyl]amino)-4,7,10,13-tetraoxapentadecanoic acid, *N*-hydroxysuccinimidylester (Pierce) for 3 h at room temperature. After removing unreacted biotin by centrifugation, 1 mg/ml streptavidin was added. After the excess streptavidin was removed by centrifugation, the pellet was resuspended in 2 mM potassium phosphate, pH 7.0, containing 0.05% polyethylene glycol and stored at 4°C. In the experiments to test the inhibition of rotation by *N*,*N*′-dicyclohexylcarbodiimide (DCCD), larger beads (streptavidin-coated microspheres, 0.56 μm, Bangs Laboratories, Carmel, IN) were used.

Rotation Assay. A flow cell was made of a Ni^{2+}-NTA-coated cover glass and a slide glass separated by two spacers with 50-μm thickness. At first, buffer R (50 mM Hepes/KOH, pH 7.5/100 mM KCl/10 mg/ml BSA/0.05% LPC/20 mM imidazole) was infused into the flow cell and incubated for 5 min to block nonspecific binding of the enzyme. Biotinylated His_{10}-tagged F_oF_1 (1–5 nM) in buffer R was infused. After 10 min, unbound F_oF_1 was washed with buffer R. Then, streptavidin-coated beads (2×10^9 particles per milliliter) in buffer R1 (50 mM Hepes/KOH, pH 7.5/100 mM KCl/10 mg/ml BSA/0.05% LPC) were infused, and incubated for 10 min. Unbound beads were removed with buffer R1 containing 5 mM $MgCl_2$, an ATP-regeneration system, and ATP at indicated concentrations, and observation of rotation was started. When indicated, ATPγS was added instead of ATP, and an ATP-regeneration system was omitted in this case. The number of the beads at the glass surface depended on the concentrations of biotinylated F_oF_1 infused to the flow cell. When nonbiotinylated enzyme was infused, it was almost the same as the case when no protein was infused, and we could not find any rotating beads in this case. Inhibitory effect of DCCD was assessed by observing the rotation of F_oF_1 incubated with 50 μM DCCD for 30 min at room temperature before infusion into the flow cell. Beads were observed with a dark-field microscopy (IX-70, Olympus) with a ×100 objective lens (numerical aperture of 1.35, Olympus) and a dark-field condenser (numerical aperture of 1.2–1.4, Olympus). Both the objective lens and the condenser were warmed by lens (condenser) heater (Tokai Hit) to maintain temperature of the flow cell at 37°C. Bead images were recorded as an eight-bit AVI file with a fast-framing charge-coupled device camera (Hi-Dcam, NAC Image Technology) at the indicated frame rate. To analyze the acquired image data, custom software (created by R.Yasuda; Cold Spring Harbor Laboratory, Cold Spring Harbor, NY) was used. Rotation rate was obtained from the average of 20 continuous revolutions without unnatural interruption.

Other Assays. ATPase activity was measured at 37°C with an ATP regeneration system (25). The assay solution was composed of buffer R1 containing 5 mM $MgCl_2$, 1 mM ATP-Na, 2 mM phospho*enol*pyruvate, 100 μg/ml lactate dehydrogenase, 100 μg/ml pyruvate kinase, and 0.2 mM NADH. DCCD inhibition of ATP hydrolyzing activity was measured as described for the inverted membrane vesicles (24), or after a 30-min preincubation

Table 1. ATPase activity sensitivity of F_oF_1 to DCCD inhibition

Samples	Residual activity +DCCD, %
Membrane vesicles	25
Reconstituted vesicles	20
F_oF_1	15

The samples were pretreated with 50 μM DCCD for 30 min and subjected to the assays. Membrane vesicles were prepared from *Escherichia coli* cells expressing F_oF_1 from thermophilic *Bacillus* PS3. Purified F_oF_1 was incorporated into reconstituted vesicles. ATPase activity was measured in the same solution used for rotation observation. Other experimental details are described in *Materials and Methods*.

with DCCD (50 μM) for the purified enzymes. To measure inhibitory effect of tributyltin chloride (TBT-Cl) on ATP hydrolyzing activity, indicated concentrations of TBT-Cl was added to the assay solution before the start of the reaction. Because the inhibitory effect of TBT-Cl on ATPase activity, as well as on rotation, tended to be relieved gradually as time passed (for an unknown reason), we collected rotation data quickly after the initiation of measurements. Reconstitution of F_oF_1 into liposomes was performed by the method described (24). Protein concentrations were determined by the BCA protein assay kit (Pierce) with BSA as a standard.

Results

Intact F_oF_1 in Detergent. In this study, we used F_oF_1 of thermophilic *Bacillus* PS3 expressed in the plasma membranes of an F_oF_1-deficient *E. coli* strain, DK8. A detergent octaethylene glycol monododecyl ether was used to solubilize F_oF_1 from the membrane vesicles and it was substituted with LPC at the next step of purification. We have tested various detergents, but this combination of detergents gave the most efficient solubilization, and the F_oF_1 preparation had the most stable, intact coupling properties. The F_oF_1 has His_{10} tags at the N terminus of the β-subunits to immobilize onto a glass surface and has a cysteine residue at the second position from N terminus of the *c*-subunit for biotinylation to attach the beads. The enzyme was purified with a Ni^{2+}-NTA column and a Soft-Link avidin column (Fig. 1 *Inset*, lane 1). These procedures should help to remove free F_1 and F_o, if any. Specific biotinylation of the *c*-subunit was confirmed by immunoblotting (Fig. 1 *Inset*, lane 2). The purified F_oF_1 in LPC comprised eight kinds of subunits and exhibited DCCD-sensitive ATPase activity; ≈85% of the activity was inhibited by DCCD in the solution used for observation of rotation (Tables 1 and 2). This degree of inhibition is similar to that of the intact F_oF_1 embedded in membranes, either in the membrane vesicles, or in the reconstituted vesicles. It has been known that DCCD covalently labels an essential carboxyl residue of the *c*-subunit, blocks proton transport, and consequently, if

Table 2. Effect of DCCD on rotation of F_oF_1

	No. of rotating beads	
Trial	+DCCD	−DCCD
1	2	10
2	1	10
3	0	9
4	2	12
5	1	11
6	1	8
Total	7	60

Rotating beads were looked for in 120 optical fields of a unit area (~45 × 55 μm^2) in 10 min in one trial. Other experimental details are described in *Materials and Methods*.

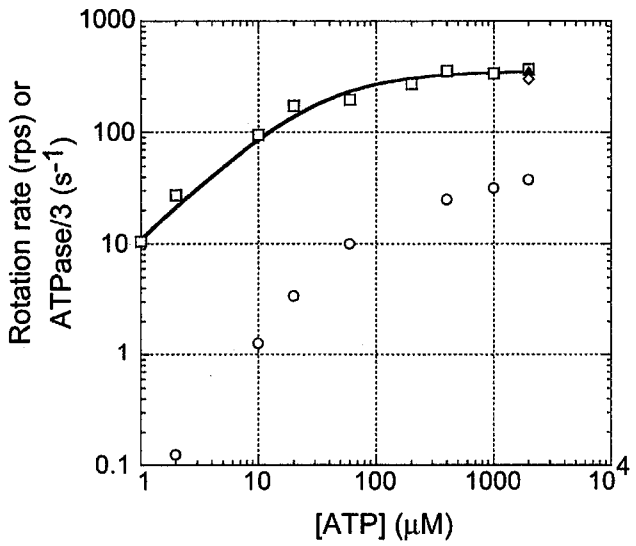

Fig. 2. Dependency of rotation rate and bulk-phase ATPase of F_oF_1 on [ATP]. □, rotation observed with an 80 nm-bead; ◇, rotation observed with a 40 nm-bead; ▲ rotation of F_1 observed with an 80 nm-bead; ○, bulk-phase ATPase activities measured in the rotation buffer. The line shows fit with Michaelis–Menten kinetics, $V = V_{max}[ATP]/(K_m+[ATP])$, where V_{max} = 352 ± 16 rps, and K_m = 31 ± 7 μM. Values are means ± SE.

F_oF_1 is intact, prevents ATP hydrolysis/synthesis. Unlike F_oF_1, ATPase activity of the isolated F_1 was not affected by DCCD at pH values of >7.5. (data not shown). Therefore, high sensitivity to DCCD inhibition is a good indication of the intactness of our F_oF_1 preparation. The reconstituted vesicles containing purified F_oF_1 showed substantial ATP-driven proton-pumping activity, comparable with that of the authentic wild-type thermophilic F_oF_1 (24). Based on these observations, we concluded that the purified F_oF_1 in LPC had intact ATPase activity that coupled proton transport. This conclusion was further confirmed by TBT-Cl sensitivity of F_oF_1 as described later.

V_{max} Rotation of F_oF_1. F_oF_1 was immobilized on a glass surface through β-subunits, and an 80-nm bead was attached to the *c*-subunit ring. Because the size of the bead was much larger than the *c*-subunit ring (≈5 nm) (26), a single bead could be tethered to several *c*-subunits in the same ring, although two beads could not attach to the same *c*-subunit ring. ATP-driven rotation of the bead attached obliquely to the *c*-subunit ring was observed at 37°C under dark-field microscopy equipped with a fast camera (Fig. 1). Functional integrity of immobilized F_oF_1 was confirmed by the observations that the number of rotating beads was drastically decreased to 12% (7:60) by DCCD-pretreatment of F_oF_1 (Table 2). In the case of rotation of F_1, on the contrary, pretreatment of F_1 with DCCD did not cause decrease in the number of the rotating molecules (data not shown). The direction of rotation was exclusively viewed counter clockwise from the membrane side. We observed the rotation at various [ATP] and found that rotation rates obeyed a simple Michaelis–Menten kinetics with a V_{max} of 352 ± 16 revolutions per second (rps) and a K_m of 31 ± 7 μM (Fig. 2, □). We used an 80-nm single bead as a rotation probe, but the rotation rate observed with a 40-nm single bead at 2 mM ATP (≈300 rps, Fig. 2, ◇) was almost the same as that of an 80-nm bead, indicating that the viscous friction in the rotating 80-nm bead did not slow down the rotation rate of F_oF_1. It is noteworthy that the rotation rate of F_oF_1 under V_{max} conditions was very similar to the rotation rate of F_1 (≈320 rps, Fig. 2, ▲) under the same conditions. Therefore, any events occurring at the F_o portion during rotation, such as the interaction between rotor (*c*-subunit ring) and stator (ab_2-subunits)

BIOCHEMISTRY

and proton transport through F_o, does not limit rotation rate of F_oF_1, at least in the absence of the electrochemical gradient of protons.

Rotation Rate Versus ATPase Activity. The bulk-phase steady-state ATPase activities of the purified F_oF_1 in the same solution used for observation of rotation were only ≈10% at 2 mM ATP, and even <1% at 2 μM ATP of the expected values from the rotation rates (Fig. 2, ○). This result indicates that >90% population of F_oF_1 molecules are not working at a given moment, or, in other words, a single molecule spends ≈90% of time in inactive state(s). Indeed, we noticed that rotating molecules usually stopped rotation after several seconds of continuous rotation. Sometimes, the same molecule resumed rotation after a while. We also often saw, under the microscopic field, that a previously nonrotating bead started rotating. The real reason why such high fractions of F_oF_1 molecules are in inactive state(s) is not known, but it should be noted that F_1 ($\alpha_3\beta_3\gamma$ subcomplex) also shows similar large discrepancy of rates between rotation and bulk-phase steady-state ATPase activity. In the case of F_1, the responsibility for the discrepancy is thought to be the ADP-Mg inhibition, which is caused from the nonturnover retention of ADP-Mg at a catalytic site (27–29). The steady-state ATPase activity of F_1 is largely suppressed by the ADP-Mg inhibition, but, uninhibited activity that is almost consistent with the rotation rate, is estimated from the initial burst activity that appears upon initiation of ATPase assays (14). We speculate that ADP-Mg inhibition occurring in F_oF_1 can explain, at least partly, the discrepancy between rotation and bulk-phase ATPase activity, although we cannot estimate its quantitative contribution because F_oF_1 does not show the uninhibited initial-burst activity. Pronounced inhibition of ATPase activity of F_oF_1 at low [ATP] in Fig. 2 might be due to the inhibition by the endogenous inhibitor, ε-subunit, that exhibits inhibition at low [ATP] (30).

Stepwise Rotation. We analyzed the time course of rotation at 2 mM ATP (Fig. 3*A*). Under V_{max} conditions, it is expected that ATP binds to F_oF_1 very quickly, and the catalytic events occurring in the enzyme determine the rates of ATP hydrolysis and rotation. Therefore, the rotation would show only the catalytic dwell. Indeed, the histogram of angular distribution of centroid of bead (Fig. 3*A Inset*) indicated the presence of three favorable positions for a bead to make a brief pause. However, the expanded time course of rotation did not always show clear steps (see Fig. 6, which is published as supporting information on the PNAS web site), and we could not define each dwell time with certainty.

At 2 μM ATP, F_oF_1 rotated with discrete 120° steps (Fig. 3*B*), and the dwell time of the pauses between adjacent step-rotations was apparently dependent on [ATP], indicating that the observed pauses were the ATP-waiting dwells. In addition, very short dwells were often seen in the intermediate position in a 120° rotation. They are not obvious in the bead-centroid distribution plots (Fig. 3*B Lower Inset*) because these dwells would be buried behind spreading distribution of the long ATP-waiting dwells. Usually, the starting time points of the short dwells could be recognized in the rotation time course as an interruption of 120° rotation, but the end points were mostly unclear; the dwells transited to the next ATP-waiting dwell without showing discrete step rotation. Therefore, the total dwell time from the start of the short dwell to the end of the ATP-waiting dwell was analyzed. The histogram of the total dwells at 2 μM ATP showed a distinct peak, and was fitted by the sum of two exponential components that assumed two rate-limiting reactions (Fig. 3*B Upper Inset*). One of the time constants was [ATP]-dependent and corresponds to the ATP-waiting dwell. From the time constant, the ATP-binding rate ($k_{on\text{-}ATP}$) of F_oF_1 was estimated to be 3.6 ± 0.1 × 10^7 $M^{-1}\cdot s^{-1}$. This value is close to that of F_1 at 23°C (3.0 ± 0.1 × 10^7 $M^{-1}\cdot s^{-1}$) (14). The other time constant (≈0.58 ms) was [ATP]-independent and corresponds to the catalytic dwell. This value is consistent with that (≈0.95 ms) obtained from the V_{max} rotation.

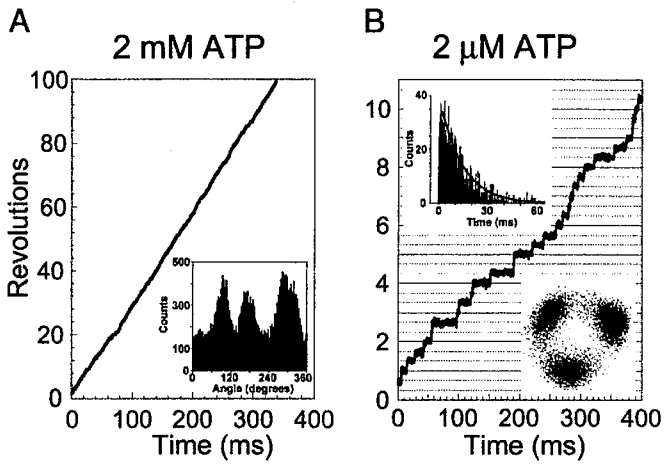

Fig. 3. Rotation of F_oF_1 driven by ATP. Bead images were recorded at 8,000 frames per second. (*A*) Time course of rotation at 2 mM ATP. (*Inset*) Histogram of angular distribution of the centroid of the bead image. (*B*) Time course of rotation at 2 μM ATP. (*Upper Inset*) Histogram of the total dwell times of rotation at 2 μM ATP. The total dwell time is defined as the time period from the start of the short dwell to the end of the ATP-waiting dwell. The black line is fit with the two rate constants, constant × [exp(−k_1t)−exp(−k_2t)], k_1 = 0.073 ± 0.002 ms^{-1} (time constant = 13.8 ± 0.4 ms) and k_2 = 1.72 ± 0.18 ms^{-1} (time constant = 0.58 ± 0.06 ms). k_1 is [ATP]-dependent and corresponds to the ATP-waiting dwell. k_2 is [ATP]-independent and corresponds to the catalytic dwell. Values are means ± SE. Total counts of dwells are 1,079. Bin width is 0.5 ms. (*Lower Inset*) Trace of the centroid of the bead image.

From these results, we learned that F_oF_1 rotates by repeating ATP-waiting dwell and catalytic dwell. However, the very short lifetime of the catalytic dwell did not allow for its further analysis, and the angular position of the catalytic dwell and the number of events occurring in the catalytic dwell were not determined. To learn these answers, we extended the duration of the catalytic dwell by adopting a slowly hydrolyzable ATP analog, ATPγS, as a substrate (15).

Rotation Driven by ATPγS. F_oF_1 rotated in 1 mM ATPγS at ≈20 rps, >10 times slower rate compared with the rate in 1 mM ATP (≈335 rps), and the discrete 120° steps were observed (Fig. 4*A Lower Inset*). The rotation in 100 μM ATPγS was apparently very similar to that observed in 1 mM ATPγS; rotation rate of ≈18 rps and 120° step rotation (data not shown). The dwell time between steps was not changed in two ATPγS concentrations and should be the catalytic dwell. The histogram of the catalytic dwell of the rotation in 1 mM ATPγS showed a peak, and was fitted with the sum of two exponential components that provided two time constants, ≈12.4 and ≈2.3 ms (Fig. 4*A Upper Inset*). Taking the F_1 study on hydrolysis of ATPγS as a reference (15), the long time constant is likely the one for cleavage of ATPγS, and the short time constant for the release of the last product. The total of these time constants (≈14.7 ms) agrees well with that (≈16.7 ms) obtained from V_{max} (≈20 rps). In 10 μM ATPγS, the 120° step was further split into two substeps (Fig. 4*B Lower Inset*). The angles of the two substep rotations were roughly 80° and 40° that are the same as observed for F_1. The pauses between adjacent 40° and 80° substep rotations depended on ATPγS concentrations, and, hence, the ATPγS-waiting dwell. The histogram of the ATPγS-waiting dwell was fitted well with a single-exponential component (Fig. 4*B Upper Inset*), and the ATPγS-binding rate ($k_{on\text{-}ATP\gamma S}$) of F_oF_1 was estimated to be

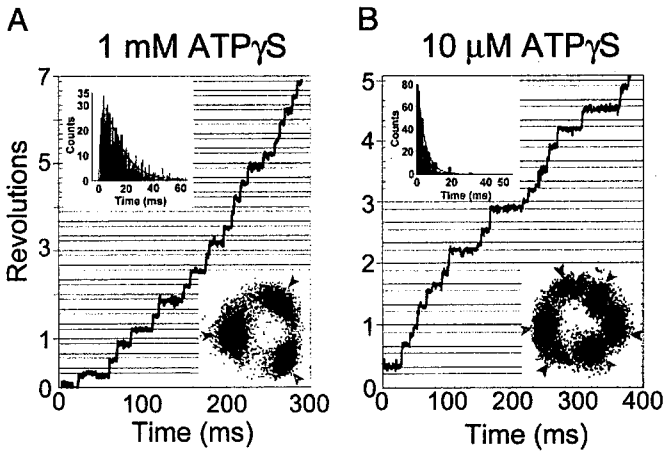

Fig. 4. Rotation of F_oF_1 driven by ATPγS. Bead images were recorded at 2,000 frames per second. Gray horizontal lines are placed 40° below black lines. (*A*) Time course of the rotation of F_oF_1 at 1 mM ATPγS. (*Upper Inset*) Histogram of the pauses before 40° substeps (catalytic dwell) in rotation at 1 mM ATPγS. The line is fit with the two rate constants, constant × [exp($-k_1$t)−exp($-k_2$t)], k_1 = 80.8 ± 3.5 s^{-1} (time constant = 12.4 ± 0.5 ms) and k_2 = 445 ± 36 s^{-1} (time constant = 2.25 ± 0.18 ms). Values are means ± SE. Total counts of dwells are 1,028. Bin width is 0.5 ms. (*Lower Inset*) Trace of the centroid of the bead image. Gray arrows indicate the positions of catalytic dwell. (*B*) Time course of the rotation of F_oF_1 at 10 μM ATPγS. (*Upper Inset*) Histogram of the pauses before 80° substep rotations (ATPγS-binding dwell) in rotation at 10 μM ATPγS. The line is a single-exponential fit, constant × exp($-k$t) where k = 238.3 ± 5.3 s^{-1} (time constant = 4.2 ± 0.1 ms). Values are means ± SE. Total counts of dwells are 202. Bin width is 2 ms. (*Lower Inset*) Trace of the centroid of the bead image. Black arrows indicate the positions of ATPγS-binding dwell.

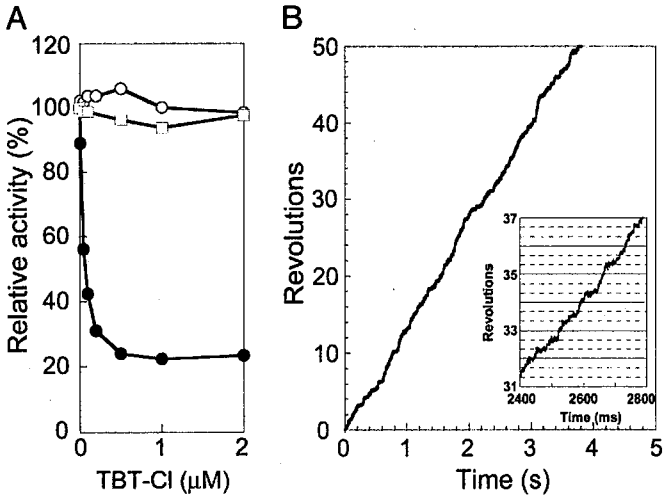

Fig. 5. Effect of TBT-Cl on ATPase activity of F_oF_1 (*A*) and rotation of F_oF_1 (*B*). (*A*) The ATPase activities of F_oF_1 were measured in the presence of indicated concentrations of TBT-Cl. Samples are F_oF_1 (●), F_oF_1 plus 0.3% lauryldodecylamine oxide (○), and F_1 (□). (*B*) Time course of the rotation of F_oF_1 in 1 mM ATP in the presence of 1 μM TBT-Cl.(*Inset*) Expanded time course of rotation.

$2.4 \pm 0.1 \times 10^7\ M^{-1}{\cdot}s^{-1}$. This value is in the same order of $k_{on\text{-}ATP}$ ($3.6 \pm 0.1 \times 10^7\ M^{-1}{\cdot}s^{-1}$) of F_oF_1, and $k_{on\text{-}ATP\gamma S}$ ($2.6 \pm 0.1 \times 10^7\ M^{-1}{\cdot}s^{-1}$) of F_1 (15). The pauses between adjacent 80° and 40° substep rotations corresponded to the catalytic dwell, and the analysis of the dwell-time histogram (not shown) gave two time constants, ≈17.3 and ≈2.4 ms, which is consistent with the values obtained from the rotation in 1 mM ATPγS.

Effect of TBT-Cl on F_oF_1 Rotation. TBT-Cl has been known as an inhibitor of F_oF_1 (31, 32). It reacts noncovalently with the F_o portion, probably with the F_oa-subunit, and prevents proton translocation-coupled ATP hydrolysis/synthesis (33). ATPase activity of our purified F_oF_1 measured in the same solution used for observation of rotation was efficiently (≈80%) inhibited by 1 μM TBT-Cl (Fig. 5*A*, ●). No inhibition was observed in the presence of 0.3% lauryldodecylamine oxide (Fig. 5*A*, ○), a detergent known to disrupt stator/rotor interface of F_o. ATPase activity of the isolated F_1 was also totally insensitive to TBT-Cl (Fig. 5*A*, □). Rotation of F_oF_1 in 1 mM ATP was slowed down significantly by TBT-Cl (Fig. 5*B*); the average rotation rate decreased to 4% (≈15 rps). Rotation of F_1 under the same condition was not affected by TBT-Cl (data not shown). We had expected to identify the angular position(s) where rotation would have paused in TBT-Cl, and 15 rps was slow enough to show any prolonged dwells. However, the rotating bead did not show any obvious pause at certain angular position (Fig. 5 *Inset*). We speculate that TBT-Cl interferes with the rotation of the F_o portion at many angular positions, and makes the step-wise rotation obscure.

Discussion

In this study, we directly observed ATP-driven rotation of single-molecule F_oF_1 immobilized on a glass surface. To do so, F_oF_1 must be solubilized and purified without losing original structural integrity. It should be noted that the previous demonstrations of rotation of purified *E. coli* F_oF_1 immobilized on a glass surface were carried out by using the enzyme preparation, of which ATPase activity in the rotation buffer and the rotation itself were totally insensitive to DCCD (34, 35), and might have been the rotation of incomplete F_oF_1, as stated in the subsequent paper (36). We have spent considerable effort to establish the procedures to isolate intact thermophilic F_oF_1 from the recombinant *E. coli* cells, and found that extraction from membranes by octaethylene glycol monododecyl ether and isolation in LPC gave the best yield and preparation. Both bulk-phase ATPase activity in the rotation buffer and the observed rotations under microscopy were efficiently inhibited by DCCD and TBT-Cl. Combination of this intact F_oF_1 and the submillisecond fast camera enabled us to learn several features of ATP-driven rotation of F_oF_1.

Firstly, F_oF_1 rotates as fast as 350 rps (37°C). We observed rotations at 25°C and 45°C and obtained the V_{max} rotation rates of ≈230 and ≈650 rps, respectively. Therefore, extrapolated rotation rate at 60°C, an optimum growth temperature of *Bacillus* PS3, can reach ≈1,600 rps. Although reservation is needed concerning whether these enormous numbers are really the case, it is certain that the rotation rate of thermophilic F_oF_1 at 25°C is much faster than the rotation rate (19 ms/120°, that is, 17 rps, at 23°C) reported for *E. coli* F_oF_1 reconstituted into liposomes measured with fluorescence resonance energy transfer (22). However, in these measurements, uphill proton gradient should be immediately established by proton-pumping ATP hydrolysis to reach an equilibrium, and the rate limiting can be the rate of passive proton leak through membranes. It is interesting to discover whether the rotation rate will increase by addition of an uncoupler. One might argue whether fast rotation of >200 rps at V_{max} is common in F_oF_1 (and F_1) from various sources. Some reported values of very high ATPase activities would predict rapid rotations such as bovine mitochondrial F_1 (≈310 rps) (37), yeast mitochondrial F_1 (≈280 rps) (38), and *E. coli* F_oF_1 (≈300 rps) (39). Much lower ATPase activities corresponding to 10 ≈ 100 rps were also reported in many papers. However, if a significant fraction of molecules in the bulk solution are in the ADP-Mg-inhibited state or other inactive states, as in the case of thermophilic F_oF_1, real ATPase activity specific for the working enzymes should be higher, and the

rotation rates can be much faster. It is intriguing to learn whether these rapid rotations are really occurring in living cells.

Second, F_oF_1 rotates in the almost same manner as F_1. V_{max} rotation rate, [ATP] dependency, ATP-waiting dwell, and catalytic dwell are all very similar to those observed for F_1. Apparently, friction in F_o motor is negligible, that is, F_o does not impose significant drag during ATP-driven rotation of F_oF_1. This finding means that F_o keeps the interaction between the c-subunit ring and ab_2 neither too strong nor too weak. The c-subunit ring seems to be able to pause rotation at the angular positions dictated by F_1. We recently proposed that b_2 in F_o act as a strong brake of ATP-driven rotation when the a-subunit is removed (40). The association of the a-subunit makes b_2 to be a proper anchor rail that allows the c-subunit ring to slide without breaking association during rotation.

Finally, an F_o-specific inhibitor, TBT-Cl, obscures the steps in ATP-driven rotation of F_oF_1. Obviously, now the F_o portion resists the rotary torque generated in F_1 portion. Because the rotor of F_o in thermophilic F_oF_1 is a decamer c-subunit ring (41), it is likely that resistance occurs at every 36°. As discussed in the recent paper (41), mismatch of the unit-rotation angle in F_1 (120°) and in F_o (36°) assumes a torsion-spring-like motion of the central rotor shaft (and/or the peripheral stalk) that makes the dwelling position of the c-subunit ring in ATP-driven rotation obscure. We don't know whether this explanation is really the case, but we expect that further study on TBT-Cl inhibition will provide the answer.

We thank J. Suzuki for technical assistance; K. Shimabukuro, E. Muneyuki, R. Iino, T. Masaike, T. Ariga, and M. Takeda for valuable discussion and technical advice; and H. Noji, R. Yasuda, and K. Adachi for creating and developing the single-molecule observation system. This work was supported by research fellowships from the Japan Society for the Promotion of Science for Young Scientists (to H.U.).

1. Boyer, P. D. (1997) *Annu. Rev. Biochem.* **66,** 717–749.
2. Yoshida, M., Muneyuki, E. & Hisabori, T. (2001) *Nat. Rev. Mol. Cell Biol.* **2,** 669–677.
3. Capaldi, R. A. & Aggeler, R. (2002) *Trends Biochem. Sci.* **27,** 154–160.
4. Pedersen, P. L. (2002) *J. Bioenerg. Biomembr.* **34,** 327–332.
5. Senior, A. E., Nadanaciva, S. & Weber, J. (2002) *Biochim. Biophys. Acta* **1553,** 188–211.
6. Abrahams, J. P., Leslie, A. G. W., Lutter, R. & Walker, J. E. (1994) *Nature* **370,** 621–628.
7. Seelert, H., Poetsch, A., Dencher, N. A., Engel, A., Stahlberg, H. & Muller, D. J. (2000) *Nature* **405,** 418–419.
8. Birkenhager, R., Hoppert, M., Deckers-Hebestreit, G., Mayer, F. & Altendorf, K. (1995) *Eur. J. Biochem.* **230,** 58–67.
9. Singh, S., Turina, P., Bustamante, C. J., Keller, D. J. & Capaldi, R. (1996) *FEBS Lett.* **397,** 30–34.
10. Jiang, W. & Fillingame, R. H. (1998) *Proc. Natl. Acad. Sci. USA* **95,** 6607–6612.
11. Boyer, P. D. (1993) *Biochim. Biophys. Acta* **1140,** 215–250.
12. Noji, H., Yasuda, R., Yoshida, M. & Kinosita, K., Jr. (1997) *Nature* **386,** 299–302.
13. Yasuda, R., Noji, H., Kinosita, K., Jr. & Yoshida, M. (1998) *Cell* **93,** 1117–1124.
14. Yasuda, R., Noji, H., Yoshida, M., Kinosita, K., Jr. & Itoh, H. (2001) *Nature* **410,** 898–904.
15. Shimabukuro, K., Yasuda, R., Muneyuki, E., Hara, K. Y., Kinosita, K., Jr. & Yoshida, M. (2003) *Proc. Natl. Acad. Sci. USA* **100,** 14731–14736.
16. Nishizaka, T., Oiwa, K., Noji, H., Kimura, S., Muneyuki, E., Yoshida, M. & Kinosita, K., Jr. (2004) *Nat. Struct. Mol. Biol.* **11,** 142–148.
17. Kaim, G., Prummer, M., Sick, B., Zumofen, G., Renn, A., Wild, U. P. & Dimroth, P. (2002) *FEBS Lett.* **525,** 156–163.
18. Hutcheon, M. L., Duncan, T. M., Ngai, H. & Cross, R. L. (2001) *Proc. Natl. Acad. Sci. USA* **98,** 8519–8524.
19. Tsunoda, S. P., Aggeler, R., Yoshida, M. & Capaldi, R. A. (2001) *Proc. Natl. Acad. Sci. USA* **98,** 898–902.
20. Nishio, K., Iwamoto-Kihara, A., Yamamoto, A., Wada, Y. & Futai, M. (2002) *Proc. Natl. Acad. Sci. USA* **99,** 13448–13452.
21. Borsch, M., Diez, M., Zimmermann, B., Reuter, R. & Graber, P. (2002) *FEBS Lett.* **527,** 147–152.
22. Diez, M., Zimmermann, B., Borsch, M., Konig, M., Schweinberger, E., Steigmiller, S., Reuter, R., Felekyan, S., Kudryavtsev, V., Seidel, C. A. & Graber, P. (2004) *Nat. Struct. Mol. Biol.* **11,** 135–141.
23. Landt, O., Grunert, H. P. & Hahn, U. (1990) *Gene* **96,** 125–128.
24. Suzuki, T., Ueno, H., Mitome, N., Suzuki, J. & Yoshida, M. (2002) *J. Biol. Chem.* **277,** 13281–13285.
25. Suzuki, T., Suzuki, J., Mitome, N., Ueno, H. & Yoshida, M. (2000) *J. Biol. Chem.* **275,** 37902–37906.
26. Stock, D., Leslie, A. G. & Walker, J. E. (1999) *Science* **286,** 1700–1705.
27. Hirono-Hara, Y., Noji, H., Nishiura, M., Muneyuki, E., Hara, K. Y., Yasuda, R., Kinosita, K., Jr. & Yoshida, M. (2001) *Proc. Natl. Acad. Sci. USA* **98,** 13649–13654.
28. Matsui, T., Muneyuki, E., Honda, M., Allison, W. S., Dou, C. & Yoshida, M. (1997) *J. Biol. Chem.* **272,** 8215–8221.
29. Jault, J. M., Matsui, T., Jault, F. M., Kaibara, C., Muneyuki, E., Yoshida, M., Kagawa, Y. & Allison, W. S. (1995) *Biochemistry* **34,** 16412–16418.
30. Kato-Yamada, Y., Bald, D., Koike, M., Motohashi, K., Hisabori, T. & Yoshida, M. (1999) *J. Biol. Chem.* **274,** 33991–33994.
31. Cain, K. & Griffiths, D. E. (1977) *Biochem. J.* **162,** 575–580.
32. Matsuno-Yagi, A. & Hatefi, Y. (1993) *J. Biol. Chem.* **268,** 6168–6173.
33. von Ballmoos, C., Brunner, J. & Dimroth, P. (2004) *Proc. Natl. Acad. Sci. USA* **101,** 11239–11244.
34. Sambongi, Y., Iko, Y., Tanabe, M., Omote, H., Iwamoto-Kihara, A., Ueda, I., Yanagida, T., Wada, Y. & Futai, M. (1999) *Science* **286,** 1722–1724.
35. Tanabe, M., Nishio, K., Iko, Y., Sambongi, Y., Iwamoto-Kihara, A., Wada, Y. & Futai, M. (2001) *J. Biol. Chem.* **276,** 15269–15274.
36. Panke, O., Gumbiowski, K., Junge, W. & Engelbrecht, S. (2000) *FEBS Lett.* **472,** 34–38.
37. Feinstein, D. L. & Moudrianakis, E. N. (1984) *J. Biol. Chem.* **259,** 4230–4236.
38. Ichikawa, N. & Mizuno, M. (2004) *Protein Expression Purif.* **37,** 97–101.
39. Moriyama, Y., Iwamoto, A., Hanada, H., Maeda, M. & Futai, M. (1991) *J. Biol. Chem.* **266,** 22141–22146.
40. Ono, S., Sone, N., Yoshida, M. & Suzuki, T. (2004) *J. Biol. Chem.* **279,** 33409–33412.
41. Mitome, N., Suzuki, T., Hayashi, S. & Yoshida, M. (2004) *Proc. Natl. Acad. Sci. USA* **101,** 12159–12164.

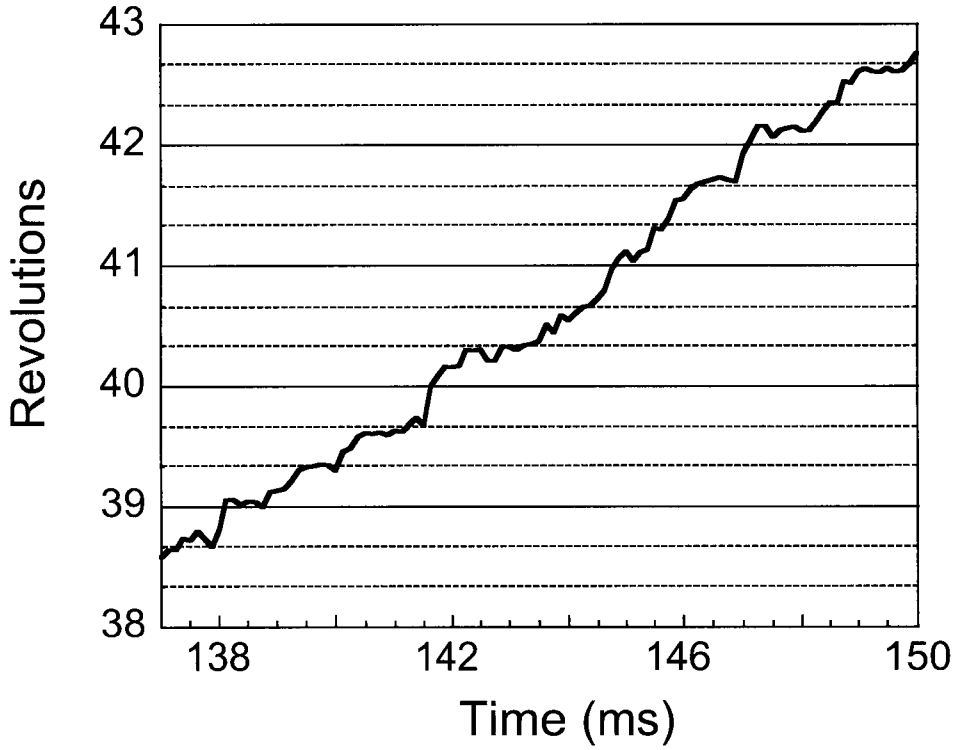

Fig. 6. Expanded time course of rotation as seen in Fig. 3A. Trace is rugged, but obvious steps cannot be defined.

Activation of pausing F_1 motor by external force

Yoko Hirono-Hara*†, Koji Ishizuka†‡, Kazuhiko Kinosita, Jr.§, Masasuke Yoshida‡, and Hiroyuki Noji*¶

*Institute of Industrial Science and ¶Precursory Research for Embryonic Science and Technology, Japan Science and Technology Corporation, University of Tokyo, Tokyo 153-8505, Japan, ‡Chemical Resources Laboratory, Tokyo Institute of Technology, Yokohama 226-8503, Japan; and §Center for Integrative Bioscience, Okazaki National Research Institutes, Okazaki 444-8585, Japan

Edited by Paul D. Boyer, University of California, Los Angeles, CA, and approved January 4, 2005 (received for review September 2, 2004)

A rotary motor F_1, a catalytic part of ATP synthase, makes a 120° step rotation driven by hydrolysis of one ATP, which consists of 80° and 40° substeps initiated by ATP binding and probably by ADP and/or P_i dissociation, respectively. During active rotations, F_1 spontaneously fails in ADP release and pauses after a 80° substep, which is called the ADP-inhibited form. In the present work, we found that, when pushed >+40° with magnetic tweezers, the pausing F_1 resumes its active rotation after releasing inhibitory ADP. The rate constant of the mechanical activation exponentially increased with the pushed angle, implying that F_1 weakens the affinity of its catalytic site for ADP as the angle goes forward. This finding explains not only its unidirectional nature of rotation, but also its physiological function in ATP synthesis; it would readily bind ADP from solution when rotated backward by an F_o motor in the ATP synthase. Furthermore, the mechanical work for the forced rotation was efficiently converted into work for expelling ADP from the catalytic site, supporting the tight coupling between the rotation and catalytic event.

ADP inhibition | ATP synthase | F1-ATPase | magnetic tweezers | single-molecule observation

The molecular rotary motor F_1-ATPase generates rotary torque driven by chemical energy liberated from ATP hydrolysis (1–4). In cells, F_1 constitutes the ATP synthase binding with its partner motor, F_o, which is embedded in a biomembrane and rotates its rotor ring driven by a proton flux down to the electrochemical potential across the membrane. F_1 and F_o are connected to each other through their rotor and stator parts, whereas their rotary directions are opposite. Thus, they push each other intramolecularly. Under physiological conditions where the proton-motive force is larger than the free energy obtained from ATP hydrolysis, F_o can generate a larger torque than F_1 and enforces F_1 to rotate in the reverse direction. Consequently, F_1 reverses its catalytic reaction to synthesize ATP from P_i and ADP. In contrast, when the free energy of ATP hydrolysis is larger, F_1 hydrolyzes ATP, inversely rotating F_o to pump protons in the opposite direction. Thus, F_1 is a reversible molecular machine for converting energy between the chemical potential of ATP and mechanical work of rotation. It has been proved that mechanically reversing F_1 molecules leads ATP synthesis (5). We recently revealed that the coupling efficiency of the mechanical ATP synthesis is very high with single-molecule manipulation and microfabrication techniques (6).

F_1 has a subunit composition of $\alpha_3\beta_3\gamma\varepsilon$. Its minimum complex as ATPase is the $\alpha_3\beta_3\gamma$ subcomplex, which is referred to hereafter as F_1. Walker's group (7–9) solved F_1's crystal structures to reveal that three α- and β-subunits are alternately arranged in a hexagonal cylinder in which the rotor subunit, γ, penetrates at the center. The catalytic site is located mainly on the β-subunit. Three β-subunits hydrolyze ATP in a cooperative manner to make a unidirectional rotation of the γ-subunit (10, 11). The kinetic model for its ATP hydrolysis coupled with the rotation was originally proposed by Boyer (12). The γ-rotation in F_1 hydrolyzing ATP was strongly supported by biochemical cross-linking (13) and a spectroscopic technique (14), and finally visualized at a single-molecule level (15). The direct observation of the rotation revealed F_1 makes a 120° stepping rotation upon each ATP hydrolysis (16). High-speed imaging of the F_1 rotation with no viscous load resolved the 120° step further, into 80° and 40° substeps (17). The kinetic analysis in these studies has made allowance for the idea that the 80° substep arises from ATP binding, and the 40° substep is triggered by ADP and/or P_i dissociation. Recently, it was demonstrated that ATP hydrolysis occurs between the 80° and 40° substeps by using a mutant F_1 that hydrolyzes ATP at an extremely slow rate (18).

In our previous work, we observed that the F_1 lapses into an inactive state during rotation and showed it to correspond to the ADP-inhibited form (19), which had been characterized by many biochemical studies (20, 21). The ADP-inhibited form is the state in which the F_1 fails to dissociate ADP to stop catalysis and rotation. The ADP-inhibited F_1 pauses after the 80° substep (19) in agreement with the idea that the 40° substep arises from the release of the product(s). The inactivation is a reversible process; the F_1 in pause spontaneously becomes active to rotate again. Recent single-molecule works showed that some other enzymes are also in equilibrium between catalytic active and inactive or less active forms (22, 23). If we identify the structural feature of an inactive enzyme and mechanically manipulate its conformation back to the catalytic active state, in principle, it is possible to activate the enzyme. However, there have been few experimental attempts to do so, one of which is a report by the Bustamante group (23) showing that the probability of the transcriptional pause of RNA polymerase is affected by external force directions. In the ATP synthase, F_o turns the F_1's catalysis direction by rotating the γ-subunit; therefore, F_1 is expected to modulate kinetic parameters upon the forced rotation of the γ-subunit. In the present study, we found that the ADP-inhibited F_1 can be mechanically activated by pushing the rotor γ-subunit in the forward direction. An elaborate analysis of this phenomenon revealed that the mechanical stress on the γ-subunit opens the catalytic site to dissociate inhibitory ADP, and that the rate constant of ADP dissociation increases with the angle of the γ-subunit. These findings have important implications for the model of the F_1's unidirectional rotation and its ATP synthesis in the ATP synthase.

Methods

Materials. A mutant $\alpha_3\beta_3\gamma$ subcomplex (α-C193S, β-His-10 at N terminus, γ-S107C/I210C) from a thermophilic *Bacillus* PS3 (referred to as F_1 unless otherwise specified) was expressed and purified as described (24). ATP, ADP, and phospho*enol*pyruvate were purchased from Sigma. Pyruvate kinase and streptavidin-coated magnetic beads (0.73 μm) were purchased from Roche Diagnostics and Seradyn (Indianapolis), respectively.

Magnetic Tweezers. A schematic diagram of magnetic tweezers is shown in Fig. 1*a*. The tweezers comprise four electromagnets, each constructed of a soft iron core (10 × 10 × 40 mm) and a copper wire with 100 turns around the core. Each pair of tweezers was electrically connected in a series and separated by an interval of 15 mm. The two electromagnet pairs were crossed at each center space and positioned 10 mm above the microscope stage. The microscope

This paper was submitted directly (Track II) to the PNAS office

†Y H.-H and K.I. contributed equally to this work

¶To whom correspondence should be addressed. E-mail: hnoji@iis.u-tokyo.ac.jp.

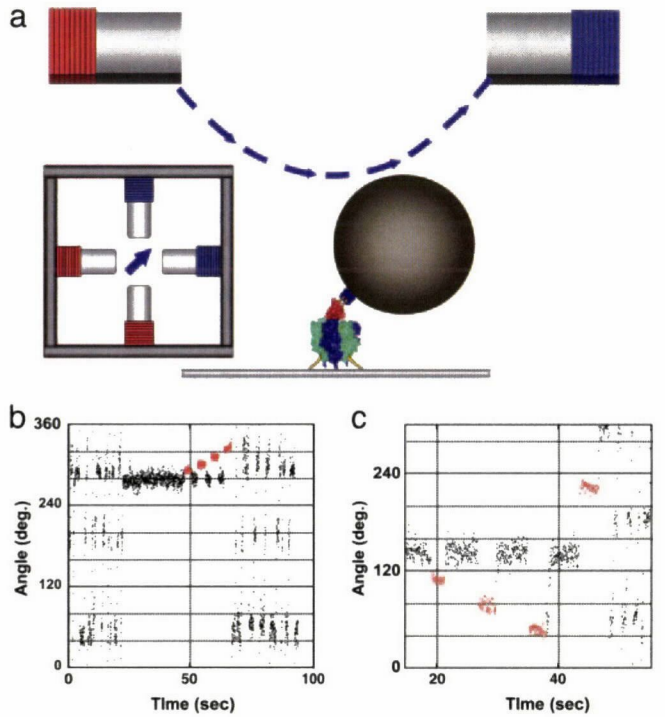

Fig. 1. Mechanical activation of the ADP-inhibited F_1 with magnetic tweezers. (*a*) Side and top views of the manipulation system with magnetic tweezers. The ≈0.6-μm magnetic beads were attached to the γ-subunit in the F_1 immobilized on the slide glass. The magnetic tweezers were mounted on the microscope 10 mm above the specimen stage to generate a magnetic field parallel to the stage. (*b*) Time course of the mechanical activation by pushing in the forward direction. After a 120° stepping rotation that can be seen as an oscillating trace, the F_1 spontaneously lapsed into the ADP-inhibited form at 280°. The F_1 was stalled and released at +10°, +20°, +30°, and +40° from the angle for inhibition with magnetic tweezers. After a +40° stalling, the F_1 regained active rotation. Red areas indicate the manipulation time by using the magnetic tweezers. (*c*) Trial of the mechanical activation by pulling in the backward direction. The F_1 was not activated when stalled and released at −20°, −40°, and −80° with magnetic tweezers. To confirm that it was alive, it was activated by being pushed >+80°.

stage and objective lens were constructed of antimagnetic materials to minimize the remanence magnetic field <0.2 G. The angle of the composite magnetic field was controlled by applying an electric current having sine components, to one pair (*y* axis) and cosine components, to the other (*x* axis), and the field intensity was controlled by changing the current amplitude. The magnetic field was measured with a gaussmeter (421 Gaussmeter, Lake Shore Cryotronics, Westerville, OH) to confirm that the magnetic tweezers generated ≈200 G at the center of the focal plane with a precision of 4% for the intensity and 5° for the angle.

Rotational Assay. A flow cell was constructed from a bottom coverslip coated with Ni^{2+}-NTA (5) and an uncoated top cover glass. F_1 of 1–2 nM in buffer A (50 mM Mops-KOH, pH 7.0/50 mM KCl/2 mM $MgCl_2$/10% BSA) was infused into the flow cell. After 2 min, the flow cell was washed with buffer A, and then the magnetic beads were infused. After 3 min, the unbound beads were washed out with buffer A, and then buffer A containing the indicated amount of Mg-ATP was infused. The rotating beads were observed as bright images (19). The images were videotaped and analyzed with custom software, see Movie 1, which is published as supporting information on the PNAS web site. For an ADP-free experiment, an ATP regenerating system (10.3 units/ml of pyruvate kinase, 1 mM phospho*enol*pyruvate) was added to buffer A. In the experiments for examining the effect of ADP on mechanical activation, purified ADP was added to buffer A (5).

Mechanical Activation. The solution contained 200 nM ATP except for the indication, in which the F_1 shows 120° stepping rotation. When the F_1 lapsed into the ADP-inhibited form pausing at ≈80° (ADP inhibition position) from the ATP-waiting position (5), a manipulation with magnetic tweezers was performed as follows: the tweezers were activated to trap the magnetic bead(s) at the ADP-inhibition angle, and then the magnetic field was rotated to the desired angle within 0.4 s. After the indicated time (0.5–300 s), the external magnetic field was turned off to check whether the F_1 was activated. All procedures were controlled with a custom computer program (H.N.). Some magnetic beads of which the magnetic moment was not parallel to the microscope stage were inclined under an external magnetic field, and those beads were not analyzed. The image of the beads was videotaped with a charge-coupled device camera at 30 frames per s with 2-ms shutter speed (TAKEX Tokyo, FC300M) and was analyzed with a custom computer program (Ryohei Yasuda, Duke University, Durham, NC).

Results

Experimental System. The F_1 motor was immobilized on a glass plate through the $\alpha_3\beta_3$ ring, and magnetic beads were attached to the γ-subunit (Fig. 1*a*). The rotation of the beads was videotaped at 30 frames per s in a bright field by using a charge-coupled device camera. To manipulate the F_1 motor, we developed magnetic tweezers consisting of two pairs of crossed electromagnets installed 10 mm above and parallel to the specimen stage of the microscope. The magnetic tweezers generate a magnetic field that is parallel to the stage. Its strength and orientation is controllable by changing the electric current on each electromagnet.

Observation of Mechanical Activation. The rotation of the F_1 was observed at 200 nM ATP, unless otherwise described, where F_1 rotates with a discrete 120° step, each initiated by ATP binding, which takes 0.3 s on average. As seen in our previous experiment, the F_1 motor spontaneously lapsed into the ADP-inhibited form to show a long pause (≈30 s) at an angle 80° forward from that for the ATP binding, that is, 40° backward from the next ATP binding angle. Hereafter, we define the origin angle, 0°, as the center angle for the ADP-inhibited form, plus as the rotary direction and minus as the opposite direction. The ADP-inhibited F_1 was manipulated with the magnetic tweezers to stall it at arbitrary angles, and then released from the tweezers. As seen in Fig. 1*b*, the F_1 was stalled for 3 s at +10°, +20°, +30°, and +40° and released each time. After it stalled at +10° to +30°, the F_1 still remained in its ADP-inhibited form, returning back to the original angle. On the other hand, the F_1 immediately restarted its rotation after being pushed to +40°. This finding means that the F_1 returned to its active form. This activation is discerned from the spontaneous recovery from the ADP-inhibited state. In the presence of 200 nM and 2 mM ATP, the average times for spontaneous activation without manipulation are 60 and 30 s, respectively, both of which are much longer than the standard manipulation time taken in the present experiment. In addition, it should be noted that any spontaneous activation did not occur after ADP-inhibited F_1 was stalled for several min at 0°, as described later. Therefore, any mechanical activation reported in this article was conducted by the manipulation.

Angle Dependency of Mechanical Activation. The probability of mechanical activation within the 3-s stall was determined at each stall angle (Fig. 2*a*). In this case, it was defined as activation, when the F_1 motor rotated >+120° from 0° after it was released from the magnetic tweezers. Other cases were regarded as an activation failure. In most of the failure cases, the F_1 motor returned to 0° (Fig. 1*b*). When pushed >+40°, the activation probability sharply in-

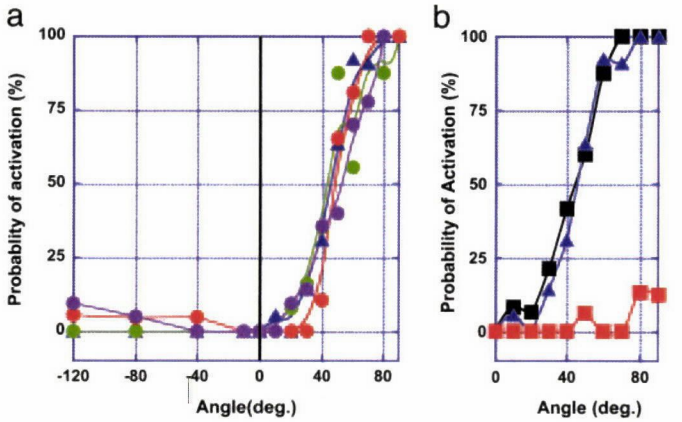

Fig. 2. Angle dependency of the probability of mechanical activation. (*a*) Probabilities of the mechanical activation were determined in the presence of 0.2 μM ATP (blue); 0.2 μM ATP, 30 mM P_i (green); 0.2 μM ATP, 1 mM ADP (red); and 0.2 μM ATP, 30 mM P_i, 1 mM ADP (purple). Each data point was determined from 17 observations on average. (*b*) Probabilities were determined in the presence of 0.2 μM ATP (blue), 2 mM ATP (black), and 33 μM ATP, 20 mM ADP (red). Each data point was determined from 15 observations on average.

creased to reach up to nearly 100% at +70°. However, when pulled up to −120°, the F_1 motor mostly returned to 0° (Fig. 1*c*). Thus, both the rotary direction and angle amplitude were important for the mechanical activation. The activation probability was also determined in the presence of 1 mM ADP and/or 30 mM P_i. No major difference in the presence of ADP was found, except for the lower probability at 30° and 40°. Similar probabilities were also obtained at 2 mM ATP (Fig. 2*b*). These findings suggest that the mechanical activation is ascribable to the release of the inhibitory ADP, as opposed to the binding of the substrate/product from the solution. In previous biochemical experiments (24, 25), the ADP-inhibited F_1 was activated by ADP depletion, for example, through gel filtration. To verify this finding, the mechanical activation was examined at 20 mM ADP, where it was completely suppressed, thus confirming the above explanation (Fig. 2*c*). At 20 mM ADP is much higher than the previously reported K_d values for ADP (26, 27), probably because the affinity of ADP decreases with the rotary angle, as shown below. Therefore, much higher ADP was needed for the suppression of the mechanical activation >40°, whereas the γ-subunit in the biochemical experiments would mostly be 0°, maintaining a higher affinity to ADP. Indeed, 2 mM ADP was enough to inhibit the mechanical activation <30°, indicating that the $K_{d(ADP)}$ for <30° is <2 mM. The $K_{d(ADP)}$ between 40° and 60° was expected to lie between 2 and 20 mM.

Time Course of Mechanical Activation. We examined how the mechanical activation depends on the stalling time. A typical time course of the experiment is shown in Fig. 3*a*, where the ADP-inhibited F_1 was stalled at 40° for 5, 5, and 15 s. Magnetic tweezers were turned off after each stalling to observe the activation. In this example, the F_1 was activated after 15 s of stalling. From these experiments, we obtained saturation curves for the activation probability, which exponentially increased with the stalling time (Fig. 3 *b* and *c*). These were well fitted with a single exponential equation that assumes a first-order reaction, ADP-inhibited form → activated form. Each fitting gave a rate constant for the mechanical activation, which exponentially increased with the rotary angle. Interestingly, the activation at 0° was too slow for this fitting, whereas the spontaneous activation occurred at the same rate as the mechanical activation at 20°. These results mean that the affinity of the inhibited F_1 to ADP at 0° is very high, and it decreases with the angle to accelerate ADP release. This finding is consistent with the observation that higher ADP was needed to suppress the

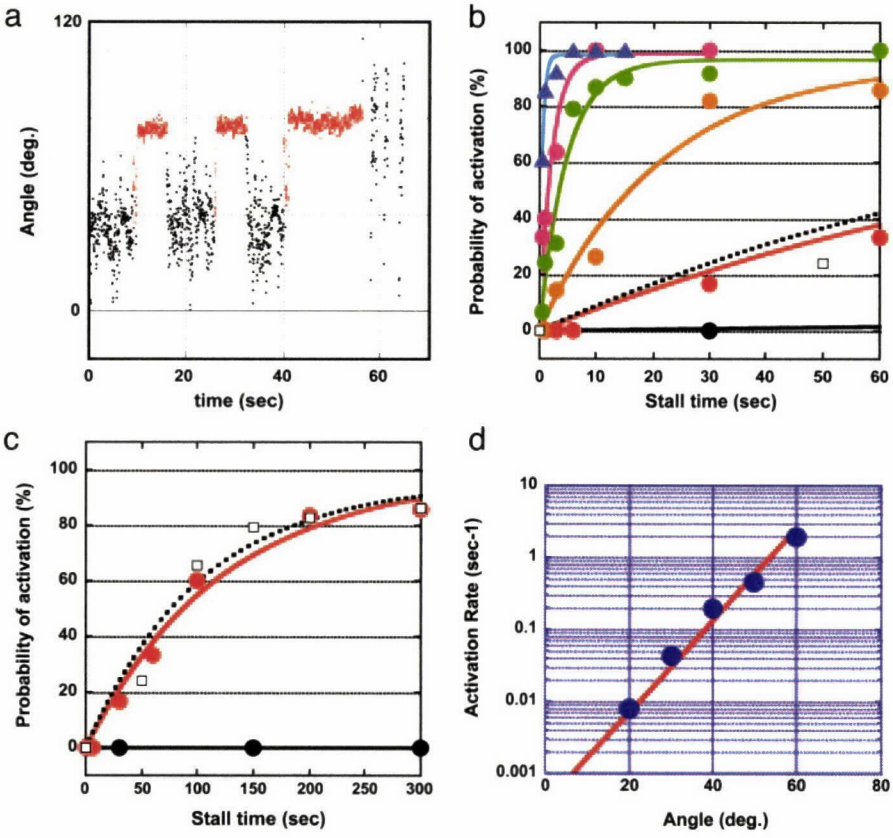

Fig. 3. Rate constant of the mechanical activation. (*a*) Time course of the mechanical activation with different stalling times. The ADP-inhibited F_1 was stalled and released at +40° after 5 s twice and after 15 s. (*b*) The probabilities of the mechanical activation by stalling at 0° (black), 20° (red), 30° (orange), 40° (green), 50° (purple), and 60° (blue) were plotted against the stalling time. Each data point was determined from 12 observations on average. (*c*) Shown is an expanded graph for probabilities of the spontaneous activation (□). (*d*) Rate constants (blue circles) were determined by fitting the curves in *b* and *c* with single exponential equations. The slope of linear fitted line (red) for these rates in semilogarithmic scale gives the angle dependency of the activation energy as $-1.3\ k_BT/10^0$.

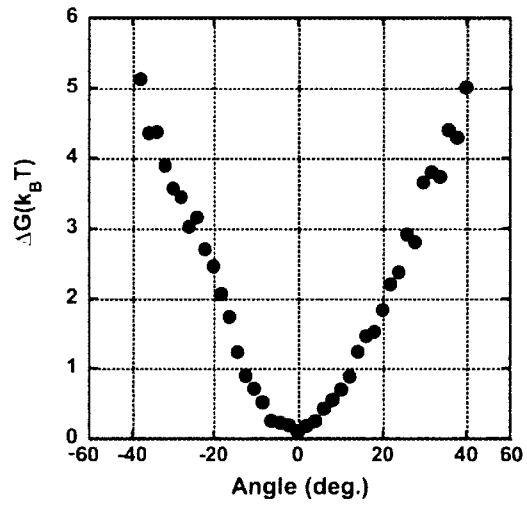

Fig. 4. The rotary potential of the ADP-inhibited form F_1. The probability density of the angle of the magnetic beads from the six molecules was transformed into potential according to the Boltzmann distribution law

activation in forward angles. Each fitting gave a saturation value of $\approx 100\%$, suggesting its irreversibility. To verify this idea, the following experiments were performed. The ADP-inhibited F_1 was stalled at $>60°$ for 6 s to activate it, and it was rotated back to 0° to stall for 6 s to inactivate it, should it occur, and then it was released from the magnetic tweezers. In most of the cases (93%), released F_1 showed its active rotation (data not shown). Thus, it was confirmed that F_1 is not reversibly inactivated again in this condition. Once F_1 is activated by stripping inhibitory ADP, the reinactivation would need either ADP binding from the solution or production of ADP in catalysis.

Activation Energy of Mechanical Activation. The rate constants of the mechanical activation, k_{act}, determined from Fig. 3 *b* and *c*, are plotted against stall angles (Fig. 3*d*). It was clearly shown that the rate increases exponentially with the angle. This finding means that the activation energy of the mechanical activation, G_a, given in the Arrehenius equation ($\ln k_{act} = \ln A - G_a/k_BT$), decreases with the angle. The activation energy change was given as $-1.3\ k_BT/10°$ from the slope in Fig. 3*d*. This finding strongly suggests that, upon the mechanical energy input through the γ-subunit, the energy state of the inhibitory ADP binding shifts to a higher state, so that the activation energy becomes relatively lower. To determine the amount of energy transferred to the F_1 by the magnetic tweezers, the work for pushing the F_1 in the ADP-inhibited form was estimated. The Brownian motion of the magnetic beads attached to the F_1 in the ADP-inhibited form was observed for >30 s without applying magnetic field, and the probability density of angle was determined to calculate the potential shape according to the Boltzmann distribution law (Fig. 4). The determined potential $>+20°$ had a linear slope, corresponding to the linear decrement of the activation energy of the mechanical activation. The energy increment of 1.5 k_BT per 10° coincides well with the activation energy decrement of 1.3 k_BT per 10°, suggesting that 85% of the mechanical energy input was transmitted to the catalytic site to weaken the binding energy of ADP. This finding is consistent with the tight coupling model between the catalytic reaction and the γ-rotation in the F_1 motor. The residual energy would remain stored as elastic energy for the other elements in our experimental system (for example, the γ-subunit itself, the $\alpha_3\beta_3$ ring, His tag, or streptavidin).

Angle Deviation Between the γ-Subunit and the Magnetic Beads. When the experimental system has highly flexible components such as the γ-subunit, the $\alpha_3\beta_3$ ring, His tags, or streptavidin, the rotary angle of the magnetic beads could deviate by a large amount from the γ-angle. Even though the angle deviation was not definitely determined in the present work, some of our experimental data suggested that the deviation is probably not so large. First, the mechanical activation was observed when the magnetic beads were rotated >20°, suggesting that the γ-subunit certainly rotates against the $\alpha_3\beta_3$ ring, which implies that the deviation is <20°. The rotary potential of the ADP-inhibited F_1 is also suggestive on this point. The determined potential comprises a loose spring-like potential within ±10° and linearly increasing potentials for over ±10°, which have slopes (= torque) of ≈35 pNnm for both sides. These values are consistent with the reported torque of ≈40 pNnm (16, 24, 28), implying that the potential >20° certainly reflects the interaction between the $\alpha_3\beta_3$ ring and the γ-subunit. Thus, the angle deviation would be at most 20°. One of the most likely candidates for elastic components is the γ-subunit, because its protruding part from the $\alpha_3\beta_3$ ring was twisted by 11° in the crystal structure of the mitochondrial F_1 modified by dicyclohexyl-carbodiimide (8, 9). Further studies on its elasticity remain to be done. It should be noted that the determined torque from the rotary potential is equal to the external torque by the magnetic tweezers because these two torque are equilibrated.

Backward Activation. Although the mechanical activation was not observed when the γ-subunit was pulled backward, up to −120°, preliminary experiments showed that the F_1 can be activated when pulled over by −160°. However, the results have been quite irregular so far. It is only certain that the activation probability was the highest in the presence of both ADP and P_i. A similar finding was reported by Vinogradov and colleagues (29, 30), that is, a submitochondrial particle containing the FoF_1-ATPase showed a higher ATP-hydrolysis activity after transient charging of the membrane potential. The most plausible explanation is that when F_1 is rotated in the ATP-synthetic direction in the presence of the ADP and P_i, the F_1 follows the ATP synthesis pathway to be efficiently activated.

Discussion

Mechanical Activation of Enzymes. The catalytically active F_1 spontaneously fails to dissociate ADP with some probability, and its rotation pauses at an angle after an 80° substep. This catalytically inactive state is called the ADP-inhibited form. In this study, we showed the mechanical activation of the F_1 motor in the ADP-inhibited form by pushing it with magnetic tweezers. When the ADP-inhibited F_1 was pushed $>+40°$ with the magnetic tweezers, the F_1 regained its catalytic activity to restart the rotation, whereas it was not readily activated when pulled back. This mechanical activation was completely suppressed by ADP, but not by ATP and/or P_i. These findings showed that the mechanical activation is triggered by the dissociation of the inhibitory ADP. Also, in biochemical experiments, ADP removal is necessary for the activation of the ADP-inhibited F_1, for example, using gel filtration. The model for the mechanical activation in the catalysis and rotation scheme is shown in Fig. 5*a*. The scheme starts from the ATP-waiting state, A, where the β-subunit with an empty catalytic site waits for the ATP to bind, and the two are bound with ATP and ADP, respectively. This state approximately corresponds to the crystal structure of MF_1 solved in 1994, except for P_i binding in the model. Upon ATP binding to the empty β, the F_1 makes an 80° substep, which triggers the following catalytic reactions on the other βs, ATP hydrolysis (B → C) and ADP and/or P_i release (C → A′). When ADP releases from the F_1, the γ-subunit rotates 40° to reset the F_1 in a new ATP-waiting state, A′. With some probability, the F_1 in the state C releases phosphate and isomerizes to the ADP-inhibited form, state D. This scheme accords with a recent biochemical study using a mutant F_1 with an inserted tryptophan residue near the phosphate binding region, which showed that F_1 releases phosphate and then slowly isomerizes to the ADP-inhibited

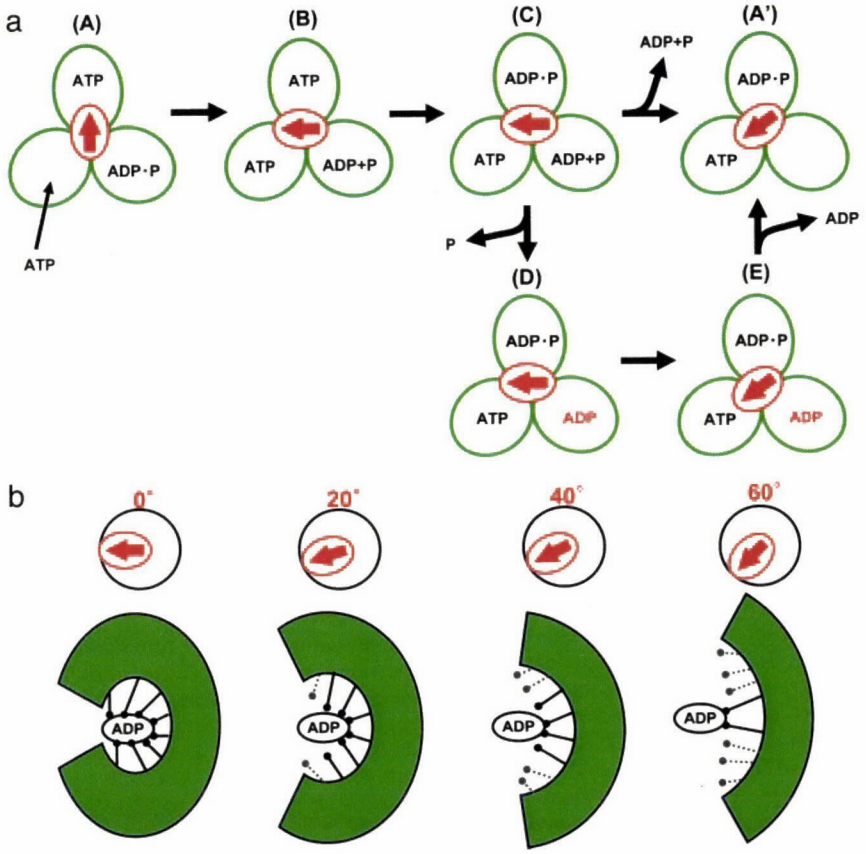

Fig. 5. The proposed model for conformational change around the catalytic site. (*a*) Reaction scheme in the catalysis and rotation model. Three green circles represent the catalytic state, and the red arrow indicates the angle of the γ-subunit. States D and E represent the ADP-inhibited form and forward-rotated form, respectively. (*b*) Schematic model of the conformational change around the catalytic site with the inhibitory ADP coupled with mechanical rotation. Upon forced rotation, the catalytic site progressively opens its conformation-breaking interactions with ADP.

form (31). Even though the biochemical experiments were conducted in an unisite condition where the number of catalytic sites occupied with a nucleotide was one at most, it is assumed that a similar isomerization occurs in F_1 that operates in a multisite catalysis mode (32, 33) (here, the trisite model is used). When the γ-subunit of the ADP-inhibited F_1 (D) is rotated >40° with the magnetic tweezers, the mechanical stress on the F_1 changes the conformation of the β-subunit carrying the inhibitory ADP, enforcing the F_1 to strip the inhibitory ADP molecule. After releasing it, the F_1 returns to a new ATP-waiting state, A′, on the catalytic active pathway. This scheme explains our experimental data well; however, it should be noted that this scheme is provisional because the angle at which the active F_1 releases ADP and P_i has not been conclusively identified yet. Additionally, the mostly same model can be proposed standing on bisite mode in which site occupancy alternates between one and two.

Angle Dependency of ADP Affinity. The most important result obtained in the present study is that the angle of the γ-subunit determines the rate constant of the ADP dissociation from the β-subunit. The time course of the mechanical activation gave the rate constant of the ADP dissociation that exponentially increases with angles of the γ-subunit in the forward direction. This finding explains well the directed rotation coupled with ADP release. Similar findings on the kinesin motor have been reported by Uemura and Ishiwata (34). They determined the ratio of the ADP-bound kinesin to the nucleotide-free from the measurement of the unbinding force of the kinesin–microtuble complex to reveal that the direction of the external force determines the affinity of kinesin with ADP. Thus, the modulation of the ADP affinity in response to the external force would be a common feature for molecular motors to give rise to unidirectional motion.

This finding is very suggestive for the ATP synthesis reaction model, in which we assume similar angle dependency of the ADP dissociation rate for active F_1. For ATP hydrolysis, the F_1 motor has to dissociate ADP in the solution, whereas it also has to efficiently bind ADP from the aqueous solution for ATP synthesis. If the ADP binding/dissociation would occur merely at a specific angle, the F_1 would not manage these two reactions. However, when active F_1 has a similar angle dependency of ADP affinity, F_1 would readily catch ADP from the solution when the F_o motor pulls F_1 back. Thus, the angle dependency of ADP release accords with a property needed for F_1 to operate its physiological function of ATP synthesis.

Spontaneous Activation. The angle dependency of the activation implies that the ADP remains difficult to strip off until the γ-subunit is moved. It was actually observed that when the F_1 was clamped at 0°, the angle for the ADP-inhibited state, ADP did not dissociate even after 300 s. In contrast, when the F_1 motor was allowed to make the rotary Brownian motion without an external force, the F_1 was spontaneously activated at the same rate as the mechanical activation at 20°. This finding means that when the thermal energy occasionally pushes the γ-subunit >20°, the inhibited F_1 dissociates ADP to regain its activity. In this sense, the spontaneous activation is also a mechanical activation caused by the thermal energy. It would be also interesting to examine ADP release in the unisite catalysis from the same view point. In the unisite catalysis, ADP release is known to be very slow, whereas the ATP hydrolysis step and the following phosphate release are fast (31, 35). The F_1 is also in a kind of ADP-inhibited form, although it has a sole bound

nucleotide. Therefore, similar mechanism could occur in the ADP release; F_1 waits for the thermal fluctuation to push forward to release the tightly bound ADP.

Structural Model of Mechanical Activation. As shown in Fig. 3*d*, the rate constant of the mechanical activation increased upon mechanical rotation of the γ-subunit, implying that the interaction between the bound ADP and the catalytic site on the β-subunit was weakened to accelerate ADP release. The analysis of the rate constants according to the Arrehenius equation suggested that the binding energy decreases in proportion to the rotary angle, by 1.3 k_BT per 10°. We discuss the structural features of the ADP-inhibited form and models to explain the mechanical activation below.

Structural studies on bovine mitochondrial F_1 (MF_1) by the Walker group (7–9) have revealed that the β-subunit can essentially use three types of conformation. The β-subunit with tightly bound ADP or ATP analog lifts the C-terminal domain up to the nucleotide binding domain enclosing the nucleotide in the crevice between the two domains. In contrast, the β-subunit without a nucleotide pulls down the C-terminal domain opening the catalytic site. Recently, an intermediate conformation was found, which weakly binds ADP in half-opened conformation. Thus, the F_1 closes the catalytic site upon ATP binding and opens its conformation after ADP release via the half-closed conformation. This conformational change is a typical induced-fit. The C-terminal domain has direct contact with the γ-subunit, thereby, this domain movement is thought to mechanically link the catalytic reactions and the γ-rotation. What are the structural features specific for the ADP-inhibited form? Considering that ADP binds tightly to the inhibited F_1, the ADP-inhibited β would be in the closed conformation (36). Further detailed structural features distinct from a catalytically active F_1 remain to be revealed. However, an interesting point is given by the recent crystal structures of MF_1 with dicyclohexyl carbodiimide (9) and complexes of ADP and beryllium fluoride (37). The catalytic site that corresponds to the ATP-binding site in other crystal structures does not bind ATP but does bind ADP. Because of the absence of the γ-phosphate, the side chain of the αR373, a catalytically crucial residue, is in a largely different conformation from other structures and forms a hydrogen bond to the 2′OH of the ribose of the ADP. Considering that isomerization to ADP inhibition occurs after phosphate release, it is possible that this structural rearrangement is a structural base of the ADP-inhibited form.

Kinetic analysis of the mechanical activation suggests that the mechanical forward rotation of the γ-subunit decreases the binding energy of ADP and the catalytic site. Therefore, we propose a simple structural model in which the mechanical forward rotation enforces the closed-β-subunit with the inhibited ADP to transform into the opened conformation, breaking the interactions between ADP and the catalytic site (Fig. 5*b*). When the interactions are unzipped sequentially with the forced rotation, it explains the linear drop of the ADP binding energy well. As an alternative model, a conformational rearrangement of a few amino acid residues, for example the αR373, which is decisive for the ADP inhibition, can be a trigger of mechanical activation. The analysis of the rotary Brownian motion showed that 85% of the energy given for forced rotation was transmitted to the catalytic site, supporting the tight mechanical linkage between the γ and the catalytic site. The structural model shown in Fig. 5*b* coincides well with progressive ATP-binding models proposed by Oster and Wang (38) and Cross (39) independently. These models explain well the efficient energy conversion and the reversibility of F_1-ATPase. In Oster and Wang's "binding-zipper" model, it is proposed that hydrogen bonds of ATP and the catalytic site are sequentially formed to drive the γ-rotation to explain the F_1's constant torque against the rotary angle (38, 40). In the near future, the angle dependency of the affinity of F_1 with ATP also will be elucidated by using this method.

Conclusion

The F_1 catalyzes ATP synthesis when the F_o enforces it to rotate in the reverse direction. It means that catalytic parameters of F_1 can be modulated by rotating the γ-subunit. In this work, we successfully activated the ADP-inhibited F_1 molecules by rotating the γ-subunit with magnetic tweezers. From the analysis of this phenomenon, it was revealed that F_1 decreases its affinity to the inhibitory ADP with the γ-rotation by using external energy with high efficiency. Theses properties of F_1 well explain its unidirectional nature of rotation and physiological function: synthesis of ATP. The molecular mechanism regarding the manner in which F_1 tunes elementary chemical steps (ATP binding, ATP hydrolysis/synthesis, and P_i release) in response to an external torque would be challenged by this method.

We thank Eiro Muneyuki for critically reading the manuscript; all members of the H.N. laboratory and former Core Research for Evolutional Science and Technology team 13 for discussion and experimental support; and Ryohei Yasuda for programming of image analysis. This work was supported in part by grants-in-aid from the Ministry of Education, Science, Sports, and Culture of Japan (to H.N., K.K., and M.Y.), the Toyota Physical and Chemical Research Institute (to H.N.), and the Bio-Oriented Technology Research Advancement Institution (to H.N.). Y.H.-H. is a Research Fellow of the Japan Society for the Promotion of Science.

1 Boyer, P. D. (1997) *Annu. Rev. Biochem.* **66,** 717–749
2 Yoshida, M., Muneyuki, E. & Hisabori, T. (2001) *Nat. Rev. Mol. Cell Biol.* **2,** 669–677
3 Kinosita, K., Jr., Yasuda, R. & Noji, H. (2000) *Essays Biochem.* **35,** 3–18
4 Senior, A. E., Nadanaciva, S. & Weber, J. (2002) *Biochim. Biophys. Acta* **1553,** 188–211
5 Itoh, H., Takahashi, A., Adachi, K., Noji, H., Yasuda, R., Yoshida, M. & Kinosita, K. (2004) *Nature* **427,** 465–468
6 Rondelez, Y., Tresset, G., Nakashima, T., Kato-Yamada, Y., Fujita, H., Takeuchi, S. & Noji, H. (2005) *Nature* **433,** 773–777
7 Abrahams, J. P., Leslie, A. G., Lutter, R. & Walker, J. E. (1994) *Nature* **370,** 621–628
8 Menz, R. I., Walker, J. E. & Leslie, A. G. (2001) *Cell* **106,** 331–341
9 Gibbons, C., Montgomery, M. G., Leslie, A. G. & Walker, J. E. (2000) *Nat. Struct. Biol.* **7,** 1055–1061
10 Ariga, T., Masaike, T., Noji, H. & Yoshida, M. (2002) *J. Biol. Chem.* **277,** 24870–24874
11 Nishizaka, T., Oiwa, K., Noji, H., Kimura, S., Muneyuki, E., Yoshida, M. & Kinosita, K., Jr. (2004) *Nat. Struct. Mol. Biol.* **11,** 142–148
12 Boyer, P. D. (1993) *Biochim. Biophys. Acta* **1140,** 215–250
13 Duncan, T. M., Bulygin, V. V., Zhou, Y., Hutcheon, M. L. & Cross, R. L. (1995) *Proc. Natl. Acad. Sci. USA* **92,** 10964–10968
14 Sabbert, D., Engelbrecht, S. & Junge, W. (1996) *Nature* **381,** 623–625
15 Noji, H., Yasuda, R., Yoshida, M. & Kinosita, K., Jr. (1997) *Nature* **386,** 299–302
16 Yasuda, R., Noji, H., Kinosita, K., Jr. & Yoshida, M. (1998) *Cell* **93,** 1117–1124
17 Yasuda, R., Noji, H., Yoshida, M., Kinosita, K., Jr. & Itoh, H. (2001) *Nature* **410,** 898–904
18 Shimabukuro, K., Yasuda, R., Muneyuki, E., Hara, K. Y., Kinosita, K., Jr. & Yoshida, M. (2003) *Proc. Natl. Acad. Sci. USA* **100,** 14731–14736
19 Hirono-Hara, Y., Noji, H., Nishiura, M., Muneyuki, E., Hara, K. Y., Yasuda, R., Kinosita, K., Jr. & Yoshida, M. (2001) *Proc. Natl. Acad. Sci. USA* **98,** 13649–13654
20 Jault, J. M., Matsui, T., Jault, F. M., Kaibara, C., Muneyuki, E., Yoshida, M., Kagawa, Y. & Allison, W. S. (1995) *Biochemistry* **34,** 16412–16418
21 Matsui, T., Muneyuki, E., Honda, M., Allison, W. S., Dou, C. & Yoshida, M. (1997) *J. Biol. Chem.* **272,** 8215–8221
22 Lu, H. P., Xun, L. & Xie, X. S. (1998) *Science* **282,** 1877–1882
23 Forde, N. R., Izhaky, D., Woodcock, G. R., Wuite, G. J. & Bustamante, C. (2002) *Proc. Natl. Acad. Sci. USA* **99,** 11682–11687
24 Noji, H., Bald, D., Yasuda, R., Itoh, H., Yoshida, M. & Kinosita, K., Jr. (2001) *J. Biol. Chem.* **276,** 25480–25486
25 Vasilyeva, E. A., Minkov, I. B., Fitin, A. F. & Vinogradov, A. D. (1982) *Biochem. J.* **202,** 9–14
26 Weber, J., Wilke-Mounts, S., Lee, R. S., Grell, E. & Senior, A. E. (1993) *J. Biol. Chem.* **268,** 20126–20133
27 Dou, C., Fortes, P. A. & Allison, W. S. (1998) *Biochemistry* **37,** 16757–16764
28 Noji, H., Hasler, K., Junge, W., Kinosita, K., Jr., Yoshida, M. & Engelbrecht, S. (1999) *Biochem. Biophys. Res. Commun.* **260,** 597–599
29 Galkin, M. A. & Vinogradov, A. D. (1999) *FEBS Lett.* **448,** 123–126
30 Zharova, T. V. & Vinogradov, A. D. (2004) *J. Biol. Chem.* **279,** 12319–12324
31 Masaike, T., Muneyuki, E., Noji, H., Kinosita, K., Jr. & Yoshida, M. (2002) *J. Biol. Chem.* **277,** 21643–21649
32 Muneyuki, E., Makino, M., Kamata, H., Kagawa, Y., Yoshida, M. & Hirata, H. (1993) *Biochim. Biophys. Acta* **1144,** 62–68
33 Masaike, T., Mitome, N., Noji, H., Muneyuki, E., Yasuda, R., Kinosita, K. & Yoshida, M. (2000) *J. Exp. Biol.* **203,** 1–8
34 Uemura, S. & Ishiwata, S. (2003) *Nat. Struct. Biol.* **10,** 308–311
35 Grubmeyer, C., Cross, R. L. & Penefsky, H. S. (1982) *J. Biol. Chem.* **257,** 12092–12100
36 Tsunoda, S. P., Muneyuki, E., Amano, T., Yoshida, M. & Noji, H. (1999) *J. Biol. Chem.* **274,** 5701–5706
37 Kagawa, R., Montgomery, M. G., Braig, K., Leslie, A. G. & Walker, J. E. (2004) *EMBO J.* **23,** 2734–2744
38 Oster, G. & Wang, H. (2000) *Biochim. Biophys. Acta* **1458,** 482–510
39 Cross, R. L. (2000) *Biochim. Biophys. Acta* **1458,** 270–275
40 Antes, T., Chandler, D., Wang, H. & Oster, G. (2003) *Biophys. J.* **85,** 695–706

The Journal of Experimental Biology 203, 1–8 (2000)
Printed in Great Britain © The Company of Biologists Limited 2000
JEB2353

ROTATION OF F_1-ATPase AND THE HINGE RESIDUES OF THE β SUBUNIT

TOMOKO MASAIKE[1], NORIYO MITOME[1], HIROYUKI NOJI[2], EIRO MUNEYUKI[1], RYOHEI YASUDA[2], KAZUHIKO KINOSITA JR[2,3] AND MASASUKE YOSHIDA[1,2,*]

[1]*The Research Laboratory of Resources Utilization, Tokyo Institute of Technology, 4259 Nagatsuta, Yokohama 226-8503, Japan,* [2]*CREST (Core Research for Evolutional Science and Technology) 'Genetic Programming' Team 13, Teikyo University Biotechnology Research Center 3F Nogawa 907, Miyamae-ku, Kawasaki 216-0001, Japan* and [3]*Department of Physics, Faculty of Science and Technology, Keio University, Yokohama 223-8522, Japan*

*Author for correspondence (e-mail: myoshida@res.titech.ac.jp)

Accepted 20 October; published on WWW 13 December 1999

Summary

Rotation of a motor protein, F_1-ATPase, was demonstrated using a unique single-molecule observation system. This paper reviews what has been clarified by this system and then focuses on the role of residues at the hinge region of the β subunit. We have visualised rotation of a single molecule of F_1-ATPase by attaching a fluorescent actin filament to the top of the γ subunit in the immobilised F_1-ATPase, thus settling a major controversy regarding the rotary catalysis. The rotation of the γ subunit was exclusively in one direction, as could be predicted by the crystal structure of bovine heart F_1-ATPase. Rotation at low ATP concentrations revealed that one revolution consists of three 120° steps, each fuelled by the binding of an ATP to the β subunit. The mean work done by a 120° step was approximately 80 pN nm, a value close to the free energy liberated by hydrolysis of one ATP molecule, implying nearly 100 % efficiency of energy conversion. The torque is probably generated by the β subunit, which undergoes large opening–closing domain motion upon binding of AT(D)P. We identified three hinge residues, βHis179, βGly180 and βGly181, whose peptide bond dihedral angles are drastically changed during domain motion. Simultaneous substitution of these residues with alanine resulted in nearly complete loss (99 %) of ATPase activity. Single or double substitution of the two Gly residues did not abolish the ATPase activity. However, reflecting the shift of the equilibrium between the open and closed forms of the β subunit, single substitution caused changes in the propensity to generate the kinetically trapped Mg-ADP inhibited form: Gly180Ala enhanced the propensity and Gly181Ala abolished the propensity. In spite of these changes, the mean rotational torque was not changed significantly for any of the mutants.

Key words: F_1-ATPase, F_1F_o-ATP synthase, motor protein, rotation, single-molecule observation.

Introduction

F_1F_o-ATP synthase, the enzyme responsible for most of the ATP synthesis in the biological world, couples H^+ translocation across membranes to synthesis/hydrolysis of ATP. It reversibly dissociates into a membrane part, F_o, a proton channel in itself, and a water-soluble part, F_1, an ATPase that is hence often called F_1-ATPase. The subunit composition of F_1 is $\alpha_3\beta_3\gamma\delta\varepsilon$; the $\alpha_3\beta_3\gamma$ complex is the catalytic core that retains the major kinetic features of F_1-ATPase.

More than 10 years before the structure of F_1-ATPase was determined, Boyer proposed the binding change mechanism in which three conformations of the β subunit with different affinities for adenine nucleotide were assumed (Boyer and Kohlbrenner, 1981; Boyer, 1993). The input of energy changes the affinity of binding sites by cooperative conformational changes. The molecular model that best explained the binding change mechanism was the physical rotation of the γ subunit relative to a ring consisting of the $\alpha_3\beta_3$ part. The crystal structure of bovine heart mitochondrial F_1 (Abrahams et al., 1994) indeed showed that the β subunits are in three different states, as predicted by the binding change mechanism: the AMP–PNP bound form (β_{TP}), the ADP bound form (β_{DP}) and the empty form (β_E). Elaborate experiments by two groups indicated that the γ subunit rotates during catalysis (Duncan et al., 1995; Sabbert et al., 1996). However, other movements such as simple conformational changes could also explain the observations, and exclusive evidence for the rotation was sought. A decisive answer was provided by visualising the rotation through single-molecule imaging.

Observation of rotation

A novel system to detect rotation

We have established a novel system to detect rotation of a single F_1-ATPase molecule (Noji et al., 1997). A fluorescent actin filament was attached to the γ subunit of $\alpha_3\beta_3\gamma$ complex

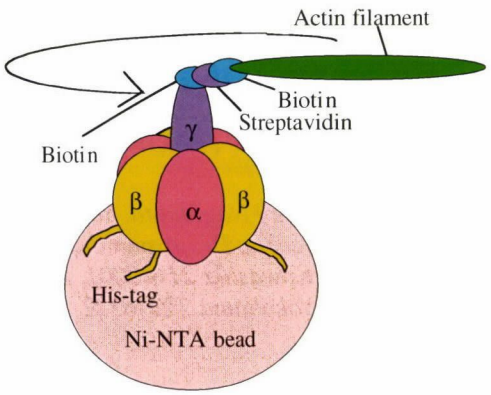

Fig. 1. The system used to observe the rotation of the γ subunit. For this assay system, mutations were introduced into the $\alpha_3\beta_3\gamma$ complex. A new cysteine was introduced into the γ subunit, to which biotin, streptavidin and biotinylated actin were attached in order. A sequence of 10 histidines at the N terminus of the β subunit (His-tag) immobilised the $\alpha_3\beta_3$ cylinder on a Ni^{2+}-nitrilotriacetic acid (Ni-NTA)-coated polystyrene bead.

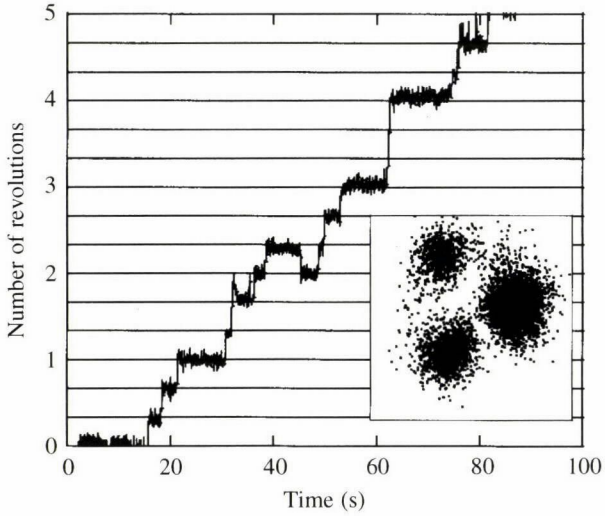

Fig. 2. Stepwise rotation at 20 nmol l^{-1} ATP. The inset shows a trace of the centroid of the actin image. Actin length = 1.1 μm.

from thermophilic *Bacillus* PS3, and the $\alpha_3\beta_3$ part was immobilised on a Ni^{2+}-nitrilotriacetic acid (Ni-NTA)-coated polystyrene bead (Fig. 1). Rotation of the actin filament in an anticlockwise direction was observed under a fluorescent microscope. The rotation was ATP-dependent and azide-sensitive (Noji et al., 1997). An actin filament that was attached to the ε subunit of $\alpha_3\beta_3\gamma\varepsilon$ rotated in the same direction, and the ε subunit therefore also constitutes part of the rotor apparatus in F_1-ATPase (Kato-Yamada et al., 1998).

Rotational steps at low ATP concentration

At ATP concentrations below 600 nmol l^{-1}, the γ subunit rotated in steps of 120°, pausing at three dwell positions (Fig. 2) (Yasuda et al., 1998). Taking into account the pseudo-threefold symmetry of $\alpha_3\beta_3\gamma$ structure and that the binding of ATP to a catalytic site is the rate-limiting step under this condition, binding of ATP to an empty β subunit seems to initiate the stepping motion, and the work done during a step is fuelled by one ATP molecule. The plot of dwell time *versus* number of events was consistently exponential and was explained better by a one-ATP-per-step model than by a two-ATPs-per-step model (Yasuda et al., 1998). Thus, consumption of three ATP molecules for one rotation was confirmed. The possibility of smaller substeps is not excluded because of the limit of time resolution of our current system.

Torque and thermodynamic efficiency

Attachment of an actin filament to the γ subunit enabled not only visualisation of the rotation but also estimation of the torque generated by the rotation. Fig. 3 shows the dependence of the rotational speed of actin filaments on the length of the filaments. The mean torque was approximately 40 pN nm (4×10^{-20} J) irrespective of the load or the actin length, under conditions in which the free energy of hydrolysis of one ATP molecule (ΔG) was 90 or 110 pN nm. The work done by a one-third rotation was approximately 84 pN nm (40 pN nm × $2\pi/3$), indicating that the thermodynamic efficiency of conversion of the chemical energy of ATP hydrolysis to the kinetic energy of rotation is

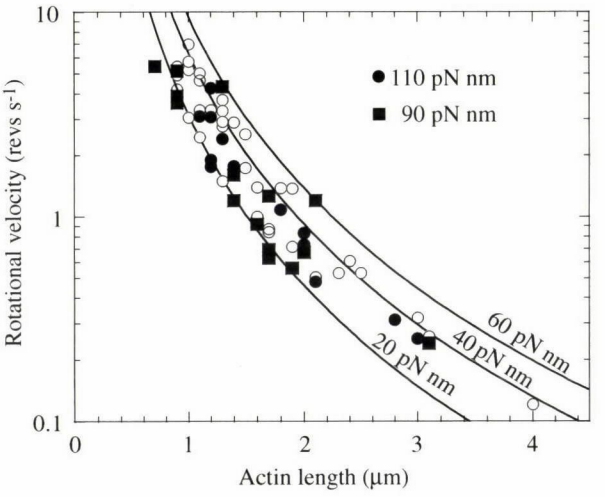

Fig. 3. Load-dependence of the rotational rate of the wild-type $\alpha_3\beta_3\gamma$ complex at ΔG=90 or 110 pN nm. ΔG is defined as (standard free energy change of ATP hydrolysis)+$\boldsymbol{RT}\log_e$[ADP][P_i]/[ATP], where $\boldsymbol{R}$ is the gas constant and T is absolute temperature. Open circles, measurements at [ATP]=2 mmol l^{-1} (because of the ATP-regenerating system, ΔG cannot be defined). Filled circles, measurements at [ATP]=2 mmol l^{-1}, [ADP]=10 μmol l^{-1} and [P_i]=0.1 mmol l^{-1} (ΔG= 110 pN nm). Filled squares, measurements at [ATP]=2 mmol l^{-1}, [ADP]=10 μmol l^{-1} and [P_i]=10 mmol l^{-1} (ΔG=90 pN nm). The mean work done by a one-third rotation is 80 pN nm, which gives approximately 100% efficiency of energy conversion. Theoretical lines give torque values of 40 pN nm, 20 pN nm and 60 pN nm. 1 pN nm=10^{-21} J.

nearly 100 %. This value contrasts with the reported values of efficiency of myosin/actin (20 %) (Ishijima et al., 1995) and kinesin/microtubule (50 %) (Svoboda et al., 1993). It is interesting to consider how the γ subunit would behave if ΔG were ≤80 pN nm. One possibility is that the rotation would slow down, keeping approximately 100 % efficiency. Another possibility is that the rotational speed would not slow down, but that the enzyme would frequently fail in rotation even though ATP was hydrolysed, resulting in the overall consumption of two or more ATP molecules per step. To test which is the case is a challenge.

The hinge loop

The hinge for domain motion

Once rotation of the γ subunit had been established, the next problem was the mechanism of rotation. It is most likely that shifting the C-terminal domain of the β subunit towards the γ subunit triggers rotation of the γ subunit. For this kind of domain motion to occur, there should be a segment corresponding to a hinge connecting the two domains. For example, the crystal structures of myosin indicated that Gly457 and Ile455 (*Dictyostelium* myosin II) of the 'switch II' region constitute a hinge, and mutations of Gly457 caused the loss of both ATPase and motor activity (Fisher et al., 1995a,b; Smith and Rayment, 1996; Sasaki et al., 1998). Gly709 and Gly720 at the each end of the helix SH1 (chicken vertebrate smooth muscle myosin) are also identified as hinge residues. In the case of G-proteins, crystallisation and mutational analyses have revealed that Gly199 of the α subunit of bovine transducin is the hinge residue, and mutation of the residue resulted in the loss of the ability to activate the effector (Lee et al., 1992; Noel et al., 1993; Lambright et al., 1996). Thus, to describe the sequence of conformational changes of the β subunit of F_1-ATPase, it is important to identify and characterise a hinge.

The hinge of the β subunit

To identify hinge residues in the β subunit, we compared the main-chain dihedral angles, φ and ψ (formed by four main-chain atoms starting from the carbonyl carbon of the previous residue and the amide nitrogen of the residue in question, respectively), of each residue in β_{DP} and β_E (refer to Introduction) of the crystal structure of bovine mitochondrial F_1 (Abrahams et al., 1994). Only five residues, Val162, Gly163, His179, Gly180 and Gly181 (numbering of *Bacillus* PS3), change either φ or ψ by more than 100° when the structure of β_{DP} is superimposed onto that of β_E. Val162 and Gly163 are residues in the Walker A motif, which is found at nucleotide binding sites in a variety of proteins, and are components of the P-loop (GGAG*V*GKT). The P-loop changes its conformation in response to nucleotide binding and hydrolysis, but this change is not a hinge-like motion. In contrast, Gly180 and Gly181 are located in the loop connecting helix B and strand β_4 (Fig. 4) (Abrahams et al., 1994). In β_{TP} and β_{DP}, His179 is also a component of the loop, but it is

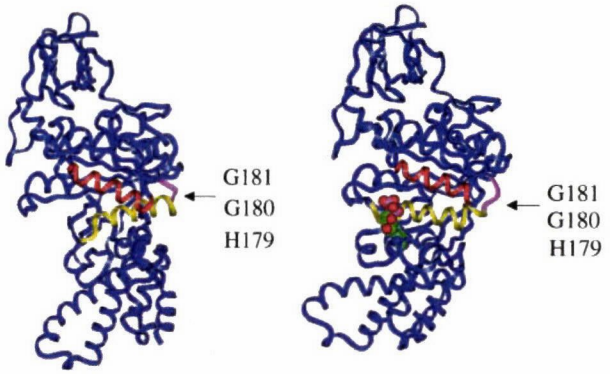

Fig. 4. Putative hinge loop of the β subunit in the empty form and the ADP form. The putative hinge loop is in pink, the Walker A sequence and helix B are in yellow, and helix C is in red. Taken from Abrahams et al. (1994) with permission.

involved in helix B in β_E. Helix B is preceded by the P-loop, and the strand β_4 is part of the 'wall' of parallel β sheet that surrounds the P-loop and helix B. The catalytic glutamic acid exists at the end of strand β_4 that is followed by helix C. As a whole, the catalytic site of the β subunit consists mostly the P-loop, helix B, strand β_4, helix C and the wall of β sheet (Figs 4, 5) (Abrahams et al., 1994). When a nucleotide binds to the catalytic site, the N-terminal region of helix B is pulled up (Fig. 5), and this motion probably triggers swinging of the whole C-terminal helical domain. These three residues (βHis179, βGly180 and βGly181) appear to allow the C-terminal domain to swing by changing their dihedral angles drastically. A large movement of His179 was already indicated by the report that the ^1H nuclear magnetic resonance peak of His179 of the free β subunit shifted downfield with increasing concentration of Mg-AMP-PNP (Tozawa et al., 1995). We replaced these residues with alanine and studied the characteristics of mutant $\alpha_3\beta_3\gamma$ complexes containing His179Ala, Gly180Ala and Gly181Ala.

Mg-ADP inhibited form

A brief scheme of ATP hydrolysis catalysed by F_1-ATPase is shown in Fig. 6. It has been known that, when the product ADP is held in a stable manner at a catalytic site in the β subunit during ATP hydrolysis, the F_1 molecule becomes inactive. This inactive form is called the Mg-ADP inhibited form (Jault et al., 1995; Matsui et al., 1997). When the ATPase reaction is started by addition of ATP, the $\alpha_3\beta_3\gamma$ complex gets trapped in the Mg-ADP inhibited form in some probability and accumulates as turnover of the catalysis repeats, and the initial rate of ATP hydrolysis (initial ATPase activity) decreases towards an equilibrium rate (steady-state ATPase activity). The transition from initial activity to steady-state activity can be simulated by exponential fitting; the half-time of the transition for the wild-type $\alpha_3\beta_3\gamma$ complex was approximately 19 s under the conditions tested. The ratio of steady-state to initial

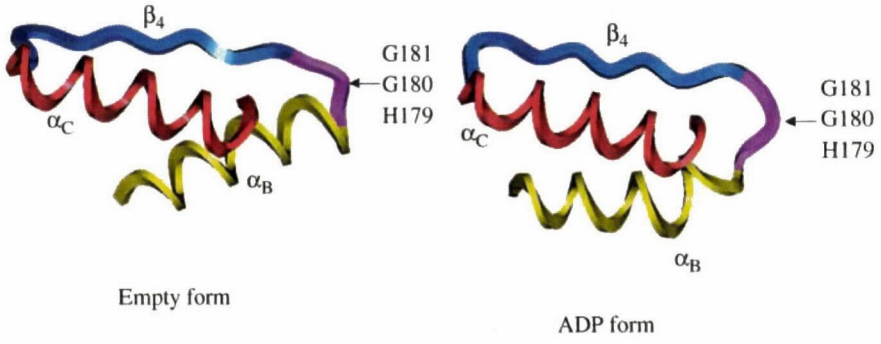

Fig. 5. Putative hinge loop and its motion. α_B, α helix B (yellow); α_C, α helix C (red); β_4, β sheet 4 (light blue); the hinge loop is in pink. The nomenclature is taken from the crystal structure (see Abrahams et al., 1994).

activities was approximately 0.4. Because the precursor of the Mg-ADP inhibited form is thought to be an intermediate of the catalytic cycle, F_1·ADP, these values reflect the relative population of F_1·ADP form during catalytic turnover.

ATPase activities of the mutants

Initial and steady-state ATPase activities of the mutants are shown in Fig. 7. In the case of the $\alpha_3\beta_3\gamma$ complex containing His179Ala, the initial ATPase activity did not change much, but the ratio of steady-state to initial activities decreased to 0.16. The half-time of the initial-to-steady-state transition was approximately 3.1 s. Thus, the propensity to fall into the Mg-ADP inhibited form increased. Interpretation of these changes is not easy because His179 becomes a part of helix B in the transition from β_{DP} (or β_{TP}) to β_E, as described above, and the replacement of His by Ala includes the loss of a hydrogen-bonding site for side chains of other residues. Therefore, His179Ala is not discussed in the next section. For the Gly180Ala mutant, the initial ATPase activity decreased to half that of the wild-type complex, but the decrease in the steady-state activity was more pronounced, to 7 % of the wild-type value. The ratio of steady-state to initial activities was approximately 0.05, and the half-time of the initial-to-steady-state transition was approximately 3.4 s. In contrast, the $\alpha_3\beta_3\gamma$ complex containing Gly181Ala showed only very little time-dependent transition of activity; the initial ATPase activity was not reduced, and no initial-to-steady-state transition was observed. Therefore, the Gly180Ala mutant demonstrates an enhanced propensity to fall into the Mg-ADP inhibited form, whereas the Gly181A mutant becomes resistant to Mg-ADP inhibition.

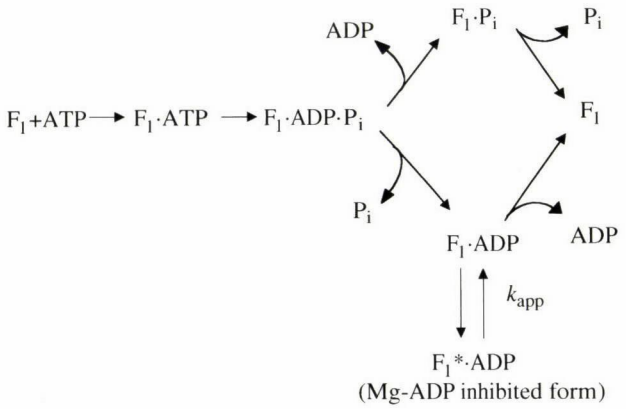

Fig. 6. A scheme of ATP hydrolysis catalysed by F_1-ATPase. P_i, inorganic phosphate; k_{app}, apparent rate of inactivation.

Changed stability of the closed form of the mutants

These observations regarding Gly180Ala and Gly181Ala can be explained by postulating a change in the stability of the closed form of the mutants (Fig. 8). At a saturating ATP concentration, the transition from open form 2 with an empty catalytic site to open form 1 with a bound ATP is very fast. In the case of Gly180Ala, the rapid initial-to-steady-state transition can be caused by the increased population of F_1·ADP, which results from stabilisation of the closed form. The stabilisation of the closed form leads to an increased activation energy for the transition from the closed form to

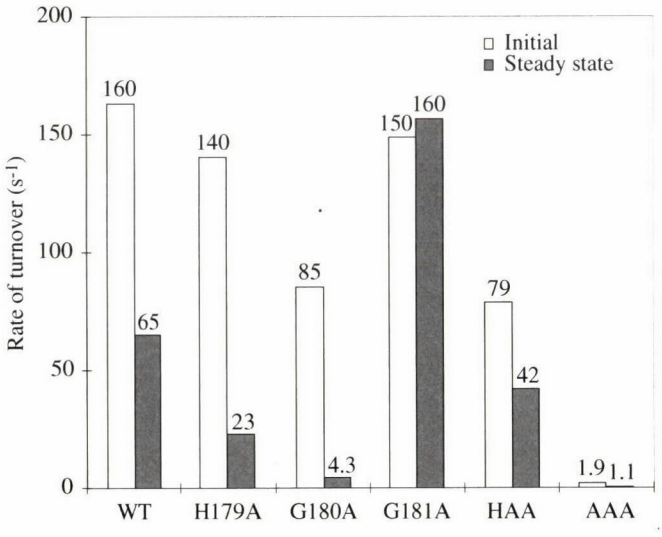

Fig. 7. ATPase activities of the mutants. ATPase activity was measured in Mops buffer: 10 mmol l^{-1} Mops-KOH (pH 7.0), 50 mmol l^{-1} KCl, 2 mmol l^{-1} $MgCl_2$ and 2 mmol l^{-1} ATP-Mg in an ATP-regenerating system. WT, wild type; H179A, $\alpha_3\beta$(His179Ala)$_3\gamma$; G180A, $\alpha_3\beta$(Gly180Ala)$_3\gamma$; G181A, $\alpha_3\beta$(Gly181Ala)$_3\gamma$; HAA, $\alpha_3\beta$(Gly180Ala/Gly181Ala)$_3\gamma$; AAA, $\alpha_3\beta$(His179Ala/Gly180Ala/Gly181Ala)$_3\gamma$.

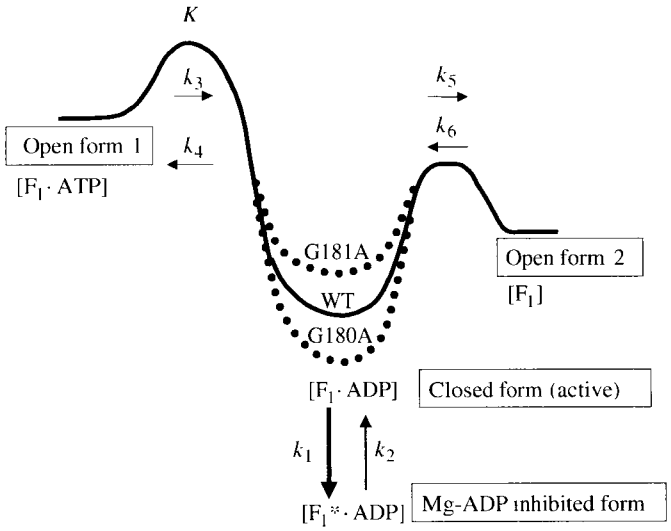

Fig. 8. A simple model to account for the observed changes in ATPase activity of the Gly mutants. We assume that F_1 and F_1 ATP are in the open form and that F_1 ADP and F_1* ADP are in the closed form. In addition, we also assume that the changes in the stability of F_1 ADP caused the observed changes in the Gly mutants (shown schematically). As the onset of Mg-ADP inhibition is relatively slow compared with ATPase turnover, it can be assumed that F_1, F_1 ATP and F_1 ADP are in rapid equilibrium. At a saturating ATP concentration and in the presence of an ATP-regenerating system, the amount of F_1 and the value of k_6 are negligible. Then, the apparent rate of inactivation due to inhibition by Mg-ADP (k_{app}) is expressed as $k_{app}=[k_1/(1+K)]+k_2$, where $K=[F_1 ATP]/[F_1 ADP]$, which is determined by the balance between k_3, k_4, k_5 and k_6. The change in the relative stability of the open and closed forms directly affects K, k_5 and k_4 and hence the apparent rate of inactivation k_{app} and the initial ATPase activity (V_{max}). In the case of Gly180Ala, stabilisation of the closed form increases [F_1 ADP], which results in a decrease in the value of K and an increase in the value of k_{app}. V_{max} is mainly determined by k_5 for this mutation, whereas it is determined mainly by k_3 in the wild type. In the case of Gly181Ala, destabilisation of the closed form decreases [F_1·ADP], which results in a decrease in k_{app} The rate-limiting step for Gly181Ala is k_3, as for the wild type. The work done by the Gly180Ala and Gly181Ala mutants differs by less than 10% from that of the wild type concerning free energy change.

open form 2, which may result in the decreased initial ATPase activity of this mutant. In contrast, the closed form of the Gly181Ala mutant appears to be less stable, and [F_1·ADP] may be lower than that in the wild-type complex. As a consequence, little or no Mg-ADP inhibited form is produced during catalysis, and the apparent rate of inactivation (k_{app}) decreases. The rate-limiting step in the catalytic cycle of this mutant may be the transition from open form 1 to the closed form, and the transition energy for this mutant is the same as that for the wild type, so that the initial ATPase activity is unchanged.

Ramachandran map of the hinge residues

The stability changes in the closed form of the mutant complexes can be partly attributed to the steric stability of the mutated residues. The change in steric stability caused by the mutations discussed above was estimated in a Ramachandran map. The map was calculated for Gly-Gly, Ala-Gly and Gly-Ala peptides with various ϕ–ψ combinations (Fig. 9). The ϕ–ψ combination of Gly180 observed in the crystal structure of β_E is plotted in the area close to 'outer limit' of the energetically allowed region (Fig. 9A). Mutation of Gly180 to alanine seems to further destabilise this ϕ–ψ combination (Fig. 9B). Consequently, the open form (empty form) becomes less stable in this mutation, and [F_1·ADP] increases. More Mg-ADP inhibited form is then generated. The situation is the reverse for the Gly181Ala mutant; the Ramachandran plot shows that Gly181 in the closed form (ADP form) takes the ϕ–ψ combination that is only allowed for glycine residue and that, when Gly181 is replaced by alanine, this ϕ–ψ combination becomes impossible (Fig. 9C,D). Thus, the Gly181Ala mutation destabilises the closed form (ADP form), the population of the closed form [F_1·ADP] decreases, and the mutant complex becomes resistant to Mg-ADP inhibition (see legend to Fig. 8).

Double and triple mutants

The two single alanine mutations had opposite effects on the stability of the closed form. To investigate these effects in one molecule, the ATPase activity of a double Ala mutant (Gly180Ala/Gly181Ala, termed the HAA mutant) was measured (Fig. 7). This mutation resulted in approximately the same initial ATPase activity as that of the single alanine mutant Gly180Ala, but the steady-state ATPase activity was 65% of that of the wild type, contrasting with that of the single Gly180Ala mutant (7%). For this double mutant, there was an additional intermediate phase in the time course of ATPase activity besides the initial and steady-state phases. Therefore, resistance to Mg-ADP inhibition could not be defined by half-time of the initial-to-steady-state transition. However, the steady-state ATPase activity indicated that resistance to Mg-ADP inhibition was regained when the second mutation βGly181Ala was introduced to the βGly180Ala mutant. It is likely that destabilisation and stabilisation of F_1·ADP occurred simultaneously, and the effects of both mutations seemed to be cancelled.

When we replaced all His-Gly-Gly residues with alanines (termed the AAA mutant), both initial and steady-state ATPase activity decreased drastically, to approximately 1% of those of the wild type (because of limits to the detection of the fast transition from initial state to steady state, the initial ATPase activity may include an error; Yasuda et al., 1998). In addition, the AAA mutant had a much faster apparent rate of inactivation than that of the wild type and even of the Gly180Ala mutant (data not shown). From these results, we can assume that stabilisation of the closed form was considerably enhanced, further impairing the opening–closing motion of the β subunit. Taken together, these results strongly indicate that the His-Gly-Gly loop contributes to the opening–closing motion of the β subunit.

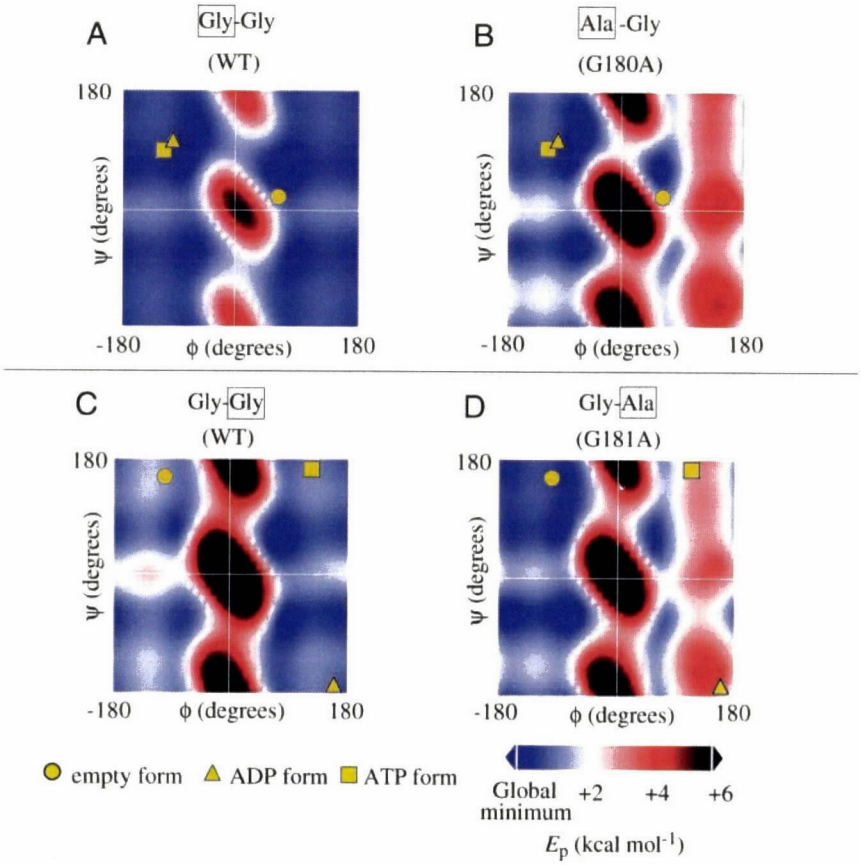

Fig. 9. Pairs of main-chain dihedral angles ϕ and ψ plotted on the Ramachandran map of the potential energy (E_p). Ramachandran maps were calculated using Discover3 (Molecular Simulations, USA) using the AMBER force field with the dielectric value of water. Each dipeptide is capped with an acetyl group and an $NHCH_3$ group. WT, wild type; G180A, $\alpha_3\beta$(Gly180Ala)$_3\gamma$; G181A, $\alpha_3\beta$(Gly181Ala)$_3\gamma$. The dihedral angles ϕ and ψ in each map indicate those of the boxed residue. Circles, empty form; triangles, ADP form; squares, ATP form.

Rotation of the hinge mutants

Rotation of these mutants was observed. As described in the previous section, the relative stability of the closed and open forms is changed by mutations at the hinge loop. Because we assume that the rotational work exerted by the hinge mutants corresponds to the potential difference between open form 1 and the closed form (Fig. 8), a change in the potential difference could lead to a change in the rotational torque. However, the γ subunit, for all the single alanine mutants, rotated with the same mean torque as that of the wild-type, irrespective of the actin length (Fig. 10). This is probably because the change in [F_1·ADP] affects the initial-to-steady-state transition rate in a more pronounced manner than it does the free energy of rotation. For example, a 10-fold increase in [F_1·ADP] will result in a 10-fold increase in the initial-to-steady-state transition rate, while it will cause only a 10 % increase in the potential difference (the work). In this case, torque should change by 10 %, a value far smaller than the experimental error range of the present rotary assay system.

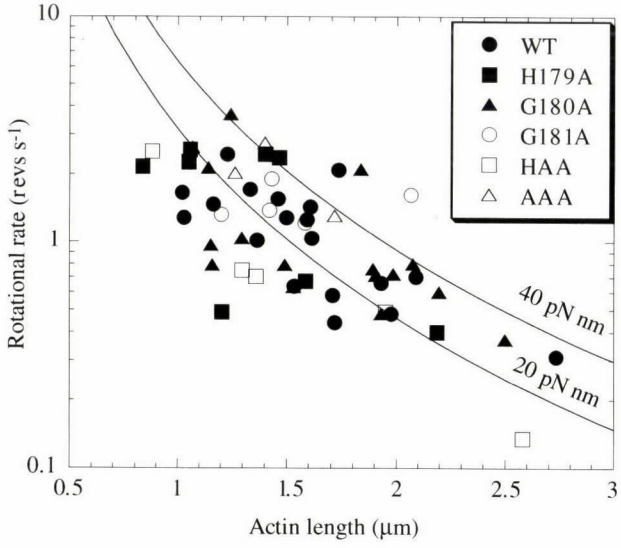

Fig. 10. Load-dependence of the rotational rate of the hinge mutants. The rotary assay was performed either in Mops buffer (10 mmol l^{-1} Mops-KOH, pH 7.0, 50 mmol l^{-1} KCl, 2 mmol l^{-1} $MgCl_2$ and 2 mmol l^{-1} Mg-ATP) or in potassium phosphate buffer (100 mmol l^{-1} potassium phosphate, 2 mmol l^{-1} $MgCl_2$, pH 7.0) using an ATP-regenerating system. According to the rotary assay of the wild type, the torque is not affected by the difference between these two buffers (H. Noji, unpublished data). Mutation of the hinge loop did not affect the rotational torque. WT, wild type; H179A, $\alpha_3\beta$(His179Ala)$_3\gamma$; G180A, $\alpha_3\beta$(Gly180Ala)$_3\gamma$; G181A, $\alpha_3\beta$(Gly181Ala)$_3\gamma$; HAA, $\alpha_3\beta$(Gly180Ala/Gly181Ala)$_3\gamma$; AAA, $\alpha_3\beta$(His179Ala/Gly180Ala/Gly181Ala)$_3\gamma$.

Perspectives

Our experimental system using an actin filament has enabled us to perform a direct 'seeing is believing' experiment. However, it is still to be improved. The population of actively rotating actin filaments is only a few per cent of the total filaments. This may be due to interference by other neighbouring F_1 molecules, to surface obstruction or to denaturation of F_1 molecules by immobilisation. Therefore, without extensive statistical analysis, it is difficult to distinguish pauses and stops that arise as natural characteristics of this enzyme from those originating from the experimental manipulations.

A simultaneous observation of rotation and ATP hydrolysis by a single molecule has not yet been successfully achieved. Therefore, we are obliged to estimate the rate of ATP consumption during rotation from measurements using unimmobilised F_1 molecules in a solution without load. At low ATP concentrations, because the rate-limiting step of the reaction is ATP binding, hydrolysis of one ATP molecule measured in a bulk solution roughly corresponds to one-third of a rotation of the filaments (Yasuda et al., 1998). However, at high ATP concentrations, the frictional load of filament rotation limits the speed of rotation, and the rate of ATP hydrolysis is probably suppressed accordingly. Measurement of the ATPase activity of a single F_1 molecule or observation of the rotation of the unloaded γ subunit is necessary to relate the timing of rotation directly to that of ATP hydrolysis. Experimental methods to measure both these in the same system are awaited.

Single-molecule experiments using F_1F_o-ATP synthase must be performed to extend our understanding of its function as a holoenzyme. The ATP synthesis reaction catalysed by F_1F_o-ATP synthase may not be merely the reverse of ATP hydrolysis by F_1-ATPase. In the process of ATP synthesis, the source of energy for rotation is not the chemical energy of ATP hydrolysis, but H^+ flow through F_o. In addition, the generation of the Mg-ADP inhibited form appears to be absent during ATP synthesis (Bald et al., 1998). Therefore, the rotation of the γ subunit during ATP synthesis needs to be confirmed. Moreover, classification of F_o subunits into rotors and stators using the rotary assay will clarify the mechanism of F_1F_o, as was achieved for F_1.

A recent report that F_1F_o undergoes contraction (Syroeshkin et al., 1998) is worth considering in exploring other movements required for ATP synthesis, although we have been unable to repeat the 'sonic wave-driven ATP synthesis' (N. Mitome, unpublished results). If this movement is essential for ATP synthesis, real-time detection of the up–down motion of a F_1F_o molecule would be the next challenge.

We acknowledge Dr Tazashi Matsui for constructing the overexpression system of TF_1 $\alpha_3\beta_3\gamma$ and Dr Takayuki Nishizaka for providing carefully prepared actin filaments.

References

Abrahams, J. P., Leslie, A. G. W., Lutter, R. and Walker, J. E. (1994). Structure at 2.8 Å resolution of F_1-ATPase from bovine heart mitochondria. *Nature* **370**, 621–628.

Bald, D., Amano, T., Muneyuki, E., Pitard, B., Rigaud, J.-L., Kruip, J., Hisabori, T., Yoshida, M. and Shibata, M. (1998). ATP synthesis by F_oF_1-ATP synthase independent of noncatalytic nucleotide binding sites and insensitive to azide inhibition. *J. Biol. Chem.* **273**, 865–870.

Boyer, P. D. (1993). The binding change mechanism for ATP synthase – some probabilities and possibilities. *Biochim. Biophys. Acta* **1140**, 215–250.

Boyer, P. D. and Kohlbrenner, W. E. (1981). The present status of the binding-change mechanism and its relation to ATP formation by chloroplasts. In *Energy Coupling in Photosynthesis* (ed. B. Selman and S. Selman-Reiner), pp. 231–240. New York: North Holland Elsevier.

Duncan, T. M., Bulygin, V. V., Zhou, Y., Hutcheon, M. L. and Cross, R. L. (1995). Rotation of subunits during catalysis by *Escherichia coli* F_1-ATPase. *Proc. Natl. Acad. Sci. USA* **92**, 10964–10968.

Fisher, A. J., Smith, C. A., Thoden, J., Smith, R., Sutoh, K., Holden, H. M. and Rayment, I. (1995a). X-ray structures of the myosin motor domain of *Dictyostelium discoideum* complexed with MgADP·BeFx and MgADP·AlF_4^-. *Biochemistry* **34**, 8960–8972.

Fisher, A. J., Smith, C. A., Thoden, J., Smith, R., Sutoh, K., Holden, H. M. and Rayment, I. (1995b). Structural studies of myosin:nucleotide complexes: a revised model for the molecular basis of muscle contraction. *Biophys. J.* **68**, 19–28.

Ishijima, A., Harada, Y., Kojima, H., Funatsu, T., Higuchi, H. and Yanagida, T. (1995). Single-molecule analysis of the actomyosin motor using nano-manipulation. *Biochim. Biophys. Res. Commun.* **199**, 1057–1063.

Jault, J. M., Matsui, T., Jault, F. M., Kaibara, C., Muneyuki, E., Yoshida, M., Kagawa, Y. and Allison, W. S. (1995). The $\alpha_3\beta_3\gamma$ complex of the F_1-ATPase from the thermophilic *Bacillus* PS3 containing the α-D261N substitution fails to dissociate inhibitory MgADP from a catalytic site when ATP binds to noncatalytic sites. *Biochemistry* **34**, 16412–16418.

Kato-Yamada, Y., Noji, H., Yasuda, R., Kinoshita, K. and Yoshida, M. (1998). Direct observation of the rotation of ε subunit in F_1-ATPase. *J. Biol. Chem.* **273**, 19375–19377.

Lambright, D. G., Sondek, J., Bohm, A., Skiba, N. P., Hamm, H. E. and Sigler, P. B. (1996). The 2.0 Å crystal structure of a heterotrimeric G protein. *Nature* **379**, 311–319.

Lee, E., Taussig, R. and Gilman, A. G. (1992). The G226A mutant of $G_{s\alpha}$ highlights the requirement for dissociation of G protein subunits. *J. Biol. Chem.* **267**, 1212–1218.

Matsui, T., Muneyuki, E., Honda, M., Allison, W. S., Dou, C. and Yoshida, M. (1997). Catalytic activity of the $\alpha_3\beta_3\gamma$ complex of F_1-ATPase without noncatalytic nucleotide binding site. *J. Biol. Chem.* **272**, 8215–8221.

Noel, J. P., Hamm, H. E. and Sigler, P. B. (1993). The 2.2 Å crystal structure of transducin-α complexed with GTPγS. *Nature* **366**, 654–662.

Noji, H., Yasuda, R., Yoshida, M. and Kinoshita, K., Jr (1997). Direct observation of the rotation of F_1-ATPase. *Nature* **386**, 299–302.

Sabbert, D., Engelbrecht, S. and Junge, W. (1996). Intersubunit rotation in active F_1-ATPase. *Nature* **381**, 623–625.

Sasaki, N., Shimada, T. and Sutoh, K. (1998). Mutational analysis

of the switch II loop of *Dictyostelium* myosin II. *J. Biol. Chem.* **273**, 20334–20340.

Smith, C. A. and Rayment, I. (1996). X-ray structure of the magnesium(II)·ADP·vanadate complex of the *Dictyostelium discoideum* myosin motor domain to 1.9 Å resolution. *Biochemistry* **35**, 5404–5417.

Svoboda, K., Schmidt, C. F., Schnapp, B. J. and Block, S. M. (1993). Direct observation of kinesin stepping by optical trapping interferometry. *Nature* **365**, 721–727.

Syroeshkin, A. V., Bakeeva, L. E. and Cherepanov, D. A. (1998). Contraction transition of F_1-F_o ATPase during catalytic turnover. *Biochim. Biophys. Acta* **1409**, 59–71.

Tozawa, K., Sekino, N., Soga, M., Yagi, H., Yoshida, M. and Akutsu, H. (1995). Conformational dynamics monitored by His-179 and His-200 of isolated thermophilic F_1-ATPase β subunit which reside at the entrance of the conical tunnel in holoenzyme. *FEBS Lett.* **376**, 190–194.

Yasuda, R., Noji, H., Kinoshita, K. and Yoshida, M. (1998). F_1-ATPase is a highly efficient molecular motor that rotates with discrete 120° steps. *Cell* **93**, 1117–1124.

2

F_1-ATPase: a highly efficient rotary ATP machine

Kazuhiko Kinosita, Jr.*†[1], Ryohei Yasuda† & Hiroyuki Noji†

**Department of Physics, Faculty of Science and Technology, Keio University, Hiyoshi, Kohoku-ku, Yokohama 223-8522, Japan, and †CREST "Genetic Programming" Team 13, Teikyo University Biotechnology Center 3F, Nogawa, Miyamae-ku, Kawasaki 216-0001, Japan*

Introduction

Think of a single protein molecule that is by itself a rotary motor. Driven by three subunits each fuelled by ATP, the motor rotates in discrete 120° steps. The efficiency of energy conversion, from the free energy of ATP hydrolysis to mechanical output of the motor, amounts to nearly 100%. Mother Nature has created such a tiny yet powerful molecular machine, not for the purpose of producing mechanical work but for the synthesis of ATP in our body by reverse operation of the rotary motor.

This rotary motor is a part of the enzyme ATP synthase. In animals, the ATP synthase resides in the inner membrane of mitochondria. The food ingested by an animal is 'burnt' (oxidized) by protein machinery embedded in the inner membrane, and the energy obtained by the oxidation is used to eject protons from inside the mitochondrion to the external space. The protons eventually flow back into mitochondria through the ATP synthase, in which

[1]*To whom correspondence should be addressed, at Keio University.*

ATP is synthesized from ADP and P_i using the proton flow as the energy source. Similar systems occur in plants and bacteria.

That oxidation and ATP synthesis are coupled by the flow of protons across the mitochondrial membrane was proposed by Peter Mitchell [1], a radical concept at that time which took many years to be accepted. For the coupling between the proton flow and ATP synthesis in the ATP synthase, another revolutionary proposal was made by Boyer [2]: the proton flow and chemical reaction are coupled by the mechanical rotation of a subunit(s) within the protein molecule. This latter proposal, too, failed to arouse enthusiasm until, in 1994, John Walker and colleagues elucidated the atomic structure of part of the ATP synthase [3]. The structure strongly supported Boyer's idea, and also suggested many experiments that have led to the proof (at least in part) of Boyer's rotational catalysis model [4–8]. Here we briefly review some of the remarkable features of this molecular machine revealed in our laboratory, and discuss its possible mechanism.

The ATP synthase: two rotary motors with a common shaft

As shown in Figure 1(a), the ATP synthase consists of two parts, a membrane-embedded portion called F_0 and a protruding portion F_1. When protons flow through F_0 from top to bottom in Figure 1(a), ATP is synthesized in F_1. The ATP synthase is a completely reversible machine: when ATP is hydrolysed in F_1, protons are pumped back in the reverse direction.

Boyer [2,9,10] proposed that F_0 is a rotary motor (or rather a turbine) driven by the proton flow, and that F_1 is another rotary motor driven by ATP hydrolysis. The two motors have a common rotary shaft (magenta in Figure 1a), but the genuine rotary directions of the two are different. When the free energy liberated by the downward flow of protons is greater than the free energy of ATP hydrolysis, the F_0 motor rotates the common shaft in the F_0's genuine direction. The F_1 motor is forcibly rotated in its reverse direction, resulting in ATP production in its catalytic sites. If the free energy of ATP hydrolysis is higher, the F_1 motor gains control and rotates the shaft in its own direction. Protons are then pumped out by F_0 against an uphill potential.

Isolated F_1 catalyses only ATP hydrolysis, and hence is called F_1-ATPase. Its subunit composition is $\alpha_3\beta_3\gamma\delta\epsilon$. One view of the crystal structure of bovine mitochondrial F_1, determined by Walker and colleagues [3], and hereafter referred to as the Walker structure, is shown in Figure 1(b). The δ and ϵ subunits were not resolved, but these are not required for the rotation of F_1. The $\alpha_3\beta_3$ cylinder forms the stator, and the central γ subunit, of which part of the protruding portion has not been resolved, would rotate in the cylinder. The catalytic sites in which ATP is synthesized/hydrolysed are on the three β subunits, each at an interface with a neighbouring α. Surprisingly, each of the three β subunits carried a different nucleotide in the crystal: one an analogue of ATP, another ADP, and the third carried none, in the clockwise order

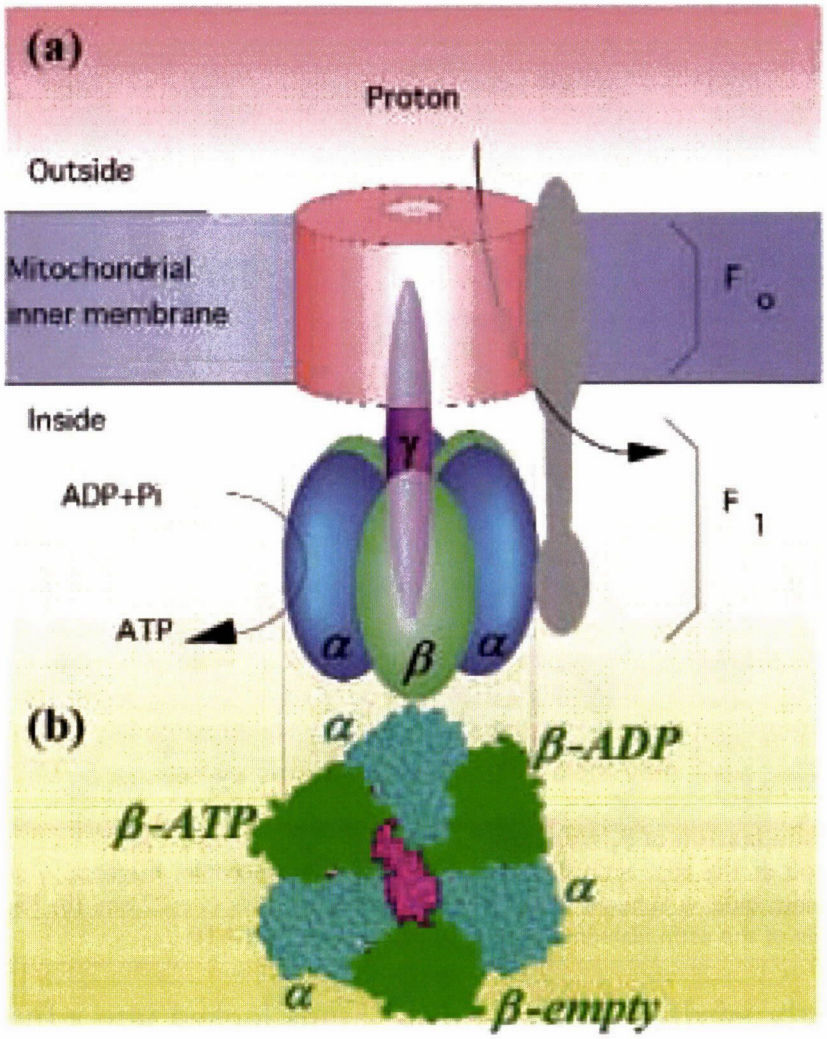

Figure 1. ATP synthase
(a) A schematic model. In a currently popular but unproven view, the red cylinder in the membrane rotates together with the γ shaft, and the grey part serves as the stator. Adapted from [12] with permission. ©1998 Cell Press. (b) Top view of the atomic structure of the F_1 part [3].

(Figure 1b). If hydrolysis were to proceed from this crystal structure, the ATP in the first β would be hydrolysed into ADP, the ADP in the second β would be released, and the third β would bind ATP from the medium. Thus the central γ is expected to rotate anticlockwise.

Proof that F_1 is indeed a rotary motor

Large-amplitude rotational motion of γ during ATP hydrolysis or synthesis had been shown by crosslinking and spectroscopic studies [4–7], but whether γ makes complete turns and does so in a unique direction was not clear until we observed the motion of γ directly under a microscope [8]. To visualize the rotation, Hiroyuki Noji prepared an $\alpha_3\beta_3\gamma$ subcomplex of bacterial origin. The $\alpha_3\beta_3$ cylinder was fixed to a glass surface, and a micrometre-sized actin filament was attached to γ via streptavidin (Figure 2a). The actin filament was

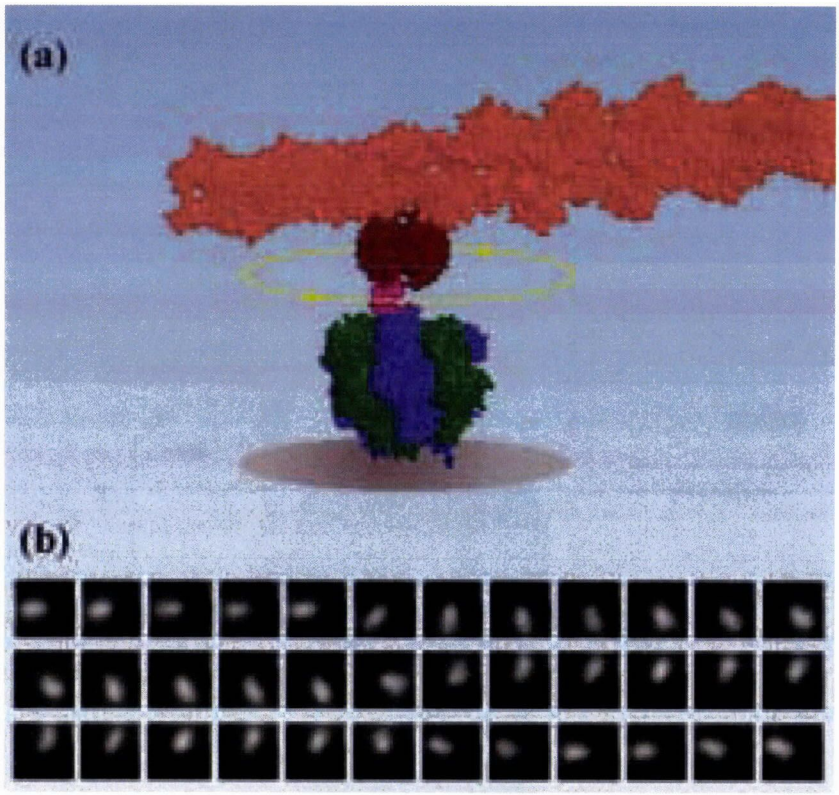

Figure 2. Visualization of F_1 rotation
(a) Orange rod at the top, actin filament; dark brown, streptavidin; magenta, γ subunit of F_1; green, β subunit; blue, α subunit. The diameter of the grey disk is $\approx$22 nm. (b) Photographs at 26 ms intervals of the actin filament rotating stepwise at 0.6 μM ATP.

fluorescently labelled. When Ryohei Yasuda looked into a fluorescence microscope, he saw a filament rotating continuously in one direction, anticlockwise as expected! The rotating filament was found on the very first day, within 30 min of the initial trial. The rotation was so beautiful that we were immediately convinced, almost, that F_1 was indeed a rotary motor. Soon a second rotating filament was found, and we were to toast Boyer after confirming the third. But the beer remained unopened; the third came only after a full month of struggle.

In our hands, at most a few percent of the actin filaments in a sample chamber rotate. A likely cause is surface obstructions. Note that the F_1 molecule is only $\approx$10 nm high, whereas the actin filaments are $\approx$1 μm or longer. Thus rotating the filament without touching the surface should be difficult. Indeed, rotating filaments often show a tendency to be stuck at a particular angle. Also, a significant fraction of F_1 is idle under normal assay conditions: MgADP, a product of the ATPase reaction, tends to bind tightly to a catalytic site and inhibit further ATP hydrolysis. Presumably, this MgADP inhibition prevents futile consumption of ATP in living cells.

Figure 3 shows typical (i.e. the most vigorously rotating) examples of rotation versus time. At a saturating concentration of ATP (2 mM), the rotation was essentially smooth and unidirectional. Rotation was slower for longer

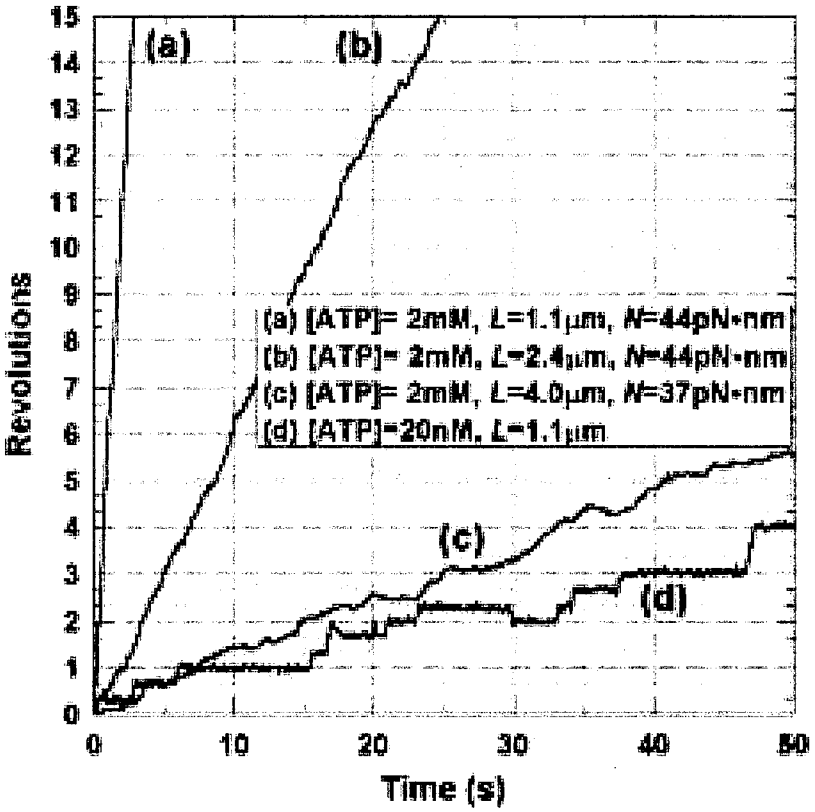

Figure 3. Rotation at high and low ATP concentrations
Traces (a–c) show the rotational rates for actin filaments of different lengths at 2 mM ATP. Analysis of the data [13] gives torque values of 44, 44 and 37 pN·nm, respectively. The rotational rates during individual steps at 20 nM ATP (trace d) are similar to the rate for the same filament length at 2 mM ATP (trace a).

actin filaments, because the viscous friction against the rotation is basically proportional to the cube of the actin length [11]. At very low ATP concentrations, the rotation became stepwise (Figures 2b and 3, trace d). The step size of 120° is precisely the one expected for the motor driven by the three β subunits separated by 120°. Note, in Figure 3 (trace d), that the motor made a back step at ≈30 s; a molecular machine must occasionally make mistakes.

The properties of the F_1 motor

Our studies [8,12–14] have revealed the following properties of F_1-ATPase. These properties have been deduced from the observations of the most actively rotating F_1, and do not necessarily represent the average behaviour of an ensemble.

(i) F_1-ATPase is a rotary motor made of a single molecule

Occasionally an actin filament rotated around its centre, like a propeller [8]. If one were to hold a long rod at the middle and rotate it like a propeller, one would have to shift one's grip continually; true rotation requires slippage between the rotor and stator, compared with the pseudo-rotation that one can

make by holding the end of a rod and twisting (not really rotating) the wrist. Thus the γ subunit must slide against the surrounding $\alpha_3\beta_3$ cylinder over infinite angles. The propeller rotation of an actin filament cannot be supported by two different F_1 molecules, and therefore a single F_1 molecule must itself be a rotary motor. Its diameter and height being only $\approx$10 nm [3], the F_1 motor is the smallest rotary motor known.

(ii) $\alpha_3\beta_3\gamma$ subunits suffice for rotation

We have demonstrated rotation in the subcomplex $\alpha_3\beta_3\gamma$ [8]. Crosslinking studies [7] have indicated that the ϵ subunit also moves relative to α, and rotation of an actin filament attached to ϵ has been demonstrated [14]. Thus ϵ is likely to be part of the rotor, although it is not a necessary part of the rotary mechanism.

(iii) Rotation is anticlockwise when viewed from the F_0 side

Except for the occasional back steps, the sense of rotation is always anticlockwise when viewed from the top in Figures 1(a) and 2(a) [8]. This direction is in accord with the Walker structure (Figure 1b), suggesting that a structure similar to that in Figure 1(b) appears during rotation.

(iv) The F_1 motor is a 120° stepper

Stepwise rotation is seen at submicromolar ATP concentrations [13] (Figures 2b and 3, trace d). Between steps, F_1 waits for the next ATP molecule to arrive. At high ATP concentrations, the waiting time is shorter than the time required to rotate an actin filament through 120°, and hence the steps are not easily discerned. So far, substeps within the 120° step have not been resolved at our highest temporal resolution of 5 ms.

(v) The F_1 motor is designed to produce a constant torque

From the measured rate of rotation, we can calculate the torque the F_1 motor produces to move the actin filament [13]. At saturating ATP concentrations where ATP binding is not rate limiting, the torque, averaged over many revolutions, is $\approx$40 pN·nm irrespective of the viscous load or the rotational rate [13] (see also Figure 3). At low ATP concentrations where the 120° steps are resolved, the torque driving each step averages $\approx$44 pN·nm, again irrespective of the filament length [13] (see also Figure 4).

(vi) Work per step is also constant

Mechanical work done (against the viscous load) in a single step is given by the angular displacement, $2\pi/3$ radians (i.e. 120°), multiplied by the torque. Because the torque is constant, 40–44 pN·nm, the work done in a step is also constant and amounts to 80–90 pN·nm.

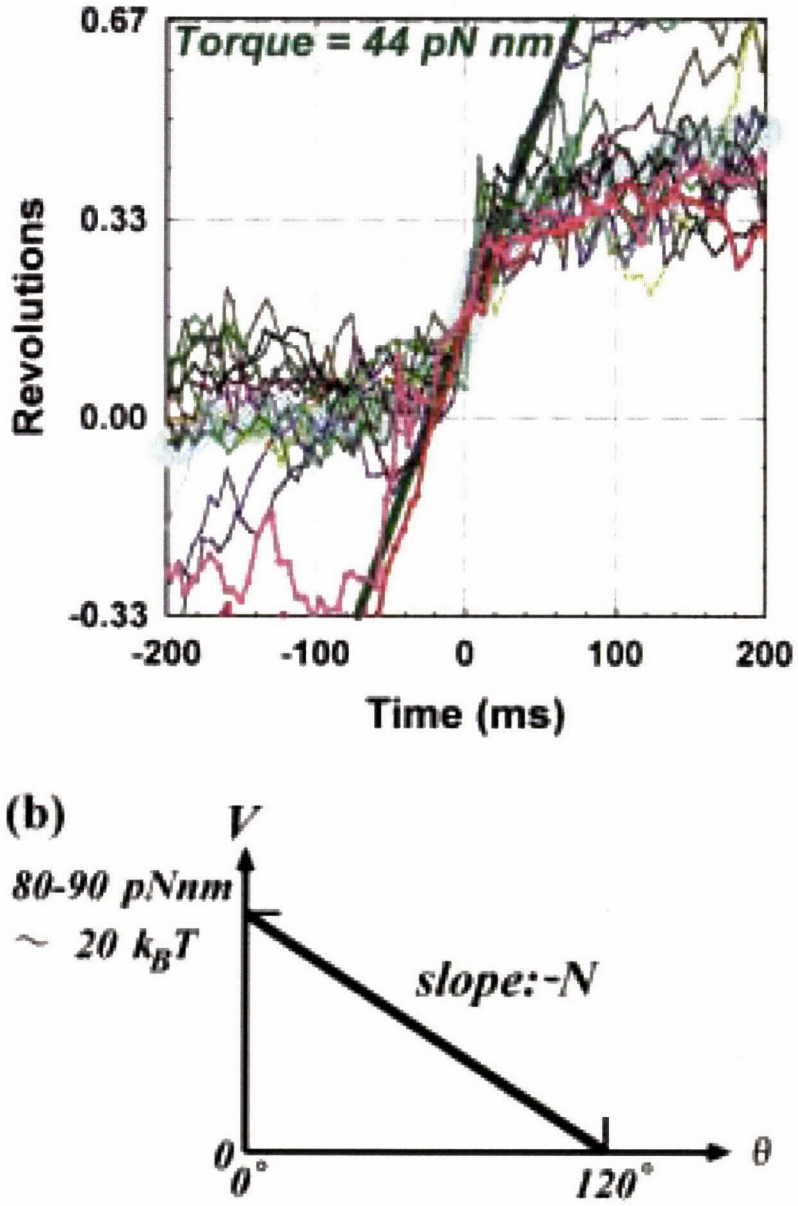

Figure 4. Time courses of individual steps
(a) Steps were measured at 0.2 μM ATP for F_1 bearing a 1.0 μm filament. Traces for individual steps are superimposed such that the middle of each step is located at time zero. Rapid succession of two steps are seen in two traces (red and pink). A thick cyan line shows the average of all traces. A thick green line shows a constant-speed rotation at 44 radians/s, corresponding to a torque of 44 pN·nm. (b) Rotational potential, $V(\theta)$, deduced from (a).

(vii) One ATP molecule is consumed per step

At low ATP concentrations where ATP binding is rate-limiting both for hydrolysis and rotation, the time-averaged rate of actin rotation was approximately equal to one-third of the number of ATP molecules hydrolysed per s [13]. This suggests that one ATP molecule is consumed per 120° step. Both the rate of rotation and the rate of ATP hydrolysis were proportional to the ATP concentration, indicating that neither of these processes required simultaneous consumption of two or more ATP molecules. At very low ATP

concentrations where the 120° steps were resolved, an analysis of the intervals between steps indicated that each step was fuelled by one ATP molecule [13].

(viii) The efficiency of energy conversion can reach ≈100%

Points (vi) and (vii) above indicate that the constant mechanical output of 80–90 pN·nm per step is produced by the consumption of one ATP molecule. The energy input, the free energy of ATP hydrolysis, ΔG, depends on the concentrations of ATP, ADP and P_i. In experiments at a controlled ΔG of 90 pN·nm, the work done per step was also ≈80 pN·nm [13]. Thus the F_1 motor can work at near 100% efficiency. The efficiency is lower at higher ΔG, because the mechanical output is constant. In cells where ΔG is 80–90 pN·nm, the efficiency could be ≈100%. This amazingly high efficiency, compared with other molecular motors [12], is probably related to the fully reversible nature of this molecular machine. In ATP synthase, the F_1 motor would pump protons at the energy conversion efficiency of ≈100%.

The rate of ATP hydrolysis quoted in point (vii) was measured in solution, and thus is an ensemble average. The hydrolysis rate of active F_1 might be higher, because some in the ensemble might have been inhibited. Hence, we cannot exclude the possibility that uncoupled, futile consumption of ATP occurs occasionally. Even so, each mechanical step is coupled to the hydrolysis of one and only one ATP molecule, and the free energy liberated in the coupled hydrolysis can be converted to mechanical work at ≈100% efficiency.

(ix) Bi-site catalysis supports rotation

At submicromolar ATP concentrations, the F_1-ATPase operates in the so-called bi-site mode [9,10], where at most two catalytic sites are filled with a nucleotide. Basically, one site binds tightly a nucleotide, ATP or ADP+P_i in reversible equilibrium, and the other two sites are empty. When a second site binds ATP from the medium, ADP and P_i are rapidly released from the first site, resulting in net hydrolysis of one ATP molecule. Our results show that rotation can occur in this bi-site catalysis: there is no need to fill all the catalytic sites. The bi-site rotation is fundamental to the rotary mechanism, and there is no clear evidence that the motor adopts a different mechanism in the tri-site regime. Because torque generation requires broken symmetry, the use of an all-filled (or all-empty) state is not advantageous.

At extremely low ATP concentrations, uni-site catalysis occurs where the tightly bound products in one catalytic site are very slowly released in the medium without the binding of a second ATP. Whether the uni-site catalysis accompanies rotation is an important yet unsettled question. Crosslinking γ to a β did not inhibit uni-site catalysis [15], indicating that uni-site catalysis can occur without rotation. However, the possibility of rotation in the absence of crosslinking cannot be dismissed.

(x) Back steps occur, probably using ATP

Occasional back steps observed at low ATP concentrations were as rapid as the forward steps [13]. The torque driving the back steps, and thus the work per step, are as high as those of the forward steps, suggesting that the back steps are also driven by ATP hydrolysis. Presumably, ATP binding to the wrong site (one of the two empty sites) in the bi-site rotation produces a back step.

(xi) ATP hydrolysis is likely to introduce a linear downhill rotational potential

Point (vi) can be explained if an angle-dependent potential energy of height 80–90 pN·nm, downhill towards the position 120° ahead, is introduced for γ rotation upon the binding (and/or subsequent hydrolysis) of ATP. We can estimate the shape of this potential as follows.

In Figure 4(a), many steps in a rotation record are superimposed. Although individual traces are noisy, their average shown in the thick cyan line indicates that the slope, the rotational rate ω, is approximately constant throughout the 120° interval. The torque N ($=\omega\xi$; where ξ is the rotational frictional drag coefficient [11,13], $\xi=1.0$ pN·nm·s for the 1 μm filament) is thus independent of the rotational angle θ, and is approximately 44 pN·nm throughout the 120° interval as shown in the thick green line. Because the potential $V(\theta)$ for γ rotation is related to N by $dV/d\theta=-N$, a linear potential profile is deduced, shown in Figure 4(b). Note that the actual potential profile should be dependent on the state of the bound nucleotides, which changes with time in each step. The profile shown in Figure 4(b) is the effective potential experienced by γ during the course of the chemical kinetics. Also, details of the actual potential profile may have been smoothed out by the combination of possible elastic linkage between γ and actin and the viscous friction on the latter.

How the F_1 motor may be designed

A rotary mechanism of human design is shown in Figure 5. This motor has three driving poles in the stator part, like the F_1 motor. The motor is powered by a unidirectional current source, while ATP hydrolysis is also practically unidirectional. Thanks to the three pairs of switches (commutators) on the shaft, the three poles change their polarities such that the shaft rotates continuously in the anticlockwise direction. The rotor is a permanent magnet, a static component. If the rotor is forcibly rotated in the reverse direction, this DC (direct current) motor becomes a DC generator and charges the external battery. The energy-conversion efficiency of modern electrical motors is quite high, often >95%. The DC motor operates in the bi-site mode in that the three driving poles never assume the same polarity. Thus there are similarities

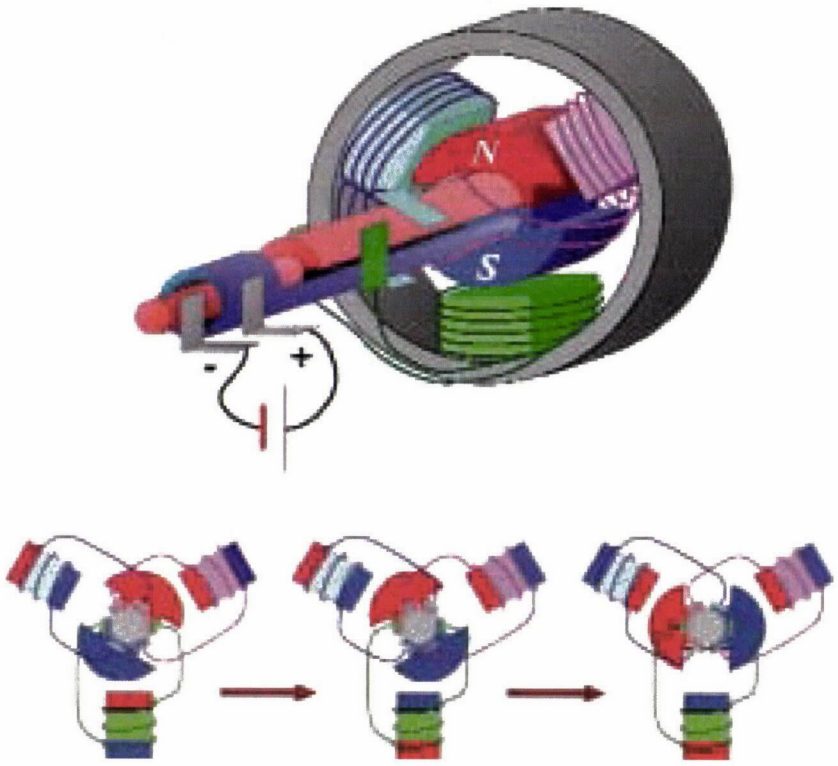

Figure 5. A three-pole DC motor
The commutators on the shaft change the polarity of stator magnets such that the shaft rotates anticlockwise continuously.

between the properties of this three-pole DC motor and those of the F_1 motor. Do these two share some operational principles?

The driving forces in the electrical motor in Figure 5 are the attraction between north and south poles and the repulsion between like poles. Such a push–pull mechanism may also operate between the γ and β subunits of the F_1 motor. Figure 6(a) shows side views of the three pairs of opposing β and α subunits, together with the central γ, in the Walker structure. The vertical black lines show the rotational axis suggested by Wang and Oster [16]: the bottom part of the $\alpha_3\beta_3$ stator has an approximate 3-fold symmetry around this axis, and thus the conformations of β and α in the bottom do not change greatly depending on the bound nucleotide. In the upper part, in contrast, the β subunits binding ATP or ADP are bent towards, and therefore push, γ, whereas the empty β retracts and pulls γ towards it. Wang and Oster [16] suggest that, because the central γ is slightly bent, co-operative push–pull actions of the three β subunits would rotate γ, as seen in Figure 6(b).

A simple F_1 model

Figure 7 shows a model for F_1 rotation based on this push–pull mechanism. The side of γ that faces the empty β in the Walker structure is designated the north pole, and thus an empty β is the south pole. A nucleotide-carrying β is north and repels the north face of γ and attracts its south face. By reciprocity, the south face of γ augments the affinity of the opposing β for a nucleotide,

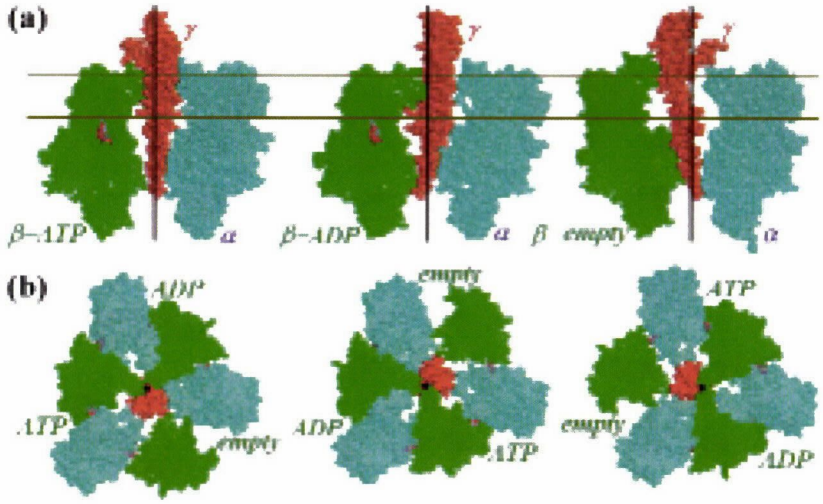

Figure 6. Nucleotide-dependent conformational changes in F_1
(a) The diagrams show the central γ subunit (orange), one β (green) to the left of γ, and one α (blue) to the right in the crystal structure [3]. The black lines indicate the rotation axis [16]. Nucleotides are shown in Corey-Pauling-Kultun (CPK) colours. (b) Top view of the cross sections of F_1 between the horizontal lines in (a).

and the north face decreases the affinity (the free energy is lowered when north and south oppose each other). To ensure rotation in a unique direction, additional control of nucleotide-binding kinetics via 'commutators' is required. A simple example is given in Figure 7(b): binding/release of ATP is allowed for β while it is on the pink side of γ, and ADP binding/release while on the green side. As shown in Figures 7(c) and 7(d), the switching ensures anticlockwise rotation of γ when ATP is hydrolysed; when the rotor is forced to rotate clockwise in the presence of ADP (and P_i), ATP is synthesized.

More elaborate switches have been proposed by Wang and Oster [16], and their model can account for many experimental observations, including the near 100% efficiency and 120° stepping with occasional back steps. In their model, as with the model in Figure 7, the motor tends to pause at angles 60° out of phase from the Walker structure (Figure 7a), an experimentally testable prediction. How the switching action is implemented in the protein structure is yet to be specified.

A switch-less F_1 model

The roles of the commutators in Figure 5 are to alternate the polarities of the stator magnets, and to do so at precise timings dictated by the rotational angle of the shaft. Unlike the magnet driven by direct current, the alternation of the polarity is inherent in the ATP-driven 'magnet', where bound ATP is eventually hydrolysed and released, restoring the south state spontaneously. Thus only co-ordination of nucleotide kinetics among the three stator magnets needs to be programmed. This could be done without switches, as shown in Figure 8, which is one version of the general model of Oosawa and Hayashi [17].

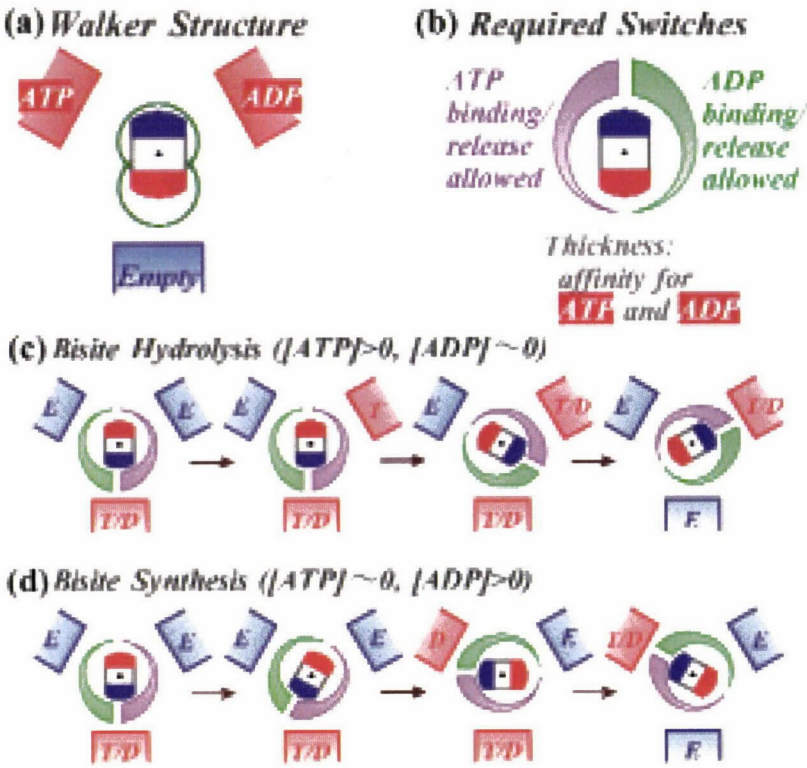

Figure 7. A simple model for the F_1 motor

(a) The γ subunit is regarded as a permanent magnet, the side of γ that faces the empty β in the Walker structure being the north pole. (b) The affinity for a nucleotide is higher when β is closer to the south pole of γ (strictly, the affinity for ATP is higher than that for ADP). Binding and release of ATP and ADP are kinetically inhibited on the green and pink sides, respectively. (c) Bound ATP (T) is in equilibrium with ADP (D) and P_i, and is released as ADP when a second ATP binds and rotates γ. E, empty. (d) Forced clockwise rotation of γ results in the uptake of ADP (and P_i) and release of ATP.

In Figure 8, the position of the 'magnetic pole' in β changes depending on the bound nucleotide. This dual-pole arrangement, combined with the higher affinity for nucleotides when the pole is closer to the south face of γ, ensures anticlockwise rotation in bi-site hydrolysis by inducing ATP binding primarily in the empty β in the anticlockwise direction (Figure 8c). Note that the angle-dependence of the nucleotide affinity results as a reaction to the nucleotide-dependent push–pull action, without requiring switches. An additional factor ensuring correct rotation is the higher affinity for ATP than for ADP. Because ATP hydrolysis on β is reversible (the free-energy difference between β binding ATP and β binding ADP+P_i is small), the affinity for the hydrolysis products has to be lower in order for β to act as an ATPase. In the original model of Oosawa and Hayashi [17], near-100% efficiency was achieved for both hydrolysis and synthesis.

The essence of the dual-pole arrangement is that the mechanical interaction between γ and individual β subunits involves a nucleotide-dependent rotational component in addition to pushing/pulling. The Walker structure gives more emphasis to pushing/pulling rather than to direct rotation, but the

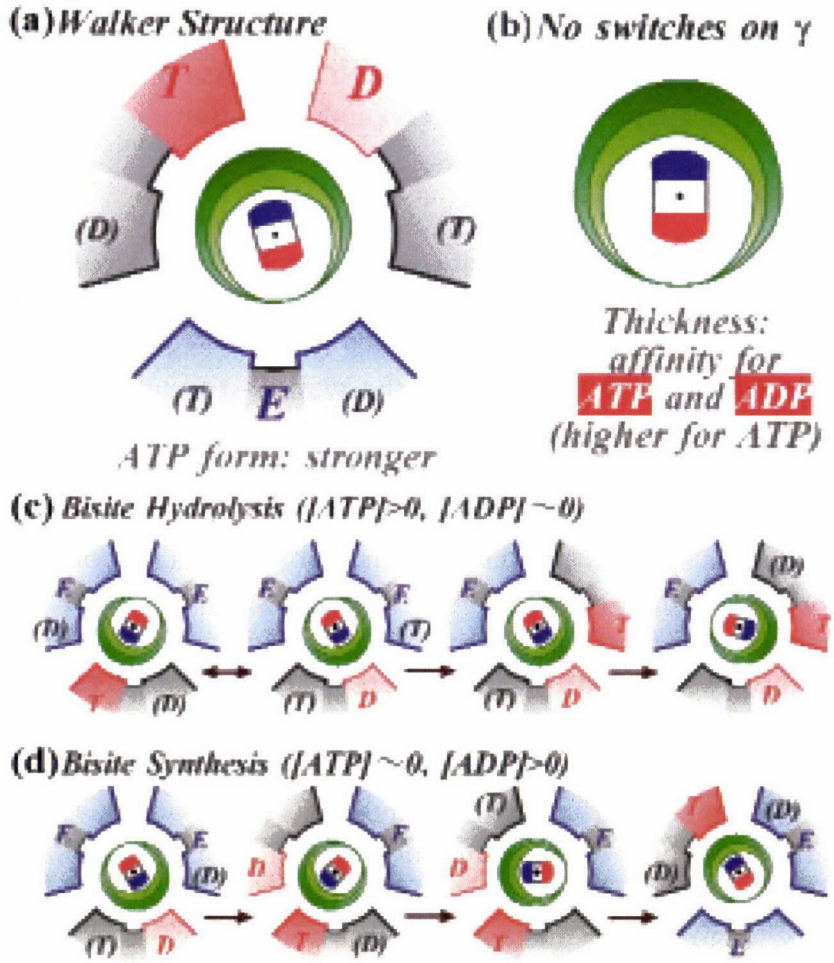

Figure 8. A switch-less model for the F_1 motor
(a) Location of the magnetic pole on β changes depending on the bound nucleotide. ATP (T) magnet is stronger than ADP (D) magnet and, hence, (b) the affinity for ATP is higher than that for ADP. (c) When only one nucleotide is bound it is reversibly interconverted between ATP and ADP+P_i. Comparison of affinities suggests that the most likely way of filling a second site is binding of ATP in the β in the anticlockwise direction. (d) When γ is forcibly rotated clockwise, the equilibrium between ATP and ADP is shifted towards ATP, which is eventually released while ADP is newly bound in the second site. E, empty.

structure of γ in the protruding portion has not been resolved. Also, key intermediates in actual rotation, particularly the state with only one bound nucleotide, may well have a different structure.

Models in Figures 7 and 8 have been introduced solely to point out several factors that may or may not be important in the mechanism of F_1 rotation. Neither is assumed to be the actual mechanism. Nor are all important factors explained in these models. For example, the magnet analogy, particularly that for γ, obscures the fact that neither γ nor β possesses reflection symmetry. The force between γ and individual β subunits must be more or less asymmetric, favouring one rotational direction over the other, as modelled by the dual poles in Figure 8. Whether the rotational potential can be approximated by a simple superposition of three pairwise interactions between individual β and γ,

as implied by the magnetic analogy, remains unclear until structures of the different intermediates are revealed. Also, in Figures 7 and 8, nucleotide kinetics on different βs are co-ordinated only through the rotation of γ, but β subunits may also communicate through the intervening α subunits.

Problems to be solved

The key to understanding the rotational mechanism is to elucidate the structure of F_1 in which only one catalytic site is filled, the structure from which the 120° step begins. It is unlikely that the two empty β subunits in this structure both resemble the empty β in the Walker structure; presumably, the asymmetric γ would induce the β 120° ahead into a conformation closer to the nucleotide-carrying β in the Walker structure.

Also important is to establish the precise relation between the nucleotide binding/hydrolysis kinetics and the rotational potential. This could be done by imaging nucleotide turnover in a single motor molecule [18] while observing its rotation through an attached actin filament. Manipulation of the filament, e.g. with optical tweezers [19], will help establish the angle dependence of the nucleotide kinetics or, conversely, the nucleotide dependence of the rotational torque. Because an attached actin filament may not faithfully reflect the orientation of γ, assessment of the latter through imaging of polarized fluorescence [20,21] from a fluorophore rigidly attached to γ will also be useful.

What happens if the free energy of ATP hydrolysis is reduced below 80 pN·nm by manipulating nucleotide and P_i concentrations? This is a fundamental question for mechanisms of molecular machines in general. The predicted behaviours depend on the model. Answering the question experimentally is not easy, because MgADP inhibition is serious at high ADP concentrations.

Presumably, the MgADP-inhibited form is the most stable state of the F_1 motor, while rotation requires instability. The Walker crystal structure probably represents this stable inhibited form [3]. The anticlockwise rotation consistent with this structure, then, implies that slight destabilization of the Walker structure, e.g. by the presence of P_i next to ADP, would make an active intermediate. Interestingly, the inhibition does not occur in the synthesis mode [10], where proton-driven rotation of γ may destabilize the inhibited form. Many articles on F_1-ATPase do not mention the degree of MgADP inhibition in the experiments described; in some cases, different interpretations could emerge if this almost inevitable inhibition was taken into account.

Will ATP be synthesized in F_1 without the aid of F_0, if one mechanically rotates γ clockwise, e.g. by manipulating attached actin with optical tweezers? The answer should be yes, but experimental proof is still awaited. Such an experiment would demonstrate that mechanical energy can be directly transformed into chemical energy.

Relatively little is known about the F_0 part of the ATP synthase. Even whether F_0 is really a rotary motor is yet to be proved. If it is, which part is the rotor and how is it connected to γ? Is the proton transport tightly coupled to the rotation as it seems to be between ATP hydrolysis and rotation in the F_1 motor? Many questions remain, demanding new experimental ideas. Boyer calls the ATP synthase a splendid molecular machine [10]. It is also a splendid toy for young, creative researchers.

Summary

- *A single molecule of F_1-ATPase is by itself a rotary motor in which a central subunit, γ, rotates against a surrounding stator cylinder made of $\alpha_3\beta_3$ hexamer.*
- *Driven by the three β subunits that hydrolyse ATP sequentially, the motor runs with discrete 120° steps at low ATP concentrations.*
- *Over broad ranges of load and speed, the motor produces a constant torque of 40 pN·nm.*
- *The mechanical work the motor does in the 120° step, or the work per ATP hydrolysed, is also constant and amounts to 80–90 pN·nm, which is close to the free energy of ATP hydrolysis. Thus this motor can work at near 100% efficiency.*

We are grateful to Professor M. Yoshida and the members of CREST (Core Research for Evolutionary Science and Technology) Team 13 for collaboration and discussion. This work was supported in part by Grants-in-Aid from the Ministry of Science, Education, Sports and Culture of Japan, and a Keio University Special Grant-in-Aid. R.Y. was a Research Fellow of the Japan Society for the Promotion of Science.

References

1. Mitchell, P. (1961) Coupling of phosphorylation to electron and hydrogen transfer by a chemi-osmotic type of mechanism. *Nature (London)* **191**, 144–148
2. Boyer, P.D. & Kohlbrenner, W.E. (1981) The present status of the binding-change mechanism and its relation to ATP formation by chloroplasts, in *Energy Coupling in Photosynthesis* (Selman, B.R. & Selman-Reimer, S., eds.), pp. 231–240, Elsevier, Amsterdam
3. Abrahams, J.P., Leslie, A.G.W., Lutter, R. & Walker, J.E. (1994) Structure at 2.8 Å of F_1-ATPase from bovine heart mitochondria. *Nature (London)* **370**, 621–628
4. Duncan, T.M., Bulygin, V.V., Zhou, Y., Hutcheon, M.L. & Cross, R.L. (1995) Rotation of subunits during catalysis by *Escherichia coli* F_1-ATPase. *Proc. Natl. Acad. Sci. U.S.A.* **92**, 10964–10968
5. Zhou, Y., Duncan, T.M., Bulygin, V.V., Hutcheon, M.L. & Cross, R.L. (1996) ATP hydrolysis by membrane-bound *Escherichia coli* F_0F_1 causes rotation of the γ subunit relative to the β subunits. *Biochim. Biophys. Acta* **1275**, 96–100
6. Sabbert, D., Engelbrecht, S. & Junge, W. (1996) Intersubunit rotation in active F-ATPase. *Nature (London)* **381**, 623–625
7. Aggeler, R., Ogilvie, I. & Capaldi, R.A. (1997) Rotation of a γ-ϵ subunit domain in the *Escherichia coli* F_1F_0-ATP synthase complex. *J. Biol. Chem.* **272**, 19621–19624

8. Noji, H., Yasuda, R., Yoshida, M. & Kinosita, Jr., K. (1997) Direct observation of the rotation of F_1-ATPase. *Nature (London)* **386**, 299–302
9. Boyer, P.D. (1993) The binding change mechanism for ATP synthase — some probabilities and possibilities. *Biochim. Biophys. Acta* **1140**, 215–250
10. Boyer, P.D. (1997) The ATP synthase - a splendid molecular machine. *Annu. Rev. Biochem.* **66**, 717–749
11. Hunt, A.J., Gittes, F. & Howard, J. (1994) The force exerted by a single kinesin molecule against a viscous load. *Biophys. J.* **67**, 766–781
12. Kinosita, Jr., K., Yasuda, R., Noji, H., Ishiwata, S. & Yoshida, M. (1998) F_1-ATPase: a rotary motor made of a single molecule. *Cell* **93**, 21–24
13. Yasuda, R., Noji, H., Kinosita, Jr., K. & Yoshida, M. (1998) F_1-ATPase is a highly efficient molecular motor that rotates with discrete 120° steps. *Cell* **93**, 1117–1124
14. Kato-Yamada, Y., Noji, H., Yasuda, R., Kinosita, Jr., K. & Yoshida, M. (1998) Direct observation of the rotation of γ subunit in F_1-ATPase. *J. Biol. Chem.* **273**, 19375–19377
15. García, J. J. & Capaldi, R. A. (1998) Unisite catalysis without rotation of the γ-ϵ domain in *Escherichia coli* F_1-ATPase. *J. Biol. Chem.* **273**, 15940–15945
16. Wang, H. & Oster, G. (1998) Energy transduction in the F_1 motor of ATP synthase. *Nature (London)* **396**, 279–282
17. Oosawa, F. & Hayashi, S. (1986) The loose coupling mechanism in molecular machines of living cells. *Adv. Biophys.* **22**, 151–183
18. Funatsu, T., Harada, Y., Tokunaga, M., Saito, K. & Yanagida, T. (1995) Imaging of single fluorescent molecules and individual ATP turnovers by single myosin molecules in aqueous solution. *Nature (London)* **374**, 555–559
19. Arai, Y., Yasuda, R., Akashi, K., Harada, Y., Miyata, H., Kinosita, Jr., K. & Itoh, H. (1999) Tying a molecular knot with optical tweezers. *Nature (London)* **399**, 446–448
20. Sase, I., Miyata, H., Ishiwata, S. & Kinosita, Jr., K. (1997) Axial rotation of sliding actin filaments revealed by single-fluorophore imaging. *Proc. Natl. Acad. Sci. U.S.A.* **94**, 5646–5650
21. Hälser, K., Engelbrecht, S. & Junge, W. (1998) Three-stepped rotation of subunits γ and ϵ in single molecules of F-ATPase as revealed by polarized, confocal fluorometry. *FEBS Lett.* **426**, 301–304

THE ROYAL SOCIETY

A rotary molecular motor that can work at near 100% efficiency

Kazuhiko Kinosita Jr[1,2*], Ryohei Yasuda[2], Hiroyuki Noji[2] and Kengo Adachi[2,3]

[1]*Department of Physics, Faculty of Science and Technology, Keio University, Hiyoshi, Kohoku-ku, Yokohama 223-8522, Japan*
[2]*Core Research for Evolutional Science and Technology—'Genetic Programming' Team 13, Tokyo University Biotechnology Center 3F, Nogawa, Miyamae-ku, Kawasaki 216-0001, Japan*
[3]*Department of Physics, Faculty of Science, Kanazawa University, Kakuma-machi, Kanazawa 920-11, Japan*

A single molecule of F_1-ATPase is by itself a rotary motor in which a central γ-subunit rotates against a surrounding cylinder made of $\alpha_3\beta_3$-subunits. Driven by the three βs that sequentially hydrolyse ATP, the motor rotates in discrete 120° steps, as demonstrated in video images of the movement of an actin filament bound, as a marker, to the central γ-subunit. Over a broad range of load (hydrodynamic friction against the rotating actin filament) and speed, the F_1 motor produces a constant torque of *ca.* 40 pN nm. The work done in a 120° step, or the work per ATP molecule, is thus *ca.* 80 pN nm. In cells, the free energy of ATP hydrolysis is *ca.* 90 pN nm per ATP molecule, suggesting that the F_1 motor can work at near 100% efficiency. We confirmed *in vitro* that F_1 indeed does *ca.* 80 pN nm of work under the condition where the free energy per ATP is 90 pN nm. The high efficiency may be related to the fully reversible nature of the F_1 motor: the ATP synthase, of which F_1 is a part, is considered to synthesize ATP from ADP and phosphate by reverse rotation of the F_1 motor. Possible mechanisms of F_1 rotation are discussed.

Keywords: molecular motor; F_1-ATPase; ATP synthase; energy conversion efficiency

1. INTRODUCTION

Molecular motors generate movement and force between two cellular components. Linear motors produce movement along a filamentous structure; for example, myosin along an actin filament (Goldman 1998; Suzuki *et al.* 1998; Dominguez *et al.* 1998; Kitamura *et al.* 1999), kinesin (Block 1998; Lohman *et al.* 1998; Mandelkow & Johnson 1998) and dynein (Shingyoji *et al.* 1998) along a microtubule, and RNA polymerase along DNA (Gelles & Landick 1998; Wang *et al.* 1998). Known linear motors are driven by free energy obtained from nucleotide hydrolysis. Usually, the molecule that contains the hydrolysis site(s), excluding the filament, is called a motor and the filament is regarded as a track, although the filament is likely to also play an active role in producing force and movement (Kinosita 1998; Kinosita *et al.* 1998).

In the case of myosin, large-amplitude bending (conformational change) occurs when it binds ATP (Suzuki *et al.* 1998; Dominguez *et al.* 1998), suggesting that the reversal of the bending upon release of the hydrolysis products may directly drive an actin filament. Thermodynamics of actomyosin ATPase (Taylor 1979), however, indicates that much of the free energy of ATP hydrolysis is used in the unbinding of myosin from actin. Thus, rebinding by actin is likely to be the source of the pulling force, at least by reinforcing the reversal of the myosin bending. Whether myosin bound to actin in fact undergoes a large-amplitude bending and, if so, whether the bending produces sufficient force to drive actin, are yet to be seen. The observation that myosin made several 5-nm steps on actin upon hydrolysis of only one ATP molecule (Kitamura *et al.* 1999) is not readily explained by a simple bending model. Kinesin is likely to 'walk' on a microtubule using its two globular ATPase domains as 'feet'. Even so, whether the force is generated when a 'leg' is bent forward, or when a detached 'foot' is bound to the microtubule, is still an open question. A key to understanding the mechanism of linear motors is to detect their nucleotide-dependent conformational changes while they are bound to the substrate filament, but decisive experiments have not been done.

Two rotary molecular motors are known to date. One is the bacterial flagellar motor that rotates a flagellum using proton flow through the motor as the energy source (DeRosier 1998). The other is the F_oF_1-ATP synthase (Boyer 1993, 1997, 2000; Junge *et al.* 1997; Kinosita *et al.* 1998, 2000; Kinosita 1999; Kagawa 1999), which comprises two rotary motors, one driven by proton flow (F_o motor) and the other by ATP hydrolysis (F_1 motor), in one molecule.

The mechanisms of the proton-driven motors, whether flagellar or of ATP synthase, are less clear compared to myosin and kinesin, because structural details have not been elucidated. It is of interest to note that, at least conceptually, these proton-driven motors could operate without major conformational changes in either the rotor or stator: electrostatic force from moving protons could produce torque if the geometry of proton channels are designed appropriately (Läuger 1977).

Large-amplitude bending occurs in the ATP-driven F_1-motor of the ATP synthase (Abrahams *et al.* 1994). The

*Author for correspondence.

bending has been shown in a functional motor complex containing both the rotor and stator, and thus this bending is likely to contribute directly to torque generation. Unlike linear motors that undergo alternate binding and unbinding to and from the substrate filaments, the rotor and stator stay together in rotary motors. The analysis of the molecular mechanism of the F_1 motor may, in this sense, be simpler, and is expected to reveal precisely how the energy of ATP hydrolysis can be converted to torque. (Note that, if linear motors produce movement by bending, as in the lever-arm model for myosin, the direct outcome of nucleotide hydrolysis is torque rather than vectorial force.)

2. ATP SYNTHASE AND ROTATIONAL CATALYSIS

(a) *ATP synthase: a reversible molecular machine*

ATP synthase is ubiquitous from bacteria to plants and animals. It is a membrane-spanning enzyme that produces ATP using proton flow across the membrane. In animals, ATP synthase resides in the inner mitochondrial membranes where an electrochemical gradient of protons, high on the outside of mitochondria, is generated by the respiratory chain of enzymes. An active researcher produces his or her bodyweight of ATP in one day.

As shown in figure 1, the ATP synthase consists of a membrane-embedded portion F_o and a protruding portion F_1, and thus is also called F_oF_1-ATP synthase. When protons flow through F_o from top to bottom, in figure 1, ATP is synthesized in F_1. The synthase is a completely reversible molecular machine in that, when ATP is hydrolysed in F_1, protons are pumped back, from bottom to top, against an electrochemical gradient. How, then, is the proton flow through F_o coupled to the synthesis–hydrolysis of ATP in F_1?

(b) *Boyer's proposal: two rotary motors with a common shaft*

Boyer proposed that the coupling is mechanical (Boyer & Kohlbrenner 1981): F_o is a motor, or turbine, driven by the proton flow, and F_1 is another motor driven by ATP hydrolysis. The two have a common shaft. Proton flow from top to bottom in figure 1 drives the shaft in a unique direction, say clockwise. ATP hydrolysis in F_1 drives the shaft in the opposite direction, counterclockwise. When the free energy obtained from the downward flow of protons is greater than the free energy of ATP hydrolysis, the F_o motor rotates the common shaft in its genuine direction. The F_1 motor is forced to rotate in its reverse direction, and thus ATP is synthesized in its catalytic sites. If the energy obtained from ATP hydrolysis is higher, the F_1 motor gains control and protons are pumped out.

Boyer's idea came from the analysis of the chemical reaction in the F_1 part. The F_1 portion can be isolated in solution, and then it only hydrolyses ATP. Hence, the isolated enzyme is called F_1-ATPase. The F_1-ATPase consists of five types of subunits in the stoichiometry of $\alpha_3\beta_3\gamma\delta\varepsilon$ (in bovine mitochondrial F_1, δ and ε are, respectively, called ε and OSCP). $\alpha_3\beta_3\gamma$-subunits suffice for ATPase activity (and for rotation, as shown in § 3(a)). Each β-subunit contributes one catalytic site for the synthesis–hydrolysis of ATP (the catalytic site resides at the interface between a β-subunit and an α-subunit, and is in part contributed from residues of α). In addition, three non-catalytic nucleotide-binding sites exist, one on each α, but we ignore these non-catalytic sites in most of this review. Now, Boyer and others have found that the three catalytic sites are completely equivalent in steady-state ATP hydrolysis by F_1-ATPase or in steady-state ATP synthesis–hydrolysis by the whole ATP synthase. The γ-subunit, a single-copy subunit, was known to be indispensable for the catalysis, but its amino-acid sequence indicated that its structure could not possess threefold symmetry. Then, for the asymmetrical γ-subunit to interact with the three β-subunits impartially, it had to rotate. The rotation could be either unidirectional or to-and-fro fluctuation, but there should have been no limit in the rotational angle.

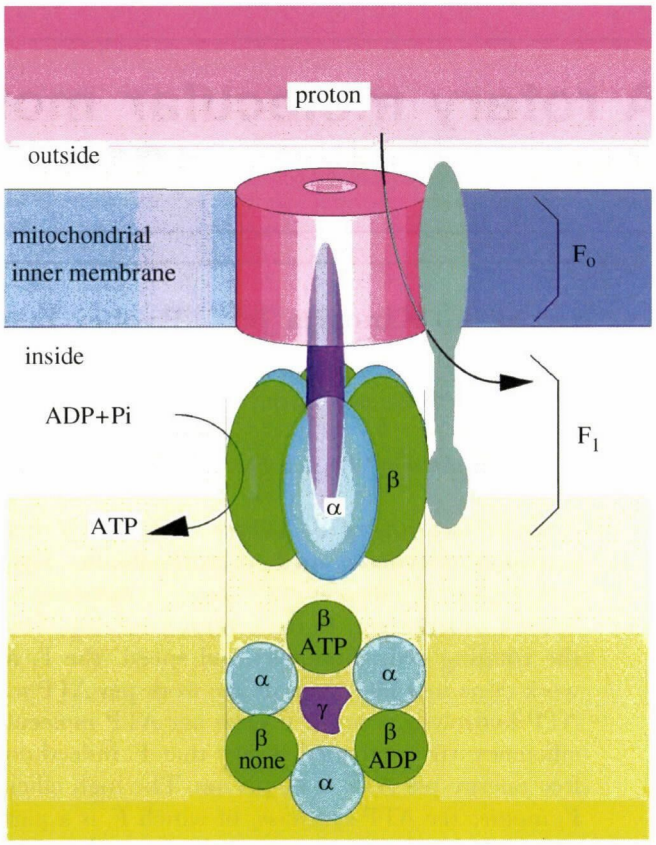

Figure 1. A schematic view of ATP synthase (Kinosita *et al.* 1998). The magenta rod at the centre represents the common shaft (the γ-subunit). In a currently popular but unproven view, the orange cylinder in the membrane rotates together with the γ-shaft and the grey part serves as the stator. The bottom diagram shows a top view of the F_1 part with catalytic nucleotides as found in the crystal (Abrahams *et al.* 1994).

(c) *Support for the rotational catalysis model*

That a subunit in a compact, functional protein molecule could slide against other subunits over infinite angles was certainly a revolutionary idea. Textbooks teach that protein subunits are held against each other by lock-and-key mechanisms, which would not readily allow mutual sliding. There were few believers, until a three-dimensional structure of F_1-ATPase was solved by Walker and colleagues (Abrahams *et al.* 1994). In the structure, which we refer to as the 'Walker structure' in this review, $\alpha_3\beta_3$ hexamer formed an orange-shaped cylinder, and part of

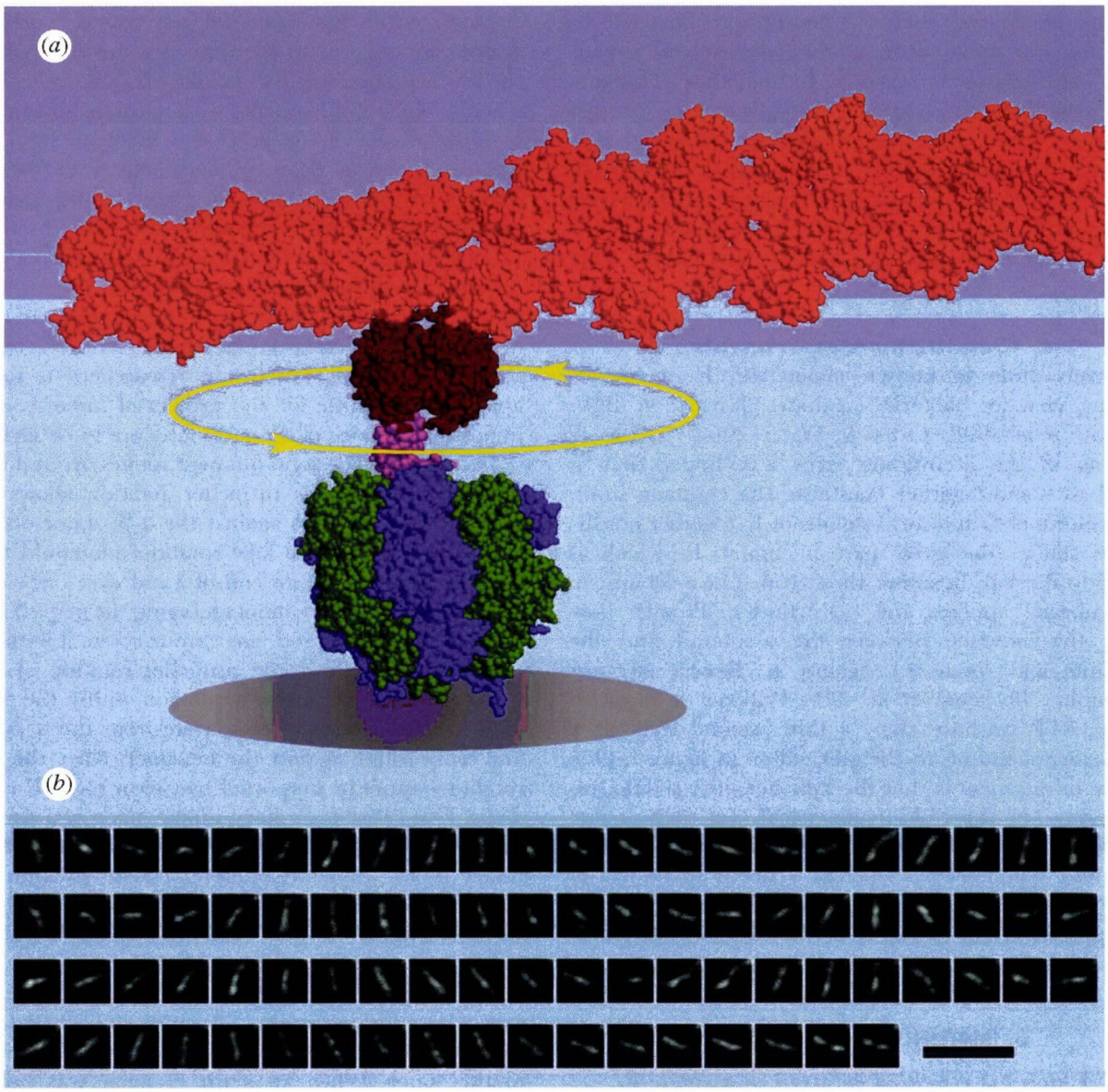

Figure 2. (*a*) The experimental system for the observation of the rotation of F_1-ATPase. The space-filling model of F_1 (blue, α; green, β; magenta, γ) is from Abrahams *et al.* (1994), actin filament (orange) from Holmes *et al.* (1990), and streptavidin (brown) from Livnah *et al.* (1993). Streptavidin has four strong binding sites for biotin, and the actin filament is heavily decorated with biotin. There is, however, only one biotin on γ. Presumably, free rotation between streptavidin and γ is prevented by steric hindrance. The diameter of the grey disk, representing the surface to which the three β-subunits are bound through histidine tags, is *ca.* 22 nm. (*b*) Sequential images, at 33 ms intervals, of a rotating actin filament (Noji *et al.* 1997). The average rate of rotation was 1.3 rev s^{-1}. Bar, 5 μm.

the γ-subunit, in the form of a coiled coil of two α-helices, penetrated the centre of the cylinder (δ- and ε-subunits were not resolved). The interface between the central γ-subunit and surrounding $\alpha_3\beta_3$-subunits was mostly hydrophobic, suggesting that the γ-shaft might rotate in the oily sleeve. Moreover, the three catalytic sites were filled with different nucleotides, one with AMPPNP (an analogue of ATP), the second with ADP, and the third with none, in a clockwise order when viewed from the top of figure 1 (see the bottom of the diagram). If this arrangement represents an active intermediate during hydrolysis, the arrangement in the next hydrolysis step would be ADP, none and ATP. The side of the γ-subunit that tends to face the ATP-carrying β-subunit would thus rotate counterclockwise.

The Walker structure strongly supported Boyer's rotational catalysis model; the γ-subunit would constitute a part of the common shaft of the two motors. The high-resolution structure immediately suggested experiments that would confirm the rotation of the γ-subunit against the $\alpha_3\beta_3$ cylinder. One strategy was to cross-link a particular residue on γ to one of the three βs. Then the link was cut and the enzyme was allowed to catalyse ATP hydrolysis (F_1 preparation; Duncan *et al.* 1995) or synthesis (whole ATP synthase; Zhou *et al.* 1997). After that, the residue was again cross-linked to a β-subunit. The second cross-linking was found to be to any of the three β-subunits, indicating that the residue on the γ-subunit faced all three β-subunits equally during catalysis. In experiments where catalysis was not allowed between the two cross-linking treatments, the second target was the same as the first one. In another set of experiments (Sabbert *et al.* 1996; Häsler *et al.* 1998), a fluorescent dye was attached to the γ-subunit. Time-resolved polarization

measurement showed that the fluorophore changed its orientation over many degrees when the enzyme underwent an ATP hydrolysis reaction. In one study (Häsler *et al.* 1998), the fluorophore appeared to adopt three distinct orientations. These experiments together indicated that the γ-subunit indeed rotates in the $\alpha_3\beta_3$ cylinder, but whether the rotation occurs in a unique direction was unanswered. The answer came from direct imaging of the rotation under a microscope, as described in the next section.

(d) *F_o awaits more experiments*

Relatively little is known about the F_o motor. A prevailing view for bacterial synthase (Junge *et al.* 1997; Fillingame *et al.* 1998; Oster & Wang 2000) is that 12 c-subunits in the membrane form a cylinder that is attached to γ and together constitute the common shaft. The δ-subunit of F_1 and ab_2-subunits of F_o together constitute the stator (the grey part in figure 1), which is attached to the $\alpha_3\beta_3$ hexamer through δ. The a-subunit in the membrane apposes the c_{12} cylinder. Protons flow through the interface between the a-subunit and the c_{12}-subunits and rotate c_{12} against a. Recent electron micrographs (Boekema *et al.* 1997; Wilkens & Capaldi 1998) of ATP synthase show a thin, second stalk at a position corresponding to the grey stator in figure 1. One difficulty in this view is that the $\alpha_3\beta_3$ hexamer should, on time-average, be threefold symmetrical, yet there is one $\delta b_2 a$ stator attached to it. Also, the c_{12} cylinder is presumably 12-fold symmetrical, whereas γ needs to be firmly attached to c_{12} but lacks its symmetry. These may not be serious problems, but certainly detract from the elegance of Boyer's proposal.

3. IMAGING F_1 ROTATION

(a) *A huge tag revealed rotation in a single F_1 molecule*

To prove that F_1-ATPase is a rotary motor that consistently rotates in a unique direction, and to investigate the details of the rotational characteristics, we imaged the rotation of single F_1 molecules under a microscope (Noji *et al.* 1997; Yasuda *et al.* 1998). A subcomplex of F_1, $\alpha_3\beta_3\gamma$ (hereafter we refer to this subcomplex simply as F_1) derived from a thermophilic bacterium, was fixed on a glass surface, or on a submicrometre-sized plastic bead sitting on a glass surface, through histidine residues engineered at the bottom of the β-subunits. A micrometre-long actin filament was attached, through biotin–streptavidin links, to the protruding portion of γ above the $\alpha_3\beta_3$ hexamer (figure 2*a*). The actin filament was fluorescently labelled, and observed under a fluorescence microscope. When ATP was infused into the observation chamber, the filament began to rotate, as shown in figure 2*b*.

Only a few per cent of the actin filaments in the observation chamber rotated, but those that rotated did so in the counterclockwise direction, as predicted from the Walker structure. This suggests that a structure similar to the Walker structure, in which rotation was inhibited for crystallization, appears as an active intermediate in the rotational kinetics. Some filaments made hundreds of revolutions without noticeable reversal.

Most of the filaments did not rotate, but there are reasons for this. First, the filaments are likely to stick on the surface, because the height of F_1 is only *ca.* 10 nm, whereas the actin filaments were 1 μm or longer. It would be difficult for F_1 to keep the filament level. Indeed, putting F_1 on a 0.2-μm bead helped to increase the number of rotating filaments. However, the increase was not dramatic because we could not control the position of F_1 such that it would be precisely at the top of the bead. Second, F_1-ATPase tends to be inhibited by its reaction product, MgADP (see §4(b)). Third, protein molecules on a surface are often damaged or denatured. In fact, the major job of single-molecule researchers is to find an appropriate surface for the protein of interest, a 'mission impossible' if none of the molecules are to be sacrificed.

In figure 2*b*, the actin filament rotates around its centre, like a propeller. The propeller rotation shows that the whole γ-subunit slides against the $\alpha_3\beta_3$ stator over unlimited angles. It is not a fake rotation one could make, for example, by holding an end of a rod over one's head and twisting one's wrist without changing the grip. If one holds the middle of a long rod, one cannot rotate it without occasional releases. Thus, the propeller rotation of the actin filament cannot be made by torsion within the γ-subunit. The γ-subunit has to be separate from the $\alpha_3\beta_3$ cylinder and truly rotate against the hexamer. Also, the propeller rotation cannot be supported by two or more F_1 molecules. Thus, F_1-ATPase is a rotary motor made of a single molecule. Its size being *ca.* 10 nm, the F_1-ATPase is the smallest rotary motor known. Counterclockwise rotation has also been demonstrated for F_1 from *Escherichia coli* (Omote *et al.* 1999; Noji *et al.* 1999) and chloroplast (Hisabori *et al.* 1999).

Of the five kinds of subunit in F_1, $\alpha_3\beta_3\gamma$ suffice for rotation. Cross-linking studies (Aggeler *et al.* 1997) have indicated that ε is probably a part of the rotor and δ belongs to the stator. When an actin filament was bound to ε instead of γ, the filament also rotated counterclockwise, although the rotary speed was somewhat lower (Kato-Yamada *et al.* 1998).

(b) *Stepping rotation*

When ATP concentration was reduced, the rotation became stepwise, as shown in figure 3. The step size of 120° is consistent with, though not a necessary consequence of, the basic threefold symmetry of the $\alpha_3\beta_3$ stator. We have been unable to resolve sub-steps at the highest temporal resolution, of 5 ms, achieved so far. Note that the motor made a clear back-step at *ca.* 45 s in figure 3. A molecular machine must occasionally make mistakes. The 120° steps have also been confirmed in F_1 without actin (K. Adachi, unpublished data), by attaching a fluorophore on γ and observing the polarization of the fluorescence from the single fluorophore under a microscope (Sase *et al.* 1997; Ha *et al.* 1998). Thus, stepping is not an artefact caused by friction between the actin filament and the stator cylinder with pseudo-threefold symmetry.

4. THE KINETICS OF ATP HYDROLYSIS

The hydrolysis kinetics of F_1-ATPase is complicated, because of the presence of three catalytic sites (and three non-catalytic sites that also bind a nucleotide), and of the

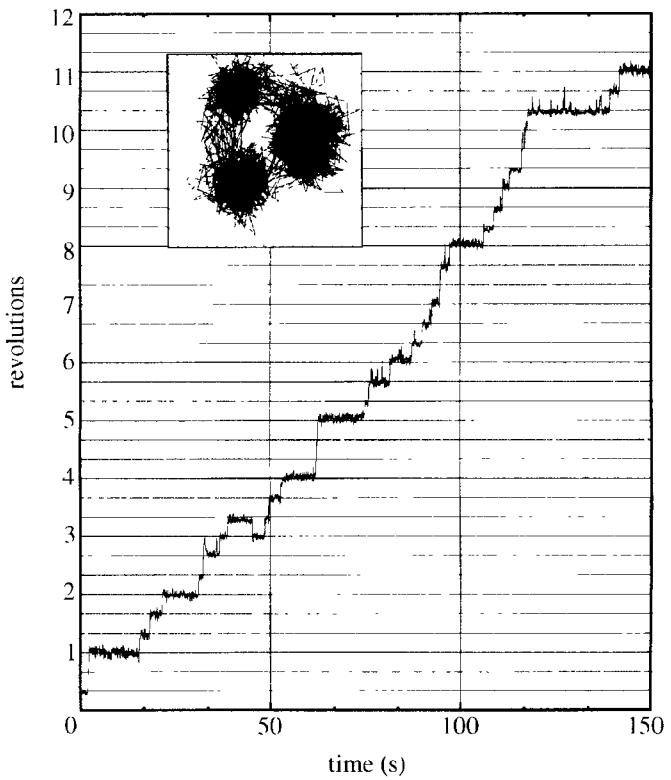

Figure 3. Stepping rotation of F_1 at 20 nM ATP (Yasuda *et al.* 1998). Inset shows the trace of the centroid of the actin filament.

MgADP inhibition. It is difficult to extract a unified view from the literature, partly because the effect of the (almost inevitable) MgADP inhibition on the experimental results is often ignored or not mentioned. The description below is an arbitrary selection from the literature. For comprehensive reviews, see Boyer (1993, 1997, 2000).

(a) *Three modes of hydrolysis reaction*

At extremely low ATP concentrations, at most one catalytic site of F_1 is filled with a nucleotide. Under this uni-site regime, ATP and its hydrolysis products are in equilibrium in the catalytic site, and the products are very slowly released into the medium (figure 4). For mitochondrial F_1, Cunningham & Cross (1988) describe the uni-site kinetics as

$$\begin{array}{lcl} & F_1 + ATP & \\ k_{+1} = 6\times10^{6}\,M^{-1}s^{-1} & \rightleftarrows & k_{-1} \leqslant 7\times10^{-6}\,s^{-1} \\ & F_1\cdot ATP & \\ k_{+2} = 12\,s^{-1} & \rightleftarrows & k_{-2} = 24\,s^{-1} \\ & F_1\cdot ADP\cdot Pi & \\ k_{+3} = 4\times10^{-3}\,s^{-1} & \rightleftarrows & k_{-3} \geqslant 5\times10^{-6}\,M^{-1}s^{-1} \\ & F_1\cdot ADP + Pi & \\ k_{+4} = 4\times10^{-3}\,s^{-1} & \rightleftarrows & k_{-4} = 4\times10^{6}\,M^{-1}s^{-1} \\ & F_1 + ADP + Pi & \end{array}$$

$$k_{+1}/k_{-1} = K_1 \geqslant 10^{12}\,M^{-1},$$
$$k_{+2}/k_{-2} = K_2 = 80.5,$$
$$k_{+3}/k_{-3} = K_3 \leqslant 8\times10^{-2}\,M,$$
$$k_{+4}/k_{-4} = K_4 = 10^{-9}\,M,$$

where Pi is inorganic phosphate, k_{+i} and k_{-i} are forward and backward rate constants, and $K_i = k_{+i}/k_{-i}$ are the equilibrium constants. Unlike myosin (Taylor 1979), the rates of ADP and phosphate releases from F_1 appear to be similar, and thus phosphate release does not necessarily precede the release of ADP. A more recent study (Milgrom *et al.* 1998) indicates that the rates of product release (k_{-3} and k_{+4}) are an order of magnitude higher and K_2 is about 0.8. The rate of ATP binding to a second catalytic site (at a higher ATP concentration) is similar to k_{+1} above (Cross *et al.* 1982). Thus, uni-site catalysis is expected when free ATP concentration is below 1 nM. Uni-site catalysis has been reported to take place even when rotation of γ is prohibited (García & Capaldi 1998). This, however, does not necessarily exclude the possibility that rotation might still accompany uni-site catalysis.

Binding of a second ATP greatly promotes the rate of hydrolysis on the first site and particularly the rates of product release from the first site (Boyer 1993, 1997). The positive cooperativity in catalysis and negative cooperativity in nucleotide binding result in an increase in the overall hydrolysis rate by a factor of more than 10^5. At submicromolar ATP concentrations, hydrolysis occurs in the bi-site mode where, at most, two catalytic sites are filled with a nucleotide (figure 4). Our result in figure 3, the observation of rotation at 20 nM ATP, then indicates that bi-site hydrolysis accompanies rotation.

At higher ATP concentrations, it has often been suggested that hydrolysis proceeds in the tri-site mode with a moderate acceleration from the bi-site mode. One indication has been that the hydrolysis rate over submicromolar to millimolar ATP concentrations, above the uni-site range, cannot be described by simple Michaelis–Menten kinetics (see, for example, dashed line in figure 6) and requires two sets of Michaelis parameters, one presumably corresponding to a second site and the other to the third site. The claim of 'acceleration' is based on an approximately tenfold difference in the values of V_{max}. Unlike the transition from uni-site to bi-site where doubling ATP concentration more than doubles the hydrolysis rate, however, the acceleration to tri-site is not readily apparent in raw data. The deviation from a simple kinetics is not large (see the example in figure 6), and is variable depending on preparations, possibly due to variability in the degree of MgADP inhibition. Milgrom *et al.* (1998) have reported that, when care was taken to avoid inhibition, one set of parameters ($K_m = 130\,\mu M$ and $V_{max} = 700\,s^{-1}$ for mitochondrial F_1 at 25 °C) sufficed for the description of the multi-site kinetics up to 1 mM ATP. Thus, F_1-ATPase may not adopt the tri-site mode. Strong support for tri-site catalysis has come from the measurement of site occupancies through the nucleotide-induced quenching of tryptophans in the catalytic sites (Weber *et al.* 1993). The interpretation of the fluorescence signal, however, is not absolutely unambiguous (Milgrom *et al.* 1998).

Because the rotation of γ has been demonstrated in the bi-site regime, we think that the bi-site mode is fundamental at least for the mechanism of rotation. Bi-site hydrolysis in ATP synthase pumps protons (Muneyuki & Hirata 1988).

(b) *MgADP inhibition*

Figure 5 shows typical time-courses of ATP hydrolysis at three ATP concentrations. The $\alpha_3\beta_3\gamma$ subcomplex of

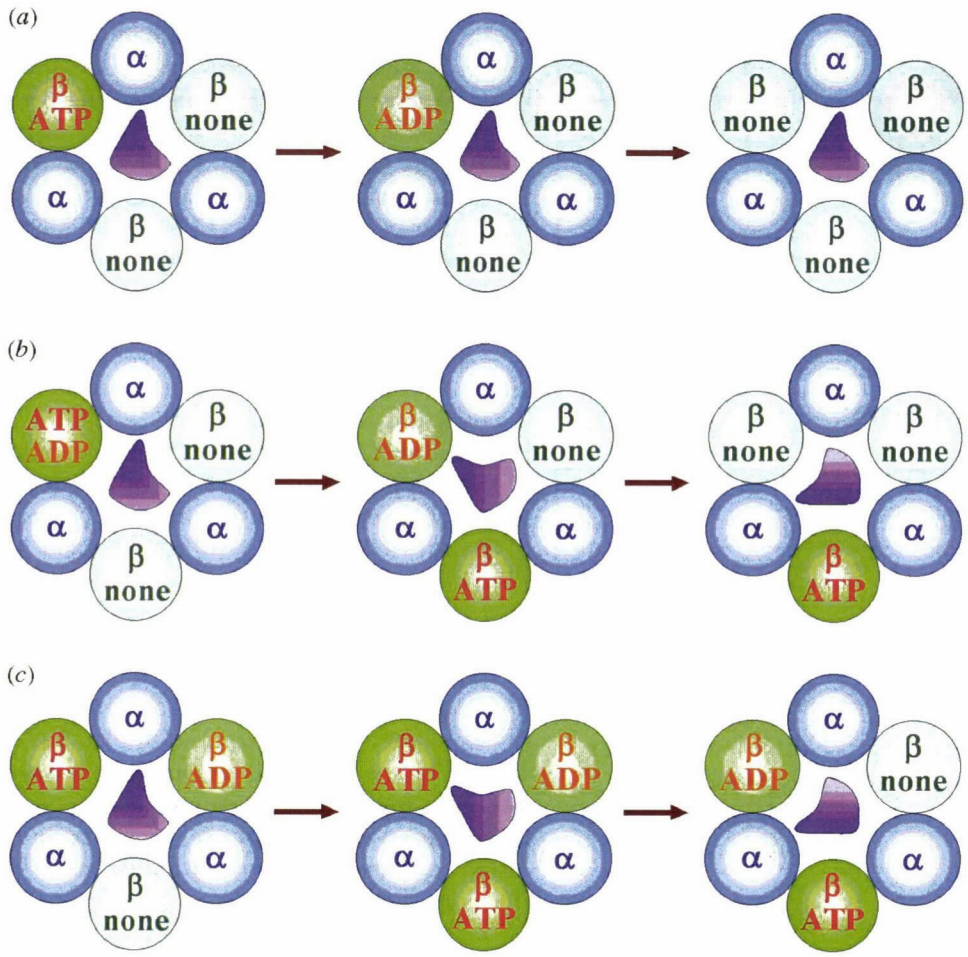

Figure 4. Three modes of ATP hydrolysis by F_1-ATPase. The timing of γ rotation, and whether γ rotates in the uni-site mode, are yet to be determined. (*a*) Uni-site hydrolysis, [ATP] < 1 nM; (*b*) bi-site hydrolysis, [ATP] *ca.* 1 μM; (*c*) tri-site hydrolysis, [ATP] > 100 μM.

bacterial origin used to demonstrate the γ rotation was suspended in solution without attaching actin. The amount of ATP hydrolysed was estimated by regenerating ATP by pyruvate kinase and coupling the reaction to the oxidation of NADH by lactate dehydrogenase (Kato *et al.* 1995). As seen, the rate of hydrolysis gradually decreased to less than half the initial value. This is the so-called MgADP inhibition, where the hydrolysis product MgADP is tightly bound to a catalytic site and inhibits further turnover of the enzyme (Boyer 1997, 2000).

The inhibition does not proceed to completion, because slow binding of ATP to non-catalytic sites tends to displace the tightly bound MgADP in the catalytic site. Under certain conditions, the hydrolysis kinetics becomes tri-phasic: full activity in the initial phase slows down due to the inhibition, and then follows partial recovery toward an intermediate hydrolysis rate (e.g. 60 μM in figure 5). In a mutant where ATP binding to the non-catalytic sites was prohibited, there was no recovery and the inhibition proceeded to completion (Matsui *et al.* 1997). In the assay in figure 5, the hydrolysis products were immediately converted back to ATP. If ATPase kinetics is measured without a regeneration system by, for example, chromatographic assay of ATP and ADP, the enzyme is more severely inhibited (E. Muneyuki, personal communication). Thus, a small amount of MgADP in the medium promotes the inhibition.

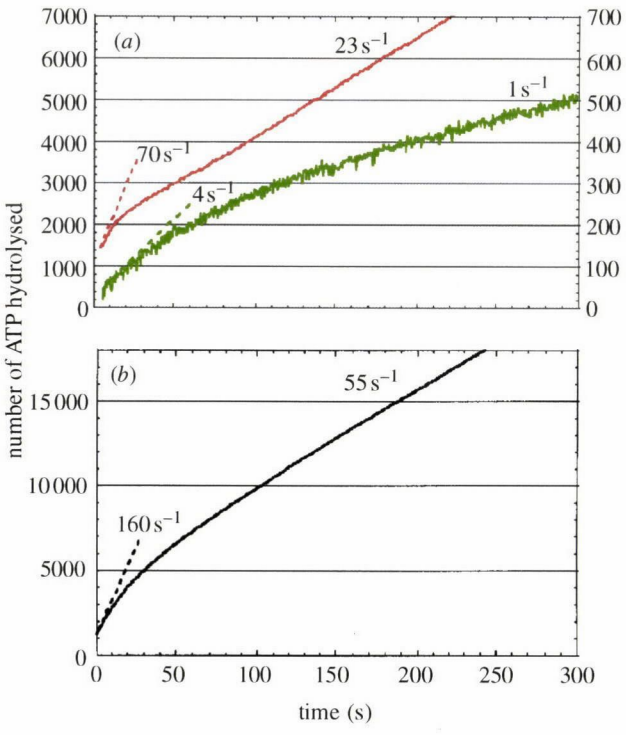

Figure 5. Time-courses of ATP hydrolysis measured in solution at 23 °C (H. Noji, unpublished data). (*a*) [ATP] = 60 μM shown in red, [ATP] = 0.6 μM shown in green; (*b*) [ATP] = 2 mM.

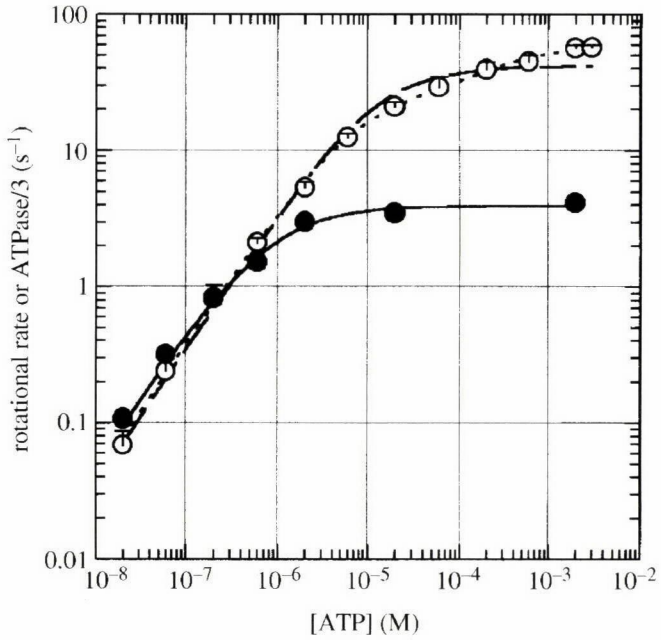

Figure 6. Comparison of the hydrolysis and rotational rates (Yasuda *et al.* 1998). The hydrolysis rate V (open circles) was measured in solution, and was fitted with $V = k_{cat}[ATP]/([ATP] + K_m^{hyd})$, where $k_{cat} = 125\,s^{-1}$ and $K_m^{hyd} = 12\,\mu M$ (dashed line), or with $V = (k_{cat}^a K_m^{hydb}[ATP] + k_{cat}{}^b[ATP]^2)/([ATP]^2 + K_m^{hydb}[ATP] + K_m^{hyda}K_m^{hydb})$, where $k_{cat}^a = 75\,s^{-1}$, $k_{cat}^b = 177\,s^{-1}$, $K_m^{hyda} = 6.6\,\mu M$, and $K_m^{hydb} = 285\,\mu M$ (dotted line). The rotational rate v was measured by attaching a short (0.8–1.2 μm) actin filament (closed circles), and was fitted with $v = v_{max}[ATP]/([ATP] + K_m^{rot})$ where $v_{max} = 3.9\,rev\,s^{-1}$ and $K_m^{rot} = 0.8\,\mu M$ (solid line).

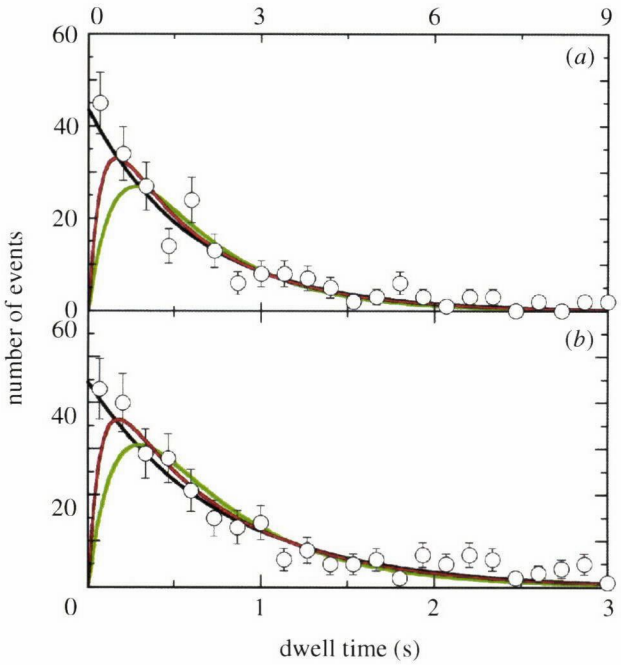

Figure 7. Histograms of dwell times between steps (Yasuda *et al.* 1998). (*a*) [ATP] = 20 nM; (*b*) [ATP] = 60 nM. Black lines indicate exponential fits: constant × exp($-k_{on}$[ATP]t), where k_{on} is the rate constant for ATP binding ($2.7 \times 10^7\,M^{-1}\,s^{-1}$ at 20 nM ATP and $2.2 \times 10^7\,M^{-1}\,s^{-1}$ at 60 nM) and t is the dwell time. Green and red lines show fits with two exponentials (simultaneous consumption of rapidly and slowly bound ATP): constant × {exp($-k_{on}^{slow}$[ATP]t) − exp($-k_{on}^{rapid}$[ATP]t)}, where k_{on}^{rapid} was fixed at $1.0 \times 10^8\,M^{-1}\,s^{-1}$ (green lines) and $2.5 \times 10^8\,M^{-1}\,s^{-1}$ (red lines).

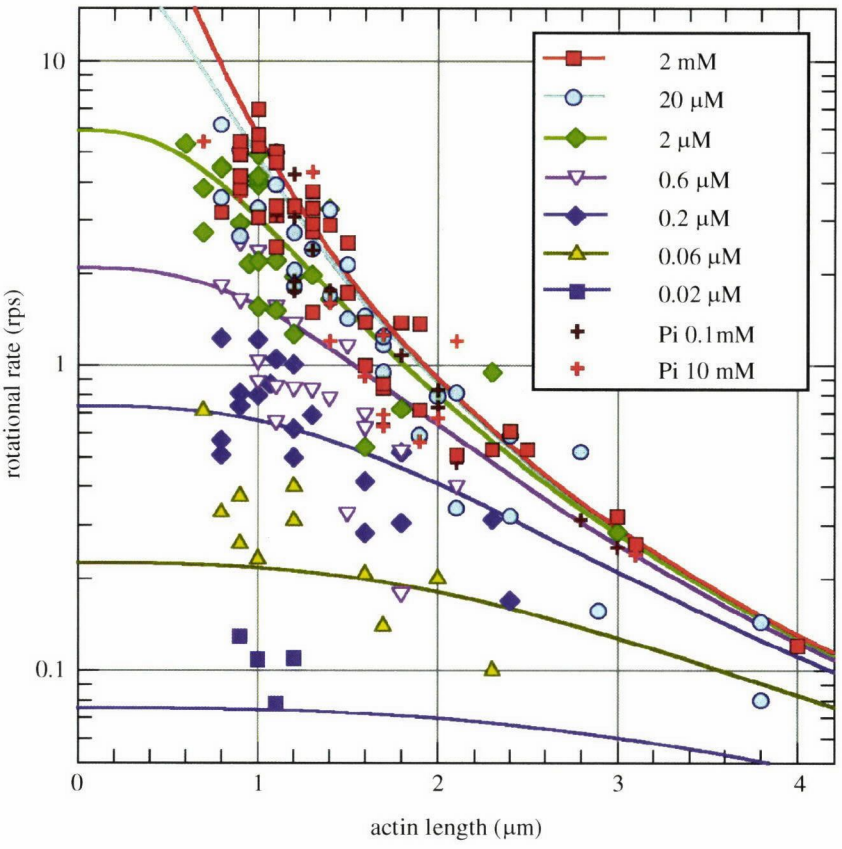

Figure 8. Load (actin length) and ATP dependence of the average velocity of rotation (Yasuda *et al.* 1998). ATP concentrations are shown in the key. ADP and phosphate concentrations were not controlled, except for the + symbols for which [ATP] = 2 mM and [ADP] = 10 μM. Lines are calculated as $1/(3\tau_{120^\circ})$, where $\tau_{120^\circ} = \tau_{ATP} + \tau_{step}$ is the time per 120° step, τ_{ATP} is the ATP cycle time at no load estimated from figure 6, and $\tau_{step} = (2\pi/3)\xi/\mathcal{N}$, where $\mathcal{N} = 40$ pN nm and ξ is the friction coefficient in equation (1). It is likely that τ_{ATP} is overestimated by *ca.* 30% because of the MgADP inhibition, and thus the calculated velocities (lines) at low [ATP] are underestimated by the same proportion.

The MgADP inhibition would economize by preventing futile consumption of ATP in cells, but it is a nuisance for researchers analysing the ATPase kinetics. Unless tightly bound nucleotides are completely removed from F_1-ATPase prior to measurement, which is not often the case, the preparation will contain an unknown amount of inhibited enzyme, possibly most of the molecules. Results on such a preparation, or on the 'steady-state' ATPase, have to be interpreted with caution.

The Walker structure is probably an MgADP-inhibited form (Abrahams *et al.* 1994). As already pointed out, the fact that the arrangement of nucleotides in this structure is consistent with the sense of observed rotation suggests that the Walker structure resembles an active intermediate that appears during rotation. An attempt to 'freeze' F_1-ATPase in this structure by cross-linking supported this view (Tsunoda *et al.* 1999). Presumably, the inhibited structure represents one of the most stable forms of this enzyme, and is separated by a relatively small activation barrier from the major kinetic pathway of the hydrolysis reaction. In this regard, it is worth noting that MgADP inhibition does not operate during synthesis (Boyer 1997, 2000), and synthesis renders inhibited enzyme back to a form capable of hydrolysis (Galkin & Vinogradov 1999). Free energy obtained by clockwise rotation of γ will lift the enzyme from the bottom of the potential well back to the major pathway, or to a possibly different path for the synthesis.

(c) *Three ATP molecules per turn*

The rate of ATP hydrolysis and the rate of γ rotation are compared in figure 6 (Yasuda *et al.* 1998). The hydrolysis rate was measured as the initial rate (figure 5), and is divided by three to facilitate the comparison. The rotational rate was measured with an actin filament of length 0.8–1.2 μm. At ATP concentrations above 1 μM, the rotational rate saturated because of the frictional load imposed on the rotating filament (see §5(a)). Below 1 μM where ATP binding was rate limiting, the rotational rate and one-third of the hydrolysis rate grossly agreed with each other, suggesting that three ATP molecules are consumed per turn.

The agreement was not perfect, a likely cause being the MgADP inhibition. Whereas the rotational rate in figure 6 is the average over selected filaments that rotated vigorously and continuously without unnatural pauses, which represented at most a few per cent of the filaments on the surface, the hydrolysis rate is the ensemble average over all enzyme molecules in the solution. Some molecules in the solution may have been inhibited from the beginning. These samples (also those shown in figure 5) contained about 0.3 M of tightly bound nucleotide per mole of F_1, implying that 30% may well have been inhibited at the beginning. Also, the initial rate was measured over the first 3–13 s and significant inhibition might have occurred during these periods.

The MgADP inhibition may also be responsible for the failure in fitting the hydrolysis rate with a simple Michaelis–Menten kinetics (solid line in figure 6). Another possible reason is that the non-catalytic sites tend to be filled with ATP earlier at higher ATP concentrations; the hydrolysis rate might be somewhat higher when the non-catalytic sites bind ATP.

(d) *One ATP molecule per step*

In figure 6, the rotational and hydrolysis rates are proportional to the ATP concentration in the sub-micromolar range. This suggests that, at least in this range, both processes are fuelled by individual ATP molecules, not by the combination of two or more ATP molecules. To further confirm this point, we analysed the dwell times between rotary steps at very low ATP concentrations where 120° steps were clearly resolved (figure 3).

Figure 7 shows histograms of the dwell times (Yasuda *et al.* 1998). If each 120° step is driven by one ATP molecule, the histogram should be exponential, as was indeed the case (black lines in figure 7). If, on the other hand, two or more ATP molecules were required for each step, the histogram would have started from the origin at the lower left, as in the green and red lines, because simultaneous arrivals of two or more ATP molecules should be a rare event. The data point to one ATP molecule per step. Experimental distinction, however, is not easy when binding of the first ATP molecule is always much faster than the second: in this case the rise of the histogram near the origin will be very steep (compare the green and red lines). As seen, the experimental histograms cannot exclude the two-ATP-molecule case if the rate constant for the first binding is much larger than $10^8\,M^{-1}s^{-1}$. Such a high rate (essentially diffusion limited) has not been reported for the hydrolysis kinetics of F_1-ATPase, whether for uni-, bi-, or tri-site modes.

For the scenario of one ATP molecule per step, the rate constant for ATP binding is estimated from the exponential constant for the histogram: $2.7\times10^7\,M^{-1}s^{-1}$ at 20 nM ATP and $2.2\times10^7\,M^{-1}s^{-1}$ at 60 nM ATP. These values agree, within experimental uncertainty, with each other and also to the slope of hydrolysis rate versus ATP concentration (figure 6). Literature values are scattered mostly between 10^5 and $10^7\,M^{-1}s^{-1}$ (both uni-site and multi-site), and our values here belong to the high end (possibly indicative of the absence of MgADP inhibition).

Judging from figures 6 and 7, we are fairly sure that each 120° step is driven by the hydrolysis of one ATP molecule. Of course this does not necessarily mean that the ATP molecule just bound is hydrolysed and released into the medium during one 120° step: it is highly likely that one ATP molecule is bound to a catalytic site and products are released from a different site, as shown in figure 4. We are less certain about the reverse statement, that each ATP hydrolysis always accompanies rotation. This is suggested by figure 6, but the hydrolysis rate in the complete absence of MgADP inhibition might be somewhat higher than the rotational rate. Futile consumption of ATP, as occurs in the myosin–actin system (Huxley 1957), cannot be ruled out completely.

5. MECHANICAL PROPERTIES OF THE F_1 MOTOR

(a) *The actin filament is a heavy burden for F_1*

When we observed the rotation of actin filaments attached to γ, we noticed that longer filaments tended to rotate slower. This seemed reasonable, because the hydrodynamic friction against a rotating filament is essentially

proportional to the cube of its length L: the frictional drag coefficient ξ is given by (Hunt *et al.* 1994)

$$\xi = (4\pi/3)\eta L^3/[\ln(L/r) - 0.447], \quad (1)$$

where $\eta (= 10^{-3}\ \mathrm{N\ m^{-2}\ s})$ is the viscosity of the medium, and $r (= 5\ \mathrm{nm})$ is the radius of the filament. Equation (1) applies to a filament rotating around one of its ends; such filaments were selected for analysis.

The rotational rate ω (in radians per second ($\mathrm{rad\ s^{-1}}$)) is related with ξ and the torque N of the motor by

$$N = \omega\xi. \quad (2)$$

To rotate an actin filament at the observed speed, the F_1 motor has to produce an enormous torque. For example, an actin filament of length 1 μm rotated at $6\ \mathrm{rev\ s^{-1}}$ ($\cong 40\ \mathrm{rad\ s^{-1}}$). This requires a torque of about 40 pN nm. If this torque is generated at the γ–β interface at the radius of 1 nm, the force that let γ slide past β amounts to 40 pN, the largest among the forces produced by known nucleotide-driven motors (Kinosita *et al.* 1998).

(b) *The F_1 motor produces a constant torque*

In figure 8, the rotational rates of actin filaments that made at least five continuous revolutions without unnatural pauses are plotted against the filament length. As seen, the data points at different ATP concentrations, distinguished by different symbols, fall approximately on the respective smooth lines that have been calculated on the assumption of constant torque. That is, we assumed that (i) F_1 produces a constant torque of 40 pN nm irrespective of the frictional load (actin length) or of the ATP concentration, and (ii) the time per one-third of a revolution is simply the sum of the ATP cycle time at no load (taken from figure 6) and the time needed to rotate the actin filament by 120° under the torque of 40 pN nm. The latter—the time needed to move the filament—was assumed to be given by $2\pi/3\ \mathrm{rad} (= 120°)$ divided by $\omega = N/\xi$, where the torque N was assumed to be 40 pN nm for all curves.

The fair agreement between the data and the curves in figure 8 indicates that the F_1 motor produces a constant torque of 40 pN nm over the range of rotational rates between 0.1 and $10\ \mathrm{rev\ s^{-1}}$ and over the range of ATP concentrations between 20 nM and 2 mM. The slower rate for a longer filament is explained by the higher friction, and the slower rate at a lower ATP concentration is due to the lower rate of ATP binding. The constant torque output of the F_1 motor is contrasted with the force of the myosin–actin motor, which decreases with the sliding speed (Huxley 1957). The bacterial flagellar motor produces a constant torque when the rotary speed is not high (Berg & Turner 1993). In this regard, the rotational rates of the F_1 motor in figure 8 are also low compared to the expected unloaded rate: figure 6 indicates that the maximal rate of ATP hydrolysis in the absence of actin is about $180\ \mathrm{s^{-1}}$, implying that the maximal rotational rate will exceed $60\ \mathrm{rev\ s^{-1}}$ at high ATP concentrations. Indeed, recent measurements show unloaded rotation at *ca.* $100\ \mathrm{rev\ s^{-1}}$ at 23 °C (R. Yasuda, unpublished data). The torque performance at high rotational rates remains to be determined.

(c) *The energy conversion efficiency can be nearly 100%*

The torque of 40 pN nm times the angular displacement of $2\pi/3\ \mathrm{rad} (= 120°)$, *ca.* 80 pN nm, is the mechanical work done in a 120° step. This value of 80 pN nm is close to the free energy obtained from the hydrolysis of one ATP molecule under intracellular conditions: $\Delta G = \Delta G_0 + k_B T \ln[\mathrm{ADP}][\mathrm{Pi}]/[\mathrm{ATP}]$, where $\Delta G_0 = -50$ pN nm is the standard free-energy change per molecule for ATP hydrolysis at pH 7, $k_B T = 4.1$ pN nm is the thermal energy at room temperature, and intracellular [ATP] and [Pi] are both in the order of 10^{-3} M, giving ΔG of −100 pN nm for [ADP] = 10 μM and −90 pN nm for [ADP] = 100 μM. Thus, the F_1 motor appears to work at an efficiency close to 100%.

Most of the observations in figure 8 were made in the presence of the ATP regenerating system, and thus the concentrations of ADP and phosphate were minimal, implying that $|\Delta G|$ was much larger than 80 pN nm. To confirm the high efficiency, therefore, we conducted experiments in the absence of the regenerating system, at [ATP] = 2 mM, [ADP] = 10 μM, and [Pi] at either 0.1 or 10 mM (crosses in figure 8). Calculated ΔG are −110 pN nm for [Pi] = 0.1 mM and −90 pN nm for [Pi] = 10 mM. As seen, the rotational rates under these conditions are also on the red line for the torque of 40 pN nm, indicating that the work per step is also *ca.* 80 pN nm. The F_1 motor is made to produce a constant work per step of *ca.* 80 pN nm, and it can work even when the energy supply per step is as low as 90 pN nm.

The scatter of data in figure 8 may make the claim of near 100% efficiency dubious. In fact, there were many more actin filaments, not shown in the figure, that rotated with irregular intermissions and thus gave lower average speed. There are, however, many factors that may impede the filament rotation, as already discussed. Another factor that has not been mentioned is that the effective viscosity close to a surface is higher than in the bulk for which equation (1) applies (Hunt *et al.* 1994): for the actin filament close to the surface, the effective viscosity can be three times as high (Noji *et al.* 1997). Of the data points in figure 8, those that are slow may have been affected by these impeding factors. On the other hand, we cannot think of experimental uncertainties that would lead to a gross overestimation of the rotational rate, determined as the average over five or more revolutions. Actin length determined from the fluorescence image is subject to error, but the error is relatively small for a long filament. In some cases, the filament was slightly curved in the image plane, or the rotating end floated from the surface. The curvature or inclination, however, do not affect the interpretation seriously, because they change the effective length as a cosine of the angle; deviation by 20° is noticeable, for which the ratio of the arc length to its chord is $(\theta/2)/\sin(\theta/2) = 1.01$ (close to 1).

We also analysed the speed of rotation in individual 120° steps observed at low ATP concentrations (Yasuda *et al.* 1998; also see §5(d)). The torque estimated from equation (2) for ω measured in each step averaged 44 pN nm, and hence the work per step averaged *ca.* 90 pN nm, in agreement with the values obtained from the rotational rate averaged over many revolutions.

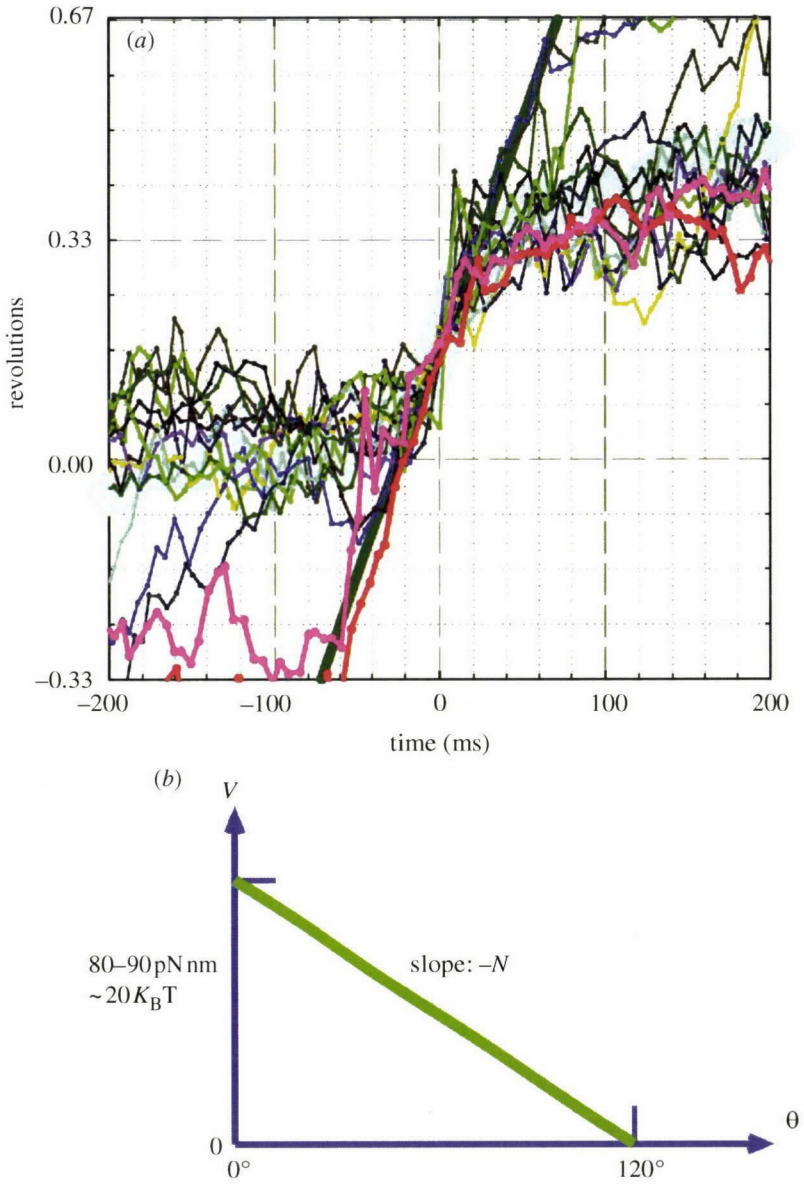

Figure 9. Time-courses of individual steps (Kinosita *et al.* 2000). (*a*) Steps were measured at 0.2 μM ATP for F_1 bearing a 1.0-μm filament. Traces for individual steps are superimposed such that the middle of each step is located at time zero. Rapid succession of two steps are seen in two traces (red and pink). The thick cyan line shows the average of all traces. The thick dark-green line shows a constant-speed rotation at 44 rad s^{-1}, corresponding to a torque of 44 pN nm. (*b*) Rotational potential, $V(\theta)$, deduced from (*a*).

Interestingly, the occasional backward steps were as fast as forward steps, implying that the work needed to produce the back step is also *ca.* 90 pN nm. Presumably, a backward step also consumes one ATP molecule. In the bi-site catalysis (figure 4), two catalytic sites remain empty for most of the time. Binding of ATP to the wrong one of the two may well cause the backward step. Or, the back step may result from premature dissociation of newly bound ATP before hydrolysis.

(d) *The torque is constant over the rotational angle*

In figure 9*a*, individual steps for a 1-μm filament rotating at 0.2 μM ATP are superimposed on each other. As seen in the thick cyan line showing the average, the steps were made at an approximately constant speed from beginning to end. The linearity is clearer in the two curves (red and pink) showing succession of two steps starting at −0.33 revolutions.

The constant speed implies, according to equation (2), a constant torque over the stepping angle of 120°. The thick green line indicates that the constant torque is about 44 pN nm. If this torque $\mathcal{N}$ (= 44 pN nm) is derived from an angle-dependent potential energy $V(\theta)$:

$$\partial V/\partial\theta = -\mathcal{N}, \tag{3}$$

then the potential will be linearly downhill as shown in figure 9*b*. The depth of the potential is given by $\mathcal{N}$ (= 44 pN nm) multiplied by $2\pi/3$, or *ca.* 90 pN nm, in accordance with the work per step of 80–90 pN nm above. The fact that the F_1 motor produces a constant torque and constant work per step irrespective of the load, speed, and ATP concentration, is easily understood if ATP binding and subsequent hydrolysis somehow produces the rotational potential depicted in figure 9*b*.

Note that the chemical state of bound nucleotides probably changes while the motor makes a 120° step, and thus the potential in figure 9*b* does not necessarily correspond to a single chemical state. There may well be several chemical states during one mechanical step, each with a different potential. The experimental potential described here (figure 9*b*) should be regarded as an effective potential.

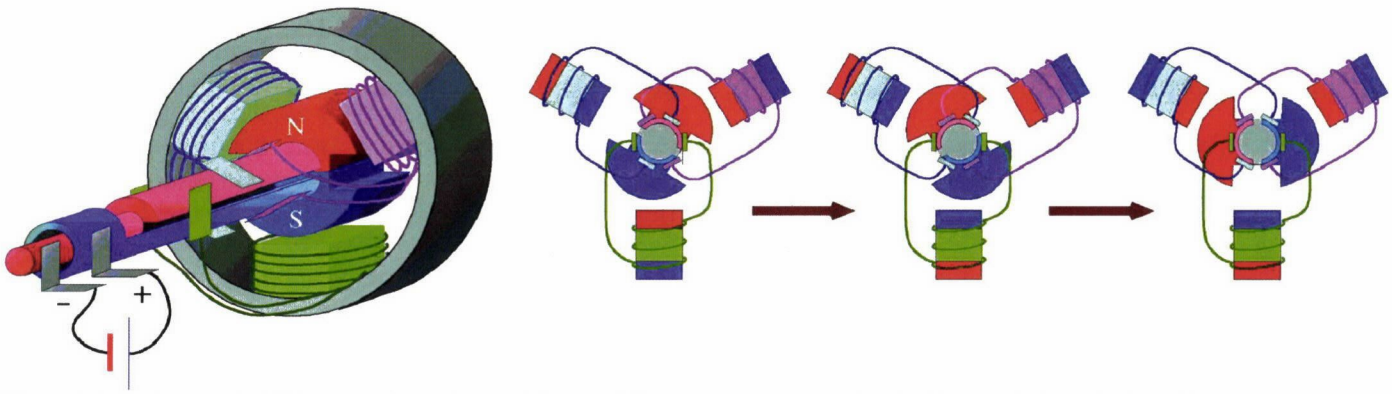

Figure 10. A three-pole DC motor (Kinosita *et al.* 2000). The commutators on the shaft control the polarity of stator magnets such that the shaft rotate continuously counterclockwise.

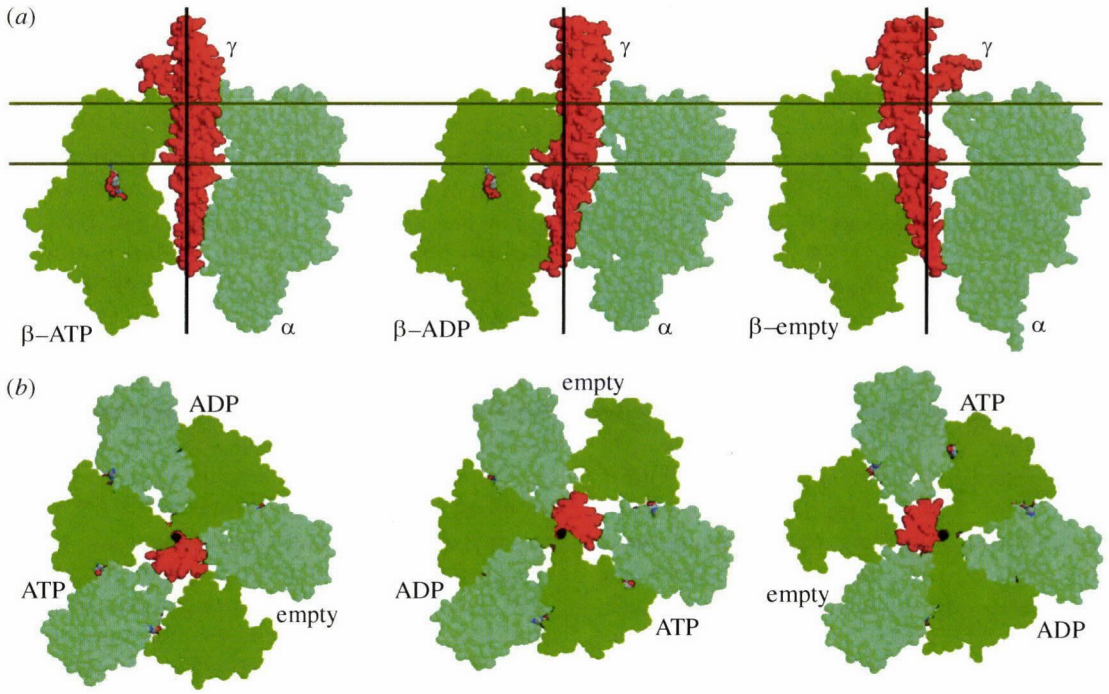

Figure 11. Nucleotide-dependent conformational changes in F_1 (Kinosita *et al.* 2000). (*a*) From the crystal structure (Abrahams *et al.* 1994), the central γ, one β to the left of γ, and one α to the right are selected and shown. The black lines indicate the rotation axis suggested by Wang & Oster (1998): the lower half of F_1 retains an approximate threefold symmetry around this axis. Nucleotides are shown in CPK colours. (*b*) Top view of sections of F_1 between the gold lines in (*a*).

The torque of 44 pN nm in figure 9*a* is the torque under the bi-site condition (submicromolar ATP). A similar torque value of 40 pN nm is deduced at 2 mM ATP (figure 8), which is in the putative tri-site regime. Thus, tri-site operation, if it occurs, does not add power to this motor.

6. POSSIBLE MECHANISMS OF ROTATION

(a) *Probable experimental facts about the F_1 motor*

Before discussing the mechanism, we summarize below probable facts about the F_1 motor. We say probable because, in general, there are few experiments from which one can draw conclusions with certainty.

(i) F_1-ATPase is a rotary motor made of a single molecule. The energy source is ATP.

(ii) $\alpha_3\beta_3\gamma$ suffice for rotation and ATP hydrolysis. γ is the rotor and $\alpha_3\beta_3$ hexamer is the stator.

(iii) The rotation of γ is counterclockwise when viewed from the F_o side.

(iv) The motor rotates in discrete 120° steps, at least at low ATP concentrations.

(v) The F_1 motor is so designed as to produce a constant torque of *ca.* 40 pN nm over broad ranges of speed and load, and of ATP concentration.

(vi) The mechanical work done in each 120° step is also constant, except for statistical variations, and amounts to 80–90 pN nm.

(vii) Hydrolysis of one ATP molecule suffices for making one step.

(viii) The energy conversion efficiency approaches 100% when the free energy of ATP hydrolysis is decreased to the intracellular level.

(ix) Bi-site catalysis supports rotation. The torque in the bi-site regime is as high as the torque in the putative tri-site regime at high ATP concentrations.

(x) Apparently, each step is made along a linear, downhill potential with a depth of 80–90 pN nm.
(xi) Back steps occur occasionally.

(b) *Analogy might help*

A mechanism that is guaranteed to rotate is shown in figure 10. This direct current (DC) motor has three driving poles in the stator part, like the F_1 motor. The motor is powered by a unidirectional current, while ATP hydrolysis is also practically unidirectional. Continuous, counterclockwise rotation of the DC motor is assured by the three pairs of switches on the shaft (commutators), which alternate the polarities of the stator magnets. The rotor is made of a static magnet. The DC motor operates in the bi-site mode in that the three stator magnets never adopt the same polarity at the same time. The DC motor becomes a DC generator if the rotor shaft is forcibly rotated in the clockwise direction. The energy-conversion efficiency of modern electrical motors is quite high, often $>95\%$. Thus, there are apparent similarities between this three-pole DC motor and the F_1 motor. There might be similarities in their operational principles, too.

The driving forces in the DC motor in figure 10 are the attraction between north and south poles and the repulsion between like poles. Wang & Oster (1998) suggest that such a push pull mechanism may also operate between the γ- and β-subunits of the F_1 motor. Figure 11*a* shows side views of the three pairs of opposing β- and α-subunits, together with the central γ, in the Walker structure. The vertical black lines show the rotational axis suggested by these authors: the bottom part of the $\alpha_3\beta_3$ stator has an approximate threefold symmetry around this axis, and thus the conformations of β and α in the bottom do not change greatly depending on the bound nucleotide. In contrast, in the upper part the βs binding ATP or ADP are bent towards, and therefore push, γ, whereas the empty β retracts and pulls γ towards it. Wang & Oster (1998) suggest that, because the central γ is slightly bent and skewed, cooperative push pull actions of the three βs would rotate γ as seen in figure 11*b*.

(c) *An F_1 model relying on switches*

Figure 12 shows a model for F_1 rotation based on the push pull mechanism above, a simplified version of the model proposed by Wang & Oster (1998). The side of γ that faces the empty β in the Walker structure is designated the north pole (N), and thus an empty β is the south pole (S). A nucleotide-carrying β is N, and repels the N face of γ and attracts its S face. By reciprocity, the S face of γ augments the affinity of opposing β for a nucleotide, and the N face decreases the affinity (the free energy is lowered when N and S oppose each other). To make this model rotate in a unique direction, additional control of nucleotide binding kinetics via 'commutators' is required. A simple example is given in figure 12*b*: binding release of ATP is allowed for β while it is on the pink side of γ, and ADP binding–release while on the green side. As shown in figure 12*c*,*d*, the switching ensures counterclockwise rotation of γ when ATP is hydrolysed; when the rotor is forced to rotate clockwise in the presence of ADP (and phosphate), ATP is synthesized. (We do not distinguish ADP, ADP plus phosphate, or phosphate alone, because the rate constants for ADP and phosphate releases are similar and because we do not yet know which event is pivotal in producing rotation.)

More elaborate switches have been proposed by Wang & Oster (1998; also see Oster & Wang 2000), and their model can account for many experimental observations including the near 100% efficiency and 120° stepping with occasional back steps. In their model, as with the model in figure 12, the motor tends to pause at angles of 60° out of phase from the Walker structure (figure 12*a*), a prediction experimentally testable. How the switching action is implemented in the protein structure is yet to be specified.

(d) *A switch-less F_1 model*

The roles of the commutators in figure 10 are to alternate the polarities of the stator magnets, and to do so at precise timings dictated by the rotational angle of the shaft. Unlike the magnet driven by direct current, the alternation of the polarity is inherent in the ATP-driven 'magnet,' where bound ATP is eventually hydrolysed and released, and the S state is restored spontaneously. Thus, only coordination of nucleotide kinetics among the three stator magnets needs be programmed. This could be done without postulating switches, as shown in figure 13, which is one version of the general model of Oosawa & Hayashi (1986).

In figure 13, the position of the 'magnetic pole' in β changes depending on the bound nucleotide. This dual-pole arrangement, combined with the higher affinity for nucleotides when the pole is closer to the S face of γ, ensures counterclockwise rotation in bi-site hydrolysis by inducing ATP binding primarily in the empty β in the counterclockwise direction (figure 13*c*). Note that the angle dependence of the nucleotide affinity is a result of the reaction to nucleotide-dependent push–pull action, and that this angle dependence does not require switches. An additional factor warranting correct rotation in this model is the higher affinity for ATP than for ADP. Because ATP hydrolysis on β is reversible (the free-energy difference between β binding ATP and β binding ADP + phosphate is small), the affinity for the hydrolysis products has to be lower in order for β to act as ATPase. In the original model of Oosawa & Hayashi (1986), near 100% efficiency was achieved for both hydrolysis and synthesis.

The essence of the dual-pole arrangement is that the hydrolysis of ATP to ADP on a β-subunit produces rotational force, and the release of ADP tends to further rotate γ. That is, direct rotational force, in addition to the pushing–pulling, is produced by a single β hydrolysing ATP. Apparently, the Walker structure gives more emphasis to pushing–pulling than direct rotation, but the structure of γ in the protruding portion has not been resolved. Also, a key intermediate(s) in actual rotation, particularly the state with only one bound nucleotide among the catalytic sites, may well have a somewhat different structure. Boyer (1997, 2000) points out that the equilibrium between ATP and its hydrolysis products on β is shifted depending on whether ATP synthase is synthesizing or hydrolysing ATP. The switch-less model predicts this behaviour because clockwise rotation of γ shifts the equilibrium towards ATP and counterclockwise rotation towards ADP (figure 13*c*,*d*).

The abstract models in figures 12 and 13 might help dissect the actual F_1 motor, but they are nothing more than a guide. The magnetic representation obscures several factors that may be important. For example, unlike the magnets, actual γ and β do not possess reflection symmetry. The force between γ and individual β must therefore be more or less asymmetrical, favouring one rotational direction over the other, as modelled by the dual poles in figure 13. Whether the rotational potential can be approximated by a simple superposition of three pairwise interactions between individual β and γ, as implied by the magnetic representation, may also be questioned. In figures 12 and 13, nucleotide kinetics on different βs are coordinated only through the rotation of γ, but βs may also communicate with each other through intervening αs.

7. PROSPECTS

(a) F_1

When do we say we have understood the mechanism of F_1 rotation, or of molecular motors in general? The F_1-ATPase has given us the unique opportunity of determining the mechanical potential that underlies the force and movement. The potential in figure 9*b*, however, is an apparent one, and we do not yet know how it is formed, except for guess work. We need to, and should be able to, determine the mechanical potential for each chemical state of the bound nucleotides. The chemical state, at least which of the binding sites are filled with a nucleotide, could be measured with single-molecule imaging of fluorescent nucleotides (Funatsu *et al.* 1995) or by introducing a probe fluorophore within the binding site (Weber *et al.* 1993). The potential could be estimated by forcibly rotating the γ-subunit, for example with optical tweezers. As we discussed above, the potential and the affinity for nucleotides are in a sense mirror images of each other: if, for example, ATP binding favours a certain orientation of γ, that orientation increases the affinity for ATP. Thus, measurement of nucleotide affinity also serves as an indirect means of estimating the potential.

When we know the potentials for individual chemical states involved in rotation, we would like to ask how each of them is formed. We wish to answer on the basis of the atomic structure of the F_1 motor. Here, the vitally important structure is yet to be solved: the structure in which only one catalytic site is filled with a nucleotide, the structure from which the bi-site stepping begins. Presumably, the transition from this structure to something similar to the Walker structure drives the rotation. The key issues are whether the two empty βs in the one-nucleotide structure adopt the conformation of the empty β in the Walker structure, and if not, whether the β with a different structure may contribute to the production of a rotational force, perpendicular to the push–pull direction in figure 11. If the force along the direction of rotation is absent, switches are required, and their physical construct should be explored.

The structure of $\alpha_3\beta_3$ hexamer without γ and without nucleotides has been solved (Shirakihara *et al.* 1997); all three β-subunits adopted a conformation closely resembling the empty β in the Walker structure. The hexamer without γ is not stable in the presence of nucleotides. In contrast, F_1-ATPase or the $\alpha_3\beta_3\gamma$ subcomplex are not stable in the absence of nucleotides (except for those from thermophilic bacteria, which are relatively stable). The γ-subunit appears to favour at least two βs to be in the nucleotide-binding conformation. F_1 bearing only one catalytic nucleotide is probably less stable, and thus shows a high affinity for a second nucleotide. Binding of ATP to the second site thus releases free energy that can be used for rotation. Because the one-nucleotide structure is probably less stable, its crystallization may not be easy. Determination of the structure may require indirect means such as the fluorescence energy transfer technique. A recent cross-linking study has suggested that the one-nucleotide structure is different from the Walker structure (Tsunoda *et al.* 1999).

Experimental determination of mechanical potential is feasible in the case of F_1, but is not easy for linear motors such as myosin and kinesin that undergo attachment–detachment cycles. These latter motors may use biased Brownian motion and selective binding as a source of movement and force, in addition to potential-driven bending (Huxley 1957; Kinosita *et al.* 1998). Such a thermal ratchet mechanism should be explored in linear motors, not in F_1 for which efficiency appears to be too high for a thermal ratchet to be operative.

The F_1 motor also offers an opportunity of demonstrating conversion of mechanical energy into chemical energy: mechanical synthesis of ATP by forced, clockwise rotation of γ. Nowadays most people believe F_1 in intact ATP synthase will do this, but experimental proof with isolated F_1 is awaited.

(b) F_o

Recently, two crystal structures have been reported that elucidate the link between γ and F_o. In a crystal of yeast F_oF_1 (Stock *et al.* 1999), a ring of ten (not 12) c-subunits was connected to γ and ε (δ in yeast nomenclature), as shown in figure 14*a*,*b* (part of the densities assigned to γ are not shown in this figure). Much of the γ-subunit was revealed (figure 14*c*,*d*) in a crystal of F_1 from *Escherichia coli* (Hausrath *et al.* 1999). Despite the differences in crystal forms, the structures of γ in the two crystals appear largely similar to each other. In particular, contact between γ and the c-ring is indicated in the yeast structure, near the putative rotation axis (black dot and line in figure 14*a*,*b*). The top of γ in figure 14*c*,*d* coincides with the contact region.

The structure in figure 14*b* suggests that, when the $\alpha_3\beta_3$ hexamer is fixed on a surface and ATP is supplied, the c-ring and ε will rotate together with γ. Indeed, an actin filament attached to ε in F_1 preparation (Kato-Yamada *et al.* 1998) or c in F_oF_1 preparation (Sambongi *et al.* 1999) was seen to rotate. Whether the c-ring (and ε) in intact ATP synthase is a rotor and rotates against its putative stator (the grey part in figure 1), however, remains to be seen. The presence of an intact stator was assumed in the F_oF_1 experiment (Sambongi *et al.* 1999), but the stator did not impede the rotation at all, and the rotation was poorly inhibited by an F_o inhibitor. In this regard, it is of interest to note that the yeast crystal contained only F_1-subunits and c, although the 'mother' solution contained a full complement of F_oF_1 (Stock *et al.* 1999). The putative stator appears to be quite labile in the presence of

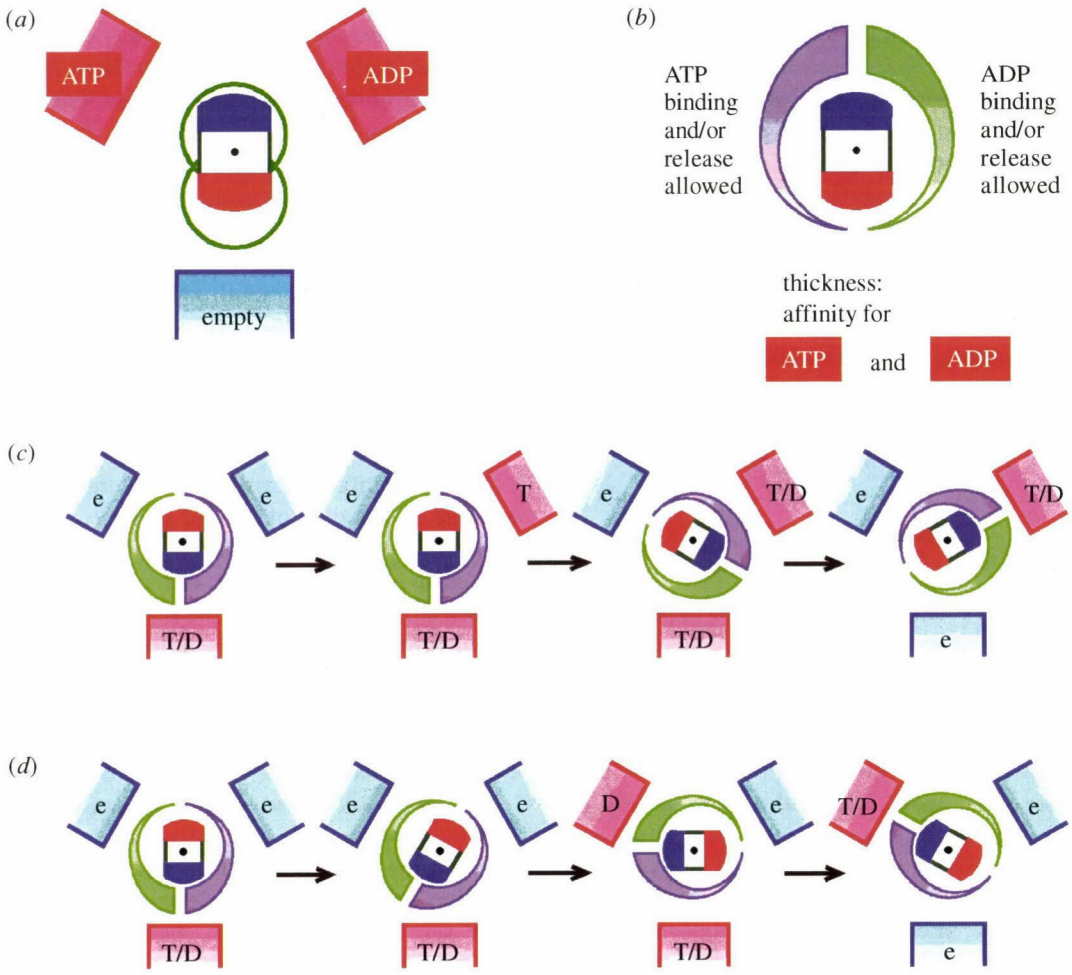

Figure 12. A simple model for the F_1 motor (Kinosita *et al.* 2000). (*a*) The Walker structure. The γ-subunit is regarded as a permanent magnet, the side of γ that faces the empty β in the Walker structure being the north pole. (*b*) The affinity for a nucleotide is higher when β is closer to the south pole of γ (strictly, the affinity for ATP is higher than that for ADP). Binding and release of ATP and ADP are kinetically inhibited on the right- and left-hand sides, respectively. (*c*) Bi-site hydrolysis ([ATP] > 0, [ADP] *ca.* 0). Bound ATP (T) is in equilibrium with ADP (D) and phosphate, and is released as ADP when a second ATP binds and rotates γ. (*d*) Bi-site synthesis ([ATP] *ca.* 0, [ADP] > 0). Forced, clockwise rotation of γ results in the uptake of ADP (and phosphate) and release of ATP.

detergent, an indispensable component for the purification of F_o or F_oF_1.

The arrangement of the c-ring in figure 14*a*,*b* apparently poses a problem. The ring is inclined against the putative rotation axis, and the attachment to γ is not at the centre of the ring. When γ rotates, the ring will make an eccentric movement. The putative stator, while moving the ring to rotate γ, has to maintain close contact with this eccentric ring by bending itself and/or γ. A proton channel(s) must also be secured. A hand-over-hand mechanism, like kinesin, may solve this dilemma, possibly by coordinating structural changes (Rastogi & Girvin 1999) in two or three c-subunits, such that at least one c-subunit is tightly bound to the stator. Occasionally, though, the grip may fail and the c-ring may swing away. Is it then ATP hydrolysis that brings the ring back to the stator surface?

If there were three stators, the c-ring would not escape, and the symmetry mismatch with the $\alpha_3\beta_3$ hexamer would also be solved. The symmetry mismatch between the three stators and ten c-subunits would be advantageous for c rotation. Two peripheral stalks, in addition to the central γ, have been seen in an electron micrograph of V-type ATPase, raising the possibility of three peripheral stalks at least for this enzyme (Boekema *et al.* 1999). Is it not possible that F_oF_1 is stripped of some stator components during detergent purification?

It is possible that, in intact synthase, γ is connected to the centre of the c-ring. A central contact with the symmetrical ring, however, would be more liable to slippage than the peripheral contact in figure 14*a*,*b*. Note that the c-ring might be neither a rotor nor a stator: it could rotate γ by a circular or conical movement without changing its orientation, like a sleeve on a crank handle.

Assignment of rotor subunits apart, the real challenge is to demonstrate, and to elucidate the mechanism of, rotation driven by proton flow. Kaim & Dimroth (1999) have shown that proton gradient alone is not sufficient for ATP synthesis and that transmembrane potential is required. We therefore like to design an experiment in which individual F_oF_1 molecules are observed while they are exposed to an electric field.

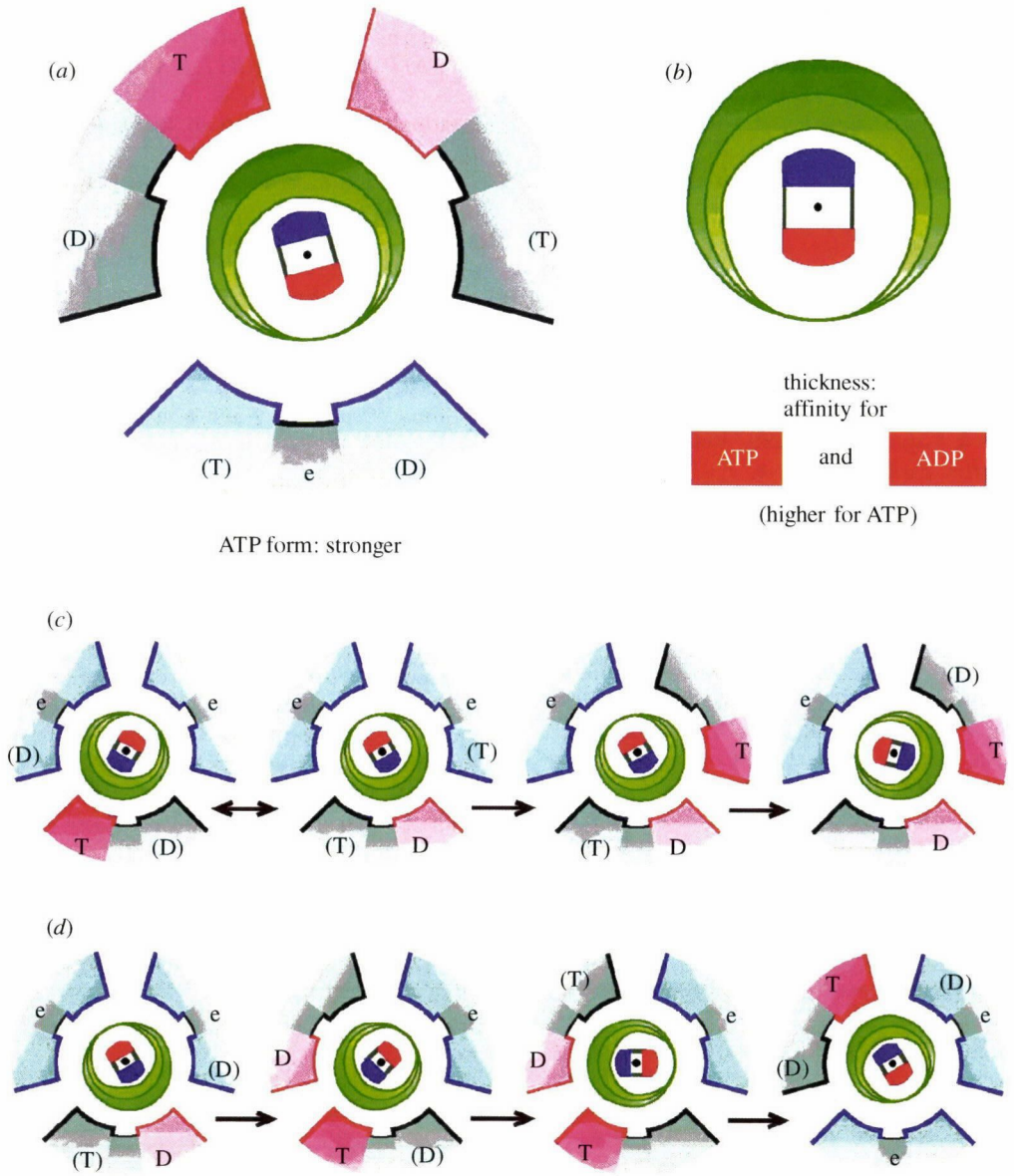

Figure 13. A switch-less model for the F_1 motor (Kinosita *et al.* 2000). (*a*) The Walker structure. Location of the magnetic pole on β changes depending on the bound nucleotide. ATP magnet is stronger than ADP magnet, and hence, (*b*) the affinity for ATP is higher than that for ADP (no switches on γ). (*c*) Bi-site hydrolysis ([ATP] > 0, [ADP] *ca.* 0). When only one nucleotide is bound, it is reversibly converted between ATP and ADP-phosphate. Comparison of affinities suggests that the most likely way of filling a second site is binding of ATP in the β in the counterclockwise direction. (*d*) Bi-site synthesis ([ATP] *ca.* 0, [ADP] > 0). When γ is forcibly rotated clockwise, the equilibrium between ATP and ADP is shifted towards ATP, which is eventually released while ADP is newly bound in the second site.

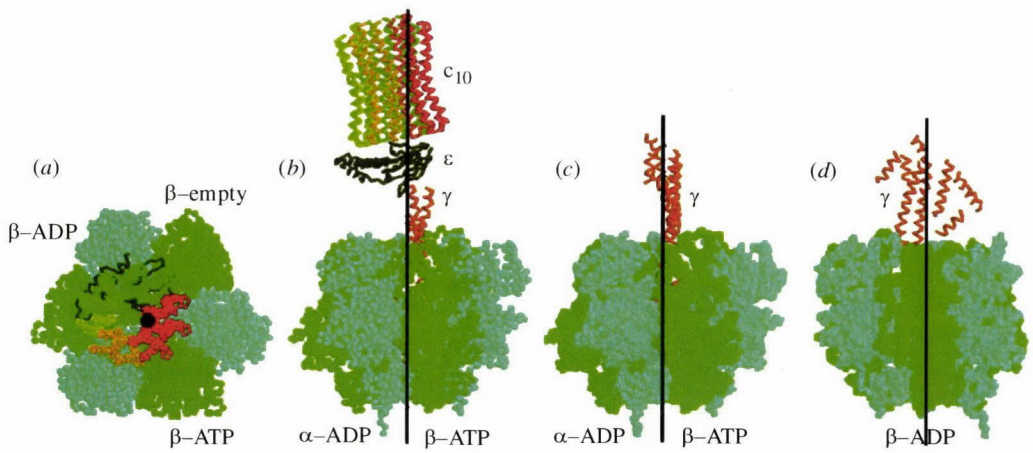

Figure 14. Crystal structures of yeast F_0F_1 (Stock *et al.* 1999) and of *Escherichia coli* F_1 (Hausrath *et al.* 1999). (*a*, *b*) Top and side views of the α-carbon model of the yeast structure. (*c*, *d*) Backbone model of the *E. coli* structure. (*d*) is rotated by 90° with respect to (*c*). Black dot in (*a*) and black lines in (*b–d*) show the putative rotation axis (Wang & Oster 1998). β-subunits in green and α-subunits in cyan.

We are grateful to Professor Masasuke Yoshida and the members of CREST Team 13 for collaboration and discussion, and to Dr Eiro Muneyuki for many useful comments. This work was supported in part by Grants-in-Aid from the Ministry of Science, Education, Sports and Culture of Japan, and a Keio University Special Grant-in-Aid. R. Yasuda was a Research Fellow of the Japan Society for the Promotion of Science.

REFERENCES

Abrahams, J. P., Leslie, A. G. W., Lutter, R. & Walker, J. E. 1994 Structure at 2.8 Å of F_1-ATPase from bovine heart mitochondria. *Nature* **370**, 621–628.

Aggeler, R., Ogilvie, I. & Capaldi, R. A. 1997 Rotation of a γ-ε subunit domain in the *Escherichia coli* F_1F_o-ATP synthase complex. *J. Biol. Chem.* **272**, 19621–19624.

Berg, H. C. & Turner, L. 1993 Torque generated by the flagellar motor of *Escherichia coli*. *Biophys. J.* **65**, 2201–2216.

Block, S. M. 1998 Kinesin: what gives? *Cell* **93**, 5–8.

Boekema, E. J., Ubbink-Kok, T., Lolkema, J. S., Brisson, A. & Konings, W. N. 1997 Visualization of a peripheral stalk in V-type ATPase: evidence for the stator structure essential to rotational catalysis. *Proc. Natl Acad. Sci. USA* **94**, 14291–14293.

Boekema, E. J., Van Breemen, J. F. L., Brisson, A., Ubbink-Kok, T., Konings, W. N. & Lolkema, J. S. 1999 Connecting stalks in V-type ATPase. *Nature* **401**, 37–38.

Boyer, P. D. 1993 The binding change mechanism for ATP synthase—some probabilities and possibilities. *Biochim. Biophys. Acta* **1140**, 215–250.

Boyer, P. D. 1997 The ATP synthase—a splendid molecular machine. *A. Rev. Biochem.* **66**, 717–749.

Boyer, P. D. 2000 Catalytic site forms and controls in ATP synthase catalysis. *Biochim. Biophys. Acta Bioenergetics*. (In the press.)

Boyer, P. D. & Kohlbrenner, W. E. 1981 The present status of the binding-change mechanism and its relation to ATP formation by chloroplasts. In *Energy coupling in photosynthesis* (ed. B. R. Selman & S. Selman-Reimer), pp. 231–240. Amsterdam: Elsevier.

Cross, R. L., Grubmeyer, C. & Penefsky, H. S. 1982 Mechanism of ATP hydrolysis by beef heart mitochondrial ATPase. Rate enhancements resulting from cooperative interactions between multiple catalytic sites. *J. Biol. Chem.* **257**, 12101–12105.

Cunningham, D. & Cross, R. L. 1988 Catalytic site occupancy during ATP hydrolysis by MF_1-ATPase. Evidence for alternating high affinity site during steady-state turnover. *J. Biol. Chem.* **263**, 18850–18856.

DeRosier, D. J. 1998 The turn of the screw: the bacterial flagellar motor. *Cell* **93**, 17–20.

Dominguez, R., Freyzon, Y., Trybus, K. M. & Cohen, C. 1998 Crystal structure of a vertebrate smooth myosin motor domain and its complex with the essential light chain: visualization of the pre-power stroke state. *Cell* **94**, 559–571.

Duncan, T. M., Bulygin, V. V., Zhou, Y., Hutcheon, M. L. & Cross, R. L. 1995 Rotation of subunits during catalysis by *Escherichia coli* F_1-ATPase. *Proc. Natl Acad. Sci. USA* **92**, 10964–10968.

Fillingame, R. H., Jones, P. C., Jiang, W., Valiyaveetil, F. I. & Dmitriev, O. Y. 1998 Subunit organization and structure in the F_o sector of *Escherichia coli* F_1F_o ATP synthase. *Biochim. Biophys. Acta* **1365**, 135–142.

Funatsu, T., Harada, Y., Tokunaga, M., Saito, K. & Yanagida, T. 1995 Imaging of single fluorescent molecules and individual ATP turnovers by single myosin molecules in aqueous solution. *Nature* **374**, 555–559.

Galkin, M. A. & Vinogradov, A. D. 1999 Energy-dependent transformation of the catalytic activities of the mitochondrial F_oF_1-ATP synthase. *FEBS Lett.* **448**, 123–126.

García, J. J. & Capaldi, R. A. 1998 Unisite catalysis without rotation of the γ-ε domain in *Escherichia coli* F_1-ATPase. *J. Biol. Chem.* **273**, 15940–15945.

Gelles, J. & Landick, R. 1998 RNA polymerase as a molecular motor. *Cell* **93**, 13–16.

Goldman, Y. E. 1998 Wag the tail: structural dynamics of actomyosin. *Cell* **93**, 1–4.

Ha, T., Glass, J., Enderle, Th., Chemla, D. S. & Weiss, S. 1998 Hindered rotational diffusion and rotational jumps of single molecules. *Phys. Rev. Lett.* **80**, 2093–2096.

Hasler, K., Engelbrecht, S. & Junge, W. 1998 Three-stepped rotation of subunits γ and ε in single molecules of F-ATPase as revealed by polarized, confocal fluorometry. *FEBS Lett.* **426**, 301–304.

Hausrath, A. C., Gruber, G., Matthews, B. W. & Capaldi, R. A. 1999 Structural features of the γ subunit of the *Escherichia coli* F_1 ATPase revealed by a 4.4-Å resolution map obtained by x-ray crystallography. *Proc. Natl Acad. Sci. USA* **96**, 13697–13702.

Hisabori, T., Kondoh, A. & Yoshida, M. 1999 The γ subunit in chloroplast F_1-ATPase can rotate in a unidirectional and counter-clockwise manner. *FEBS Lett.* **463**, 35–38.

Holmes, K. C., Popp, D., Gebhard, W. & Kabsch, W. 1990 Atomic model of the actin filament. *Nature* **347**, 44–49.

Hunt, A. J., Gittes, F. & Howard, J. 1994 The force exerted by a single kinesin molecule against a viscous load. *Biophys. J.* **67**, 766–781.

Huxley, A. F. 1957 Muscle structure and theories of contraction. *Progr. Biophys. Biophys. Chem.* **7**, 255–318.

Junge, W., Lill, H. & Engelbrecht, S. 1997 ATP synthase: an electrochemical transducer with rotatory mechanics. *Trends Biochem. Sci.* **22**, 420–423.

Kagawa, Y. 1999 Biophysical studies on ATP synthase. *Adv. Biophys.* **36**, 1–25.

Kaim, G. & Dimroth, P. 1999 ATP synthesis by F-type ATP synthase is obligatorily dependent on the transmembrane voltage. *EMBO J.* **18**, 4118–4127.

Kato, Y., Sasayama, T., Muneyuki, E. & Yoshida, M. 1995 Analysis of time-dependent change of *Escherichia coli* F_1-ATPase activity and its relationship with apparent negative cooperativity. *Biochim. Biophys. Acta* **1231**, 275–281.

Kato-Yamada, Y., Noji, H., Yasuda, R., Kinosita Jr, K. & Yoshida, M. 1998 Direct observation of the rotation of γ subunit in F_1-ATPase. *J. Biol. Chem.* **273**, 19375–19377.

Kinosita Jr, K. 1998 Linear and rotary molecular motors. *Adv. Exp. Med. Biol.* **453**, 5–14.

Kinosita Jr, K. 1999 Real time imaging of rotating molecular machines. *FASEB J.* **13**, S201–S208.

Kinosita Jr, K., Yasuda, R., Noji, H., Ishiwata, S. & Yoshida, M. 1998 F_1-ATPase: a rotary motor made of a single molecule. *Cell* **93**, 21–24.

Kinosita Jr, K., Yasuda, R. & Noji, H. 2000 F_1-ATPase: a highly efficient rotary ATP machine. *Essays Biochem.* **35**. (In the press.)

Kitamura, K., Tokunaga, M., Hikikoshi Iwane, A. & Yanagida, T. 1999 A single myosin head moves along an actin filament with regular steps of 5.3 nanometres. *Nature* **397**, 129–134.

Lauger, P. 1977 Ion transport and rotation of bacterial flagella. *Nature* **268**, 360–362.

Livnah, O., Bayer, E. A., Wilchek, M. & Sussman, J. L. 1993 Three-dimensional structures of avidin and the avidin-biotin complex. *Proc. Natl Acad. Sci. USA* **90**, 5076–5080.

Lohman, T. M., Thorn, K. & Vale, R. 1998 Staying on track: common features of DNA helicases and microtubule motors. *Cell* **93**, 9–12.

Mandelkow, E. & Johnson, K. A. 1998 The structural and mechanochemical cycle of kinesin. *Trends Biol. Sci.* **23**, 429–433.

Matsui, T., Muneyuki, E., Honda, M., Allison, W. S., Dou, C. & Yoshida, M. 1997 Catalytic activity of the $\alpha_3\beta_3\gamma$ complex of F_1-ATPase without a noncatalytic nucleotide binding site. *J. Biol. Chem.* **272**, 8215–8221.

Milgrom, Y. M., Murataliev, M. B. & Boyer, P. D. 1998 Bi-site activation occurs with the native and nucleotide-depleted mitochondrial F_1-ATPase. *Biochem. J.* **330**, 1037–1043.

Muneyuki, E. & Hirata, H. 1988 Kinetic analysis of proton translocation catalyzed by F_oF_1ATPase. *FEBS Lett.* **234**, 455–458.

Noji, H., Yasuda, R., Yoshida, M. & Kinosita Jr, K. 1997 Direct observation of the rotation of F_1-ATPase. *Nature* **386**, 299–302.

Noji, H., Hasler, K., Junge, W., Kinosita Jr, K., Yoshida, M. & Engelbrecht, S. 1999 Rotation of *Escherichia coli* F_1-ATPase. *Biochem. Biophys. Res. Commun.* **260**, 597–599.

Omote, H., Sambonmatsu, N., Saito, K., Samboingi, Y., Iwamoto-Kihara, A., Yanagida, T., Wada, Y. & Futai, M. 1999 The γ-subunit rotation and torque generation in F_1-ATPase from wild-type or uncoupled mutant *Escherichia coli*. *Proc. Natl Acad. Sci. USA* **96**, 7780–7784.

Oosawa, F. & Hayashi, S. 1986 The loose coupling mechanism in molecular machines of living cells. *Adv. Biophys.* **22**, 151–183.

Oster, G. & Wang, H. 2000 Reverse engineering a protein: the mechanochemistry of ATP synthase. *Biochim. Biophys. Acta.* (In the press.)

Rastogi, V. K. & Girvin, M. E. 1999 Structural changes linked to proton translocation by subunit c of the ATP synthase. *Nature* **402**, 263–268.

Sabbert, D., Engelbrecht, S. & Junge, W. 1996 Intersubunit rotation in active F-ATPase. *Nature* **381**, 623–625.

Sambongi, H., Iko, Y., Tanabe, M., Omote, H., Iwamoto-Kihara, A., Ueda, I., Yanagida, T., Wada, Y. & Futai, M. 1999 Mechanical rotation of the c subunit oligomer in ATP synthase (F_oF_1): direct observation. *Science* **286**, 1722–1724.

Sase, I., Miyata, H., Ishiwata, S. & Kinosita Jr, K. 1997 Axial rotation of sliding actin filaments revealed by single-fluorophore imaging. *Proc. Natl Acad. Sci. USA* **94**, 5646–5650.

Shingyoji, C., Higuchi, H., Yoshimura, M., Katayama, E. & Yanagida, T. 1998 Dynein arms are oscillating force generators. *Nature* **393**, 711–714.

Shirakihara, Y., Leslie, A. G. W., Abrahams, J. P., Walker, J. E., Ueda, T., Sekimoto, Y., Kambara, M., Saika, K., Kagawa, Y. & Yoshida, M. 1997 The crystal structure of the nucleotide-free $\alpha_3\beta_3$ subcomplex of F_1-ATPase from the thermophilic *Bacillus* PS3 is a symmetric trimer. *Structure* **5**, 825–836.

Stock, D., Leslie, A. G. W. & Walker, J. E. 1999 Molecular architecture of the rotary motor in ATP synthase. *Science* **286**, 1700–1705.

Suzuki, Y., Yasunaga, T., Ohkura, R., Wakabayashi, T. & Sutoh, K. 1998 Swing of the lever arm of a myosin motor at the isomerization and phosphate-release steps. *Nature* **396**, 380–383.

Taylor, E. W. 1979 Mechanism of actomyosin ATPase and the problem of muscular contraction. *CRC Crit. Rev. Biochem.* **6**, 103–164.

Tsunoda, S. P., Muneyuki, E., Amano, T., Yoshida, M. & Noji, H. 1999 Cross-linking of two β subunits in the closed conformation in F_1-ATPase. *J. Biol. Chem.* **274**, 5701–5706.

Wang, H. & Oster, G. 1998 Energy transduction in the F_1 motor of ATP synthase. *Nature* **396**, 279–282.

Wang, M. D., Schnitzer, M. J., Yin, H., Landick, R., Gelles, J. & Block, S. M. 1998 Force and velocity measured for single molecules of RNA polymerase. *Science* **282**, 902–907.

Weber, J., Wilke-Mounts, S., Lee, R. S.-F., Grell, E. & Senior, A. E. 1993 Specific placement of tryptophan in the catalytic sites of *Escherichia coli* F_1-ATPase provides a direct probe of nucleotide binding: maximal ATP hydrolysis occurs with three sites occupied. *J. Biol. Chem.* **268**, 20 126–20 133.

Wilkens, S. & Capaldi, R. A. 1998 ATP synthase's second stalk comes into focus. *Nature* **393**, 29.

Yasuda, R., Noji, H., Kinosita Jr, K. & Yoshida, M. 1998 F_1-ATPase is a highly efficient molecular motor that rotates with discrete 120° steps. *Cell* **93**, 1117–1124.

Zhou, Y., Duncan, T. M. & Cross, R. L. 1997 Subunit rotation in *Escherichia coli* F_oF_1-ATP synthase during oxidative phosphorylation. *Proc. Natl Acad. Sci. USA* **94**, 10 583–10 587.

Microscopic Analysis of Polymerization and Fragmentation of Individual Actin Filaments

Shin'ichi Ishiwata[1,2,3,4], Junko Tadashige[1], Ichiro Masui[1], Takayuki Nishizaka[4], and Kazuhiko Kinosita, Jr[4,5]

Introduction

The dynamics of polymerization (and annealing of fragments) and depolymerization (and fragmentation) of actin filaments (F-actin) is a key process in diverse cellular functions, including cell motility. Up to the present, there have been many spectroscopic studies in solution, which have clarified time-dependent but averaged properties, as well as electron microscopic and other studies; but a single filament analysis, which is effective in clarifying not only time-dependent but also nonaveraged properties, has not yet been reported. Thus, direct observation of the polymerization-depolymerization dynamics of individual actin filaments is worthy of investigation.

The polymerization process consists of nucleation and growth phase, and at a steady state, annealing and fragmentation of polymerized filaments occur. The essential elements of these processes have been experimentally clarified and theoretically formulated (Oosawa and Kasai 1962; Oosawa and Asakura 1975). Actin filaments, like microtubules, have a structural polarity, such that the polymerization and depolymerization rates at the two ends of the filaments are different (Oosawa and Asakura 1975; Woodrum et al. 1975; Kondo and Ishiwata 1976; Hayashi and Ip 1976; Pollard and Cooper 1986). The end of the filaments at which the polymerization rate is larger is defined as the barbed (B-) end and the other is called the pointed (P-) end.

After the steady state of polymerization is attained, a treadmill process is expected to occur (Wegner 1976). The B-end of the filament is where filament assembly occurs, while depolymerization occurs at the P-end, such that the length of the filament is maintained nearly constant. The treadmill process has been experimentally demonstrated in solution (cf Wegner 1976; Korn et al. 1987). After actin monomers (G-actin) with ATP are polymerized, the bound

[1] Department of Physics, School of Science and Engineering
[2] Advanced Research Institute for Science and Engineering
[3] Materials Research Laboratory for Bioscience and Photonics, Waseda University, Tokyo 169-8555, Japan
[4] Core Research for Evolutional Science and Technology (CREST) Genetic Programming Team 13, Japan
[5] Department of Physics, Faculty of Science and Technology, Keio University, Yokohama 223-8522, Japan

Results and Problems in Cell Differentiation, Vol. 32
C. dos Remedios (Ed.): Molecular Interactions of Actin

ATP is hydrolyzed and inorganic phosphate (Pi) is released, leaving ADP attached.

When the rate of polymerization is greater than that of ATP hydrolysis, actin molecules with ATP should cap that end of the filaments. Depending on whether each end of the actin filaments is capped by either ATP-bound actin (ATP-cap) or ADP-bound actin (ADP-cap), dynamic instability of the filaments may occur (Korn et al. 1987; Carlier 1989). However, in contrast to microtubules, the dynamic instability has not yet been experimentally proved in actin filaments. Thus, the examination of whether this dynamic process occurs is a challenging problem.

About a decade ago, it became possible to visualize single actin filaments under a fluorescence microscope by labeling the filaments with rhodamine-phalloidin (Rh-Ph; Yanagida et al. 1984) or with fluorescein 5-isothiocyanate (FITC; Honda et al. 1986). In both studies, phallotoxins (Wieland et al. 1975) were added in order to suppress the depolymerization of actin filaments due to extremely low concentration (an order of nM) of actin, lower than the critical concentration for polymerization. Because the filament structure is stabilized, it became possible to visualize single filaments for a sufficiently long time to examine quantitatively not only the polymerization process but also the fragmentation process. Thus, the use of fluorescent-dye conjugated phallotoxins was very useful for stably and clearly visualizing the filament under a conventional fluorescence microscope without disturbance of background fluorescence (cf. Ishiwata 1998). The advantage of this technique is that Rh-Ph does not bind to G-actin and the fluorescence intensity of Rh-Ph increases several-fold upon binding to actin filaments (Harada et al. 1991; Huang et al. 1992).

In this chapter, we describe the properties of the polymerization and fragmentation processes of single actin filaments examined by direct observation through the fluorescence image of actin filaments in the presence of phallotoxins under a conventional fluorescence microscope (Tadashige et al. 1992; Masui et al. 1995).

We ask the reader to bear in mind that although the stabilization by phallotoxins is convenient for visualizing single actin filaments, there are several disadvantages to this method: (1) The greatest disadvantage is that spontaneous depolymerization is suppressed (Estes et al. 1981; Coluccio and Tilney 1984; Sampath and Pollard 1991), (2) The structure of actin filaments may be modified by the binding of phallotoxins (Drubin et al. 1993; Lorenz et al. 1993), so that the results may not represent polymerization properties of pure actin filaments. In this respect, however, this method can, conversely, be considered unique in studying the interaction of phallotoxins with actin filaments.

We have recently succeeded in visualizing polymerization and depolymerization of single actin filaments by using fluorescent dye(rhodamine)-labeled actin without using rhodamine-phallotoxins (phalloidin or phallacidin) under evanescent field illumination (Takahashi and Ishiwata 1998; Fujiwara et al. 1998). Thus it is now possible to visualize at a video rate both polymerization and depolymerization processes for every filament. The results will be published in more detail elsewhere.

How to Image the Polymerization (and Fragmentation) Process of Actin Filaments

To analyze polymerization and fragmentation of individual actin filaments under a fluorescence microscope, it is necessary to observe the same filaments at least for 30 min. Although single filaments are visualized in solution under a conventional fluorescence microscope, it is difficult to trace the polymerization process for each filament floating in solution because of its violent Brownian motion (Yanagida et al. 1984; Isambert et al. 1995).

To overcome this difficulty, we fixed short actin filaments to a glass surface through the cross-linked HMM molecules, as schematically illustrated in Fig. 1 [myosin easily adheres to a collodion(nitrocellulose)-coated glass surface], so that we can keep observing the same filaments. Thus, a short filament adhering to the glass surface was used as a nucleus for observing the polymerization process and as a tool to fix the long filaments so as to observe the fragmentation (severing) process.

To visualize the polymerization process at a constant concentration of G-actin, the actin solution was infused into a flow cell just after the addition

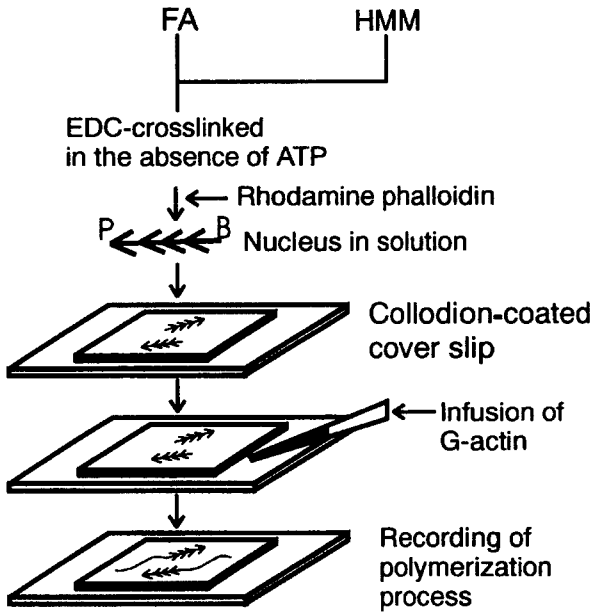

Fig. 1. Scheme showing how to measure the polymerization rate of actin on single actin filaments under a fluorescence microscope. Actin filaments decorated with HMM in the absence of ATP were cross-linked with 1-ethyl-3-(3-dimethyl-aminopropyl)-carbodiimide (EDC) and labeled with Rh-Ph to clearly identify the nuclei (Nishizaka et al. 1993). The EDC cross-linked acto-HMM complexes were mildly sonicated to make filaments short and used as nuclei for polymerization of actin. Immediately after the addition of salt, G-actin solution was infused into the flow cell sandwiched between a pair of coverslips, one of which was coated with nitrocellulose (collodion). The polymerization process was observed under an inverted fluorescence microscope and recorded on a videotape through a SIT camera (C1000; Hamamatsu Photonics). The length of the actin filaments was analyzed using a digital image processor (DIPS-C2000; Hamamatsu Photonics) (Nishizaka et al. 1995)

of salt to the G-actin solution, and the initial process of polymerization was recorded on a videotape at a rate of 30 frames s^{-1}. The length of actin filaments was determined by accumulating and averaging the images for 1 s every 5 (and 6, 7 or 10) min. Thus, the accuracy of the estimation of length change was less than 0.2 μm.

Visualization of the Polymerization Process of Actin Filaments

Figure 2 illustrates a series of fluorescence micrographs showing the polymerization process of individual actin filaments. The concentration of Rh-Ph was reduced to 15 nM, 1/7 that of phalloidin (or phallacidin), which was sufficiently high to image actin filaments. Under this condition, polymerization occurred only at one end of the actin nuclei, corresponding to the B-end.

Judging from the polymerization rate of actin (about 100 nm min^{-1} = 0.6 molecules s^{-1} assuming that the pitch of an actin monomer along the

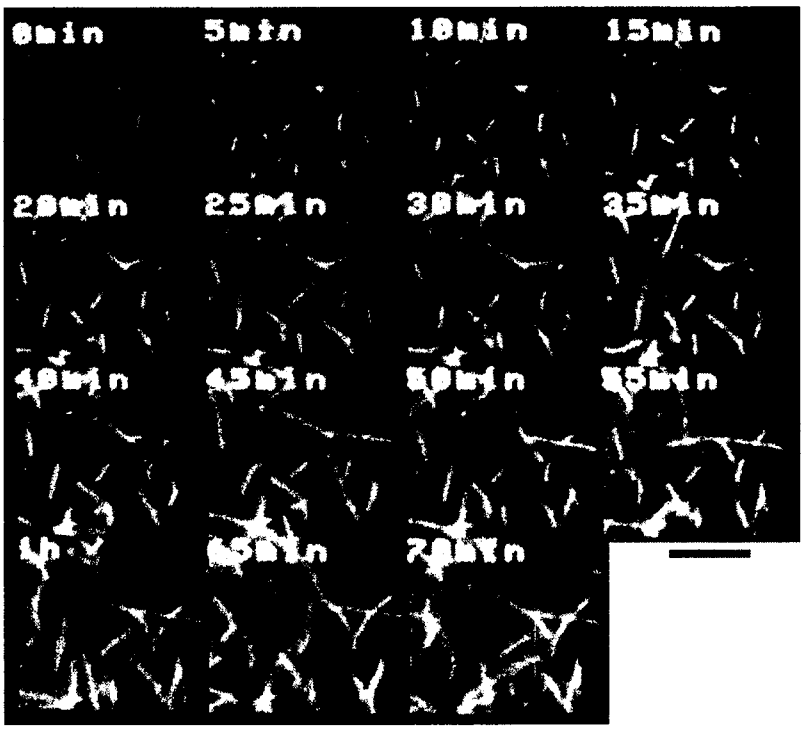

Fig. 2. Fluorescence images showing the time course of the polymerization on single actin filaments. Fluorescence images were recorded for several seconds every 5 min to minimize the photobleaching after the addition of the following actin solution. Condition: 5 μg ml^{-1} G-actin, 30 mM KCl, 1 mM $MgCl_2$, 4 mM ATP, 2 mM MOPS (pH 7), 105 nM phalloidin (Molecular Probes, Inc.), 15 nM Rh-Ph (Molecular Probes, Inc.) and oxygen scavenger system (Harada et al. 1991). The solvent was mixed with G-actin solution containing only ATP and MOPS immediately before the experiments, to minimize the spontaneous polymerization in solution. Temperature 25 °C. Bar, 5 μm

long-pitch helical strand of F-actin to be 5.5 nm) and the concentrations of nuclei and G-actin, the decrease in the concentration of G-actin can be neglected during initial observation (10 min) period. The polymerization rate (shown in Figs. 4 and 5 below) was estimated from the initial phase of elongation for 10 min (cf Fig. 3). We noticed that about one third of the nuclei among those attached to the glass surface did not elongate (see the upper left in each micrograph of Fig. 2). This is probably because G-actin was not accessible to the ends of the nuclei due to an obstacle such as nitrocellulose. Some filaments, which showed bending Brownian motion out of focus, were omitted from the length measurements.

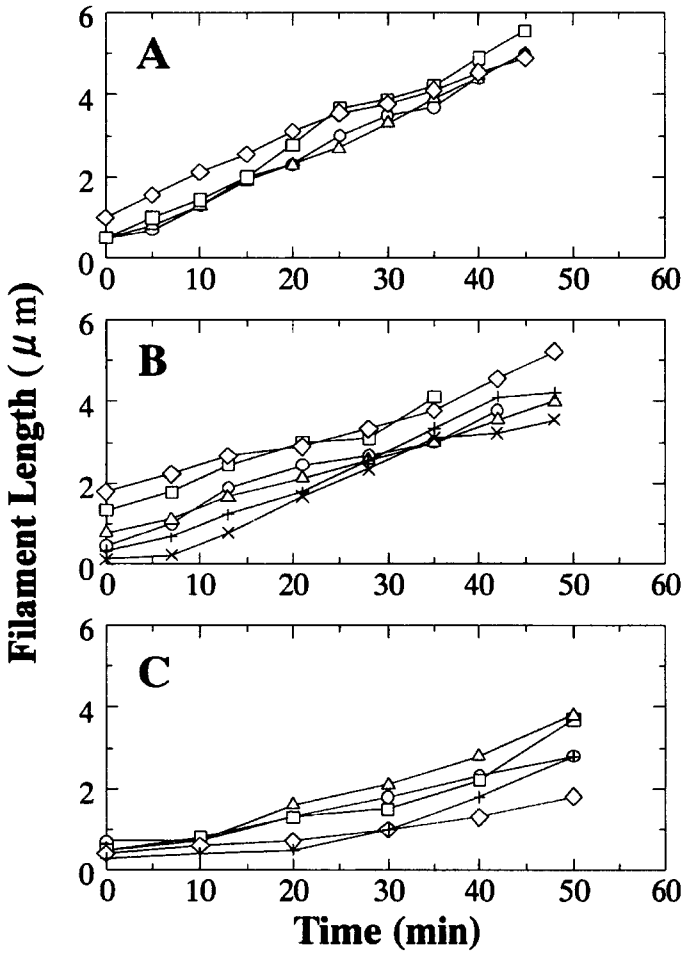

Fig. 3A–C. Time course of polymerization at the B-end of F-actin obtained under a fluorescence microscope at different actin concentrations. Conditions: G-actin, 5 μg ml^{-1} (**A**, images are shown in Fig. 2), 4 μg ml^{-1} (**B**) and 3 μg ml^{-1} (**C**); other solvent conditions, the same as in Fig. 2 (the concentrations of phalloidin and Rh-Ph were maintained at 105 nM and 15 nM, respectively, irrespective of the concentrations of G-actin. Although the total concentration of phalloidin was less than the highest actin concentration examined, we estimated that it was high enough for the binding at the initial stage of polymerization). The filament length at time zero corresponds to the length of nucleus. Temperature 25 °C

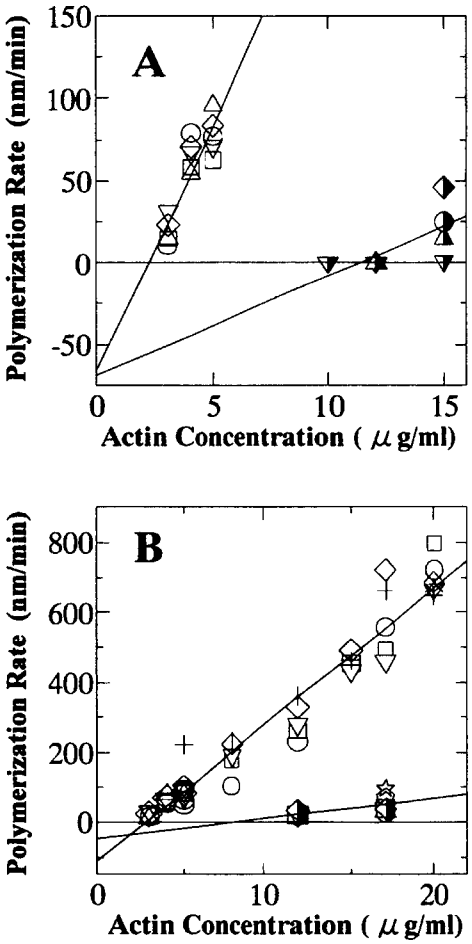

Fig. 4A,B. Initial rate of polymerization vs G-actin concentration in the presence of phalloidin. The polymerization rates at the B- and P-ends of F-actin were examined. When polymerization occurred at both ends of the filament, we decided the end elongated longer to be a B-end and that shorter to be a P-end. (**A**): polymerization at the B-end in the presence of 1 mM Mg^{2+} (open symbols) or 1 mM Ca^{2+} (half-filled symbols). Conditions as in Fig. 3, except that 1 mM $CaCl_2$ was added in half-filled symbols instead of 1 mM $MgCl_2$. (**B**) Polymerization at the B-end (open symbols and crosses) or the P-end (half-filled symbols, open star and pentagon) in the presence of Mg^{2+}. The data in **A** are also included. Different symbols show different preparations of actin. Temperature, 2 °C

Measurement of the Polymerization Process of Actin Filaments

Figure 3 shows an example of the time course of polymerization of individual actin filaments at three different concentrations of G-actin in the presence of phalloidin. The density of nuclei attached to the glass surface was common to all the experiments. On increasing the concentration of infused G-actin, the average rate of polymerization increased.

The polymerization rate varied from filament to filament (Fig. 3). Even in the same filament, the polymerization rate was not constant over 40–50 min but changed with time beyond the resolution of length determination. The accessibility of G-actin to the ends of the filaments may have fluctuated with time due to the adhesion to the nitrocellulose. Also, these results may be attributable to the nonhomogeneity of the local concentration of G-actin and/or the stochastic and cooperative properties of the polymerization process in the presence of phalloidin.

Depolymerization was suppressed by the presence of phalloidin, but there is a possibility that spontaneous fragmentation occurred. This could be one of the causes of length fluctuations during the polymerization process. In practice, however, we did not notice distinct fragmentation, at least in the middle of the filaments.

The rate of fragmentation in the absence of phalloidin was previously estimated in solution experiments to be $7 \times 10^{-7} s^{-1}$ (Kinosian et al. 1993), suggesting that in practice, fragmentation in the presence of phallotoxins does not occur within the period of measurements.

At low concentrations of G-actin, there was a tendency for the polymerization rate to increase with time (Fig. 3). The polymerization curve at $3 \mu g ml^{-1}$ G-actin was convex downward, whereas the curve at $5 \mu g ml^{-1}$ G-actin was nearly straight. This suggests that the polymerization kinetics change with the elongation of the filaments. The shorter the filament, the more the binding of G-actin may be disturbed.

Relation Between Polymerization Rate and Actin Concentration

The average rate of polymerization vs G-actin concentration relation is summarized in Fig. 4. In Fig. 4A, the relation observed at the B-end of F-actin in the presence of Mg^{2+} or Ca^{2+} is compared, while in Fig. 4B, the relation at the B- and P-ends is shown over a comparatively broader range of G-actin concentration.

These experiments were done in the presence of a constant concentration of phalloidin. Contrary to our expectation and differing from previous results obtained in solution (Estes et al. 1981; Coluccio and Tilney 1984; Sampath and Pollard 1991), the critical concentration of polymerization was not zero under all the conditions. This result was not changed even if the polymerization rates were estimated between 40 and 50 min in Fig. 3, where the polymerization rates were larger than the initial ones. However, when the same concentration of phallacidin was used instead of phalloidin, the result was as expected (Fig. 5). In both cases, the same concentration of Rh-Ph, one seventh that of phalloidin (or phallacidin), coexisted in order to visualize single actin filaments.

The relation between the polymerization rate (r) and G-actin concentration (c) can be expressed by:

$$r = k^+c - k^-,$$

where k^+ and k^- are the rate constants for polymerization and depolymerization, respectively. Thus, under the conditions examined in the presence of phalloidin, k^+ was estimated to be $29.6 (nm\,min^{-1})/(\mu g\,ml^{-1})$ $(= 7.5 \times 10^6 M^{-1} s^{-1})$ and $6.2 (nm\,min^{-1})/(\mu g\,ml^{-1})$ $(= 1.6 \times 10^6 M^{-1} s^{-1})$ for the B-end in the presence of Mg^{2+} and Ca^{2+}, respectively (Fig. 4A), and $39.3 (nm\,min^{-1})/(\mu g\,ml^{-1})$ $(= 1.0 \times 10^7 M^{-1} s^{-1})$ and $5.9 (nm\,min^{-1})/(\mu g\,ml^{-1})$ $(= 1.5 \times 10^6 M^{-1} s^{-1})$ for the B-end and the P-end in the presence of Mg^{2+}, respectively (Fig. 4B). In calculating the values in the parentheses, we assumed that the molecular weight of actin is 42 kDa, and the number density of actin molecules along the filament is 2 molecules/5.5 nm.

On the other hand, in the presence of phallacidin, k^+ at the B-end was estimated to be 34.9 $(nm\,min^{-1})/(\mu g\,ml^{-1})$ (= $8.9 \times 10^6 M^{-1} s^{-1}$) and 5.8 $(nm\,min^{-1})/(\mu g\,ml^{-1})$ (= $1.5 \times 10^6 M^{-1} s^{-1}$) in the presence of Mg^{2+} and Ca^{2+}, respectively (Fig. 5).

The values of k^+ obtained above in the presence of Mg^{2+} (Figs. 4B, 5) were a little larger than, but consistent with, those obtained in solution under the same solvent conditions except for the absence of phallotoxins (the values of k^+ at the B- and P-ends were, respectively, $6.3 \times 10^6 M^{-1} s^{-1}$ and $1.1 \times 10^6 M^{-1} s^{-1}$; Suzuki and Mihashi 1989). This differs, however, from the results that the addition of phallotoxins reduced the value of k^+ by 20 to 50% (Coluccio and Tilney 1984; Wendel and Dancker 1987; Sampath and Pollard 1991). Such an apparent discrepancy may be attributable to the difference in experimental conditions. Note that the value of k^- was almost zero in the presence of phallacidin, consistent with the previous solution experiments (Estes et al. 1981; Coluccio and Tilney 1984; Sampath and Pollard 1991).

We found that the addition of 10 mM Pi in the presence of phallacidin slightly increased the value of k^+ to 39.0 $(nm\,min^{-1})/(\mu g\,ml^{-1})$ (= $9.9 \times 10^6 M^{-1} s^{-1}$) and 6.9 $(nm\,min^{-1})/(\mu g\,ml^{-1})$ (= $1.8 \times 10^6 M^{-1} s^{-1}$) in the presence of Mg^{2+} and Ca^{2+}, respectively, that is, by about 1.1 to 1.2 times (Fig. 5). This demonstrates that Pi does not significantly affect the polymerization rate but stabilizes the filament structure (Nonomura et al. 1975) through the decrease

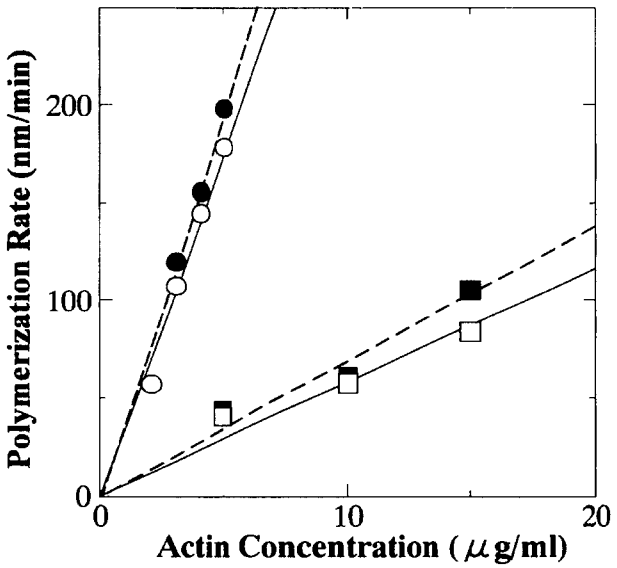

Fig. 5. Initial rate of polymerization at the B-end vs G-actin concentration in the presence of phallacidin. Effects of Pi and divalent cations (Mg^{2+} or Ca^{2+}) were examined. Conditions: various concentrations of G-actin, 30 mM KCl, 2 mM $MgCl_2$ (circles) or $CaCl_2$ (squares), 4 mM ATP, 2 mM MOPS (pH 7), 2 $mg\,ml^{-1}$ BSA, 1.5 mM NaN_3, with (closed symbols) or without (open symbols) 1.5 mM Pi, 105 nM phallacidin, 15 nM Rh-Ph, 10 mM DTT, 0.3% (w/v) methylcellulose and oxygen scavenger system (Harada et al. 1991). The time course of polymerization of actin filaments was indistinguishable from that in the presence of phalloidin shown in Fig. 3, except that the polymerization curve was slightly convex upward at every G-actin concentration we examined

in the rates of both depolymerization (Rickard and Sheterline 1986, 1988; Funatsu 1986) and fragmentation as described below (Fig. 6).

It is also to be noted that, irrespective of the species of phallotoxins, in other words, independent of whether the critical concentration was zero (Fig. 5 for phallacidin) or not (Fig. 4 for phalloidin), the polymerization rate, k^+, was nearly the same under the same solvent conditions. On the other hand, the value of k^+ for Mg-actin was five-to-six times larger than that for Ca-actin (Figs. 4A, 5). This is in contrast to previous results obtained in solution that k^+ for Mg-actin was, at most, only two times larger than that for Ca-actin (see Estes et al. 1992). This apparent discrepancy may be attributable to the structural changes induced by the binding of phallotoxins and the difference in experimental conditions. Another possibility is that the HMM-cross linked nucleus may have amplified a small difference between the polymerization properties of Mg-actin and Ca-actin.

What is most notable in the above experiments is that the critical concentration for polymerization was practically zero in the presence of 105 nM phallacidin with 15 nM Rh-Ph (Fig. 5) but not zero in the presence of 105 nM phalloidin with 15 nM Rh-Ph (Fig. 4). At first sight, the reason for this difference appears to be attributable to the larger dissociation constant of phalloidin than that of phallacidin with F-actin. In practice, however, the dissociation constants of phalloidin and Rh-Ph with F-actin are, respectively, reported to be 67 and 40 nM (Molecular Probes Data Book; Huang et al. 1992), and those of fluorescent dye-conjugated phallotoxins such as coumarin-, NBD- and bodipy-phallacidin are, respectively, reported to be 24, 18 and 38 nM (Huang et al. 1992). Thus, although the dissociation constant of phallacidin has not yet been reported, there seems to be no large difference between phalloidin and phallacidin. If the dissociation constant itself is practically indistinguishable, the reason for the above difference may be attributable to the different rate constants.

The apparent association rate constant of Rh-Ph for F-actin is reported to be two-to-three orders of magnitude smaller than the rates of polymerization and depolymerization (De la Cruz and Pollard 1994, 1996; $6 \times 10^3\,M^{-1}s^{-1}$ at 20 °C; and $5 \times 10^4\,M^{-1}s^{-1}$ at 40 °C, Hotta and Ishiwata 1997). If this is also the case for the newly polymerized ends of the filaments, there would be an appreciable probability that the actin molecules once attached to the filament ends are detached, so that the apparent polymerization rate becomes reduced, resulting in the nonzero critical concentration.

This was not the case at least for phallacidin (as observed in Fig. 5), suggesting that the association rate constant of phallotoxins for the ends of the filaments is much larger than that for the bulk of the filaments. In fact, there is a report suggesting that phalloidin binds to the filament ends more rapidly than to the bulk of the filament (Cano et al. 1992). We infer that the rate constant of attachment to the filament ends of phalloidin may be still much slower than that of phallacidin.

Such a subtle difference may be produced by the structural change of actin molecules incorporated into the filament ends. The result shown in Fig. 4A,

that the apparent critical concentration for polymerization was larger in the presence of Ca^{2+} than of Mg^{2+}, can be ascribable to this mechanism, and may be related to the difficulty of nucleus formation for Ca-actin. That is, the association rate of phalloidin to the polymerized filament end may be slower for Ca-actin than for Mg-actin. This difference may be overcome in the presence of phallacidin, because the association rate constant of phallacidin at the polymerized ends is large enough to overcome the smaller association rate constant to Ca-actin. These mechanisms should be quantitatively examined in future.

Fragmentation of Actin Filaments: Effect of Anions at High Ionic Strength

Finally, the fragmentation of individual actin filaments was visualized using the same technique as described above. In this case, however, the long actin filaments polymerized beforehand in the presence of Rh-Ph were attached to the glass surface through the short fragments decorated with cross-linked HMM as shown in Fig. 6 (a similar technique has been used before: Bearer 1991; Maciver et al. 1991; Nishizaka et al. 1993). Various salt solutions were then infused into the cell and their effects on the fragmentation were examined under a continuous flow of the solutions.

As observed in a series of micrographs summarized in Fig. 6, shortening of the filaments in the presence of 3 M KSCN occurred mainly by severing with a lifetime of about 2 min (upper micrographs, –Pi) and 10 min (lower micrographs, +Pi), and finally all the filaments disappeared. Gradual depolymerization from the ends of the filaments was not detected. We examined various kinds of salts composed of K^+ as the cation, and Cl^-, I^-, SCN^-, etc as anions.

We found that the severing abilities were in the order of the Hofmeister series (lyotropic number) for anions, ie, the order according to which the hydrophobic interaction is destroyed: SCN^-, I^-, Cl^-, CH_3COO^-, SO_4^{2-}, etc (for the Hofmeister series, see Melander et al. 1984; Cacace et al. 1997). This is in spite of the fact that severing was largely retarded by phalloidin (for the effect of KI in the presence of phalloidin, see Dancker et al. 1975).

The present results are consistent with the previous results obtained by the phase-contrast image analysis of the dissociation process from the P-end of thin filaments in the I-Z-I brush of myofibrils (Funatsu and Ishiwata 1985; Funatsu et al. 1988), which was prepared by mildly etching the P-end of thin filaments with 0.5 M KCl treatment (Ishiwata and Funatsu 1985). The dissociation rate in the presence of 0.5 M salts in the absence of phallotoxins was in the order of SCN^-, I^-, NO_3^-, Cl^- and SO_4^{2-}, being consistent with the Hofmeister series (Funatsu 1986).

These results suggest that a hydrophobic interaction between actin molecules is important for the stabilization of the filament, even after the polymer structure is stabilized by the binding of phalloidin. However, we cannot completely eliminate the possibility that the interaction between phalloidin and

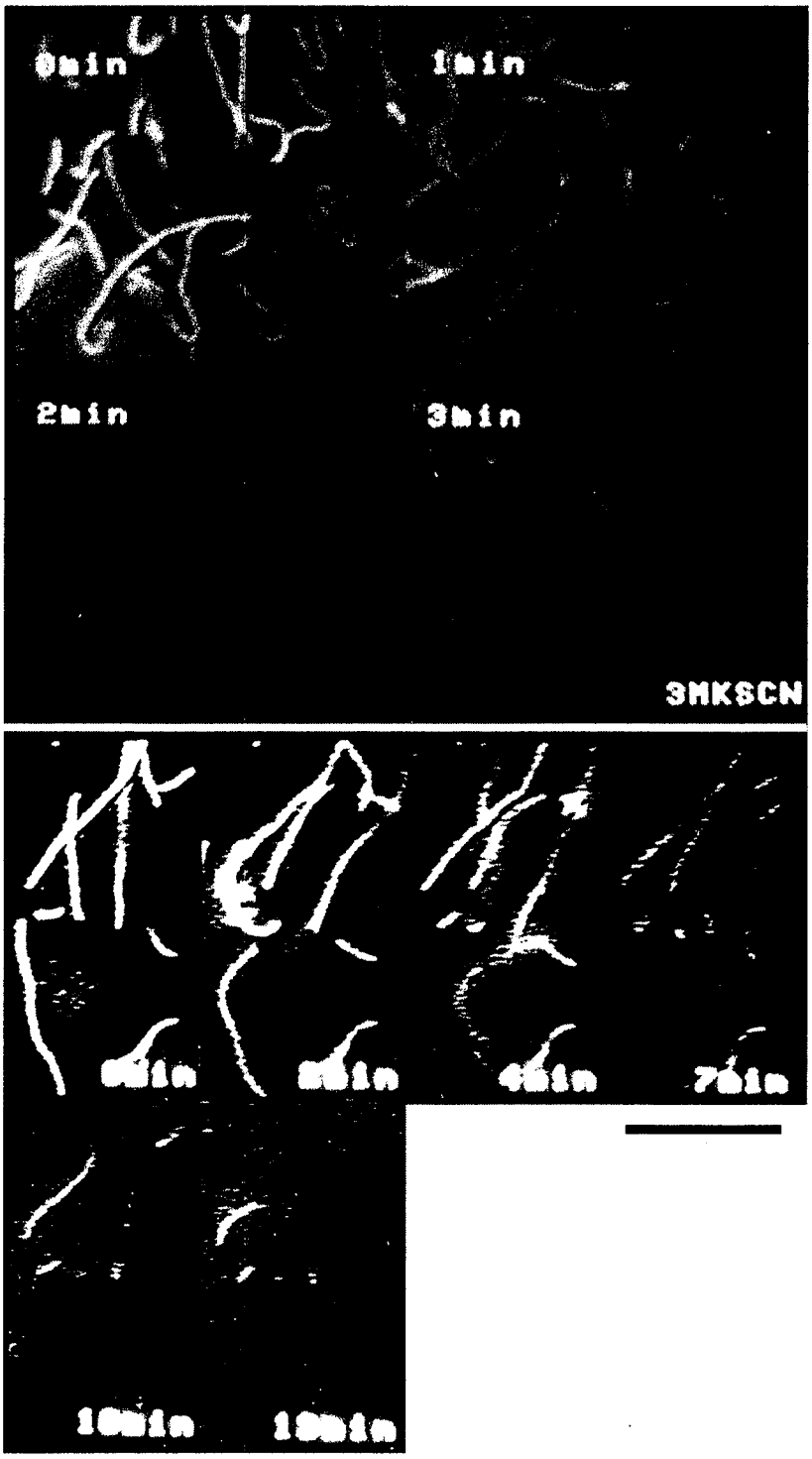

Fig. 6. Fluorescence images showing the time course of fragmentation of actin filaments in the presence of high concentrations of chaotropic anions. To record the time course of fragmentation of actin filaments, the filaments polymerized onto the nuclei of EDC-cross-linked acto-HMM complex in solution were infused into the cell, so that the filaments were attached to the glass surface through the short nuclei portion of the filaments and the polymerized portion of the filaments showed Brownian motion. The assay solvent was then infused. The time (min) after the infusion of the solvent is shown in each micrograph. Conditions as in Fig. 3, except that 3 M KSCN was added instead of 30 mM KCl and in the absence (upper micrographs) or presence (lower micrographs) of 10 mM Pi. Temperature 25 °C. Bars 5 μm

actin is weakened by the anions in the order of the Hofmeister series. It is to be noted that PO_4^{2-} was exceptional because it did not obey the Hofmeister series, ie, in practice, the shortening of the filaments did not occur in the presence of 0.5 M Pi.

The importance of hydrophobic interaction in the polymerization of actin has been recognized for many years (Oosawa and Asakura 1975). Nowadays, this discussion is based on the 3D atomic structure of G-actin (Kabsch et al. 1990) and the molecular model of F-actin (Holmes et al. 1990). These authors suggested that the hydrophobic loop located between subdomains 3 and 4 plays a role in stabilization of F-actin and this suggestion was supported by data from actin mutants or isoforms (Holmes et al. 1990; Allen et al. 1996b; Kuang and Rubenstein 1997).

Although we cannot add any information on the interaction between actin monomers on the atomic level, the results obtained here not only confirmed that the hydrophobic interaction is essential for maintaining the polymer structure but also demonstrated that other kinds of interactions exist between actin monomers, which are stabilized by phalloidin and Pi.

The manner in which phalloidin binds in the 3D structure of F-actin (Drubin et al. 1993; Lorenz et al. 1993; Steinmetz et al. 1998) suggests that phalloidin functions as a glue making connections among actin monomers in the filament. In practice, phalloidin can restore the polymerizability and also the ability of actin to activate myosin ATPase in monomers which have been impaired by chemical modifications of Lys 61 residue with FITC (Miki 1987), with several lysine residues with (m-maleimidobenzoyl)-N-hydroxysuccinimide ester (MBS) (Miki and Hozumi 1991), and by large hydrophobic probes at Cys-374 (Moens et al. 1994). Thus, actin filaments are stabilized by the cooperative nature of several kinds of molecular forces acting between actin and the regulators, ie, phallotoxins and Pi.

It is interesting that the addition of 10 mM Pi substantially lengthened the lifetime of F-actin in the presence of 3 M KSCN (Fig. 6), implying that Pi stabilized the structure of F-actin against the chaotropic effects of anions (for KI, see Dancker and Fischer 1989). For many years, the stabilizing effect of Pi has been well known. For example, with the addition of mM Pi: (1) the fragility of F-actin observed by negative staining in the electron microscope appeared to become stiffer (Nonomura et al. 1975); (2) the depolymerization rate observed in cuvette was slowed down (Rickard and Sheterline 1986, 1988; Carlier 1989); (3) subdomain 2 of the actin monomer in F-actin became oriented so as to interact strongly with the adjacent actin monomers (Orlova and Egelman 1992); and (4) severing activity of gelsolin (Allen et al. 1996a) and actophorin (Maciver et al. 1991) was reduced.

Pi does not greatly accelerate the polymerization rate, as seen in Fig. 5, and suppresses not only the depolymerization but also the fragmentation as observed in Fig. 6, such that Pi shifts the polymerization-depolymerization equilibrium to the polymerization side. The present results strongly suggest that Pi is a stabilizer of the hydrophobic interaction between actin monomers

which is essential for the polymerization of actin. On the other hand, phalloidin stabilizes the F-actin-ADP-Pi complex (Dancker and Hess 1990). Thus, phallotoxins and Pi function as allosteric effectors that synergistically stabilize the structure of actin filaments.

Conclusions

The polymerization and fragmentation processes of individual actin filaments can be visualized by imaging the polymerized filaments through binding of the fluorescent dye, Rh-Ph, under a conventional fluorescence microscope. Thus, the polymerization process at the B- and P-ends of actin filaments can be analyzed in the presence of Mg^{2+} or Ca^{2+}. By measuring the rate of polymerization at various G-actin concentrations, we confirmed that the depolymerization process was inhibited by the attachment of phallotoxins to the filaments (phallacidin was more effective than phalloidin), but the polymerization rate itself was not significantly affected, such that the critical concentration of polymerization was essentially zero. Also, the fragmentation process of filaments due to the addition of high concentrations of chaotropic salts such as KSCN and KI (except Pi) can be observed and stabilization of the hydrophobic interactions by Pi was confirmed. The present study demonstrates that the polymerization and fragmentation dynamics on single actin filaments can be examined quantitatively by fluorescence microscopy.

Acknowledgments. The authors would like to thank Dr JMQ Davies of Waseda University for his critical reading of the manuscript. The authors also thank Miss Ikuko Fujiwara for her assistance in preparing figures. This research was supported in part by Grants-in-Aid for Scientific Research, for Scientific Research on Priority Areas and for the HighTech Research Center Project from the Ministry of Education, Science, Sports and Culture of Japan, and Core Research for Evolutional Science and Technology (CREST) from the Japan Science and Technology Corporation (JST), and a Waseda University Special Grant-in-Aid.

References

Allen PG, Laham LE, Way M, Janmey PA (1996a) Binding of phosphate, aluminum fluoride, or beryllium fluoride to F-actin inhibits severing by gelsolin. J Biol Chem 271:4665–4670

Allen PG, Shuster CB, Kas J, Chaponnier C, Janmey PA, Herman IM (1996b) Phalloidin binding and rheological differences among actin isoforms. Biochemistry 35:14062–14069

Bearer EL (1991) Direct observation of actin filament severing by gelsolin and binding by gCap39 and CapZ. J Cell Biol 115:1629–1638

Cacace MG, Landau EM, Ramsden JJ (1997) The Hofmeister series: salt and solvent effects on interfacial phenomena. Q Rev Biophys 30:241–277

Cano ML, Cassimeris L, Joyce M, Zigmond SH (1992) Characterization of tetramethylrhodaminylphalloidin binding to cellular F-actin. Cell Motil Cytoskel 21:147–158

Carlier M-F (1989) Role of nucleotide hydrolysis in the dynamics of actin filaments and microtubules. Int Rev Cytol 115:139–170

Coluccio LM, Tilney LG (1984) Phalloidin enhances actin assembly by preventing monomer dissociation. J Cell Biol 99:529–535

Dancker P, Fischer S (1989) Stabilization of actin filaments by ATP and inorganic phosphate. Z Naturforsch C44:698–704

Dancker P, Hess L (1990) Phalloidin reduces the release of inorganic phosphate during actin polymerization. Biochim Biophys Acta 1035:197–200

Dancker P, Löw I, Hasselbach W, Wieland Th (1975) Interaction of actin with phalloidin: Polymerization and stabilization of F-actin. Biochim Biophys Acta 400:407–414

De la Cruz EM, Pollard TD (1994) Transient kinetic analysis of rhodamine phalloidin binding to actin filaments. Biochemistry 33:14387–14392

De la Cruz EM, Pollard TD (1996) Kinetics and thermodynamics of phalloidin binding to actin filaments from three divergent species. Biochemistry 35:14054–14061

Drubin DG, Jones HD, Wertman KF (1993) Actin structure and function: Roles in mitochondrial organization and morphogenesis in budding yeast and identification of the phalloidin-binding site. Mol Biol Cell 4:1277–1294

Estes JE, Selden LA, Gershman LC (1981) Mechanism of action of phalloidin on the polymerization of muscle actin. Biochemistry 20:708–712

Estes JE, Selden LA, Kinosian HJ, Gershman LC (1992) Tightly-bound divalent cation of actin. J Muscle Res Cell Motil 13:272–284

Fujiwara I, Takahashi S, Tadakuma H, Ishiwata S (1998) Visualization of polymerization process of single actin filaments under total reflection microscope. Biophysics (Japanese) 38:S63 (Abstr)

Funatsu T (1986) Structural stability and capping proteins of actin filaments. Doct Diss Waseda University

Funatsu T, Ishiwata S (1985) Characterization of β-actinin: A suppressor of the elongation at the pointed end of thin filaments in skeletal muscle. J Biochem 98:535–544

Funatsu T, Asami Y, Ishiwata S (1988) β-actinin: A capping protein at the pointed end of thin filaments in skeletal muscle. J Biochem 103:61–71

Harada Y, Sakurada K, Aoki T, Thomas DD, Yanagida T (1991) Mechanochemical coupling in actomyosin energy transduction studied by in vitro movement assay. J Mol Biol 216:49–68

Hayashi T, Ip W (1976) Polymerization polarity of actin. J Mechanochem Cell Motil 3:163–169

Holmes KC, Popp D, Gebhard W, Kabsch W (1990) Atomic model of the actin filament. Nature 347:44–49

Honda H, Nagashima H, Asakura S (1986) Directional movement of F-actin in vitro. J Mol Biol 191:131–133

Hotta M, Ishiwata S (1997) Temperature dependence of association and dissociation rate constants of rhodamine phalloidin with actin filaments. J Muscle Res Cell Motil 18:491 (Abstr)

Huang Z, Haugland RP, You W, Haugland RP (1992) Phalloidin and actin binding assay by fluorescence enhancement. Anal Biochem 200:199–204

Isambert H, Venier P, Maggs AC, Fattoum A, Kassab R, Pantaloni D, Carlier M-F (1995) Flexibility of actin filaments derived from thermal fluctuations. Effect of bound nucleotide, phalloidin, and muscle regulatory proteins. J Biol Chem 270:11437–11444

Ishiwata S (1998) The use of fluorescent probes. In: Current Methods in Muscle Physiology (ed by Sugi H) Oxford University Press, Oxford, UK, pp 199–222

Ishiwata S, Funatsu T (1985) Does actin bind to the ends of thin filaments in skeletal muscle? J Cell Biol 100:282–291

Kabsch W, Mannherz HG, Suck D, Pai EF, Holmes KC (1990) Atomic structure of the actin: DNase I complex. Nature 347:37–44

Kinosian HJ, Selden LA, Estes JE, Gershman LC (1993) Actin filament annealing in the presence of ATP and phalloidin. Biochemistry 32:12353–12357

Kondo H, Ishiwata S (1976) Uni-directional growth of F-actin. J Biochem 79:159–171

Korn ED, Carlier M-F, Pantaroni D (1987) Actin polymerization and ATP hydrolysis. Science 238:638–644

Kuang B, Rubenstein PA (1997) Beryllium fluoride and phalloidin restore polymerizability of a

mutant yeast actin (V266G, L267G) with severely decreased hydrophobicity in a subdomain 3/4 loop. J Biol Chem 272:1237–1247

Lorenz M, Popp D, Holmes KC (1993) Refinement of the F-actin model against X-ray fiber diffraction data by the use of a directed mutation algorithm. J Mol Biol 234:826–836

Maciver SK, Zot HG, Pollard TD (1991) Characterization of actin filament severing by actophorin from *Acanthamoeba castellani.* J Cell Biol 115:1611–1620

Masui I, Tadashige J, Nishizaka T, Ishiwata S (1995) Microscopic analysis of polymerization process on a single actin filament. Proc Annu Meet Phys Soc Jpn 29:pA3 (Abstr)

Melander WR, Corradini D, Horvath C (1984) Salt-mediated retention of proteins in hydrophobic-interaction chromatography. Application of solvophobic theory. J Chromatogr 317:67–85

Miki M (1987) The recovery of the polymerizability of Lys-61-labelled actin by the addition of phalloidin. Fluorescence polarization and resonance-energy-transfer measurements. Eur J Biochem 164:229–235

Miki M, Hozumi T (1991) Interaction of maleimidobenzoyl actin with myosin subfragment 1 and tropomyosin-troponin. Biochemistry 30:5625–5630

Moens PDJ, Yee D, dos Remedios CG (1994) Determination of the radial coordinate of Cys-374 in F-actin using fluorescence resonance energy transfer spectroscopy: Effect of phalloidin on random assembly. Biochemistry 33:13102–13108

Nishizaka T, Yagi T, Tanaka Y, Ishiwata S (1993) Right-handed rotation of an actin filament in an in vitro motile system. Nature 361:269–271

Nishizaka T, Miyata H, Yoshikawa H, Ishiwata S, Kinosita Jr K (1995) Unbinding force of a single motor molecule of muscle measured using optical tweezers. Nature 377:251–254

Nonomura Y, Katayama E, Ebashi S (1975) Effect of phosphates on the structure of the actin filament. J Biochem 78:1101–1104

Oosawa F, Asakura S (1975) Thermodynamics of the polymerization of proteins. Academic Press, New York

Oosawa F, Kasai M (1962) Theory of linear and helical aggregations of macromolecules. J Mol Biol 4:10–21

Orlova A, Egelman EH (1992) Structural basis for the destabilization of F-actin by phosphate release following ATP hydrolysis. J Mol Biol 227:1043–1053

Pollard TD, Cooper JA (1986) Actin and actin-binding proteins. A critical evaluation of mechanisms and functions. Annu Rev Biochem 55:987–1035

Rickard JE, Sheterline P (1986) Cytoplasmic concentrations of inorganic phosphate affect the critical concentration for assembly of actin in the presence of cytochalasin D or ADP. J Mol Biol 191:273–280

Rickard JE, Sheterline P (1988) Effect of ATP removal and inorganic phosphate on length redistribution of sheared actin filament populations. Evidence for a mechanism of end-to-end annealing. J Mol Biol 201:675–681

Sampath P, Pollard TD (1991) Effects of cytochalasin, phalloidin, and pH on the elongation of actin filaments. Biochemistry 30:1973–1980

Steinmetz MO, Stoffler D, Müller SA, Jahn W, Wolpensinger B, Goldie KN, Engel A, Faulstich H, Aebi U (1998) A correlative analysis of actin filament assembly, structure, and dynamics. J Mol Biol 276:1–6

Suzuki N, Mihashi K (1989) Subunit flow in F-actin under steady-state conditions. Application of a novel method to determination of the rate of subunit exchange of F-actin at the terminals. Biophys Chem 33:177–193

Tadashige J, Nishizaka T, Ishiwata S (1992) Direct observation of the dynamic process of polymerization and depolymerization on single actin filaments. Biophysics (Japanese) 32:S194 (Abstr)

Takahashi S, Ishiwata S (1998) Direct observation of polymerization process of single actin filaments under fluorescence microscope. Biophys J 74:A46 (Abstr)

Wegner A (1976) Head to tail polymerization of actin. J Mol Biol 108:139–150

Wendel H, Dancker P (1987) Influence of phalloidin on both the nucleation and the elongation phase of actin polymerization. Biochim Biophys Acta 915:199–204

Wieland T, de Vries JX, Schäfer AJ, Faulstich H (1975) Spectroscopic evidence for the interaction of phalloidin with actin. FEBS Lett 54:73–75

Woodrum DT, Rich SA, Pollard TD (1975) Evidence for biased bidirectional polymerization of actin filaments using heavy meromyosin prepared by an improved method. J Cell Biol 67:231–237

Yanagida T, Nakase M, Nishiyama K, Oosawa F (1984) Direct observation of motion of single F-actin filaments in the presence of myosin. Nature 307:58–60

Seitz.[15] Of course, these results should be regarded as lower bounds of the errors in more realistic circumstances. In particular, if motion of the substratum is nonuniform, then σ values may double or even triple those found in this simple test.

Summary

The optical flow algorithm presented here is a robust method that rapidly yields a high-density field of substrate displacement vectors based on two optical images. We found that one of the limiting factors, at least for inexperienced experimentalists, is the consistency of focusing or the drift in microscope focus. However, with properly collected images the standard error of the measurement was estimated to be on the order of ± 0.10 pixels. Finally, although the discussion has been focused on the displacement of flexible substrata, a similar method should be applicable for detecting movements on other types of images, as long as the movement involves a certain degree of local coordination.

Acknowledgments

This research was supported by the Computational Science Graduate Fellowship funded by the Department of Energy to W. A. Marganski, NIH Grant GM61806 to M. Dembo, and NIH Grant GM32476 and NASA Grant NAG2-1495 to Y.-L. Wang.

[15] P. Seitz, *Opt. Eng.* **27,** 535 (1988).

[11] Single-Molecule Imaging of Rotation of F_1-ATPase

By KENGO ADACHI, HIROYUKI NOJI, and KAZUHIKO KINOSITA, JR.

Introduction

A single molecule of F_1-ATPase has been shown to be a rotary motor, driven by adenosine triphosphate (ATP) hydrolysis, in which the central γ subunit rotates against a surrounding cylinder made of alternately arranged three α and three β subunits.[1–5] Together with another (yet putative) proton-driven rotary motor F_0, it constitutes the F_0F_1-ATP synthase that synthesizes ATP from adenosine

[1] P. D. Boyer, *Biochim. Biophys. Acta* **1140,** 215 (1993).
[2] P. D. Boyer, *Biochim. Biophys. Acta* **1458,** 252 (2000).
[3] K. Kinosita, Jr., R. Yasuda, H. Noji, and K. Adachi, *Philos. Trans. R. Soc. Lond. B* **355,** 473 (2000).
[4] K. Kinosita, Jr., R. Yasuda, and H. Noji, *Essays Biochem.* **35,** 3 (2000).
[5] H. Noji and M. Yoshida, *J. Biol. Chem.* **276,** 1665 (2001).

0076-6879/03 $35.00

diphosphate (ADP) and inorganic phosphate using proton flow as the energy source. Isolated F_1 composed of $\alpha_3\beta_3\gamma_1\delta_1\varepsilon_1$ subunits only hydrolyzes ATP, and hence is called F_1-ATPase. Its subcomplex $\alpha_3\beta_3\gamma$ suffices for rotation driven by ATP hydrolysis. Single-molecule imaging of this subcomplex has revealed detailed mechanical and kinetic properties of the motor activity, and high-resolution atomic structures of F_1 are already available.[6,7] At present, F_1-ATPase is one of the best characterized molecular motors, or nucleotide-driven molecular machines. It is possible to learn a lot from this rotary machine about the molecular mechanism of chemomechanical energy transduction.

Because all molecular machines work stochastically, their operations can never be synchronized with each other in a rigorous sense. Thus, it is necessary to watch the individual behaviors closely. With F_1-ATPase, for example, we have been able to show that it rotates in a unique direction,[8] that it does so in discrete 120° steps,[9,10] and that 120° steps are resolved into ~90° and ~30° substeps at low ATP concentrations.[11] We have also been able to measure its rotary torque, and have shown that its energy conversion efficiency can reach ~100%.[9,12] We believe that it would be very difficult, if not impossible, to obtain these results without dealing with individual molecules. Here we describe in detail the techniques involved, hoping that they may also be applicable to other molecular machines, in particular to the detection of conformational changes underlying their function (note that a conformational change accompanies reorientation, or partial rotation, of one part against the other).

For the detection of rotation (or conformational changes), we recommend the complementary use of large and small probes. Here we describe two examples, an actin filament as a probe that is large compared to the rotary motor, and a single fluorophore as a small and less perturbing probe. We begin with the preparation of materials, and proceed to the setting of functional motor molecules on a glass surface and then to imaging and analysis.

Preparation of Proteins

The $\alpha_3\beta_3\gamma$ subcomplex of F_1 derived from thermophilic *Bacillus* PS3 is expressed in *Escherichia coli*.[13] To fix the subcomplex on a glass surface, 10 histidines

[6] J. P. Abrahams, A. G. W. Leslie, R. Lutter, and J. E. Walker, *Nature* **370,** 621 (1994).

[7] Y. Shirakihara, A. G. W. Leslie, J. P. Abrahams, J. E. Walker, T. Ueda, Y. Sekimoto, M. Kambara, K. Saika, Y. Kagawa, and M. Yoshida, *Structure* **5,** 825 (1997).

[8] H. Noji, R. Yasuda, M. Yoshida, and K. Kinosita, Jr., *Nature* **386,** 299 (1997).

[9] R. Yasuda, H. Noji, K. Kinosita, Jr., and M. Yoshida, *Cell* **93,** 1117 (1998).

[10] K. Adachi, R. Yasuda, H. Noji, H. Itoh, Y. Harada, M. Yoshida, and K. Kinosita, Jr., *Proc. Natl. Acad. Sci. U.S.A.* **97,** 7243 (2000).

[11] R. Yasuda, H. Noji, M. Yoshida, K. Kinosita, Jr., and H. Itoh, *Nature* **410,** 898 (2001).

[12] H. Noji, D. Bald, R. Yasuda, H. Itoh, M. Yoshida, and K. Kinosita, Jr., *J. Biol. Chem.* **276,** 25480 (2001).

[13] T. Matsui and M. Yoshida, *Biochim. Biophys. Acta* **1231,** 139 (1995).

(His tag) have been incorporated genetically at the N terminus of the β subunit. To label the stalk region of the γ subunit with a probe, γ-Ile-210* or γ-Ser-107* has been replaced with cysteine, and α-Cys-193, the only cysteine in the wild-type $\alpha_3\beta_3\gamma$ subcomplex, has been replaced with serine by site-directed mutagenesis. The mutant $\alpha_3\beta_3\gamma$ subcomplex is purified as follows.[12]

Purification of F_1

1. Incubate cell lysate at 65° for 15 min, and remove the denatured *E. coli* protein by centrifugation (e.g., 216,000*g* for 30 min at 4°).
2. Apply the supernatant containing F_1 on an Ni^{2+}-NTA Superflow column (Qiagen) equilibrated with 50 m*M* imidazole, pH 7.0, and 100 m*M* NaCl. Wash the column with 100 m*M* imidazole, pH 7.0, and 100 m*M* NaCl, and then elute the enzyme with 500 m*M* imidazole, pH 7.0, and 100 m*M* NaCl.
3. Add ammonium sulfate to the fraction containing the enzyme to the final concentration of 10% saturation. Apply the solution to a butyl-Toyopearl column (Tosoh, Tokyo, Japan) equilibrated with 500 m*M* imidazole, pH 7.0, 100 m*M* NaCl, and 10% saturated ammonium sulfate. To remove endogenously bound nucleotides, wash the column with 10 column volumes of a solution containing 100 m*M* potassium phosphate, pH 7.0, 2 m*M* EDTA, and 10% saturated ammonium sulfate.
4. Elute the enzyme with 50 m*M* Tris–HCl, pH 8.0, and 2 m*M* EDTA, and store as precipitate in 70% saturated ammonium sulfate containing 2 m*M* dithiothreitol (DTT) at 4°.

Conjugation of F_1 with Streptavidin

For rotation assay with actin filaments, we use the cysteine mutant at γ-Ser-107; with the γ-Ile-210-Cys mutant, we rarely find rotating actin filaments.

1. Collect the mutant subcomplex (γS107C) stored as precipitate by centrifugation at low speed (e.g., 18,800*g* for 15 min at 4°), and dissolve in buffer A (20 m*M* MOPS–KOH, pH 7.0, 100 m*M* KCl) containing 5 m*M* dithiothreitol.
2. Incubate for 30 min at room temperature to fully reduce the sole cysteine (S107C) at the γ subunit.

* In thermophilic *Bacillus* PS3, the precursory polypeptide of γ subunit contains four amino acid residues at the N terminus to be truncated. The amino acid sequence of the γ subunit registered in the DNA databank starts from an Ala residue, which is the first amino acid residue after the truncation. In our expression vector, the precursory sequence of γ has been removed from the cloned DNA sequence and the residual DNA sequence starting from the Ala residue has been conjugated after the Met residue (start codon) to express the γ subunit. In this article, as well as our previous reports, the numbers of amino acids in the γ subunit have been determined from the DNA sequence including the Met residue in the expression vector, and are therefore larger by one than these in the DNA databank.

3. To remove dithiothreitol and possibly dissociated subunits, pass the solution through a size-exclusion column (Superdex 200 HR 10/30; Amersham Pharmacia Biotech, Piscataway, NJ) equilibrated with buffer A.
4. Incubate the enzyme with a two molar excess of 6-{*N'*-[2-(*N*-maleimide) ethyl]-*N*-piperazinylamido}hexyl-D-biotinamide(biotin-PEAC$_5$-maleimide, Dojindo, Kumamoto, Japan) in buffer A for 6 hr on ice.
5. Remove unbound biotin with a gel filtration column (PD-10, Amersham Pharmacia Biotech) equilibrated with buffer A. Specific biotinylation of the γ subunit is confirmed by Western blotting with horseradish peroxidase avidin D (Vector Laboratories, Burlingame, CA), and the capacity for streptavidin binding is confirmed by an assay using 4-hydroxyazobenzene-2-carboxylic acid (HABA).[14]
6. Add eight molar excess of streptavidin (Pierce, Rockford, IL) to the biotinylated enzyme, and incubate for 1 hr at 23°.
7. Purify the enzyme conjugated with streptavidin on a Superdex 200 column equilibrated with buffer A.

Fluorescent Biotinylated Actin Filament

Actin is extracted from acetone powder of rabbit skeletal muscles and purified as previously described.[15] Actin is covalently biotinylated at Cys-374 with biotin maleimide, and labeled with TMR–phalloidin.

1. Incubate 50 μM F-actin with 500 μM biotin-PEAC$_5$-maleimide in buffer B (10 m*M* MOPS–KOH, pH 7.0, 100 m*M* KCl, 1 m*M* $MgCl_2$) for 6 hr on ice.
2. Quench the reaction by adding 0.2% 2-mercaptoethanol, and collect F-actin by centrifugation (350,000*g* for 60 min at 4°).
3. Depolymerize the pellet in buffer C (2 m*M* Tris–HCl, pH 8.0, 0.2 m*M* $CaCl_2$, 0.2 m*M* ATP) overnight on ice, and clean the obtained G-actin by centrifugation (350,000*g* for 60 min at 4°).
4. Polymerize G-actin in buffer B overnight on ice. Then repeat the depolymerization protocol (step 3 above).
5. Remove unreacted biotin with a gel filtration column (PD-10) equilibrated with buffer C. Biotinylated G-actin is obtained.
6. Polymerize 5 μM biotinylated G-actin in buffer B containing 12.5 μM phalloidin–tetramethylrhodamine B isothiocyanate conjugate (TMR–phalloidin, Fluka, Ronkonkoma, NY). To remove free dye and nucleotides, precipitate F-actin by centrifugation (100,000*g* for 30 min at 4°), and resuspend in buffer D (10 m*M* MOPS–KOH, pH 7.0, 50 m*M* KCl, 2 m*M*

[14] Y. Kunioka and T. Ando, *J. Biochem.* (*Tokyo*) **119,** 1024 (1996).
[15] J. A. Spudich and S. Watt, *J. Biol. Chem.* **246,** 4866 (1971).

$MgCl_2$). This washing procedure is repeated twice. Estimate the final concentration of F-actin using $\varepsilon_{1\%}^{290\,nm} = 0.63$. Typically, about 70% of the actin is recovered through the washing. The amount of free ATP and ADP in 370 n*M* actin prepared in this way has been estimated by luciferin–luciferase assay[16] to be $\leq$50 n*M* after conversion of ADP to ATP by incubation with 0.2 mg/ml creatine kinase and 2.5 m*M* creatine phosphate for 30 min at room temperature, and does not increase for at least several weeks.

Labeling F_1 with Single Fluorophore

To detect the rotation of the γ subunit by the measurement of fluorophore orientation, the fluorophore should be firmly attached to γ. We have tested several combinations of γ-mutants (S107C, I210C, or S107C/I210C) and fluorescent dyes that are suitable for general single-fluorophore imaging (tetramethylrhodamine-5-maleimide, Molecular Probes, Eugene, OR; Cy3-maleimide or Cy3-bismaleimide, Amersham Pharmacia). We looked for the combination that would give the highest fluorescence anisotropy in solution, a measure of the wobble of the fluorophore on a protein molecule. Among those tested, the subcomplex $\alpha_3\beta_3\gamma$(I210C) labeled with Cy3-maleimide at the sole cysteine in γ gave the highest fluorescence anisotropy of 0.32 (λ_{ex} = 550 nm; λ_{em} = 590 nm; measured in a Hitachi F-4500 spectrofluorometer), indicating that the fluorophore wobble on the subcomplex was within a cone of having a semiangle <25°.[17] A bis-functionalized dye conjugated to two properly spaced cysteines would be the best approach for firm attachment, but bridging between the two reactive sites is not necessarily guaranteed. In our experience, a fluorophore, even without covalent attachment, often finds a (hydrophobic) site that embraces the fluorophore firmly enough. Trial and error is our preferred approach. The procedure for Cy3 labeling is given below.

1. Using the mutant subcomplex (γI210C), follow steps 1–3 of the procedure for the conjugation of F_1 with streptavidin above.
2. Mix the subcomplex in the column eluent with 1.1-fold molar excess of Cy3-maleimide in buffer A (20 m*M* MOPS–KOH, pH 7.0, 100 m*M* KCl) and incubate for 30 min at room temperature.
3. Remove unreacted Cy3-maleimide with a Superdex 200 column equilibrated with buffer A to terminate the reaction. Determine the labeling ratio by assuming $\varepsilon_{555}^{Cy3} = 150{,}000\,M^{-1}\,cm^{-1}$,[18] $\varepsilon_{280}^{Cy3} = 15{,}000\,M^{-1}\,cm^{-1}$, and $\varepsilon_{280}^{F1} = 154{,}000\,M^{-1}\,cm^{-1}$.[19]

[16] M. Deluca and W. D. McElroy, *Methods Enzymol.* **57,** 3 (1978).
[17] K. Kinosita, Jr., S. Kawato, and A. Ikegami, *Biophys. J.* **20,** 289 (1977).
[18] L. A. Ernst, R. K. Gupta, R. B. Mujumdar, and A. S. Waggoner, *Cytometry* **10,** 3 (1989).
[19] T. Matsui, E. Muneyuki, M. Honda, W. S. Allison, C. Dou, and M. Yoshida, *J. Biol. Chem.* **272,** 8215 (1997).

Preparation of Surfaces for F_1 Attachment

Ni^{2+}-NTA Polystyrene Beads for Observation of Actin Rotation

Amino polystyrene beads of 0.224 μm diameter (Polysciences, Warrington, PA) are covalently coated with amino-NTA [*N*-(5-amino-1-carboxypentyl) iminodiacetic acid, Dojindo] via ethylene glycol bis[succinimidylsuccinate] (EGS, Pierce) linkage as follows:

1. Dissolve EGS in *N,N*-dimethylformamide at 100 m*M* and add 1 volume to 9 volumes of 1% (w/v) bead suspension in 100 m*M* MOPS–KOH, pH 7.0. Incubate for 15 min at room temperature.
2. Add 100 m*M* amino-NTA to the mixture, and incubate for 1 hr at room temperature.
3. Wash the beads four times with 100 m*M* MOPS–KOH, pH 7.0, by centrifugation (e.g., 10,000*g* for 10 min).
4. Wash the beads four times with 10 m*M* $NiCl_2$ and 10 m*M* glycine to form Ni^{2+}-NTA. Remove unbound Ni^{2+} by washing four times with 100 m*M* MOPS–KOH, pH 7.0.

Ni^{2+}-NTA Glass Coverslip for Single-Fluorophore Imaging

Unless coverslips are properly cleaned, dust or impurities show up as numerous light spots under conditions for single-fluorophore imaging. Some dust particles, even bright ones, are apparently photobleached in one step, due possibly to detachment and more likely to actual photobleaching. These cannot be readily distinguished from genuine single fluorophores, and thus preparation of clean glass surfaces is crucial to single-fluorophore imaging.[20]

1. Immerse glass coverslips (Micro Cover Glass, No. 1, 24 × 36 mm^2 and 18 × 18 mm^2, Matsunami, Osaka, Japan) in 20 *N* KOH for 1 day to clean the surfaces. We use a ceramic container that holds each coverslip vertically and separately throughout the procedure.
2. Wash the coverslips extensively with ultrapure water.
3. Incubate the coverslips in 0.01% (v/v) acetic acid containing 2% (v/v) 3-glycidyloxypropyltrimethoxysilane (Fluka) for 3 hr at 90°. The pH should be adjusted to pH 5.
4. Wash the coverslips with ultrapure water.
5. Incubate the coverslips in 0.01 *M* $NaHCO_3$, pH 10.0, containing 10% (w/v) amino-NTA (Qiagen) for 16 hr at 60°. In this procedure, the coverslips are stacked in a small dish in a small amount of solution, because amino-NTA

[20] K. Adachi, K. Kinosita, Jr., and T. Ando, *J. Microsc. (Oxford)* **195,** 125 (1999).

is expensive. We reuse the reaction solution several times because of the stability of amino-NTA.

6. Wash the coverslips with ultrapure water.
7. Incubate the coverslips in 10 m*M* $NiCl_2$ (or $NiSO_4$) and 5 m*M* glycine, pH 8.0, for 2 hr at room temperature. The glycine is added to modify unreacted epoxy group.
8. Wash the coverslips with ultrapure water.
9. Store the coverslips in ultrapure water until use (within a few weeks).

Rotation Assay Using Actin Filaments

Flow Chamber

A flow chamber is constructed with two coverslips (bottom, 24 × 36 mm^2; top, 18 × 18 mm^2) separated by two greased spacers (Parafilm cover sheet) of ~50 μm thickness.[8] The volume of the chamber is typically 10 μl. We fix a subcomplex of F_1 on surface-bound beads (0.224 μm in diameter) through 10 histidines (His tag) linked to the amino terminus of each β. The purpose of the bead pedestal is to let F_1 on the top rotate freely, without surface obstructions or impeding factors such as the higher than bulk friction near the glass surface.[21] A fluorescently labeled actin filament is attached to γ of F_1 through streptavidin–biotin linkage. Glucose oxidase, catalase, and glucose make up an oxygen-scavenger system[22] that serves to retard photobleaching of fluorescent dye. Creatine kinase and creatine phosphate are an ATP-regenerating system that maintains the initial ATP concentration.

1. Infuse 1 chamber volume of 0.1% (w/v) Ni^{2+}-NTA beads in buffer D (10 m*M* MOPS–KOH, pH 7.0, 50 m*M* KCl, 2 m*M* $MgCl_2$) containing 2 m*M* $MgCl_2$ into the flow chamber, and allow the beads to adhere to the glass surface for 15 min. The bead density will be several beads per 5 × 5 μm^2.
2. Wash the chamber twice with 3 volumes of buffer D′ [buffer D containing 10 mg/ml bovine serum albumin (BSA)].
3. Infuse 1 volume of 10 n*M* streptavidin-F_1 in buffer D′. After 2 min, wash the chamber twice with 3 volumes of buffer D′.
4. Dilute labeled actin filaments from the 370 n*M* stock 10 times in buffer D′ before use, and infuse 1.5 volumes of the 37 n*M* actin into the flow chamber. After 15 min, wash the chamber with 3 volumes of buffer D′.
5. Infuse 2 volumes of buffer D′ containing 0.5% 2-mercaptoethanol, 6 mg/ml glucose, 0.2 mg/ml glucose oxidase, 30 U/ml catalase, an ATP regenerating system consisting of 2.5 m*M* creatine phosphate and 0.2 mg/ml creatine kinase, and a desired amount of MgATP.

[21] A. J. Hunt, F. Gittes, and J. Howard, *Biophys. J.* **67,** 766 (1994).
[22] Y. Harada, K. Sakurada, T. Aoki, D. D. Thomas, and T. Yanagida, *J. Mol. Biol.* **216,** 49 (1990).

Observation

We observe the flow chamber on an inverted fluorescence microscope (TMD300, Nikon; excitation filter: HQ525/50, dichroic mirror: Q555, emission filter; HQ590/50, Chroma Technology) with an intensified (KS-1381, Videoscope) charge-coupled device (CCD) camera (Dage MTI) at 23°. Actin rotation can be observed for 30–40 min. In the absence of Ni^{2+}-NTA beads, or with untreated amino beads, few actin filaments are bound to the glass surface. Washing with 500 m*M* imidazole in buffer D′ (10 m*M* MOPS–KOH, pH 7.0, 50 m*M* KCl, 2 m*M* $MgCl_2$, 10 mg/ml BSA) removes nearly 80% of actin filaments, whereas 500 m*M* KCl in buffer D′ removes only ~20%. In this way, we confirm that the actin filaments are attached to the F_1 subcomplex fixed on the Ni^{2+}-NTA beads through histidine tags.

In the presence of ATP, rotating fluorescent actin filaments are found on the surfaces of the chamber. On the bottom surface, the filaments rotate counterclockwise. On the inverted microscope where the light beam is reflected once before reaching a video camera or eye, an observed image corresponds to the view from above, or, for the F_1 on the bottom surface, the view from the F_0 side. At low (<1 μM) ATP concentrations, rotation is resolved into discrete 120° steps (Fig. 1).

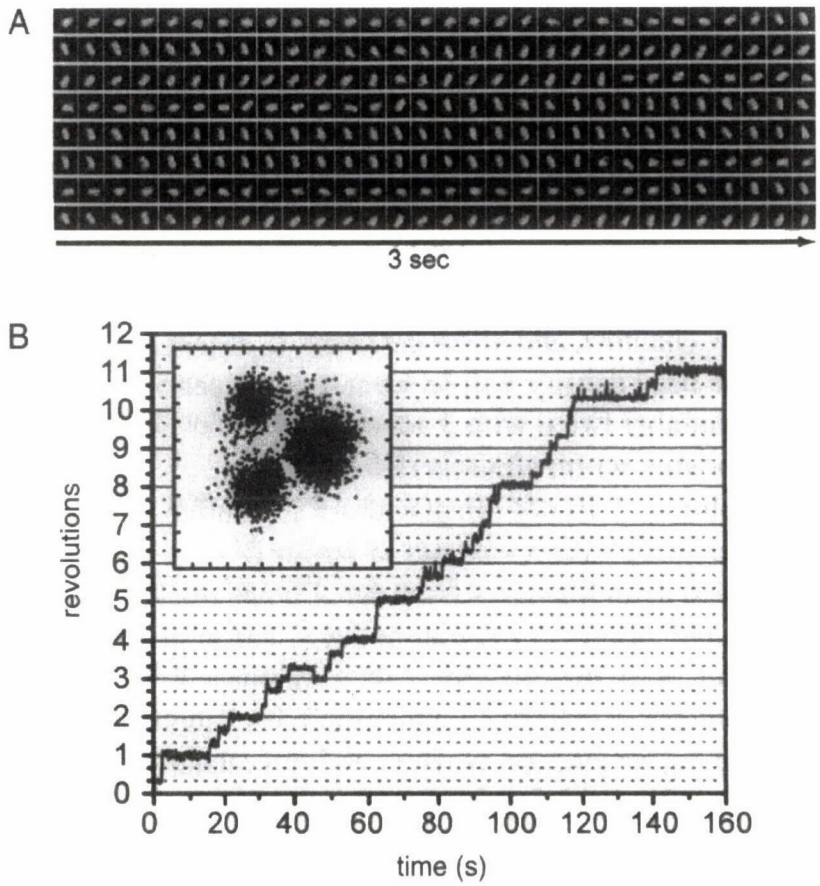

FIG. 1. Stepwise rotation of F_1-ATPase at 20 n*M* ATP. (A) Sequential images, at 0.1-sec intervals, of an actin filament of length 1.1 μm attached to the γ subunit of F_1-ATPase. (B) Time course of the rotation in (A). Inset shows the trace of centroid of the actin image.

Determination of Torque

When an actin filament is attached to the γ subunit of F_1, F_1 rotates the filament against hydrodynamic friction. The Reynolds number for an actin filament moving in water is extremely low, $<10^{-4}$. The torque generated by F_1-ATPase is therefore balanced with hydrodynamic friction. When a filament rotates around an axis at the middle of the filament, the friction is given by[21]:

$$\xi = (\pi/3)\eta\omega L^3/[\ln(L/2r) - 0.447]$$

where $\eta(=10^{-3}$ N m^{-2} sec) is the viscosity of water at room temperature, ω is the angular velocity, L is the length of the filament, and $r(=5$ nm) is the radius of the actin filament. Most filaments rotate around an axis away from the mid point. The friction in these cases is estimated as the sum of two parts:

$$\xi = (4\pi/3)\eta\omega\{L_1^3/[\ln(L_1/r) - 0.447] + L_2^3/[\ln(L_2/r) - 0.447]\}$$

where L_1 is the length from one edge to the axis and L_2 from the other edge. [In some of our earlier publications,[3,9,23] this equation for the case of $L_2 = 0$ was incorrectly cited as $(4\pi/3)\eta\omega L^3/[\ln(L/2r) - 0.447]$, where "2" in the denominator should have been omitted.] Note that these equations are applicable to filaments rotating well above a surface; filaments close to a surface experience much higher friction.[21] We try not to overestimate the torque, and thus we use these equations without introducing possibly ambiguous corrections.

We determine the position of rotation axis, the length of the filament, and the angular velocity as follows.

Axis. Find, in sequential images of a rotating filament, a fixed point. Placing a cursor on the monitor screen will help.

Length. Make sure that the video camera is not saturated, because, due to diffraction, an actin filament may appear longer (and thicker) by up to the wavelength of light, ~550 nm for TMR fluorescence. We define the edges of a filament as the points at which the fluorescence intensity is half-way between the highest intensity and background. To obtain reliable torque values, we recommend analyzing long ($\gtrsim 2$ μm) filaments.

Angular Velocity. The rotation angle can be determined, image by image, manually on a screen. If a digital image processor is available, the easiest method is to calculate the centroid of the filament image, which will move on a circular trajectory.[8] Alternatively, calculate the long and short axes of the filament from quadratic moments of the filament image. The latter method works even when the rotation axis is close to the middle of the filament.

At high ATP concentrations, F_1 bearing an actin filament shows continuous rotation (Fig. 2A and B). The angular velocity, however, is not strictly constant, presumably due to thermal fluctuations. We determine the angular velocity, and

[23] K. Kinosita, Jr., *FASEB J.* **13**, S201 (1999).

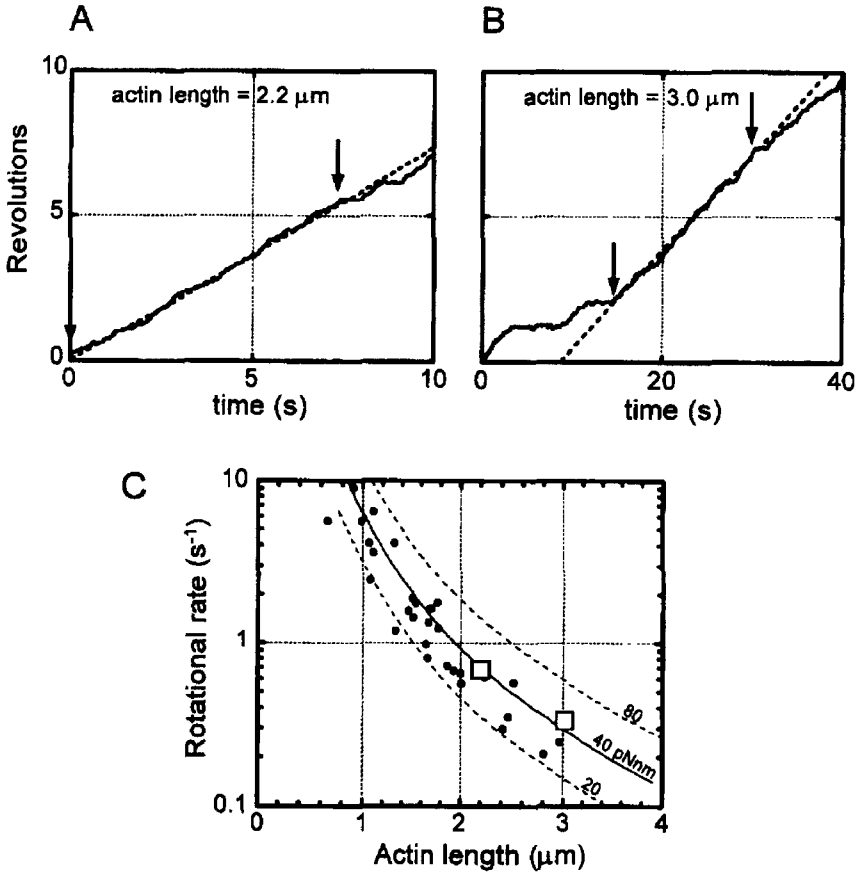

FIG. 2. Estimation of the torque of F_1. (A and B) Time courses of the rotation of an actin filament of length of 2.2 μm (A) or 3.0 μm (B) at 2 m*M* ATP. The average velocities are determined by averaging over five continuous revolutions (between arrows) as 0.69 and 0.33 revolution per second (dashed lines). (C) Rotational rate versus the length of the actin filament rotating around an axis at an edge. For actin filaments having a rotary axis away from the edge, $(L_1^3 + L_2^3)^{1/3}$ is plotted as the length because a torque value determined from the value is virtually as same as that determined from L_1 and L_2 within an experimental error. Large diamonds indicate the data in (A) and (B).

hence the torque, by averaging over at least five continuous revolutions that are not interrupted by unnatural pauses such as the last part of Fig. 2A and the first part of Fig. 2B. These pauses often occur at a certain angle(s), suggesting obstruction by nearby debris or glass surface (the filament may be oblique to the surface). Another reason might be that F_1 lapses at intervals into a catalytic inactive state called the MgADP-inhibited state. During this state, which lasts for ~30 sec in the wild-type $\alpha_3\beta_3\gamma$ subcomplex of thermophilic F_1, F_1 exhibits rotational fluctuation about a certain angle; continuous rotation resumes after a while.[24] The pauses by MgADP inhibition are readily distinguished, because they occur at angles 120° apart.[24]

Figure 2C shows rotational rate versus the length of the actin filament in the presence of 2 m*M* ATP. Most data are on or below the line representing the constant

[24] Y. Hirono-Hara, H. Noji, M. Nishiura, E. Muneyuki, K. Y. Hara, R. Yasuda, K. Kinosita, Jr., and M. Yoshida, *Proc. Natl. Acad. Sci. U.S.A.* **98**, 13649 (2001).

torque of 40 pN nm. We think that higher velocity values are more reliable, because any obstructions against rotation would reduce the velocity, and conclude that F_1 exerts a constant torque of about 40 pN nm regardless of the length of the filament.

Optics for Single-Fluorophore Imaging

The optical system is located in a clean room and mounted on a vibration isolation table. An optical layout for single-fluorophore polarization imaging is illustrated in Fig. 3. A 532-nm laser beam (DPSS 532-200, Coherent) is first focused onto a rotating diffuser disk (lemon-skin filter, Nikon, Tokyo, Japan) to average out speckle pattern and interference fringes. The linearly polarized laser beam is passed through a quarter-wave plate to make it circularly polarized. That the resulting excitation beam is isotropic in the image plane is confirmed by observing the beam through a polarizer placed on the sample stage. In experiments where the excitation

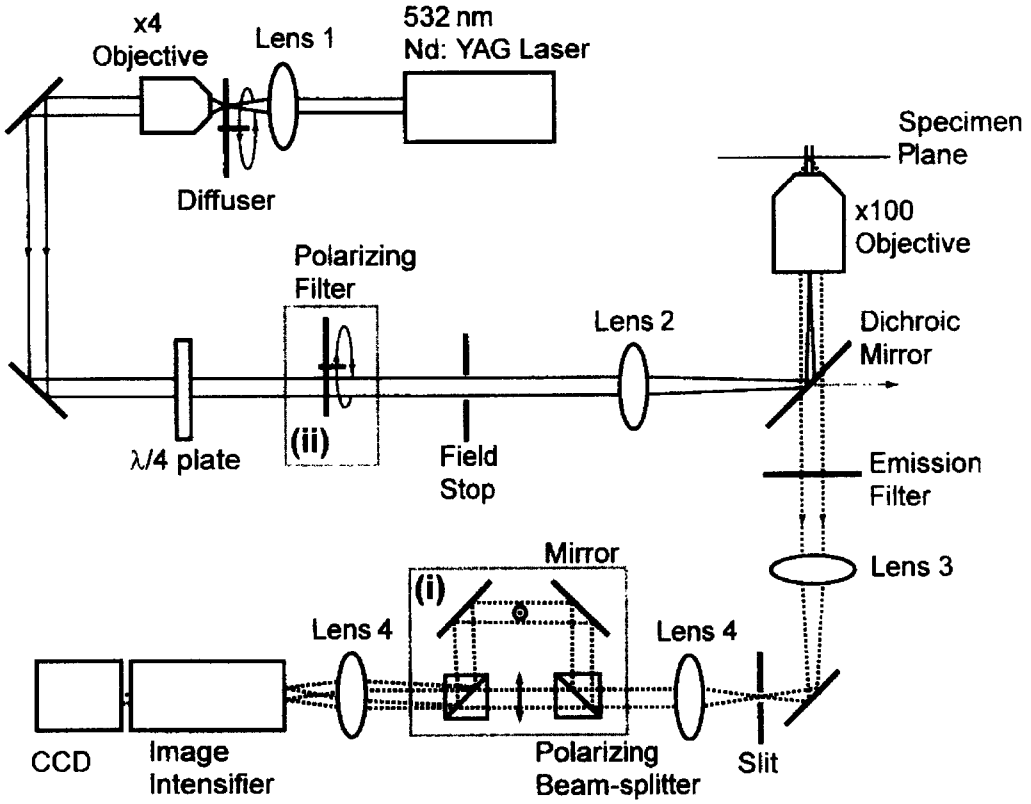

FIG. 3. Optical system for single fluorophore imaging. An Nd : YAG laser (532 nm) is used as the excitation light source. Lens 1 focuses the beam onto a rotating diffuser disk and the scattered beam is collimated with the ×4 objective. Lenses 4 produce a parallel beam in between. The focal lengths are lens 1, 50 mm; lens 2, 350 mm; lens 3, 180 mm; lens 4, 80 mm. Lens 3 is originally provided inside the microscope body, and the slit is positioned at the side camera port. Either (i) or (ii) is inserted, depending on the experimental demand. In the actual system, the excitation beam travels through the microscope from left to right.

polarization is rotated, a rotating sheet polarizer (HN32, Polaroid) is inserted after the quarter-wave plate [(ii) in Fig. 3]. The beam is introduced into a fluorescence microscope (IX70, Olympus) through a field diaphragm and a condenser lens (Lens 2, Fig. 3). A custom-made holder for a dichroic mirror (550DRLP, Chroma Technology; separation wavelength, 550 nm, Brattleboro, VT) allows entrance of the excitation beam from the right-hand side and exit of the unreflected portion to the left, preventing scattering in the body and thus reducing the background noise.[25] Lens 2 has a long focal length such that only the center of the objective aperture is illuminated; depolarization by the objective is thus avoided.

Fluorescence is collected through an oil-immersion objective (PlanApo 100×, NA 1.4, Olympus) and detected through a bandpass filter (BP590/50, Chroma Technology) with an image intensifier (VS4-1845, Videoscope, Sterling, VA) coupled to a CCD camera (CCD-300T-IFG, Dage MTI, Michigan City, IN). We have found that, whereas a water-immersion objective combined with quartz coverslips gives a lower background luminescence and usually a higher signal-to-noise ratio,[25] the signal itself from a single fluorophore is higher with the oil-immersion objective; for Cy3 and rhodamine fluorescence, therefore, we generally use the oil objective. When fluorescence emission is to be decomposed into vertically and horizontally polarized components, a dual-view apparatus[26] [(i) in Fig. 3] is inserted before the camera, onto which the two components are simultaneously projected. On the intermediary image plane after Lens 3 (Fig. 3), a rectangular slit is placed that defines the edges of the pair of images so that they can be positioned side by side without overlapping. We check whether the two components are detected with the same sensitivity by observing a thin layer of isotropic fluorescent solution sandwiched between coverslips. If disparity is found, we place coverslips in one of the split beams.

Rotation Assay Using Single-Fluorophore

Flow Chamber

Preparation of a flow chamber is carried out on a clean bench. The chamber is constructed of a bottom coverslip (24 × 36 mm^2) coated with Ni^{2+}-NTA and an uncoated top coverslip (18 × 18 mm^2) separated by two greased spacers. One chamber volume is typically ~10 μl. BSA is not used as blocking agent in the buffer for single-fluorophore imaging to avoid dust or impurities.

1. Infuse 50 p*M* Cy3-$\alpha_3\beta_3\gamma$ in buffer E (10 m*M* MOPS–KOH, pH 7.0, 50 m*M* KCl, 4 m*M* $MgCl_2$) into a flow chamber.
2. Allow 2 min for surface attachment, and wash the chamber with 5 chamber volumes of buffer E.

[25] I. Sase, H. Miyata, J. E. T. Corrie, J. S. Craik, and K. Kinosita, Jr., *Biophys. J.* **69,** 323 (1995).
[26] K. Kinosita, Jr., H. Itoh. S. Ishiwata, K. Hirano, T. Nishizaka, and T. Hayakawa, *J. Cell. Biol.* **115,** 67 (1991).

3. Infuse 5 volumes of degassed buffer E containing 0.5% 2-mercaptoethanol, 216 μg/ml glucose oxidase, 360 μg/ml catalase, 4.5 mg/ml glucose, 0.2 mg/ml creatine kinase, 2.5 m*M* creatine phosphate, and a desired amount of ATP.
4. To prevent evaporation, seal the open edges of the chamber with colorless nail lacquer.

Imaging

The orientations of individual fluorophores, and thus of γ, are assessed by two methods: (i) from the polarization of emitted fluorescence with the dual-view apparatus[27] and (ii) from the polarization dependence of the efficiency of light absorption by rotating the excitation polarization.[28] Method (i) has theoretically unlimited time resolution, and method (ii) is superior in angular resolution.

The flow chamber is observed using a fluorescent microscope in a clean room controlled at 23°. The laser power is decreased appropriately with neutral density filters; higher power increases emission from a single fluorophore but decreases the time to photobleaching. We set the excitation intensity at 1.1 mW over a sample area of 24 μm in diameter, Cy3 fluorophores can be observed for ~30 sec. We videotape dozens of fluorescent spots in a field of view until most of them are photobleached, and then move to a new field. A chamber is observed for a total of ~30 min. Usually, we cannot distinguish rotating fluorophores until we analyze the recorded images.

In method (i), a vertically oriented fluorophore will show up in the *V* (vertically polarized) image, and a horizontal one will appear in the *H* (horizontally polarized) image. Alternate appearance, as shown in Fig. 4A, indicates rotation of the γ-shaft. For method (ii), the polarization axis of excitation light is rotated continuously in the sample plane at 1 Hz, in the counterclockwise direction when viewed from above the microscope. A higher rotary rate may be employed when F_1 rotation is fast, at the expense of higher signal-to-noise ratio. Under rotating excitation, fluorophores are expected to fluorescence when the excitation polarization becomes parallel with their absorption transition moment. The fluorophore in Fig. 4B remains vertical from beginning to end, presumably being on an inactive F_1. In contrast, the fluorophore in Fig. 4C is initially at an 8 o'clock–2 o'clock orientation, turned into a 4 o'clock–10 o'clock orientation in the second row, and then turned through a vertical orientation to the 8 o'clock–2 o'clock orientation.

Analysis of Polarization

Images recorded on a Hi8 video recorder (EVO-9650, Sony) are analyzed with a digital image processor (C2000, Hamamatsu Photonics) and personal computer.

[27] I. Sase, H. Miyata, S. Ishiwata, and K. Kinosita, Jr., *Proc. Natl. Acad. Sci. U.S.A.* **94,** 5646 (1997).
[28] T. Ha, T. Enderle, D. S. Chemla, P. R. Selvin, and S. Weiss, *Phys. Rev. Lett.* **77,** 3979 (1996).

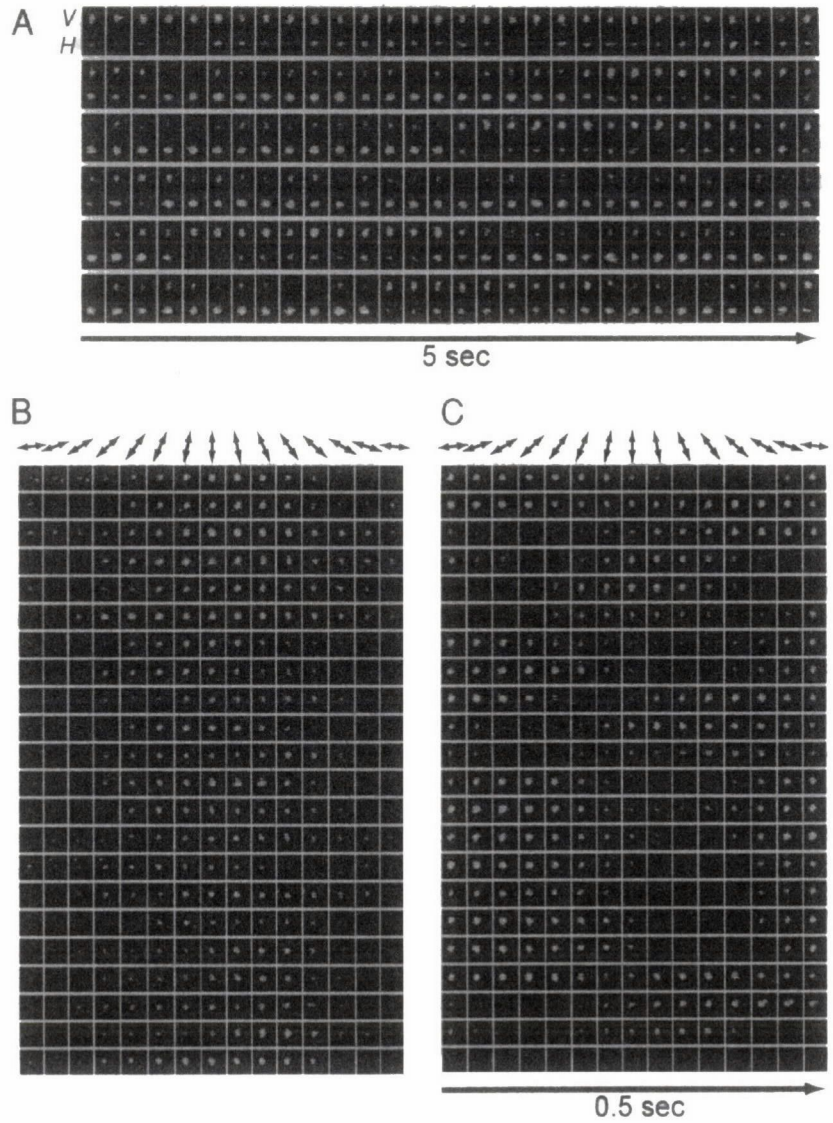

FIG. 4. (A) Sequential fluorescence images obtained with method (i). Images of a single Cy3-F_1 molecule rotating in the presence of 20 n*M* ATP are shown at 167-ms intervals. *V*, vertically polarized fluorescence; *H*, horizontally polarized fluorescence. Each image has been averaged spatially over 3 × 3 pixels; the size of the images shown is 15 × 30 pixels (1.5 × 3.0 μm^2). (B and C) Sequential fluorescence images obtained with method (ii). Single Cy3-F_1 at 20 n*M* ATP; 33-ms intervals. Each image has been averaged spatially over 3 × 3 pixels; the size of the images shown is 17 × 17 pixels. Arrows at the top indicate the direction of excitation polarization. In (C), the fluorophore was photobleached in the last row.

Fluorescence intensity of a spot is calculated as the integrated intensity over a square of 8 × 8 pixels (0.79 × 0.79 μm^2) enclosing the spot; background intensity calculated in the same way in the area after photobleaching is subtracted.

In method (i), time courses of spot intensities for *V* (vertically polarized fluorescence) and *H* (horizontally polarized fluorescence) are plotted as in Fig. 5A. Alternations of the two curves are the signature of rotation. Polarization ($P = [V - H]/[V + H]$) is calculated (Fig. 5C). At the low ATP concentration,

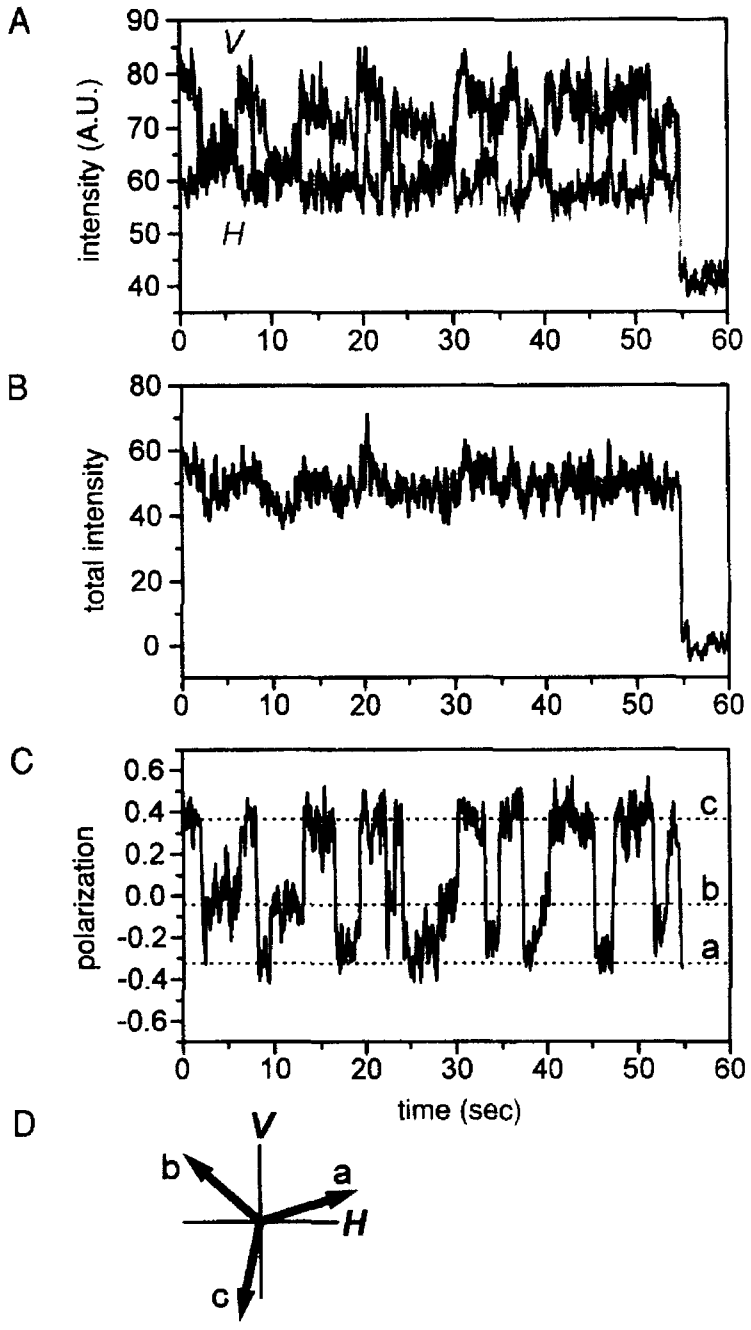

FIG. 5. (A) Time courses of spot intensities for V and H in Fig. 4A, median filtered over eight video frames (0.27 sec). The fluorophore was photobleached at ~55 sec. (B) Time course of the total intensity, $V + H$, calculated from (A). (C) Time course of the polarization, $P = (V - H)/(V + H)$, calculated from (A) and (B). Dashed lines (a, b, and c) are calculated P for the three orientations in (D): $P = 0.4 \times [\sin^2(\theta + 18°) - \cos^2(\theta + 18°)]$, where $\theta = 0°$, 120°, and 240°.

rotation of F_1 is expected to be stepwise, and indeed we see three levels of polarization, a, b, and c, in Fig. 5C. The three polarization values can be explained by the three orientations separated by 120° (Fig. 5D).

In method (ii), the fluorescence intensity oscillates with time as shown in Fig. 6A. When a fluorophore lies at an angle θ in the sample plane, its intensity is

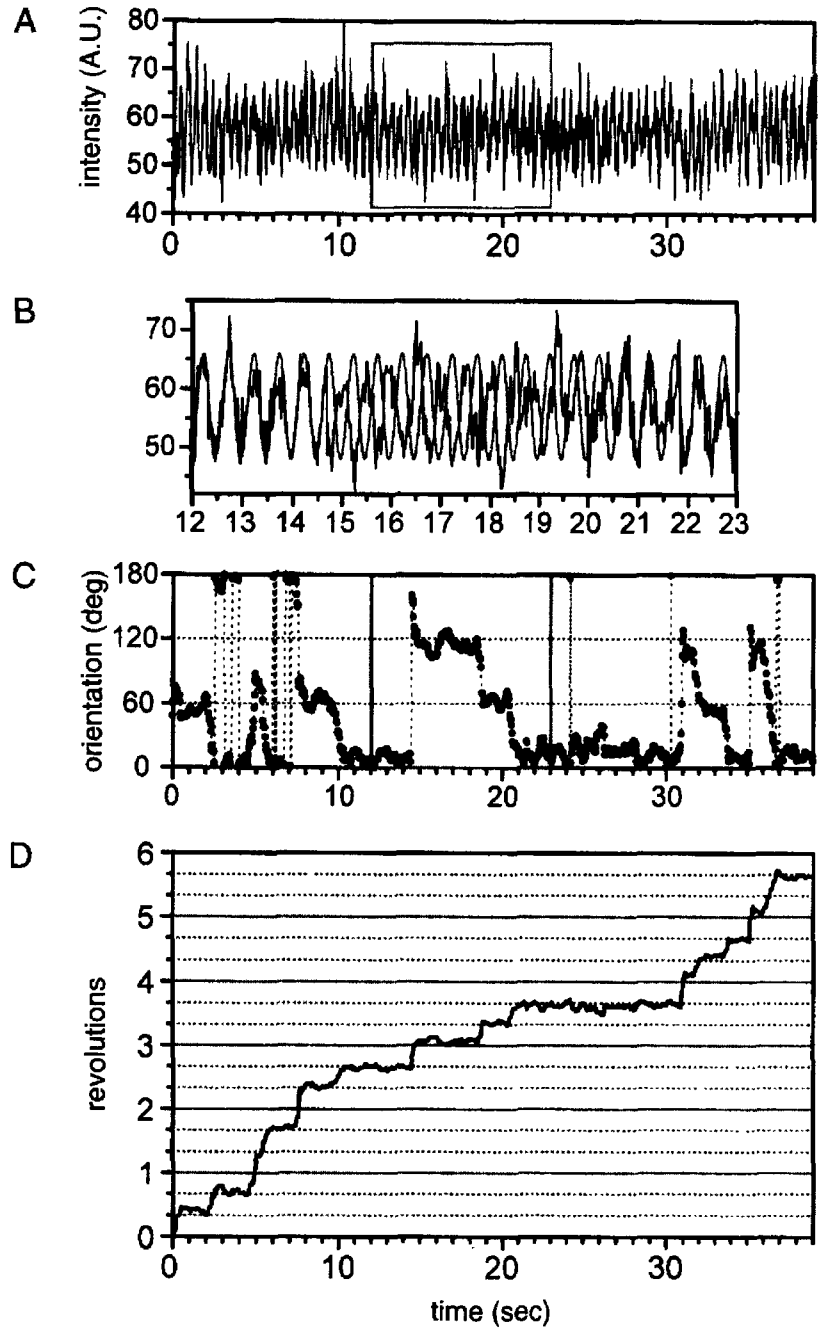

FIG. 6. (A) Time course of the fluorescence intensity in Fig. 4C. (B) Expanded view of the time course in (A) between 12 and 23 sec. (C) Time course of the fluorophore angle calculated from (A). (D) Accumulated rotation angle estimated from (C).

expected to flicker as a periodic function of time: $\cos^2[360°(t/T) - \theta] \propto \cos[360°(2t/T) - 2\theta]$, where t is time and $T(= 1$ sec) is the period of excitation rotation. Thus, the orientation at time t, $\theta(t)$, is determined by fitting the observed intensity, $I(t)$, with this function over the period between t and $t + T/2$. Figure 6C shows $\theta(t)$ calculated from Fig. 6A; values between 0° and 180° are chosen. The orientation steps among three levels. If this fluorophore had remained

at θ at $t = 12$ sec, $I(t)$ would have flickered as in the gray curve (Fig. 6B). In fact it changed its orientation at 14.7, 18.6, and 20.7 sec. The accumulated rotation angle, as shown in Fig. 6D, is obtained from Fig. 6C by assuming that all steps are counterclockwise; negative 60° steps (or positive 120° steps) in Fig. 6C are interpreted as counterclockwise 120° steps. The positive 60° step at ~5 sec is interpreted as rapid succession of two counterclockwise 120° steps within the 0.5-sec fitting window used for the angle analysis.

Conclusion

Single-molecule imaging with a large or small probe is a versatile tool for the investigation of the mechanisms of protein machines, revealing their conformational changes in real time (note that rotation we observe in F_1 is a conformational change in a large scale). Probes that are large compared to protein molecules are easily observed by conventional microscopy. Interpretation of the images is often straightforward, and intense signals from a large probe allows precise analysis. Asymmetric probes such as the actin filament are smart probes in that they amplify reorientational motions (= conformational changes) in a protein molecule without requiring a sophisticated instrument. In contrast, probes smaller than protein molecules, such as single fluorophores, are much less perturbing and enable observation under no load. By virtue of gene engineering, a single fluorophore can be attached at any desired site on a protein molecule, reporting the behavior of that particular site. We hope this article will encourage many laboratories to join the venture of single-molecule physiology, where one studies conformational dynamics of molecular machines in real time while they are at work.

Acknowledgments

We thank Masasuke Yoshida, Ryohei Yasuda, Hiroyasu Itoh, and the members of CREST (Core Research for Evolutional Science and Technology) Team 13 for suggestions and discussion, and Kerstin Steinert of Qiagen for the Ni^{2+}-NTA protocol. This work was supported in part by Grants-in-Aid from the Ministry of Education, Science, Sports, and Culture of Japan and CREST.

Annu. Rev. Biophys. Biomol. Struct. 2004. 33:245–68
doi: 10.1146/annurev.biophys.33.110502.132716

First published online as a Review in Advance on January 16, 2004

ROTATION OF F_1-ATPASE: How an ATP-Driven Molecular Machine May Work

Kazuhiko Kinosita, Jr.,[1] Kengo Adachi,[1] and Hiroyasu Itoh[2,3]
[1]*Center for Integrative Bioscience, Okazaki National Research Institutes, Higashiyama 5-1, Myodaiji, Okazaki 444-8585, Japan; email: kazuhiko@ims.ac.jp; adachi@ims.ac.jp*
[2]*Tsukuba Research Laboratory, Hamamatsu Photonics KK, and* [3]*CREST "Creation and Application of Soft Nano-Machine, the Hyperfunctional Molecular Machine" Team 13*, Tokodai, Tsukuba 300-2635, Japan; email: hiritoh@hpk.trc-net.co.jp*

Key Words molecular motor, single-molecule physiology, torque generation, efficiency of energy conversion, free energy

■ **Abstract** F_1-ATPase is a rotary motor made of a single protein molecule. Its rotation is driven by free energy obtained by ATP hydrolysis. In vivo, another motor, F_o, presumably rotates the F_1 motor in the reverse direction, reversing also the chemical reaction in F_1 to let it synthesize ATP. Here we attempt to answer two related questions, How is free energy obtained by ATP hydrolysis converted to the mechanical work of rotation, and how is mechanical work done on F_1 converted to free energy to produce ATP? After summarizing single-molecule observations of F_1 rotation, we introduce a toy model and discuss its free-energy diagrams to possibly answer the above questions. We also discuss the efficiency of molecular motors in general.

CONTENTS

INTRODUCTION

F_1-ATPase

F_1-ATPase is a part of the enzyme ATP synthase that synthesizes ATP from ADP and inorganic phosphate (Pi) using proton flow across the membrane as the energy source (10, 26, 60, 67). The membrane-embedded F_o portion conducts protons, which drive the catalytic synthesis of ATP in the water-soluble F_1 portion. The ATP synthase is a reversible molecular machine in that hydrolysis of ATP in F_1 can pump protons through F_o in the opposite direction against an electrochemical gradient of protons. To explain the energetic coupling between the proton flow in F_o and synthesis/hydrolysis of ATP in F_1, Boyer & Kohlbrenner (12) and Oosawa and colleagues (17, 43) independently proposed rotational catalysis at about the same time, although a full account of the latter's model (44) appeared late. The prediction was that both F_o and F_1 are rotary motors, F_o being powered by proton flow and F_1 by ATP hydrolysis, and that the genuine rotary directions of the two are opposite to each other yet the two have a common rotary shaft (rotor). When the drop of proton electrochemical potential across the membrane exceeds the free energy obtained by ATP hydrolysis, F_o wins and F_1 is forced to rotate in its reverse direction, resulting in the synthesis of ATP in its catalytic sites. If the free energy of ATP hydrolysis is larger, rotation is in the direction of F_1 and protons are pumped back. Crystal structures of F_1 (1) and F_oF_1 (53) suggested that the two are indeed rotary motors, and unidirectional rotation, counterclockwise when viewed from the F_o side, was videotaped for an isolated F_1 attached to a glass surface (40). For the whole ATP synthase, reorientation of γ under proton-motive force has been indicated in a cross-linking study (68), and single-molecule study (9a) has suggested rotation. Proton driven rotation, clockwise and stepwise, has recently been demonstrated in a fluorescence resonance energy transfer study (70).

Isolated F_1, consisting of $\alpha_3\beta_3\gamma\delta\varepsilon$ subunits (in bacteria), only hydrolyzes ATP and hence is called F_1-ATPase. An $\alpha_3\beta_3\gamma$ subcomplex suffices for rotation and hydrolysis activities: The central γ subunit rotates inside a cylinder made of three α and three β subunits arranged alternately (Figures 1 and 2) when ATP is hydrolyzed in three catalytic sites each hosted primarily by a β subunit. In this article, we focus on this simplest subcomplex and, hereafter, refer to it simply as F_1.

The Question

The central question we ask in this article is, How are the chemical reactions, synthesis or hydrolysis of ATP, in the catalytic sites coupled to the mechanical

rotation of γ? Hydrolysis of one molecule of ATP accompanies a free-energy drop ΔG of

$$\Delta G = \Delta G_0 + k_B T \ln[\mathrm{ADP}][\mathrm{Pi}]/[\mathrm{ATP}], \quad 1.$$

where $\Delta G_0 = -50$ pN · nm is the standard free-energy change at pH 7 (6; also see recent beautiful work in Reference 56), and $k_B T = 4.1$ pN · nm is the thermal energy at room temperature (k_B, the Boltzmann constant; T, absolute temperature). Under physiological conditions of [ATP] $\sim 10^{-3}$ M, [ADP] $\sim 10^{-4}$ M, and [Pi] $\sim 10^{-3}$ M, ΔG is about -90 pN · nm. ΔG is negative under all practical conditions, implying that the reaction always proceeds in the direction of hydrolysis and that spontaneous net synthesis of ATP never happens in solution. How, then, is this chemical reaction, which is destined to proceed in one direction, converted to unidirectional rotation that can do work against an external opposing torque?

In this article, we first summarize rotational characteristics of F_1 revealed by single-molecule observations. The results allow us to deduce potential energies for γ rotation in various chemical states. We then try to answer the central question on the basis of these potential energies. In doing so, we introduce a toy model that can reproduce the experimental potential energies and that, if fabricated by future nanotechnology, would work as an ATP-driven rotary motor. Our goal is to show a possible, concrete mechanism of chemo-mechanical energy transduction that bears some essential features of the actual F_1 motor. We discuss how a motor senses free energy of ATP hydrolysis and how it responds to an external load. Our discussion is yet premature and may contain incorrect statements, but we hope that some of the concepts we present here may be useful in interpreting or designing future experiments.

ROTATION OF F_1

Single-Molecule Observations of F_1 Rotation

Counterclockwise rotation was first imaged in F_1 from a thermophilic bacterium by attaching a fluorescent actin filament to γ while fixing the $\alpha_3\beta_3$ cylinder to a glass surface (40). Since then, counterclockwise rotation has been confirmed in F_1 from *Escherichia coli* (39, 41) and plants (19). Rotation of tags other than actin has been imaged successfully (2), including a single fluorophore (2a), spherical bead or bead duplex (18, 65), metal bar (52), or a single donor-acceptor pair for fluorescence resonance energy transfer (9, 63). Subunits attached to γ rotate counterclockwise during ATP hydrolysis, suggesting that they are part of the common rotor shaft in the whole ATP synthase: the ε subunit (24) and the ring of c subunits in F_o (37, 49, 55), but not the a subunit of F_o (37), which is considered to be part of the stator. V_1-ATPase, a relative of F_1-ATPase, also rotates in the same direction (21).

Below we summarize the rotational characteristics of the F_1 motor that are essential to the understanding of the mechanism of chemo-mechanical coupling.

Most of the quoted results were obtained with F_1 from a thermophilic bacterium (40). Details of earlier work have been reviewed elsewhere (26, 67).

120 STEP PER ATP For ATP concentrations, [ATP], from 20 nM to 6 mM, rotation occurs in discrete 120° steps (2a, 64, 65). The time-averaged stepping rate depends on [ATP] in a Michaelis-Menten manner, with a V_{max} of 390 steps s^{-1} and K_m of 15 μM (65). Statistical analysis of intervals between steps at various [ATP] indicates that each step is driven by the hydrolysis of one ATP molecule (2a, 64, 65). The average stepping rate of single molecules above, however, is somewhat higher than the hydrolysis rate measured in solution (65), apparently suggesting that the coupling ratio, the number of 120° steps per ATP molecules consumed, is greater than 1. Presumably, the hydrolysis rate is underestimated, because part of F_1 in solution is inhibited by MgADP (10, 18, 23, 26, 32), whereas a single-molecule observation focuses on active molecules in the field of view (26). Our expectation is that the coupling ratio is close to but slightly less than 1.

ANGLE-INDEPENDENT TORQUE When a micrometer-sized actin filament is attached to γ, F_1 rotates slowly because of the hydrodynamic friction against the moving actin filament. The frictional drag coefficient, ξ, is given (2, 20) by:

$$\xi = (4\pi/3)\eta L^3/[\ln(L/r) - 0.447] \qquad 2.$$

for an actin filament of length L and radius r (~5 nm) rotating around one end, where η is the viscosity of the medium and is $\sim 10^{-3}$ Nm^{-2} s at room temperature. (This equation was mistyped in some of our earlier work.) If, instead of actin, a spherical bead of radius a is attached off axis such that the distance between the bead center and rotation axis is x, ξ is given by:

$$\xi = 8\pi\eta a^3 + 6\pi\eta a x^2. \qquad 3.$$

The torque N needed to rotate the filament against the friction is given by:

$$N = \omega\xi, \qquad 4.$$

where ω is the speed of rotation (in radians s^{-1}). From the rotation speed during each 120° step, the torque F_1 produces against the friction is estimated to be ~44 pN · nm; the torque appears independent of the rotary angle, because the rotation speed is constant during a 120° step (25). A similar value of 40 pN · nm is obtained from the rotation speed averaged over many revolutions, under the condition of high enough [ATP] in which F_1 bearing an actin filament rotates smoothly without apparent steps (64). Thus, the work F_1 can do in a 120° step amounts to 80–90 pN · nm or ~20 k_BT, calculated as 40–44 pN · nm × $(2/3)\pi$ radian (=120°). This is almost equal to the physiological $|\Delta G|$ for ATP hydrolysis above, suggesting that the energy conversion efficiency, the average work done in a 120° step divided by $|\Delta G|$, can reach ~100% (but see below). The torque of ~44 pN · nm may be somewhat underestimated, because the friction near a glass surface

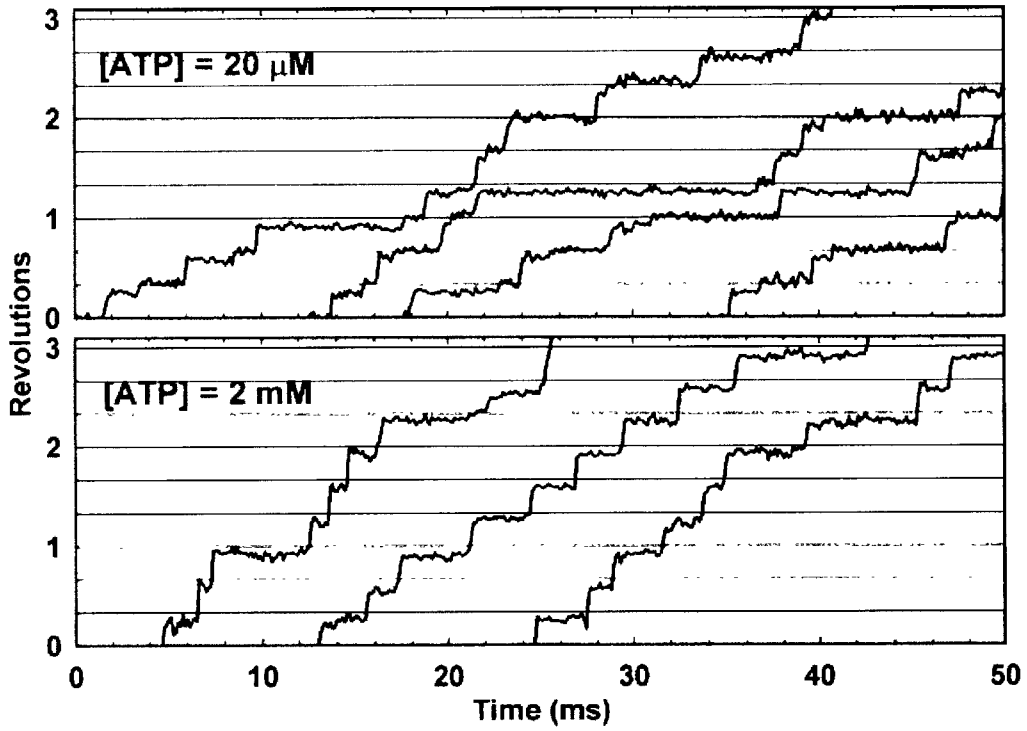

Figure 3 Substeps in F_1 rotation at 20 μM ATP (*upper panel*) recorded with a temporal resolution of 0.125 ms (65). With this resolution, substeps are not discerned at 2 mM ATP (*lower panel*), implying that the ATP-waiting dwell is <0.125 ms and the next 90° rotation is complete within 0.125 ms of ATP binding; it also implies that F_1 is completely reset and ready to bind a next ATP by the end of a 30° substep. Horizontal solid lines are separated by 120°, and dotted lines are drawn 30° below.

is higher than the estimate in Equations 2 and 3 (20). A slightly higher value, 50 pN · nm, has been estimated from the curvature of an actin filament attached to γ (45). Here, the torque of F_1 is balanced by the elastic recoil of a bent actin, which, unlike friction, is a conservative force.

80°–90° SUBSTEP BY ATP BINDING AND 40°–30° SUBSTEP BY PRODUCT RELEASE A 40-nm gold bead attached to γ (Figure 1) does not impede rotation, at least as far as the average stepping rate is concerned, even though the bead is approximately four times as large as F_1. Figure 3 shows time courses of the bead rotation recorded at 8000 frames s^{-1} (65). At 20 μM ATP, the 120° steps are resolved into ~90° and ~30° substeps, as seen in most parts of the record. The dwell before a 90° substep is much longer, on average, at lower [ATP], and the average dwell is inversely proportional to [ATP]. This implies that the 90° substep is triggered by binding of ATP. Because the 90° rotation is complete within 0.125 ms of ATP binding (Figure 3, *lower panel*), most of the 90° rotation seems to be driven directly by ATP binding, and not by a subsequent process such as ATP hydrolysis.

The dwell time before a 30° substep is independent of [ATP]. Analysis indicates that the dwell consists of at least two reactions, each taking ~1 ms (65). Because a

30° substep is immediately (<0.125 ms) followed by a 90° substep at 2 mM ATP (Figure 3, *lower panel*), the 30° substep completely resets the motor to the initial ATP-waiting state. The simplest scenario is that the 30° substep is driven by the release of a hydrolysis product, ADP or Pi, whichever is released last.

When F_1 falls into the MgADP-inhibited state and stops rotating, it stalls at the ~80° position (18). This is consistent with the idea that the 30° substep is associated with ADP release, of which the failure leads to inhibition. Or, the 30° substep may be driven by Pi release, which induces a conformational change in F_1 (31). When rotation is driven by ATP-γ-S, which is slowly hydrolyzed by F_1, video-rate substeps of ~80° and ~40° are observed (50), indicating that ATP hydrolysis occurs before the 30° substep and supporting the contention that ATP binding drives most (80°) of the 90° substep. A fluorescent ATP analog (Cy3-ATP) also induces video-rate substeps of ~80° and ~40° in a mutant F_1, and binding/release of Cy3-ATP has been imaged simultaneously with the substep rotation (37a). This study, combined with the ATP-γ-S study above (50), indicates that one of the two ~1 ms reactions preceding the 30° substep is the ATP hydrolysis in a site that bound ATP one step ago. These more recent results suggest that 80° rather than 90° is closer to the actual substep size, the difference being an experimental error, or that the 80° rotation is driven by ATP binding and the remaining 10° by another process such as ATP hydrolysis.

Potential Energy for γ Rotation

The scheme that emerges from these studies for the potential energy of γ rotation is shown in Figure 4. We distinguish at least three states (A)-(C), (A) being the ATP-waiting state and (A′) being the next ATP-waiting state. For the chemical species involved in rotation, two basic schemes have been proposed: a bi-site scheme in which the occupancy of catalytic sites alternates between 1 and 2 (Figure 4*b*), and a tri-site scheme alternating between 2 and 3 (Figure 4*c*). Previously, we suggested that the bi-site scheme would be the norm because earlier studies (35) indicated bi-site operation at least at low [ATP] and because the rotation rate is characterized by a single K_m down to 20 nM ATP (65). Site occupancy probed by a tryptophan residue engineered in the catalytic sites, however, is more than 2 at $\geq$10 μM ATP, and steady-state hydrolysis activity correlates well with the fraction of molecules with an occupancy number of $\geq$2 (42, 47, 59). Weber & Senior (59, 60) thus conclude that three-site filling is a must for rotation. A crystal structure in which three sites are occupied with a nucleotide (34) also supports a tri-site scheme. Work in our lab is as yet inconclusive: Rotation driven by Cy3-ATP proceeds in a tri-site mode (37a), whereas analysis of fluorescence resonance energy transfer apparently suggests bi-site if crystal structures of mitochondrial F_1 are undistorted by crystal packing (63). The average stepping rate is proportional to [ATP] down to 0.6 nM ATP (N. Sakaki, unpublished results), suggesting that, if it operates in a tri-site mode, two catalytic sites bind a nucleotide extremely tightly, apparently in contradiction to the binding data above. Boyer (11) suggests that bi-site is fundamental, but retention of the ADP to be released may lead to three-site filling.

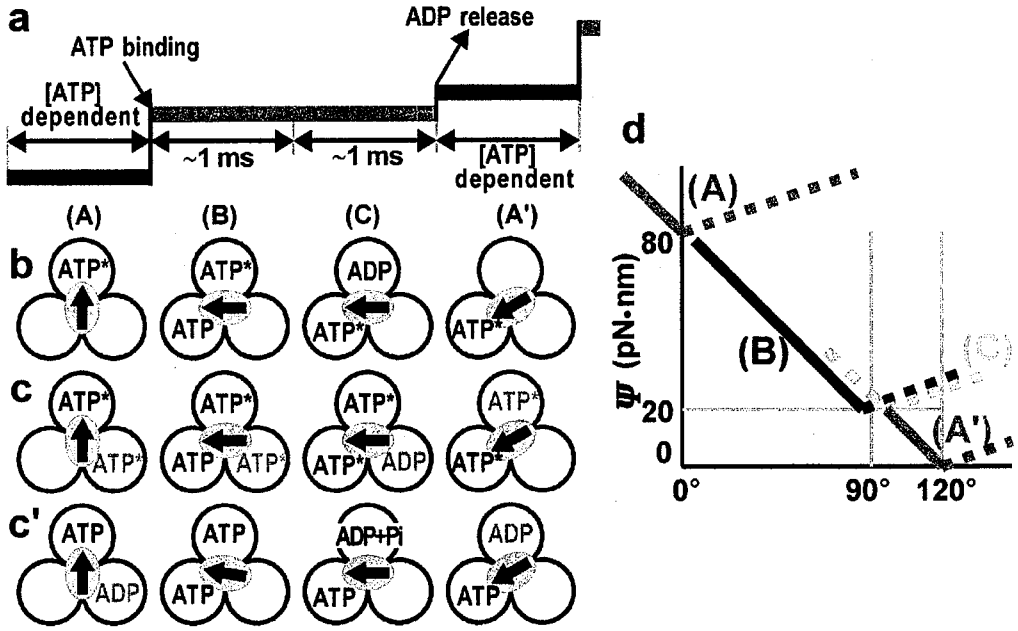

Figure 4 Potential energy for γ rotation deduced from the substep behavior (65). (*a*) Schematic diagram of 90° and 30° substeps. (*b*) Corresponding nucleotide states in a bi-site scheme. The central arrow shows the orientation of γ. ATP* represents ATP or ADP + Pi; ADP may be ADP + Pi or Pi. (*c*) A tri-site scheme. Light shade indicates difference in site occupancy. (*c'*) A tri-site scheme that is closer to *b* is also possible, in which site occupancy remains 2 and becomes 3 only during the 90° substep. (*d*) Potential energies for the four chemical states (A)-(A'). The γ orientation in state (A) is taken as 0°. The vertical shifts of the potential curves in this figure are arbitrary. See Figures 7 and 8 and associated explanations in text.

ATP binding may indeed assist release of a retained ADP (K. Adachi, unpublished data) (Figure 4*c'*). More work is needed before concluding firmly that three sites must be filled for rotation to occur. In this article, we define states (A) and (A') in Figure 4 as the ATP-waiting state, and (B) as the state immediately after ATP binding, regardless of the actual occupancy number.

The scheme in Figure 4*a* and the angle-independent torque of 40–44 pN · nm suggest a potential energy diagram for γ rotation in each chemical state, as in Figure 4*d*. Here, solid lines reflect the experimental constant torque, and dashed lines are added to provide minima at the experimentally observed stationary angles. In the ATP-waiting state (A), γ rests at the potential minimum at 0°. Binding of ATP changes the state to (B), whereupon γ slides down the constant slope toward the minimum at 90°. The chemical transition from (B) to (C) is mechanically almost silent. Release of the last hydrolysis product restores state (A'), whereupon γ slides down the slope for the last 30°. As noted above, the minima for (B) and (C) may well be closer to 80°, or the minimum for (B) near 80° and that for (C) near 90°.

F_1 rotation can be driven by GTP and ITP, but not by CTP and UTP at concentrations up to 300 μM (38). The Michaelis-Menten constant, K_m, for hydrolysis

differs among ATP, GTP, and ITP, but all these purine nucleotides drive an actin filament at similar speeds, implying similar torque. Thus, it appears that the potential energies in Figure 4*d* are the properties intrinsic to F_1, and nucleotides are either able or unable to drive transitions among the potential curves.

How an ATP-Driven Molecular Machine May Work

The potential diagram in Figure 4*d* is our experimental answer to the prime question of how a molecular machine can convert free energy of ATP hydrolysis into work. We believe that protein machines work by changing their conformations. In the case of F_1, rotation of γ is in itself a sequence of conformational changes of F_1, and individual β subunits, in particular, undergo large conformational changes in response to nucleotide binding (Figure 2). Each potential curve in Figure 4*d* thus represents the change in conformational energy of the protein (F_1) in that chemical state, as γ is rotated to designated angles. Before discussing how these potentials could explain rotation, let us summarize in Figure 5 what the experiments have told us. A protein molecule, shown in green, is to do mechanical work by changing its conformation between the upright posture and bent one.

MAJOR WORK IS DONE BY ATP BINDING, AND SOME BY PRODUCT RELEASE At least in F_1, the major, work-producing conformational change (80°–90° rotation) is driven by ATP binding. Another change, back to the original conformation upon product release, also does some positive work. ATP hydrolysis per se does not contribute much to work output. In other words, major free-energy drops, which can be converted to work, occur upon ATP binding and product release (brown arrows in Figure 5). Indeed, on a protein machine such as F_1 and myosin, ATP and its hydrolysis products ADP + Pi are near equilibrium, as demonstrated by spontaneous ATP synthesis on these proteins in the presence of high concentrations of ADP and Pi (30, 48, 61, 66). Exploiting binding and release, rather than hydrolysis, seems natural if one is to design an efficient protein machine: Upon substrate binding, many bonds are newly formed between the substrate and protein, whereas hydrolysis would result mainly in bond reorganization without a gross change in the total number of bonds.

NUCLEOTIDE AFFINITY CHANGES AS ROTATION (CONFORMATIONAL CHANGE) PROCEEDS If ATP binding drives a conformational change in a protein molecule, that particular conformational change will accompany an increase in the affinity for ATP, by the law of action and reaction. Likewise, if ADP (Pi) release drives another conformational change, that will accompany a decrease in the affinity for ADP (Pi). These points are crucial in understanding the mechanism of the F_1 motor and molecular machines in general.

A highly schematic explanation is given in Figure 5 for the case of ATP binding. Starting from the upper left, initial binding of ATP (light color) is accomplished by the formation of multiple weak bonds (violet dots). The fact that ATP binding

induces bending (conformational change) of the protein implies that the ATP molecule pulls the protein toward it by forming more bonds (second from left). As a result, the ATP molecule in the bent protein is now tightly held in the bent protein, implying higher affinity. Constant torque can be explained by sequential increase in the number of bonds. A more realistic view for the particular case of F_1 has been given by molecular dynamics simulation (3).

The magnitude of affinity changes can be estimated by referring to Figure 4*d* (65). As γ is rotated from 0° to 90°, curve (B) for the ATP-bound state becomes lower (more stable) than curve (A) for the state before ATP binding. The stabilization upon the 90° rotation amounts to >60 pN · nm in energy, or to an increase in the affinity for ATP of more than $\exp(60\ \text{pN} \cdot \text{nm}/k_BT) \sim 2 \times 10^6$-fold. Similarly, rotation from 90° to 120° is accompanied by a decrease in the affinity for ADP (Pi) of more than $\exp(20\ \text{pN} \cdot \text{nm}/k_BT) \sim 100$-fold.

THE PRIMARY ROLE OF HYDROLYSIS IS TO RESET THE MACHINE If work is done by binding and release, why is ATP hydrolyzed? The reason is that, after the ATP-driven conformational change, the ATP molecule is so tightly bound that the reaction stops there (second from left in Figure 5). To remove this blocking ATP, the protein machine splits it into two entities so that individual products, each held by a smaller number of bonds, can escape one by one.

In the case of F_1, which synthesizes ATP efficiently upon reverse rotation, we propose (25, 26) that hydrolysis may well produce some work (rotation), although direct evidence is not yet available. The model below considers this possibility.

A CAMSHAFT MODEL OF F_1 ROTATION

Here we present a simple mechanical model (Figure 6) that is based on the models of Oosawa & Hayashi (44) and of Wang & Oster (57). The purpose is to show a relatively concrete example of the mechanism of chemo-mechanical energy conversion that mimics some of the essential features of the F_1 motor. For the purpose of illustration, we design the model to work in a bi-site scheme at moderate ATP concentrations, because a smaller number of chemical pathways need to be considered in bi-site. Most of the discussion below, however, is independent of the details of chemical pathways and thus is applicable to a tri-site scheme as well.

A Push-Pull Mechanism for Torque Generation

As seen in Figure 2, crystal structures of mitochondrial F_1 (1, 15) have shown that a β subunit binding a nucleotide is bent in such a way that its upper portion pushes γ toward and beyond the central axis. An empty β, on the other hand, retracts and pulls γ toward it; an isolated β subunit (62) or βs in an $\alpha_3\beta_3$ complex without γ (51) adopt a conformation similar to the empty β in the whole F_1,

although a recent simulation shows otherwise (8). Wang & Oster (57) have proposed that these push-pull actions against the slightly slant and skewed γ constitute the driving force of rotation. This is consistent with the fact that, in the upper and lower portions of the central cavity of the $\alpha_3\beta_3$ cylinder where γ makes extensive contacts with the cylinder wall (Figure 2, *top*), the cylinder wall is covered with hydrophobic residues (1), allowing lateral slippage while responding to push and pull. The contact at the γ tip (at the lower end of and as illustrated in the top part of Figure 2) seems relatively unimportant, because up to 12 residues can be removed without affecting torque (36). Another major contact is made between γ and the top surface of a β, near the orifice. The contact area of β, the so-called DELSEED motif (yellow atoms in Figure 2, *top*, *left*), contains a cluster of conserved acidic residues, suggesting a role in torque generation. Complete elimination of the negative charges, however, did not affect the rotational characteristics (16), although molecular dynamics simulation suggests a role for this region (29). Thus, we also assume that the push-pull actions by β are the major source of the torque, and we model γ as a camshaft and let bending/unbending of β push/pull the camshaft (Figure 6*a*).

The push, or bending of β, is driven by ATP binding (Figure 6*b*), and conversely a bent β shows a higher affinity for ATP than an unbent β does. The pull, or unbending of β, is driven by the release of ADP (Figure 6*c*), which is assumed to dissociate last, and unbending leads to a lower affinity for ADP (and Pi). The central camshaft is so designed that ATP-driven bending of a β rotates the γ shaft by 80° (Figure 6*e*, *e*1–*e*10), and unbending of another β upon ADP release drives the last 30° from 90° to 120° (Figure 6*e*, *e*13–*e*16). By repeating the sequence in Figure 6*e*, the central γ shaft continues to make counterclockwise 120° steps (see Supplementary Movie 1; follow the Supplemental Material link from the Annual Reviews home page at http://www.annualreviews.org).

The Mechanism Warranting Unidirectional Rotation

In principle, simple pushes and pulls would rotate the shaft in either direction. In our model, there are two stages in which the γ shaft could rotate clockwise (wrong direction). The first is the situation in Figure 6*e*1, in which two βs are empty: Binding of ATP to the wrong β (β_3) would lead to clockwise rotation. Binding to the wrong β, however, is prevented by virtue of the slope of the camshaft. The radii of the cam are varied in such a way that the correct β (β_2) is already bent slightly, whereas β_3 is completely unbent. Thus, the correct β has a higher affinity for ATP, and thus, in most cases, this β binds the next ATP. In a tri-site scheme, the situation of two βs being empty does not arise. However, when ADP is to be released, one of three filled sites needs to be selected. This is equivalent to the choice of an ATP binding site, because ATP will bind to the site from which ADP has dissociated.

The next critical stage is in Figure 6*e*10, in which two βs bind ATP tightly and either ATP could be hydrolyzed. If the β that has just bound ATP (β_2) hydrolyzes

the ATP, the shaft would make a backward substep upon release of the hydrolysis products. To prevent this uncoupling scenario, we postulate (as in References 25, 26, and 44) that hydrolysis of ATP drives a small amount of counterclockwise rotation of γ (Figure 6*d*). That is, the tip of the toy β is twisted to the right (as it faces γ) when its bound ATP is split into ADP + Pi, and further as Pi is released. The law of action and reaction states, then, that twisting the tip of β to the right drives the equilibrium between ATP and ADP + Pi toward hydrolysis, and twisting to the left shifts the equilibrium toward ATP synthesis. Once we assume the coupling between the tip motion and hydrolysis/synthesis reactions, rotation in the correct direction is warranted: In Figure 6*e*10, β_1 can hydrolyze ATP by twisting its tip to the right, but β_2 cannot because the tip motion is obstructed by the cam wall. A theoretical calculation has indicated that a β that presumably has just bound ATP favors ATP over ADP + Pi (13).

Clockwise Rotation Leads to ATP Synthesis

The model predicts synthesis of ATP when the γ shaft is forcibly rotated clockwise. This can be seen by following Figure 6*e* in the reverse order (also see Supplementary Movie 2; follow the Supplemental Material link from the Annual Reviews home page at http://www.annualreviews.org). Clockwise rotation pulls in and thus bends β_1, thereby increasing its affinity for ADP (Figure 6*e*, *e*16–*e*14). Here, bending β_1 also tends to increase its affinity for ATP, but because the slope of the camshaft twists the tip of β_1 to the right, the affinity for ADP is higher. Thus, ADP and then Pi bind (Figure 6*e*, *e*13–*e*12). Further rotation twists the β_1 tip to the left (Figure 6*e*, *e*11–*e*10) to facilitate the conversion of ADP + Pi to ATP, which remains tightly bound. At this angle, the ATP that has been synthesized in the previous step is still tightly bound by β_2, but further clockwise rotation (Figure 6*e*, *e*10–*e*1) pries the catalytic site open and releases the ATP. Clockwise rotation of γ in a molecular dynamics simulation has demonstrated that the affinity for ATP decreases with rotation, as expected (7).

Recently, we have shown that ATP is indeed synthesized when the γ shaft of actual F_1 is forcibly rotated clockwise by electric magnets, through a magnetic bead attached to γ (22). An external torque applied to one point on the motor suffices to reverse the chemo-mechanical linkage and force the chemical reaction in remote catalytic sites to proceed in reverse, increasing chemical free energy. This is not a trivial result: consider whether one can pull back a linear motor, such as myosin or kinesin, to let it synthesize ATP, and, if one can, where to pull.

POTENTIAL DIAGRAMS FOR THE CAMSHAFT MODEL

Here we derive potential diagrams for the camshaft model, which basically reproduce the experimental potential diagram in Figure 4*d*, to discuss the motor's behaviors under various ΔG and under various external loads.

Free-Energy Diagrams

The three sets of curves at the bottom of Figure 7*a* show the angle-dependent energy, $\psi_i^L(\theta)$, that we assume for the interaction between γ and a β binding a ligand, L, where L is ATP (T), ADP + Pi (H), ADP (D), Pi (P), or none (E); and i = 1, 2, or 3 designates one of the three βs. These potential energies reflect the shape of the camshaft. We assume that an empty β is stable when it is unbent and that a β binding a ligand is stable when it is bent. Thus, $\psi_1^T(\theta)$, for example, is low for θ between $-30°$ and $80°$, where β_1 remains fully bent; and $\psi_1^T(\theta)$ is highest at $\theta = 100°$, where β_1 with its tip twisted to the left is forced to unbend fully. $\psi_i^L(\theta)$ for L = H, D, and P have the same shape as $\psi_i^T(\theta)$, except that their heights are lower and they are shifted to the right, reflecting the twist of the β tip. $\psi_i^E(\theta)$ is assumed to be a mirror image of $\psi_i^D(\theta)$ except for a lower height. $\psi_i^L(\theta)$ for different i are related by translation of $\pm 120°$.

The overall potential energy $\Psi_0^{L1L2L3}(\theta)$ for γ rotation is assumed to be given by the simple sum of three energies:

$$\Psi_0^{L1L2L3}(\theta) = \psi_1^{L1}(\theta) + \psi_2^{L2}(\theta) + \psi_3^{L3}(\theta). \qquad 5.$$

Experiments with a chimera of fast and slow βs indicate that, at least for kinetics, the properties of individual βs are additive (4). As seen in Figure 7*a* (*top*), the total potential energies in Equation 5 essentially reproduce the experimental potential diagram in Figure 4*d*: $\Psi_0^{TEE}(\theta)$, for example, represents the ATP-waiting state, and $\Psi_0^{TTE}(\theta)$ represents the state after ATP binding. In fact, the shape and height of the individual potential, $\psi_i^L(\theta)$, have been chosen arbitrarily, solely to reproduce the experimental diagram. The choice is nothing but one out of many possibilities that could underlie the experimental potentials.

In Figure 7*a* (*top*) and in all subsequent potential diagrams including Figure 7*b*, a constant is added to each potential energy such that each curve represents the free energy of the system including the motor and its environment. That is, starting from an arbitrarily chosen initial state, the following constants are added (subtracted for a reverse reaction) for every chemical transition in a β.

$$\mathrm{E} \rightarrow \mathrm{T}: -\ln K_{a0}^{ATP} - k_B T \ln[\mathrm{ATP}] \qquad 6a.$$

$$\mathrm{T} \rightarrow \mathrm{H}: -\ln K_{hyd0} \qquad 6b.$$

$$\mathrm{H} \rightarrow \mathrm{D}: -\ln K_{d0}^{Pi(1st)} + k_B T \ln[\mathrm{Pi}] \qquad 6c.$$

$$\mathrm{H} \rightarrow \mathrm{P}: -\ln K_{d0}^{ADP(1st)} + k_B T \ln[\mathrm{ADP}] \qquad 6d.$$

$$\mathrm{D} \rightarrow \mathrm{E}: -\ln K_{d0}^{ADP(2nd)} + k_B T \ln[\mathrm{ADP}] \qquad 6e.$$

$$\mathrm{P} \rightarrow \mathrm{E}: -\ln K_{d0}^{Pi(2nd)} + k_B T \ln[\mathrm{Pi}], \qquad 6f.$$

where K_0 is the equilibrium constant for the forward reactions (in the absence of the interaction between β and γ). These constants satisfy the conditions:

$$K_{a0}^{ATP} \cdot K_{hyd0} \cdot K_{d0}^{Pi(1st)} \cdot K_{d0}^{ADP(2nd)} = K_{a0}^{ATP} \cdot K_{hyd0} \cdot K_{d0}^{ADP(1st)} \cdot K_{d0}^{Pi(2nd)} = \exp(-\Delta G_0/k_B T), \quad 7.$$

where ΔG_0 is the standard free-energy change for ATP hydrolysis.

For example, starting from TEE, angle-dependent free energies for subsequent states are given by:

$$\Psi^{TEE}(\theta) = \Psi_0^{TEE}(\theta) \quad 8a.$$

$$\Psi^{TTE}(\theta) = \Psi_0^{TTE}(\theta) - \ln K_{a0}^{ATP} - k_B T \ln[ATP] \quad 8b.$$

$$\Psi^{HTE}(\theta) = \Psi_0^{HTE}(\theta) - \ln K_{a0}^{ATP} - k_B T \ln[ATP] - \ln K_{hyd0} \quad 8c.$$

$$\Psi^{DTE}(\theta) = \Psi_0^{DTE}(\theta) - \ln K_{a0}^{ATP} - k_B T \ln[ATP] - \ln K_{hyd0} - \ln K_{d0}^{Pi(1st)} + k_B T \ln[Pi] \quad 8d.$$

$$\Psi^{ETE}(\theta) = \Psi_0^{ETE}(\theta) - \ln K_{a0}^{ATP} - k_B T \ln[ATP] - \ln K_{hyd0} - \ln K_{d0}^{Pi(1st)} + k_B T \ln[Pi] - \ln K_{d0}^{ADP(2nd)} + k_B T \ln[ADP] \quad 8e.$$

$$= \Psi_0^{ETE}(\theta) + \Delta G_0 + k_B T \ln[ADP][Pi]/[ATP] \quad 8f.$$

$$= \Psi_0^{ETE}(\theta) + \Delta G. \quad 8g.$$

Note that $\Psi^{ETE}(\theta)$ for ETE obtained by unbinding of ATP from β_1 and binding of ATP to β_2 is given simply by $\Psi_0^{ETE}(\theta)$, which is $\Psi_0^{TEE}(\theta - 120^\circ)$, because hydrolysis is not involved.

For the equilibrium constants, we choose arbitrarily the following values: $K_{a0}^{ATP} = 6.1 \times 10^{11}\ M^{-1}$, $K_{hyd0} = 0.13$, $K_{d0}^{Pi(1st)} = 2.0 \times 10^{-3}$ M, $K_{d0}^{ADP(2nd)} = 1.5 \times 10^{-3}$ M, $K_{d0}^{ADP(1st)} = 1.0 \times 10^{-5}$ M, and $K_{d0}^{Pi(2nd)} = 0.31$ M. Note that these are just parameters and that actual equilibrium constants exhibit angle dependence determined by the difference between the initial and final $\psi(\theta)$s involved in the relevant chemical transition. For example, the affinity $K_{a1}^{ATP}(\theta)$ of β_1 for ATP is given by:

$$K_{a1}^{ATP}(\theta) = K_{a0}^{ATP} \cdot \exp\left\{\left[\psi_1^E(\theta) - \psi_1^T(\theta)\right]/k_B T\right\}, \quad 9.$$

which takes a maximal value of $6.7 \times 10^{14}\ M^{-1}$ at θ between -10° and 80° and a minimal value of $2.6\ M^{-1}$ at $\theta = 120^\circ$. The angle dependence can readily be appreciated from the vertical difference between the relevant two curves in Figure 7*a* (*top*). For example, $K_{hyd}(\theta)$, which is related to the difference between HTE and TTE curves, remains low and constant (=0.13) between -20° and 80°, and takes high values favoring hydrolysis between 80° and 120°, reaching a maximal value of 7.0×10^5 at 100°. Note that the angle-dependent equilibrium constants also satisfy Equation 7 at each angle. For example, to bind ADP (not ATP) and Pi from the medium for ATP synthesis, K_a^{ATP}, K_d^{ADP}, and K_d^{Pi} need all be small at some angle, which requires that K_{hyd} be large at the same angle. In our model, this happens around 90° for β_1.

Major Reaction Pathways

Now we discuss the rotation mechanism on the basis of the free-energy diagrams. In Figure 7*a* (top) we show the major reaction pathway at the indicated nucleotide concentrations. We choose TEE to be the starting state, where the potential minimum is at 0° and the motor waits for ATP at this angle. When ATP binds to the correct site (on β_2), the potential shifts to the red TTE curve. At 0°, however, the TTE curve is above the TEE curve, indicating that ATP binding is an uphill reaction. This is because the chosen ATP concentration, 2 μM, is low; the motor has to wait long for ATP to bind. The uphill part only poses a kinetic barrier, because as rotation proceeds the TTE curve becomes lower than TEE, stabilizing bound ATP. Indeed, Equation 8b indicates that the rate of passage over the (entropic) barrier at 0°, or the rate of ATP binding, should be proportional to [ATP], which is the expected kinetics. It is possible, however, that the motor binds ATP by crossing from TEE to TTE around 15°, where the barrier height is lower. This could happen through thermal fluctuation of the γ angle, and the rate of ATP binding would no longer be proportional to [ATP]; kinetic barrier in this pathway is actually high, because ATP must arrive at the moment where γ happens to fluctuate counterclockwise by ~15°. Experimentally, the stepping rate of the F_1 motor is proportional to [ATP] down to <1 nM, suggesting that ATP binding occurs by an upward jump from TEE to TTE. The rate of binding of a fluorescent ATP analog indeed becomes lower when γ is rotated slightly counterclockwise from an ATP-waiting angle (K. Adachi, unpublished data). It seems that closure of the binding site poses a kinetic barrier and impedes binding, in addition to stabilizing a bound nucleotide; higher affinity for ATP upon counterclockwise rotation results from decrease in the rate of ATP release.

Once ATP is bound, the motor slides down the slope of the TTE curve to 80°, producing an apparent torque of ~50 pN · nm. That is, an actin filament or bead attached to γ can be rotated at a speed commensurate with this much torque (Equation 4). Note that in the world of molecular machines, mass is negligible, or motion is always overdamped, and thus a linear potential produces motion at a constant speed. When γ reaches 80°, the motor again waits for thermal activation to hydrolyze ATP and, upon activation, switches onto the HTE curve to reach 90°. One of the two experimentally observed ~1 ms reactions around 90° likely corresponds to this process. At 90°, both PTE and DTE curves are below the HTE curve, because [ADP] and [Pi] are low in this diagram, and thus either ADP or Pi is readily released. The ETE curve is further below, and the motor lands on this curve by releasing the last hydrolysis product. The last 30° is again a torque-generating downhill process, except for the first 10°, which is slightly uphill and which might correspond to the observed second ~1 ms reaction. At 120°, the motor waits for the next ATP.

In our scheme, torque is given as the slope of the potential energy, which is an intrinsic property of the motor. Thus, the torque is independent of speed or nucleotide concentrations. A cargo attached to the rotor rotates at a speed commensurate

with Equation 4, as long as internal impeding factors such as friction are negligible. Indeed, the apparent torque calculated from Equation 4 is independent of [ATP] and of speed up to ~30 revolutions s^{-1}, compared with the full speed of 130 revolutions s^{-1} (64, 65): Internal friction does not manifest its effect up to one fourth of the maximal speed. Another rotary motor, the flagellar motor that is driven by proton flow, also shows nearly speed-independent torque at low speeds (5).

Other Pathways

We consider five chemical states, T, H, D, P, and E, for each β, and thus there are a total of 125 chemical states, each associated with a unique potential energy, $\Psi_0(\theta)$. More states would appear in our free-energy diagram showing $\Psi(\theta)$s, in which the same chemical state can have a different vertical offset, in multiples of ΔG, depending on the net number of ATP hydrolyzed/synthesized to reach that state. In Figure 7*a* (*top*) we present only five of these $\Psi(\theta)$s. Now we show that these indeed constitute the major pathway, at least at moderate concentrations of nucleotides.

In Figure 7*b* we show all states that are accessible from TEE (*bottom*) or TTE (*top*): Destinations from T are E (unbinding) or H (hydrolysis), and destinations from E are T, D, or P (all bindings). From TEE at 0° (an ATP-waiting state), TTE at 80° is the most likely destination because the barrier to TTE is low (almost absent at the indicated ATP concentration) and the minimum of TTE at 80° is the lowest. This is why we show the path TEE → TTE as the major pathway in Figure 7*a* (*top*). The other, equally stable destination is TET at −40° (binding to the wrong site), but a high barrier exists because β_3 is fully unbent and its affinity for ATP is low. Binding of ATP to this wrong site could still happen rarely and might account for occasional backward 120° steps observed at low ATP concentrations (64). In the model, however, the major path from TET at −40° is to return to TEE at 0°, without hydrolysis of ATP. Completion of a backward 120° step through hydrolysis of ATP, i.e., reaching EET at −120° through HET and DET, is a minor path.

Another path from TEE at 0° is toward HEE at 0° (hydrolysis without rotation). Because the barrier to HEE is only a few k_BT high, the motor fluctuates between the two states, or ATP and ADP + Pi are near equilibrium at 0°. This can account for the extensive exchange of Pi oxygens during catalysis at low [ATP] (10). From HEE, there is another pathway to EEE through DEE or PEE. This is the so-called uni-site catalysis (26) and does not accompany rotation in our model, in accord with the experiment showing ATP hydrolysis in F_1 in which γ is cross-linked to β (14).

Thus, although the pathway shown in Figure 7*a* (*top*) is the major one in that it crosses the lowest barriers and follows free-energy minima, there are many other paths that can be populated to some extent. Some are just detours that return to the major pathway without expenditure of ATP, as in the example of TEE → TET → TEE or TEE → HEE → TEE. Others constitute uncoupled pathways in

which ATP hydrolysis occurs without rotation, such as the uni-site hydrolysis or reverse rotation failing to synthesize ATP (see below). It is also possible that a forward 120° step is made without expending ATP, as in the example of TEE to ETE simply by binding and unbinding of ATP. A backward 120° step, however, occurs through an equivalent sequence toward EET, with the same (and small) probability: On the free-energy diagram the three states, TEE, ETE, and EET, are related by a purely horizontal 120° shift unless ATP hydrolysis or synthesis is involved. Naturally, there is no unidirectional motion without expenditure of free energy. The extent to which the nonmajor pathways are populated depends on the rate constants of chemical reactions and rotation. We do not discuss kinetics here because too many angle-dependent rates are involved and most are experimentally unknown. Formalisms for kinetic analysis are given in References 44 and 57.

EFFICIENCY OF CHEMO-MECHANICAL ENERGY CONVERSION

Hereafter, we focus on the major pathway shown in Figure 7*a* (*top*), and we further neglect PTE to simplify the diagram. The discussion below is based on free-energy diagrams that are basically experimental, and does not depend on the details of the model, such as whether it operates in the bi-site or tri-site scheme. TEE implies an ATP-waiting state, TTE the state after ATP binding (to an unspecified site), HTE after hydrolysis of ATP (in an unspecified site), DTE after Pi release, and ETE the ATP-waiting state after a 120° step accompanying hydrolysis of one ATP molecule has occurred. An alternative representation for a tri-site pathway, among others, is TED → TTD → TTE → HTE → DTE, which is similar to the bi-site scheme except that the last 30(40)° substep is driven by Pi release and that ADP stays on F_1 until prompted by subsequent ATP binding (Figure 4*c'*). Another, more genuine tri-site scheme is TEH → TTH → HTH → HTD → HTE, in which ATP binds to β_2, hydrolysis occurs in β_1, and product release is from β_3.

Responses to Decreasing ΔG in the Absence of External Load

Figure 8*a* shows a free-energy diagram for nucleotide concentrations at which the free energy decreases relatively smoothly and linearly as rotation proceeds. When a large cargo such as an actin filament or bead is attached to γ, the motor will do an apparent work of ~100 pN · nm or 25 k_BT per 120° step against the viscous load, which is approximately equal to the free-energy input, ΔG, under the chosen conditions. The situation, however, is different from work against a conservative force (see below), and the cargo simply stirs the solution, producing heat. Net heat production per ATP hydrolyzed, including the heat associated with the chemical reactions and possible loans from the environment, is not 100 pN · nm and is given by $-\Delta H$, which is ~45 pN · nm at pH 7 (28). The heat output is independent of ΔG or of whether a cargo is attached to γ, unless the motor does work against a conservative force.

Now we reduce ΔG, first by decreasing [ATP] (Figure 8*b*). In the free-energy diagram, all curves after ATP binding are brought up by the term $-k_BT$ ln[ATP] (Equations 8b–e). ATP binding is now uphill, and the motor must borrow some free energy (negative entropy) from the environment. That is, the motor must wait at $\sim 0^\circ$ for the rare event of ATP binding.

We can further reduce ΔG by increasing [ADP] and [Pi] (Figure 8*c*). Then the curve DTE is brought up by the term k_BT ln[Pi], and ETE is further brought up by the term k_BT ln[ADP]. The result is that both Pi and ADP releases are uphill: Immediate rebinding occurs in proportion to [Pi] and [ADP], which are both high. Thus, the motor cannot readily release the products and would dwell around 90°. However, in the rare event that the motor happens to release both products, rotate to $\sim 120^\circ$, and bind a next ATP, it can proceed onto the curve ETT and reach 200° (dashed curve in Figure 8*c*). Although the probability of the forward stepping should be extremely low under the chosen conditions, it is still much higher than the reaction back to TEE at 0°. As long as ΔG is negative, the motor eventually rotates counterclockwise however rarely it may step.

Changes in the rates of ATP binding and product rebinding enable the motor to "sense" the nucleotide concentrations, or free energy of the environment. Note that, irrespective of ΔG, rotation occurs along the same slopes and thus at the same speed. If one calculated the amount of apparent work from the rotary speed during forward stepping, it would still be ~ 100 pN · nm, whereas ΔG is only about -20 pN · nm in Figure 8*c*. The apparent efficiency could thus exceed 100%. Thermodynamic efficiency, however, has to be discussed for the situation when a motor works against a conservative force that pushes back the motor (see below). To deal with the case of viscous load, the concept of generalized efficiency has been introduced (69) and developed as Stokes efficiency (58), which is based on the rotary speed averaged over a long time including interstep dwells and which is bound by 100%; for a high Stokes efficiency, the motor torque must be angle-independent, as in the F_1 motor. Experiments at varying [ATP] have shown that the apparent amount of work in a 120° step is independent of [ATP], as discussed above (64). Experiments at high [ADP] are difficult because of the MgADP inhibition.

Rotation Against a Conservative Force

A different scenario arises when an external torque is applied to the motor. A conservative torque, such as one exerted by a magnet or bent actin, operates on a motor regardless of whether the motor is moving. The magnitude of torque depends on the motor angle, not speed. In contrast, the viscous torque disappears when the motor stops. The viscous torque impedes motor movement, but it never pushes back the motor, whereas a conservative torque does.

Below we examine the case of angle-independent external torque (Figure 8*d–i*). The torque F_o applies on F_1 is expected to be relatively smooth, because the rotor of F_o possesses 10- to 14-fold symmetry (13a, 53, 67). An externally applied force on a linear molecular motor, e.g., with an optical trap, is practically constant over the size of the motor step.

Figure 8*d–f* shows diagrams of free energy (including the potential energy of the external torque) at increasing opposing torque for the nucleotide concentrations in Figure 8*a*. As seen, the motor moves forward (counterclockwise) as long as the total free energy decreases over a 120° step (TEE → ETE), or as long as $\Delta G + W$ is negative, where W (>0) is the work done against the external opposing torque N_{ext} ($W = N_{ext} \cdot 2\pi/3$). That is, the motor can do positive work (output) up to the amount, $-\Delta G$ (input), determined by the nucleotide concentrations. When W exceeds $-\Delta G$ (Figure 8*f*), the motor rotates in reverse, pushed by the external torque. The reverse rotation leads to ATP synthesis, basically in the sequence ETE → DTE → HTE → TTE → TEE, although under the conditions of Figure 8*f*, the motor tends to hop between these states. A more comfortable situation for synthesis is shown in Figure 8*g*, in which the above sequence is almost guaranteed (thanks to the higher concentrations of ADP and Pi).

Here we discuss the efficiency of chemo-mechanical energy conversion, first considering solely the major pathway; the discussion ignoring uncoupled pathways sets an upper limit for the efficiency. For forward rotation, the input is $-\Delta G$, which is determined by nucleotide concentrations, and the output is W, which is determined by the external torque. The efficiency of chemical to mechanical energy conversion would thus apparently be $W/|\Delta G|$, which is independent of the motor properties except for the step size. The efficiency would approach 100% as W and $|\Delta G|$ become comparable. When W equals $|\Delta G|$, the motor fluctuates equally in both directions, hydrolyzing and resynthesizing ATP. When $W > |\Delta G|$, the efficiency of mechanical to chemical energy conversion (ATP synthesis) would be given by $|\Delta G|/W$, again independent of motor properties. When $W < |\Delta G|$, the difference is dissipated as an increase in entropy (and heat if $W < |\Delta H| = 45$ pN · nm). When $W > |\Delta H|$, the difference in energy is supplied, in the form of heat, by the environment as the heat bath.

According to the argument above, a motor would always achieve 100% efficiency when W equals $|\Delta G|$. In fact, there are many uncoupled pathways that reduce the efficiency and that critically depend on the make of a particular motor. The efficiency above, $W/|\Delta G|$ or $|\Delta G|/W$, is thus an upper limit. Actual efficiency depends on kinetic parameters (rate constants) that dictate the probabilities of branching among various pathways.

Uncoupling scenarios can be seen even on a diagram depicting the major pathway. In Figure 8*f*, for example, there is a possibility that the motor, starting on the ETE curve at 120°, slides along the ETE line toward the left without picking up ADP and Pi. It encounters a small barrier at 0°, but there is a certain probability that the motor crosses the barrier toward left. That is, an external torque may simply rotate the motor clockwise without synthesizing ATP. The probability of this scenario is high under a higher torque, as one expects: If one rotates the motor too fast, the motor will certainly fail to pick up ADP and Pi or to synthesize ATP.

Another example is given in Figure 8*h*, in which $|\Delta G|$ is quite large (136 pN · nm) and might be expected to drive counterclockwise rotation against the large external torque of 60 pN · nm ($W = 123$ pN · nm). The shape of the TEE (or ETE)

curve, however, is such that the motor yields to the external torque and tends to rotate clockwise without hydrolyzing or synthesizing ATP. There must be an upper limit to the force (torque) a motor can produce, and it is about 50 pN · nm for this particular motor. Near the upper limit, the tendency toward uncoupled, backward motion increases, as seen in Figure 8*e*. One cannot let a motor do an arbitrarily large amount of work by increasing $|\Delta G|$. "Give" (yielding under a high backward force) is a common phenomenon for linear molecular motors in an optical trap (33, 54).

Dissipation and Friction

Let us confine the discussion to the case of coupling ratio being close to 1 (see Reference 46 for more general discussion). Then, the efficiency is close to $W/|\Delta G|$ or $|\Delta G|/W$, determined by $|\Delta G|$ and W alone. This implies that the magnitude of friction, internal or external, has little effect on the efficiency. A poorly designed motor with high internal friction simply runs slowly, with the same efficiency as a low friction motor. The efficiency also remains the same if an external friction is added, by attaching a large cargo to the rotor. The cargo only slows down the motor.

One might think that dissipation could occur via free-energy drop without motor motion, such as the initial ATP binding, before subsequent rotation, at high [ATP]. In Figure 9*a*, for example, the overall ΔG is assumed to be the same as in Figure 8*a*, but [ATP] (or K_{a0}^{ATP}) is set high and [ADP] (or K_{d0}^{ADP}) is set correspondingly low. Thus, ATP binding (downward arrow) dissipates free energy because no work is done during the binding, except for the internal work on the protein machine that is independent of [ATP]. The dissipation, however, is canceled at the moment of ADP binding (upward arrow), which is now uphill and requires a loan of free energy from the environment. Again, the overall efficiency is unchanged, although the motor runs slower because of the uphill portion.

HOW TO DESIGN AN ATP-DRIVEN MOLECULAR MACHINE

In principle, one could conceive of a motor that makes multiple steps per ATP hydrolyzed (27); the motor could even be smart enough to make only one step under a high load to produce a correspondingly high force. Though attractive, working out a possible, reasonably detailed design for such a motor is not easy for us. We therefore restrict our discussion to one-step motors.

We presume that the most desirable characteristics of a molecular machine are high efficiency of energy conversion and high speed. If so, the design shown in Figure 8 is close to ideal, as an ATP-driven rotary motor under the nucleotide concentrations of Figure 8*a*, *d*–*f* and as a torque-driven ATP synthesizer under the nucleotide concentrations of Figure 8*g*.

Linear potentials that produce angle-independent torque, or position-independent force for a linear motor, are better than curved potentials. Figure 9*b*, for

example, shows parabolic potentials (solid lines), which may be expected for a linear molecular motor (such as kinesin) that makes a diffusional search (shallow potential on the left) followed by binding to a specific site (deep potential on the right). Such a design, however, suffers from extreme slowing down in the presence of an opposing load, because the barrier between the two potentials rises sharply (dotted lines). Linear potentials do not suffer from this effect (Figure 8*d–f*). Linear potentials are also advantageous when a molecular machine is to be driven by an external force (Figure 8*f*), because they allow smooth, less bumpy and thus faster motion.

To obtain a high efficiency of energy conversion at a high speed, free energy must decrease smoothly, as in Figure 8*a*, without an uphill portion that degrades speed and without a vertical drop that degrades the efficiency. Even with a well-designed motor, however, these conditions are met only under one specific set of nucleotide concentrations. In other words, a molecular machine must be designed to work best in its working environment; its performance drops in other environments.

If one is to avoid uncoupling, or give, at a high load, one needs a barrier(s) against uncoupled pathways. This problem is serious for a machine to be driven by an external force, such as the ATP synthase. Potential diagrams that are too smooth, such as those in Figure 8*f* or 8*h*, are liable to uncoupling. Ideally, barriers should be introduced in positions outside the normal pathway, such as the small bumps around -20° in Figure 8*f*. An arbitrarily high barrier, however, cannot be introduced, because it must disappear in another chemical state (to let the motor cross that point); the appearance/disappearance of the barrier must be driven by a chemical reaction with a limited drop in free energy. A solution that sacrifices speed is to allow the presence of some bumps or uphill portions in the major pathway, as in Figure 8*g*. A highly bumpy diagram, as shown in Figure 8*i*, warrants tight coupling (and $\sim$100% energy-conversion efficiency near the balancing $|\Delta G|$, which is 30 pN · nm in Figure 8*i*), although speed is greatly reduced.

The free-energy diagrams in Figure 8 are derived from the experimental potential energies in the actual F_1 motor, with equilibrium constants chosen to mimic, approximately, the behavior of F_1 under a variety of nucleotide concentrations. It seems that the F_1 motor is designed to be an almost ideal ATP synthesizer working under physiological conditions when driven by moderate torque (Figure 8*g*). For ATP-driven rotation, fast operation requires a relatively low [ADP] (Figure 8*a*), which is a condition adopted in in vitro studies. If the motor is to work as an ion pump in vivo, as with V_0V_1-ATPase, effective K_d^{ADP} needs to be increased.

ACKNOWLEDGMENTS

We thank members of the Kinosita lab and the former CREST Team 13 for collaboration and discussion. Critical comments by Y. Oono (University of Illinois), E. Muneyuki (Tokyo Institute of Technology), and H. Nakanishi (Kyushu University) are particularly appreciated. This work was supported by Grants-in-Aid from the Ministry of Education, Culture, Sports, Science and Technology of Japan.

The *Annual Review of Biophysics and Biomolecular Structure* is online at http://biophys.annualreviews.org

LITERATURE CITED

1. Abrahams JP, Leslie AGW, Lutter R, Walker JE. 1994. Structure at 2.8 Å resolution of F_1-ATPase from bovine heart mitochondria. *Nature* 370:621–28
2. Adachi K, Noji H, Kinosita K Jr. 2003. Single-molecule imaging of rotation of F_1-ATPase. *Methods Enzymol.* 361:211–27

2a. Adachi K, Yasuda R, Noji H, Itoh H, Harada Y, et al. 2000. Stepping rotation of F_1-ATPase visualized through angle-resolved single-fluorophore imaging. *Proc. Natl. Acad. Sci. USA* 97:7243–47

3. Antes I, Chandler D, Wang H, Oster G. 2003. The unbinding of ATP from F_1-ATPase. *Biophys. J.* 85:695–706
4. Ariga T, Masaike T, Noji H, Yoshida M. 2002. Stepping rotation of F_1-ATPase with one, two, or three altered catalytic sites that bind ATP only slowly. *J. Biol. Chem.* 277:24870–74
5. Berg HC. 2003. The rotary motor of bacterial flagella. *Annu. Rev. Biochem.* 72:19–54
6. Berg JM, Tymoczko JL, Stryer L. 2001. *Biochemistry.* New York: Freeman. 974 pp. 5th ed.
7. Böckmann RA, Grubmüller H. 2002. Nanoseconds molecular dynamics simulation of primary mechanical energy transfer steps in F_1-ATP synthase. *Nat. Struct. Biol.* 9:198–202
8. Böckmann RA, Grubmüller H. 2003. Conformational dynamics of the F_1-ATPase β-subunit: a molecular dynamics study. *Biophys. J.* 85:1482–91
9. Börsch M, Diez M, Zimmermann B, Reuter R, Gräber P. 2002. Stepwise rotation of the γ-subunit of EF_oF_1-ATP synthase observed by intramolecular single-molecule fluorescence resonance energy transfer. *FEBS Lett.* 527:147–52

9a. Börsch M, Diez M, Zimmermann B, Trost M, Steigmiller S, Gräber P. 2003. Stepwise rotation of the γ-subunit of EF_oF_1-ATP synthase during ATP synthesis: a single-molecule FRET approach. *Proc. SPIE* 4962:11–21

10. Boyer PD. 1997. The ATP synthase: a splendid molecular machine. *Annu. Rev. Biochem.* 66:717–49
11. Boyer PD. 2002. Catalytic site occupancy during ATP synthase catalysis. *FEBS Lett.* 512:29–32
12. Boyer PD, Kohlbrenner WE. 1981. The present status of the binding-change mechanism and its relation to ATP formation by chloroplasts. In *Energy Coupling in Photosynthesis*, ed. BR Selman, S Selman-Reimer, pp. 231–40. Amsterdam: Elsevier
13. Dittrich M, Hayashi S, Schulten K. 2003. On the mechanism of ATP hydrolysis in F_1-ATPase. *Biophys. J.* 85:2253–66

13a. Fillingame RH, Angevine CM, Dmitriev OY. 2003. Mechanics of coupling proton movements to *c*-ring rotation in ATP synthase. *FEBS Lett.* 555:29–34

14. García JJ, Capaldi RA. 1998. Unisite catalysis without rotation of the γ-ε domain in *Escherichia coli* F_1-ATPase. *J. Biol. Chem.* 273:15940–45
15. Gibbons C, Montgomery MG, Leslie AGW, Walker JE. 2000. The structure of the central stalk in bovine F_1-ATPase at 2.4 Å resolution. *Nat. Struct. Biol.* 7:1055–61
16. Hara KY, Noji H, Bald D, Yasuda R, Kinosita K Jr, Yoshida M. 2000. The role of the DELSEED motif of the β subunit in rotation of F_1-ATPase. *J. Biol. Chem.* 275:14260–63
17. Hayashi S, Oda N, Oosawa F. 1982. A loose coupling model of H^+-ATPase. *Proc. 20th Annu. Meet. Biophys. Soc. Jpn.* p. 119. (Abstr.)

18. Hirono-Hara Y, Noji H, Nishiura M, Muneyuki E, Hara KY, et al. 2001. Pause and rotation of F_1-ATPase during catalysis. *Proc. Natl. Acad. Sci. USA* 98:13649–54
19. Hisabori T, Kondoh A, Yoshida M. 1999. The γ subunit in chloroplast F_1-ATPase can rotate in a unidirectional and counterclockwise manner. *FEBS Lett.* 463:35–38
20. Hunt AJ, Gittes F, Howard J. 1994. The force exerted by a single kinesin molecule against a viscous load. *Biophys. J.* 67:766–81
21. Imamura H, Nakano M, Noji H, Muneyuki E, Ohkuma S, et al. 2003. Evidence for rotation of V_1-ATPase. *Proc. Natl. Acad. Sci. USA* 100:2312–15
22. Itoh H, Takahashi A, Adachi K, Noji H, Yasuda R, et al. 2004. Mechanically driven ATP synthesis by F_1-ATPase. *Nature.* 427:465–68
23. Jault JM, Dou C, Grodsky NB, Matsui T, Yoshida M, Allison WS. 1996. The $\alpha_3\beta_3\gamma$ subcomplex of the F_1-ATPase from the thermophilic *Bacillus* PS3 with the βT165S substitution does not entrap inhibitory MgADP in a catalytic site during turnover. *J. Biol. Chem.* 271:28818–24
24. Kato-Yamada Y, Noji H, Yasuda R, Kinosita K Jr, Yoshida M. 1998. Direct observation of the rotation of ε subunit in F_1-ATPase. *J. Biol. Chem.* 273:19375–77
25. Kinosita K Jr, Yasuda R, Noji H. 2000. F_1-ATPase: a highly efficient rotary ATP machine. *Essays Biochem.* 35:3–18
26. Kinosita K Jr, Yasuda R, Noji H, Adachi K. 2000. A rotary molecular motor that can work at near 100% efficiency. *Philos. Trans. R. Soc. London Sci. Ser. B* 355:473–89
27. Kitamura K, Tokunaga M, Iwane AH, Yanagida T. 1999. A single myosin head moves along an actin filament with regular steps of 5.3 nanometres. *Nature* 397:129–34
28. Kodama T. 1985. Thermodynamic analysis of muscle ATPase mechanisms. *Physiol. Rev.* 65:467–551
29. Ma J, Flynn TC, Cui Q, Leslie AGW, Walker JE, Karplus M. 2002. A dynamic analysis of the rotation mechanism for conformational change in F_1-ATPase. *Structure* 10:921–31
30. Mannherz HG, Schenck H, Goody RS. 1974. Synthesis of ATP from ADP and inorganic phosphate at the myosin-subfragment 1 active site. *Eur. J. Biochem.* 48:287–95
31. Masaike T, Muneyuki E, Noji H, Kinosita K Jr, Yoshida M. 2002. F_1-ATPase changes its conformations upon phosphate release. *J. Biol. Chem.* 277:21643–49
32. Matsui T, Muneyuki E, Honda M, Allison WS, Dou C, Yoshida M. 1997. Catalytic activity of the $\alpha_3\beta_3\gamma$ complex of F_1-ATPase without noncatalytic nucleotide binding site. *J. Biol. Chem.* 272:8215–21
33. Mehta AD, Rock RS, Rief M, Spudich JA, Mooseker MS, Cheney RE. 1999. Myosin-V is a processive actin-based motor. *Nature* 400:590–93
34. Menz RI, Walker JE, Leslie AGW. 2001. Structure of bovine mitochondrial F_1-ATPase with nucleotide bound to all three catalytic sites: implications for the mechanism of rotary catalysis. *Cell* 106:331–41
35. Milgrom YM, Murataliev MB, Boyer PD. 1998. Bi-site activation occurs with the native and nucleotide-depleted mitochondrial F_1-ATPase. *Biochem. J.* 330:1037–43
36. Müller M, Pänke O, Junge W, Engelbrecht S. 2002. F_1-ATPase, the C-terminal end of subunit γ is not required for ATP hydrolysis-driven rotation. *J. Biol. Chem.* 277:23308–13
37. Nishio K, Iwamoto -Kihara A, Yamamoto A, Wada Y, Futai M. 2002. Subunit rotation of ATP synthase embedded in membranes: a or β subunit rotation relative to the c subunit ring. *Proc. Natl. Acad. Sci. USA* 99:13448–52

37a. Nishizaka T, Oiwa K, Noji H, Kimura S, Muneyuki E, et al. 2004. Chemomechanical coupling in F_1-ATPase

revealed by simultaneous observation of nucleotide kinetics and rotation. *Nature Struct. Mol. Biol.* 11:142–48
38. Noji H, Bald D, Yasuda R, Itoh H, Yoshida M, Kinosita K Jr. 2001. Purine but not pyrimidine nucleotides support rotation of F_1-ATPase. *J. Biol. Chem.* 276:25480–86
39. Noji H, Häsler K, Junge W, Kinosita K Jr, Yoshida M, Engelbrecht S. 1999. Rotation of *Escherichia coli* F_1-ATPase. *Biochem. Biophys. Res. Commun.* 260:597–99
40. Noji H, Yasuda R, Yoshida M, Kinosita K Jr. 1997. Direct observation of the rotation of F_1-ATPase. *Nature* 386:299–302
41. Omote H, Sambonmatsu N, Saito K, Sambongi Y, Iwamoto-Kihara A, et al. 1999. The γ-subunit rotation and torque generation in F_1-ATPase from wild-type or uncoupled mutant *Escherichia coli*. *Proc. Natl. Acad. Sci. USA* 96:7780–84
42. Ono S, Hara KY, Hirao J, Matsui T, Noji H, Yoshida M, Muneyuki E. 2003. Origin of apparent negative cooperativity of F_1-ATPase. *Biochim. Biophys. Acta* 1607:35–44
43. Oosawa F, Hayashi S. 1983. Coupling between flagellar motor rotation and proton flux in bacteria. *J. Phys. Soc. Jpn.* 52:4019–28
44. Oosawa F, Hayashi S. 1986. The loose coupling mechanism in molecular machines of living cells. *Adv. Biophys.* 22:151–83
45. Pänke O, Cherepanov DA, Gumbiowski K, Engelbrecht S, Junge W. 2001. Viscoelastic dynamics of actin filaments coupled to rotary F-ATPase: angular torque profile of the enzyme. *Biophys. J.* 81:1220–33
46. Parmeggiani A, Jülicher F, Ajdari A, Prost J. 1999. Energy transduction of isothermal ratchets: generic aspects and specific examples close to and far from equilibrium. *Phys. Rev. E* 60:2127–40
47. Ren H, Allison WS. 2000. Substitution of βGlu^{201} in the $\alpha_3\beta_3\gamma$ subcomplex of the F_1-ATPase from the thermophilic *Bacillus* PS3 increases the affinity of catalytic sites for nucleotides. *J. Biol. Chem.* 275:10057–63
48. Sakamoto J. 1984. Effect of dimethylsulfoxide on ATP synthesis by mitochondrial soluble F_1-ATPase. *J. Biochem.* 96:483–87
49. Sambongi Y, Iko Y, Tanabe M, Omote H, Iwamoto-Kihara A, et al. 1999. Mechanical rotation of the c subunit oligomer in ATP synthase (F_oF_1): direct observation. *Science* 286:1722–24
50. Shimabukuro K, Yasuda R, Muneyuki E, Hara KY, Kinosita K Jr, Yoshida M. 2003. Catalysis and rotation of F_1 motor: cleavage of ATP at the catalytic site occurs in 1 ms before 40° substep rotation. *Proc. Natl. Acad. Sci. USA.* 100:14731–36
51. Shirakihara Y, Leslie AGW, Abrahams JP, Walker JE, Ueda T, et al. 1997. The crystal structure of the nucleotide-free $\alpha_3\beta_3$ subcomplex of F_1-ATPase from the thermophilic *Bacillus PS3* is a symmetric trimer. *Structure* 5:825–36
52. Soong RK, Bachand GD, Neves HP, Olkhovets AG, Craighead HG, Montemagno CD. 2000. Powering an inorganic nanodevice with a biomolecular motor. *Science* 290:1555–58
53. Stock D, Leslie AGW, Walker JE. 1999. Molecular architecture of the rotary motor in ATP synthase. *Science* 286:1700–5
54. Svoboda K, Schmidt CF, Schnapp BJ, Block SM. 1993. Direct observation of kinesin stepping by optical trapping interferometry. *Nature* 365:721–27
55. Tsunoda SP, Aggeler R, Noji H, Kinosita K Jr, Yoshida M, Capaldi RA. 2000. Observations of rotation within the F_oF_1-ATP synthase: deciding between rotation of the F_oc subunit ring and artifact. *FEBS Lett.* 470:244–48
56. Turina P, Samoray D, Gräber P. 2003. H^+/ATP ratio of proton transport-coupled ATP synthesis and hydrolysis catalysed by CF_oF_1-liposomes. *EMBO J.* 22:418–26
57. Wang H, Oster G. 1998. Energy transduction in the F_1 motor of ATP synthase. *Nature* 396:279–82

58. Wang H, Oster G. 2002. The Stokes efficiency for molecular motors and its applications. *Europhys. Lett.* 57:134–40
59. Weber J, Senior AE. 2001. Bi-site catalysis in F_1-ATPase: Does it exist? *J. Biol. Chem.* 276:35422–28
60. Weber J, Senior AE. 2003. ATP synthesis driven by proton transport in F_1F_0-ATP synthase. *FEBS Lett.* 545:61–70
61. Wolcott RG, Boyer PD. 1974. The reversal of the myosin and actomyosin ATPase reactions and the free energy of ATP binding to myosin. *Biochem. Biophys. Res. Commun.* 57:709–16
62. Yagi H, Tozawa K, Sekino N, Iwabuchi T, Yoshida M, Akutsu H. 1999. Functional conformation changes in the TF_1-ATPase β subunit probed by 12 tyrosine residues. *Biophys. J.* 77:2175–83
63. Yasuda R, Masaike T, Adachi K, Noji H, Itoh H, Kinosita K Jr. 2003. The ATP-waiting conformation of rotating F_1-ATPase revealed by single-pair fluorescence resonance energy transfer. *Proc. Natl. Acad. Sci. USA* 100:9314–18
64. Yasuda R, Noji H, Kinosita K Jr, Yoshida M. 1998. F_1-ATPase is a highly efficient molecular motor that rotates with discrete 120° steps. *Cell* 93:1117–24
65. Yasuda R, Noji H, Yoshida M, Kinosita K Jr, Itoh H. 2001. Resolution of distinct rotational substeps by submillisecond kinetic analysis of F_1-ATPase. *Nature* 410:898–904
66. Yoshida M. 1983. The synthesis of enzyme-bound ATP by the F_1-ATPase from the thermophilic bacterium PS3 in 50% dimethylsulfoxide. *Biochem. Biophys. Res. Commun.* 114:907–12
67. Yoshida M, Muneyuki E, Hisabori T. 2001. ATP synthase—a marvellous rotary engine of the cell. *Nat. Rev. Mol. Cell Biol.* 2:669–77
68. Zhou Y, Duncan TM, Cross RL. 1997. Subunit rotation in *Escherichia coli* F_oF_1-ATP synthase during oxidative phosphorylation. *Proc. Natl. Acad. Sci. USA* 94: 10583–87
69. Derényi I, Bier M, Astumian RD. 1999. Generalized efficiency and its application to microscopic engines. *Phys. Rev. Lett.* 83:903–6
70. Diez M, Zimmermann B, Börsch M, König M, Schweinberger E, et al. 2004. Proton-powered subunit rotation in single membrane-bound F_0F_1-ATP synthase. *Nat. Struct. Mol. Biol.* 11:135–41

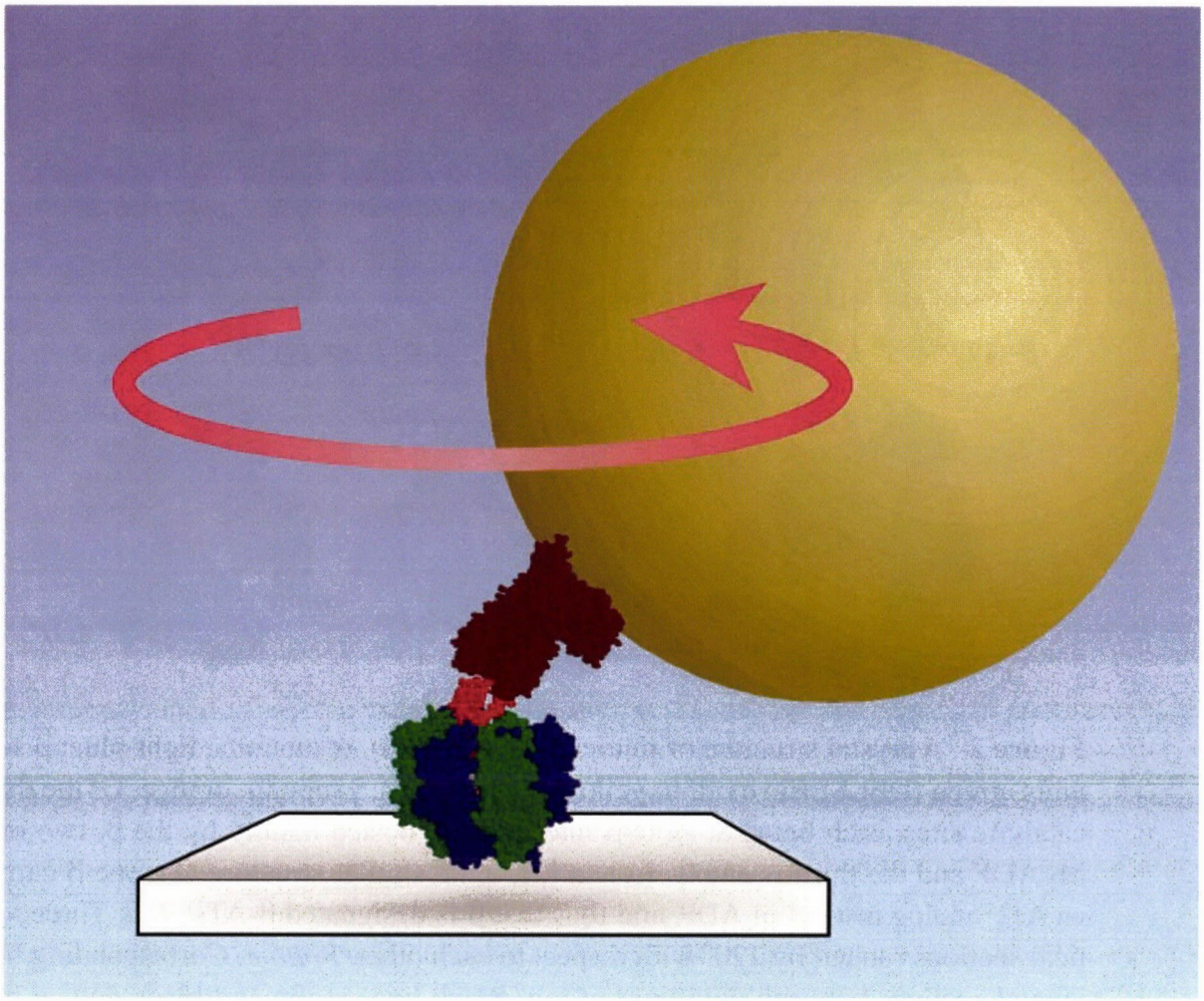

Figure 1 Observation of F_1 rotation (65). Three β subunits (*green*) were attached to a glass surface through histidine residues engineered on the N terminus. To the central γ subunit (*red*), a 40-nm gold bead was attached through BSA and streptavidin (both *brown*). Rotation was observed by dark-field microscopy. A larger bead can be observed under an ordinary microscope, and a fluorescent actin filament attached to γ was observed under a fluorescence microscope (40). The α subunit is in blue. The 40-nm bead and proteins in the figure are approximately to scale.

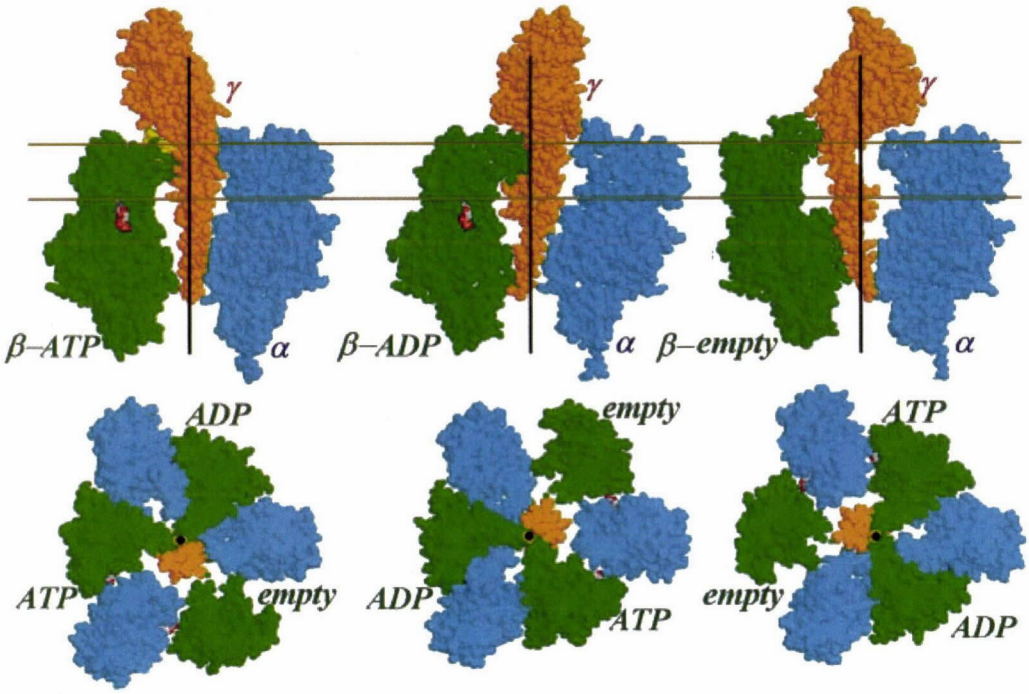

Figure 2 A crystal structure of mitochondrial F_1 (15). α subunits, light-blue; β subunits, green (DELSEED motif in yellow at upper left); γ subunit, orange. Of the three catalytic sites, each being at an α-β interface but hosted mainly by the β, two bind MgADP and the third is empty. In another, quite similar structure (1), one β carries an ATP analog instead of ADP, and thus that β is designated β-ATP. *Top*: Three vertical sections rotated by 120° with respect to each other. *Bottom*: Corresponding horizontal sections between gold lines at top. Black lines at top and black dots at bottom represent the putative axis of γ rotation (57).

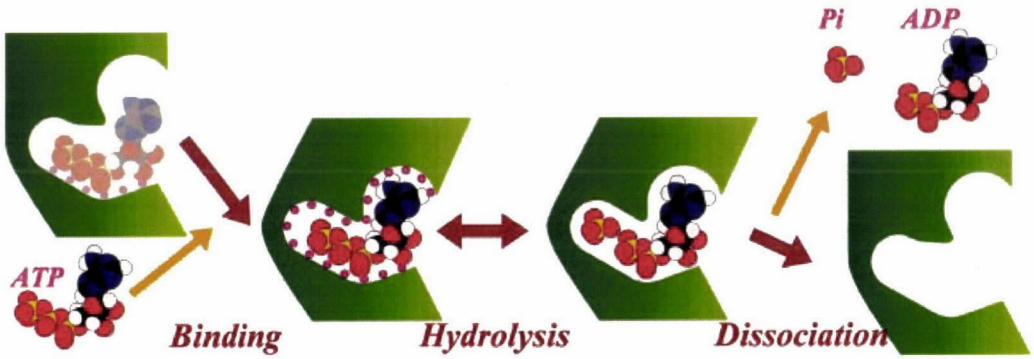

Figure 5 How an ATP-driven molecular machine may work. An ATPase protein (shown in *green*) does work by changing its conformation. In this example, the protein bends when it binds ATP and unbends upon release of hydrolysis products. Brown arrows indicate how free energy decreases, accompanying work output, during the reaction. Major work is done in the process of ATP binding (and product release), not much in conjunction with hydrolysis. Violet dots represent bonds between ATP and the protein. Light-colored ATP on the left represents the state after initial binding. The ATP pulls and bends the protein by progressively making more bonds while the ATP is bound more tightly by the protein.

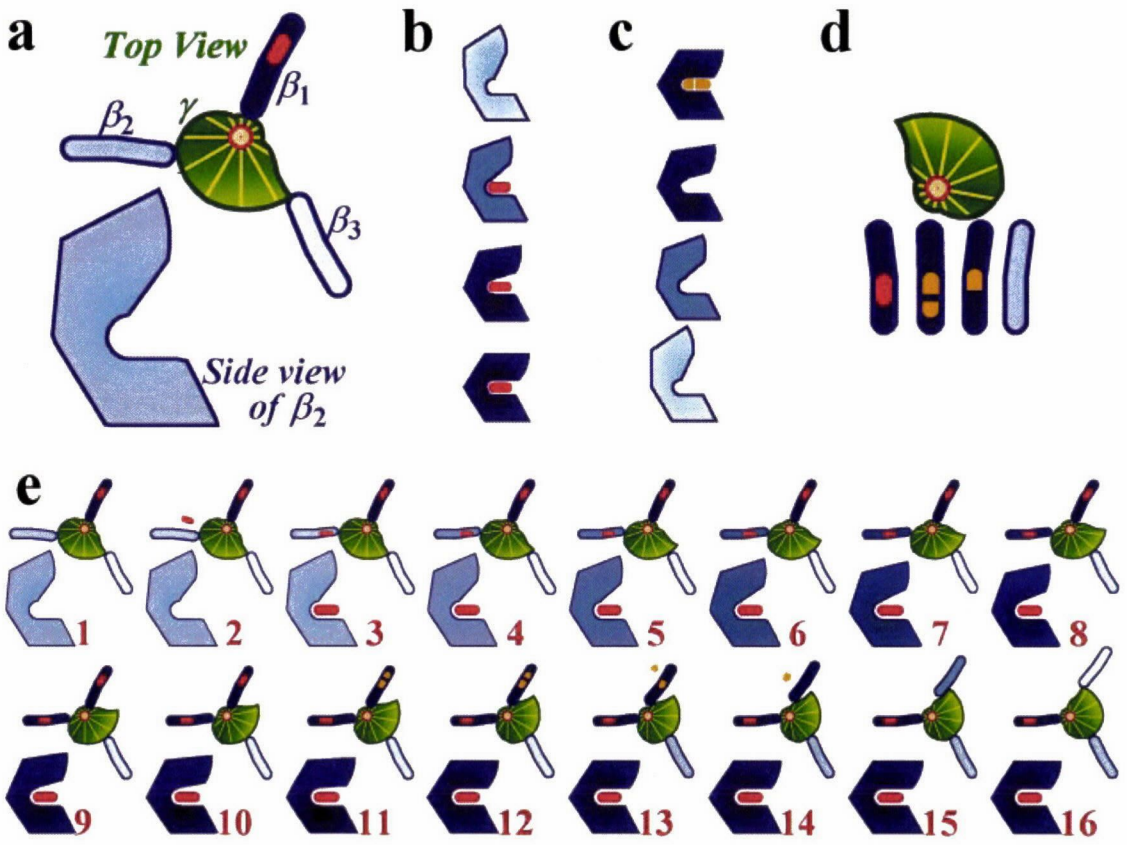

Figure 6 A camshaft model for the F_1 motor. Red oblong represents ATP, which is split into larger (ADP) and smaller (Pi) orange pieces. (*a*) The cam (γ) is supposed to stay in contact with the upper tip of βs, as if a thin oil layer exists at the interfaces. (*b*) The basic driving force comes from a push by a β binding ATP (β_2 in *e*1–*e*10), and (*c*) a pull by a β from which ADP and Pi leave (β_1 in *e*13–*e*16). The shade of blue reflects the degree of bending of β. (*d*) In addition, the upper tip of β is assumed to be twisted upon ATP hydrolysis, such that the tip motion produces a small amount of counterclockwise rotation (*e*10–*e*14). Conversely, a β with its tip twisted to the right (facing γ) has a higher affinity for ADP, whereas a tip twisted to the left favors ATP. (*e*) Sequence of events during hydrolysis. When γ is forced to rotate clockwise by an external torque (reversed sequence), the twist of the tip to the right in *e*16–*e*13 helps preferential binding of ADP over ATP.

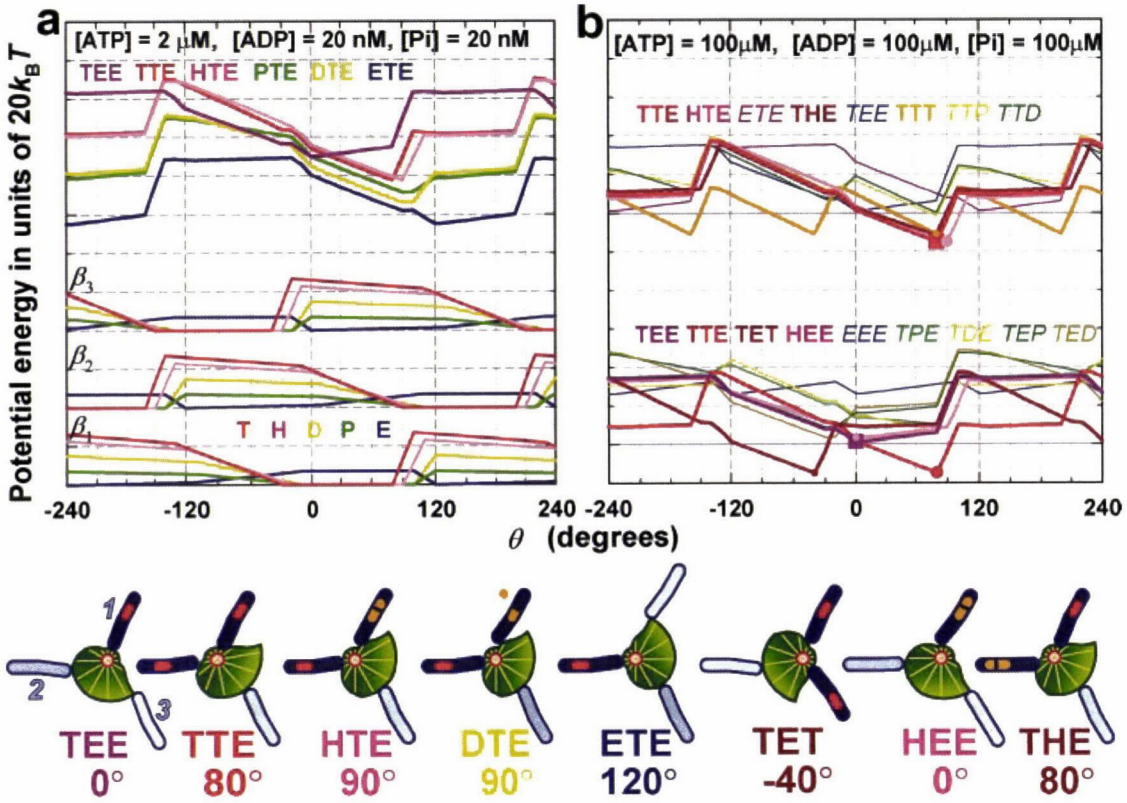

Figure 7 Potential energies for the camshaft model. T, ATP; H, hydrolysis products (ADP + Pi); D, ADP; P, Pi; E, empty. (*a*) Potential diagrams for the interaction between γ and an individual β (*bottom*), and the diagram for a major reaction pathway (*top*). (*b*) Diagrams showing all possible intermediates accessible from TEE (*bottom*) and TTE (*top*). Except for the three sets of curves at the bottom of (*a*), curves in a set are shifted vertically such that they represent angle-dependent free energy of the motor and environment, as explained in text.

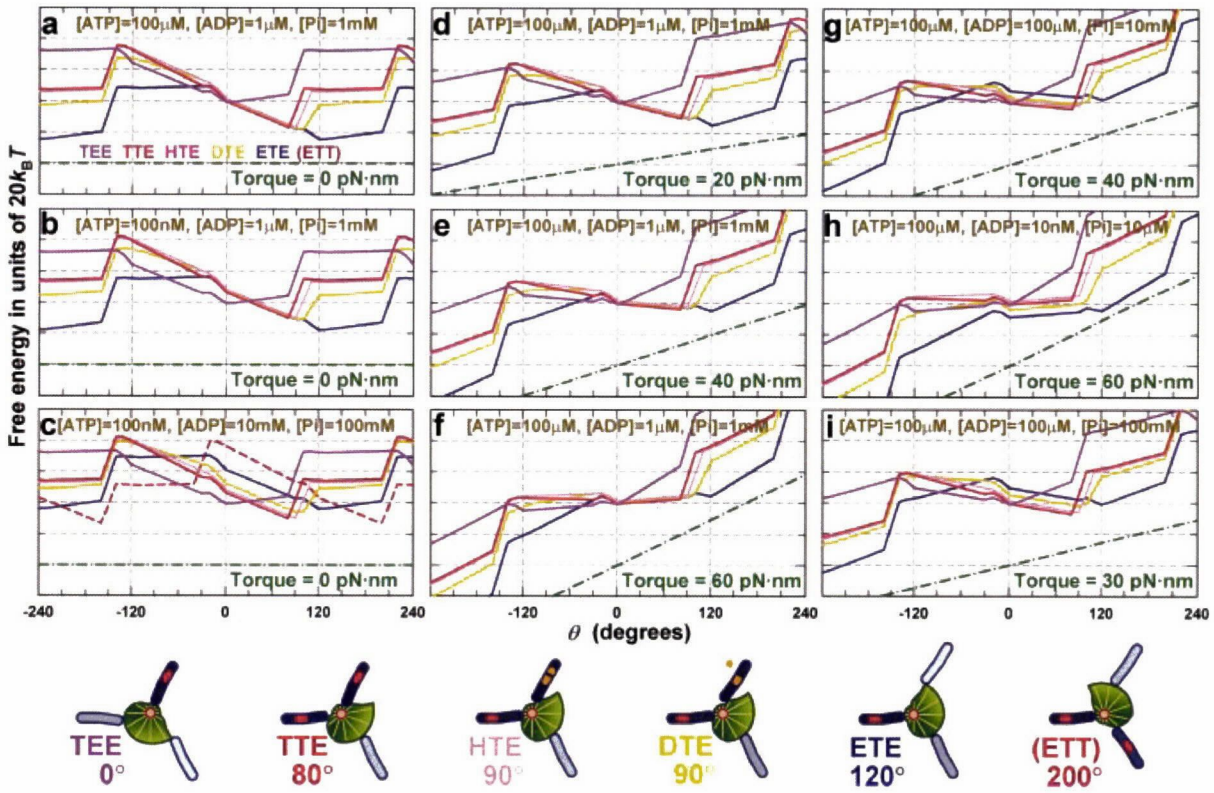

Figure 8 Potential diagrams under different ΔG and external torque. In (*a*)–(*i*), nucleotide concentrations are shown at the top and torque is shown at the bottom. The potential energy for the external torque is shown in a green line and has been added to all free-energy curves.

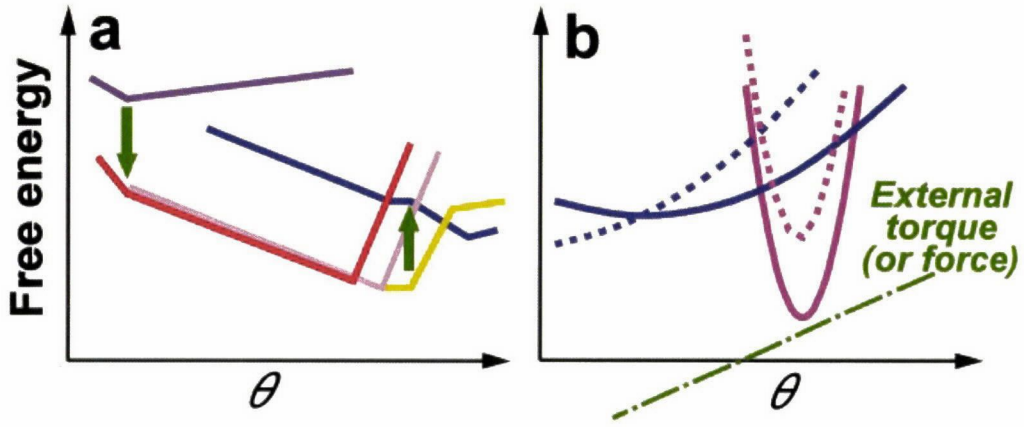

Figure 9 Designing a molecular machine. (*a*) A portion of free-energy diagram (around 0°–120°) for the camshaft model showing TEE (*purple*) to ETE (*blue*). ΔG is the same as in Figure 8*a*, but [ATP] (or K_{a0}^{ATP}) is higher and [ADP] (or K_{d0}^{ATP}) is lower. Thus, ATP binding is downhill (*downward arrow*), whereas ADP release is uphill (*upward arrow*). (*b*) Parabolic potential energies present a high barrier in the presence of an external torque (*dotted lines*).

Adv. Exp. Med. Biol., in press

HOW TWO-FOOT MOLECULAR MOTORS MAY WALK

Kazuhiko Kinosita, Jr.[1], M. Yusuf Ali[2], Kengo Adachi[1], Katsuyuki Shiroguchi[1], and Hiroyasu Itoh[3,4]

1. INTRODUCTION

Myosins and kinesins each constitute a large family of linear molecular motors that track along a filamentous rail, myosins along an actin filament and kinesins along a microtubule. These motors are powered by free energy derived from ATP hydrolysis, and the mechanisms of chemo-mechanical conversion in these motors have been under intensive study (Kinosita et al., 1998; Vale and Milligan, 2000; Mehta, 2001; Vale, 2003; Schliwa and Woehlke, 2003; Endow and Barker, 2003). Most of myosins and kinesins have two globular domains that bind to the filamentous rail and that hydrolyze ATP in a rail-dependent manner. The two domains are usually called "heads" or "motor domains" and are connected via a neck-like structure to a common stalk. Some of the two-headed motors are processive, in that a single molecule moves along a rail for many ATPase cycles without detaching from the rail. These processive motors appear to "walk," using the two heads alternately in a hand-over-hand fashion, as has recently been demonstrated for myosin V (Yildiz et al., 2003) and conventional kinesin (Asbury et al., 2003; Yildiz et al., 2004). Unlike walking of a human being, molecular motors cannot rely on inertia, which is negligible for biological molecules that work in water or membranes. A human has a right and a left foot, but the two heads of a molecular motor are identical (Fig. 1*a*). How, then, do they walk? In this article, we focus on the mechanism(s) that warrant forward, not backward, stepping. Because we discuss walking mechanisms in this article, we call the heads "feet" and necks "legs."

[1]Okazaki Institute for Integrative Bioscience, National Institutes of Natural Sciences, Higashiyama 5-1, Myodaiji, Okazaki 444-8787, Japan [2]Department of Physics, Faculty of Physical Sciences, Shahjalal University of Science and Technology, Sylhet-3114, Bangladesh. [3]Tsukuba Research Laboratory, Hamamatsu Photonics KK, and [4]CREST "Creation and Application of Soft Nano-Machine, the Hyperfunctional Molecular Machine" Team 13*, Tokodai, Tsukuba 300-2635, Japan.

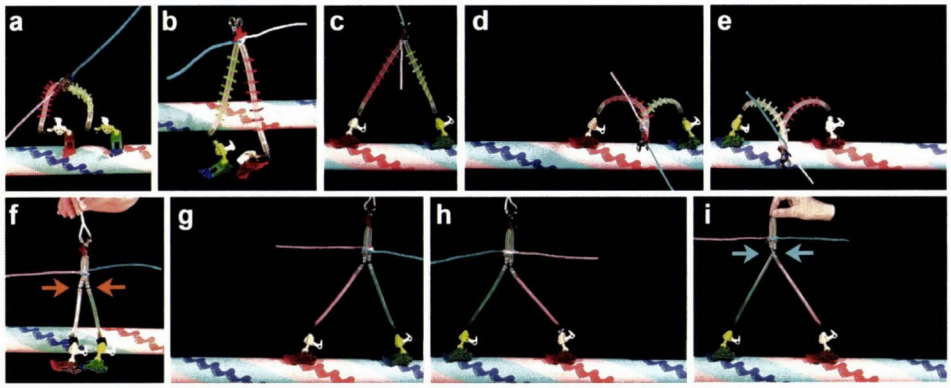

Figure 1. Walking with two identical feet. The legs are made of elastic vinyl pipes, which can accommodate both torsional and flexural strains. (**a**) Two feet of a molecular motor are identical, because they are coded by the same gene. (**b**) The two legs are joined in twofold symmetry. Thus the two feet would be oriented in opposite directions, one toe facing east if the other faces west, unless the legs are flexible. (**c**) When two feet land simultaneously during walking, both toes must be oriented forward, because the landing sites on the rail are all identical. Elastic legs would thus be severely distorted. In the configuration shown in this image (*b*), most of the strain is in torsion of the legs (note the directions of the small bars on the legs) whereas bending is relatively small. (**d**) By turning one of the feet by 360°, much of the torsional strain is relieved, resulting in severe bending. The total strain is the same as in *c*. (**e**) When the motor moves forward by one step and attains the same posture as in *d*, a cargo (pink and blue long bars) attached to the body rotates by 180°. A 180° rotation also accompanies every step if the motor steps with the posture in *c*. (**f**) Flexible joints in the legs (arrows) allow the two feet to adopt the same orientation. (**g**) With flexible joints, landing with two feet does not introduce strain. (**h**) But, because of the basic twofold symmetry, the body still tends to rotate 180° every time the motor steps. (**i**) With flexible joints, though, the 180° rotations can be prohibited by an external force without introducing too much strain in the legs. Note that the two legs are now crossed near the junction (arrows); a small torque suffices to bring about this configuration.

2. HINTS ON WALKING MECHANISMS

2.1. Walking with Two Identical Feet

The two legs of a myosin or kinesin molecule emerge from a coiled coil of α-helices (the stalk, or "body"), each helix extending into a leg (see Figs. 2*c* and *d*). Because the coiled coil is twofold symmetric, as confirmed for kinesin (Kozielski et al., 1997) and myosin (Li et al., 2003), the two identical legs are also arranged, basically, in the same twofold symmetry: if there were no flexibility, the two feet would be oriented in opposite directions, making it extremely difficult to walk on landing spots that are unidirectionally oriented on a rail (Figs. 1*b-e*). In fact, each leg of kinesin is a single polypeptide chain and is considered flexible over the entire length, unless it is "docked" onto the foot (Fig. 2*d*); in a crystal structure of kinesin dimer where both legs were docked (Kozielski et al., 1997), the two feet were not arranged in twofold symmetry, indicating that the short undocked portion is already flexible. Myosin's legs are reinforced with light chains (Figs. 2*a* and *b*), and thus are probably semi-rigid. Flexibility likely resides at the leg-body junction. Indeed, analyses of rotational Brownian motion of myosin II (conventional myosin) indicated the presence of a flexible joint near the leg-body junction (Kinosita et al., 1984; Ishiwata et al., 1987), and electron micrographs of myosin

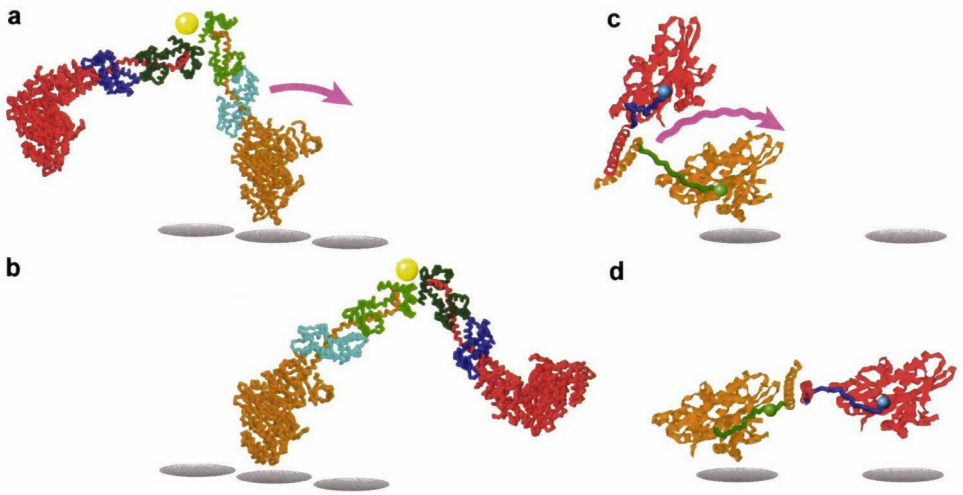

Figure 2. Postulated lever action in two-foot motors. The motors in this figure move toward right. **(a, b)** Scallop myosin. This myosin is non-processive and thus does not "walk." Nevertheless, we show possible walking postures in order to indicate lever action (arrow) in myosin: the orange leg (the long α-helix) rotates between *a* and *b*. Flexible joints likely exist around the location indicated by the yellow ball, beyond which the two α-helices form a coiled coil (the "stalk"; not shown in the figure). Thus, the red leg presumably undergoes rotational diffusion around the yellow ball. The lever action of the orange leg biases the Brownian motion of the red foot forward. Each figure is composed of two structures of scallop myosin subfragment 1 (S1), arranged arbitrarily. The orange foot/leg in *a* represents the structure of S1 binding MgADP·VO_4, and that in *b* is S1 without a nucleotide (Houdusse et al., 2000). The red foot/leg is S1 binding MgADP, which mimics a structure after detachment from actin (Houdusse et al., 1999). Cyan/blue, essential light chains; green/dark green, regulatory light chains. The gray disks with a diameter of 5.5 nm represent binding sites on an actin filament. **(c, d)** Conventional kinesin. The blue and green legs ("neck linkers") between the balls are presumably flexible, and thus the red foot undergoes Brownian motion. The flexible green leg in *c* "docks" onto the orange foot, in an ATP-dependent process, through Brownian motion (wavy arrow). After docking (*d*), the Brownian motion of the red foot occurs around the green ball, and thus is biased toward the forward binding site. The docking is equivalent with the lever action in myosin. The gray disks with a diameter of 4 nm represent binding sites on a microtubule. The figures are constructed from a structure of a dimeric kinesin (Kozielski et al., 1997) by assigning arbitrary structures to the neck linkers (except the green one in *d*) and orienting the central coiled coil (stalk) arbitrarily.

V revealed the angle between the two legs to be quite variable (Walker et al., 2000). In a crystal of the coiled coil portion of myosin II, the end next to the legs was disordered (Li et al., 2003).

The flexibility in the undocked legs of kinesin and that at the body-leg junction of myosin allows the two feet to adopt the same orientation, which is a required posture when the two feet simultaneously land during walking. Because the two feet and legs are identical, the landed posture with least strain must be the same whether one or the other foot leads, although the flexibility may allow many other postures without imposing much strain. If the motor reaches the unique, most stable posture after every step, then symmetry dictates that the body must turn around its axis by 180° as the leading and trailing feet swap (Howard, 1996; also see Figs. 1*g* and *h*). Hua et al. (2002) sought for, but did not observe, the 180° reorientations that would accompany every step in kinesin. They thus suggested inchworm walking in which one foot always

leads. We also failed to observe the 180° reorientations in myosin V (Ali et al., 2002) and myosin VI (Ali et al., 2004). Recent studies, however, have established that myosin V and kinesin walks in a hand-over-hand fashion in which the two feet alternate in the lead. A single fluorophore attached to one of the two feet of myosin V (Yildiz et al., 2003) or kinesin (Yildız et al., 2004) advanced, for every two ATP hydrolysis cycles, over a distance twice the motor's step size which is the distance traveled by the body of the motor in one ATP cycle; inchworm walking would advance the fluorophore by a distance equaling the step size. Also, in some mutant kinesins, dwells between steps were alternately long and short, indicating an asymmetric hand-over-hand walking with two different conformations for two-foot landing (Asbury et al., 2003). Why, then, have the 180° reorientations not been detected so far? Previous observations were made by attaching a large probe, a microtubule or micron-sized bead, to the motor. The attached probe may well have broken the symmetry of the motor, as in the mutations, and impeded the reorientation. With the assumed flexibility, the torque needed to break the symmetry is small (Fig. 1*i*). Genuine motion of these motors, without a cargo, might still involve 180° reorientations, although the flexible joints likely obscure the rotation.

2.2. Lever Action and Biased Diffusion

Until recently, researchers working on myosin and kinesin had somewhat different views. Because myosin's legs are likely stiff, prevailing theory states that a landed leg acts as a lever (Huxley, 1969; Holmes and Geeves, 2000): when a landed ankle is bent forward, the leg leans forward, carrying the body forward (Figs. 2*a* and *b*). The tilting is best evidenced for myosin V (Walker et al., 2000; Moore et al., 2001; Veigel et al., 2001; Burgess et al., 2002; Forkey et al., 2003). The lifted leg thus easily finds a forward landing site. Kinesin's legs, in contrast, are flexible and unlikely to serve as a stiff lever. Instead, a lower part of a landed leg docks onto the landed foot such that the upper leg emerges from a forward part of the foot (Figs. 2*c* and *d*). This biases the Brownian motion of the lifted foot forward, and the foot lands on a forward site. The relatively small bias could be efficient, because kinesin's legs are short and must be fully extended to reach a forward or backward site: of the two sites that are available, only the forward site can be reached after the docking of the landed foot. The docking in kinesin may be regarded as the equivalent of the lever action in myosin, and then the two schemes are apparently quite similar. Myosin researchers, however, tend to stress the lever action whereas kinesin researchers diffusional search. The distinction seems to be coupled to the question of which process produces force: lever action itself in myosin, and landing of the diffusing foot in kinesin. Is this really so?

3. SPIRAL MOTION OF MYOSIN AROUND AN ACTIN FILAMENT

3.1. Observation of Spiral Motion

Myosin V is now one of the best characterized molecular motors. It moves toward the barbed, or plus (fast-growing) end of an actin filament using two long (~23 nm) legs each reinforced with six light chains (Cheney et al., 1993; see Fig. 3). The movement is processive (Mehta et al., 1999; Rief et al., 2000; Sakamoto et al., 2000). The step size

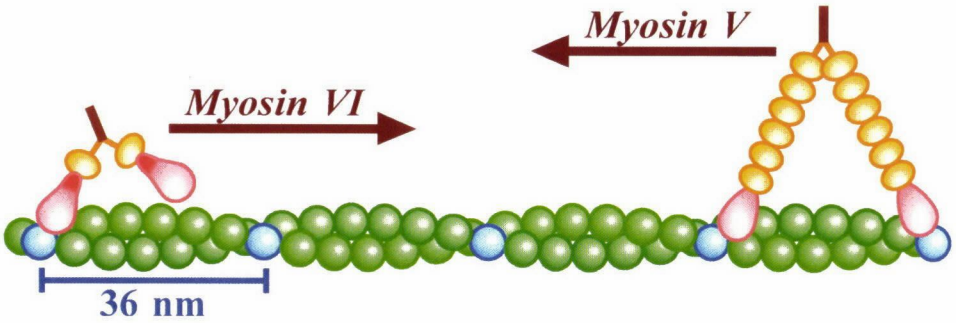

Figure 3. Myosin V and myosin VI. Myosin V has two legs each reinforced with six light chains (orange) and walks on an actin filament (green) toward the barbed, or plus, end (left in the figure). Myosin VI, on the other hand, moves toward the pointed, or minus, end. Previously, myosin VI was thought to bind one light chain per leg, and thus myosin VI was considered short-legged as shown in this figure. The red portion in the feet of myosin VI indicates an extra insert not seen in other myosins. Every 13th monomer of the actin filament is shown in blue. Walking along one side of an actin filament implies an average step size of ~36 nm. Adapted from Ali et al. (2004).

of myosin V has been estimated to be about 36 nm (Mehta et al., 1999; Rief et al., 2000; Rock et al., 2001; Tanaka et al., 2002), which coincides with the helical repeat of an actin filament of 36 nm (Holmes et al., 1990; see Fig. 3). Electron micrographs of myosin V (Walker et al., 2000) have shown that bound feet are separated by ~36 nm on an actin filament, corroborating the step size measurements. In most of these previous studies, however, myosin V could approach an actin filament from only one side, and thus myosin V may have been forced to step on the actin sites that are 36-nm apart (Fig. 3).

To address this possibility, we designed an experiment in Fig. 4*a*, where myosin V could freely rotate around an actin filament that was suspended between two large (4.5 μm) beads. We attached a duplex of 1-μm beads to myosin V to facilitate visualization of rotation. The microscope focus was set such that the bead closer to the observer appeared white and the bead farther from the observer black. As seen in Fig. 4*b*, the bead duplex moved in a left-handed spiral around the right-handed double helix of actin. The rotational pitch was 2.2±0.3 μm per turn, compared to the pitch of the actin double helix of 72 nm. The slight left-handed spiral can be explained if the step size of myosin V is slightly less than the actin helical repeat (half pitch) of 36 nm: in Fig. 4*a*, stepping on blue subunits that are 36-nm apart produces straight motion without spiraling, whereas slightly smaller strides, e.g. on the purple subunits, would lead to a left-handed spiral.

The average step size of myosin V is calculated from the spiral pitch in the following way. If the step size is $(36 - x)$ nm, then myosin V will rotate toward left by $180° \times (x/36)$ per step. To accumulate one turn, myosin V has to make $360° / [180° \times (x/36)] = (72/x)$ steps, or to proceed over a distance of $(72/x) \times (36 - x)$ nm. This latter distance is equal to the spiral pitch of 2200 nm. Thus, $(72/x) \times (36 - x) = 2200$. Solving for x yields $x = 1.1$ nm, and thus the step size is 34.9 nm. (This calculation is slightly different from the one in Ali et al. (2002), but the answer is essentially the same.) With this average step size, the predominant landing site from the position in Fig. 4*a* is on the blue subunit, or the 13th subunit counting both strands. Occasionally myosin V lands on the 11th subunit (purple), and less frequently on the 15th or 9th.

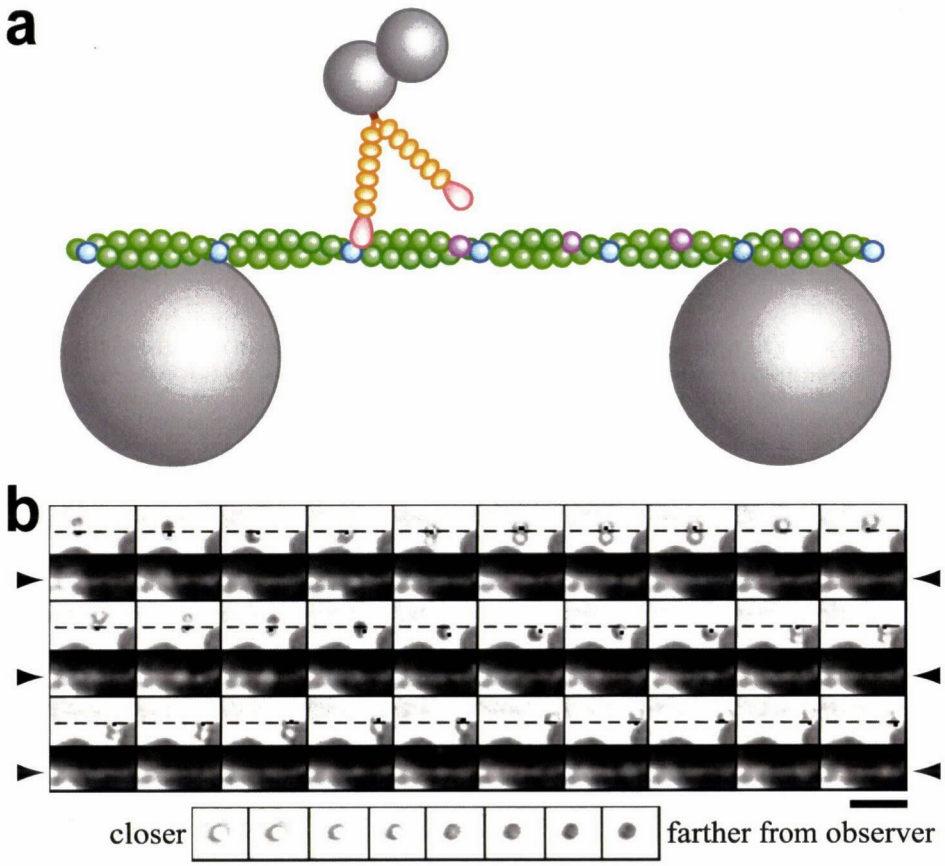

Figure 4. Spiral motion of myosin V around an actin filament. (**a**) Experimental setup. An actin filament, fluorescently labeled, was suspended between beads of diameter 4.5 μm placed on a glass surface. To myosin V, a duplex of 1-μm beads was attached. (**b**) Sequential images, at 1-s intervals, of spiral motion of myosin V at 400 μM ATP. Upper frames in a row show transmitted images of the bead duplex, where a bead closer to the observer appears white and a bead farther away black (see control images at bottom). Lower frames show fluorescence images of the actin filament (between arrow heads). The dashed line in the upper frames show the position of the actin filament deduced from the lower frames. The dot in the upper frames indicates the center of the bead which we judged to be attached to actin. Bar, 5 μm. Adapted from Ali et al. (2002).

The step size we obtained under no load (viscous load is negligibly small for the slow translational motion) is not so different from the previous estimates. Previous steps of ~36 nm were not imposed by experimental geometry. Myosin V naturally walks almost straight, on one side of an actin filament. The implication is that the lever action in myosin V occurs, on the average, almost precisely forward, or in a plane including the actin filament, to let the lifted foot aim from above, not obliquely from side, at the landing sites on the filament. The slight tendency to spiral to the left is explained if forward bias by the lever action is not sufficient to comfortably place the lifted foot on the 13th subunit. Or, the ankles of myosin V may have an intrinsic tendency to bend slightly to the left. When many molecules of myosin II carry an actin filament forward,

the filament rotates as a right-handed screw (Nishizaka et al., 1993) with a pitch of ~1 μm (Sase et al., 1997). Although myosin II is not processive and thus does not walk, the right-handed spiral can be explained if myosin II "kicks" actin by bending a landed ankle slightly obliquely to the right. The structure of the foot (motor domain) of myosin V is similar to that of myosin II (Coureux et al., 2003; Holmes et al., 2003), but a small difference in the direction of ankle action is not inconceivable.

3.2. Myosin VI May Move Like Kinesin

Myosin VI moves, unlike most other myosins, toward the pointed, or minus, end of an actin filament (Wells et al., 1999; Homma et al., 2001). It is a processive motor (Rock et al., 2001; Nishikawa et al., 2002), and thus is considered to "walk" using its two feet. Myosin VI has only one typical light-chain binding site per leg (Wells et al., 1999) and was initially considered short-legged (Fig. 3). Nevertheless, its step size was long, ~30 nm (Rock et al., 2001) or ~36 nm (Nishikawa et al., 2002), apparently incompatible with the expected physical size of the legs. Again, these measurements were made in a configuration that allowed myosin VI to approach from one side of an actin filament, raising the possibility that this constraint somehow forced the short-legged myosin VI to stride on the 36-nm spaced landing sites on one side of the filament. We thought that, if we allowed myosin VI to rotate freely around an actin filament, it would spiral more extensively toward left than myosin V. It might even spiral to the right with a pitch of 72 nm, if its natural step size is smaller than 18 nm such that the motor tracks along one strand of the actin double helix. So we tested this idea, again using the actin-bridge assay (Fig. 4*a*).

A result is shown in Fig. 5*a*, where the bead duplex spiraled as a right-handed screw with a pitch of ~1.4 μm. Many more right-handed spirals were observed, the pitch averaging 2.4 μm. The shallow right-handed spiral indicates an average step size slightly greater than 36 nm (e.g., walking on purple subunits in Fig. 5*b*); the average step size calculated as above is 37.1 nm. There were, however, many more bead duplexes (>80%) that failed to show clear rotation (>0.5 revolution) during a processive run of a few μm. If these represent straight motion, the step size would be 36 nm (on blue actin subunits in Fig. 5*b*). Or, these may also be a part of long-pitch right-handed spiral. In any event, the average step size of myosin VI somewhat exceeds 36 nm, being the longest among known molecular motors. Other long steppers include myosin V, and myosin XI with the average step size of 35 nm (Tominaga et al., 2003).

The long strides of myosin VI are obviously incompatible with walking with short legs. In an electron micrograph (Nishikawa et al., 2002), legs of myosin VI were somehow extended, possibly by unzipping of the stalk coiled coil. Another possibility that the insert unique to myosin VI (red part in Fig. 3) may adopt an extended conformation (Rock et al., 2001) has been denied by a recent study (Bahloul et al., 2004) which shows that the insert is actually a second calmodulin (light chain) binding domain. More recent work (B. R. Rami and J. A. Spudich, Stanford University, and H. L. Sweeney and C. Franzini-Armstrong, Pennsylvania University, personal communication) shows that the coiled coil is indeed unzipped over a considerable length and the unzipped portion is flexible (Fig. 5*b*). The long and flexible legs can account for the unconstrained step size of 36-37 nm. Thus, myosin VI seems to walk almost like kinesin, relying on biased diffusion. A lower part of the legs of myosin VI is

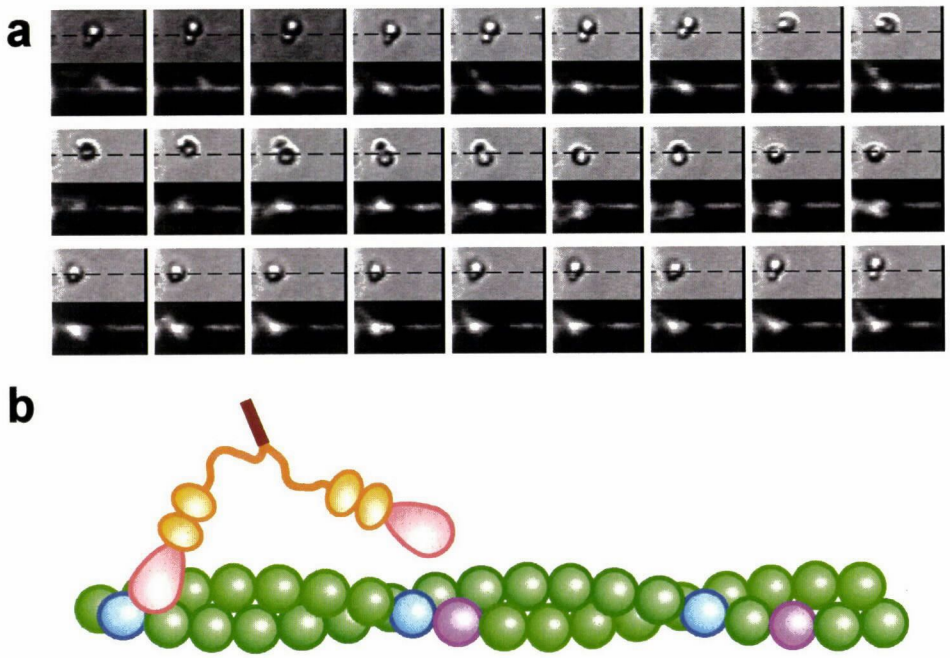

Figure 5. Spiral motion of myosin VI around an actin filament. (**a**) Sequential images, at 0.4-s intervals, of spiral motion of myosin VI at 400 μM ATP. See Fig. 4 for details. This bead duplex (1 and 0.45-μm) carried a short actin filament, which also rotated as seen in the fluorescence images in the lower frames. Of the bead duplexes examined, only ~15% showed right-handed spiral, as seen in these images. Others moved straight without spiraling. (**b**) A recent study (Bahloul et al., 2004) shows that the extra insert in the leg sequence (red part in Fig. 3) actually binds a calmodulin light chain. Also, the coiled coil beyond the light-chain binding region was found to be unzipped. Myosin VI can thus span >36 nm, as required by the right-handed spiraling. Adapted from Ali et al. (2004).

presumably semi-rigid, and its lever action would serve the purpose of biasing the diffusion of a lifted foot forward.

4. TOE UP-DOWN MECHANISM

4.1. Moving Forward against a Backward Force

Myosin and kinesin both appear to walk forward by biasing the diffusion of the lifted foot by an action of the landed ankle, either lever action or docking. Does this mechanism really warrant that the lifted foot lands on a forward, not backward, site? Such a mechanism, alone, would not work properly when the body is pulled backward, particularly when the legs are flexible as in kinesin and myosin VI. If the legs are flexible over a large part, diffusion will even be biased backward (Fig. 6*a*). In kinesin, the free energy difference between the docked and undocked states is small (Rice et al., 2003), implying that docking would fail when the body is pulled back by a load. Then, there will be little bias for diffusion, or backward diffusion may be preferred (Fig. 2*c*).

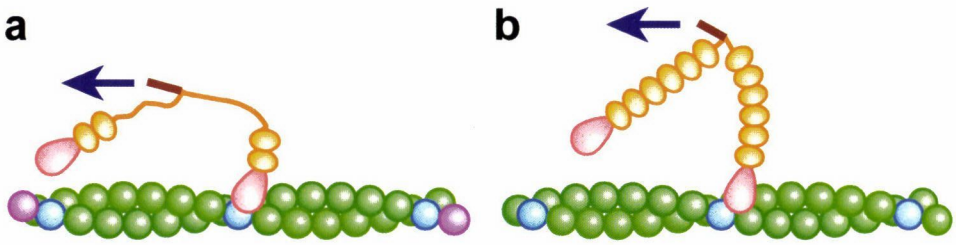

Figure 6. How to move forward against a backward force (arrows). (**a**) If legs are flexible over a considerable length, diffusion would move the lifted foot toward a backward site. (**b**) Under a high backward force, the presumably semi-rigid leg of myosin V may also be bent backward, such that the diffusion is biased backward.

Myosin V might appear to be free from these problems, but its legs cannot be perfectly rigid. Veigel et al. (2002) have estimated its leg stiffness to be 0.2 pN/nm, implying that the body would be pulled back by 10 nm under 2 pN of backward force (Fig. 6*b*). Also, the ankle of the landed foot may yield under the external force, because sustaining 2 pN at the end of the 23-nm leg requires a torque of 46 pN·nm, comparable to the torque of the powerful rotary motor F_1-ATPase (Yasuda et al., 1998; Kinosita et al., 2004). In spite of these problems, all these motors are known to move forward under a few pN of backward load. An additional mechanism, other than biasing the translational diffusion of the lifted foot by moving the effective pivot forward, must be involved.

4.2. Toe Up-Down Mechanism

The mechanism we propose (Ali et al., 2004) is the ankle action in the lifted foot: proper up-down motion of the lifted toe will orient the sole correctly such that landing on a forward site is favored over a backward site even if the body is pulled backward. The toe up-down mechanism warrants forward motion even if legs are completely flexible.

To illustrate the mechanism, let us again use the toy model introduced in Fig. 1. First we deal with the case of semi-rigid legs as in myosin V (Fig. 7). We assume the presence of a flexible joint near the leg-body junction (Fig. 1*f*), and thus there will be little torsional strain in the two legs. Bending strain, however, cannot be relieved by the flexible joint. In Fig. 7, a posture with a bent leg is attained only at the expense of a high energetic cost, or is rarely attained (unless coupled to a reaction accompanying a large drop in free energy).

Figure 7*a*1 shows a posture of the motor after the trailing foot (green) is lifted from the rail. The ankle of the leading foot (red) is already bent forward (lever action), such that the pivot for rotary diffusion of the lifted leg is forward of the landed foot (red) and is ready to bring the green foot forward. However, if the lifted toe is up, as in Fig. 7*a*1, the sole will be misoriented after a forward swing (Fig. 7*a*2), making forward landing difficult. Forced landing would bend the leg severely (Fig. 7*a*3). Natural landing sites for the toe-up foot will be next to the landed foot (Fig. 7*a*4), front or back, and thus the motor will hardly walk forward.

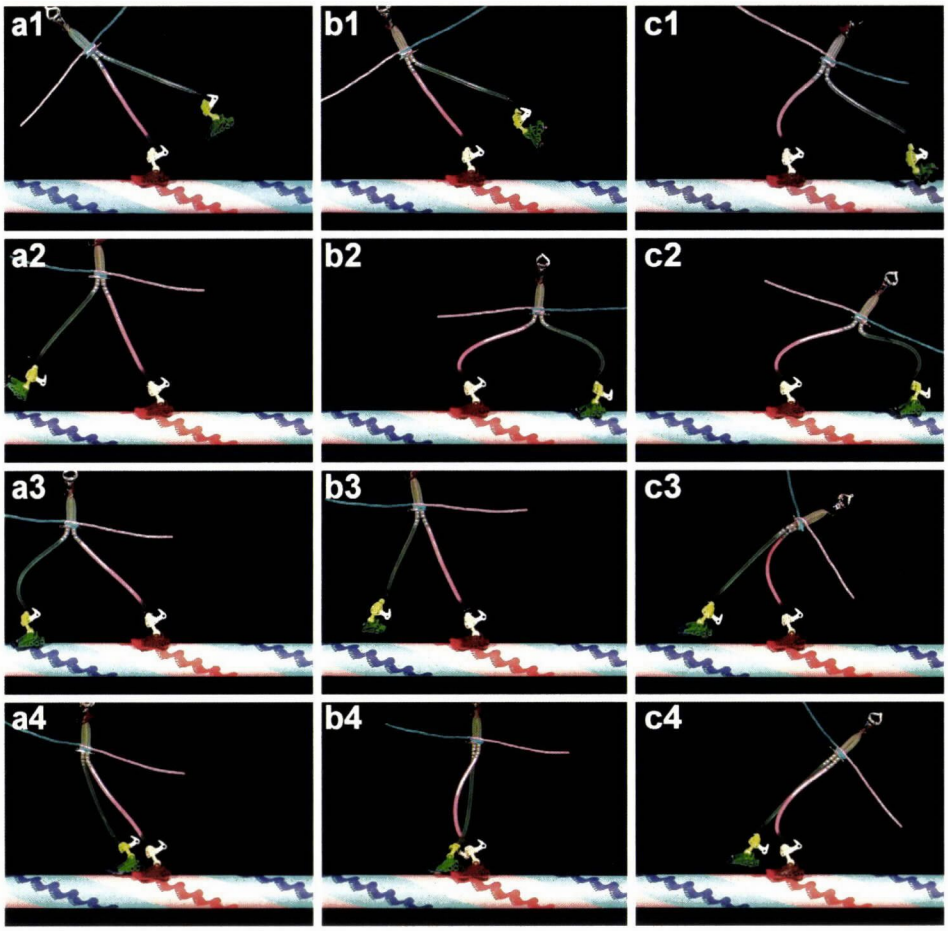

Figure 7. Toe up-down mechanism for the case of semi-rigid legs. (**a**) If the lifted toe is up, landing on a forward site is difficult, and natural landing would be on a nearby site (*a*4), if one is available. (**b**) If the toe goes down upon lifting of the foot, landing with the least strain will be on a distant forward site. (**c**) A backward force will pull the pivot backward (*c*1), but, as long as the lifted toe is down, landing on a distant forward site is favored. Under a high force, landing on a nearby site is equally probable (*c*4). Note that, in *c*4, bending of the red leg is caused by the external force. Adapted from Ali et al. (2004).

If, on the other hand, the lifted toe goes down, as in Fig. 7*b*1, re-landing on the backward site will be prohibited (Fig. 7*b*2), whereas landing on a distant forward site will be smooth and natural (Fig. 7*b*3). Landing on a nearby site would result in a strain (Fig. 7*b*4) and thus is much less likely.

A nice feature of the toe up-down mechanism is that it operates properly even in the presence of a backward force that tends to pull back the pivot beyond the position of the landed foot (Fig. 7*c*1). Thanks to the sole orientation, backward landing is still prohibited (Fig. 7*c*2), whereas a small thermal agitation will allow landing on a distant forward site (Fig. 7*c*3). Landing on a nearby site is also allowed under a high backward force (Fig. 7*c*4), but this is the condition where the motor begins to stall.

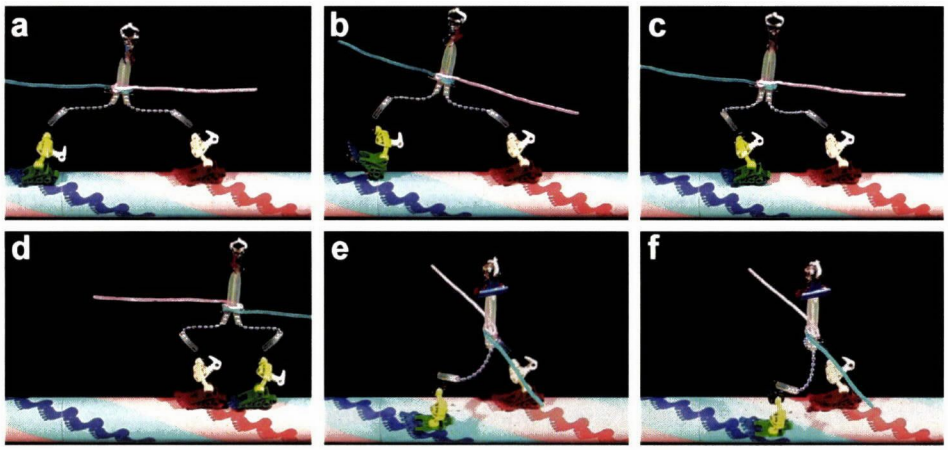

Figure 8. Toe up-down mechanism for the case of completely flexible legs. The legs in the model are made of metal chains. (**a**) The size of the legs are such that landing on a distant forward site is allowed only when the legs are fully extended and the leading toe is down and trailing toe up. (**b, c**) With the green toe up, forward landing is impossible. (**d**) As long as the green toe is down, there is no hope in backward landing. (**e, f**) If a lower part of legs is stiff, oblique landing on a side of the cylindrical rail is also prohibited. The postures here represent the lowest possible position for the green foot, which fails to reach a blue foot mark below.

The toe up-down mechanism also works with flexible legs, as long as landing sites are widely separated such that landing requires almost full extension of the legs. This is because, on a fully extended leg, the orientation of the sole is restricted, in the same way as in a rigid leg. In Fig. 8, the legs of the toy model are made of flexible chains. Suppose, for the moment, that only those landing sites (foot marks) that are at the top of the rail cylinder are available. This situation applies to kinesin on a microtubule. The green foot can land on the forward site if its toe is down (Fig. 8*a*), but it cannot land if the toe is up (Figs. 8*b* and *c*). When the green toe is down, forward movement is warranted because landing on the backward site is impossible (Fig. 8*d*). The preferential forward landing also operates in the presence of backward force. In Fig. 8*d*, even if the red ankle yields to a backward force and bends backward (kinesin "undocks" by backward pull), the green foot cannot reach the backward site as long as its toe remains down. Forward landing (Fig. 8*a*) would still be possible, when the body happens to move forward by Brownian motion (a rare event when the backward force is high).

On an actin filament along which myosin VI moves, all foot marks in Fig. 8 are basically available for landing. Unless the legs are too long, however, landing on a distant backward site is prohibited when the green toe is down (Fig. 8*d*). In addition, the presumably stiff lower portion of the legs of myosin VI opposes oblique landing on a side of the filament (Figs. 8*e* and *f*). Thus, toe-down landing will be made primarily on a distant forward site (Fig. 8*a*), and occasionally on sites next to the landed foot. The frequency of landing on a nearby site depends critically on the make of the legs and ankles (less easy if shanks are long and ankles are bent acutely), and also on the backward load. The large variation in the size of individual steps of myosin VI (Rock

et al., 2001; Nishikawa et al., 2002) may result from mixing of ~36-nm strides with short ones (±5.5 nm for the adjacent landing sites).

4.3. How to Walk Forward

In our view, at least four mechanisms are needed to let a two-foot motor walk forward: (1) the lever action or docking in the landed foot, (2) diffusion of the lifted foot, (3) toe up-down in the lifted foot, and (4) preferential detachment of the rear foot. (1) The lever action has been considered, by many myosin researchers, to play the central role in throwing the lifted leg forward. Its true significance, however, might be in preventing the pivot from pulled back too much by a backward force (Fig. 6). (2) Diffusion around the pivot is the only way by which the lifted foot move, whether forward or backward. It is quite unlikely that ATP-dependent conformational changes alone, in the landed and/or lifted feet, carry the lifted foot all the way onto a landing site. Passive diffusion must be involved, which assists forward and backward movements equally. (3) Toe up-down in the lifted foot, we propose, plays the major role in selecting a forward landing site over backward ones. (4) When both feet land, it must be the rear foot that is lifted first. This is accomplished by a strain dependence of the nucleotide kinetics in the feet. For kinesin, for example, pulling a landed foot forward has been shown to increase the affinity of that foot for ADP (Uemura and Ishiwata, 2003). This would take place in the rear foot, and the affinity for a microtubule binding site is weakened when kinesin's foot binds ADP.

In somewhat different contexts, a human being also uses the four mechanisms above when he/she walks. The major differences, apart from the distinction between the right and left feet, are that a human relies on inertia, particularly in (2) and (4), and that gravity helps in (2) and (3).

5. ACKNOWLEDGMENTS

We thank M. Fukatsu for the toy model, and S. Ishiwata, S. Uemura, and the members of Kinosita lab for discussion. This work was supported in part by Grants-in-Aid from the Ministry of Education, Culture, Sports, Science and Technology of Japan. M. Y. Ali was, and K. Shiroguchi is, a Research Fellow of the Japan Society for the Promotion of Science.

6. REFERENCES

Ali, M. Y., Uemura, S., Adachi, K., Itoh, H., Kinosita, K. Jr., and Ishiwata, S., 2002, Myosin V is a left-handed spiral motor on the right-handed actin helix, *Nat. Struct. Biol.* **9**:464-467

Ali, M. Y., Homma, K., Iwane, A. H., Adachi, K., Itoh, H., Kinosita, K. Jr., Yanagida, T., and Ikebe, M., 2004, Unconstrained steps of myosin VI appear longest among known molecular motors, *Biophys. J.* **86**:3804-3810.

Asbury, C. L., Fehr, A. N., and Block, S. M., 2003, Kinesin moves by an asymmetric hand-over-hand mechanism, *Science* **302**:2130-2134.

Bahloul, A., Chevreux, G., Wells, A. L., Martin, D., Nolt, J., Yang, Z., Chen, L.-Q., Potier, N., Dorsselaer, A. V., Rosenfeld, S., Houdusse, A., and Sweeney, H. L., 2004, The unique insert in myosin VI is a structural calcium-calmodulin binding site *Proc. Natl. Acad. Sci. USA* **101**:4787-4792.

Burgess, S., Walker, M., Wang, F. J., Sellers, R. J., White, H. D., Knight, P. J., and Trinick, J., 2002, The

prepower stroke conformation of myosin V, *J Cell Biol.* **159**:983-991.
Cheney, R E., O'Shea, M K., Heuser, J E., Coelho, M V., Wolenski, J S., Espreafico, E. M., Forscher, P., Larson, R. E., and Mooseker, M S., 1993, Brain myosin-V is a two-headed unconventional myosin with motor activity, *Cell* **75**:13-23
Coureux, P.-D., Wells, A. L., Ménétrey, J., Yengo, C. M., Morris, C. A., Sweeney, H L., and Houdusse, A., 2003, A structural state of the myosin V motor without bound nucleotide, *Nature* **425**:419-423.
Endow, S. A., and Barker, D. S., 2003, Processive and nonprocessive models of kinesin movement, *Annu Rev. Physiol.* **65**:161-175.
Forkey, J N., Quinlan, M E., Shaw, M A., Corrie, J. E T., and Goldman, Y. E., 2003, Three-dimensional structural dynamics of myosin V by single-molecule fluorescence polarization, *Nature* **422**:399-404.
Holmes, K. C., Popp, D., Gebhard, W., and Kabsch, W., 1990, Atomic model of the actin filament, *Nature* **347**:44–49
Holmes, K C., and Geeves, M. A., 2000, The structural basis of muscle contraction, *Phil Trans. R Soc B* **355**: 419-431
Holmes, K. C., Angert, I., Kull, F. J., Jahn, W., and Schröder, R. R., 2003, Electron cryo-microscopy shows how strong binding of myosin to actin releases nucleotide, *Nature* **425**:423-427.
Homma, K., Yoshimura, M., Saito, J., Ikebe, R., and Ikebe, M., 2001, The core of the motor domain determines the direction of myosin movement, *Nature* **412**. 831-834
Houdusse, A., Kalabokis, V. N., Himmel, D., Szent-Györgyi, A. G., and Cohen, C., 1999, Atomic structure of scallop myosin subfragment S1 complexed with MgADP: A novel conformation of the myosin head, *Cell* **97**, 459-470
Houdusse, A., Szent-Györgyi, A G., and Cohen, C., 2000, Three conformational states of scallop myosin S1, 2000, *Proc Natl Acad Sci USA* **97**, 11238-11243
Howard, J., 1996, The movement of kinesin along microtubules, *Annu Rev. Physiol* **58** 703-729
Hua, W., Chung, J., and Gelles, J., 2002, Distinguishing inchworm and hand-over-hand processive kinesin movement by neck rotation measurements, *Science* **295** 844-848.
Huxley, H E., 1969, The mechanism of muscular contraction, *Science* **164**:1356-1366
Ishiwata, S., Kinosita, K. Jr., Yoshimura, H., and Ikegami, A., 1987, Rotational motions of myosin heads in myofibril studied by phosphorescence anisotropy decay measurements, *J. Biol. Chem.* **262**:8314-8317
Kinosita, K. Jr., Ishiwata, S., Yoshimura, H., Asai, H., and Ikegami, A., 1984, Submicrosecond and microsecond rotational motions of myosin head in solution and in myosin synthetic filaments as revealed by time-resolved optical anisotropy decay measurements, *Biochem.* **23**:5963-5975.
Kinosita, K. Jr., Yasuda, R., Noji, H., Ishiwata, S., and Yoshida, M., 1998, F_1-ATPase: a rotary motor made of a single molecule, *Cell* **93**:21-24.
Kinosita, K., Jr., Adachi, K., and Itoh, H., 2004, Rotation of F_1-ATPase: how an ATP-driven molecular machine may work, *Annu. Rev. Biophys. Biomol. Struct.* **33**:245-268.
Kozielski, F., Sack, S., Marx, A., Thormählen, M., Schönbrunn, E., Biou, V., Thompson, A., Mandelkow, E.-M., and Mandelkow, E., 1997, The crystal structure of dimeric kinesin and implications for microtubule-dependent motility, *Cell* **91**:985-994.
Li, Y, Brown, J H., Reshetnikova, L., Blazsek, A., Farkas, L., Nyitray, L., and Cohen, C., 2003, Visualization of an unstable coiled coil from the scallop myosin rod, *Nature* **424**:341-345.
Mehta, A. D., Rock, R. S., Rief, M., Spudich, J. A., Mooseker, M. S., and Cheney, R. E., 1999, Myosin-V is a processive actin-based motor, *Nature* **400**:590-593.
Mehta, A., 2001, Myosin learns to walk, *J. Cell Sci.* **114**:1981-1998.
Moore, J R., Krementsova, E. B., Trybus, K. M., and Warshaw, D. M., 2001, Myosin V exhibits a high duty cycle and large unitary displacement, *J. Cell Biol.* **155**:625-635
Nishikawa, S., Homma, K., Komori, Y., Iwaki, M., Wazawa, T., Iwane, A. H., Saito, J., Ikebe, R., Katayama, E., Yanagida, T., and Ikebe, M., 2002, Class VI myosin moves processively along actin filaments backward with large steps, *Biochem Biophys. Res. Commun.* **290** 311-317.
Nishizaka, T., Yagi, T., Tanaka, Y., and Ishiwata, S., 1993, Right-handed rotation of an actin filament in an in vitro motile system, *Nature* **361**:269-271.
Rice, S., Cui, Y., Sindelar, C., Naber, N., Matuska, M., Vale, R., and Cooke, R., 2003, Thermodynamic properties of the kinesin neck-region docking to the catalytic core, *Biophys. J* **84**: 1844-1854
Rief, M., Rock, R S., Mehta, A. D., Mooseker, M. S., Cheney, R. E., and Spudich, J A., 2000, Myosin-V stepping kinetics: A molecular model for processivity, *Proc. Natl. Acad. Sci. USA.* **97**: 9482-9486.
Rock, R. S., Rice, S E., Wells, A. L., Purcell, T. J., Spudich, J. A., and Sweeney, H. L., 2001, Myosin VI is a processive motor with a large step size, *Proc. Natl Acad. Sci. USA.* **98**:13655-13659
Sakamoto, T., Amitani, I., Yokota, E., and Ando, T., 2000, Direct observation of processive movement by individual myosin V molecules, *Biochem. Biophys Res Commun.* **272**:586–590
Sase, I., Miyata, H., Ishiwata, S., and Kinosita, K. Jr., 1997, Axial rotation of sliding actin filaments revealed

by single-fluorophore imaging, *Proc Natl Acad Sci USA* **94** 5646-5650
Schliwa, M., and Woehlke, G., 2003, Molecular motors, *Nature* **422**:759-765.
Tanaka, H., Homma, K., Iwane, A. H., Katayama, E., Ikebe, R., Saito, J., Yanagida, T., and Ikebe, M., 2002, The motor domain determines the large step of myosin-V, *Nature* **415**:192-195.
Tominaga, M., Kojima, H., Yokota, E., Orii, H., Nakamori, R., Katayama, E., Anson, M., Shimmen, T., and Oiwa, K., 2003, Higher plant myosin XI moves processively on actin with 35 nm steps at high velocity, *EMBO J.* **22**:1263-1272.
Uemura, S., and Ishiwata, S., 2003, Loading direction regulates the affinity of ADP for kinesin, *Nat Struct Biol* **10** 308-311.
Vale, R. D., and Milligan, R. A., 2000, The way things move: looking under the hood of molecular motor proteins, *Science* **288** 88-95.
Vale, R. D., 2003, Myosin V motor proteins: marching stepwise towards a mechanism, *J. Cell Biol.*, **163**.445-450
Veigel, C., Wang, F., Bartoo, M. L., Sellers, J. R., and Molloy, J. E., 2002, The gated gait of the processive molecular motor, myosin V, *Nat. Cell Biol.* **4**.59-65.
Walker, M. L., Burgess, S. A., Sellers, J. R., Wang, F., Hammer, J. A., Trinick, J., and Knight, P. J., 2000, Two-headed binding of a processive myosin to F-actin, *Nature* **405**.804-807.
Wells, A. L., Lin, A. W., Chen, L.-Q., Safer, D., Cain, S. M., Hasson, T., Carragher, B. O., Milligan, R. A., and Sweeney, H. L., 1999, Myosin VI is an actin-based motor that moves backwards, *Nature* **401**.505-508.
Yasuda, R., Noji, H., Kinosita, K. Jr., and Yoshida, M., 1998, F_1-ATPase is a highly efficient molecular motor that rotates with discrete 120° steps, *Cell* **93** 1117-1124.
Yildiz, A., Forkey, J. N., McKinney, S. A., Ha, T., Goldman, Y. E., and Selvin, P. R., 2003, Myosin V walks hand-over-hand: Single fluorophore imaging with 1.5-nm localization, *Science* **300**:2061-2065.
Yildiz, A., Tomishige, M., Vale, R. D., and Selvin, P. R., 2004, Kinesin walks hand-over-hand, *Science* **303**:676-678.

DISCUSSION

Pollack: Could you comment on how single-headed kinesins could advance along a microtubule?

Kinosita: Some part of kinesin would stick non-specifically to the microtubule, as has been shown for KIF1A, and another part would pull the molecule forward, by a lever action or by extending itself forward by diffusion followed by binding to a microtubule site.

Gonzalez: Without strain, on which direction would myosin V move?

Kinosita: If there were no strain-dependent regulation of nucleotide kinetics, either foot, front or rear, could be lifted from actin. The motor would still move forward, but the efficiency would be low, because lifting the front foot would not contribute to forward motion while ATP is expended.

Pollack: (comment) With single filaments sliding past one another, you do see backward steps of $n \times 2.7$ nm.

Sugi: One single question is the biased diffusion you mentioned in your talk is the same as so-called Brownian ratchet mechanism?

Kinosita: The Brownian ratchet, in my opinion, is a broad term that applies to almost

any mechanisms of molecular machines. Moving the pivot forward, by a lever action, to help forward landing is a kind of ratchet. Assuring forward landing by bringing the toe up, without necessarily the pivot motion, is another way of realizing a ratchet.

Kushmerick: You stated the ATP synthesis by F_1-ATPase may be nearly 100% efficient. What is the efficiency of the H^+ proton-driven component of F_oF_1 ATP synthase? Is the overall F_oF_1 rotary motor reversible?

Kinosita: For ATP synthesis, I expect the number efficiency (the number of ATP molecules synthesized per 120-degree rotation) to be close to one, under favorable nucleotide concentrations and at low rotary speeds. The energetic efficiency (free energy for ATP synthesis divided by mechanical work done on the gamma subunit) is critically dependent on the nucleotide concentrations and applied torque, and would be high only near reversal (low torque). Peter Gräber's group, among others, has shown that F_oF_1 ATP synthase is reversible, and that synthesis/hydrolysis in F_1 is balanced by the proton flow through F_o. When the proton motive force across F_o is greater than the free energy needed for ATP synthesis, ATP is synthesized. ATP is hydrolyzed when the proton motive force is lower. They have shown that synthesis of one ATP molecule requires translocation of about four protons, but, in addition, some protons may leak through the membrane or the F_o motor. Thus, experimental determination of the efficiency of synthesis is very difficult.

生物物理 41 (6), 315-317 (2001)

ひとくう

あれ！ 顕微鏡対物レンズが縮んでいる？(対物レンズの温度依存性)

科学技術振興事業団CREST
「生命活動プログラム」チーム13
塩 育

1. はじめに

タンパク質などの生体物質が働くようすを1分子単位で観察・操作する「1分子生理学」と呼ばれる新しい研究分野が生まれつつある. この研究のためには光学顕微鏡が不可欠であり, 生体物質の動きが非常に小さいため, 解析には数ナノメートルの精度が必要である.

しかし現存の光学顕微鏡には安定性の問題があり, 実験誤差のおもな原因の1つとなっている.

X-Y (水平面) 座標軸方向は研究者の苦心により安定性確保の対策がとれる場合もあるが, *Z* 軸 (垂直) 方向の最大の不安定要素は対物レンズの温度依存性にあると言われており, 研究者が対処できる問題ではない. そこで次の方法でこれを実際に測定してみたところ, 対物レンズの筒は単純に伸びるという想定を裏切って焦点が対物レンズ側に移動した. しかもその移動量が予想外に大きかったので報告する.

2. 使用機材と測定方法

2.1 被測定レンズ

- Nikon CF Plan Apo 60× N.A.1.40
- Nikon CF fluor 100× N.A.1.30
- Olympus Plan Apo 60× N.A.1.40

2.2 おもな使用機材

- Olympus 倒立顕微鏡IX-70：
  左サイドポート部測定光学系 (ナイフエッジ法) 追加
- Nikon 倒立顕微鏡TMD：
  落射蛍光照明部改造・左サイドポート部測定光学系追加
- 画像記録・解析装置
  ビデオカメラ：HAMAMATSU C5405 1/2 インチ
  Camera Controller：HAMAMATSU C2741
  DIPS：HAMAMATSU C2000
- 加温装置：
  東海ヒット社 レンズウォーマー

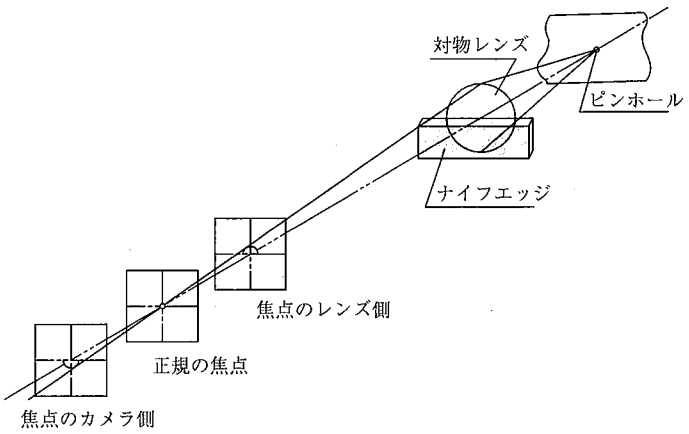

図1 ナイフエッジ法の原理
ピンホールからの光は対物レンズにより拡大され, 正規の焦点面に再結像する. 対物レンズの瞳面を半分覆うと, 正規の焦点前後面では図のような半円となる.

Microscope Objectives Effectively Shrink Upon Warming

Megumu SHIO
CREST Genetic Programming Team 13

表1　各種対物レンズの温度依存性測定結果
顕微鏡対物レンズの物点（焦点面）が室温の変化等により変化する量を単位温度あたりで表した値（μm／℃）で表示する．とは1℃上昇すると対物レンズを下記の数値だけ物体の方向に近づけなくてはならない方向を示す（焦点距離が短くなる方向の値）．数値の単位はμm

対物レンズ	測定法1 ビーズ拡大像の直径測定法		測定法2 ナイフエッジ法		測定法3 ナイフエッジ法	
	結果1	結果2	結果1	結果2	結果1	結果2
Nikon CF Plan Apo 60×	−0.62	−0.72	−0.63	−0.66	−0.63	
Nikon CF fluor 100×	−1.28		1.16			
Olympus Plan Apo 60×	−0.58	0.58	−0.58	−0.56	−0.67	−0.68

2.3 測定方法（ここにもひとくふう）

測定には，3通りの方式を用いた（表1）．測定法1は，対物レンズによるビーズの拡大像の直径変化から焦点位置の変化を求めるものである（ビーズ拡大像の直径測定法）．まず，ピエゾ駆動によりZ軸ステージを0.1 μmずつ動かし，それぞれの部位におけるビーズの拡大像をCCDカメラで記録しておく．これを基準尺とし，室温を上昇させて顕微鏡全体を暖めたときのビーズ拡大像の直径から焦点位置の変化を換算した．

測定法2と3は，いずれもナイフエッジ法[1]応用式を用い，2は室温を上昇させ，3は対物レンズ部のみをレンズウォーマーで暖めて測定を行った．ナイフエッジ法の原理を以下に述べる（図1）．対物レンズ瞳面に，レンズ面の真半分を遮光するようにナイフエッジを挿入しておく．ピンホールからの光を対物レンズで拡大投影し，CCDカメラの撮像面に再結像させる．撮像面がちょうど焦点であれば，スポット像が得られる．しかし，撮像面が焦点よりもレンズ側であれば上方半円像となり，カメラ側であれば下方半円像となる．したがって，カメラの撮像面をレンズ側の位置から次第に遠ざけていき，上方半円像が下方半円像に変わる境目が正規の焦点ということになる．実際には，半円像の上下の逆転は，画像解析により光の重心移動から検出する（重心移動がゼロとなる点が焦点である）．

この測定法の感度は非常に高いが，測定できる試料面の範囲が非常に狭い（100倍の対物レンズでは試料面でZ軸方向300 nm）．そこで，カメラ移動方式の光学系を考案した（図2）．試料面には，ピンホールの代わりに直径1～2 μmのビーズを固定する．

対物レンズの瞳部に直接ナイフエッジを置くことは，高倍率対物レンズでは（レンズがきっちり詰まっており）現実には不可能である．そこで，倒立顕微鏡サイドポート側に瞳面を中継するリレーレンズ系を増設し，投影瞳面にナイフエッジを置いた．

3. 測定結果の検討

測定結果を表1に示す．対物レンズの筒は40 mm近くあるので，温度上昇時には（筒長が伸び，対物レンズ取付けねじ終面より焦点面が長くなり）対物レンズを物体より遠ざける方向に移動させないと合焦しないと予想していた．しかし，3つの測定法による結果はどれも，対物レンズを物体に近づける必要があるというものだった．今回の測定で，単純に筒が伸び縮みするのでなく，レンズと金物の複雑な関係があることに気づいた．

同一の測定法での再現性はよいが，測定法を変えると0.1 μmの差が認められ，換算法には問題が残されて

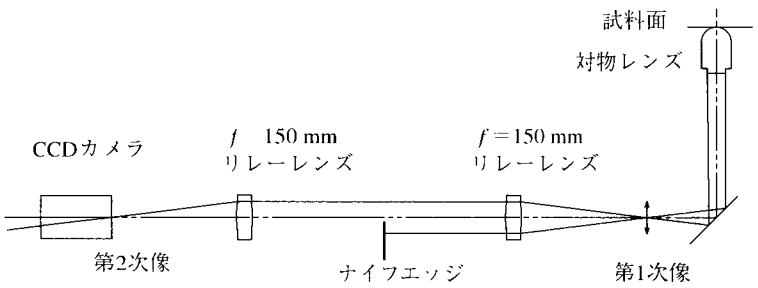

図2　ナイフエッジ法を用いて実測した光学系
対物レンズの瞳面はリレーレンズで中継され，この面にナイフエッジを設置した．寸法は記載しないが，実測装置サイズをそのまま縮小している．

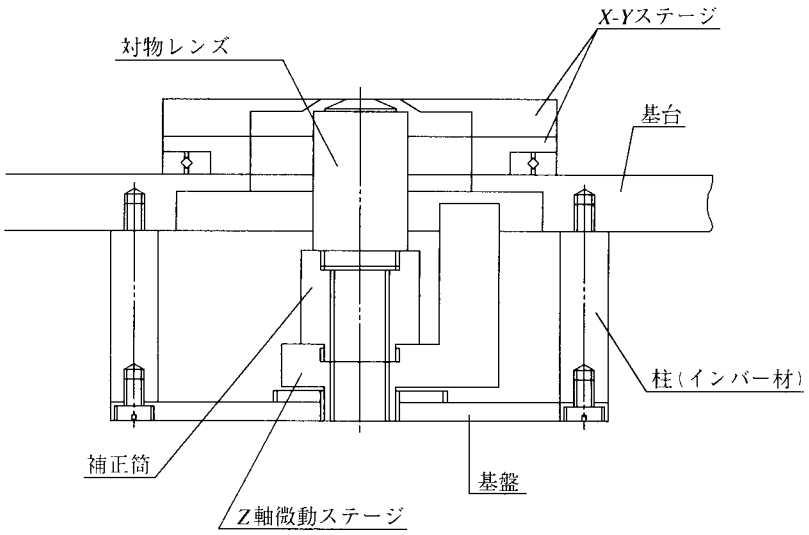

図3　補正機構の構成図（測定結果確認用）
基盤上の中央部（対物レンズ・補正筒・Z軸微動ステージ）と周辺部（柱・基台・X-Y軸ステージ）の温度依存性の総和が等しくなっている

いる.

4. ひとくふう

焦点移動の方向と測定値を確認し、また、実際の使用の際の不安定性を少しでも解消するため、図3のような工夫をし、補正機構を試作した. 補正の原理はステージ部に熱膨張係数のきわめて低いインバー材の柱を用いて、基盤を吊り下げ、この基盤上に補正筒と対物レンズを組上げた. 対物レンズの温度依存性はマイナス方向にあるので、補正筒にはプラス方向となる真鍮を用いた.

結果は良好で、安定性が桁違いに向上した. 焦点移動方向も誤りないと確認できた. しかしながら、この補正方式は指定のレンズには適応できるが、レンズ交換時には別途補正が必要である. 研究が進むにつれて、より安定性の高い顕微鏡が望まれるが、対物レンズのような顕微鏡の基本コンポーネントに問題がある場合、研究者にはどうすることもできない.

5. まとめ

対物レンズの温度依存性を測定したところ、焦点距離が1.0 μm／℃以上移動し、対物レンズの筒が単純に伸びるという想定とは逆方向であった.

顕微鏡の不安定要素はこの焦点移動の問題だけではない. メーカーさん何とか解決して下さい. 我々は苦し紛れにこんな工夫をしていますが、切実な問題です. 対物レンズの焦点移動はせめて1℃の温度変化で0.1 μm以下にして下さい.

文　献

1）久保田　広（1964）光学, pp.210-213, 岩波書店, 東京.

塩　育（しお　めぐむ）
科学技術振興事業団 CREST「生命活動プログラム」チーム13
連絡先：〒216-0001　川崎市宮前区野川907　帝京大学生物工学研究センター内3F
E-mail: m-shio@mvi.biglobe ne jp
shio@phys keio.ac.jp

生体の科学　54(1)：36-40，2003

座談会に関連して

F_1-ATPaseのステップ回転：ATP駆動の分子機械が働く仕組み

木下一彦　足立健吾　伊藤博康

たんぱく質の分子は，たった1個だけでも立派に働くので，分子機械と呼ばれる。例えば，図1に示してあるのは1個の回転モーター分子で，中央上部に突き出ている黒っぽい棒状の部品(サブユニット)が，それを取り囲む六つの灰色の部品の中で回る。われわれの体の中には，この分子モーターがたくさんあり，くるくると回り続けている。原子が縦・横・奥行きそれぞれ数十個並んだ塊がたんぱく質の分子。こんなに小さな分子が，たった1個だけで働くのである。

この回転分子モーターは，F_1-ATPaseないしF_1(エフワン)と呼ばれている。体内では，回転により，生体内のエネルギー通貨であるATPを化学合成している。回転による化学合成とは，いったいどういう仕掛けなのだろうか。反対方向に回るときには，ATPを分解して，そのエネルギーを使って文字通りモーターとして働くのだが，合成の時と同じ仕掛けを使うのだろうか。

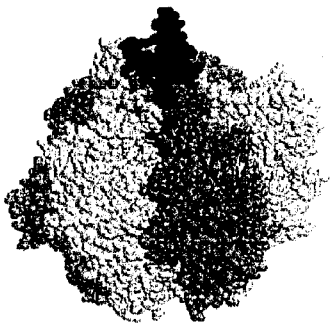

図1　F_1-ATPaseの立体構造[3]
中央の一番黒いのがγ，白っぽい三つがα，灰色の三つがβサブユニット。

体の中には，他にもいろいろな分子機械があって，栄養を運んだり，筋肉を縮ませたり，DNAを複製したり，さまざまな仕事をしている。分子機械を作るための分子機械もある。これらの分子機械が働く仕組みを探りたい。個々の分子機械の仕掛けだけでなく，できたら共通原理，人間の作ったマクロの機械のものとはおそらく異なる原理を見出したいと考えている。

1．ATP加水分解により働く分子機械

生理的条件下では，ATPがADPと無機燐酸に加水分解されるとき，自由エネルギーが放出される(＝反応が分解方向に進む)。たんぱく質(ないしRNA)でできた生体分子機械の多くが，このエネルギーを使って仕事をする。しかしその仕組みが，まだよくわかっていない。

一般に，ATP駆動の分子機械は，三つの段階を経て働くと考えられる。すなわち，(1)ATPの活性部位への結合，(2)活性部位内でのATPの分解，(3)分解産物(ADPと燐酸)の活性部位からの解離，の3段階である。

F_1モーターは，体の外に取り出すと，もっぱらATPを分解して，そのエネルギーにより回転する。すなわちATP駆動の回転モーターとして働く。われわれは，光学顕微鏡下の一分子観察(一分子生理学)により，少なくともF_1モーターの場合には，第1のATP結合の過程で大部分の仕事が行われる(力が発生する)ことを見出した。残りの

Kazuhiko Kinosita, Jr., Kengo Adachi　[著者連絡先] 岡崎国立共同研究機構 統合バイオサイエンスセンター
(〒444-8585 岡崎市明大寺町東山5-1 山手1号館4F)
Hiroyasu Ito [著者連絡先] 浜松ホトニクス(株) 筑波研究所 (〒300-2635 つくば市東光台5-9-2)

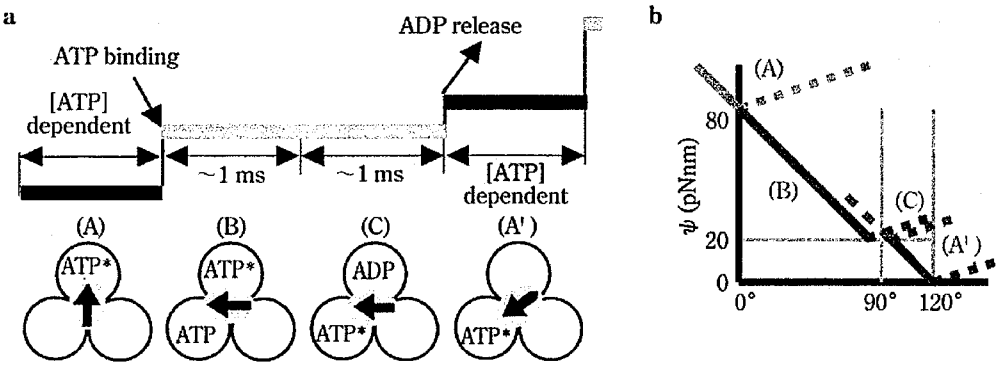

図2　サブステップの解釈(a)とそれから推定されるγ回転のポテンシャルエネルギー(b)
ATP*はATPないしADP＋燐酸を表し，ADPは燐酸ないしADP＋燐酸かもしれない。(b)の各線は，(a)の下側の(A)-(A')の四つの化学状態に対応するポテンシャルエネルギー。この図では結合ヌクレオチドの数が1-2-1-2-…と変化しながら回転することになるが(bi-site説)，2-3-2-3-…かもしれない(tri-site説)。

仕事は，第3の分解産物解離の過程で行われる。活性部位内では，溶液中と違って，加水分解過程が可逆なため(合成反応も比較的容易に起こる)，第2の過程はたいした仕事をしない。

ATPの分解により得られるいわば「化学」エネルギーを，回転という「力学」エネルギーに変換するのに，分解反応のところでなく結合・解離過程を利用する，というところがみそである。他にも共通の原理で働くATP駆動分子機械が多いのではないかと推察している。

2．F_1モーター

F_1-ATPaseは，ATP合成酵素という大きなたんぱく質分子の一部分である。ATP合成酵素は，われわれの体の中ではミトコンドリアの内膜中に存在する。われわれが栄養をとり酸素を吸うのはミトコンドリアに供給するためで，ミトコンドリアは食物を酸素でゆっくりと燃やし(酸化し)，このとき得られるエネルギーを使って，ミトコンドリア内部から外側に水素イオン(プロトン)を運び出す。プロトンはいずれミトコンドリア内に戻ってくるが，その通り道になるのがATP合成酵素である。ATP合成酵素は，膜に埋まったF_0と呼ばれる部分と，外に飛びだしたF_1からなる。F_0部分をプロトンが流れると，F_1でATPが合成される。逆にF_1でATPを加水分解させた場合には，F_0がプロトンを逆向きに運ぶポンプとして働く。

プロトンの流れとATPの合成・分解という化学反応がどうして結びつくのか。ボイヤー[1]および大沢ら[2]は，F_0がプロトン駆動の回転モーター，F_1がATP駆動の回転モーターで，両者の回転軸が共通であると考えた。ただし両者の回転方向は逆で，生体内ではプロトンの駆動力が大きいためF_0モーターの方が勝ち，F_1は無理矢理逆回転させられてATPを作ってしまうというわけである。

単離されたF_1は，$\alpha_3\beta_3\gamma_1\delta_1\varepsilon_1$というサブユニット構成を持ち，ATPの分解のみ行う(δとεはATP分解および回転には不要)。結晶構造[3]を見ると，$\alpha_3\beta_3$の筒の中央にγが突き刺さっている(図1)。ATP分解(および合成)の活性部位は，三つのβにそれぞれ一ヵ所ずつある。

われわれは1997年に，顕微鏡下で，F_1が確かに回転モーターであることを示した[4]。γにアクチン線維を結合させ，その回転を直接目で見ることができたのである。回転の向きは結晶構造から予想したように図1の上から見て反時計回りで，三つのβが順番にATPを分解することにより回転が生じることが示唆された。さらにわかったことは，(a)回転は120度おきのステップ状に起き，各ステップはATP1分子の分解により駆動される[5,6]，(b)各ステップにおいてなされる力学的仕事は一定で，約80-90 pN・nmという値であり，生体内でATP1分子を加水分解するときに得られる自由エネルギーにほぼ等しい[5]，(c)このモーターのトルク(回転力)は回転角によらずほぼ一定で約40 pN・nm[7]，などである。とくに(a)(b)は，このモーターのエネルギー変換効率が100%近くに達し得ることを示唆する。しかしながら，ATPの

加水分解がどのようにして回転を引き起こすのかは，よくわからなかった。

3．サブステップの発見

最近われわれは，γに直径40 nmという小さな金粒子を結合させ，その回転を毎秒8千駒の高速で撮影することに成功した[8]。2 mM ATP存在下ではF_1モーターはフルスピードで回転し，その速度は毎分8千回転に達した。この速度でも回転は120度ステップに分かれ，ステップするときの瞬間速度は毎分10万回転を越えた。一方，ATP濃度を下げて平均回転速度を落としてやると，120度ステップが約90度と30度の二つのサブステップに分かれるのが見えてきた。詳しい解析の結果，図2 aのようなスキームが示唆された。すなわち，90度サブステップはATPの結合により駆動され，30度サブステップのほうは加水分解産物の解離に伴って起きるというものである。両者の間には二つの約1ミリ秒の反応があるが，これらは回転をほとんど伴わない。高濃度ATPではサブステップが見られないが，これは30度サブステップが終わったとたんにATPが結合して90度サブステップが起きるから，というわけである。すなわち，30度サブステップの直後には，モーターは次のATPを受け取って新たな反応サイクルを開始する準備ができている。

ATPの結合が90度サブステップを駆動するということは，作用反作用の法則に従えば，γが90度反時計方向に回転するに従い(図2 aのA→B)，太矢印の左側のβのATPに対する親和性が増加していくことを意味する(解析[8]によれば90度で二百万倍以上の増加)。同様に，C→A'の30度サブステップにおいては太矢印の右側のβのADPに対する親和性が減少していく(30度で百倍以上)。とすると，このモーターを(F_0モーターにより)逆回転させたときATPが合成される仕組みがわかってくる。すなわち，図のA'から始めてγを力ずくで時計回りに回転させると，まず太矢印の右側のβのADPに対する親和性が高まるのでこのβが溶液中からADP(と燐酸)を結合し，さらに回転を続けると，今度は太矢印の左側のβに結合していた合成済みのATPに対する親和性が低くなってこのATPが放り出される，というわけである。

4．ATPの加水分解をいかに使うか

水溶液中でADPと燐酸を混ぜてもATPが自然に合成されることはないが，そこにF_1があると，たんぱく質上では(活性部位内に)ATPが合成されてしまう。リニアー分子モーターであるミオシンでも同様のことが起きることが知られている。ATP駆動の分子機械の多くは，ヌクレオチドを強く結合することにより，活性部位内でATPとADP+燐酸の2状態の間に自由エネルギー差がほとんどない(両者が行き来する)状況を作り出すようである。だとすると，自由エネルギーの大

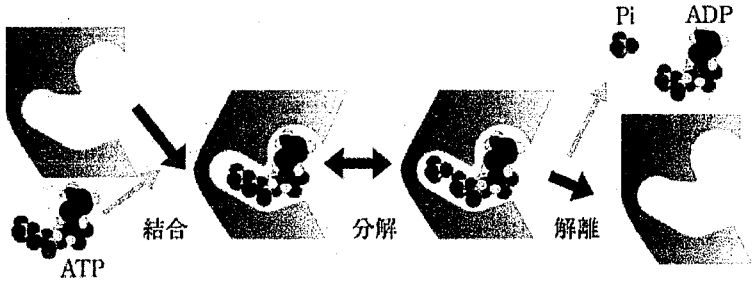

図3 ATP駆動の分子機械が働く仕組み

ATP結合により放出される自由エネルギーによって構造変化を起こして仕事をする。ADP(ないし燐酸[10])の解離の時にも仕事をさせられる。後者はATP結合の時と逆向きの構造変化だが，F_1のような「賢い」分子機械は，これも正しい方向への回転に利用するようである(たぶん三つのβサブユニットの構造変化が順に起きることによりうまくγを回す)。図中の三つの太矢印は，ATP(+たんぱく質分子)の自由エネルギーが3段階に分かれて下がっていくことを示す(水中では同じだけ一気に下がる)。結合と解離の時の自由エネルギー減少を，仕事(力学的エネルギー)に転換するのである。

部分は，ATPの活性部位への結合に伴って放出されることになる[7]。効率よい分子機械を作ろうと思ったら，ATP結合の時に仕事をさせるのに限る。

たんぱく質分子の身になってみればまことにもっともで，空の活性部位にATPが結合(解離)するときには自分の身に大きな変化(たくさんのボンドの生成)が起きるが，加水分解に伴う変化は比較的小さい。ATP結合のとき自分の構造を大きく変え，それにより外部に仕事をするのがよい(図3)。少なくともF_1の場合，この構造変化の仕掛けはたんぱく質側に内在するようで，ヌクレオチドは出来合いの仕掛けを駆動するだけらしい。すなわち，F_1はATPだけでなくGTPやITPでも回転させることができ，回転力は変わらない。しかしUTPやCTPは，回転機構を駆動できない。プリン環があれば，細部に多少の違いがあっても，回転に必要な構造変化を引き起こせるわけである[9]。

それではなんのために加水分解するのかというと，90度サブステップの後はATPが強く結合され，そのままでは次の反応を起こすことができないので，二つに分解することによりそれぞれに対する親和性を下げ，解離を促すというわけである。

加水分解の役目は分子機械を初期状態にリセットするだけかというと，おそらくそうではない。加水分解により少しだけ回転が起きるように(分解と回転がカップルするように)F_1がデザインされているとすると，正しい方向への回転が保証され，さらにATPの分解・合成をそれぞれ効率よく行わせることができる[7]。この点をうまく説明するF_1モーターモデルを，今作っているところである。

5．一分子生理学

分子1個を観察し，必要なら操作を加えることにより，分子機械の働く仕掛けに迫る一分子生理学。なぜ分子1個を相手にする必要があるのか。

F_1-ATPaseのステップ回転を見ると，ステップのタイミングは確率的で，次のステップがいつ起きるかを予想することができない。いわば，各瞬間にサイコロを振って，出た目に応じてステップするかどうかを決めている。ヒトの作るステッピングモーターが，必ず10ミリ秒ごとに1ステップというように，規則正しく動くのと対照的である。

分子機械の動きが確率的なのは，熱運動(ブラウン運動)のせいである。たんぱく質分子がヒトの大きさだとすると，周囲の水分子は大きさ・重さともにパチンコ玉程度。その水分子のブラウン運動の平均速度は何と時速1000 km，ジャンボジェットなみで，音速に近い。この激しいブラウン運動にさらされて，しかもそれをうまく利用しながら働く分子機械の動作は，必然的に不規則な，確率的なものとなる。したがって，二つ以上の分子機械の動作を同期させることは，原理的に不可能なのである。分子機械を本当に理解しようと思ったら，どうしても1個1個が働くところを見ないといけない。

F_1モーターの回転軸に小さな磁石を付けることはすでにできている。だから，もしたくさんのF_1モーターがタイミングを合わせて一斉に回ってくれるのなら，マクロの磁気測定により簡単に回転が検出できるはずである。実際には動きがバラバラだから，止まっていないで動いているらしいぞ，と推定するのがせいぜいである。一方向に回り続けるのかどうか，あるいはどちらに回るのか，の判定など至難であろう。1個を見てしまえばその場で，F_1モーターは反時計回り[4]，RNA合成酵素によるDNAの回転は右ねじの向き[11]，ミオシンVのアクチン線維の回りの回転は左ねじ[12]，とわかる。ステップの詳細解析となったら，一分子観察以外にはまず考えられない。

一分子観察のもう一つの御利益は，分子の個性が見えてくること，つまり個々の分子の振舞いは多数の平均とは異なることがわかることである。しかし本来，分子は均一なものとして定義されている。見かけ上の個性は，その分子のおかれた微環境ないし履歴のせいである。一分子観察のために無理やりガラス表面に結合させられた分子達は，そのせいでやむを得ず個性を発揮してしまうことも多い。実際，われわれの実験系では，99%以上の分子がガラス面上で死んでいることが多い。そのような実験系で得られた結果に意味があ

るのだろうか。

一分子生理学では，「生きた」分子から得られた結果だけが論文に載る。死んだ分子は無視され，死にかけを数えるかどうかは実験者に任される。したがって，ほとんどの分子が生きているという幸運な実験系でない限り，単純な統計処理は客観性を欠く。それでどうして科学たり得るのか。われわれの基本的立場は，同一の分子が何度も同じ動作(例えばステップ)を繰り返す例を選んで，同一分子の複数動作に関する統計を取ることである。例えば連続15ステップ以上が観察された分子だけにつき，ステップ幅やステップ間の時間間隔の解析を行う。長時間統計なら意味がある，アンサンブル統計は要注意，というわけである。

そもそも，「生きている」ことの定義すら実験者任せである。生体内と同じ振舞いをしているのかどうかと問われても，(われわれは)まず答えられない。われわれの採用する定義は，「面白い」かどうか。分子モーターが相手なら，面白いのは，速く動くもの，長い距離動くもの，何回も回転するもの，などである。生体内では，分子モーターはほとんどの時間寝ているかもしれない。しかしわれわれは，寝ているモーターよりは，活発に動くモーターに興味を持つ。顕微鏡下でその精妙な動きを見てしまったら，たとえそれが非生理的な動きであろうと，仕掛けをどうしても探りたくなる。報告したくなる。

ほとんどが失敗に終わる一分子実験。それでも，目の前で演じられる分子劇に魅せられてみたい，そういう人の参加をお待ちします。

[http：//www. K2. ims. ac. jp に動画あり]

文 献

1) Boyer PD：*Biochim Biophys Acta* **1140**：215-250, 1993
2) Oosawa F, Hayashi S：*Adv Biophys* **22**：151-183, 1986
3) Abrahams JP, Leslie AGW, Lutter R, Walker JE：*Nature* **370**：621-628, 1994
4) Noji H, Yasuda R, Yoshida M, Kinosita K Jr：*Nature* **386**：299-302, 1997
5) Yasuda R, Noji H, Kinosita K Jr, Yoshida M：*Cell* **93**：1117-1124, 1998
6) Adachi K, Yasuda R, Noji H et al：*Proc Natl Acad Sci USA* **97**：7243-7247, 2000
7) Kinosita K Jr, Yasuda R, Noji H, Adachi K：*Phil Trans R Soc Lond B* **355**：473-489, 2000
8) Yasuda R, Noji H, Yoshida M et al：*Nature* **410**：898-904, 2001
9) Noji H, Bald D, Yasuda R et al：*J Biol Chem* **276**：25480-25486, 2001
10) Masaike T, Muneyuki E, Noji H et al：*J Biol Chem* **277**：21643-21649, 2002
11) Harada Y, Ohara O, Takatsuki A et al：*Nature* **409**：113-115, 2001
12) Ali MY, Uemura S, Adachi K et al：*Nature Struct Biol* **9**：464-467, 2002

Na/K-ATPase and Related ATPases
K. Taniguchi and S. Kaya (Editors)

Rotation of ATP synthase

R. Yasuda[a], H. Noji[a], K. Adachi[a], T. Nishizaka[a], Y. Kato-Yamada[b], M. Yoshida[b] and K. Kinosita, Jr[a,c]

[a] CREST "Genetic Programming" Team 13
Teikyo University Biotechnology Research Center, Nogawa 907, Kawasaki 216-0001, Japan.
[b] Research Laboratory of Resources Utilization, Tokyo Institute of Technology, Yokohama 226-8503, Japan
[c] Department of Physics, Keio University, Yokohama 223-8522, Japan.

We have shown that a single F_1 molecule is a rotary motor by visualizing the swiveling motion of an actin filament attached to the putative rotor of a surface-fixed F_1. At low [ATP], the rotation was resolved into 120° steps, consistent with the three fold symmetrical structure of F_1. The thermodynamic efficiency of this motor was estimated as nearly 100 %.

1. Overview of the ATP synthase

The ATP synthase is a membrane protein that synthesizes ATP from ADP and Pi in animals, plants, and bacterial cells. In the case of an animal cell, the ATP synthase is located in mitochondrial inner membranes. The respiratory chain pumps protons from the inside to outside of mitochondria. When protons go back through the ATP synthase from the outside to inside of mitochondria, the ATP synthase synthesizes ATP.

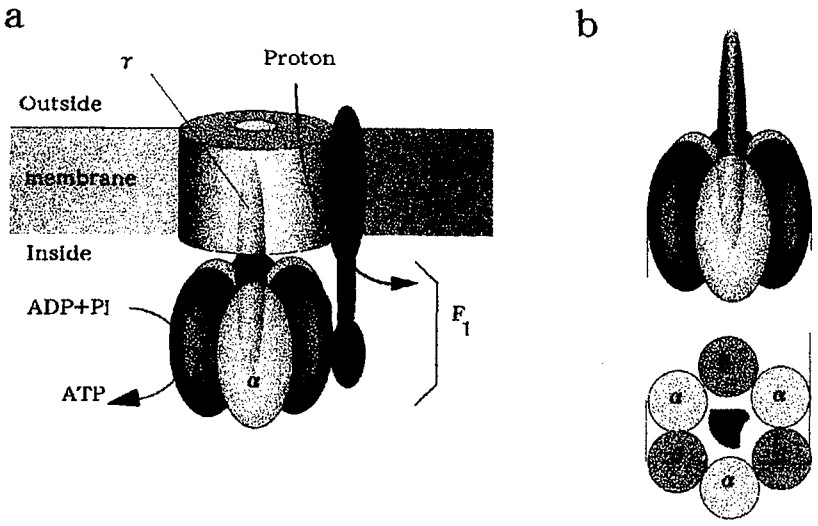

Figure 1: Schematic illustration of the ATP synthase. **a**: Whole complex. **b**: F_1 [3].

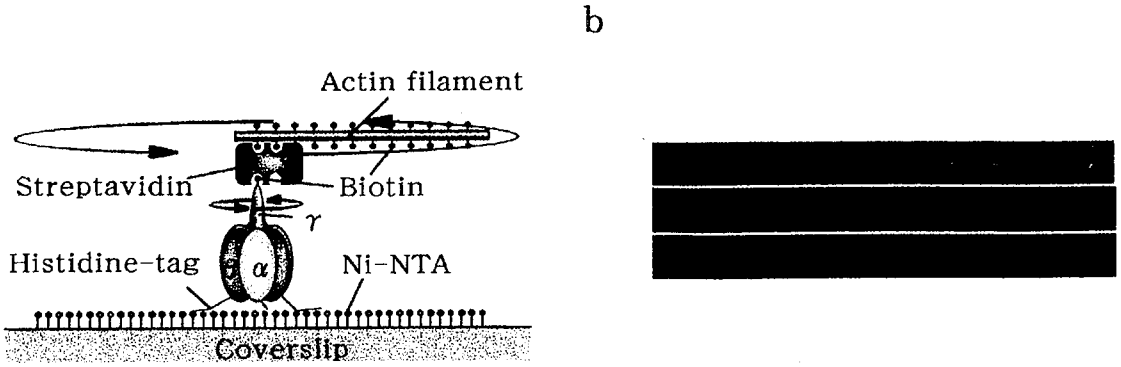

Figure 2: Visualization of the F_1 rotation. **a**: The system to visualize the rotation of F_1. **b**: Successive images of the actin filament attached to F_1. Intervals between frames = 133 ms, actin length = 2.6 μm, rotation speed = $\sim$ 0.5 r.p.s.

The structure of the ATP synthase is illustrated in figure 1a. The membrane-embedded portion is called F_o, and the portion protruding from the membrane is called F_1. When protons flow through the F_o, three β subunits of F_1 catalyzes ATP synthesis. The ATP synthase is a completely reversible protein machine. In the reverse reaction, F_1 hydrolyzes ATP to pump protons through F_o. Isolated F_1 only catalyzes ATP hydrolysis.

In the early 1980s, P. Boyer proposed that the γ subunit rotates during catalysis from kinetic analyses [1, 2]. His rotation hypothesis predicts that the rotation of the γ couples the proton flow through F_o with ATP hydrolysis/synthesis in F_1. Thus, F_o is a rotary motor driven by proton flow, F_1 is another rotary motor driven by ATP hydrolysis, and γ is their common shaft. This hypothesis gained a support from the crystal structure of F_1, in which a central γ subunit is surrounded by three α subunits and three catalytic β subunits [3] (figure 1b). Crosslinking [4] and spectroscopic [5] experiments also suggested a large movement, but not necessarily continuous rotation, of the γ subunit. To prove the rotation hypothesis, evidence for the unidirectional rotation had been awaited.

2. Visualization of the F_1 rotation

The rotation of the γ subunit with $\sim$ 2 nm diameter inside the ATP synthase with $\sim$ 10 nm diameter cannot be resolved under an optical microscope. We developed a novel system to visualize the rotation of an isolated F_1 (figure 2a) [6]. To fix an F_1 molecule on a coverslip, histidine-tags were attached to three βs, and the coverslip was coated with Ni^{2+}-nitrilotriacetic acid (Ni-NTA). Because of the high affinity between histidines and Ni^{2+}, $\alpha_3\beta_3$ cylinder would be fixed on the coverslip with the orientation described in figure 2a. The γ and a fluorescently labeled actin filament were biotinylated and linked via streptavidin.

Actin filaments with lengths of 1 - 4 μm were seen to rotate unidirectionaly under a fluorescence microscope in the presence of ATP (figure 2b). The rotation speed ranged between 0.1 - 5 r.p.s. at 2 mM [ATP], depending on the length of the actin : shorter actin rotated faster.

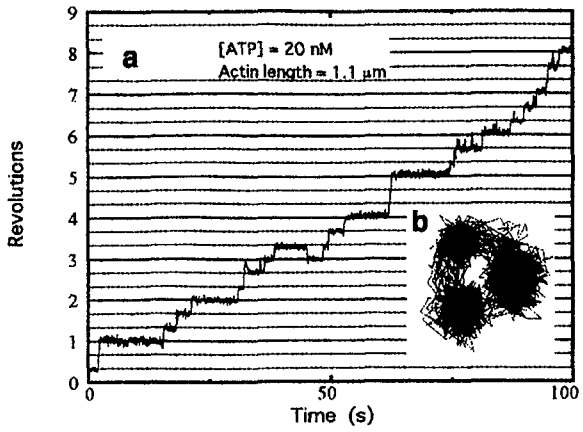

Figure 3: Time course of the stepwise rotation of an actin filament attached to F_1 at 20 nM ATP [7] . **a:** The stepwise rotation. **b:** The trace of the center of the actin filament. The actin paused at three angles.

3. F_1 rotates with 120° steps

Coupling between the mechanical event and the ATP hydrolysis is an important factor for understanding of the rotation mechanism of F_1. To investigate the coupling, we reduced [ATP] to detect a single mechanical event at the moment of an ATP hydrolysis [7]. At low [ATP] (< 0.6 μM), the actin rotation is resolved into 120° steps with occasional backward steps (figure 3), in contrast with the smooth rotation at high [ATP] ($\sim$ mM). The three stepped rotation is consistent with the three fold symmetrical structure of F_1.

To clarify whether a single step corresponds to one cycle of ATP hydrolysis, the rate of the rotation of short filaments (0.7-1.2 μm) was compared with the rate of ATP hydrolysis at various [ATP] (figure 4a). At low [ATP] where we observed the stepwise rotation (< 0.6 μM), the rotation rate was similar to one third of the rate of ATP hydrolysis, consistent with the model that one ATP makes one 120° step. On the other hand, at higher [ATP], the rotation was saturated around $\sim$ 5 r.p.s., while one third of the rate of ATP hydrolysis increased to $\sim$ 100 r.p.s. This apparanet discrepancy is presumably due to the high viscous load imposed on the actin.

The coupling between the step and the ATP hydrolysis was also investigated through statistical analysis of the dwell time between two steps (Figure 4b). If only one ATP is consumed in a single step, the histogram of the dwell time will decay with a single exponential manner (solid line in figure 4b). If more than one ATP were consumed, the histogram would have a peak, because the probability that two ATPs arrive at the protein in a short dwell time would be low (dashed line in figure 4b [8]). The data (open circles) show a single exponential decay, thus, only one ATP is consumed in a single step at least at low [ATP].

a

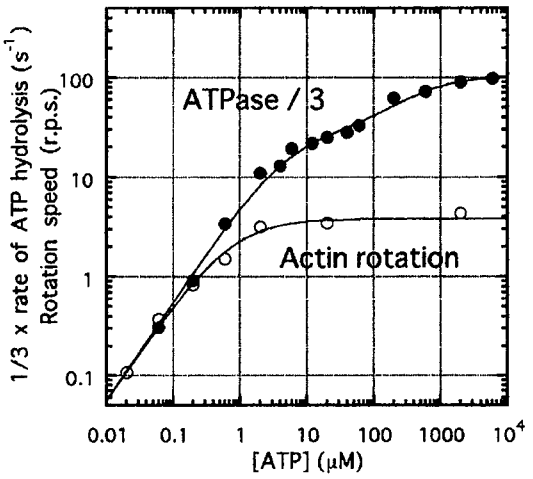

b

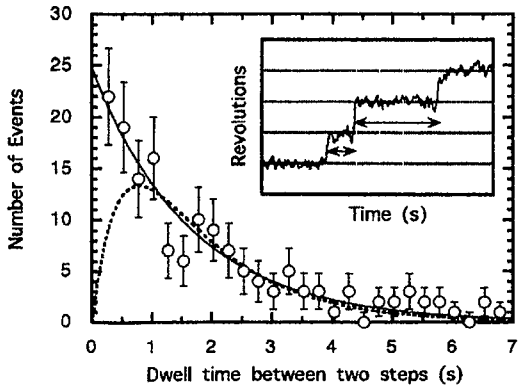

Figure 4: **a:** Relationship between one third of the rate of ATP hydrolysis (filled circles) and the rotation speed of actin filaments with 0.7-1.2 μm length (open circles). **b:** Histogram of dwell times between two steps. Inset: definition of the dwell time.

4. Thermodynamic efficiency

In the system described above, F_1 rotated against the high viscous friction imposed on the actin filament. Thus, longer actin filaments rotated slower at a saturating [ATP] (open circles in figure 5).

The torque required to rotate an actin filament is calculated as $T = \xi \cdot \omega$, where ω is the rotation velocity in radians/s and ξ is the frictional coefficient. The actin filament is approximated by a rod with length L and diameter D = 10 nm, thus, $\xi = 4\pi\eta L^3/[3 \cdot (\ln(L/D) - 0.447)]$ where η (viscosity of the solution) = 1×10^{-3} Pa·s [9]. Theoretical curves in figure 5 (solid and dashed lines) give the torque produced by F_1 as ~40 pN·nm. If a single ATP molecule makes one 120° ($2\pi/3$ radian) step at high [ATP], the work W done by F_1 in a single ATP turn over can be obtained as $W = T \cdot 2\pi/3 \sim 80$ pN·nm. This value is close to the free energy of ATP hydrolysis in cells, thus, the thermodynamic efficiency of F_1 is estimated to be close to 100 %.

To estimate the thermodynamic efficiency more directly, the work done in a single step at low [ATP] was measured. Closed circles in figure 5 show the rotation speed at moments of forward steps. The torque produced in a step is also estimated as ~ 40 pN·nm, and thus, the work done in a single step, or in a single ATP hydrolysis, is estimated as ~ 80 pN·nm, suggesting 100 % thermodynamic efficiency.

Surprisingly, the work done in backward steps (open squares in Figure 5) is similar to that in forward steps. Because the work is 20 times as large as the thermal energy (4 pN·nm), backward steps cannot be caused by thermal fluctuation, suggesting at least one ATP is consumed in a backward step.

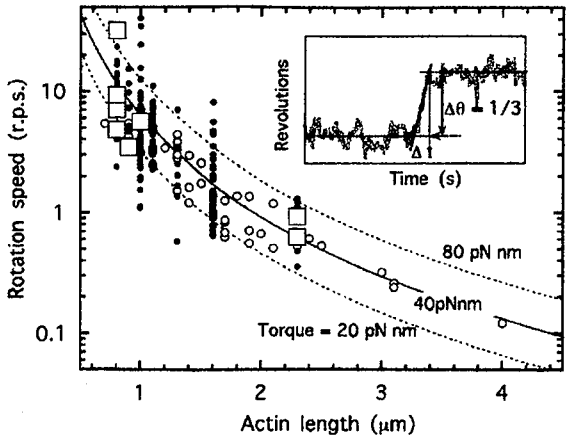

Figure 5: Relationship between the rotation speed and length of actin filaments. Open circles show the rotation speed at high [ATP] (2 mM). Filled circles and open squares show the rotation speed in forward steps and backward steps, respectively. Inset: Velocity in a step, v, was measured as $v = \Delta\theta/\Delta t$.

5. Detection of rapid rotation

At high [ATP], the rotation speed of the actin was lower than 1/3 of the ATP hydrolysis rate and the rotation was smooth rather than stepwise. The high viscous load imposed on the actin may have prevent rapid rotation and blurred stepwise movement. To reduce the viscous friction, we attached to the γ a smaller marker, an aggregate of nano-beads (40 nm ϕ), instead of the actin filament. The viscous friction against the marker was estimated to be $\sim 10^{-2} - 10^{-3}$ times that against 1 μm actin. The bead rotation could be observed under a laser dark field microscope using a fast framing CCD. At 2 mM [ATP], the rotation speed of the beads reached $\sim$ 100 r.p.s., the value much higher than that of actin filaments ($0.1 - 5$ r.p.s.) and close to one third of the rate of ATP hydrolysis ($1/3 \times 300\,s^{-1}$). Three stepped rotation was observed at this [ATP], showing that a single ATP turnover produces a single 120° step at high [ATP] as well as low [ATP].

6. Conclusions

By attaching a large marker to a small protein molecule, we have shown the rotation of F_1 and measured rotation features such as the size of the single mechanical event, torque and thermodynamic efficiency. Because a large marker can magnify small angular reorientation of a protein, it would allow us to visualize directly the mechanical processes of proteins. Thus, this method would be a powerful tool to understand how protein machines work.

References

[1] Boyer, P.D. 1993 *Biochim. Biophys. Acta* **1140**, 215-250.

[2] Boyer, P.D. 1997 *Annu. Rev. Biochem.* **66**, 717-749.

[3] Abrahams, J.P., Leslie, A.G.W., Lutter, R. and Walker, J.E. 1994 *Nature* **370** 621-628.

[4] Duncun, T.M., Bulygin, V.V., Zhou, Y., Hutcheon, M.L. and Cross, R.L. 1995 *Proc. Natl. Acad. Sci. USA* **92**, 10964-10968.

[5] Sabbert, D., Engelbrecht, S. and Junge, W. 1996 *Nature* **386**, 299-302.

[6] Noji, H., Yasuda, R., Yoshida, M., and Kinosita, K., Jr. 1997 *Nature* **386**, 299-302.

[7] Yasuda, R., Noji, H., Kinosita, K., Jr. and Yoshida, M. 1998 *Cell* **93**, 1117-1124.

[8] Higuchi, H., Muto, E., Inoue, Y. and Yanagida, T. 1997 *Proc. Natl. Acad. Sci. USA* **94** 4395-4400.

[9] Jefrey, D.J. and Onishi, Y. 1981 *Quant. J. Mecha. Appl. Math* **34**, 129-137.

[10] Elston, T., Wang, H. and Oster, G. 1998 *Nature* **391**, 510-513.

第3章

4 私の生物物理学

―― 生物物理はHowの世界

木下一彦

私は，今から30年ほど前に大学を卒業する間近まで，生物学が大っ嫌いだった。その当時の生物学は，雄しべが何本，花びら何枚というたぐいで，単なる記憶の学問だったのである。物理学科にいた私に生物への目を開かせたのは，一枚の電顕写真であった(図1)。筋収縮の滑り説の根拠となった写真である。太い線維と細い線維が互いに入

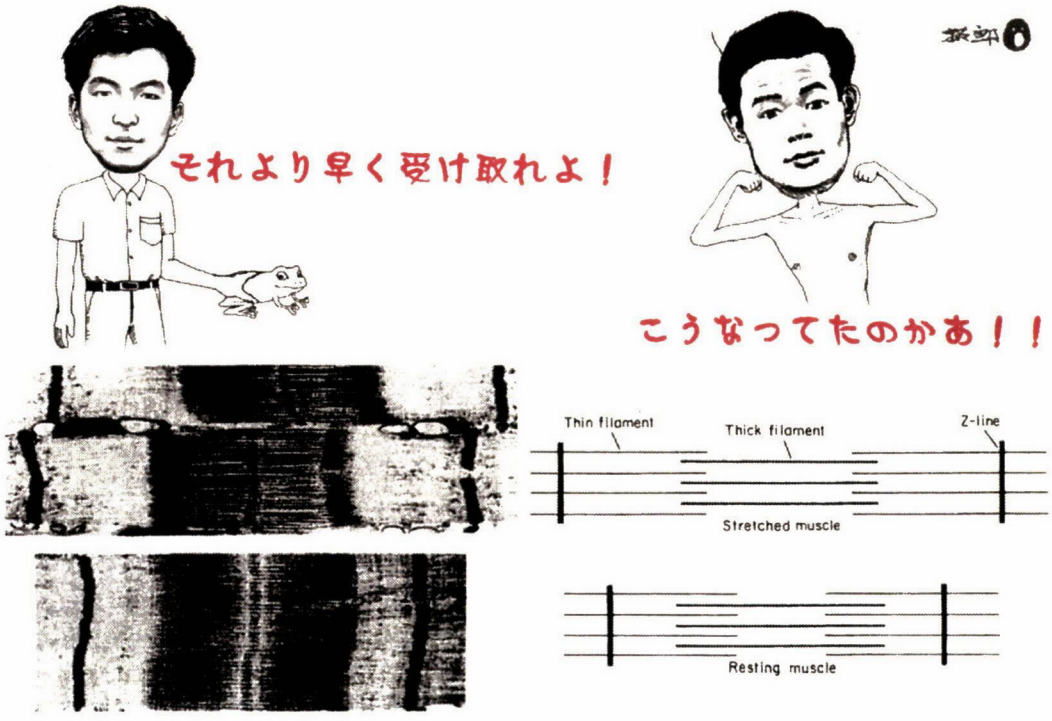

図1　筋収縮の滑り説

左下が電子顕微鏡写真(H. E. Huxley による)，その右は説明図。筋肉の中には太い線維(ミオシン分子よりなる thick filament) と細い線維 (アクチン分子よりなる thin filament) がある。筋肉の収縮は，両線維がそれぞれの長さを変えることなく，互いの間に滑り込むことにより起きる。収縮前 (上) と収縮後 (下) の電子顕微鏡写真を比べると，太い線維の長さが変わらないことがよくわかる。

れ子になっており，互いの間に滑り込むことにより筋肉が収縮する。はーぁなるほど，そうなってるのかぁ。初めて，生き物の世界にも“説明”があると認識した。しかも一目でわかるという明快さである。私には考えつけそうもない説明である。

もっとも，その場で納得してしまったのはその頃の私がシロウトだったからで，今だったらそう簡単に信じない。話がそれるが，信じるというのは宗教行為で，科学者が何かを信じているというときは，きちんとした根拠が示せません，ということの告白にすぎないと，信じている。同様に，「これは真実です」と心の底から言う人がいたら，その人は真の科学者ではないと思う。

ところで，図1の電顕写真を紹介してくれたのは，その上に写っている同級のI氏で，今でも公私ともに親しくさせてもらっている。大学祭で，蛙の筋肉を使った実験をしよう，と誘ってくれたのである。私は蛙をさわることができないのだが（ウサギなら持てる），私が実験の道に進むことになったのは，この時の数週間の高揚による。I氏が蛙を解剖し，私が測定装置らしきものの一部を作った。この役割分担は，その後数十年にわたり固定されてしまった。I氏がいなかったら，私が生物物理の世界に入ることはなかったであろう。

ひるがえってみると，若い頃物理学に惹かれたのは，単純かつ万能な説明に圧倒されたからである。大学に入ってみると，単純ではすまないことを思い知らされた。そこで生物に逃げたわけだが，悪い選択ではなかったと思う。生物物理学における私の初心は，自分でも説明をしたい，というところにあったわけである。残念ながら，この初心は，自分が実験をしている間は貫けなかった。

実験をしていると，あれこれ小さな工夫ができるし，たいした意味はなくてもデータが出てくるから，いくら続けても飽きることがなかった。これがくせ者で，説明が目的であることを忘れてしまったのである。いや，時には考えるのだが，自分の実験能力の範囲ではとても確かめようもなく，空想に終わっていた。自分の力の範囲内でできることはきちんとしたデータを出すこと，もしかしたらそれを誰かが使

ってくれるかもしれない，という態度に終始した。なんのことはない，もっとも嫌っていた記述の学問の，隅の隅に棲息することになったのである。

学生さんに来ていただける身分となり，同時に，実験をすると息切れがする年になってしまった。くやしいけれど，何をやっても学生さんのほうが上手という事態になってしまった。すると，説明のための実験を，学生さんにお願いすればよいのだということがわかった。しかも他人には，力の範囲をはるかに超えていそうなことでも，平気で頼めるのである。だませば不可能も可能になることを教えてくれたのは，Y氏である。だますというのはけしからん表現だと叱る人がいるのでお断りしておくが，彼に直接言われたわけではない。彼の所の学生さんがとんでもない快挙を成し遂げたのを見て，勝手に教わった。自分で自分をだますのは難しい。若い人には，うまくだまされなさいよ，できるかもしれないと信じなさい，と話すことにしている。

他人様が，タンパク質の分子たった1個でできた回転モーターが存在することを，光学顕微鏡の下で見せてくれた。モーターの回転軸と

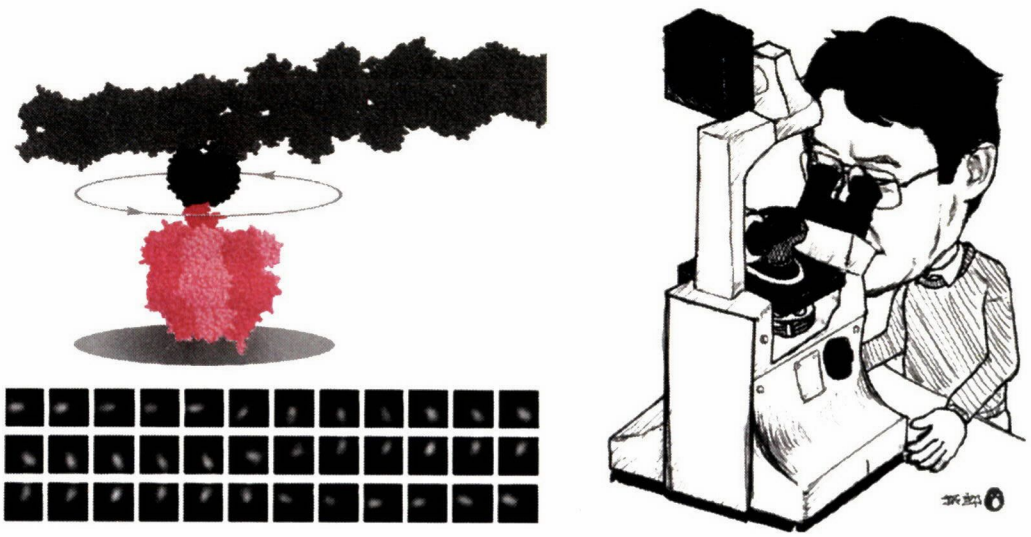

図 2　タンパク質一分子でできた回転モーターF_1-ATPase（赤）
上中央の赤いモーター分子の中で，一番濃い赤の部分が回転する。それを証明するため，アクチン線維（上部の横向きの長い棒；右端が切れているが実際の長さは図に示されている部分の百倍くらい）を目印として付けた。下の連続写真に見られるように，顕微鏡下でアクチン線維は120度おきに回転し，F_1-ATPaseはステッパーモーターであることがわかった。我々の体の中では，このモーターが逆回転することにより，エネルギーの素であるATPを合成している。

目されるサブユニットに，長い棒を付けてみたところ，目の前で棒が回るのが見えたのである（図2）。あまりに見事な回転ぶりだったので，一目で，これはほとんど真実であろうと直感した。この実験を自分でやっていたらどんなによかっただろう。くやしいからこのモーターの実験には手を出さない。図2の漫画は嘘である。

身近な他人様たちにお願いして，このモーターの回転の機構を説明してもらいたいと思っている。それだけでなく，いろいろな分子機械の働く仕掛けを，片端から説明できるようにして欲しい。分子機械は，体を曲げたり伸ばしたり捻ったり，構造変化をすることにより働くのだと思っている。構造変化の原因でもあり結果でもあるのが，他の分子（ATPのような低分子や別のタンパク質分子）との結合・解離，場合によると光や電位などである。具体的にはこうなんだよ，と動画を使って説明したい。

いろいろな生物研究者と話してみて，私の求めている「説明」は，常にHowであることに気づく。一方，多くの研究者の求めているのは，Who does Whatである。私に言わせれば，次々と名前を付けることである。いわく，目の中で光を吸収するのはRhodopsin，Rhodopsinが光子を1個吸収したという信号はTransducinに伝わり，それがPhosphodiesteraseを活性化し，……。生き物の働きを支えているのがどのような役者なのか，役者を捜し出して名前を付け（確かに存在し他と区別できるという主張），その役割を一言で表す。もしかして雄しべが何本の記述の学問に戻ったという印象をもたれるかもしれないが，全く違う。役者の同定は，立派な説明になっている。

だけれどしかし，である。私は，役者一人一人が一体どう振る舞うのか，その力の素はどのように得られるのか，突き詰めてみたい。配役リストだけではとても満足できないのである。生物物理屋の多くは私と同じらしい。講演を聴くとき，名前（しかも多くの場合アルファベットの略号）がたくさん出てくると退屈するのが生物物理屋，たくさん出ないと退屈するのが細胞生物学者，という分類になる。細胞生

物学者の前で回転モータータンパク質がどう働くか一時間も話すと，飽きられる。

分子1個でできた役者の振る舞いを理解するには，やはり分子1個を見ないといけない。熱運動にさらされて働く分子たちだから，その動きは確率的で，全員一緒に調子を合わせることはあり得ないのである。あなたがタンパク質分子だとすると，水分子はパチンコ玉くらい。その熱運動の速度は時速1000 km，ジャンボジェットなみである。この速度で雨あられと降り注ぐパチンコ玉の中でのタンパク質分子機械の働きを，一言で記述するだけではかわいそうである。何とかしてよく観察してあげないといけない。

私たちは，もっぱら光学顕微鏡を使って観察している。電子顕微鏡ほどの分解能はないが，同じ分子を連続して，動画として観察できるのが強みである。図2のように，分子機械は自分の何百倍もある大きな目印を付けられてもちゃんと働く。分子機械よりずっと小さな蛍光色素分子1個を付ければ，細かい構造変化を捉えることもできる。大小の目印を使い分け，さらに“光ピンセット”や“磁気ピンセット”などによる分子操作も駆使して，“1分子生理学”をやりたいと思っている。

さて，ここまで話を引っ張ってきたのは，ページをめくってから図3を見て欲しかったからである。筋収縮の滑り説は受け入れられたとして，ミオシンがアクチンに対して滑る，その仕掛けがまだよくわからない。しかし図3を見ると，2本足を順に使って，着地した足を前方に折り曲げることにより前進するという，人間が歩くような動作をしているように思える。今年（2000）『*Nature*』にこの写真が発表されたとき，30年前にHuxleyの電顕写真を見て以来の衝撃を受けた。今回は予備知識があり，「やっぱりこうだったか」，なのではあるが，論文を読まずとも写真だけで「うーん」とうなった。もちろん，私も今やプロの科学者ですから，歩行説を100％信じているわけではないですよ。

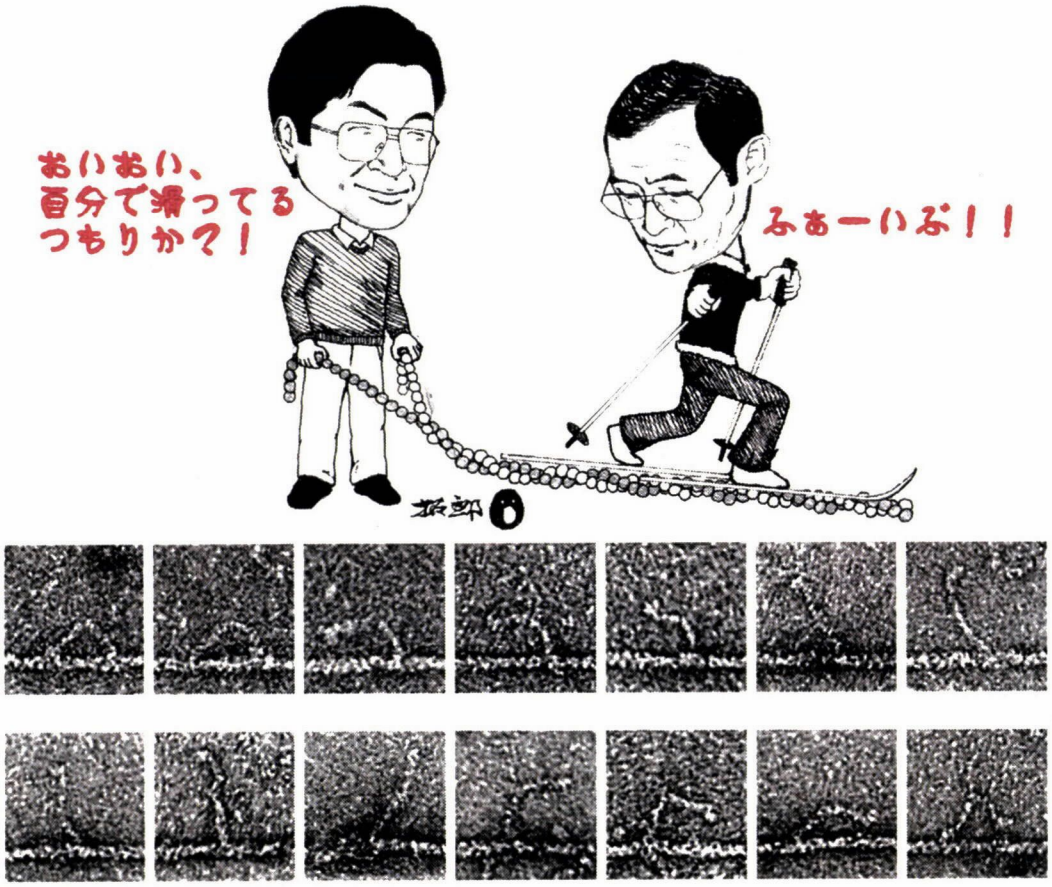

図 3　ミオシンの一種であるミオシン V（ファイブ）が，2 本足を振り回しながらアクチン線維の上を“歩く”かのように見える電子顕微鏡写真（P. J. Knight らによる）

連続写真ではなく，適当に選んだ写真をそれらしく並べたもの。2 番目の写真など，2 本の足が前方に折れ曲がり，スキーのテレマーク姿勢のように見える。真珠のネックレスをひねったようならせん構造をもつアクチン線維は，単なる足場ではなく，アクチンが主役となってミオシンを動かすのだという説もないわけではない。

後　記

この原稿は，2000 年 11 月に書き上げたものである。出版に際し，編者から，細胞・器官・個体の世界にどうアプローチするか，一言述べよとのお達しをいただいた。実は，細胞までは手を出したことがある。しかし，非才の身で How を考えてみても，結局はアカの他人により新たな役者が見つかってチョンであった。最近は事情が少し違ってきて，自分の後方にアクチンを重合しながらそれを推進力にして前進するバクテリアなど，少数の役者が“いかに”ふるまうかが説明の鍵である例も増えてきた。今一番印象が強いのは，細胞が誘引物質に向かって運動するとき，ある役者は細胞膜の誘引物質に近い側に整列

し，別の役者は反対側に揃い，という見事な映像である。細胞の世界も，Who と What だけではなくなってきたんだな，とちょっとほっとする。その上の世界は私にはわからない。ヒトの脳を理解できるとしたら，超天才が必要だろうなぁ，とひとごとのように思う。